Sustainable recovery and advanced use of nanostructured cellulose from agri-food residues

Annachiara Pirozzi

UNIVERSITY OF SALERNO

DEPARTMENT OF INDUSTRIAL ENGINEERING

Ph.D. Course in Industrial Engineering
Curriculum in Chemical Engineering - XXXV Cycle

SUSTAINABLE RECOVERY AND ADVANCED USE OF NANOSTRUCTURED CELLULOSE FROM AGRI-FOOD RESIDUES

Supervisor   **Ph.D. student**
Prof. Francesco Donsì   *Annachiara Pirozzi*

Scientific Referees
Prof. Giovanna Ferrari
Dott. Gennaro Gentile
Prof. Luis Serrano Cantador

Ph.D. Course Coordinator
Prof. Francesco Donsì

Acknowledges

I would like to warmly thank my supervisor, Prof. Francesco Donsì, for giving me the opportunity to work within the frame of Panacea project and for providing invaluable guidance and direction throughout my Ph.D. program. His extensive experience, knowledge, and high standards have played a pivotal role in shaping me into a better researcher. I am truly grateful for his continuous support and for pushing me to overcome the challenges that I encountered along the way.

I would also like to extend my sincere thanks to the scientific members of my thesis advisory and exam committee, particularly Prof. Giovanna Ferrari, for her unwavering support and guidance throughout my academic journey, from my Bachelor's degree to the Ph.D. program.

Prof. Pataro, Dr. Roberta Ferrari, and all my colleagues have supported me throughout these three years in ProdAl Scarl.; I am also grateful to them.

It was a great delight to have been at the University of Córdoba during the pre-doctoral visiting research activity. Special thanks must go to Luis, Esther, Edoardo, and all the people I had the pleasure of collaborating with for their hospitality and for the support received.

Futhermore, I thank with love to my whole family, representing for me precious support and encouragement. In particular, I want to express my deepest appreciation my husband, helping me navigate and overcome the challenges I faced during this demanding path in the most positive way. His unwavering belief in my abilities has been invaluable, and I am truly grateful for his presence in my life. Thank you for always being by my side.

Finally, I thank myself, my own perseverance and dedication. I am proud of the hard work and effort I have put into my research, and I am grateful to myself for the determination to succeed.

List of Contributions

Pubblications on international peer reviewed journals

Caiyun Liu, **Annachiara Pirozzi**, Giovanna Ferrari, Eugene Vorobiev, Nabil Grimi (2020). Effects of pulsed electric fields on vacuum drying and quality characteristics of dried carrot, *Food and Bioprocess Technology*, 13:45-52. doi:10.1007/s11947-019-02364-1.

Caiyun Liu, **Annachiara Pirozzi**, Giovanna Ferrari, Eugene Vorobiev, Nabil Grimi (2020). Impact of pulsed electric fields on vacuum drying kinetics and physicochemical properties of carrot, *Food Research International*, 137:109658. doi:10.1016/j.foodres.2020.109658.

Annachiara Pirozzi, Gianpiero Pataro, Francesco Donsì, Giovanna Ferrari (2020). Edible coating and pulsed light to increase the shelf life of food products, *Food Engineering Reviews*, 13, 544-569. doi:10.1007/s12393-020-09245-w.

Annachiara Pirozzi, Vittoria Del Grosso, Giovanna Ferrari, Francesco Donsì (2020). Edible coatings containing oregano essential oil nanoemulsion for improving postharvest quality and shelf life of tomatoes, *Foods*, 9, 1605. doi:10.3390/foods9111605.

Annachiara Pirozzi, Vittoria Del Grosso, Giovanna Ferrari, Francesco Donsì (2021). Combination of edible coatings containing oregano essential oil nanoemulsion and pulsed light treatments for improving the shelf life of tomatoes, *Chemical Engineering Transactions*, 87. doi:10.3303/CET2187011.

Annachiara Pirozzi, Roberta Capuano, Roberto Avolio, Gennaro Gentile, Giovanna Ferrari, Francesco Donsì (2021). O/W Pickering Emulsions Stabilized with Cellulose Nanofibrils Produced through Different Mechanical Treatments, *Foods*, 10, 1886. doi:10.3390/foods10081886.

Annachiara Pirozzi, Giovanna Ferrari, Francesco Donsì (2021). The Use of Nanocellulose in Edible Coatings for the Preservation of Perishable Fruits and Vegetables, *Coatings*, 11, 190. doi:10.3390/coatings11080990.

Annachiara Pirozzi, Giovanna Ferrari, Francesco Donsì (2022). Cellulose Isolation from Tomato Pomace Pretreated by High-Pressure Homogenization, *Foods*, 11, 266. doi:10.3390/foods11030266.

Linda Gali, **Annachiara Pirozzi**, Francesco Donsì (2023). Biopolymer- and lipid-based carriers for the delivery of plant-based ingredients. *Pharmaceutics*, 15, 927. doi:10.3390/pharmaceutics15030927.

Annachiara Pirozzi, Esther Rincón Rubio, Francesco Donsì, Luis Serrano, Eduardo Espinosa Víctor (2023). Nanoncellulose-based aerogels for dyes removal, *Chemical Engineering Transactions,* Under review.

Annachiara Pirozzi, Giovanna Pappalardo, Francesco Donsì (2023). Recovery of nanocellulose from agri-food residues trough chemical and physical processes, *Chemical Engineering Transactions,* Under review.

Annachiara Pirozzi, Francesco Donsì (2023). Structuring vegetable oils through the formation of capillary suspensions: comparison of wheat middlings and pure cellulose processed by high-pressure homogenization, *Chemical Engineering Transactions,* Under review.

Annachiara Pirozzi, Esther Rincón Rubio, Francesco Donsì, Eduardo Espinosa Víctor, Luis Serrano (2023). Quality index of nanostructured cellulose from barley straw by-product in aerogel materials as efficient dye removal systems, Under submission.

Annachiara Pirozzi, Paolo Bettotti, Giovanna Ferrari, Tiziano Facchinelli, Elvira D'Amato, Marina Scarpa, Francesco Donsì (2023). Oil-in-water Pickering emulsions stabilized by nanostructured cellulose: comparison of cellulose nanocrystals and nanofibrils, Under submission.

Annachiara Pirozzi, Alfredo Posocco, Giovanna Ferrari, Francesco Donsì (2023). Oil structuring through capillary suspension prepared with wheat middlings agri-food residues, Under review.

Pubblications on international peer reviewed journals

Annachiara Pirozzi, Vittoria Del Grosso, Giovanna Ferrari, Gianpiero Pataro, Francesco Donsì (2021). Combination of edible coatings containing oregano essential oil nanoemulsion and pulsed light treatments for improving the shelf life of tomatoes. Proceeding of the 3rd *International Conference on Engineering Future Food* (Virtually participation 23-26.05.2021).

Annachiara Pirozzi, Giovanna Ferrari, Francesco Donsì (2021). Mechanical cell disruption of agri-food residues through high-pressure homogenization as a green approach for the isolation of cellulose nanofibrils. Proceeding of the 35th *International Conference: Healthy Individuals, Resilient Communities, and Global Food Security* (SwissTech Convention Center of Lausanne, Swizerland 01-04.11.2021).

Annachiara Pirozzi, Alfredo Posocco, Giovanna Ferrari, Francesco Donsì (2022). Capillary suspensions for oil structuring with agri-food residues micronized via high-pressure homogenization in oil. Proceeding of the *36th International Conference: Healthy Individuals, Resilient Communities, and Global Food Security* (Aviva Stadium, Dublin, Ireland 07-09.11.2022).

Annachiara Pirozzi, Paolo Bettotti, Giovanna Ferrari, Tiziano Facchinelli, Elvira D'Amato, Marina Scarpa, Francesco Donsì (2022). Nanostructured cellulose particles for O/W Pickering emulsions stabilization. Proceeding of the *36th International Conference: Healthy Individuals, Resilient Communities, and Global Food Security* (Aviva Stadium, Dublin, Ireland 07-09.11.2022).

Annachiara Pirozzi, Silvia Bianco, Emanuela Maresca, Martina Aulitto, Giovanna Ferrari, Patrizia Contursi, Francesco Donsì (2022). Active edible coatings reinforced with micronized bacterial cellulose. Proceeding of the *4th International Congress on Technological Innovation in the Packaging Industry: Advances in the Packaging Industry* (Museo Donnaregina, Naples, Italy 24-25.11.2022).

Annachiara Pirozzi (2023). Sustainable recovery and advanced use of nanostructured cellulose from agri-food residues. Proceeding of the *16th European PhD Workshop on Food Engineering and Technology* (University of Copenhagen, Copenhagen, Denmark 9-10.05.2023). To do.

Annachiara Pirozzi, Esther Rincón Rubio, Francesco Donsì, Luis Serrano, Eduardo Espinosa Víctor (2023). Nanocellulose-based aerogels for dyes removal. Proceeding of the *5th International Conference on Nano Technology Based Innovative Applications For The Environment* (Fondazione Querini Stampalia, Venice, Italy 25-28.06.2023). To do.

Annachiara Pirozzi, Giovanna Pappalardo, Francesco Donsì (2023). Recovery of nanocellulose from agri-food residues trough chemical and physical processes. Proceeding of the *4th International Conference on Engineering Future Food* (Grand Hotel Baglioni, Florence, Italy 20-22.09.2023). To do.

Annachiara Pirozzi, Francesco Donsì (2023). Structuring vegetable oils through the formation of capillary suspensions: comparison of wheat middlings and pure cellulose processed by high-pressure homogenization. Proceeding of the *4th International Conference on Engineering Future Food* (Grand Hotel Baglioni, Florence, Italy 20-22.09.2023). To do.

Contents

VIII

Lists of figures

XIII

XVI

XVIII

Lists of tables

XX

Abstract

In recent years, there has been a growing interest in the development of sustainable alternative materials due to the environmental impacts related to the high disposal of fossil oil-based products. In this regard, cellulose is a key constituent and an attractive feedstock as one of the most abundant, cost effective, renewable, and biodegradable biopolymers in nature. Cellulose is characterized by noteworthy structure and properties due to its unique molecular structure, consisting of a highly ordered polymer of cellobiose unbranched chains of β-1, 4-linked glucose units, which act as a framework for the three-dimensional polysaccharide structure. The promising chemical (such as hydrophilicity, chirality, degradability, and broad chemical variability) and mechanical (non-toxic, biocompatible, renewable, and biodegradable) properties of cellulose have aroused increasing interest as building blocks for the development of new biomaterials, especially through advanced nanotechnology tools, which enables further promotion of its techno-functional attributes. Nevertheless nowadays, cellulose is isolated from wood sources, and as structural plant component is much more difficult to deconstruct. Indeed, its innate close polymeric alignment and its intimate relationship with other lignocellulosic components such as hemicellulose and lignin limit the accessibility to cellulose. A delignification process with effective harsh acid or alkaline chemical hydrolysis treatment to split cellulose and hemicelluloses from lignin is a crucial step and undoubtedly the most challenging. However, these current methods are expensive and energy consuming and utilize chemicals which entail special disposal, handling or production procedures. Taking into account environmental sustainability, it is counterproductive to combine energy-severe, wasteful processes on wood sources.

In the context explained above, the works carried out during this Ph.D. thesis have demonstrated that the process required to enhance cellulose accessibility and recovery is strongly influenced by the nature of the native biomass. Consequently, agri-food residues/by-products (AFRs) represent a new and promising feedstock for the development of new sustainable processes to isolate cellulose established on nonconventional technologies with low environmental and economic impacts and high efficiency,

emphasizing the stringent need to also diversify and valorize the biobased waste with circular economy strategies. In this context, high-pressure homogenization (HPH), nonthermal and purely physical treatment, is here exploited for the first time to increase the efficiency of mild chemical hydrolysis processing for isolation of cellulose from agri-food residues (increasing the cumulative yield extraction of about 20%), while leading to a drastic reduction in the use of chemicals, shortening the processing times by process intensification, enhancing purity, inducing a defibrillated cellulose structure, are enabling the concurrent recovery of high-value-added bioactive compounds with high antioxidant capacity in the side streams. Moreover, the fluid-mechanical stresses (high shear, elongation, turbulence and hydrodynamic cavitation) occurring during the HPH treatment, in combination with mild hydrolysis, improved the cellulose defibrillation and contributed to trimming down the length of the fibers. The comprehensive utilization of AFRs feedstocks has attracted considerable interest also for the development of new sustainable processes established on bottom-up green constructing strategy. The work was undertaken for the recovery of the biofilm by-product derived from Kombucha tea fermentation process using micronized AFRs as carbon source in alternative to the conventional synthetic media to decrease the culture media costs and enhance the yield production, to obtain nanostructured cellulose with remarkable biological and physico-mechanical properties. These isolation routes allowed the achievement of cellulose pulp with tailored morphological properties from underused AFRs feedstocks or by-products of fermentation processes (evaluated through light scattering for particle size distribution, optical and scanning electron microscopy, and FT-IR analysis), decreasing the severity of conventional chemical processes and increasing the exploitation of low-cost industrial by-products. From the overall results collected in this section, the efficient cellulose extraction has been accomplished along with the valorization of the value-added compounds still contained in the AFRs biomass.

To further improve the financial performance and sustainability of biomass biorefineries, to develop more sustainable materials, and thanks to the hierarchical structure of cellulose, the top-down processes have been employed enabling the isolation of nanocellulose (NCs) into cellulose nanocrystals (CNCs) or cellulose nanofibrils (CNFs), depending on the treatment carried out and operating processing conditions. NCs can be successfully obtained from AFRs isolated cellulose fiber through mechanical (ball milling and HPH) and TEMPO [(2,2,6,6-tetramethylpiperidin-1-yl) oxy radical]-mediated oxidation processes or a combination of these methods. A systematic characterization of the structural properties of the nanomaterials obtained after each process revealed that different treatments allowed to extract the cellulose nanoparticles with different morphological and physical properties. Therefore, these findings demonstrated that NCs could be successfully extracted from AFRs cellulose pulp, offering a sustainable

alternative to conventional chemical procedures on wood sources, and changing the process and/or its operating conditions it is possible to tune the properties of nanoparticles, according to the desired end product and application.

The final part of present study reported the feasibility of using NCs in different innovative applications such as (i) Pickering emulsion stabilizer, (ii) oil-structuring through capillary suspensions, (iii) decontamination systems of dyes from wastewater, (iv) reinforcement in edible coatings, and (v) network structure to capture CO_2 via covalent bonding.

In summary:

i. The morphological structure of mechanically pre-treated NCs exhibited high mobility and flexibility at the oil-water interface, resulting in an efficient emulsifying ability at different environmental stimuli, with the fibrils wrapping around the oil droplets for their stabilization. Remarkably, the high defibrillation degree of NCs obtained via HPH contribute to forming an interconnected network structure of the emulsion droplets, promoting their efficient steric and electrostatic stabilization.

ii. The HPH mechanical treatment can be applied to the lignocellulosic particles directly in oil, to efficiently cause particle break-up, and, at the same time, to induce the activation of fibers, which is important in the formation of capillary bridges and a three-dimensional network, to regulate the apparent viscosity and yield stress of the capillary suspension, when water as secondary fluid is added. Therefore, oil structuring with lignocellulosic particles treated by HPH may support the development of more sustainable and health-beneficial oleogels in replacement of solid fats, enabling to reduce of the caloric content, increase the dietary fiber content, as well as exploit the recovery of valuable bioactive compounds still present in the residues. Moreover, the antioxidant compounds released in the suspension allow reducing the oxidation of sunflower oil used in the capillary suspensions due to the water addition.

iii. Low-density and high porosity NCs-based aerogels have been successfully obtained and considered promising adsorbent materials for wastewater treatment, owing to their low-cost and high adsorption capacity. Indeed, NC-based aerogels have a high adsorption capacity for methylene blue, which could be ascribed to the internal porous structure and the electrostatic interaction between NCs and cationic dye molecules. In particular, they exhibited a methylene blue capacity removal equal to or higher than 90%.

iv. An exploratory study of sodium alginate-based edible coatings reinforced with bacterial NCs on strawberries' shelf life was also conducted. The developed edible coatings contribute to prolonging the shelf life, by reducing the growth of the endogenous microbial

flora (total microbial load, yeasts, and molds) over 27 days at refrigerated conditions in comparison with the control.

v. The optimization of amination to functionalize NCs was experimentally investigated, and the aerogels synthesis was achieved by freeze-drying technology. The as-prepared aerogels show the potential for substantial adsorption of CO_2, offering new opportunities for the design of novel functional biomaterials with controlled properties.

This Ph.D. thesis demonstrates the possibility of developing and tailoring the properties of physically or chemically modified NCs by different sustainable approaches. Therefore, this thesis is aligned with the importance of circular economy with the exploitation of AFRs and developing innovative and environmentally friendly processes and (nano)materials.

Highlights

1. Mild chemical and mechanical treatments represent a promising strategy to isolate cellulose from agri-food residues and to obtain nanostructured celluloses with tailored structure (ranging from nanofibrils to nanocrystals) by simply controlling the process intensity. These tailored structures can be exploited for controlling the techno-functional properties of nanocellulose.

2. Key role of nanoparticles on the stabilization of Pickering emulsions against environmental stimuli have been demonstrated. Rational combination of nanocellulose allows designing tailor-made emulsions of interest for the food or cosmetic industry.

3. Edible oleocolloids are obtained using agri-food residues as gelator and water as the secondary fluid through a purely physical and nonthermal process. Wheat middlings particles, micronized directly in oil through high-pressure homogenization, form a 3D network sustained by capillary forces upon water addition, with the strength of the oleocolloids that could be modulated by the water phase.

4. High-quality (ligno)cellulose nanofibers from barley straw by-products could be used for the production of nanocellulose-based aerogels as efficient bio-adsorbent for dye removal from wastewater.

5. Reinforcement of edible coatings with microbial nanocellulose-contributes to enhance the coating properties, as well as to increase of shelf life and the quality of strawberries.

6. Amine-functionalized nanocellulose shows promising ability for carbon dioxide (CO_2) adsorption, which could be one of the favorable alleviation approaches for global warming.

Keywords

Agri-food residues; Bioactive compounds; Cellulose; Nanocellulose; High-pressure homogenization; Ball milling; Pickering emulsion; Oleocolloids; Capillary force; Aerogels; Wastewater treatment; Edible coating; Shelf life; Amine modification; CO_2 capture.

Chapter I
State of the art

1. Introduction

As the awareness of our impact on the planet increased, the demand for new sustainable materials has grown rapidly in recent years, as evidenced by the UN agenda 2030 [1]. One of the compounds that has the potential to be used for developing high-performance functional composite materials is the lignocellulosic biomass. Lignocellulosic biomass is the most abundant renewable biomass on Earth, with approximately 200 billion tons per year of lignocellulosic biomass supply by worldwide from the forestry residue and agricultural wastes [2-6]. Lignocellulosic biomass is composed of cellulose, hemicelluloses, and lignin, as well as other minor components. Cellulose is the most abundant renewable organic carbohydrate polymer produced in the biosphere and widely distributed in higher plants, in several marine animals, and, to a lesser degree, in algae, fungi, bacteria, invertebrates, and even amoeba [7]. Cellulose is characterized by noteworthy structure and properties due to its unique molecular structure, consisting of a long chain of highly ordered polymer of cellobiose unbranched chains of β-1, 4-linked glucose units, which act as a framework for the three-dimensional polysaccharide structure [8]. The promising chemical (such as hydrophilicity, chirality, degradability, and broad chemical variability) and mechanical (non-toxic, biocompatible, renewable, and biodegradable) properties of cellulose have aroused increasing interest as building blocks for the development of new biomaterials, especially through advanced nanotechnology tools, enabled further promotion of its techno-functional attributes [9].

In the global scenario, among the available sources of renewable feedstock for cellulose isolation, lignocellulosic biomass, including agricultural residues, stands out. In contrast, the use of the vastly available by-products and wastes, also known as agri-food residues (AFRs), is currently mainly limited to livestock feed, providing a limited added value, or landfill or energy production by combustion, causing potential environmental issues [10]. Therefore, new strategies for the exploitation of AFRs represent a great

opportunity for more sustainable routes for the recovery of high value-added compounds, as well as for mitigating their environmental burden [11].

2. Agri-food residues (AFRs) and biorefinery processes

Along the whole food supply chain, 931 million tonnes of food waste were generated in 2019, 61% of which came from households, 26% from food service, and 13% from retail. This suggests that 17% of total global food production may be wasted (11% in households, 5% in food service, and 2% in retail) [12]. Food loss and waste are a big source of greenhouse gas emissions, making them a major contributor to the three planetary crises of climate change, nature and biodiversity loss, and pollution and waste. This is why Sustainable Development Goal 12.3 aims to halve food waste and reduce food loss by 2030. In particular, the wastage of resources (food, water, and energy) is related to the production-consumption chain (Figure I.1):

- Food loss is the decrease in the quantity or quality of food discarded, incinerated, or otherwise disposed of along the production, postharvest and processing stages;
- Food waste refers to the decrease in the quantity or quality of food resulting during the retail and final consumption stages from the decisions and actions by retailers, food service providers, and consumers.
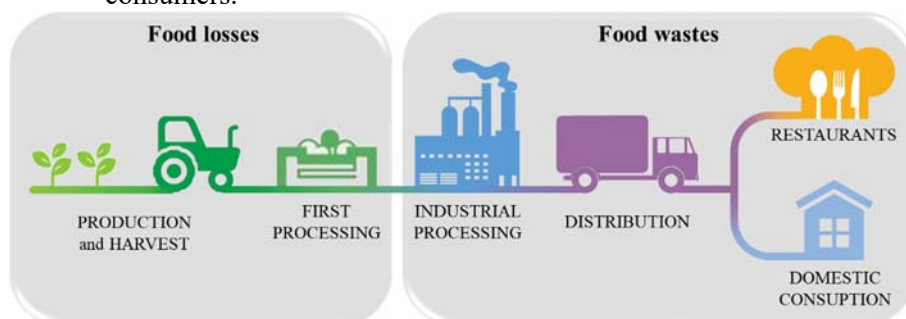
Figure I.1 *Food losses and food waste along the food supply chain.*

The agricultural industry, in collaboration with the scientific community, has directed efforts toward the design of appropriate methods for the exploitation of AFRs to extract and purify high value-added compounds [13] including dietary fiber, antioxidants, oligosaccharides, vitamins, pectin, enzymes, pigments, organic acids inter alia, of special interest for innovative applications in different fields (i.e food ingredients, nutraceuticals, cosmeceutical, bioderived fine chemicals, biofuels, etc). It is currently known that the full use of waste with functional properties could lead the food industry to decrease residues and increase its profitability [14]. Therefore, the partial (or even total) use of industrial and agricultural wastes not only is an advantage from the environmental point of view, but it could also solve some

economic issues. Indeed this leads to the minimization of residues by means of waste treatment or management and to the development of high value-added products that can provide better profits [15].

This valorization approach can be carried out together with other strategies in a multi-product biorefinery, pursuing sustainable management of the AFRs via the recovery of their main bioactive constituents [16]. The development of an integrated biorefinery based on AFRs would allow to accomplish some of the three dimensions considered on the sustainable development [17]:

- *Environmental sustainability*, through the valorization of whole residues based on the zero-waste concept;
- *Economic sustainability*, by means of manufacturing multiple high value-added products which could enter different markets;
- *Social sustainability*, since this approach would benefit different sectors by means of the creation of qualified jobs and covering the increasing demands of consumers in bio-based products.

In this scenario, the food waste biorefinery concept has gained prominence in the last years and new technologies for the valorization of food waste have been developed [18]. Phytochemicals/bioactive compounds extraction have been widely studied and tested from different fruit and vegetable processing wastes, such as those from:

- *Grape pomace* (grape skin, seeds, stems, and remaining pulp) anthocyanins, procyanidins, flavonoids, and stilbenes with important biological activities [19,20];
- *Coffee spent grounds* and *coffee silver-skin* active molecules [20-22];
- *Olive oil industry by-products* lignans, secoiridoids, and especially hydroxytyrosol endowed with anti-inflammatory and antiplatelet properties [23,24];
- *Citrus pomace* hydroxycinnamic acids and flavonoids, mainly flavanone glycosides, flavanones, and flavone aglycons [25-27];
- *Pomegranate by-products* ellagitannins punicalagin and punicalin, endowed with very high antioxidant potency [26,28,29];
- *Apple pomace* quercetin glycosides, kaempferol, catechin, procyanidins, and especially the dihydrochalcone phlorizin [25,26,30,31];
- Skin, leaves, and bulbs of *onions* quercetin, kaempferol glycosides, and anthocyanins [25,32];
- *Carrot pomace* hydroxycinnamic acid derivatives, particularly chlorogenic acid [25,33];
- *Potato peels* phenolic acids and derivatives, especially chlorogenic acids [25];
- *Tomato pomace* flavanones and flavonols, mainly quercetin, rutin, and kaempferol glycoside derivatives [25,34];

- Lignocellulosic AFRs, such as *wheat straw* [26], *wheat bran* [35] and *distiller's grain* [36], *sawdust* [37,38], phenolic compounds, mainly deriving from hydrothermal and/or autohydrolysis processing of lignin.

Among the aforementioned pathways, the lignocellulosic matrix of plant cell walls in these AFRs could be also used as a source for cellulose (or even nanocellulose) isolation [15], due to their renewability, availability, biocompatibility, and different awesome properties. Therefore, the usage of residues would be an optimal sustainable and renewable source of cellulose instead of wood sources, reducing at the same time the amount of generated waste by food/beverage industries, diminishing their environmental impact, and supplying an additional profit.

3. Cellulose and its nanostructures

In recent years, cellulose has received increasing interest as a renewable raw material for producing biodegradable polymeric products and contributing to replacing fossil resources, considering their depletion, fluctuation in oil prices, and negative environmental impacts [39]. In the global scenario, the use of the vastly available by-products and wastes, also known as AFRs, is currently limited to livestock feed, providing a limited added value, or landfill or energy production by combustion, causing potential environmental issues [10]. By virtue of its abundance and very low cost, agro-industrial waste possesses a high chemical, material, and energy potential [40,41]. In the process, vast amounts of AFRs are being produced each year that are used mainly as feed for livestock or agricultural supplements when the lignocellulosic matrix of plant cell walls in these agricultural residues could be used as a source of cellulose or even nanocellulose, for reducing and/or mitigating the environmental impact.

3.1. Structure, chemistry, and properties

Cellulose is the most abundant carbohydrate polymer on Earth, with approximately 10^9 tons produced annually [42]. On the molecular scale, cellulose exhibits a unique structure. Specifically, the chemical composition of cellulose is $(C_6H_{10}O_5)_n$, where *n* is the degree of polymerization and represents the number of anhydroglucose units, ranging from hundreds to thousands or even tens of thousands. It is a highly ordered polymer of cellobiose (D-glucopyranosyl-β-1,4-d-glucopyranose) chains, aggregated by numerous strong intermolecular hydrogen bonds between hydroxyl groups of adjacent macromolecules, forming cellulose microfibrils, also known as elementary fibrils. As shown in Figure I.2, these microfibrils are tethered together by hemicellulose to microfibril bundles, and the resulting hierarchical structure is surrounded by lignin and hemicellulose [43].

Each monomer units bear three hydroxyl groups, whose ability to form hydrogen bonds plays a major role in crystalline packing and govern the physical properties of cellulose [44]. Moreover, the nucleophilic hydroxyl groups can on the one hand be modified with electrophiles to increase the functionality of cellulose; and on the other hand, they form inter- and intra-chain hydrogen bonds. These hydrophilic interactions are, in combination with hydrophobic interactions of the axial C-H bonds, the reason for the high mechanical strength and the non-solubility of cellulose.
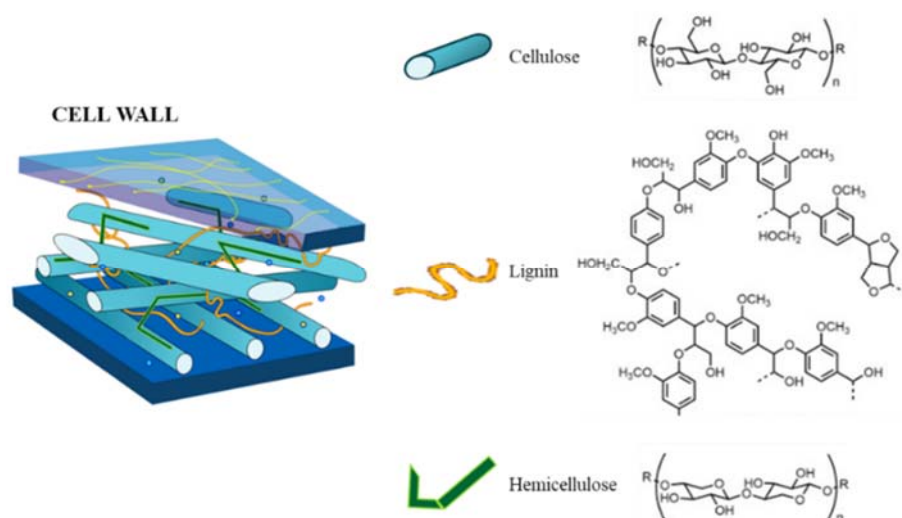
Figure I.2 *The hierarchical structure of lignocellulosic biomass with cellulose surrounded by lignin and hemicellulose.*

Cellulosic materials consist of disorganized amorphous and highly ordered, crystalline regions, where crystalline regions have higher density in comparison to amorphous regions. Crystalline and amorphous regions are found in native cellulose fibers in variable ratios, as a function of the plant species, with the growing conditions or the part of the plant. Since the presence of crystalline and amorphous domains (Figure I.3), cellulose microfibers are potential points for chemical and biochemical attacks. Research has established that the amorphous regions of cellulosic fibers are more susceptible to enzymatic degradation, easily releasing the individual crystallites under harsh acid treatment [45,46], and the highly ordered (crystalline) regions can be extracted to obtain nanocrystals [47].
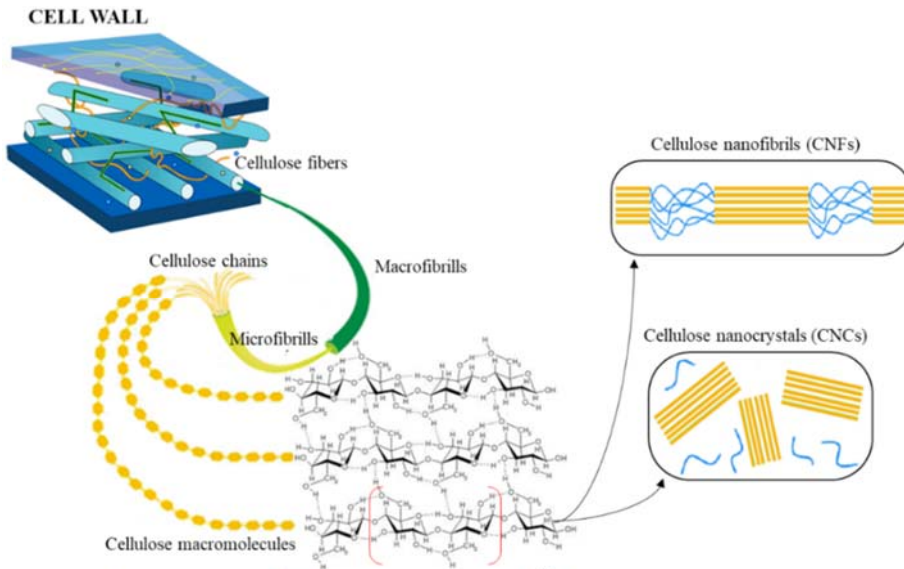
Figure I.3 *Crystalline (⬛) and amorphous (🔵) regions of cellulose fibers.*

Cellulose is characterized by noteworthy structure and properties [48]. This renewable natural biopolymer, together with the materials deriving from it, has attracted considerable interest, especially for application in environmentally friendly and biocompatible products and in foods [49,50]. Moreover, the unique molecular structure confers to cellulose unique properties, such as hydrophilicity, chirality, degradability, and broad chemical variability initiated by the high donor reactivity of the OH groups.

Cellulose isolation and modification, especially through advanced nanotechnology tools, enabled the further promotion of its techno-functional attributes [9]. Owing to their hierarchical order in a supramolecular structure and organization given by the hydrogen bond network between hydroxyl groups, nanoparticles can be efficiently isolated from cellulose [51] via mechanical and chemical methods, or through their combination. The various types of cellulose nanoparticles (also known as nanocellulose, NCs) can be classified based on their shape, dimension, function, and preparation method, which in turn primarily depend on the cellulose origin, the isolation and processing conditions as well as the eventual pre- or post-treatments [52,53]. The physicochemical characteristics of cellulose at the nanoscale, such as high specific surface area and aspect ratio, high crystallinity, purity, excellent mechanical properties, and low thermal expansion and density [8,53-58], open new prospects for NCs use in several fields, including biomedical, environmental, and energy applications [59].

3.2. Nanocellulose (NCs)

The cellulosic materials having at least one dimension in the nanometer range, based on structure and particle diameters [60], are usually classified (Figure I.4) into:

- cellulose nanocrystals (CNCs), also referred to as nanocrystalline cellulose (NCC) or cellulose nanowhiskers (CNWs);
- cellulose nanofibers (CNFs), also referred to as nano-fibrillated cellulose (NFC);
- bacterial cellulose (BC).

CNCs and CNFs can be extracted through a top-down process, whereas BC is synthesized through a bottom-up approach [61]. Although all types are similar in chemical composition, they are different in morphology, particle size, crystallinity, and some properties due to the different sources and extraction methods (Table I.1) [55,62].
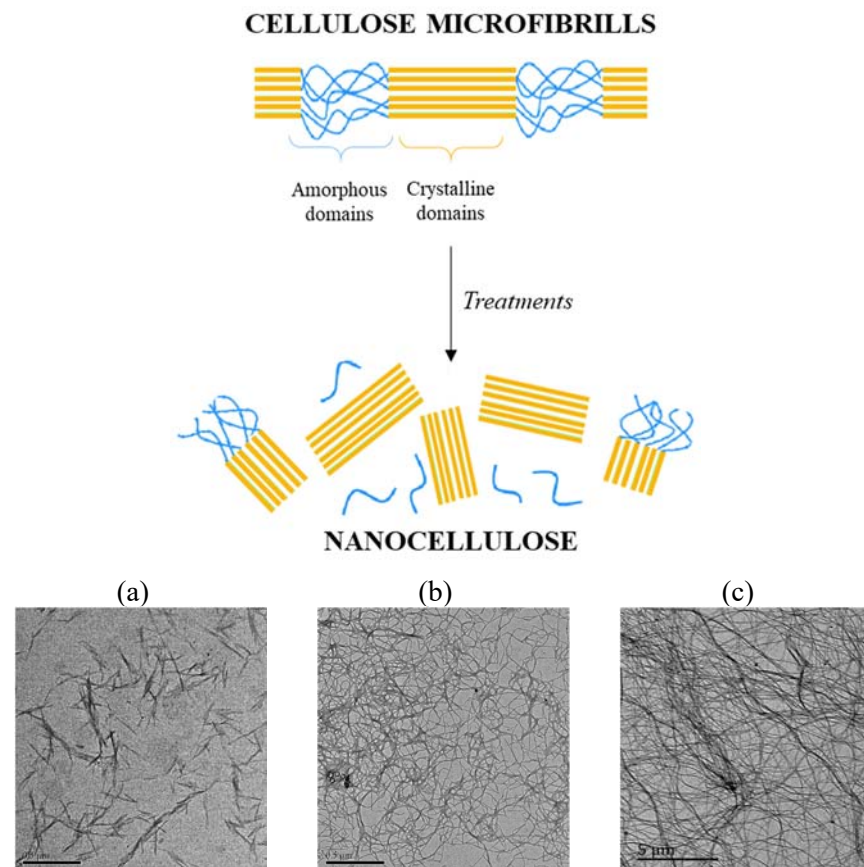
Figure I.4 *Schematic representation of NCs isolation and high-resolution TEM images of (a) CNCs, (b) CNFs, and (c) BC [63].*

Chapter I

Table I.1 *NCs production from wood and non-wood sources with different isolation methods.*

Source	Method of isolation	Type of NCs	Main results	Application	Reference
Eucalyptus kraft pulp	Enzymatic hydrolysis combined with mechanical ball milling pre-treatment	CNFs	The CNFs present a length of 294.0 ± 66.8 nm and a diameter of 24.0 ± 4.3 nm, maximum degradation temperature of 347.4 °C and crystallinity index is 82.75%.	-	[64]
Palm date fruits wastes, fruits wastes, and sugarcane molasses	Bacterial biosynthesis	CNFs	The diameter of the CNFs scales in the range of 10 - 90 nm. The crystallinity index is 81 - 84%.	CNFs film	[65]
Corn husks wastes	TEMPO oxidation combined with mechanical HPH	CNFs	The average length of the CNFs extracted is 150 ± 50 nm and the width ranged from 15-25 nm. The crystallinity of NCs is 64.5%.	Transparent membranes	[66]
Licorice residues	TEMPO oxidation combined with enzymatic pre-treatment and HPH post-treatment	CNFs	The CNFs have a diameter of 273 ± 142 nm and the crystallinity is in the range of 61.1-81.4%.	Composite films	[67]
Wheat straw, kenaf, and fax fibers	Sulfuric acid hydrolysis combined with ultrasonic fibrillation	CNFs	CNFs from wheat straw has particles with a diameter of 10 - 45 nm, from kenaf fibers 10 - 28 nm, and fax fibers 15 - 65 nm, while the lengths of the fibers are up to 10 μm. The crystallinity index is 73, 80, and 62% for wheat straw, kenaf fibers, and fax fibers, respectively.	Reinforcing fillers for paper and cardboard	[68]

Oil palm fronds leaves	Sulfuric acid hydrolysis	CNFs	NCs formed have diameters ranging between 10 - 30 nm, crystallinity index of 45.5%, and degradation temperature of 120 - 450 °C.	Reinforcing fillers for nanocomposites	[69]
Bamboo, cotton linter, and sisal	TEMPO oxidation combined with mechanical HPH	CNFs	The average lengths of CNFs extracted from bamboo, cotton linter, and sisal are 755, 635, and 464 nm, respectively. The widths of the ranged from 5 - 14 nm depending on the source. The crystallinity index is 60, 67, and 84% for bamboo, cotton linter, and sisal, respectively.	Composite film	[70]
Eucalyptus kraft pulp	Enzymatic hydrolysis combined with HPH	CNFs	The average length of NCs ranged between 278 - 550 nm.	Reinforcing fillers for film	[71]
Aspen wood	TEMPO oxidation	CNFs	The diameters CNFs are in the range of 6–26 nm and the crystallinity index is about 71 - 72%.	Composite film	[72]
Jute, soft, and hard spinifex grasses	TEMPO oxidation and nitro-oxidation	CNFs	The mean width is about 4.0 - 7.1 nm, 4.2 - 6. 5 nm, and 4.4 - 7.0 nm for jute, soft spinifex grasses, and hard spinifex grasses, respectively; the lengths are 1.4 - 3.2 nm, 1.5 - 3.9 nm, and 1.6 - 4.7 nm for jute, soft spinifex grasses, and hard spinifex grasses, respectively.	Reinforcing agent	[73]
Yerba mate residues	Oxalic acid hydrolysis	CNFs	CNFs diameters are 11 - 15 nm, aspect ratios (L/D) 12 – 24, and crystallinity index 64 - 76%.	-	[74]

9

Peach palm	Chemical treatments followed by mechanical grinding	CNFs	CNFs are 100 nm wide, with high crystallinity index (49.8-54.5%) and great thermal stability.	Composite biopolymer	[75]
Cotton gin motes and cotton gin waste	Sulfuric acid hydrolysis with and without TEMPO oxidation post-treatment	CNCs	CNCs obtained are diameters lower than 10 nm and lengths of ca. 100 - 300 nm resulting in high aspect ratios (12 - 33).	Cellulose nanomaterials	[76]
Oil palm tree wastes	Chemical treatments	CNFs	The thicknesses of the CNFs sheets are about 150 nm and a maximum decomposition temperature of 274 - 297 °C.	-	[77]
Bagasse (sugarcane wastes)	Enzyme pretreatment followed by mechanical grinding	CNFs	The degree of crystallinity ranges between 58.29 - 61.85%. The average diameter is 23.58 ± 8.63 nm and the length of CNFs varies from 200 - 1,000 nm.	Nanopaper/film	[78]
Oil palm trunk, banana peel, and coconut husk	Ni(II)-catalyzed hydrolysis	CNFs	CNFs have a diameter of less than 100 nm (ranging from 8.8 - 67.8 nm). The gravimetric yield ranges from 59.6-86.2%, while the crystallinity index is about 79 - 91%.	Reinforcement agents in composites	[79]
Coir fibers	Chemical treatments combined with ultrasonic fibrillation	CNFs	CNFs show a narrow diameter range of 2 - 4 nm and a relatively high crystallinity of 54%.	Reinforcing agents	[80]
Panax ginseng, spent tea residue, waste cotton cloth, and old corrugated cardboard	Sulfuric acid hydrolysis	CNFs	The extraction yield is 43.8, 24.6, 69.3, and 55.4% for Panax ginseng, spent tea residue, waste cotton cloth, and old corrugated cardboard, respectively. The	Reinforcing agents	[81]

			degree of crystallinity is 62.2 - 83.6%. The average width is 15.6 ± 4.5 nm, 30.5 ± 9.2 nm, 26.6 ± 13.1 nm, and 46.2 ± 7.2 nm for Panax ginseng, spent tea residue, waste cotton cloth, and old corrugated cardboard, respectively		
Ginkgo leaves	TEMPO oxidation combined with mechanical homogenization	CNFs	The average cross-sectional width of NCs is about 5 nm and the fiber length is about 400 nm.	Adsorption media	[82]
Banana peel and bract	Ball milling assisted ultra-sonication	CNFs	The diameter of CNFs is in the range of 100 nm, the peak of disintegration temperature is 346 °C, and the crystallinity index is 75.8%.	Biodegradable polymer	[83]
Eucalyptus globulus	TEMPO oxidation and enzymatic hydrolysis	CNFs	The average sizes are 22.3 and 629.1 mn for diameter and length, respectively. The yield of nanofibrillation is 95.6 - 97.1% and 20.5 - 38.9% for TEMPO oxidation and for enzymatic hydrolysis, respectively.	Nanopapers	[84]
Corn and rape stalk pulps	TEMPO oxidation combined with mechanical homogenization	CNFs	The average values of CNFs yield are 55% and 30% for corn and rape stalk pulps, respectively. The height of the CNFs was 1 - 2 nm.	Paper additives	[85]
Eucalyptus globulus	TEMPO oxidation combined with mechanical homogenization	CNFs	The diameter is between 8.7 - 14.1 nm and the yield of nanofibrillation is about 90 wt%.	Fillers material for paper	[86]

Sugarcane	Sulfuric acid hydrolysis	CNCs	The average width of CNCs is around 9.8 ± 6.3 nm, and the average length is 280.1 ± 73.3 nm. The crystallinity index is 68.54% and the rate of degradation is reached 268 °C.	Biomedical application	[87]
Amorpha fruticosa Linn.	Acetic acid hydrolysis	CNFs	CNFs have a mean diameter of about 10 nm and a length of about 10 μm, The degree of crystallinity is 54.67% and the maximum decomposition temperature of 337 °C.	Transparent nanopaper	[88]
Organosolv Straw Pulp	Sulfuric acid hydrolysis followed by ultrasound treatment	CNFs	NCs have a diameter of particles in the range from 10 - 40 nm and the rate of degradation is reached in the temperature range of 220 - 260 °C. The crystallinity degree is about 72.5%.	Nanocomposite materials	[89]
Waste pulp residues	Mechanical disintegration	CNFs	CNFs have a diameter of 10-100 nm and thermal stability of 303 - 320 °C.	Permeable membranes	[90]
Gelidium elegans red algae	Sulfuric acid hydrolysis	CNCs	CNCs have an average diameter and length of 21.8 ± 11.1 nm and 547.3 ± 23.7 nm, respectively. The degree of crystallinity is about 73% and it exhibits high thermal stability which started to degrade at 261 °C.	Reinforcing agents for nanocomposites or nano-fillers for polymer matrices	[91]
Corncob residue	Sulfuric acid hydrolysis	CNCs	The diameter and length of CNCs are 198 ± 51 nm and 5.5 ± 1.9 nm, respectively. The	Reinforcing agents	[92]

			crystallinity is 63.8%, and CNCs exhibited the best stability with the maximum thermal degradation occurring at 360 °C.		
	TEMPO oxidation and pulp refining	CNFs	CNFs have thin nanofibers (2.1 ± 1.1 nm of diameter) and the highest aspect ratio (about 438 nm of length) and the crystallinity is 49.9%. The maximum thermal degradation occurred between 330-340 °C.	Nanopaper or reinforce polymer composites	
Sunflower stalks	Sulfuric acid hydrolysis	CNCs	Acicular structure ranges from 5-10 nm in diameter and 150 - 200 nm in length, while a 69.8% of crystallinity index. The thermal decomposition of NCs is at 304 °C.	Reinforcing agents	[93]
	Steam explosion	CNFs	Fibers with an average diameter in the range of 5-10 nm with a good network. The degree of crystallinity is 93.7%	Reinforcing agents	
Pinecones	Mechanical grinding combined with chemical pretreatment	CNFs	The synthesized NCs fibers' diameter is in the range of 5 - 20 nm. The crystallinity index is 5-70% and the thermal stability is around 350 °C.	Reinforcing agents	[94]
Garlic straw residues	Sulfuric acid hydrolysis	CNCs	19.6 wt% extraction of the total amount of cellulose. The isolated CNCs have a broad polydispersity, with a diameter	Reinforcing agents	[95]

			between 4-7 nm and a length ranging from 400-700 nm. The degree of crystallinity is 68.8% and the thermal stability is around 200 °C.		
Rice straw, wheat straw, barley straw	Sulfuric acid hydrolysis	CNCs	Grains were fibrous in shape with a length of 120 - 800 nm and width of 10-25 nm, crystallinity index ranging from 63.4 - 71%, and yield extraction of 64-75 wt%.	Reinforcing fillers for film	[96]
Bamboo	Microwave liquefaction combined with chemical treatment and ultrasonic processes	CNFs	CNFs have a diameter of 20-30 μm, crystallinity of about 67.4%, and a maximum decomposition temperature of 374 °C.	Reinforcing agents for thermally stable composites	[97]

3.2.1. Cellulose nanocrystals (CNCs)

CNCs (Figure I.4a) are the mostly commonly used NCs, which are mainly produced through chemical hydrolysis/heat-controlled techniques (with sulfuric acid being the most utilized acid) of the amorphous section of cellulose fibers [98]. Extraction of the crystals from cellulose fibers involves selective hydrolysis of amorphous cellulose regions, resulting in highly crystalline particles with source-dependent dimensions [99]. The specific characterization depends on the process conditions and the source, but it is possible to detect some common features. Important parameters that affect the crystals' properties are the shape and size. Different studies have demonstrated, through specific test analysis on dimensions and morphology, such as transmission electronic microscopy (TEM), that CNCs exhibit elongated crystalline rod-like shapes or whisker shape with 2 - 20 nm in diameter and 100 - 500 nm in length (Figure I.4a), and have high rigidity compared to nanofibrils because a higher proportion of the amorphous regions are removed [100]. Moreover, thanks to the high crystallinity (around 54 - 88%), CNCs have high axial stiffness (105 - 168 GPa) [101], high Young's modulus (20 - 50 GPa) [102], high tensile strength (~9 GPa) [103], low coefficient of thermal expansion (~0.1 ppm/K) [104], high thermal stability (~260 °C) [105], high aspect ratio (~10 - 70) [106], low density (1.5 - 1.6

g/cm^3) [107], lyotropic liquid crystalline behavior, and shear-thinning rheology [108,109]. Analyzing the chemical composition, the presence of hydroxyl groups on the surface makes them suitable for functionalization: this process allows to change the electrostatic surface charge in order to enhance the interaction with some chemical groups or provide a more efficient dispersion in any solvent or polymeric matrix. The possible chemical modifications are esterification (conversion of the hydroxyl group into esters using acids), etherification (conversion of the hydroxyl group into organic radicals), amidation (conversion of oxidized CNCs into amide), oxidation, and so on [110]. Thanks to all these qualities, CNCs are considered a promising material.

3.2.2. Cellulose nanofibers (CNFs)

CNFs (Figure I.4b) are a bundle of stretched cellulose nanofibers having both crystalline and amorphous regions of cellulose filaments, obtained mainly through mechanical treatments, chemical methods, or through the combination of chemical and mechanical treatments. The peculiar CNFs' structure makes the analysis on dimensions quite hard, because it consists of a complex network, so defining an average length or diameter is not immediate. Furthermore, it exerts a high resistance to flow in aqueous suspension, resulting in a gel-like behavior also at relatively low concentrations (below 1 wt%), making it arduous to manage [111]. However, it has been found that CNFs have, typically, a diameter of 5 - 50 nm and a length of few micrometers [112,113]. These values are highly influenced by the methods and pre-treatment used (more than CNCs). The presence of amorphous regions makes the structure more flexible and suitable for many applications. The flexibility depends on the degree of crystallinity that affects the mechanical properties of the particles and on the contribution in the matrix in which they can be dispersed. The use of chemicals, acid above all, increases the crystallinity because they cause the separation of the amorphous parts [114]. The fibrils, at the end of the process, have a high self-assembly capability due to the exposure of some chains after the stretching [115]. Another important characteristic of CNFs is the high thermal stability, due to the absence or mild use of chemical reagents (in the case of chemical pre-treatments) that results in a not-so damaged, highly compact structure [116]. CNFs are extremely interesting in technological terms, because they combine in a good way the properties of cellulose and the advantages of nanometric scale, keeping more or less the same structural characteristics with better results because of the higher contact surface area, and also because the extracting methods have a mild environmental impact.

Chapter I

3.2.3. Bacterial cellulose (BC)

BC (Figure I.4c) is naturally produced by several bacterial genera. More in detail, BC is obtained by cultivating bacteria for a few days in an aqueous culture media containing glucose, phosphate, carbon, and nitrogen sources [117]. The cell membrane of the bacteria used to produce BC is composed of a cellulosic network structure of ribbon-shaped fibrils that are less than 100 nm wide, assembled from bundles of much finer nanofibrils [118], with a diameter of 2 - 4 nm. The fibrils are fairly straight and continuous and have low polydispersity in terms of their dimensions. The structural characteristics, as well as physico-mechanical properties of BCs strictly depend on the microbial strain type, the synthesis method (cell and cell-free system), and culture conditions. The bundles exhibit excellent intrinsic properties owing to their high crystallinity (84 - 89%) [119]. Along with an elastic modulus of 78 GPa, BC is reported to have high water holding capacity and a molecular weight up to 8000 Da [120].

4. Conventional chemical techniques for NCs isolation

Cellulose can be isolated from several vegetal natural fibers, which can be classified into bast fibers (jute, flax, hemp, ramie, and kenaf), leaf fibers (abaca, sisal, and pineapple), seed fibers (coir, cotton, and kapok), core fibers (kenaf, hemp, and jute), grass and reed fibers (wheat, corn, and rice) and all other types (wood and roots) [121]. Nevertheless, to assess the human activity as feed-stock selection, cellulose sources can be classified as shown in Figure I.5.

- *Primary source* for the cellulose fiber isolation, such as fibers for textile or paper, wood for building, industrial crops for bioethanol;
- *Secondary source* is the non-processed by-product from the transformation process in the food industry or residue from agricultural/forestry activities, such as bark, straw, leaves, and husks;
- *Tertiary source* is the waste from the use, transformation, and conversion of cellulosic biomass, such as pulp, bagasse, and food residues.

Most of the time, primary sources have been used for the production of CNFs and CNCs; however, recently, the interest has focused on the other two sources. For these reasons, the conventional chemical/enzymatic treatments for the isolation of NCs from wood sources are well-established top-down processes. The major differences between woody and non-woody biomass are their physical properties and chemical compositions, and accordingly the treatments for (nano)cellulose isolation vary with the raw materials used.

Raw materials
- **Wood** (pine, spruce, fir)
- **Natural fibers** (cotton, jute, sisal, bamboo,)
- **Alternative sources** (tunicates, algae, bacteria)

Sources for cellulose isolation

Processed wastes
Sugarcane/beet pulp bagasse, pulp and peper effluents, processing wastes from food and beverage industries

Non processed wastes
Straw, bark, husk, shells, leaves
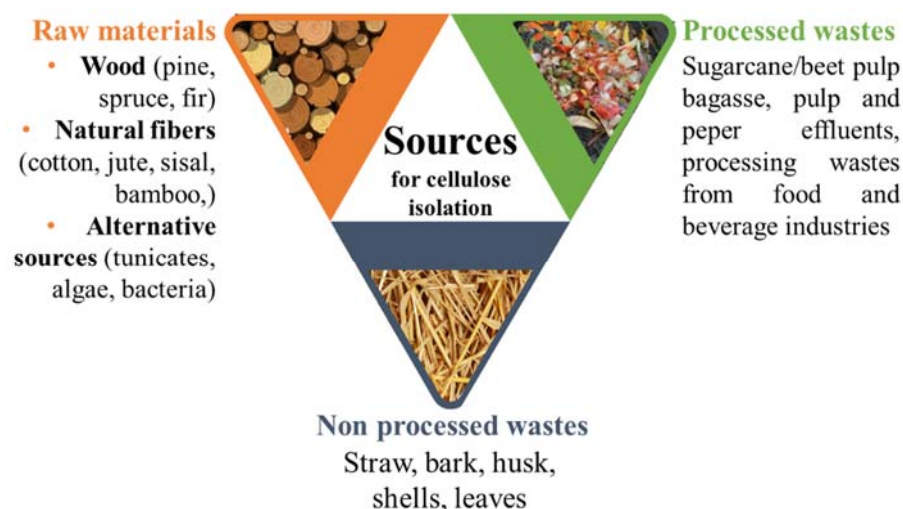
Figure I.5 *Cellulose sources classification based on the activity from which is obtained.*

The conventional production of cellulose nanoparticles requires previous treatments of the feedstock (Figure I.6), which follow these steps:

- *Delignification or pulping process*. In most cases, this step is mandatory as it allows removing as much as possible of the non-cellulosic components, i.e. hemicelluloses, lignin, and pectin. Usually. This process implies the thermochemical treatment of the cellulosic fibers, with different chemicals, such as NaOH [88-90], KOH [42,125], steam explosion [126], and organic solvents [93-95], with different treatment severity in terms of operating temperature and time. It can be mechanically assisted, such as with microwaves and/or ultrasounds treatments [130–132].

- *Beaching or purification process*. This step is necessary to remove lignin and obtain a more homogeneous final product. In most of cases, it consists of single or multiple steps of chlorine treatment in acid conditions at high temperature [133,134]. Moreover, the bleaching step of cellulose fibers not only enables to remove lignin but leads to a reduction in their diameter, and an improvement in their properties (crystallinity, modulus, aspect ratio, and surface area). The main drawback of this procedure is that it is not environmentally adequate.
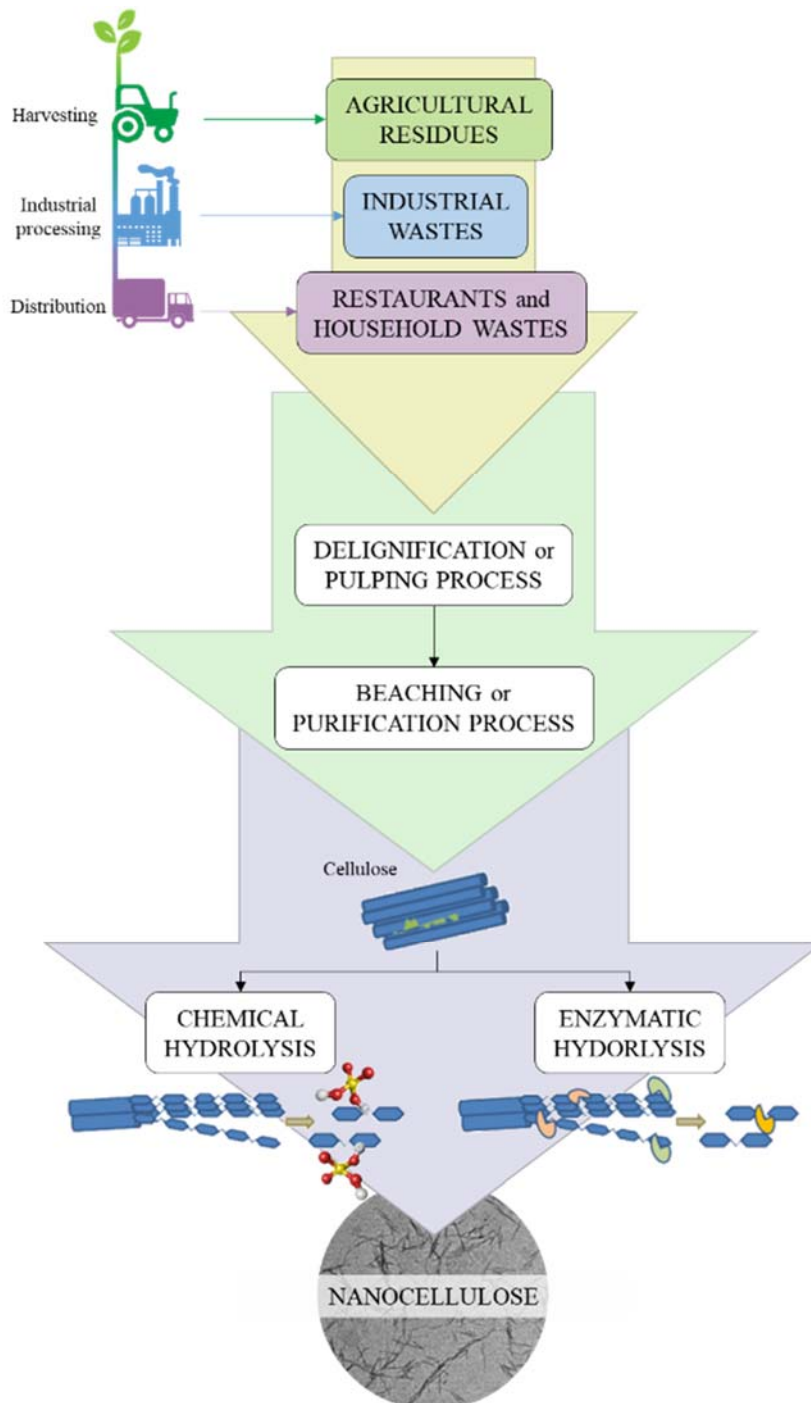
Figure I.6 *Conventional processes of NCs biorefinery: from the agricultural and industrial residues to the cellulose nanoparticles.*

After the transformation processes of lignocellulosic biomasses for the isolation of cellulose, the glycosidic bonds have to be broken down to obtain the nanodomain of cellulose. Generally, the processes of NCs production are based on chemical or enzymatic hydrolysis. However, the choice of process depends on the type of NCs being prepared, i.e., CNFs or CNCs, since the route through which NCs are isolated has a large effect on the morphology and chemical and mechanical properties of the obtained nanomaterials.

4.1. Chemical methods

Chemical hydrolysis offers great advantages to produce CNCs by partially breaking the glucosidic bonds [135]. Chemical hydrolysis involves acid hydrolysis, TEMPO hydrolysis, esterification, etherification, and amidation. Chemical treatments have shown great promise in biomass solubilization because (i) it requires a simple device; (ii) it has ease of operation; (iii) high conversion efficiency, and (iv) relatively low costs.

4.1.1. Acid hydrolysis

Acid hydrolysis is the oldest and most efficient chemical method for the production of NCs from cellulosic materials. This is because acids are capable of hydrolysing the hemicellulose portion and redistributing the lignin of the plant material, hence improving cellulose extraction [136]. Here, the acid easily dissolves and removes the amorphous region while the crystalline parts are retained [137]. Figure I.7 shows that the hydrolysis of cellulose begins with the reaction of acidic proton and oxygen that bonds two glucose units, forming the corresponding conjugated acid. Then, a cleavage of the C-O bond occurs, and a cyclic carbocation is formed. During the final step, after a rapid addition of water, a glucose molecule is formed, and a proton is released.
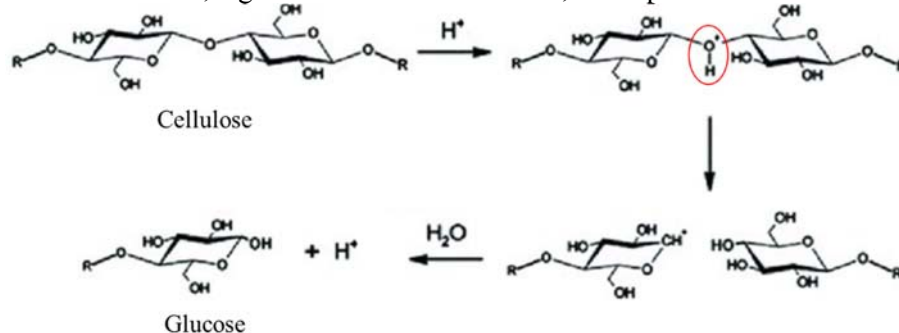
Figure I.7 *Mechanism of acid hydrolysis of cellulose for NCs production.*

HCl, H_2SO_4, HBr, and H_3PO_4 are generally utilized for chemical hydrolysis; however, H_2SO_4 is mainly used because it can strongly improve the isolation of CNCs as well as make the NCs dispersed as a stable colloid system because of the esterification of the hydroxyl group by sulfate ions

[138]. In this process, the reaction time and temperature, with the type of acid and concentration, affect the size and morphology, as well as the properties of NCs [62].

The main drawbacks and limitations of this method are the production of acidic wastewater, the high-water usage to neutralize the pH of NCs suspension, long processing time, high operational and maintenance costs, risk of equipment corrosion, the formation of inhibitors, and not being environmentally friendly [139].

4.1.2. Alkaline treatment

Alkali treatment is another chemical method to isolate NCs, which is considered less toxic and hazardous then acid treatment. Among different alkalis such as calcium hydroxide, potassium hydroxide, and ammonia, sodium hydroxide is the common alkali used for biomass treatment because it causes the breakage of intermolecular α- and β-aryl ether linkages between hemicellulose and lignin [140]. The hypnotized mechanism of alkaline hydrolysis is shown in Figure I.8.
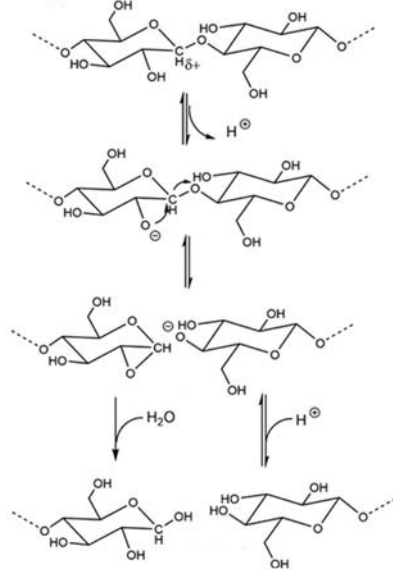
Figure I.8 *Mechanism of alkaline hydrolysis of cellulose for NCs production [141].*

The alkaline digestion process used as pre-treatment prior to acid hydrolysis targets the glycosidic side chains and esters, and this is followed by lignin removal, mercerization, and partial recrystallization of cellulose [139]. As a result of the partial elimination of hemicellulose and significant delignification, and the removal of ash and other cellulosic constituents by the alkali treatment, the resulting micro-fibrillated cellulose is more crystalline than the starting raw material. The alkali treatment enabled to [142] (i) swell

cellulose; (ii) increase the internal surface area; (iii) decrease the degree of polymerisation and crystallinity of cellulose; (iv) partially solvate the hemicellulose; (v) destroy the structural linkages between lignin and carbohydrate by saponification of intermolecular ester bonds; and (vi) disrupt the lignin structure by breaking its glycosidic ether bond.

However, the main disadvantages related to this pre-treatment are the black-generated hydrolyzate and processing time.

4.1.3. TEMPO-mediated oxidation

TEMPO-mediated oxidation is another conventional chemical method to produce NCs from lignocellulosic materials. In this technique, the oxidising agent 2,2,6,6-tetramethylpiperidine-1-oxyl radical (TEMPO) in water is commonplace to catalyse the regioselective conversion of primary hydroxyl groups on C-6 into aldehyde groups and carboxyl groups. The TEMPO-mediated oxidation treatment is generally carried out in the presence of sodium hypochlorite (NaClO) as the primary oxidant agent and sodium bromide (NaBr) as catalysts under alkaline conditions (pH ranged between 9 and 11) [143]. After the reaction, the aldehyde groups formed as intermediates always remain in the oxidized NCs [144]. These aldehyde groups are thermally unstable and cause discoloration of the oxidized celluloses when heated or dried at more than 80 °C. Moreover, the residual aldehyde groups disturb the dispersion of the oxidized celluloses as individual fibrils in water by the partial formation of hemiacetal linkages between the fibrils [143]. The chemical mechanism of TEMPO oxidization of cellulose is illustrated in Figure I.9.
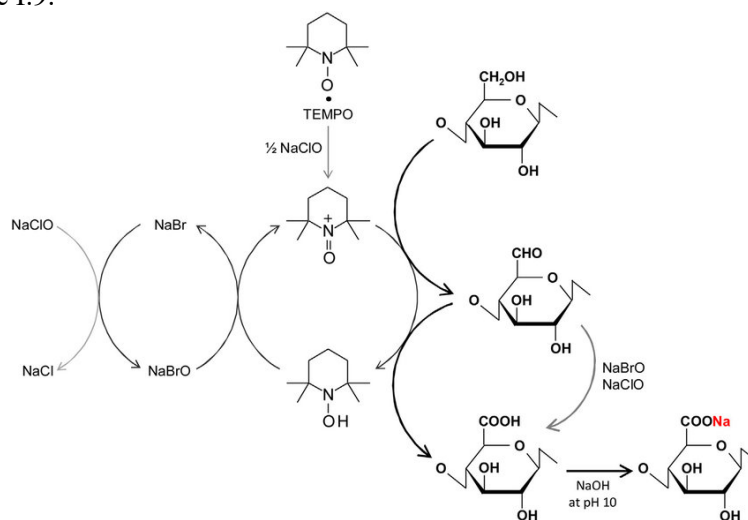
Figure I.9 *Mechanism of TEMPO-mediated oxidation of cellulose for NCs production [145].*

Chapter I

The TEMPO oxidation method has low energy consumption, simple operation, and mild reaction conditions [146]. However, it has several drawbacks, such as limited oxidation position and toxic reagents [147], since the TEMPO system contains hypohalite that can generate chlorine, extremely harmful to the environment.

4.1.4. Ammonium persulfate oxidation

Ammonium persulfate (APS) oxidation is another chemical method utilized to produce NCs. Because of its low toxicity and high solubility in water, APS has been recognized as a viable candidate to be utilized for producing H_2O_2 and SO_4^{2-} free radicals at acidic medium and high operating temperature, which are effective in solubilizing the amorphous portion of cellulose, and lignin content [148]. APS decomposes in aqueous solution through two reaction pathways that occur simultaneously (Figure I.10). The homolysis of the peroxide bond in ammonium persulfate using heat activates the S_2O_8 anion. The fast decomposition of the peroxydisulfate forms the sulfate-free radical ($SO_4\bullet^-$), which penetrates the amorphous region of the cellulose chain to co-hydrolyze the β-1,4 bond between glucose units, reducing the overall chain length and increasing the crystallinity of the nanofiber. The subsequent decomposition reactions are the rapid formation of hydrogen sulfate (HSO_4^-), sulfate-free radical ($SO_4\bullet^-$), and peroxyl radical ($HO\bullet$). The sulfate-free radical oxidizes the C6 to its aldehyde form, followed by peroxyl radical oxidation to form carboxylic acid groups on the nanofiber surface. The by-product of the oxidation reaction is the formation of sulfate ions and sulfuric acid [149].
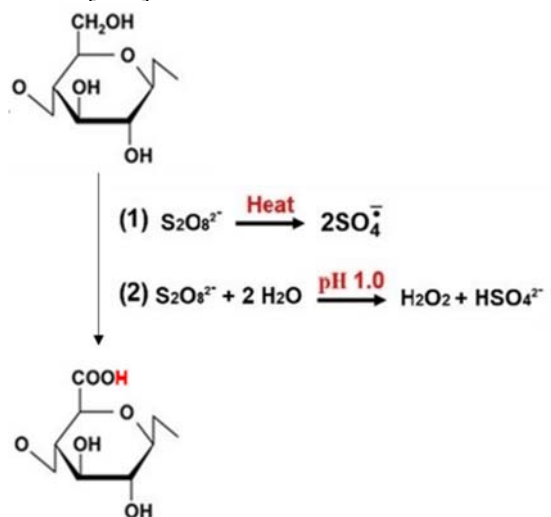
Figure I.10 *Mechanism of ammonium persulfate (APS) oxidation of cellulose for NCs production.*

APS is economical, selective for cellulose, and environmentally safe; however, the oxidation process requires long processing time. This is the major disadvantage, which limits the APS oxidation utilization in the industrial-scale production of NCs.

4.1.5. Ionic liquid method

The ionic liquids (IL) are liquid salts composed of an organic cation and a nonpolar or organic anion at room temperature or near room temperature. Ionic liquids have special properties such as non-flammability, high chemical and thermal stability ($T_{decomposition} > 200\ °C$), low melting point ($T_{melting\ point} < 100\ °C$), good solubility in polar and non-polar solvents, very low or even negligible vapor pressure, and easy recovery [150–152]. Dissolution of cellulose in IL (Figure I.11) is favorable on account of the capability of ILs to form strong hydrogen bonding between equatorial hydroxyl groups of cellulose and anions of IL [153] and coulombic interactions [154]. Such interactions between IL and biomass have been shown to cleave the lignocellulose polymer network and effectively isolate hemicellulose and lignin from the complex [154,155].
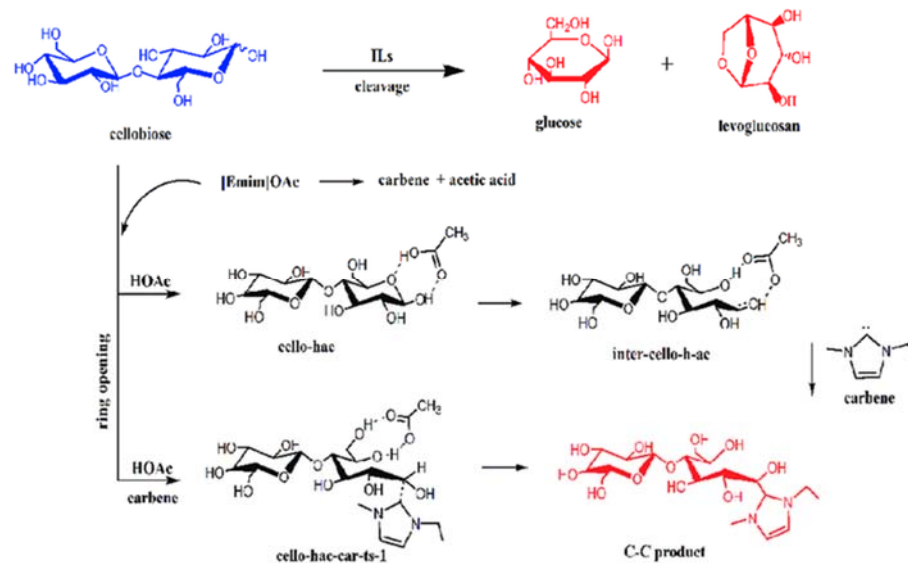
Figure I.11 *Mechanism of dissolution of cellulose in ionic liquid for NCs production.*

The cost of ILs is an important consideration for industrial applications. The recovery and reuse of ILs are very crucial for the practical employment of ILs based technology. Therefore, the high cost and toxicity of ILs have unfortunately limited their commercial implementation.

Chapter I

4.2. Enzymatic methods

Chemical hydrolysis processes are the most widely employed methods for obtaining nanosized cellulose. Nevertheless, as highlighted in the previous sections, these procedures have some drawbacks, mainly related to the environmental aspects, long processing time, and high amount of water required in the neutralization steps. In this scenario, another emerging possibility for producing NCs is the use of enzymatic hydrolysis, which is a promising environmentally-friendly and sustainable process. Enzymes, such as ligninase, xylanase, and cellulose, are used to modify and/or degrade the lignin and hemicelluloses contents while maintaining the cellulose portion [156]. On the other hand, as for acid hydrolysis, the enzymatic process mainly utilizes the selective action of cellulose on the glycosidic bond in the amorphous region to hydrolyze the NCs [99], as shown in Figure I.12.
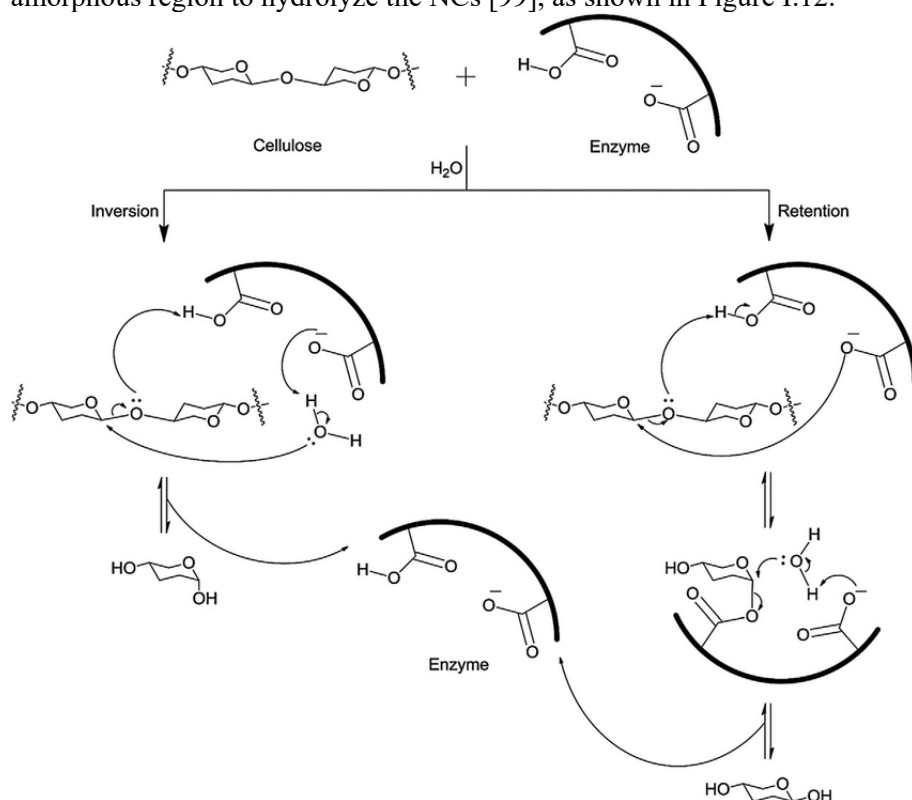
Figure I.12 *Mechanism of the enzyme-catalyzed hydrolysis for NCs production [157].*

Although this route is advantageous since the enzymatic hydrolysis is not corrosive and could be carried out at room temperature, the cost of enzymes and long processing time may be inconveniences [140].

4.3. Biological methods

Biological treatment for the isolation of NCs requires the use of a biological reaction by microorganisms (i.e. bacteria and fungi) or the direct use of cellulosic enzymes to hydrolyse or break down the structure of lignocellulosic biomass [139]. The principal source of microorganisms archetypally used is the soft-rot fungi, brown-rot fungi, and white-rot fungi, as well as bacteria from the genera of *Acetobacter*, *Alcaligenes*, *Sarcina*, *Agrobacterium*, *Rhizobium*, or *Pseudomonas* [25]. White-rot fungi are microorganisms most effective since are effective degraders of lignin and hemicellulose. The NCs isolation via fermentation can be obtained with the usage of yeasts, single-cell organisms that convert carbohydrates into alcohol. Out of 45 yeast strains, three strains (UBU-SK6, UBU-JK8, and UBU-JK9/1) showed the highest cellulose-degrading capabilities in the solid medium [158]. To improve the isolation of NCs through degradation and the crystallinity of obtained nanomaterial, enzymatic hydrolysis can be combined with a bacterial enzyme cocktail [159].

The main advantages of the biological treatment for NCs isolation are the (i) reduction of the bioconversion cost; (ii) decrease in contamination probability of microbes; (iii) improvement of the mixing rate; and (iv) increase in the kinetics [160]. However, the disadvantages of this method are related to the high cost and slower procedure to respect to chemical methods.

5. Innovative and "hurdle" approaches for NCs isolation

Several processes have been widely used to extract NCs from cellulosic materials, as described in detail in the previous sections. All these methods lead to different types of nanofibrillar materials, depending on the cellulose raw material and on the disintegration process itself. Nevertheless, several disadvantages are related to conventional chemical and enzymatic hydrolysis.

Innovative isolation processes of cellulose nanoparticles include physical treatments, which apply a high shear force to cleavage the cellulose fibers in the longitudinal axis, resulting in the nanofibrillated cellulose [56,156]. However, the NCs obtained by mechanical action have a large size and uneven distribution [146]. Besides, energy consumption is another main drawback for the production of CNFs by mechanical isolation processes [156]. Therefore, the mechanical process is generally combined with other pre-treatment methods, e.g., chemical and/or enzyme hydrolysis (Figure I.13). It is worth noting that appropriate pre-treatments (i) promote the accessibility of hydroxyl groups; (ii) increase the inner surface; (iii) alter crystallinity; and (iv) break cellulose hydrogen bonds, thus enhancing surface areas, and therefore, boost the reactivity of the fibers [161]. Moreover, these pre-treatments allow to reduce the energy consumption to an amount of 1,000 kWh/ton from 20,000 to 30,000 kWh/ton for cellulosic fibers [162].
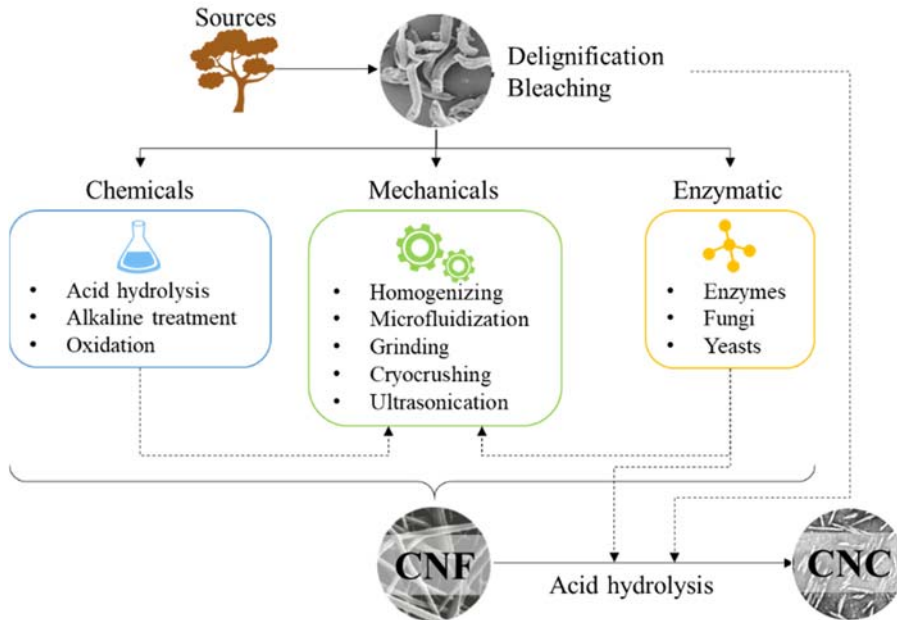
Figure I.13 *Conventional treatments and a combination of them with mechanical processes to obtain cellulose nanoparticles.*

5.1. Mechanical treatments

There are many mechanical methods to disrupt cellulosic fibers into NCs, such as refining and homogenizing [162–165], microfluidization [166–168], grinding [169], cryocrushing [170], and high-intensity ultrasonication [171,172]. Figure I.14 shows micrographs of NCs obtained by different mechanical methods.
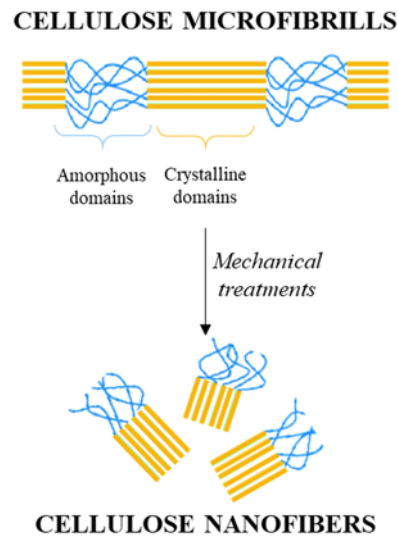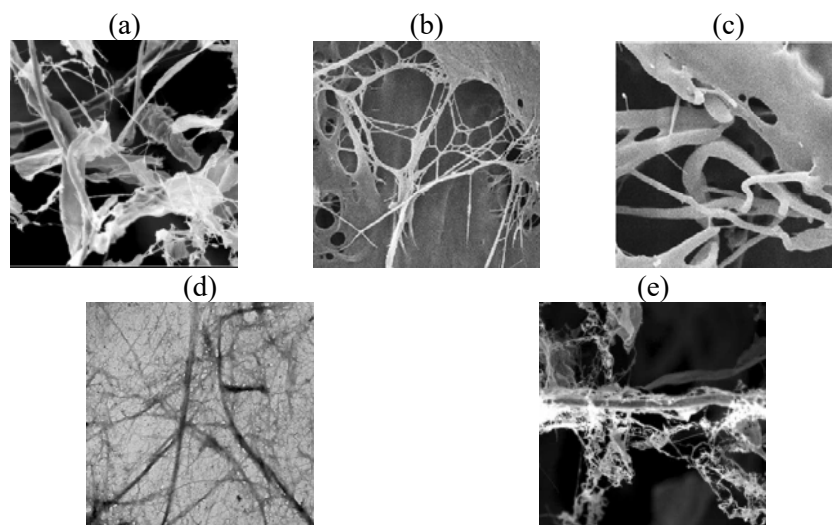
Figure I.14 *Schematic representation of CNFs isolated by mechanical treatment and the NCs micrographs obtained by different mechanical methods: (a) homogenization [173], (b) microfluidization [174], (c) micro-grinding [174], (d) cryocrushing [114], and (e) high-intensity ultrasonication [173].*

The main drawback related to the mechanical methods is the high consumption of energy, which can cause a dramatic decrease in both the yield and fibril length. Thus, a hurdle approach is proposed. Cellulosic biomasses can be pre or post-treated by mechanical processes, which greatly enhance the rupture of chemical bonds within the biomass polymeric network. These destructive actions also beneficially create reactive centers on the surface of the samples, which are prone to the next conventional hydrolysis but with a lower amount of chemicals.

5.1.1. High-Pressure Homogenization (HPH)

HPH process is the leading mechanical method to recover NCs, and in particular CNFs, from purified cellulose. The process includes pumping the cellulose slurry at high pressure into a vessel through a very small nozzle (at micron size), resulting in acceleration and depressurization of the fluid and the breakage of the jet [175]. The fluid-mechanical stresses on the cellulose biomasses occurring within the interaction chambers during HPH treatment were previously reported to induce (i) a significant reduction in particle size [11]; (ii) an increase in the surface area [116]; as well as (iii) the disruption of the well-arranged cellulose-hemicellulose-lignin complexes, causing what is referred to as fiber activation or cellulose defibrillation [117]. High velocity and pressure (Figure I.15) as well as impact and shear forces on fluid generate shear rates, turbulence, and hydrodynamic cavitation in the stream [176] and

decrease the size of the fibers to the nanoscale [177]. The pressure applied is in the range of 50 - 200 MPa while the diameter of the nozzle is about 5 - 20 µm, according to the viscosity of the suspension.
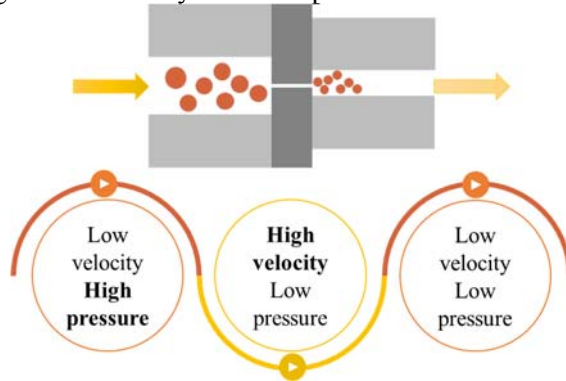
Figure I.15 *Velocity and pressure changes along the HPH valve.*

HPH, thanks to these several disruptive forces, partially disintegrates the structural organization of cellulosic materials and the obtained fibers have diameters between 20 and 100 nm and lengths of several micrometers [178].

In spite of the good results, the simplicity, and the eco-friendly process without the use of any organic solvents, the NCs isolation through HPH presents some drawbacks, such as the clogging of the narrow gap, high-energy consumption and mechanical damage of the crystalline microfibril structure. In fact, the CNFs isolated through HPH treatment generally exhibit low crystallinity than the starting cellulose, which was observed to decrease by increasing the number of passes from 0 to 30 [156], due to the breakage of intermolecular hydrogen bonds which leads to crystal collapse [179,180]. In order to overcome the aforementioned drawbacks, the lignocellulosic materials are generally pre-treated before the HPH process, such as acid hydrolysis, TEMPO-mediated oxidation, enzymatic reactions, alkali swelling, and the like, which can contribute to the removal of lignin and hemicellulose.

5.1.2. Ball milling (BM)

BM is a simple, fast, and cost-effective green technology with enormous potential for the isolation of CNFs [181]. During the BM mechanical process, cellulose is kept in a hollow cylindrical container that is partially filled with balls of ceramic, zirconia, or metal [137,182]. This hollow cylindrical container rotates and the high-energy collision between the balls disintegrates the cellulose fibers [112,183]. More specifically, at the beginning the particles get trapped on the ball surface; meanwhile, the deformation of individual particles starts because of the compressive forces formed during the collision of balls (Figure I.16). As milling progresses, the energy required to break the particle keeps increasing and attained the equilibrium between welding and fracturing [184].
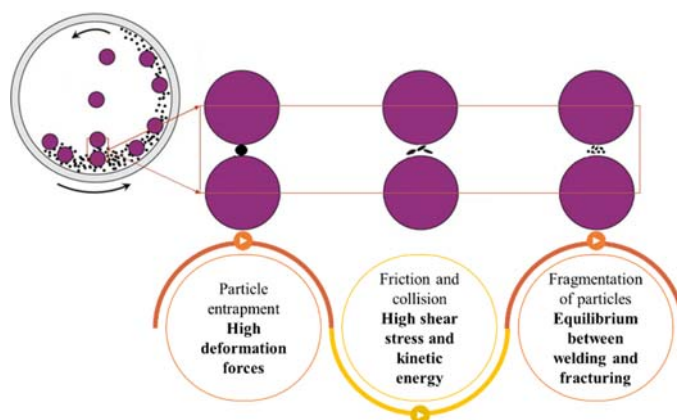
Figure I.16 *Mechanical forces involved during high-energy BM process.*

BM mechanical process is an effective method for NCs production, especially in a wet state for maintaining the fibrous state and preventing defibrillation to an amorphous one [185]. It is essentially a top-down procedure, which fundamentally results in the cyclic deformation of the initial cellulosic material, with subsequent degradation and rupture of the rigid structure of the lignocellulosic biomass [139]. Therefore, the obtained NCs exhibit a reduction in diameter, an increase in homogeneity, crystallinity, electrostatic and thermal stability [152-155]. Ball size, ball-to-cellulose weight ratio, grinding time, moisture content, and carboxylic charge can affect the chemico-physical properties of isolated CNFs [137].

Despite its efficiency and environmentally friendly properties, high power and energy consumption and the generation of a large amount of heat energy during processing are the most important limitations of BM [139]. Consequently, to overcome this issue, several alternatives that combine two different treatment methods were proposed: (i) high-intensity ultrasonication [190]; (ii) bleaching by $NaClO_2$ and alkaline hydrolysis using NaOH and KOH [191]; (iii) $Al_2(SO_4)_3$ pre-treatment [192]; (iv) enzymatic pre-treatment [193]; and (v) hydrothermal pre-treatment [194].

5.1.3. Microfluidization

Microfluidizer, another mechanical process similar to HPH treatment, concomitantly uses hydraulic shear, impact, attrition, impingement, intense turbulence, and cavitation, to affect size reduction [195]. The simplified working principle of microfluidizer is shown in Figure I.17. Microfluidizer is composed of an intensifier pump, which accelerates under high pressure the slurry into the interaction chamber, and an interaction chamber, in which impact forces against colliding streams and the channel walls occur [166].
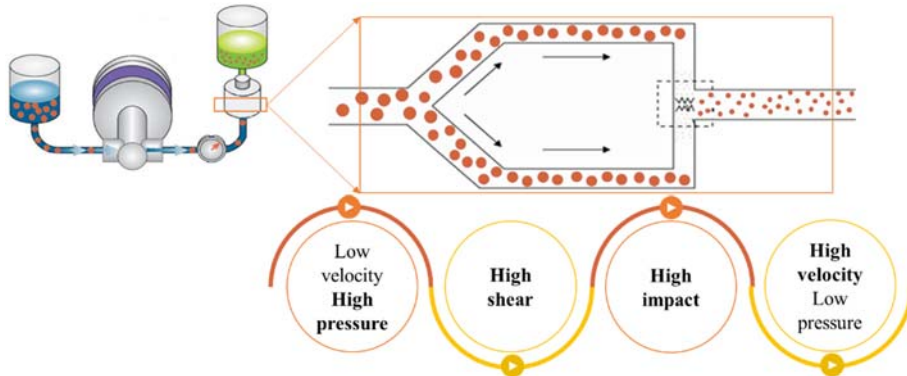
Figure I.17 *Velocity and pressure changes and mechanical forces in the microfluidizer valve.*

This mechanical approach allows to defibrillate the fibers to nanoscale dimensions, with several micrometers in length and less than 100 nm in diameter [142,196].

However, this procedure uses a high amount of energy; combined treatments have been recommended as a pathway to decrease the energy consumption in the mechanical and furthermore decrease the amount of chemicals used for bleaching during the manufacturing process [197].

5.1.4. Grinding

Another mechanical strategy to break up cellulose into nanosize fibers is grinding. In grinding equipment, there is a static upper stone and rotating grind stone at 1,400 - 1,500 rpm and the pulp slurry passes between these two stones (Figure I.18).
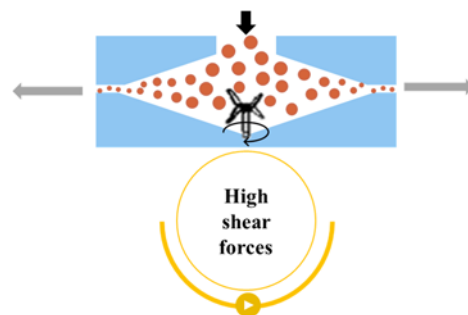
Figure I.18 *Mechanical forces involved during grinding process.*

The mechanisms involved in grinder for NCs defibrillation are to break down the hydrogen bond and cell wall structure by high shear forces and to evaporate the water content and raise solid content (which caused to boost up specific fibrillation energy) by heating generated from the friction of stones [50,137,162]. As a result, the individualization of the pulp to nanoscale fibers occurs from native cellulose fibers [162].

Although grinding is an environmentally-friendly method for preparing NCs, the disadvantages of this process are high-energy consumption, overheating of raw materials, low recovery and low uniformity of NCs, reduction in crystallinity, and possible structural alteration due to surface oxidation [139].

5.1.5. Cryocrushing

Cryocrushing is another technique used for the mechanical fibrillation of cellulose pulp. In this process, fibers are immersed in water, which is adsorbed in the cellulose cavity. Water-soaked cellulose is then immersed in liquid nitrogen, which solidifies the water content, and is subsequently crushed by mortar and pestle [137,198,199]. The application of high-impact forces (Figure I.19) leads to the rupture of the cell wall due to exerting pressure by ice crystals and thus, liberating CNFs [50,162].
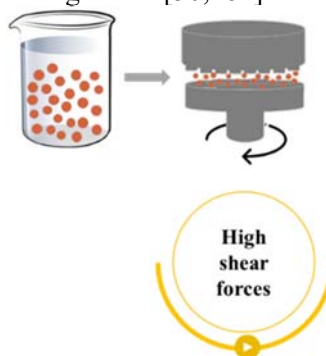
Figure I.19 *Mechanical forces involved during cryocrushing process.*

This process has a simple setup, does not require the use of organic solvent, and there is no wastewater generation. Nevertheless, the drawbacks are high cost, high-energy consumption, low recovery, and productivity with low uniformity of NCs [139].

5.1.6. Ultrasonication (US)

US is a mechanical method for the disintegration of cellulose allowing to reduce the diameter of the fibers, which exploited the hydrodynamic forces of the high frequency (≥ 20 kHz) ultrasound with oscillation power without the use of chemicals. During ultrasound treatment, acoustic cavitation (Figure I.20) leads to a powerful mechanical oscillating power, resulting in the formation, expansion, and implosion of microscopic gas bubbles and liquid molecules when absorbed by the ultrasonic energy of high-intensity waves [156,200,201]. In this way, the energy is transmitted to the cellulose chains, causing in this way their disaggregation into smaller entities [202].
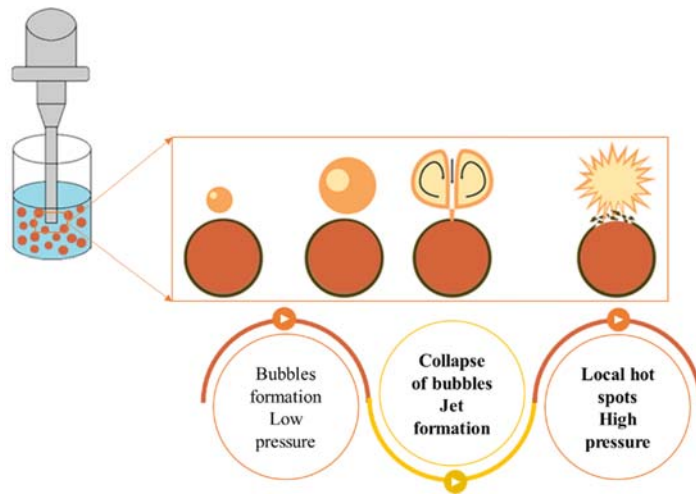
Figure I.20 *Acustic cavitation phenomena involved during US process.*

The NCs suspension produced by US treatment exhibited a reduction in diameter, an increase in homogeneity, crystallinity, electrostatic and thermal stability [203]. However, as all the aforementioned mechanical methods, US involves high consumption of energy, generation of heat and noise, and is not useful at industrial scale.

5.2. Effect of treatments on NCs isolation

In the present work, an overview of different alternatives of CNFs or CNCs production pathways from different industrial and AFRs was proposed. A key factor for the choice of treatment to be used is the morphology and therefore the width and length of NCs to be obtained. To this purpose, Figure I.21 is a schematic representation of NCs size as a function of applied treatment.
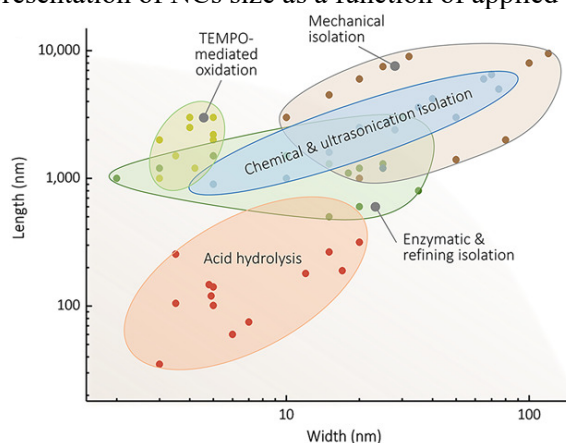
Figure I.21 *Dimensions of NCs produced through chemical, enzymatic, and/or mechanical isolation approaches [204].*

NCs produced through mechanical methods have a large width with a broad distribution: for instance, the NCs obtained from the HPH (even when including the mechanical pre-treatments) exhibit a width span from 10 to 100 nm. Accordingly, a variety of pre-treatments (chemical or enzymatic) have been utilized to accelerate the isolation process and to produce NCs with smaller width. The main purpose of chemical pre-treatments is to remove lignin and hemicellulose from the resources, to facilitate the isolation of cellulose, and to destruct and/or defibrillate into cellulose fibers. Using similar approaches, CNFs with width of 15 - 55 nm, were successfully isolated [205–207]. Enzyme pre-treatment is another strategy to improve the isolation degree by breaking non-covalent interactions presented in the amorphous structure of cellulose. In this way, using for example endoglucanase hydrolysis and HPH processing, CNFs with a width of 10 - 50 nm and several micrometers in length have been successfully produced [208,209].

6. Surface modification methods of NCs

NCs is a nanometric material that can be obtained through sustainable and environmentally-friendly processes, and which exhibits excellent intrinsic properties, such as impressive physical properties, high mechanical strength, renewability, biocompatibility, biodegradability, and transparency [210]. Despite all these aforementioned advantages, NCs exhibit limitations that restrict its widespread applications, such as poor thermal stability and interfacial adhesion [211], incompatibility with hydrophobic polymers [212,213], and absorption of moisture [142,156]. Due to the abundance of hydroxyl groups (OH) present on the surface [214], the NCs show a high agglomeration tendency, resulting in larger particles, with less dispersion and applicability difficulty [215].

One approach to overcome these limitations is the surface modification, which is a method that can increase the NCs' hydrophobic character and their electrostatic stability [215]. The NCs surface modification can be classified in (i) solvent exchange; (ii) physical modifications; and (iii) chemical modifications, as shown in Figure I.22.
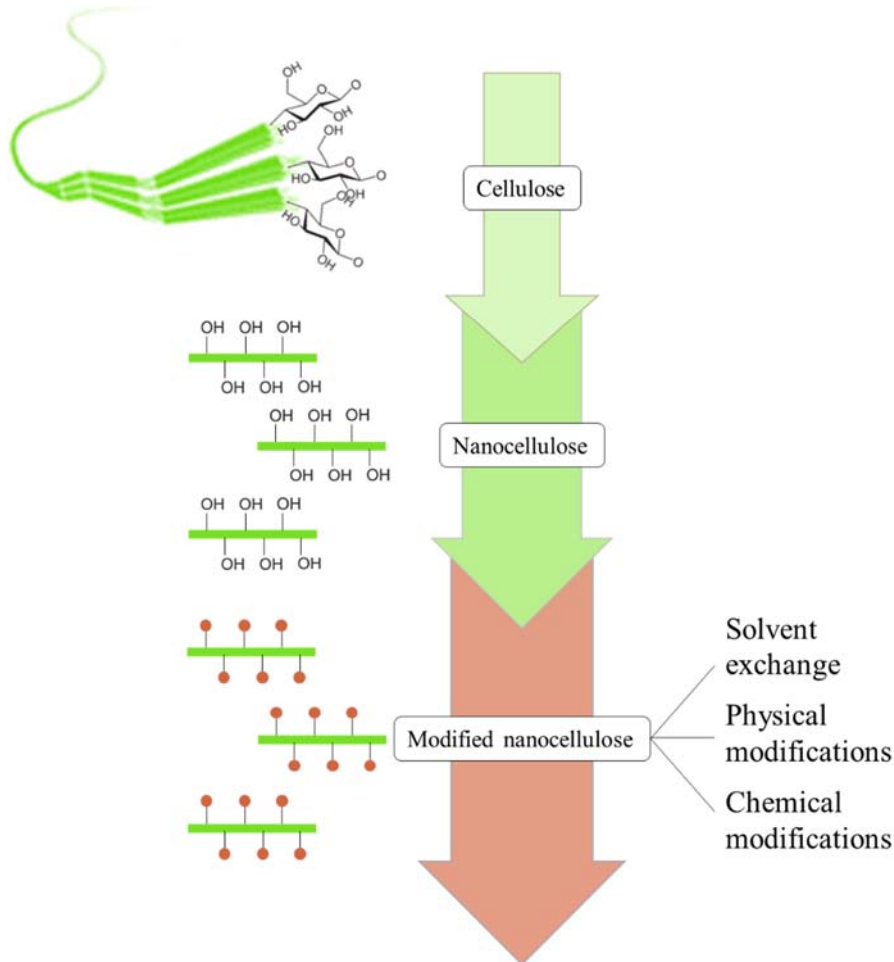
Figure I.22 *Surface modification of NCs with different routes.*

6.1. Solvent exchange

The solvent exchange method is commonly used to modify NCs and to prepare, for example, NCs-reinforced epoxy composites as bulk structural materials. In this approach, a water-miscible solvent with a higher boiling temperature than water (i.e. dimethylformamide, DMF), is added to water-dispersed NCs, and then the solvents are removed under reduced pressure by using a rotary evaporator to give a dispersion of NCs in the solvent (Figure I.23). Then, a certain amount of epoxy material is added to the dispersion of NCs in the solvent. The remaining solvent is finally removed by rotary evaporation. In this way, an epoxy dispersion with a specific NCs content is obtained [216].
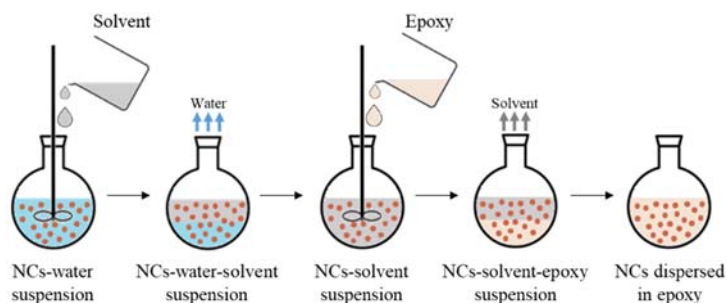
Figure I.23 *Schematic illustration of NCs modification through solvent exchange.*

Such a process drastically reduces the use of chemicals, does not degrade the cellulose nanoparticles as compared to other methods, and simplifies the modification process [217]. Nevertheless, the complete removal of the solvent is extremely difficult, and the residual solvent may have adverse effects on composite parts [216].

6.2. Physical modifications

To mitigate the aggregation of NCs, ensure the good stability, and enhance their dispersion in non-polar polymer matrices, physical modifications have also been applied as a simple and versatile route [215,218]. The physical modifications alter the dispersion of the fibers, increasing their hydrophobicity without generating covalent bonds [219]. There are many different approaches to physically modifying cellulosic substrates.

6.2.1. Adsorption

The physical adsorption approach (Figure I.24) has been used to modify the surface of (nano)cellulose [220]. This process relies on physical interactions between the adsorbed molecule (such as surfactants) and the cellulosic substrate. These secondary interactions could be the affinity between hydrophilic groups, the surface structure, electrostatic interactions, hydrogen bond formation or Van der Waals interactions [221,222].
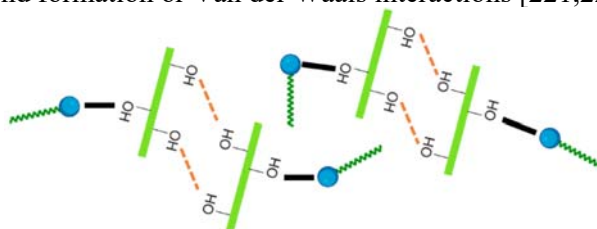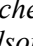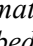
Figure I.24 *Schematization of the adsorption mechanism for NCs modification (adsorbed molecules ⬤∿∿; hydrogen bonds ▬ ▬ ▬; covalent bonds ▬▬▬).*

35

The physical adsorption can be further enhanced via electrostatic interaction where a charged amphiphilic compound is adsorbed onto an oppositely charged surface [223].

6.2.2. Plasma

Plasma is a widely used physical surface modification process for polymeric materials. The plasma surface treatment is environmentally friendly because it does not require the use of solvents [220]. Plasma, basically a glow-discharge, is characterized by an electric discharge producing partially ionized gas under vacuum at ambient temperatures. Therefore it causes only a surface modification of organic substrates through altering the chemistry of a few outermost molecular layers [224]. Plasma surface treatment is a cost-effective and easy technique to run at industrial scale to modify surfaces for various applications, and depending on the conditions and the plasma species, surface properties, such as morphology, hydrophobicity, and adhesion can be altered [225]. The increase in the NCs hydrophobicity, achieving a very high contact angle, is depicted in Figure I.25.
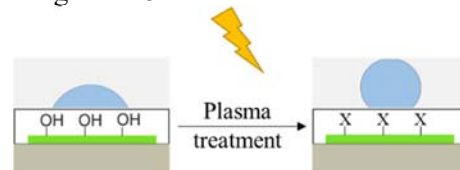
Figure I.25 *Schematic representation of NCs surface modification using plasma treatment.*

6.2.3. Corona

The corona treatment is a low-temperature visible electrical discharge that alters the properties of the treated surface. It causes surface oxidation of the polymer that is activated, changing its surface energy [226]. The corona is an easy-to-apply and low-cost technology that is frequently used by the packaging industry to increase the surface tension and polarity of films in order to improve their printing capacity, wettability, and adhesion properties [227]. Corona discharge promotes, therefore, a drastic reduction in the contact angle of water with the surface of the nanoparticles of cellulose fibers [228], as schematically shown in Figure I.26.
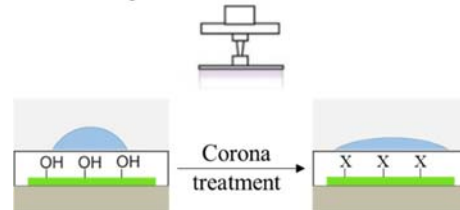
Figure I.26 *Schematic representation corona treatment on NCs surface.*

6.2.4. Laser

Laser, acronym for Light Amplification by Stimulated Emission of Radiation, is one of the most precise physical methods for surface modification [229]. During laser treatment, very small, concentrated spots of high-intensity light are produced, with a minimum heat release process. There is an interaction between laser radiation and the substance during the treatment, which can result in different effects depending on the fiber's unique chemistry and morphology [219]. For example, kenaf fiber bundles undergoing laser treatment allow to increase the fiber-resin interfacial bonding, reducing water absorption and therefore enhancing the durability and properties of the composite. Meanwhile, at high fluence, it was observed the appearance of small pores, cracks, or fibrils on the fiber surface after laser treatment [230].

6.3. Chemical modifications

The chemical modification is characterized by the covalent attachment of a polymer grafting onto NCs surface. This method changes the polarity of the nanoparticle, allowing a wide range of applications [201]. Among the main chemical modification, the most used are silylation, etherification, amidation, acetylation, carbanylation, esterification, etherification, oxidation, alkali treatment, and silynation. These last five chemical treatments are the common methods for cellulose modification to prepare adsorbent materials.

6.3.1. Silylation

Silylation is a promising surface-modification route to introduce silyl groups (R_3Si) onto the surface of NCs, improving in this way the compatibility of NCs with non-polar matrices [218]. Silanes are considered as effective coupling agents as they have strong affinity for hydroxyl groups even at room temperature [231]. The general formula of the silanes is $(RO)_3Si(CH_2)_n$-R , which shows two classes of functionality (i) RO = alkoxy groups, generally methoxy and ethoxy, is involved in the reaction with the cellulosic substrate to form a Si-O-fiber covalent bond (Figure I.27) and give methanol and ethanol as by-products during coupling reactions; (ii) R - amino; and others.
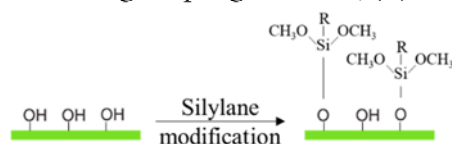
Figure I.27 *Mechanism of silylation reaction with NCs.*

Chapter I

Owing to its simplicity, silylation was also exploited as an intermediated step for further functionalization and modification: silanes were first covalently grafted onto NCs and consequently served as reactive sites to attach other compounds, such as fluorescent moieties [232] and alkene functionalized through thiolene click chemistry [233].

6.3.2. Esterification

Owing to its ease and straightforwardness, modification of hydroxyl groups present at the surface of NCs through esterification is widely used. The hydrophobization of NCs can occur with an acid anhydride, an organic acid, or an acyl halide leads to an ester group, as shown in Figure I.28. There are two acetylation mechanisms, including fibrous (heterogeneous) and solution (homogeneous) esterification, that can be recognized depending on whether a non-solvent is applied or not. Among all esterification reactions, acetylation, i.e. the substitution of hydroxyl groups (-OH) present onto the surface of NCs cellulose with acetyl groups (-COCH$_3$), is widely studied especially to increase the NCs hydrophobicity and decrease in this way the water absorption. Significantly then, the acelylation is used to prepare moisture-resistant NCs composites [234]. Nevertheless, different objectives such as dispersive/re-dispersive behavior improvement [196-199] and properties enhancement [238] were reported as well.
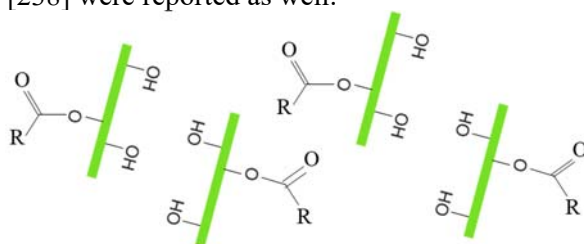
Figure I.28 *Schematic illustration of the surface modifications of NCs through esterification reaction.*

6.3.3. Etherification

Etherification is a cost-effective and highly efficient chemical modification step of NCs to change properties and functions of lignocellulosic materials [222]. The general formula of ethers organic compounds is R-O-R', where R and R' represent the alkyl or aryl groups. Ethers can be classified into two varieties: symmetrical ethers if R and R' groups are the same on both sides of the oxygen atom and asymmetrical ethers if they are different [239]. The modification process through etherification (Figure I.29) is simple and proceeds generally by activating the fibers with an aqueous alkali hydroxide, mostly sodium hydroxide, and converting indiscriminately hydroxyl groups with monochloroacetic acid or its sodium salt to carboxymethyl moieties [222].
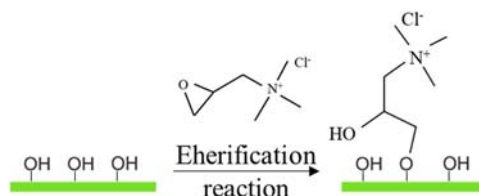
Figure I.29 *Etherification reaction of surface hydroxyl groups of NCs with epoxypropyltrimethylammonium chloride.*

Nevertheless, this process presents some drawbacks related to the use of the toxic halocarbon reactant. In addition, the resulting CNFs are even more hydrophilic than the original ones, which can be very limitation in applications involving non-polar media.

6.3.4. Covalent graft copolymerization

The hydroxy groups of NCs can act as chemical handles. Due to this uniqueness, small organic molecules can be grafted to NCs or a macromolecular polymer can be grown from its backbone [218]. Polymer grafting, characterized by covalent attachment, involves the reaction between polymers with the reactive functional end groups present on the surface of NCs, to improve the apolar character of nanoparticles. Surface grafting of polymer chains is considered an effective and versatile method to achieve a highly stable suspension in non-polar solvents because interfacial properties can be tuned depending on the nature of the grafted polymers [53]. Polymer grafting can be performed by means of various polymerization techniques, as represented in Figure I.30: "grafting from" and "grafting onto".
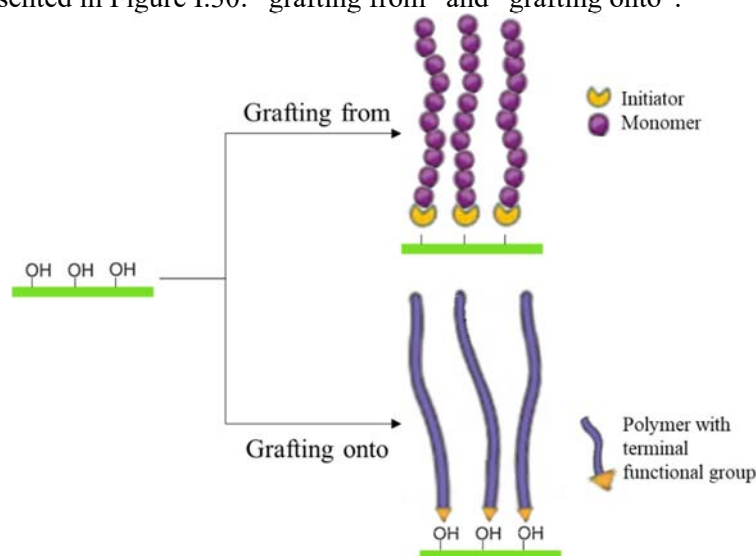
Figure I.30 *Schematic illustration of the "grafting from" and "grafting onto" approaches from NCs substrate.*

Chapter I

Grafting from

The grafting from approach, also denoted as surface-initiated polymerization, allows to increase the grafting density of the polymer brushes on the surface and to ensure their stability in different application conditions. In this method, the NCs is functionalized with an initiator, after which polymers can grow directly from its surface. There are two general mechanisms involved in this approach, which are:

- the ring-opening polymerization (ROP), in which the hydroxyl groups on the surface of NCs act as the initiator while the amount of monomer used to initiate the groups influences the degree of polymerization of the polymer chains;
- the radical polymerization (RP), in which the reaction between a monomer of interest with the initiator material occurs only after the immobilization of the initiator itself on NCs surface, and then the polymerization process starts [231].

The low steric hindrance and viscosity of the medium enable high grafting density on the surface. However, it is difficult to determine the final molecular weight of the polymer and the purification of the grafted NCs, as well as there is the formation of a large amount of free polymers [240].

Grafting onto

The "grafting onto" approach, on the other hand, relies on the attachment of the pre-synthetic polymer chains, carrying the reactive end groups onto the hydroxyl groups of the NCs surface. Unlike "grafting from", in this approach the molecular weight of the pre-synthesized polymer can be determined beforehand [202-204]. However, the downside of this approach is the higher viscosity of the processed material and its ability to only achieve a lower grafting density than "grafting from" approach due to the high steric hindrance and the packed chains on the surface [244].

6.3.5. Amidation

Amidation is one of the most common surface-modification routes applied to tailor the surface of NCs where amide linkage is formed by a reaction between amine and carboxylic moieties. This modification route is characterized by two steps, as shown in Figure I.31: the introduction of carboxy groups (-COO-) on NCs surface, often through TEMPO-mediated oxidation, followed by the amine attachment between these carboxylate groups (-COO-) and the amine functions (-NH2) on anchoring sites [53].
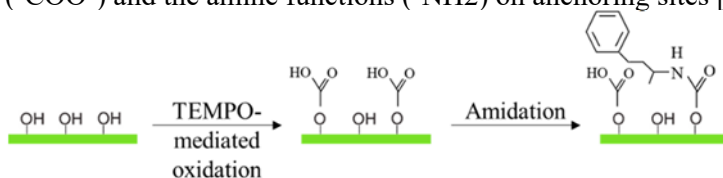
Figure I.31 *Schematic representation of amidation modification using aromatic 1-methyl-3-phenylpropylamine.*

The amidation modification allows obtaining a good dispersion and stabilization of NCs in organic solvents, which feature opens the door to further applications for nanocomposites. Furthermore, with the new sorption and barrier properties, modified NCs can be used as nanocomposites in packaging materials [245].

6.3.6. Urethanization

The process of functionalization through the urethanization method is also known as carbanylation or carbamation. This method involves the reaction between isocyanate (R-N=C=O) and hydroxyl (-OH) groups of NCs (Figure I.32) and results in the formation of covalent bonds [117,246] for enhancing the hydrophobicity of NCs [117].
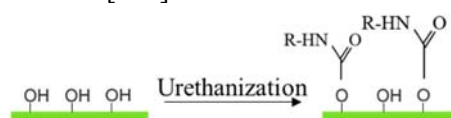
Figure I.32 *Schematic representation of urethanization modification on NCs.*

6.3.7. Phosphorylation

The modification of NCs through the amalgamation of phosphate (PO_4^{3-}) ester groups on the nanocellulosic surface occurs via direct reaction between a cellulosic pulp and inorganic phosphoric acid (Figure I.33). As result, phosphorylation of NCs enhances its properties, such as flame-retarding behavior in textiles application [247], compatibility with calcium phosphate opening pathways toward the hybrid material formation, and capability of binding metal ions for water and industrial effluents purification [248].
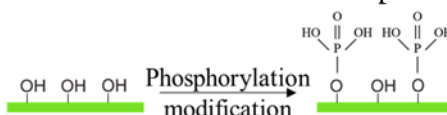
Figure I.33 *Schematic illustration of the phosphorylation of NCs.*

7. Innovative applications of NCs

Continuous environmental pollution and ever-increasing depletion of non-renewable sources have encouraged intense research in sustainable alternative solutions to conventional petroleum-based materials using biobased materials for applications in various fields of industry [249] such as pharmaceutical, cosmeceutical, food, composite materials, electronic devices, civil construction and biomedical materials (Figure I.34). In this regard, due to the renewability, biocompatibility, biodegradability, impressive physical properties, and mechanical strength, NCs have emerged as a widely used nanoscale material in material science, in particular as a reinforcing material,

template support or other functional materials, in both pure and composite forms [167,211-213]. Moreover, the multitude of functional groups on NCs surface permits physical and/or chemical modifications (as described in detail in the previous paragraph) and are further tuneable according to later application needs.
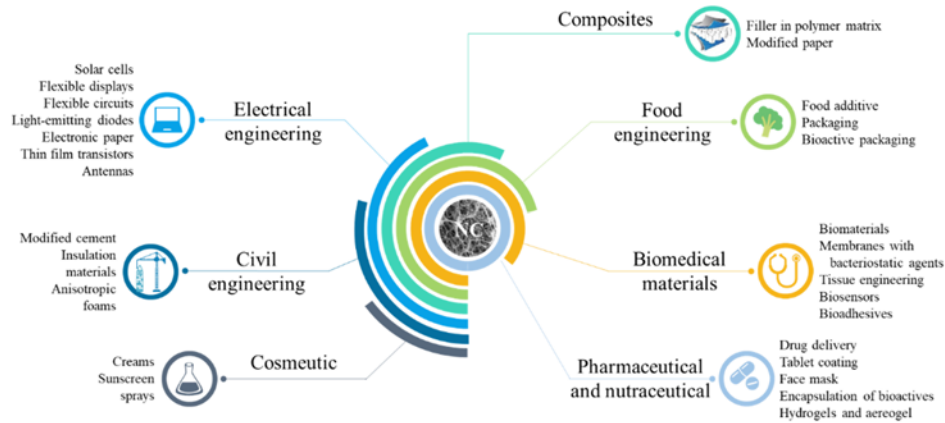
Figure I.34 *Potential applications of NCs in different fields.*

NCs applications can be classified into high-volume, low-value, and novel applications.

- *High-volume applications* consist of automotive interiors, automotive body components, buildings, and construction;
- *Low-value applications* consist of aerogels-oil and gas industry, construction, air and water filtration, and industrial-viscosity modifiers;
- *Novel applications* include some exceptionally advanced high technologies such as photonic structures-films, electronics-organic light-emitting diodes, and industrial and medical-additive manufacturing.

NCs also displays broader applications in a variety of materials related domains where physical characteristics such as weight, strength, rheology, and optical properties are highly affected in a positive manner. Some of the most important and emerging applications of NCs in terms of NCs-reinforced nanocomposites, biomedical applications, and energy materials are presented in the following sub-paragraphs.

7.1. Nanocomposites

The desirable mechanical traits and unique morphology of NCs, such as high stiffness and strength, as well as biodegradability, low weight, renewability, and low cost [240,253,254], make it highly desirable and reliable

reinforcement block instead of synthetic fibers to keep our environment safe [255]. Therefore, owing to its unique structural features, NCs have gained prominence and opened countless opportunities for novel applications in many emerging fields, such as building polymer composites [256]. Nanocomposites consist of a multiphase product in which at least one phase has a dimension of 1 - 100 nm [257], such as in the case of easily accessible nanofiller of CNCs, CNFs and BCs. The nanocomposites mechanical performance can be directly affected by (i) the nature of polymer matrix; (ii) the nature of NCs [162]; (iii) the dispersion and distribution of NCs within the polymer; (iv) the interaction between nanoparticles and matrix [156]; and (v) the nature and strength of interfacial bonding between NCs and the polymer [258].

Table I.2 sheds light on the most recent developments on the multitude of available routes for the fabrication of NCs composites. In particular, the incorporation of NCs as reinforcing agent into a polyolefin and polyester-based matrix, as well as in rubber and epoxy resins matrices has attracted relevant attention because it imparts an immense improvement in structural and mechanical properties, increasing their application potential. However, the innate hydrophilic nature of NCs makes it incompatible and leads to its poor dispersibility/miscibility with non-polar solvents. The modification of NCs surfaces addresses this issue of incompatibility with non-polar media. Several literature studies have highlighted that the unique structural and functional tunability of NCs/modified-NCs with polymeric matrices could lead to the immense improvement of the mechanical performance of the reinforced nanocomposites. Although their mechanical properties hardly meet industrial needs, from an engineering perspective, the recreation of the superior mechanical properties of natural structures (for example, cellulose has a tensile strength and Young's modulus up to about 350 MPa and 20 GPa) is quite challenging.

Table I.2 *Mechanical properties obtained from some representative studies of NCs-reinforced nanocomposites.*

Filler	Polymeric matrix	Processing technique	NCs concentration (wt %)	Mechanical properties	Reference
NCs-reinforced polyolefin nanocomposites					
Sisal CNCs	High-density polyethylene (HDPE)	Melt extrusion and solution casting from toluene	0 - 5	TS: 13.8 - 28.0 MPa EB: 17.0 - 832%	[259]
	Low-density polyethylene (LDPE)		0 - 5	TS: 10.1 - 11.2 MPa EB: 44.7 - 542%	
Wood CNCs	High-density polyethylene (HDPE)	Grafting method	7	TS: 29 MPa YM: 1.6 GPa EB: 4%	[260]

Kraft pulp CNFs	High-density polyethylene (HDPE)	Injection molding	10	TS: 26 - 39 MPa YM: 1.14 - 2.70 GPa EB: 3.0 - 9.8%	[261]
Kraft pulp CNFs	High-density polyethylene (HDPE)	Melt extruding and injection molding	0 - 25.3	TS: 25.2 - 43.4 MPa YM: 1.14 - 1.97 GPa	[262]
Cotton CNFs	High-density polyethylene (HDPE)	Physical pre-treatment and polyoxyethylene dispersion agent method prior to the extrusion process	10 - 50	TS: 30.4 - 53.9 MPa YM: 0.75 - 3.2 GPa	[263]
Wheat straws CNFs	Low-density polyethylene (LDPE)	Melt extrusion	6 - 14	TS: 4.5 - 6.0 MPa YM: 0.33 - 0.45 GPa EB: 3 - 30%	[264]
Kraft pulp CNFs	High-density polyethylene (HDPE)	Melt extruding and injection molding	10	TS: 39.6 MPa YM: 2.25 GPa	[265]
Eucalyptus Grandis CNFs	Polyethylene (PE)	Solution casting	1 - 90	TS: 7 - 70 MPa YM: 31 - 2837 MPa EB: 4 - 863%	[266]
NCs-reinforced polyester nanocomposites					
Grafting magnesium stearate modified CNFs	Polypropylene (PP) resin	Melt extruding and injection molding	5	TS: 45.4 - 49.4 MPa YM: 1.8 - 2.0 MPa	[267]
Enzymatic CNFs	Polylactic acid (PLA) and polyethylene oxide (PEO)	Electrospinning membrane	1	TS: 1.0 - 5.4 MPa EB: 30 - 74%	[268]
Cotton fibers CNCs	Polyethylene oxide (PEO)	Extrusion	0.01 - 0.09	TS: 7 - 9.5 MPa YM: 0.22 - 0.30 GPa EB: 0.4 - 0.9%	[269]
Softwood sulfate fluff pulp CNFs	Polylactic acid (PLA) and polyethylene oxide (PEO)	Melt extruding and injection molding	10 - 30	TS: 26 - 40 MPa YM: 0.7 - 1.2 GPa EB: 11.3 - 450.0%	[270]
CNCs	Polylactic acid (PLA)	Solution casting and injection molding	2.5 - 20	TS: 32 - 56 MPa YM: 2.2 - 3.6 GPa EB: 2.5 - 798.0%	[271]
CNFs	Polyethylene glycol (PEG)	Solution casting	0.1 - 1.0	TS: 45.7 - 51.3 MPa YM: 1.35 - 1.77 GPa	[272]
Cellulose nanospheres, rod-like CNCs, and CNFs	Polylactic acid (PLA)	Solution casting	1	TS: 50 - 75 MPa YM: 2.0 - 4.5 GPa EB: 4 - 7%	[273]
Polyethylene glycol-grafted CNFs	Polylactic acid (PLA)	Solution casting	0.1	TS: 64 - 343 MPa YM: 2.4 - 4.8 GPa EB: 3.8 - 34.9%	[274]
CNCs and CNFs	Poly (3-hydroxybutyrate-co-3-hydroxyvalerate) (PHBV)	Melt extrusion	1 - 7	TS: 29.1 - 37.8 MPa YM: 0.6 - 0.8 GPa EB: 7.5 - 16.4%	[275]

CNFs	Poly ε-caprolactone (PCL)	Solution casting	0.1 - 5	TS: 39.7 - 43.7 MPa YM: 300 - 380 MPa EB: 900 - 1128%	[276]
CNCs	Polycarbonate (PC)	Solution casting	0.3	TS: 67 - 93 MPa YM: 1.7 - 2.4 GPa EB: 51 - 57%	[277]
NCs-reinforced polyurethane nanocomposites					
Spinifex grass CNFs	Thermoplastic polyurethane (TPU)	Melt extrusion	0.5	TS: 41.7 - 58.3 MPa YM: 14.5 - 16.6 MPa EB: 1011 - 1096%	[278]
BC	Polyurethane (PU)	Solution casting	0.3 - 1	TS: 2 - 6 MPa YM: 100 - 600 MPa	[279]
Diisocyante (IPDI) monomer modified CNCs	Polyurethane (PU)	Solution casting	1 - 5	TS: 5 - 14 MPa EB: 160 - 190 MPa	[280]
CNCs	Polyurethane (PU)	Aluminium mould	0.2 - 0.8	TS: 0.13 - 0.21 MPa YM: 3.1 - 5.5 MPa	[281]
NCs-reinforced rubber nanocomposites					
CNCs	Natural rubber (NR) latex films	Dipping method	0.5 - 5	TS: 2.3 - 6.8 MPa	[282]
Cotton fibers CNFs	Natural rubber (NR)	Vulcanization process	0.5	TS: 6.1 MPa YM: 10.7 MPa	[283]
Wood CNFs	Natural rubber (NR)	Demulsification and coprecipitation process	4 - 20	TS: 4.4 - 9.7 MPa YM: 1.8 - 10.9 MPa EB: 253 - 463%	[284]
Softwood bisulfite pulp CNFs	Poly[styrene-co-(2-ethylhexyl acrylate)] with cationic (TTAB) or anionic (SDS) surfactants	Solution casting	0 - 5	TS: 16.9 - 965 kPa EB: > 1400%	[285]
CNFs modified with protein and peptide	Styrene-butadiene rubber (SBR)	Vulcanization process	3 - 9	TS: 4.2 - 12.3 MPa YM: 2.8 - 26.8 MPa	[286]
T. pungens and wood CNFs	Natural rubber (NR)	Solution casting	0.1 - 2	TS: 18 - 29 MPa EB: 1,000 - 1,900%	[287]
CNFs	Natural rubber (NR)	Vulcanization process	0.1 - 1	TS: 28 - 43 MPa	[288]
NCs-reinforced epoxy nanocomposites					
CNFs	Epoxy resin diglycidyl ether of bisphenol A (DGEBA)	BM and a solvent exchange method	20	TS: 50 - 60 MPa	[216]
Iodine-catalyzed chemical modificated CNFs	Epoxy matrix EPON 828 and Epikure 3140	Solution casting	0.01 - 1	TS: 29.0 - 45.2 MPa YM: 917 - 1674 MPa	[289]
Acetyl, hexanoyl, and dodecanoyl surface modified CNCs	Epoxy resin	Solution casting	1 - 5	TS: 78 - 112 MPa YM: 1.2 - 1.6 GPa EB: 8 - 12%	[290]

45

CNCs	Epoxy resin Dowex 50W-X2	Solution casting	1 - 5	TS: 40 - 62 MPa YM: 2.0 - 2.6 GPa	[291]
CNFs	Epoxy resin diglycidyl ether of bisphenol A (DGEBA)	Vacuum drying	2	TS: 30 - 65 MPa YM: 1.2 - 1.6 GPa EB: 1.3 - 3.5%	[292]
Wood pulp CNFs	Epoxy resin diglycidyl ether of bisphenol A (DGEBA)	Vacuum drying	0.3 - 3	TS: 20 - 56 MPa YM: 2.0 - 3.6 GPa EB: 1.8 - 3.5%	[293]
Cotton CNFs	Epoxy resin EPON 828	Solution casting or vacuum drying	4 - 24	TS: 2.2 - 5.7 GPa	[294]
BC	Epoxy resin diglycidyl ether diphenolate ethyl ester (DGEDP-ethyl)	Vacuum drying	5 - 30	TS: 60 - 105 MPa YM: 2 - 8 GPa EB: 1.2 - 1.9%	[295]

Note: Tensile strength (TS), Young's modulus (YM), and elongation at break (EB)

The field of NCs-based nanocomposites is still growing rapidly and there is room to optimize the mechanical properties of cellulosic materials by tuning their architectures or interparticle interactions to achieve the optimized outcome [218].

7.2. Paper industry

The paper industry is perhaps the largest consumer of cellulose and NCs. The paper process is usually carried out in different steps, including preparing the paper components, wet refining, forming of wet sheet, pressing, drying, calendering, and finishing [296]. In this process, NCs are the perfect candidate in papermaking since they can act as a strengthening agent, a component of the retention system, printing a quality aid, a binder of coating, and a barrier agent controlling water vapor and oxygen transmission [297]. Several studies have focused attention on the usage of NCs in the production of paper both as a substrate material and as an additive or in coatings, because it is a biodegradable natural polymer able to reinforce paper features and create high-performance biomaterials. Table I.3 summarizes recent studies pointing out as NCs can be preferentially used as eco-friendly substitutes of synthetic reinforcing materials currently used in the paper industry.

Table I.3 *Effect of NCs-filler in papermaking on barrier properties from some representative studies.*

NCs filler	NCs concentration (wt %)	Effect of NCs filler	Reference
NCs bionanofiller in paper-making process			
Corn and rape stalk pulps CNFs	0.5	CNFs greatly enhance the mechanical strength and durability of papers	[85]
Bleached soft wood sulfite fibers CNFs	10	Surface-modified CNFs with lactic acid improved the draining efficiency (~56%) when compared to conventional sodium chloride-aided draining	[298]
Eucalyptus and corn CNFs	0.3 - 1.5	CNFs are highly effective in stabilizing flocs and minimizing overdosing effects. CNFs can contribute to improving the wet end in the paper machine if combined with the optimal flocculant and dose	[299]
Cellulose nanofibrils from orange tree pruning	1.5 - 4.5	Mechanical properties of the paperboard were improved substantially after reinforcement, compensating for the losses in properties due to the hornification phenomenon of recycled paperboard	[300]
Wheat straw, kenaf and flax fibers CNFs	1	High level of effectiveness of NCs in reinforcing paper and cardboard, improving their quality indicators of mass types	
NCs coating material in paper-making process			
CNCs	0.75 - 1	CNC-composite barrier coating material exhibited a 71% reduction in water absorption, 27% in water vapor transmission rate and resistance to air permeation > 88% compared to the control coating	[301]
CNCs and CNFs	2.5 - 10	The multi-layered coating system with CNFs and CNCs had highly effective barrier against gas, oil and grease and oxygen transmission	[302]
CNFs	1.5	The three-layers coating made of a mixture of NCs and sorbitol showed a higher effective barrier against oxygen and water vapor transmission than the porous paper substrates	[303]
CNCs	3	The thin yet multi-layered coating of NCs with poly(lactic acid) applied on a paperboard increases the barrier properties with bio-based and biodegradable material	[304]

Despite the wide availability, environmentally friendly design, renewability, and enormous mechanical properties, the NCs as bionanofiller in the pulp and paper industry under the above-mentioned conditions is still used to manufacturing on a small to pilot scale rather than commercial scale.

7.3. Food industry

The aforementioned properties, in particular the high surface area, aspect ratio, rheological behavior, water absorption, and absence of cytotoxic and genotoxic properties, give to NCs ample opportunity for practical applications

in food sector as reinforced agents in the development of active packaging, food additives, and food stabilizers.

In food packaging, NCs can be a sustainable and biodegradable alternative to the current synthetic packaging barrier films, with the enhanced barrier, thermo-mechanical, rheological, and anti-bacterial properties. Recent research trends have shown the possible usage of NCs as base materials in traditional plastic packaging or as edible coatings/films. For example, Nguyen et al. (2021) reported the application of coating layers made of biorenewable NCs and nanochitin deposited on polypropylene films through the layer-by-layer (LbL) technique. The resulting film is highly transparent, unfavourable to bacterial adhesion, and thermally recyclable, hence it is promising for advanced food packaging applications [305]. To limit the environmental pollution caused by non-degradable plastic packaging edible coatings (ECs) represent a consolidated technology to improve the postharvest quality of fruits and vegetables by slowing down respiration rate, water loss, and oxidation processes [306], as well as helping to maintain the physiological properties. However, the performance of most ECs is insufficient to meet practical applications, in particular with reference to conjugating restricted thickness with adequate mechanical and barrier properties. Therefore, recent studies have focused on the implementation of different types of filler to improve coating properties.

The synergistic interaction between reinforcement agents and the polymeric material, through hydrogen bonding or ionic complexation, enables the ECs mechanical properties to be increased and permeability of moisture and gases to be reduced [307]. Among the different reinforcing agents, NCs with their size lying in the range of the nanometers have attracted increasing attention as a promising material for tailoring ECs properties in food preservation [48]. In general, the addition of NCs into nanocomposite coatings results in a slight increase in thickness, mainly related to the higher solid content in the coating solutions and the interruption of the original polymeric structure by NCs, as extensively shown in Table I.4. Therefore, the effect of NCs incorporation on coating thickness can be correlated well with the concentration of NCs in the formulation.

Table I.4 *Effect of NCs on thickness and mechanical properties of edible coatings and films.*

Film-forming material	NCs		Thickness (μm)	Mechanical properties		References
	Type	Concentration (wt%)		TS (MPa)	EB (%)	
Chitosan	CNFs	1.5	14.5-21.2	-	-	[308]
Tapioca, potato, corn	CNFs	0	2.99	0.047	6.67	[309]
		10	6.33	0.055	22.67	
		20	5.71	0.056	30.51	
Faba bean protein isolate	CNCs	0	-	4.3	105.0	[310]
		3		3.8	48.1	
		5		5.3	48.2	
		7		6.5	46.3	

Cassava starch	CNCs	0	-	7.15 ± 0.60	22.75 ± 2.34	[311]
		0.14		8.19 ± 0.90	19.23 ± 2.25	
		0.3		9.91 ± 0.70	5.85 ± 1.43	
		0.6		10.99 ± 0.5	1.31 ± 0.25	
Okara fiber and pectin	CMCs	0.5	123 ± 70	6.567 ± 0.33	16.67 ± 0.35	[312]
Konjac glucomannan	BNC	0	39 ± 6	46.43	6.34	[313]
		1	40 ± 12	50.36	8.58	
		2	41 ± 0	69.29	9.44	
		3	41 ± 15	74.05	8.18	
		4	42 ± 10	82.01	5.70	
Cassia-gum	CNCs	0	89 ± 5	18.53	28.87	[314]
		2	90 ± 3	24.77	31.88	
		4	93 ± 2	32.85	34.75	
		6	98 ± 4	28.75	36.51	
Polyvinyl alcohol	NCs	1	-	6.42 ± 0.59	89.99 ± 11.77	[315]
		3		9.47 ± 1.62	106.94 ± 7.04	
		5		11.17 ± 1.08	117.52 ± 10.28	
κ-carrageenan	CNCs	0	20	38.33 ± 3.79	21.50 ± 3.72	[316]
		1	30	38.43 ± 5.94	22.93 ± 1.50	
		3	40	39.83 ± 0.38	23.83 ± 2.71	
		5	25	40.07 ± 2.80	24.33 ± 3.00	
		7	25	52.73 ± 0.70	28.27 ± 2.39	
		9	35	39.10 ± 1.04	25.83 ± 2.61	
k-CA biopolymer	CNCs	0	80	49.0	27.5	[317]
		1		59.2	23.1	
		3		66.6	20.7	
		5		80.9	18.9	
		8		85.1	15.4	
Whey protein	CNCs	0	-	1.30	47	[318]
		1		1.65	35	
		3		2.10	34	
		4		2.29	35	
		5		2.30	35	
		10		2.70	25	
		15		3.15	24	
Corn nanostarch	CNCs	0	300	3.41 ± 0.17	-	[319]
		0.2		5.99 ± 0.30		
		0.4		7.28 ± 0.36		
		0.6		8.61 ± 0.43		
		0.8		11.25 ± 0.56		
		1		7.78 ± 0.39		
Agar	BNC	0	-	22.10 ± 0.64	10.76 ± 2.30	[320]
		0.045		27.95 ± 1.42	14.50 ± 0.88	
		0.075		31.26 ± 2.26	27.47 ± 1.08	
		0.12		34.20 ± 1.35	21.53 ± 1.62	
		0.15		44.51 ± 1.86	13.02 ± 1.70	
Whey protein	CNCs	0	-	2.30 ± 0.35	46.07 ± 23.25	[321]
		2		3.41 ± 0.87	20.82 ± 9.85	
		5		3.49 ± 0.91	26.54 ± 9.12	
		8		4.93 ± 0.49	17.63 ± 3.93	
Chitosan	BNC	0	90	21.07 ± 1.64	33.84 ± 2.51	[322]
		2	100	27.03 ± 1.46	29.71 ± 2.15	
		4	100	41.32 ± 2.20	23.76 ± 1.52	
		6	110	34.75 ± 1.02	25.11 ± 2.93	

Note: Tensile strength (TS), and elongation at break (EB)

Chapter I

The incorporation of NCs in coating solutions is generally reported to significantly affect the barrier properties of the films. In some polymeric matrices, the transmission rate of water vapor was reported to increase with NCs addition, because of (i) the increase of hydrophilicity within the polymer [323]; (ii) the change in polymer adsorption since the crystallinity, internal structure, and interaction forces are changed [324]; (iii) the higher concentration of NCs which causes its agglomeration in the film matrix [314]. However, in other cases, the water-vapor barrier properties were reported to increase, because of the increased surface-volume ratio and compactness of film network [322], due to the formation of a network of hydrogen bridges between NCs and the polymeric matrix, which resulted in a winding path for the water molecules, hindering their propagation through films [314,319]. The effect of NCs incorporation in film-forming solution on the barrier properties can therefore be related to the chemical nature of NCs (chemical structure, polarity, degree of crystallinity) and its concentration, as well as the hydrophilicity and hydrophobicity of the film matrix. In addition to using NCs as reinforcement material, ECs can be loaded with different bioactive compounds (as illustrated in Figure I.35) to develop active edible coatings with specific functionalities, such as antimicrobial, anti-browning, antioxidant, coloring, and flavoring, or even nutritive actions [325].
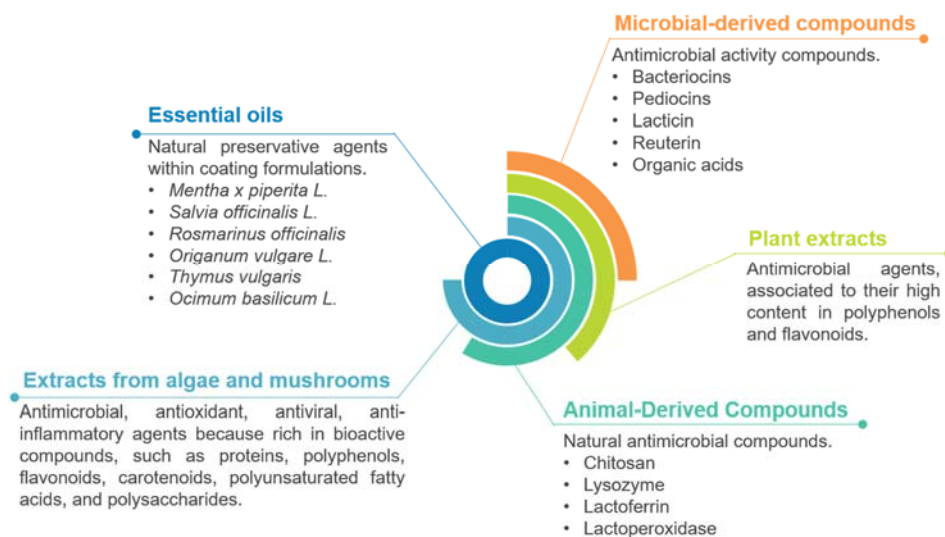
Figure I.35 *Natural compounds frequently used in edible active coatings.*

Examples of NCs addition in active systems are mainly reported in active films for food packaging, where the role of NCs is of stabilization and physical entrapment of the active species. As shown in Table I.5, the main effects of NCs addition to films are related to (i) ensuring high loading of the antimicrobial agents [326] because of the intrinsic high surface area of NCs;

(ii) improving the controlled release characteristics of the bioactive agents loaded in the biopolymer matrix, by affecting their permeation rate [327]; and, therefore (iii) increasing the antioxidant properties of the film [328], when the payload bioactives are antimicrobial agents [329].

Table I.5 *Antioxidant and antimicrobial properties of films reinforced with. NCs.*

Film-forming material	Additives		Effect of NCs on active film	References
	Reinforcing agent	Active agent		
Sodium caseinate (4% w/w)	CNFs (2.5 - 5 wt%)	Cinnamon bark essential oil-nanoemulsion (5 wt%)	NCs decrease the release rate of the essential oil from sodium caseinate matrix and improve the antioxidant properties of the film	[327]
Soy protein (5% w/v)	CNFs (0 - 0.6 wt%)	Clove essential oil (2.5 wt%)	MFC's presence favors the release of the active compounds of CEO. A higher concentration of MFC increases the antioxidant properties as well as the antimicrobial activity	[328]
Mucilage (50% v/v)	CNFs (3 - 6 wt%)	-	NCs incorporation successfully enhances the mechanical, hydrophobic, antioxidant, and antimicrobial properties of the mucilage composite films	[326]
Gelatin/agar (2% w/v)	CNFs (0.75 wt%)	Clove essential oil-based Pickering emulsion (0, 0.02, 0.1, 0.2 wt%)	Composite film is transparent and shows high UV-light barrier properties and water-resistant properties, and improved antioxidant activity	[330]
Poly (butylene adipate-co-terephthalate) (PBAT) (15% w/w)	CNFs (0.5, 1, 3 wt%)	Cinnamon essential oil	Films showed good thermal stability, higher oil release, decreased water vapor permeability values and prevented microbial attack through the release of the essential oil	[331]

Overall, the incorporation of NCs in ECs represents a promising approach for improving ECs' mechanical and barrier properties, stability, and eventual controlled release of active agents, with a potential impact in the preservation of the quality and extension of the shelf life of perishable fruits and vegetables with all-natural systems [48].

NCs are also extensively used as a food additive to improve food homogeneity and replace undesired food additives such as flour substitutes, fat substitutes, frozen food and beverage additives, thickeners, suspension agents, foam stabilizers, high-temperature stabilizers [332,333]. At present, the research on NCs as a food additive has not been carried out in a comprehensive way. Nevertheless, the usage of NCs as an additive in (i) ice cream was reported to enhance the anti-melting properties and improves the sensory properties of taste [334]; (ii) soy milk powder had the role of thickener, shearing dilution, and a slippery taste at the entrance [335]; and (iii)

in baking products was used to replace fats, improving the quality of wheat flours decreasing the browning index [336].

Different experimental findings suggested an innovative application, consisting in using NCs as food-grade particle stabilizer of lipids in Pickering emulsion, benefiting the development of functional foods. NCs are an emerging and novel alternative to synthetic stabilizer particles, due to their sustainability, biodegradability, and nontoxicity. More specifically, Pickering emulsions stabilized by NCs particles have attracted increasing interest in different fields, because they confer noteworthy stability against coalescence, adjustable permeability, and good elastic responses [337,338]. It was demonstrated that nanosized cellulosic materials possess several advantages deriving from their nanometric sizes, such as high tensile strength, stiffness, and surface functional groups. When used as a stabilizer in O/W emulsions, NCs are reported to significantly enhance the properties and performance in comparison with conventional systems [339]. Moreover, the morphological structure of cellulose nanoparticles can influence the stability of emulsions. In this sense, cellulose through HPH treatment resulted to be characterized by fibril bundles, with lengths in the range of ~10 - 100 µm and irregular widths. This kind of defibrillated NCs exhibited higher mobility and flexibility at the oil-water interface than NCs obtained via BM, resulting in an efficient emulsifying ability at different pH values, with the fibrils wrapping around the oil droplets for their stabilization. Nevertheless, the finding showed that cellulose nanoparticles could stabilize emulsions containing high oil phase, and moreover defibrillated NCs stabilize emulsions, which have good ability to resist the environment change, limiting the occurrence of coalescence phenomena and significantly slowing down gravitational separation [189].

7.4. Biomedical applications

NCs, either as an individual material or part of mixture or composite, have found broad application in biomedical field (Figure I.36) including in implants; skin replacements for burnings and wounds; blood vessel growth; nerves, gum, and dura mater reconstruction; drug releasing system; wound dressing materials and also in biosensors and diagnostics [249,340]. NCs are so interesting for biomedical materials because of their mechanical properties, nanofibrous network, and natural source, which is increasingly important to consumers with regard to health-care products [117].
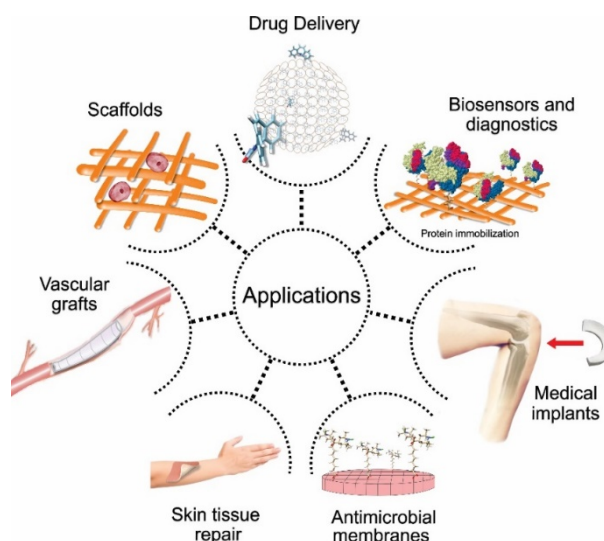
Figure I.36 *Biomedical applications of cellulose nanoparticles [178].*

The biocompatible and biodegradable nature of NCs makes this material ideal for development in the field of tissue engineering, acting to replace or repair damaged organs and tissues [341]. Many studies have been undertaken in developing NCs composites for tissue scaffolds. The NCs with all the requirements of tissue engineering technology, such as superior water absorption, water retention, biocompatibility, and mechanical properties, has been used as a major component or as reinforcement in many formulations for tissue engineering. More in detail, the main application of NCs scaffolds is the repair of skin, vascular, neural, muscular, hepatic, and ophthalmological tissue [342].

To achieve a higher therapeutic effect of a pharmaceutical drug and/or natural compound in a specific diseased site, NCs are a promising material for the delivery of drug molecules. Previous studies have demonstrated the presence of positive molecular interactions between CNFs and poorly-soluble drugs. Indeed, CNFs have been applied to stabilize crystalline nanoparticles of drugs and preserve the nanoparticulate morphology, both in aqueous suspension during storage but also upon freeze drying of these suspensions [343–348]. CNCs were also utilized as a vehicle for drug-delivery systems. Indeed, CNCs was used as (i) stabilizer of the alginate matrix to produce higher encapsulation and control the release rate of theophylline (in the treatment of respiratory-related illness) and of bovine serum albumin (BSA) [349,350]; (ii) as a drug carrier of doxorubicin hydrochloride (DOX) and tetracycline hydrochloride (TET) thanks to the negatively charged surface which interacts with the positive charge of drugs [351]; and (iii) as the element for encapsulation of hydrophobic anticancer compounds, such as etoposide (ETOP), docetaxel (DTX) and paclitaxel (PTX) showing a slower and controlled release of the drugs [341].

NCs can also be used as stimulus-responsive material for sensors and biodiagnostic, for detecting heat, ions, organic vapors, and biological organisms. For example, Wang et al. 2016 demonstrated that CNCs can be used in combination with silver nanoparticles to develop colorimetric and non-enzymatic biosensors for detecting glucose [352]. A NCs-based biosensor was designed to make use of enzymatic stimuli for the detection of cholesterol [353]. Ling et al. (2019) reported the design of NCs-based biosensors for facile detection of human neutrophil elastase [354].

7.5. Energy materials and devices

Recent years have seen an upsurge in research aiming to use of NCs in most energy applications, due to nanoscale functionality, sustainability, and biodegradability. In order to provide a high volumetric capacitance, NCs provide the required mechanical support for freestanding and flexible materials and are combined with a conductive material, usually a polymer [247]. Among other applications, high-performance energy storage units (such as lithium-ion batteries, supercapacitors and solar cells, and electrochemical energy storage devices) [355]; conductive NCs sheets for the development of conductive displays, sensors, transducers, and actuators [356]; high performing supercapacitors [357–359] and optoelectronics [360–364] are the main ongoing advances in the energy and devices field.

7.6. Other applications

7.6.1. Adsorption, filtration, and purification

NCs composites can find several application fields, for example in (i) adsorbent in environmental remediation pollutants for water decontamination [365,366] and/or for air purification [367]; (ii) catalytic degradation of toxic organic compounds [368]; (iii) adsorbents for oil contamination [369]; (iv) repellents [370,371]; and (v) sensors for waterborne pathogens [372]. Typically, NCs are valued in adsorption and separation processes at relatively low cost due to their high hydrophilicity, morphology, and mechanical properties to form supports, membranes, and pure or hybrid aerogels, solid materials featuring a porous structure and an extremely low density.

Several authors have shown the great performance of NCs and functionalized NCs for chemical contaminant remediation (heavy metal, dye, and organic oil removal) due to their high water permeability, high surface area, good mechanical properties, and versatile surface chemistry. For example, CNCs isolated thought acid hydrolysis, incorporated with succinic acid, was used to remove lead(II) and cadmium(II) ions from water [373]; CNFs containing carboxylate groups prepared by oxidation methods were used for chromium(III), nickle(II), and uranyl(II) ion removal [374,375].

A recent study by Sharma demonstrated that carboxycellulose nanofibers extracted from an arid spinifex grass using the nitro-oxidation method can be used as an effective flocculating or coagulating agent to remove cadmium(II) ions from water [376]. In addition, thiol-modified nanofibers were found to be effective for chromium(VI) and lead(II) removal [377], and amine-modified CNCs were capable of removing negatively charged chromium(VI) metal ions from water [378].

NCs membranes or NCs aerogels often showed also to be effective media for pressure-driven filtration operations both for water and air purification. Electrospun cellulose acetate membranes functionalized with CNCs showed an adsorption rate for cationic Victoria Blue 2B dye between 80 and 99% compared to pristine cellulose acetate membranes [379]. The amino-functionalized CNCs, obtained by grafting with ethylenediamine through a reductive amination treatment, was demonstrated to be an effective adsorbent material to remove anionic dyes from aqueous solutions [380]. NCs membranes were found to be excellent CO_2 barriers, allowing CO_2 to be efficiently separated from N_2 and CH_4, even under high humidity [381]. The aerogel of cellulose nanofibrils functionalized through TEMPO-mediated oxidation proved to be efficient air filters with insignificant pressure drops with a better performer than conventional filters [367].

NCs-based systems have been also widely used in chromatographic columns to separate chiral enantiomers, necessary for pharmaceutical, clinical, food, and environmental sciences [117,247,382–384]. Traditionally, various chromatographic techniques have been used, such as high-pressure liquid chromatography (HPLC), gas chromatography (GC), supercritical fluid chromatography (SCFC), and capillary liquids. Owing to the long analysis times and the use of very costly chiral stationary phases, CNCs can be used as a valuable chiral stationary phase, due to the ability to transform into a chiral liquid-crystalline phase at a critical concentration and with tunable hydrophobicity and hydrophilicity [385–387].

7.6.2. Cosmetics

NCs are also increasingly used in the field of cosmetic formulations [388], due to its easy penetration through the skin toward the targeted tissue [389]. NCs have drawn attention mostly as a thickening agent and texture modifier in cosmetics and skincare formulations as are capable to alter gelation temperature and viscosity [249]. For example, polyvinyl alcohol and polystyrene films incorporated with cinnamate-functionalized CNCs displayed an excellent UV-shielding capacity for sunscreen and transparency with enhanced Young's moduli [390]. Moreover, the high hydrophilic nature and ability of NCs to form stable dispersions in water are harnessed to produce cosmetics products suitable for hair, eyelashes, eyebrows, and nails [391]. Because of its three-dimensional, nanoporous structure, this biopolymer has proven to be an effective material that is suitable for cosmetic product

formulations. In general, the usage of NCs in cosmetics is an excellent and simple route to ensure high and greener products, with improved mechanical properties. In parallel, the World Health Organization (WHO) expressed concerns about the effect, toxicity, and safety of nanomaterials on human health, and administrative directives have been introduced [392].

8. References

1.   Assembly U.G Transforming Our World: The 2030 Agenda for Sustainable Development. In *A New Era in Global Health*; 2018.

2.   Sánchez, Ó.J.; Cardona, C.A. Trends in biotechnological production of fuel ethanol from different feedstocks. *Bioresour. Technol.* 2008.

3.   Yang, Z.; Xu, S.; Ma, X.; Wang, S. Characterization and acetylation behavior of bamboo pulp. *Wood Sci. Technol.* **2008**, doi:10.1007/s00226-008-0194-5.

4.   Ragauskas, A.J.; Williams, C.K.; Davison, B.H.; Britovsek, G.; Cairney, J.; Eckert, C.A.; Frederick, W.J.; Hallett, J.P.; Leak, D.J.; Liotta, C.L.; et al. The path forward for biofuels and biomaterials. *Science (80-.).* 2006.

5.   McKendry, P. Energy production from biomass (part 1): Overview of biomass. *Bioresour. Technol.* **2002**, doi:10.1016/S0960-8524(01)00118-3.

6.   Das, A.M.; Hazarika, M.P.; Goswami, M.; Yadav, A.; Khound, P. Extraction of cellulose from agricultural waste using Montmorillonite K-10/LiOH and its conversion to renewable energy: Biofuel by using Myrothecium gramineum. *Carbohydr. Polym.* **2016**, doi:10.1016/j.carbpol.2015.12.070.

7.   Habibi, Y.; Lucia, L.A.; Rojas, O.J. Cellulose nanocrystals: Chemistry, self-assembly, and applications. *Chem. Rev.* **2010**, doi:10.1021/cr900339w.

8.   Kargarzadeh, H.; Mariano, M.; Huang, J.; Lin, N.; Ahmad, I.; Dufresne, A.; Thomas, S. Recent developments on nanocellulose reinforced polymer nanocomposites: A review. *Polymer (Guildf).* 2017.

9.   Jiang, J.; Zhu, Y.; Jiang, F. Sustainable isolation of nanocellulose from cellulose and lignocellulosic feedstocks: Recent progress and perspectives. *Carbohydr. Polym.* **2021**, doi:10.1016/j.carbpol.2021.118188.

10.   Collazo-Bigliardi, S.; Ortega-Toro, R.; Chiralt Boix, A. Isolation and characterisation of microcrystalline cellulose and cellulose nanocrystals from coffee husk and comparative study with rice husk. *Carbohydr. Polym.* **2018**, doi:10.1016/j.carbpol.2018.03.022.

11.   Pirozzi, A.; Ferrari, G.; Donsì, F. Cellulose Isolation from Tomato Pomace Pretreated by High-Pressure Homogenization. *Foods* **2022**, *11*, 266, doi:doi.org/10.3390/foods11030266.

12.   UNEP *Food Waste Index Report 2021*; 2021; ISBN 9789280738513.

13. Leyva-López, N.; Lizárraga-Velázquez, C.E.; Hernández, C.; Sánchez-Gutiérrez, E.Y. Exploitation of agro-industrial waste as potential source of bioactive compounds for aquaculture. *Foods* 2020.

14. Ayala-Zavala, J.F.; Vega-Vega, V.; Rosas-Domínguez, C.; Palafox-Carlos, H.; Villa-Rodriguez, J.A.; Siddiqui, M.W.; Dávila-Aviña, J.E.; González-Aguilar, G.A. Agro-industrial potential of exotic fruit byproducts as a source of food additives. *Food Res. Int.* 2011.

15. García, A.; Gandini, A.; Labidi, J.; Belgacem, N.; Bras, J. Industrial and crop wastes: A new source for nanocellulose biorefinery. *Ind. Crops Prod.* **2016**, doi:10.1016/j.indcrop.2016.06.004.

16. Contreras, M. del M.; Karimi, K.; Taamalli, A.; Castro, E. Editorial: New Insights Into the Valorization of Agricultural and Agroindustrial Byproducts Through Biorefinery Cascade Processing. *Front. Energy Res.* 2021.

17. Fava, F.; Totaro, G.; Diels, L.; Reis, M.; Duarte, J.; Carioca, O.B.; Poggi-Varaldo, H.M.; Ferreira, B.S. Biowaste biorefinery in Europe: Opportunities and research & development needs. *N. Biotechnol.* **2015**, doi:10.1016/j.nbt.2013.11.003.

18. Cristóbal, J.; Caldeira, C.; Corrado, S.; Sala, S. Techno-economic and profitability analysis of food waste biorefineries at European level. *Bioresour. Technol.* **2018**, doi:10.1016/j.biortech.2018.03.016.

19. Ilyas, T.; Chowdhary, P.; Chaurasia, D.; Gnansounou, E.; Pandey, A.; Chaturvedi, P. Sustainable green processing of grape pomace for the production of value-added products: An overview. *Environ. Technol. Innov.* 2021.

20. Abbasi-Parizad, P.; De Nisi, P.; Scaglia, B.; Scarafoni, A.; Pilu, S.; Adani, F. Recovery of phenolic compounds from agro-industrial by-products: Evaluating antiradical activities and immunomodulatory properties. *Food Bioprod. Process.* **2021**, doi:10.1016/j.fbp.2021.03.015.

21. Hejna, A. Potential applications of by-products from the coffee industry in polymer technology – Current state and perspectives. *Waste Manag.* 2021.

22. Kovalcik, A.; Obruca, S.; Marova, I. Valorization of spent coffee grounds: A review. *Food Bioprod. Process.* 2018.

23. Freitas, C.S.; Da Silva, G.A.; Perrone, D.; Vericimo, M.A.; Dos S. Baião, D.; Pereira, P.R.; Paschoalin, V.M.F.; Del Aguila, E.M. Recovery of antimicrobials and bioaccessible isoflavones and phenolics from soybean (glycine max) meal by aqueous extraction. *Molecules* **2019**, doi:10.3390/molecules24010074.

24. Tsouko, E.; Alexandri, M.; Fernandes, K.V.; Freire, D.M.G.; Mallouchos, A.; Koutinas, A.A. Extraction of phenolic compounds from palm oil processing residues and their application as antioxidants. *Food Technol. Biotechnol.* **2019**, doi:10.17113/ftb.57.01.19.5784.

25. Fermoso, F.G.; Serrano, A.; Alonso-Fariñas, B.; Fernández-Bolaños, J.; Borja, R.; Rodríguez-Gutiérrez, G. Valuable Compound Extraction, Anaerobic Digestion, and Composting: A Leading Biorefinery Approach for Agricultural Wastes. *J. Agric. Food Chem.* 2018.

26. Mourtzinos, I.; Goula, A. Polyphenols in Agricultural Byproducts and Food Waste. In *Polyphenols in Plants*; 2019.

27. M'hiri, N.; Ioannou, I.; Ghoul, M.; Mihoubi Boudhrioua, N. Phytochemical characteristics of citrus peel and effect of conventional and nonconventional processing on phenolic compounds: A review. *Food Rev. Int.* 2017.

28. Panzella, L.; Napolitano, A. Natural phenol polymers: Recent advances in food and health applications. *Antioxidants* 2017.

29. Verotta, L.; Panzella, L.; Antenucci, S.; Calvenzani, V.; Tomay, F.; Petroni, K.; Caneva, E.; Napolitano, A. Fermented pomegranate wastes as sustainable source of ellagic acid: Antioxidant properties, anti-inflammatory action, and controlled release under simulated digestion conditions. *Food Chem.* **2018**, doi:10.1016/j.foodchem.2017.10.131.

30. Eberhardt, M. V.; Lee, C.Y.; Liu, R.H. Antioxidant activity of fresh apples. *Nature* **2000**, doi:10.1038/35016151.

31. Panzella, L.; Petriccione, M.; Rega, P.; Scortichini, M.; Napolitano, A. A reappraisal of traditional apple cultivars from Southern Italy as a rich source of phenols with superior antioxidant activity. In Proceedings of the Food Chemistry; 2013.

32. Wiltshire, E.J.; Eady, C.C.; Collings, D.A. Induction of anthocyanin in the inner epidermis of red onion leaves by environmental stimuli and transient expression of transcription factors. *Plant Cell Rep.* **2017**, doi:10.1007/s00299-017-2132-1.

33. Akhtar, S.; Rauf, A.; Imran, M.; Qamar, M.; Riaz, M.; Mubarak, M.S. Black carrot (Daucus carota L.), dietary and health promoting perspectives of its polyphenols: A review. *Trends Food Sci. Technol.* 2017.

34. Kelebek, H.; Selli, S.; Kadiroğlu, P.; Kola, O.; Kesen, S.; Uçar, B.; Çetiner, B. Bioactive compounds and antioxidant potential in tomato pastes as affected by hot and cold break process. *Food Chem.* **2017**, doi:10.1016/j.foodchem.2016.09.190.

35. Laddomada, B.; Caretto, S.; Mita, G. Wheat bran phenolic acids: Bioavailability and stability in whole wheat-based foods. *Molecules* 2015.

36. Wang, X.; Wang, S.; Huang, S.; Zhang, L.; Ge, Z.; Sun, L.; Zong, W. Purification of polyphenols from distiller's grains by macroporous resin and analysis of the polyphenolic components. *Molecules* **2019**, doi:10.3390/molecules24071284.

37. Meullemiestre, A.; Kamal, I.; Maache-Rezzoug, Z.; Chemat, F.; Rezzoug, S.A. Antioxidant activity and total phenolic content of oils extracted from Pinus pinaster sawdust waste. Screening of different innovative isolation

techniques. *Waste and Biomass Valorization* **2014**, doi:10.1007/s12649-013-9237-8.

38. Meullemiestre, A.; Petitcolas, E.; Maache-Rezzoug, Z.; Chemat, F.; Rezzoug, S.A. Impact of ultrasound on solid-liquid extraction of phenolic compounds from maritime pine sawdust waste. Kinetics, optimization and large scale experiments. *Ultrason. Sonochem.* **2016**, doi:10.1016/j.ultsonch.2015.07.022.

39. Araújo, D.J.C.; Machado, A.V.; Vilarinho, M.C.L.G. Availability and Suitability of Agroindustrial Residues as Feedstock for Cellulose-Based Materials: Brazil Case Study. *Waste and Biomass Valorization* **2019**, doi:10.1007/s12649-018-0291-0.

40. Ortega, C. Renewable resources for biorefineries. *Green Process. Synth.* **2015**, doi:10.1515/gps-2015-0008.

41. Tuck, C.O.; Pérez, E.; Horváth, I.T.; Sheldon, R.A.; Poliakoff, M. Valorization of biomass: Deriving more value from waste. *Science (80-.).* 2012.

42. Urruzola, I.; Robles, E.; Serrano, L.; Labidi, J. Nanopaper from almond (Prunus dulcis) shell. *Cellulose* **2014**, doi:10.1007/s10570-014-0238-y.

43. Brandt, A.; Gräsvik, J.; Hallett, J.P.; Welton, T. Deconstruction of lignocellulosic biomass with ionic liquids. *Green Chem.* 2013.

44. Siqueira, G.; Bras, J.; Dufresne, A. Cellulosic bionanocomposites: A review of preparation, properties and applications. *Polymers (Basel).* 2010.

45. Flauzino Neto, W.P.; Silvério, H.A.; Dantas, N.O.; Pasquini, D. Extraction and characterization of cellulose nanocrystals from agro-industrial residue - Soy hulls. *Ind. Crops Prod.* **2013**, doi:10.1016/j.indcrop.2012.06.041.

46. Tang, Y.; Shen, X.; Zhang, J.; Guo, D.; Kong, F.; Zhang, N. Extraction of cellulose nano-crystals from old corrugated container fiber using phosphoric acid and enzymatic hydrolysis followed by sonication. *Carbohydr. Polym.* **2015**, doi:10.1016/j.carbpol.2015.02.063.

47. Kunaver, M.; Anžlovar, A.; Žagar, E. The fast and effective isolation of nanocellulose from selected cellulosic feedstocks. *Carbohydr. Polym.* **2016**, doi:10.1016/j.carbpol.2016.04.076.

48. Pirozzi, A.; Ferrari, G.; Donsì, F. The use of nanocellulose in edible coatings for the preservation of perishable fruits and vegetables. *Coatings* 2021.

49. Klemm, D.; Heublein, B.; Fink, H.P.; Bohn, A. Cellulose: Fascinating biopolymer and sustainable raw material. *Angew. Chemie - Int. Ed.* 2005.

50. Abdul Khalil, H.P.S.; Davoudpour, Y.; Islam, M.N.; Mustapha, A.; Sudesh, K.; Dungani, R.; Jawaid, M. Production and modification of nanofibrillated cellulose using various mechanical processes: A review. *Carbohydr. Polym.* 2014.

51. Dufresne, A. Nanocellulose: A new ageless bionanomaterial. *Mater. Today* 2013.

52. Kargarzadeh, H.; Ahmad, I.; Thomas, S.; Dufresne, A. *Handbook of Nanocellulose and Cellulose Nanocomposites*; Kargarzadeh, H., Ahmad, I., Thomas, S., Dufresne, A., Eds.; Wiley-VCH Verlag GmbH & Co. KGaA: Weinheim, Germany, 2017;

53. Trache, D.; Tarchoun, A.F.; Derradji, M.; Hamidon, T.S.; Masruchin, N.; Brosse, N.; Hussin, M.H. Nanocellulose: From Fundamentals to Advanced Applications. *Front. Chem.* 2020.

54. Fukuzumi, H.; Saito, T.; Iwata, T.; Kumamoto, Y.; Isogai, A. Transparent and high gas barrier films of cellulose nanofibers prepared by TEMPO-mediated oxidation. *Biomacromolecules* **2009**, doi:10.1021/bm801065u.

55. Moon, R.J.; Martini, A.; Nairn, J.; Simonsen, J.; Youngblood, J. Cellulose nanomaterials review: Structure, properties and nanocomposites. *Chem. Soc. Rev.* **2011**, doi:10.1039/c0cs00108b.

56. Abdul Khalil, H.P.S.; Bhat, A.H.; Ireana Yusra, A.F. Green composites from sustainable cellulose nanofibrils: A review. *Carbohydr. Polym.* 2012.

57. Mondal, S. Review on Nanocellulose Polymer Nanocomposites. *Polym. - Plast. Technol. Eng.* 2018.

58. Amara, C.; El Mahdi, A.; Medimagh, R.; Khwaldia, K. Nanocellulose-based composites for packaging applications. *Curr. Opin. Green Sustain. Chem.* **2021**, doi:10.1016/j.cogsc.2021.100512.

59. Tayeb, A.H.; Amini, E.; Ghasemi, S.; Tajvidi, M. Cellulose nanomaterials-binding properties and applications: A review. *Molecules* 2018.

60. Thomas, P.; Duolikun, T.; Rumjit, N.P.; Moosavi, S.; Lai, C.W.; Bin Johan, M.R.; Fen, L.B. Comprehensive review on nanocellulose: Recent developments, challenges and future prospects. *J. Mech. Behav. Biomed. Mater.* 2020.

61. Rana, A.K.; Frollini, E.; Thakur, V.K. Cellulose nanocrystals: Pretreatments, preparation strategies, and surface functionalization. *Int. J. Biol. Macromol.* **2021**, *182*, 1554–1581, doi:10.1016/j.ijbiomac.2021.05.119.

62. Lavoine, N.; Desloges, I.; Dufresne, A.; Bras, J. Microfibrillated cellulose - Its barrier properties and applications in cellulosic materials: A review. *Carbohydr. Polym.* 2012.

63. Cellulose Lab Nanocellulose, Cellulose NanoCrystal (CNC or NCC), Cellulose Nanofibrils (CNF) and Bacterial Cellulose (BC) Supplier Available online: https://www.celluloselab.com/.

64. Squinca, P.; Bilatto, S.; Badino, A.C.; Farinas, C.S. Nanocellulose Production in Future Biorefineries: An Integrated Approach Using Tailor-Made Enzymes. *ACS Sustain. Chem. Eng.* **2020**, doi:10.1021/acssuschemeng.9b06790.

65. Abol-Fotouh, D.; Hassan, M.A.; Shokry, H.; Roig, A.; Azab, M.S.; Kashyout, A.E.H.B. Bacterial nanocellulose from agro-industrial wastes: low-cost and enhanced production by Komagataeibacter saccharivorans MD1. *Sci. Rep.* **2020**, doi:10.1038/s41598-020-60315-9.

66. Chen, Q.; Xiong, J.; Chen, G.; Tan, T. Preparation and characterization of highly transparent hydrophobic nanocellulose film using corn husks as main material. *Int. J. Biol. Macromol.* **2020**, doi:10.1016/j.ijbiomac.2020.04.250.

67. Wang, S.; Wang, X.; Liu, W.; Zhang, L.; Ouyang, H.; Hou, Q.; Fan, K.; Li, J.; Liu, P.; Liu, X. Fabricating cellulose nanofibril from licorice residues and its cellulose composite incorporated with natural nanoparticles. *Carbohydr. Polym.* **2020**, doi:10.1016/j.carbpol.2019.115464.

68. Barbash, V.A.; Yashchenko, O. V. Preparation and application of nanocellulose from non-wood plants to improve the quality of paper and cardboard. *Appl. Nanosci.* **2020**, doi:10.1007/s13204-019-01242-8.

69. Hussin, F.N.N.M.; Attan, N.; Wahab, R.A. Extraction and Characterization of Nanocellulose from Raw Oil Palm Leaves (Elaeis guineensis). *Arab. J. Sci. Eng.* **2020**, doi:10.1007/s13369-019-04131-y.

70. Chen, Q.; Liu, Y.; Chen, G. A comparative study on the starch-based biocomposite films reinforced by nanocellulose prepared from different non-wood fibers. *Cellulose* **2019**, doi:10.1007/s10570-019-02254-x.

71. Lourenço, A.F.; Gamelas, J.A.F.; Sarmento, P.; Ferreira, P.J.T. Enzymatic nanocellulose in papermaking – The key role as filler flocculant and strengthening agent. *Carbohydr. Polym.* **2019**, doi:10.1016/j.carbpol.2019.115200.

72. Jonasson, S.; Bünder, A.; Niittylä, T.; Oksman, K. Isolation and characterization of cellulose nanofibers from aspen wood using derivatizing and non-derivatizing pretreatments. *Cellulose* **2019**, doi:10.1007/s10570-019-02754-w.

73. Zhan, C.B.; Sharma, P.R.; Geng, L.H.; Sharma, S.K.; Wang, R.F.; Joshi, R.; Hsiao, B.S. Structural characterization of carboxyl cellulose nanofibers extracted from underutilized sources. *Sci. China Technol. Sci.* **2019**, doi:10.1007/s11431-018-9441-1.

74. Dahlem, M.A.; Borsoi, C.; Hansen, B.; Catto, A.L. Evaluation of different methods for extraction of nanocellulose from yerba mate residues. *Carbohydr. Polym.* **2019**, doi:10.1016/j.carbpol.2019.04.064.

75. Franco, T.S.; Potulski, D.C.; Viana, L.C.; Forville, E.; de Andrade, A.S.; de Muniz, G.I.B. Nanocellulose obtained from residues of peach palm extraction (Bactris gasipaes). *Carbohydr. Polym.* **2019**, doi:10.1016/j.carbpol.2019.04.035.

76. Jordan, J.H.; Easson, M.W.; Dien, B.; Thompson, S.; Condon, B.D. Extraction and characterization of nanocellulose crystals from cotton gin motes and cotton gin waste. *Cellulose* **2019**, doi:10.1007/s10570-019-02533-7.

77. Okahisa, Y.; Furukawa, Y.; Ishimoto, K.; Narita, C.; Intharapichai, K.; Ohara, H. Comparison of cellulose nanofiber properties produced from different parts of the oil palm tree. *Carbohydr. Polym.* **2018**, doi:10.1016/j.carbpol.2018.06.089.

78. Liu, X.; Jiang, Y.; Qin, C.; Yang, S.; Song, X.; Wang, S.; Li, K. Enzyme-assisted mechanical grinding for cellulose nanofibers from bagasse: energy consumption and nanofiber characteristics. *Cellulose* **2018**, doi:10.1007/s10570-018-2071-1.

79. Yahya, M.; Chen, Y.W.; Lee, H.V.; Hassan, W.H.W. Reuse of Selected Lignocellulosic and Processed Biomasses as Sustainable Sources for the Fabrication of Nanocellulose via Ni(II)-Catalyzed Hydrolysis Approach: A Comparative Study. *J. Polym. Environ.* **2018**, doi:10.1007/s10924-017-1167-2.

80. Yue, D.; Qian, X. Isolation and rheological characterization of cellulose nanofibrils (CNFs) from coir fibers in comparison to wood and cotton. *Polymers (Basel).* **2018**, doi:10.3390/polym10030320.

81. Chen, Y.W.; Lee, H.V. Revalorization of selected municipal solid wastes as new precursors of "green" nanocellulose via a novel one-pot isolation system: A source perspective. *Int. J. Biol. Macromol.* **2018**, doi:10.1016/j.ijbiomac.2017.08.143.

82. Ma, H.; Hsiao, B.S. Nanocellulose Extracted from Defoliation of Ginkgo Leaves. In Proceedings of the MRS Advances; 2018.

83. Harini, K.; Ramya, K.; Sukumar, M. Extraction of nano cellulose fibers from the banana peel and bract for production of acetyl and lauroyl cellulose. *Carbohydr. Polym.* **2018**, doi:10.1016/j.carbpol.2018.08.081.

84. Serra, A.; González, I.; Oliver-Ortega, H.; Tarrès, Q.; Delgado-Aguilar, M.; Mutjé, P. Reducing the amount of catalyst in TEMPO-oxidized cellulose nanofibers: Effect on properties and cost. *Polymers (Basel).* **2017**, doi:10.3390/polym9110557.

85. Balea, A.; Merayo, N.; De La Fuente, E.; Negro, C.; Blanco, Á. Assessing the influence of refining, bleaching and TEMPO-mediated oxidation on the production of more sustainable cellulose nanofibers and their application as paper additives. *Ind. Crops Prod.* **2017**, doi:10.1016/j.indcrop.2016.12.050.

86. Pinto, F.; Gominho, J.; André, R.N.; Gonçalves, D.; Miranda, M.; Varela, F.; Neves, D.; Santos, J.; Lourenço, A.; Pereira, H. Improvement of gasification performance of Eucalyptus globulus stumps with torrefaction and densification pre-treatments. *Fuel* **2017**, doi:10.1016/j.fuel.2017.06.008.

87. Lam, N.T.; Chollakup, R.; Smitthipong, W.; Nimchua, T.; Sukyai, P. Characterization of Cellulose Nanocrystals Extracted from Sugarcane Bagasse for Potential Biomedical Materials. *Sugar Tech* **2017**, doi:10.1007/s12355-016-0507-1.

88. Zhuo, X.; Wei, J.; Xu, J.F.; Pan, R.T.; Zhang, G.; Guo, Y.L.; Dong, X.Y.; Long, L.; Li, Y.F. Nanocellulose isolation from amorpha fruticosa by

an enzyme-assisted pretreatment. *Appl. Environ. Biotechnol.* **2017**, doi:10.26789/AEB.2017.01.005.

89. Barbash, V.A.; Yaschenko, O. V.; Shniruk, O.M. Preparation and Properties of Nanocellulose from Organosolv Straw Pulp. *Nanoscale Res. Lett.* **2017**, doi:10.1186/s11671-017-2001-4.

90. Sehaqui, H.; Mautner, A.; Perez De Larraya, U.; Pfenninger, N.; Tingaut, P.; Zimmermann, T. Cationic cellulose nanofibers from waste pulp residues and their nitrate, fluoride, sulphate and phosphate adsorption properties. *Carbohydr. Polym.* **2016**, doi:10.1016/j.carbpol.2015.08.091.

91. Chen, Y.W.; Lee, H.V.; Juan, J.C.; Phang, S.M. Production of new cellulose nanomaterial from red algae marine biomass Gelidium elegans. *Carbohydr. Polym.* **2016**, doi:10.1016/j.carbpol.2016.06.083.

92. Liu, C.; Li, B.; Du, H.; Lv, D.; Zhang, Y.; Yu, G.; Mu, X.; Peng, H. Properties of nanocellulose isolated from corncob residue using sulfuric acid, formic acid, oxidative and mechanical methods. *Carbohydr. Polym.* **2016**, doi:10.1016/j.carbpol.2016.06.025.

93. Fortunati, E.; Luzi, F.; Jiménez, A.; Gopakumar, D.A.; Puglia, D.; Thomas, S.; Kenny, J.M.; Chiralt, A.; Torre, L. Revalorization of sunflower stalks as novel sources of cellulose nanofibrils and nanocrystals and their effect on wheat gluten bionanocomposite properties. *Carbohydr. Polym.* **2016**, doi:10.1016/j.carbpol.2016.04.120.

94. Rambabu, N.; Panthapulakkal, S.; Sain, M.; Dalai, A.K. Production of nanocellulose fibers from pinecone biomass: Evaluation and optimization of chemical and mechanical treatment conditions on mechanical properties of nanocellulose films. *Ind. Crops Prod.* **2016**, doi:10.1016/j.indcrop.2015.11.083.

95. Kallel, F.; Bettaieb, F.; Khiari, R.; García, A.; Bras, J.; Chaabouni, S.E. Isolation and structural characterization of cellulose nanocrystals extracted from garlic straw residues. *Ind. Crops Prod.* **2016**, doi:10.1016/j.indcrop.2016.04.060.

96. Oun, A.A.; Rhim, J.W. Isolation of cellulose nanocrystals from grain straws and their use for the preparation of carboxymethyl cellulose-based nanocomposite films. *Carbohydr. Polym.* **2016**, doi:10.1016/j.carbpol.2016.05.020.

97. Xie, J.; Hse, C.Y.; Shupe, T.F.; Pan, H.; Hu, T. Extraction and characterization of holocellulose fibers by microwave-assisted selective liquefaction of bamboo. *J. Appl. Polym. Sci.* **2016**, doi:10.1002/app.43394.

98. Trache, D.; Hussin, M.H.; Haafiz, M.K.M.; Thakur, V.K. Recent progress in cellulose nanocrystals: Sources and production. *Nanoscale* 2017.

99. Abitbol, T.; Rivkin, A.; Cao, Y.; Nevo, Y.; Abraham, E.; Ben-Shalom, T.; Lapidot, S.; Shoseyov, O. Nanocellulose, a tiny fiber with huge applications. *Curr. Opin. Biotechnol.* 2016.

100. John, M.J.; Thomas, S. Biofibres and biocomposites. *Carbohydr. Polym.* 2008.

101.   Camarero-Espinosa, S.; Boday, D.J.; Weder, C.; Foster, E.J. Cellulose nanocrystal driven crystallization of poly(d, 1 -lactide) and improvement of the thermomechanical properties. *J. Appl. Polym. Sci.* **2015**, doi:10.1002/app.41607.

102.   Usov, I.; Nyström, G.; Adamcik, J.; Handschin, S.; Schütz, C.; Fall, A.; Bergström, L.; Mezzenga, R. Understanding nanocellulose chirality and structure-properties relationship at the single fibril level. *Nat. Commun.* **2015**, doi:10.1038/ncomms8564.

103.   Zhang, J.; Zhang, J.; Luo, N.; Zhang, X.; Xu, L.; Wu, J.; Yu, J.; He, J. All-Cellulose Nanocomposites Reinforced with in Situ Retained Cellulose Nanocrystals during Selective Dissolution of Cellulose in an Ionic Liquid. *ACS Sustain. Chem. Eng.* **2016**, doi:10.1021/acssuschemeng.6b01034.

104.   Nishino, T.; Matsuda, I.; Hirao, K. All-cellulose composite. *Macromolecules* **2004**, doi:10.1021/ma049300h.

105.   Petersson, L.; Kvien, I.; Oksman, K. Structure and thermal properties of poly(lactic acid)/cellulose whiskers nanocomposite materials. *Compos. Sci. Technol.* **2007**, doi:10.1016/j.compscitech.2006.12.012.

106.   Ye, C.; Malak, S.T.; Hu, K.; Wu, W.; Tsukruk, V. V. Cellulose Nanocrystal Microcapsules as Tunable Cages for Nano- and Microparticles. *ACS Nano* **2015**, doi:10.1021/acsnano.5b03905.

107.   Liu, H.; Liu, D.; Yao, F.; Wu, Q. Fabrication and properties of transparent polymethylmethacrylate/cellulose nanocrystals composites. *Bioresour. Technol.* **2010**, doi:10.1016/j.biortech.2010.02.045.

108.   Shafiei-Sabet, S.; Hamad, W.Y.; Hatzikiriakos, S.G. Rheology of nanocrystalline cellulose aqueous suspensions. *Langmuir* **2012**, doi:10.1021/la303380v.

109.   Ureña-Benavides, E.E.; Ao, G.; Davis, V.A.; Kitchens, C.L. Rheology and phase behavior of lyotropic cellulose nanocrystal suspensions. *Macromolecules* **2011**, doi:10.1021/ma201649f.

110.   George, J.; Sabapathi, S.N. Cellulose nanocrystals: Synthesis, functional properties, and applications. *Nanotechnol. Sci. Appl.* **2015**, doi:10.2147/NSA.S64386.

111.   Xu, X.; Liu, F.; Jiang, L.; Zhu, J.Y.; Haagenson, D.; Wiesenborn, D.P. Cellulose nanocrystals vs. Cellulose nanofibrils: A comparative study on their microstructures and effects as polymer reinforcing agents. *ACS Appl. Mater. Interfaces* **2013**, doi:10.1021/am302624t.

112.   Nechyporchuk, O.; Belgacem, M.N.; Bras, J. Production of cellulose nanofibrils: A review of recent advances. *Ind. Crops Prod.* **2016**.

113.   Sakurada, I.; Nukushina, Y.; Ito, T. Experimental determination of the elastic modulus of crystalline regions in oriented polymers. *J. Polym. Sci.* **1962**, doi:10.1002/pol.1962.1205716551.

114.   Alemdar, A.; Sain, M. Isolation and characterization of nanofibers from agricultural residues - Wheat straw and soy hulls. *Bioresour. Technol.* **2008**, doi:10.1016/j.biortech.2007.04.029.

115.   Jiang, F.; Han, S.; Hsieh, Y. Lo Controlled defibrillation of rice straw cellulose and self-assembly of cellulose nanofibrils into highly crystalline fibrous materials. *RSC Adv.* **2013**, doi:10.1039/c3ra41646a.

116.   Feng, Y.H.; Cheng, T.Y.; Yang, W.G.; Ma, P.T.; He, H.Z.; Yin, X.C.; Yu, X.X. Characteristics and environmentally friendly extraction of cellulose nanofibrils from sugarcane bagasse. *Ind. Crops Prod.* **2018**, doi:10.1016/j.indcrop.2017.10.041.

117.   Thomas, B.; Raj, M.C.; Athira, B.K.; Rubiyah, H.M.; Joy, J.; Moores, A.; Drisko, G.L.; Sanchez, C. Nanocellulose, a Versatile Green Platform: From Biosources to Materials and Their Applications. *Chem. Rev.* 2018.

118.   Iguchi, M.; Yamanaka, S.; Budhiono, A. Bacterial cellulose - a masterpiece of nature's arts. *J. Mater. Sci.* **2000**, doi:10.1023/A:1004775229149.

119.   Czaja, W.; Romanovicz, D.; Brown, R. malcolm Structural investigations of microbial cellulose produced in stationary and agitated culture. *Cellulose* **2004**, doi:10.1023/b:cell.0000046412.11983.61.

120.   Klemm, D.; Schumann, D.; Kramer, F.; Heßler, N.; Hornung, M.; Schmauder, H.P.; Marsch, S. Nanocelluloses as innovative polymers in research and application. *Adv. Polym. Sci.* 2006.

121.   Faruk, O.; Bledzki, A.K.; Fink, H.; Sain, M. Progress in Polymer Science Biocomposites reinforced with natural fibers : 2000 – 2010. *Prog. Polym. Sci.* **2012**, doi:10.1016/j.progpolymsci.2012.04.003.

122.   Abraham, E.; Deepa, B.; Pothan, L.A.; Jacob, M.; Thomas, S.; Cvelbar, U.; Anandjiwala, R. Extraction of nanocellulose fibrils from lignocellulosic fibres: A novel approach. *Carbohydr. Polym.* **2011**, doi:10.1016/j.carbpol.2011.06.034.

123.   Li, R.; Fei, J.; Cai, Y.; Li, Y.; Feng, J.; Yao, J. Cellulose whiskers extracted from mulberry: A novel biomass production. *Carbohydr. Polym.* **2009**, doi:10.1016/j.carbpol.2008.09.034.

124.   Siqueira, G.; Bras, J.; Dufresne, A. Luffa cylindrica as a lignocellulosic source of fiber, microfibrillated cellulose, and cellulose nanocrystals. *BioResources* **2010**.

125.   Ludueña, L.; Fasce, D.; Alvarez, V.A.; Stefani, P.M. Nanocellulose from rice husk following alkaline treatment to remove silica. *BioResources* **2011**, doi:10.15376/biores.6.2.1440-1453.

126.   Deepa, B.; Abraham, E.; Cherian, B.M.; Bismarck, A.; Blaker, J.J.; Pothan, L.A.; Leao, A.L.; de Souza, S.F.; Kottaisamy, M. Structure, morphology and thermal characteristics of banana nano fibers obtained by steam explosion. *Bioresour. Technol.* **2011**, doi:10.1016/j.biortech.2010.09.030.

127.   Chen, W.; Yu, H.; Liu, Y.; Hai, Y.; Zhang, M.; Chen, P. Isolation and characterization of cellulose nanofibers from four plant cellulose fibers using a chemical-ultrasonic process. *Cellulose* **2011**, doi:10.1007/s10570-011-9497-z.

128.   Jiang, F.; Hsieh, Y. Lo Chemically and mechanically isolated nanocellulose and their self-assembled structures. *Carbohydr. Polym.* **2013**, doi:10.1016/j.carbpol.2013.02.022.

129.   Oksman, K.; Etang, J.A.; Mathew, A.P.; Jonoobi, M. Cellulose nanowhiskers separated from a bio-residue from wood bioethanol production. *Biomass and Bioenergy* **2011**, doi:10.1016/j.biombioe.2010.08.021.

130.   Li, W.; Zhao, X.; Liu, S. Preparation of entangled nanocellulose fibers from APMP and its magnetic functional property as matrix. *Carbohydr. Polym.* **2013**, doi:10.1016/j.carbpol.2013.01.052.

131.   Lu, Z.; Fan, L.; Zheng, H.; Lu, Q.; Liao, Y.; Huang, B. Preparation, characterization and optimization of nanocellulose whiskers by simultaneously ultrasonic wave and microwave assisted. *Bioresour. Technol.* **2013**, doi:10.1016/j.biortech.2013.07.047.

132.   Purkait, B.S.; Ray, D.; Sengupta, S.; Kar, T.; Mohanty, A.; Misra, M. Isolation of cellulose nanoparticles from sesame husk. In Proceedings of the Industrial and Engineering Chemistry Research; 2011.

133.   Fahma, F.; Iwamoto, S.; Hori, N.; Iwata, T.; Takemura, A. Effect of pre-acid-hydrolysis treatment on morphology and properties of cellulose nanowhiskers from coconut husk. *Cellulose* **2011**, doi:10.1007/s10570-010-9480-0.

134.   Rosa, M.F.; Medeiros, E.S.; Malmonge, J.A.; Gregorski, K.S.; Wood, D.F.; Mattoso, L.H.C.; Glenn, G.; Orts, W.J.; Imam, S.H. Cellulose nanowhiskers from coconut husk fibers: Effect of preparation conditions on their thermal and morphological behavior. *Carbohydr. Polym.* **2010**, doi:10.1016/j.carbpol.2010.01.059.

135.   Löbmann, K.; Svagan, A.J. Cellulose nanofibers as excipient for the delivery of poorly soluble drugs. *Int. J. Pharm.* **2017**, *533*, doi:10.1016/j.ijpharm.2017.09.064.

136.   Wang, J.; Hao, X.; Wen, P.; Zhang, T.; Zhang, J. Adsorption and desorption of cellulase on/from lignin pretreated by dilute acid with different severities. *Ind. Crops Prod.* **2020**, *148*, 112309, doi:10.1016/J.INDCROP.2020.112309.

137.   Nasir, M.; Hashim, R.; Sulaiman, O.; Asim, M. Nanocellulose: Preparation methods and applications. In *Cellulose-Reinforced Nanofibre Composites: Production, Properties and Applications*; 2017 ISBN 9780081009659.

138.   Phanthong, P.; Reubroycharoen, P.; Hao, X.; Xu, G.; Abudula, A.; Guan, G. Nanocellulose: Extraction and application. *Carbon Resour. Convers.* **2018**, doi:10.1016/j.crcon.2018.05.004.

139.   Teo, H.L.; Wahab, R.A. Towards an eco-friendly deconstruction of agro-industrial biomass and preparation of renewable cellulose nanomaterials: A review. *Int. J. Biol. Macromol.* **2020**, *161*, 1414–1430, doi:10.1016/J.IJBIOMAC.2020.08.076.

140.   Reshmy, R.; Philip, E.; Paul, S.A.; Madhavan, A.; Sindhu, R.; Binod, P.; Pandey, A.; Sirohi, R. Nanocellulose-based products for sustainable applications-recent trends and possibilities. *Rev. Environ. Sci. Biotechnol.* **2020**, *19*, 779–806, doi:10.1007/s11157-020-09551-z.

141.   Berglund, J.; Azhar, S.; Lawoko, M.; Lindström, M.; Vilaplana, F.; Wohlert, J.; Henriksson, G. The structure of galactoglucomannan impacts the degradation under alkaline conditions. *Cellulose* **2019**, *26*, 2155–2175, doi:10.1007/s10570-018-1737-z.

142.   Noremylia, M.B.; Hassan, M.Z.; Ismail, Z. Recent advancement in isolation, processing, characterization and applications of emerging nanocellulose: A review. *Int. J. Biol. Macromol.* **2022**, *206*, 954–976, doi:10.1016/J.IJBIOMAC.2022.03.064.

143.   Isogai, A. Individualization of nano-sized plant cellulose fibrils: Achieved by direct surface carboxylation using TEMPO catalyst. *Int. Conf. Nanotechnol. For. Prod. Ind. 2009* **2009**, *1*, 49–72.

144.   Saito, T.; Isogai, A. TEMPO-mediated oxidation of native cellulose. The effect of oxidation conditions on chemical and crystal structures of the water-insoluble fractions. *Biomacromolecules* **2004**, *5*, 1983–1989, doi:10.1021/bm0497769.

145.   Isogai, A.; Saito, T.; Fukuzumi, H. TEMPO-oxidized cellulose nanofibers. *Nanoscale* **2011**, *3*, 71–85, doi:10.1039/c0nr00583e.

146.   Wang, J.; Liu, X.; Jin, T.; He, H.; Liu, L. Preparation of nanocellulose and its potential in reinforced composites: A review. *J. Biomater. Sci. Polym. Ed.* **2019**, *30*, 919–946, doi:10.1080/09205063.2019.1612726.

147.   Zhang, H.; Chen, Y.; Wang, S.; Ma, L.; Yu, Y.; Dai, H.; Zhang, Y. Extraction and comparison of cellulose nanocrystals from lemon (Citrus limon) seeds using sulfuric acid hydrolysis and oxidation methods. *Carbohydr. Polym.* **2020**, *238*, 116180, doi:10.1016/J.CARBPOL.2020.116180.

148.   Ng, L.Y.; Wong, T.J.; Ng, C.Y.; Amelia, C.K.M. A review on cellulose nanocrystals production and characterization methods from Elaeis guineensis empty fruit bunches. *Arab. J. Chem.* **2021**, *14*, 103339, doi:10.1016/J.ARABJC.2021.103339.

149.   Haunreiter, K.J.; Dichiara, A.B.; Gustafson, R. Nanocellulose by Ammonium Persulfate Oxidation: An Alternative to TEMPO-Mediated Oxidation. *ACS Sustain. Chem. Eng.* **2022**, *10*, 3882–3891, doi:10.1021/acssuschemeng.1c07814.

150.   Bhat, A.H.; Khan, I.; Usmani, M.A.; Umapathi, R.; Al-Kindy, S.M.Z. Cellulose an ageless renewable green nanomaterial for medical

applications: An overview of ionic liquids in extraction, separation and dissolution of cellulose. *Int. J. Biol. Macromol.* **2019**, *129*, 750–777, doi:10.1016/J.IJBIOMAC.2018.12.190.

151.   Bhatia, S.K.; Jagtap, S.S.; Bedekar, A.A.; Bhatia, R.K.; Patel, A.K.; Pant, D.; Rajesh Banu, J.; Rao, C. V.; Kim, Y.G.; Yang, Y.H. Recent developments in pretreatment technologies on lignocellulosic biomass: Effect of key parameters, technological improvements, and challenges. *Bioresour. Technol.* **2020**, *300*, 122724, doi:10.1016/J.BIORTECH.2019.122724.

152.   Arora, A.; Nandal, P.; Singh, J.; Verma, M.L. Nanobiotechnological advancements in lignocellulosic biomass pretreatment. *Mater. Sci. Energy Technol.* **2020**, *3*, 308–318, doi:10.1016/J.MSET.2019.12.003.

153.   Rieland, J.M.; Love, B.J. Ionic liquids: A milestone on the pathway to greener recycling of cellulose from biomass. *Resour. Conserv. Recycl.* **2020**, *155*, 104678, doi:10.1016/J.RESCONREC.2019.104678.

154.   Liu, Z.; Wang, H.; Li, Z.; Lu, X.; Zhang, X.; Zhang, S.; Zhou, K. Characterization of the regenerated cellulose films in ionic liquids and rheological properties of the solutions. *Mater. Chem. Phys.* **2011**, *128*, 220–227, doi:10.1016/J.MATCHEMPHYS.2011.02.062.

155.   Wen, J.L.; Yuan, T.Q.; Sun, S.L.; Xu, F.; Sun, R.C. Understanding the chemical transformations of lignin during ionic liquid pretreatment. *Green Chem.* **2014**, *16*, 181–190, doi:10.1039/c3gc41752b.

156.   Abdul Khalil, H.P.S.; Davoudpour, Y.; Islam, M.N.; Mustapha, A.; Sudesh, K.; Dungani, R.; Jawaid, M. Production and modification of nanofibrillated cellulose using various mechanical processes: A review. *Carbohydr. Polym.* **2014**, *99*, 649–665, doi:10.1016/J.CARBPOL.2013.08.069.

157.   Achinas, S.; Euverink, G.J.W. Consolidated briefing of biochemical ethanol production from lignocellulosic biomass. *Electron. J. Biotechnol.* **2016**, *23*, 44–53, doi:10.1016/J.EJBT.2016.07.006.

158.   Thongekkaew, J.; Kongsanthia, J. Screening and Identification of Cellulase Producing Yeast from Rongkho Forest, Ubon Ratchathani University. *Bioeng. Biosci.* **2016**, *4*, 29–33, doi:10.13189/bb.2016.040301.

159.   Mariño, M.; Da Silva, L.L.; Durán, N.; Tasic, L. Enhanced materials from nature: Nanocellulose from citrus waste. *Molecules* **2015**, *20*, 5908–5923, doi:10.3390/molecules20045908.

160.   Zaki, M.; Abdul Khalil, H.P.S.; Sabaruddin, F.A.; Bairwan, R.D.; Oyekanmi, A.A.; Alfatah, T.; Danish, M.; Mistar, E.M.; Abdullah, C.K. Microbial treatment for nanocellulose extraction from marine algae and its applications as sustainable functional material. *Bioresour. Technol. Reports* **2021**, *16*, 100811, doi:10.1016/J.BITEB.2021.100811.

161.   Szczesna-antczak, M.H.; Kazimierczak, J.; Antczak, T. Nanotechnology - Methods of Manufacturing Cellulose Nanofibres. *FIBRES Text. East. Eur.* **2012**, *2*, 8–12.

162.   Siró, I.; Plackett, D. Microfibrillated cellulose and new nanocomposite materials: A review. *Cellulose* 2010.

163.   Zuluaga, R.; Putaux, J.-L.; Restrepo, A.; Mondragon, I.; Ganan, P. Cellulose microfibrils from banana farming residues : isolation and characterization. *Cellulose* **2007**, *14*, 585–592, doi:10.1007/s10570-007-9118-z.

164.   Malainine, M.E.; Mahrouz, M.; Dufresne, A. Thermoplastic nanocomposites based on cellulose microfibrils from Opuntia ficus-indica parenchyma cell. *Compos. Sci. Technol.* **2005**, *65*, 1520–1526, doi:10.1016/J.COMPSCITECH.2005.01.003.

165.   Dufresne, A.; Danie`, D.; Dupeyre, D.; Vignon, M.R. *Cellulose Microfibrils from Potato Tuber Cells: Processing and Characterization of Starch-Cellulose Microfibril Composites*; 2000;

166.   Ferrer, A.; Filpponen, I.; Rodríguez, A.; Laine, J.; Rojas, O.J. Valorization of residual Empty Palm Fruit Bunch Fibers (EPFBF) by microfluidization: Production of nanofibrillated cellulose and EPFBF nanopaper. *Bioresour. Technol.* **2012**, *125*, 249–255, doi:10.1016/J.BIORTECH.2012.08.108.

167.   Lee, S.-Y.; Chun, S.-J.; Kang, I.-A.; Park, J.-Y. Preparation of cellulose nanofibrils by high-pressure homogenizer and cellulose-based composite films. *J. Ind. Eng. Chem.* **2009**, *15*, 50–55, doi:10.1016/J.JIEC.2008.07.008.

168.   Lee, S.; Chun, S.; Doh, G.; Kang, I.; Lee, S. Influence of Chemical Modification and Filler Loading on Fundamental Properties of Bamboo Fibers Reinforced Polypropylene Composites. *J. Compos. Mater.* **2009**, *43*, doi:10.1177/0021998309339352.

169.   Panthapulakkal, S.; Sain, M. Preparation and Characterization of Cellulose Nanofibril Films from Wood Fibre and Their Thermoplastic Polycarbonate Composites. *Int. J. Polym. Sci.* **2012**, *2012*, doi:10.1155/2012/381342.

170.   Castoldi, R.; Correa, V.G.; de Morais, G.R.; de Souza, C.G.M.; Bracht, A.; Peralta, R.A.; Peralta-Muniz Moreira, R.F.; Peralta, R.M. Liquid nitrogen pretreatment of eucalyptus sawdust and rice hull for enhanced enzymatic saccharification. *Bioresour. Technol.* **2017**, *224*, 648–655, doi:10.1016/J.BIORTECH.2016.11.099.

171.   Frone, A.N.; Panaitescu, D.M.; Spataru, D.D.; Radovici, C.; Trusca, R.; Somoghi, R. Preparation and characterization of PVA composites with cellulose nanofibers obtained by ultrasonication. *BioResources* **2011**, doi:10.15376/biores.6.1.487-512.

172.   Qua, E.H.; Hornsby, P.R.; Sharma, H.S.S.; Lyons, G.; Mccall, R.D. Preparation and Characterization of Poly(vinyl alcohol) Nanocomposites Made from Cellulose Nanofibers. **2009**, doi:10.1002/app.30116.

173.   Dilamian Babak Noroozi, M.; Dilamian Á Noroozi, M.B. A combined homogenization-high intensity ultrasonication process for individualizaion of cellulose micro-nano fibers from rice straw., doi:10.1007/s10570-019-02469-y.

174.   Spence, K.L.; Venditti, R.A.; Rojas, O.J.; Habibi, Y.; Pawlak, J.J. A comparative study of energy consumption and physical properties of microfibrillated cellulose produced by different processing methods., doi:10.1007/s10570-011-9533-z.

175.   Kubo, M.T.K.; Augusto, P.E.D.; Cristianini, M. Effect of high pressure homogenization (HPH) on the physical stability of tomato juice. *Food Res. Int.* **2013**, doi:10.1016/j.foodres.2012.12.004.

176.   Floury, J.; Desrumaux, A.; Lardières, J. Effect of high-pressure homogenization on droplet size distributions and rheological properties of model oil-in-water emulsions. *Innov. Food Sci. Emerg. Technol.* **2000**, doi:10.1016/S1466-8564(00)00012-6.

177.   Frone, A.N.; Panaitescu, D.M.; Donescu, D. Some aspects concerning the isolation of cellulose micro- and nano-fibers. *UPB Sci. Bull. Ser. B Chem. Mater. Sci.* **2011**.

178.   Rojas, J.; Bedoya, M.; Ciro, Y. Current Trends in the Production of Cellulose Nanoparticles and Nanocomposites for Biomedical Applications. In *Cellulose*; 2015.

179.   Wu, C.; McClements, D.J.; He, M.; Zheng, L.; Tian, T.; Teng, F.; Li, Y. Preparation and characterization of okara nanocellulose fabricated using sonication or high-pressure homogenization treatments. *Carbohydr. Polym.* **2021**, doi:10.1016/j.carbpol.2020.117364.

180.   Li, J.; Wei, X.; Wang, Q.; Chen, J.; Chang, G.; Kong, L.; Su, J.; Liu, Y. Homogeneous isolation of nanocellulose from sugarcane bagasse by high pressure homogenization. *Carbohydr. Polym.* **2012**, doi:10.1016/j.carbpol.2012.07.038.

181.   Piras, C.C.; Fernández-Prieto, S.; De Borggraeve, W.M. Ball milling: A green technology for the preparation and functionalisation of nanocellulose derivatives. *Nanoscale Adv.* 2019.

182.   Pradhan, D.; Jaiswal, A.K.; Jaiswal, S. Emerging technologies for the production of nanocellulose from lignocellulosic biomass. *Carbohydr. Polym.* **2022**, *285*, 119258, doi:10.1016/J.CARBPOL.2022.119258.

183.   Zhang, L.; Tsuzuki, T.; Wang, X. Preparation of cellulose nanofiber from softwood pulp by ball milling. *Cellulose*, doi:10.1007/s10570-015-0582-6.

184.   Ambika, S.; Devasena, M.; Nambi, I.M. Synthesis, characterization and performance of high energy ball milled meso-scale zero

valent iron in Fenton reaction. *J. Environ. Manage.* **2016**, *181*, 847–855, doi:10.1016/J.JENVMAN.2016.06.054.

185. Phanthong, P.; Karnjanakom, S.; Reubroycharoen, P.; Hao, X.; Abudula, A.; Guan, G. A facile one-step way for extraction of nanocellulose with high yield by ball milling with ionic liquid. *Cellulose* **2017**, doi:10.1007/s10570-017-1238-5.

186. Barakat, A.; Mayer-Laigle, C.; Solhy, A.; Arancon, R.A.D.; De Vries, H.; Luque, R. Mechanical pretreatments of lignocellulosic biomass: towards facile and environmentally sound technologies for biofuels production. **2014**, doi:10.1039/c4ra07568d.

187. Kim, H.J.; Lee, S.; Kim, J.; Mitchell, R.J.; Lee, J.H. Environmentally friendly pretreatment of plant biomass by planetary and attrition milling. *Bioresour. Technol.* **2013**, *144*, 50–56, doi:10.1016/J.BIORTECH.2013.06.090.

188. Avolio, R.; Bonadies, I.; Capitani, D.; Errico, M.E.; Gentile, G.; Avella, M. A multitechnique approach to assess the effect of ball milling on cellulose. *Carbohydr. Polym.* **2012**, *87*, 265–273, doi:10.1016/j.carbpol.2011.07.047.

189. Pirozzi, A.; Capuano, R.; Avolio, R.; Gentile, G.; Ferrari, G.; Donsì, F. O/W pickering emulsions stabilized with cellulose nanofibrils produced through different mechanical treatments. *Foods* **2021**, doi:10.3390/foods10081886.

190. Xuran, C.M.E.; Min, L.; Huang, W.Y.; Ewulonu, C.M.; Liu, Á.X.; Wu, Á.M.; Huang, Á.Y.; Liu, X. Ultrasound-assisted mild sulphuric acid ball milling preparation of lignocellulose nanofibers (LCNFs) from sunflower stalks (SFS). *Cellulose* **2019**, *26*, 4371–4389, doi:10.1007/s10570-019-02382-4.

191. Ferreira, R.R.; Souza, A.G.; Nunes, L.L.; Shahi, N.; Rangari, V.K.; Rosa, D. dos S. Use of ball mill to prepare nanocellulose from eucalyptus biomass: Challenges and process optimization by combined method. *Mater. Today Commun.* **2020**, doi:10.1016/j.mtcomm.2019.100755.

192. Shen, F.; Su, S.; Zhang, X.; Yang, J.; Qiu, M.; Qi, X. Mechanochemical-assisted production of 5-hydroxymethylfurfural from high concentration of cellulose. *Cellulose* **2020**, *27*, 3013–3023, doi:10.1007/s10570-020-03008-w.

193. Zeng, J.; Liu, L.; Li, J.; Dong, J.; Cheng, Z. Properties of cellulose nanofibril produced from wet ball milling after enzymatic treatment vs. mechanical grinding of bleached softwood kraft fibers. *BioResources* **2020**, *15*, 3809–3820, doi:10.15376/biores.15.2.3809-3820.

194. Jang, S.K.; Hoon Lee, J.; Jung, C.D.; Yu, J.H.; Weon Choi, J.; Choi, I.G.; Kim, H. High yield solvent extraction of hydrothermal and ball-milling treated lignin prior to enzymatic hydrolysis for co-valorization of lignin and cellulose in Miscanthus sacchariflorus. *Fuel* **2020**, *269*, 117428, doi:10.1016/J.FUEL.2020.117428.

195.   Singh, Y.; Meher, J.G.; Raval, K.; Khan, F.A.; Chaurasia, M.; Jain, N.K.; Chourasia, M.K. Nanoemulsion: Concepts, development and applications in drug delivery. *J. Control. Release* **2017**, *252*, 28–49, doi:10.1016/J.JCONREL.2017.03.008.

196.   Kassab, Z.; Mansouri, S.; Tamraoui, Y.; Sehaqui, H.; Hannache, H.; Qaiss, A.E.K.; El Achaby, M. Identifying Juncus plant as viable source for the production of micro- and nano-cellulose fibers: Application for PVA composite materials development. *Ind. Crops Prod.* **2020**, *144*, 112035, doi:10.1016/J.INDCROP.2019.112035.

197.   Araya-Chavarría, K.; Rojas, R.; Ramírez-Amador, K.; Sulbarán-Rangel, B.; Rojas, O.; Esquivel-Alfaro, M.; Sulbarán-Rangel Belkissulbaran, B.; Esquivel-Alfaro mesquive, M. Cellulose Nanofibers as Functional Biomaterial from Pineapple Stubbles via TEMPO Oxidation and Mechanical Process Statement of Novelty. *Waste and Biomass Valorization* **2022**, *13*, 1749–1758, doi:10.1007/s12649-021-01619-3.

198.   Frone, A.; Nicoleta, D.; Donescu, D. Some aspects concerning the isolation of cellulose micro- and nano-fibers. *Sci. Bull. Politeh. Bucharest* **2011**, *73*.

199.   Frone, A.N.; Panaitescu, D.; Donescu, D.; Spataru, C.I.; Radovici, C.; Trusca, R.; Somoghi, R. Preparation and characterization of PVA composites with cellulose nanofibers obtained by ultrasonication. *Bioresources* **2011**, *6*, 487.

200.   Chen, P.; Yu, H.; Liu, Y.; Chen, W.; Wang, X.; Ouyang, M. Concentration effects on the isolation and dynamic rheological behavior of cellulose nanofibers via ultrasonic processing. *cn123Cellulose* **2013**, *20*, 149–157, doi:10.1007/s10570-012-9829-7.

201.   Phanthong, P.; Reubroycharoen, P.; Hao, X.; Xu, G.; Abudula, A.; Guan, G. Nanocellulose: Extraction and application. *Carbon Resour. Convers.* **2018**, *1*, 32–43, doi:10.1016/J.CRCON.2018.05.004.

202.   González del Campo, M.M.; Caja-Munoz, B.; Darder, M.; Aranda, P.; Vázquez, L.; Ruiz-Hitzky, E. Ultrasound-assisted preparation of nanocomposites based on fibrous clay minerals and nanocellulose from microcrystalline cellulose. *Appl. Clay Sci.* **2020**, *189*, 105538, doi:10.1016/J.CLAY.2020.105538.

203.   Ferreira, R.R.; Souza, A.G.; Nunes, L.L.; Shahi, N.; Rangari, V.K.; Rosa, D. dos S. Use of ball mill to prepare nanocellulose from eucalyptus biomass: Challenges and process optimization by combined method. *Mater. Today Commun.* **2020**, *22*, 100755, doi:10.1016/J.MTCOMM.2019.100755.

204.   Yang, N.; Zhang, W.; Ye, C.; Chen, X.; Ling, S. Nanobiopolymers Fabrication and Their Life Cycle Assessments. *Biotechnol. J.* **2019**, *14*, 1700754, doi:10.1002/biot.201700754.

205.   Ae, K.A.; Yano, H. Comparison of the characteristics of cellulose microfibril aggregates of wood, rice straw and potato tuber. *Cellulose* **2009**, *16*, 1017–1023, doi:10.1007/s10570-009-9334-9.

206.   Abe, K.; Yano, H. Comparison of the characteristics of cellulose microfibril aggregates isolated from fiber and parenchyma cells of Moso bamboo (Phyllostachys pubescens). *Cellulose* **2009**, *17*, 271–277, doi:10.1007/s10570-009-9382-1.

207.   Abe, K. Nanofibrillation of dried pulp in NaOH solutions using bead milling. *Cellulose* **2016**, *23*, 1257–1261, doi:10.1007/s10570-016-0891-4.

208.   Pä, M.; Ankerfors, M.; Kosonen, H.; Nykä, A.; Ahola, S.; O ̈ Sterberg, | M; Ruokolainen, | J; Laine, J.; Larsson, P.T.; Ikkala, O.; et al. Enzymatic Hydrolysis Combined with Mechanical Shearing and High-Pressure Homogenization for Nanoscale Cellulose Fibrils and Strong Gels. *Biomacromolecules* **2007**, *8*, 1934–1941, doi:10.1021/bm061215p.

209.   Henriksson, M.; Henriksson, G.; Berglund, L.A.; Lindström, T. An environmentally friendly method for enzyme-assisted preparation of microfibrillated cellulose (MFC) nanofibers. *Eur. Polym. J.* **2007**, *43*, 3434–3441, doi:10.1016/J.EURPOLYMJ.2007.05.038.

210.   Mondal, S. Preparation, properties and applications of nanocellulosic materials. *Carbohydr. Polym.* **2017**, *163*, 301–316, doi:10.1016/J.CARBPOL.2016.12.050.

211.   Kalia, S.; Kaith, B.S.; Kaur, I. Pretreatments of natural fibers and their application as reinforcing material in polymer composites—A review. *Polym. Eng. Sci.* **2009**, *49*, 1253–1272, doi:10.1002/pen.21328.

212.   Heux, L.; Chauve, G.; Bonini, C. Nonflocculating and chiral-nematic self-ordering of cellulose microcrystals suspensions in nonpolar solvents. *Langmuir* **2000**, *16*, 8210–8212, doi:10.1021/la9913957.

213.   Hubbe, M.; Rojas, O.J.; Lucia, L.A.; Sain, M. Cellulosic nanocomposites: A review. *BioResources* **2008**, *3*, 929–980.

214.   Kang, H.; Liu, R.; Huang, Y. Graft modification of cellulose: Methods, properties and applications. *Polymer (Guildf).* **2015**, *70*, A1–A16, doi:10.1016/J.POLYMER.2015.05.041.

215.   Souza, A.G.; Santos, D.F.; Ferreira, R.R.; Pinto, V.Z.; Rosa, D.S. Innovative process for obtaining modified nanocellulose from soybean straw. *Int. J. Biol. Macromol.* **2020**, *165*, 1803–1812, doi:10.1016/J.IJBIOMAC.2020.10.036.

216.   Pruksawan, S.; Samitsu, S.; Fujii, Y.; Torikai, N.; Naito, M. Toughening Effect of Rodlike Cellulose Nanocrystals in Epoxy Adhesive. *ACS Appl. Polym. Mater.* **2020**, *2*, 1234–1243, doi:10.1021/acsapm.9b01102.

217.   Roman, C.; García-Morales, M.; Eugenio, M.E.; Ibarra, D.; Martín-Sampedro, R.; Delgado, M.A. A sustainable methanol-based solvent exchange method to produce nanocellulose-based ecofriendly lubricants. *J. Clean. Prod.* **2021**, *319*, 128673, doi:10.1016/J.JCLEPRO.2021.128673.

218. Ghasemlou, M.; Daver, F.; Ivanova, E.P.; Habibi, Y.; Adhikari, B. Surface modifications of nanocellulose: From synthesis to high-performance nanocomposites. *Prog. Polym. Sci.* **2021**, *119*, 101418, doi:10.1016/J.PROGPOLYMSCI.2021.101418.

219. Pakharenko, V.; Pervaiz, M.; Pande, H.; Sain, M. Chemical and Physical Techniques for Surface Modification of Nanocellulose Reinforcements. In *Interface/Interphase in Polymer Nanocomposites*; 2016; pp. 283–310 ISBN 9781119185093.

220. Rodríguez-Fabià, S.; Torstensen, J.; Johansson, L.; Syverud, K. Hydrophobisation of lignocellulosic materials part I: physical modification. *Cellulose* **123AD**, *1*, 5375–5393, doi:10.1007/s10570-022-04620-8.

221. Hubbe, M.A.; Rojas, O.J.; Lucia, L.A. Green Modification of Surface Characteristics of Cellulosic Materials at the Molecular or Nano Scale: A Review. *BioResources* **2015**, *10*, 6095–6206.

222. Habibi, Y. Key advances in the chemical modification of nanocelluloses. *Chem. Soc. Rev.* **2014**, *43*, 1519–1542, doi:10.1039/c3cs60204d.

223. Bassyouni, M.; Zoromba, M.S.; Abdel-Aziz, M.H.; Mosly, I. Extraction of Nanocellulose for Eco-Friendly Biocomposite Adsorbent for Wastewater Treatment. *Polymers (Basel).* **2022**, *14*, doi:10.3390/polym14091852.

224. Heine, D.R.; Petersen, M.K.; Grest, G.S. Effect of particle shape and charge on bulk rheology of nanoparticle suspensions. *J. Chem. Phys.* **2010**, *132*, doi:10.1063/1.3419071.

225. Chaiwong, C.; Rachtanapun, P.; Wongchaiya, P.; Auras, R.; Boonyawan, D. Effect of plasma treatment on hydrophobicity and barrier property of polylactic acid. *Surf. Coatings Technol.* **2010**, *204*, 2933–2939, doi:10.1016/J.SURFCOAT.2010.02.048.

226. Belgacem, M.N.; Bataille, P.; Sapieha, S. Effect of corona modification on the mechanical properties of polypropylene/cellulose composites. *J. Appl. Polym. Sci.* **1994**, *53*, 379–385, doi:10.1002/app.1994.070530401.

227. Lopes, T.A.; Bufalino, L.; Claro, P.I.C.; Martins, M.A.; Tonoli, G.H.D.; Mendes, L.M. The effect of surface modifications with corona discharge in pinus and eucalyptus nanofibril films. *Cellulose* **2018**, *25*, 55017–5033, doi:10.1007/s10570-018-1948-3.

228. Gassan, J.; Gutowski, V.S. Effects of corona discharge and UV treatment on the properties of jute-fibre epoxy composites. *Compos. Sci. Technol.* **2000**, *60*, 2857–2863, doi:10.1016/S0266-3538(00)00168-8.

229. Nourbakhsh, S. Comparison between laser application and atmospheric air plasma treatment on nanocellulose coating of polyester and nylon 66 fabrics. *J. Laser Appl.* **2015**, *27*, 012005, doi:10.2351/1.4902832.

230.   Clancy, T.C.; Frankland, S.J.V.; Hinkley, J.A.; Gates, T.S. Molecular modeling for calculation of mechanical properties of epoxies with moisture ingress. *Polymer (Guildf).* **2009**, *50*, 2736–2742, doi:10.1016/J.POLYMER.2009.04.021.

231.   Chin, K.M.; Sung Ting, S.; Ong, H.L.; Omar, M. Surface functionalized nanocellulose as a veritable inclusionary material in contemporary bioinspired applications: A review. *J. Appl. Polym. Sci.* **2018**, *135*, doi:10.1002/app.46065.

232.   Yang, Q.; Pan, X. A Facile Approach for Fabricating Fluorescent Cellulose. *J Appl Polym Sci* **2010**, *117*, 3639–3644, doi:10.1002/app.32287.

233.   Tingaut, P.; Hauert, R.; Zimmermann, T. Highly efficient and straightforward functionalization of cellulose films with thiol-ene click chemistry. *J. Mater. Chem.* **2011**, *21*, 16066, doi:10.1039/c1jm11620g.

234.   Cunha, A.G.; Zhou, Q.; Per Larsson, T.; Berglund, L.A. Topochemical acetylation of cellulose nanopaper structures for biocomposites: mechanisms for reduced water vapour sorption. *Cellulose* **2014**, 2773–2787, doi:10.1007/s10570-014-0334-z.

235.   Mashkour, M.; Afra, E.; Resalati, H.; Mashkour, M. Moderate surface acetylation of nanofibrillated cellulose for the improvement of paper strength and barrier properties. *RSC Adv.* **2015**, *5*, 60179, doi:10.1039/c5ra08161k.

236.   Dong, F.; Yan, M.; Jin, C.; Li, S. Characterization of Type-II Acetylated Cellulose Nanocrystals with Various Degree of Substitution and Its Compatibility in PLA Films. *Polymers (Basel).* **2017**, *9*, 346, doi:10.3390/polym9080346.

237.   Xingman, Z.; Xinxing, L.; White, K.L.; Lin, S.; Wu, H.; Cao, S.; Huang, L.; Chen, L. Effect of the degree of substitution on the hydrophobicity of acetylated cellulose for production of liquid marbles. *Cellulose* **2016**, *23*, 811–821, doi:10.1007/s10570-015-0856-z.

238.   Zhang, X.; Ma, P.; Zhang, Y. Structure and properties of surface-acetylated cellulose nanocrystal/poly(butylene adipate-co-terephthalate) composites. *Polym. Bull* **2016**, *73*, 2073–2085, doi:10.1007/s00289-015-1594-y.

239.   Nguyen, D.T.; Pham, Q.T. A theoretical and experimental study on etherification of primary alcohols with the hydroxyl groups of cellulose chain (n = 1–3) in acidic condition. *J. Mol. Struct.* **2021**, *1236*, 130314, doi:10.1016/J.MOLSTRUC.2021.130314.

240.   Dufresne, A. Processing of Polymer Nanocomposites Reinforced with Polysaccharide Nanocrystals. *Molecules* **2010**, *15*, 4111–4128, doi:10.3390/molecules15064111.

241.   Berger, S.; Synytska, A.; Ionov, L.; Eichhorn, K.-J.; Stamm, M. Stimuli-Responsive Bicomponent Polymer Janus Particles by "Grafting

from"/"Grafting to" Approaches. *Macromolecules* **2008**, *41*, 9669–9676, doi:10.1021/ma802089h.

242.	Wang, H.; He, J.; Zhang, M.; Chiu Tam, K.; Ni, P. A new pathway towards polymer modified cellulose nanocrystals via a "grafting onto" process for drug delivery. *Polym. Chem.* **2015**, *6*, 4206–4209, doi:10.1039/c5py00466g.

243.	Harrisson, S.; Drisko, G.L.; Malmstrom, E.; Hult, A.; Wooley, K.L. Hybrid Rigid/Soft and Biologic/Synthetic Materials: Polymers Grafted onto Cellulose Microcrystals. *Biomacromolecules* **2011**, *12*, 1214–1223, doi:10.1021/bm101506j.

244.	Hansson, S.; Trouillet, V.; Tischer, T.; Goldmann, A.S.; Carlmark, A.; Barner-Kowollik, C.; Malmström, E. Grafting Efficiency of Synthetic Polymers onto Biomaterials: A Comparative Study of Grafting-from versus Grafting-to. *Colloid Polym. Sci.* **2012**, doi:10.1021/bm3013132.

245.	Le Gars, M.; Delvart, A.; Roger, P.; Belgacem, M.N.; Bras, J. Amidation of TEMPO-oxidized cellulose nanocrystals using aromatic aminated molecules. *Colloid Polym. Sci.* **2020**, 603–617, doi:10.1007/s00396-020-04640-5.

246.	Lin, N.; Dufresne, A. Nanocellulose in biomedicine: Current status and future prospect. *Eur. Polym. J.* **2014**, doi:10.1016/j.eurpolymj.2014.07.025.

247.	Thakur, V.; Guleria, A.; Kumar, S.; Sharma, S.; Singh, K. Recent advances in nanocellulose processing, functionalization and applications: a review. *Mater. Adv.* **2021**, *2*, 1872, doi:10.1039/d1ma00049g.

248.	Liu, P.; Borrell, P.F.; Božič, M.; Kokol, V.; Oksman, K.; Mathew, A.P. Nanocelluloses and their phosphorylated derivatives for selective adsorption of Ag+, Cu2+ and Fe3+ from industrial effluents. *J. Hazard. Mater.* **2015**, *294*, 177–185, doi:10.1016/J.JHAZMAT.2015.04.001.

249.	Dhali, K.; Ghasemlou, M.; Daver, F.; Cass, P.; Adhikari, B. A review of nanocellulose as a new material towards environmental sustainability. *Sci. Total Environ.* **2021**, *775*, 145871, doi:10.1016/J.SCITOTENV.2021.145871.

250.	Motaung, T.E.; Linganiso, L.Z. Critical review on agrowaste cellulose applications for biopolymers. *Int. J. Plast. Technol.* **2018**, *22*, 185–216, doi:10.1007/s12588-018-9219-6.

251.	Aoudi, B.; Boluk, Y.; El-Din, M.G. Recent advances and future perspective on nanocellulose-based materials in diverse water treatment applications. *Sci. Total Environ.* **2022**, *843*, 156903, doi:10.1016/J.SCITOTENV.2022.156903.

252.	Nasir, M.; Hashim, R.; Sulaiman, O.; Asim, M. Nanocellulose: Preparation methods and applications. *Cellul. Nanofibre Compos. Prod. Prop. Appl.* **2017**, 261–276, doi:10.1016/B978-0-08-100957-4.00011-5.

253.   George, J.; Sreekala, M.S.; Thomas, S. A Review on Interface Modification and Characterization of Natural Fiber Reinforced Plastic Composites. *Polym. Eng. Sci.* **2001**, *41*, 9.

254.   Li, X.; Lope, G.T.; Panigrahi, S. Chemical Treatments of Natural Fiber for Use in Natural Fiber-Reinforced Composites: A Review. *J Polym Env.* **2007**, *15*, 25–33, doi:10.1007/s10924-006-0042-3.

255.   Joshi, S. V.; Drzal, L.T.; Mohanty, A.K.; Arora, S. Are natural fiber composites environmentally superior to glass fiber reinforced composites? *Compos. Part A Appl. Sci. Manuf.* **2004**, *35*, 371–376, doi:10.1016/J.COMPOSITESA.2003.09.016.

256.   Lee, K.Y.; Aitomäki, Y.; Berglund, L.A.; Oksman, K.; Bismarck, A. On the use of nanocellulose as reinforcement in polymer matrix composites. *Compos. Sci. Technol.* **2014**, *105*, 15–27, doi:10.1016/J.COMPSCITECH.2014.08.032.

257.   Manocha, L.M.; Valand, J.; Patel, N.; Warrier, A.; Manocha, S. Nanocomposites for structural applications. *Indian J. Pure Appl. Phys.* **2006**, *44*, 135–142.

258.   Barthelat, F. Architectured materials in engineering and biology: fabrication, structure, mechanics and performance. *Int. Mater. Rev.* **2015**, *60*, 413–430, doi:doi.org/10.1179/1743280415Y.0000000008.

259.   Mokhena, T.C.; Luyt, A.S. Investigation of Polyethylene/Sisal Whiskers Nanocomposites Prepared Under Different Conditions. *Polym. Compos.* **2014**, *35*, 2221–2233, doi:10.1002/pc.22887.

260.   Hendren, K.D.; Baughman, T.W.; Deck, P.A.; Foster, E.J.; Foster, E.J. In situ dispersion and polymerization of polyethylene cellulose nanocrystal-based nanocomposites. *J. Appl. Polym. Sci.* **2020**, *137*, 485000, doi:10.1002/app.48500.

261.   Sakakibara, K.; Moriki, Y.; Yano, H.; Tsujii, Y. Strategy for the Improvement of the Mechanical Properties of Cellulose Nanofiber-Reinforced High-Density Polyethylene Nanocomposites Using Diblock Copolymer Dispersants. *ACS Appl. Mater. Interfaces* **2017**, *9*, 25, doi:10.1021/acsami.7b13963.

262.   Sato, A.; Kabusaki, D.; Okumura, H.; Nakatani, T.; Nakatsubo, F.; Yano, H. Surface modification of cellulose nanofibers with alkenyl succinic anhydride for high-density polyethylene reinforcement. *Compos. Part A Appl. Sci. Manuf.* **2016**, *83*, 72–79, doi:10.1016/J.COMPOSITESA.2015.11.009.

263.   Li, J.; Song, Z.; Li, D.; Shang, S.; Guo, Y. Cotton cellulose nanofiber-reinforced high density polyethylene composites prepared with two different pretreatment methods. *Ind. Crops Prod.* **2014**, *59*, 318–328, doi:10.1016/J.INDCROP.2014.05.033.

264.   Alidadi-Shamsabadi, M.; Behzad, T.; Bagheri, R.; Nari-Nasrabadi, B. Preparation and Characterization of Low-Density

Polyethylene/Thermoplastic Starch Composites Reinforced by Cellulose Nanofibers. *Polym. Compos.* **2015**, *36*, 2309–2316, doi:10.1002/pc.23144.

265.   Yano, H.; Omura, H.; Honma, Y.; Okumura, H.; Sano, H.; Nakatsubo, F. Designing cellulose nanofiber surface for high density polyethylene reinforcement. *Cellulose* **2018**, *25*, 3351–3362, doi:10.1007/s10570-018-1787-2.

266.   Maia, T.H.S.; Larocca, N.M.; Beatrice, C.A.G.; de Menezes, A.J.; de Freitas Siqueira, G.; Pessan, L.A.; Dufresne, A.; França, M.P.; de Almeida Lucas, A. Polyethylene cellulose nanofibrils nanocomposites. *Carbohydr. Polym.* **2017**, *173*, 50–56, doi:10.1016/J.CARBPOL.2017.05.089.

267.   Cui, X.; Honda, T.; Asoh, T.A.; Uyama, H. Cellulose modified by citric acid reinforced polypropylene resin as fillers. *Carbohydr. Polym.* **2020**, *230*, 115662, doi:10.1016/J.CARBPOL.2019.115662.

268.   Ghafari, R.; Scaffaro, R.; Maio, A.; Gulino, E.F.; Lo Re, G.; Jonoobi, M. Processing-structure-property relationships of electrospun PLA-PEO membranes reinforced with enzymatic cellulose nanofibers. *Polym. Test.* **2020**, *81*, 106182, doi:10.1016/J.POLYMERTESTING.2019.106182.

269.   Pereda, M.; Kissi, N. El; Dufresne, A. Extrusion of Polysaccharide Nanocrystal Reinforced Polymer Nanocomposites through Compatibilization with Poly(ethylene oxide). *Appl. Mater. Interfaces* **2014**, *6*, 9365–9375, doi:10.1021/am501755p.

270.   Singh, A.A.; Genovese, M.E.; Mancini, G.; Marini, L.; Athanassiou, A. Green Processing Route for Polylactic Acid−Cellulose Fiber Biocomposites. *Sustain. Chem. Eng.* **2020**, *8*, 4128–4136, doi:10.1021/acssuschemeng.9b06760.

271.   Muiruri, J.K.; Liu, S.; Yeo, J.C.C.; Koh, J.J.; Kong, J.; Thitsartarn, W.; Teo, W.S.; He, C. Synergistic Toughening of Poly(lactic acid)–Cellulose Nanocrystal Composites through Cooperative Effect of Cavitation and Crazing Deformation Mechanisms. *Appl. Polym. Mater.* **2019**, *1*, 509–518, doi:10.1021/acsapm.8b00201.

272.   Fujisawa, S.; Saito, T.; Kimura, S.; Iwata, T.; Isogai, A. Surface Engineering of Ultrafine Cellulose Nanofibrils toward Polymer Nanocomposite Materials. *Biomacromolecules* **2013**, *14*, 1541–1546, doi:10.1021/bm400178m.

273.   Yu, H.-Y.; Zhang, H.; Song, M.-L.; Zhou, Y.; Yao, J.; Ni, Q.-Q. From Cellulose Nanospheres, Nanorods to Nanofibers: Various Aspect Ratio Induced Nucleation/Reinforcing Effects on Polylactic Acid for Robust-Barrier Food Packaging. *Appl. Mater. Interfaces* **2017**, *9*, 43920–43938, doi:10.1021/acsami.7b09102.

274.   Geng, S.; Yao, K.; Zhou, Q.; Oksman, K. High-Strength, High-Toughness Aligned Polymer-Based Nanocomposite Reinforced with Ultralow Weight Fraction of Functionalized Nanocellulose. *Biomacromolecules* **2018**, *19*, 4075–4083, doi:10.1021/acs.biomac.8b01086.

275.   Jun, D.; Guomin, Z.; Mingzhu, P.; Leilei, Z.; Dagang, L.; Rui, Z. Crystallization and mechanical properties of reinforced PHBV composites using melt compounding: Effect of CNCs and CNFs. *Carbohydr. Polym.* **2017**, *168*, 255–262, doi:10.1016/J.CARBPOL.2017.03.076.

276.   Deng, S.; Ma, J.; Guo, Y.; Chen, F.; Fu, Q. One-step modification and nanofibrillation of microfibrillated cellulose for simultaneously reinforcing and toughening of poly(ε-caprolactone). *Compos. Sci. Technol.* **2018**, *157*, 168–177, doi:10.1016/J.COMPSCITECH.2017.10.029.

277.   Park, S.-A.; Eom, Y.; Jeon, H.; Mo Koo, J.; Seong Lee, E.; Jegal, J.; Yeon Hwang, S.; Oh, D.X.; Park, J. Preparation of synergistically reinforced transparent bio-polycarbonate nanocomposites with highly dispersed cellulose nanocrystals. *Green Chem.* **2019**, *21*, 5212–5221, doi:10.1039/c9gc02253h.

278.   Amin, K.N.M.; Amiralian, N.; Annamalai, P.K.; Edwards, G.; Chaleat, C.; Martin, D.J. Scalable processing of thermoplastic polyurethane nanocomposites toughened with nanocellulose. *Chem. Eng. J.* **2016**, *302*, 406–416, doi:10.1016/J.CEJ.2016.05.067.

279.   Yuwawech, K.; Wootthikanokkhan, J.; Wanwong, S.; Tanpichai, S. Polyurethane/esterified cellulose nanocrystal composites as a transparent moisture barrier coating for encapsulation of dye sensitized solar cells. *J. Appl. Polym. Sci.* **2017**, *134*, 45010, doi:10.1002/app.45010.

280.   Girouard, N.M.; Xu, S.; Schueneman, G.T.; Shofner, M.L.; Meredith, J.C. Site-Selective Modification of Cellulose Nanocrystals with Isophorone Diisocyanate and Formation of Polyurethane-CNC Composites. *Appl. Mater. Interfaces* **2016**, *8*, 1458–1467, doi:10.1021/acsami.5b10723.

281.   Septevani, A.A.; Evans, D.A.C.; Annamalai, P.K.; Martin, D.J. The use of cellulose nanocrystals to enhance the thermal insulation properties and sustainability of rigid polyurethane foam. *Ind. Crops Prod.* **2017**, *107*, 114–121, doi:10.1016/J.INDCROP.2017.05.039.

282.   Blanchard, R.; Ogunsona, E.O.; Hojabr, S.; Berry, R.; Mekonnen, T.H. Synergistic Cross-linking and Reinforcing Enhancement of Rubber Latex with Cellulose Nanocrystals for Glove Applications. *Appl. Polym. Mater* **2020**, *2*, 887–898, doi:10.1021/acsapm.9b01117.

283.   Wu, X.; Lu, C.; Xu, H.; Zhang, X.; Zhou, Z. Biotemplate Synthesis of Polyaniline@Cellulose Nanowhiskers/ Natural Rubber Nanocomposites with 3D Hierarchical Multiscale Structure and Improved Electrical Conductivity. *Appl. Mater. Interfaces* **2014**, *6*, 21078–21085, doi:10.1021/am505924z.

284.   Han, J.; Lu, K.; Yue, Y.; Mei, C.; Huang, C.; Wu, Q.; Xu, X. Nanocellulose-templated assembly of polyaniline in natural rubber-based hybrid elastomers toward flexible electronic conductors. *Ind. Crops Prod.* **2019**, *128*, 94–107, doi:10.1016/J.INDCROP.2018.11.004.

285.	Nechyporchuk, O.; Pignon, F.; Botelho Do Rego, A.M.; Belgacem, M.N. Influence of ionic interactions between nanofibrillated cellulose and latex on the ensuing composite properties. *Compos. Part B Eng.* **2016**, *85*, 188–195, doi:10.1016/J.COMPOSITESB.2015.09.030.

286.	Sinclair, A.; Zhou, X.; Tangpong, S.; Bajwa, D.S.; Quadir, M.; Jiang, L. High-Performance Styrene-Butadiene Rubber Nanocomposites Reinforced by Surface-Modified Cellulose Nanofibers. *Omega* **2019**, *8*, 13189–13199, doi:10.1021/acsomega.9b01313.

287.	Hosseinmardi, A.; Annamalai, P.K.; Wang, L.; Martin, D.; Amiralian, N. Reinforcement of natural rubber latex using lignocellulosic nanofibers isolated from spinifex grass. *Nanoscale* **2017**, *9*, 9510, doi:10.1039/c7nr02632c.

288.	Hosseinmardi, A.; Annamalai, K.; Martine, B.; Pennells, J.; Martin, D.J.; Amiralian, N. Facile Tuning of the Surface Energy of Cellulose Nanofibers for Nanocomposite Reinforcement. *Omega* **2018**, *3*, 15933–15942, doi:10.1021/acsomega.8b02104.

289.	Abraham, E.; Kam, D.; Nevo, Y.; Slattegard, R.; Rivkin, A.; Lapidot, S.; Shoseyov, O. Highly Modified Cellulose Nanocrystals and Formation of Epoxy-Nanocrystalline Cellulose (CNC) Nanocomposites. *Appl. Mater. Interfaces* **2016**, *8*, 28086–28095, doi:10.1021/acsami.6b09852.

290.	Peng, S.X.; Shrestha, S.; Yoo, Y.; Youngblood, J.P. Enhanced dispersion and properties of a two-component epoxy nanocomposite using surface modified cellulose nanocrystals. *Polymer (Guildf)*. **2017**, *112*, 359–368, doi:10.1016/J.POLYMER.2017.02.016.

291.	Fox, D.M.; Rodriguez, R.S.; Devilbiss, M.N.; Woodcock, J.; Davis, C.S.; Sinko, R.; Keten, S.; Gilman, J.W. Simultaneously Tailoring Surface Energies and Thermal Stabilities of Cellulose Nanocrystals Using Ion Exchange: Effects on Polymer Composite Properties for Transportation, Infrastructure, and Renewable Energy Applications. *Appl. Mater. Interfaces* **2016**, *8*, 27270−27281, doi:10.1021/acsami.6b06083.

292.	Emami, Z.; Meng, Q.; Pircheraghi, G.; Manas-Zloczower, I. Use of surfactants in cellulose nanowhisker/epoxy nanocomposites: effect on filler dispersion and system properties. *Cellulose* **2015**, *22*, 3161–3176, doi:10.1007/s10570-015-0728-6.

293.	Shrestha, S.; Chowdhury, R.A.; Toomey, M.D.; Betancourt, D.; Montes, F.; Youngblood, J.P. Surface hydrophobization of TEMPO-oxidized cellulose nanofibrils (CNFs) using a facile, aqueous modification process and its effect on properties of epoxy nanocomposites. *Cellulose* **2019**, *26*, 9631–9643, doi:10.1007/s10570-019-02762-w.

294.	Tang, L.; Weder, C. Cellulose Whisker/Epoxy Resin Nanocomposites. *Appl. Mater. Interface* **2010**, *2*, 1073–1080, doi:10.1021/am900830h.

295.	Yue, L.; Liu, F.; Mekala, S.; Patel, A.; Gross, R.A.; Manas-Zloczower, I. High Performance Biobased Epoxy Nanocomposite Reinforced

with a Bacterial Cellulose Nanofiber Network. *Sustain. Chem. Eng.* **2019**, *7*, 5986–5992, doi:10.1021/acssuschemeng.8b06073.

296.		Saba, N.; Jawaid, M. Recent advances in nanocellulose-based polymer nanocomposites. In *Cellulose-Reinforced Nanofibre Composites: Production, Properties and Applications*; 2017 ISBN 9780081009659.

297.		Kumar Das, A.; Nazrul Islam, M.; Ashaduzzaman, M.; Nazhad, M.M. Nanocellulose: its applications, consequences and challenges in papermaking. *J. Packag. Technol. Res.* **2020**, *4*, 253–260, doi:10.1007/s41783-020-00097-7.

298.		Sethi, J.; Oksman, K.; Illikainen, M.; Sirviö, J.A. Sonication-assisted surface modification method to expedite the water removal from cellulose nanofibers for use in nanopapers and paper making. *Carbohydr. Polym.* **2018**, *197*, 92–99, doi:10.1016/J.CARBPOL.2018.05.072.

299.		Merayo, N.; Balea, A.; Fuente, E. de la; Blanco, Á.; Negro, C. Interactions between cellulose nanofibers and retention systems in flocculation of recycled fibers. *Cellulose* **2017**, *24*, 677–692, doi:10.1007/s10570-016-1138-0.

300.		Espinosa, E.; Arrebola, R.I.; Bascón-Villegas, I.; Sánchez-Gutiérrez, M.; Domínguez-Robles, J.; Rodríguez, A. Industrial application of orange tree nanocellulose as papermaking reinforcement agent. *Cellulose* **2020**, *27*, 10781–10797, doi:10.1007/s10570-020-03353-w.

301.		Tyagi, P.; Hubbe, M.A.; Lucia, L.; Pal, L. High performance nanocellulose-based composite coatings for oil and grease resistance. *Cellulose* **2018**, *25*, 3377–3391, doi:10.1007/s10570-018-1810-7.

302.		Tyagi, P.; Lucia, L.A.; Hubbe, M.A.; Pal, L. Nanocellulose-based multilayer barrier coatings for gas, oil, and grease resistance. *Carbohydr. Polym.* **2019**, *206*, 281–288, doi:10.1016/J.CARBPOL.2018.10.114.

303.		Herrera, M.A.; Mathew, A.P.; Oksman, K. Barrier and mechanical properties of plasticized and cross-linked nanocellulose coatings for paper packaging applications. *Cellulose* **2017**, *24*, 3969–3980, doi:10.1007/s10570-017-1405-8.

304.		Koppolu, R.; Lahti, J.; Abitbol, T.; Swerin, A.; Kuusipalo, J.; Toivakka, M. Continuous Processing of Nanocellulose and Polylactic Acid into Multilayer Barrier Coatings. *Appl. Mater. Interfaces* **2019**, *11*, 11920–11927, doi:10.1021/acsami.9b00922.

305.		Nguyen, H.; Hong, T.; Tan, L.; Jeon, H.; Oh, D.X. Biorenewable, transparent, and oxygen/moisture barrier nanocellulose/nanochitin-based coating on polypropylene for food packaging applications. *Carbohydr. Polym.* **2021**, *271*, 118421, doi:10.1016/j.carbpol.2021.118421.

306.		Pirozzi, A.; Del Grosso, V.; Ferrari, G.; Pataro, G.; Donsì, F. Combination of edible coatings containing oregano essential oil nanoemulsion

and pulsed light treatments for improving the shelf life of tomatoes. *Chem. Eng. Trans.* **2021**, *87*, 1–6, doi:10.3303/CET2187011.

307.   Jafarzadeh, S.; Mohammadi Nafchi, A.; Salehabadi, A.; Oladzad-abbasabadi, N.; Jafari, S.M. Application of bio-nanocomposite films and edible coatings for extending the shelf life of fresh fruits and vegetables. *Adv. Colloid Interface Sci.* 2021.

308.   Ghosh, T.; Nakano, K.; Katiyar, V. Curcumin doped functionalized cellulose nanofibers based edible chitosan coating on kiwifruits. *Int. J. Biol. Macromol.* **2021**, doi:10.1016/j.ijbiomac.2021.06.098.

309.   Shih, Y.T.; Zhao, Y. Development, characterization and validation of starch based biocomposite films reinforced by cellulose nanofiber as edible muffin liner. *Food Packag. Shelf Life* **2021**, doi:10.1016/j.fpsl.2021.100655.

310.   Rojas-lema, S.; Nilsson, K.; Trifol, J.; Langton, M.; Gomez-caturla, J.; Balart, R.; Garcia-garcia, D.; Moriana, R. "Faba bean protein films reinforced with cellulose nanocrystals as edible food packaging material." *Food Hydrocoll.* **2021**, 107019, doi:10.1016/j.foodhyd.2021.107019.

311.   Yao Désiré, A.; Charlemagne, N.; Degbeu Claver, K.; Fabrice Achille, T.; Marianne, S. Starch-based edible films of improved cassava varieties Yavo and TMS reinforced with microcrystalline cellulose. *Heliyon* **2021**, doi:10.1016/j.heliyon.2021.e06804.

312.   Lin, D.; Zheng, Y.; Wang, X.; Huang, Y.; Ni, L.; Chen, X.; Wu, Z.; Huang, C.; Yi, Q.; Li, J.; et al. Study on physicochemical properties, antioxidant and antimicrobial activity of okara soluble dietary fiber/sodium carboxymethyl cellulose/thyme essential oil active edible composite films incorporated with pectin. *Int. J. Biol. Macromol.* **2020**, doi:10.1016/j.ijbiomac.2020.10.005.

313.   Liu, Z.; Lin, D.; Lopez-Sanchez, P.; Yang, X. Characterizations of bacterial cellulose nanofibers reinforced edible films based on konjac glucomannan. *Int. J. Biol. Macromol.* **2020**, doi:10.1016/j.ijbiomac.2019.12.109.

314.   Cao, L.; Ge, T.; Meng, F.; Xu, S.; Li, J.; Wang, L. An edible oil packaging film with improved barrier properties and heat sealability from cassia gum incorporating carboxylated cellulose nano crystal whisker. *Food Hydrocoll.* **2020**, doi:10.1016/j.foodhyd.2019.105251.

315.   Jancy, S.; Shruthy, R.; Preetha, R. Fabrication of packaging film reinforced with cellulose nanoparticles synthesised from jack fruit non-edible part using response surface methodology. *Int. J. Biol. Macromol.* **2020**, doi:10.1016/j.ijbiomac.2019.09.066.

316.   Yadav, M.; Chiu, F.C. Cellulose nanocrystals reinforced κ-carrageenan based UV resistant transparent bionanocomposite films for sustainable packaging applications. *Carbohydr. Polym.* **2019**, doi:10.1016/j.carbpol.2019.01.114.

317.   Kassab, Z.; Aziz, F.; Hannache, H.; Ben Youcef, H.; El Achaby, M. Improved mechanical properties of k-carrageenan-based nanocomposite films reinforced with cellulose nanocrystals. *Int. J. Biol. Macromol.* **2019**, doi:10.1016/j.ijbiomac.2018.12.030.

318.   Jiang, S. juan; Zhang, T.; Song, Y.; Qian, F.; Tuo, Y.; Mu, G. Mechanical properties of whey protein concentrate based film improved by the coexistence of nanocrystalline cellulose and transglutaminase. *Int. J. Biol. Macromol.* **2019**, doi:10.1016/j.ijbiomac.2018.12.254.

319.   Chen, Q.J.; Zhou, L.L.; Zou, J.Q.; Gao, X. The preparation and characterization of nanocomposite film reinforced by modified cellulose nanocrystals.   *Int.   J.   Biol.   Macromol.   **2019**, doi:10.1016/j.ijbiomac.2019.04.063.

320.   Wang, X.; Guo, C.; Hao, W.; Ullah, N.; Chen, L.; Li, Z.; Feng, X. Development and characterization of agar-based edible films reinforced with nano-bacterial cellulose. *Int. J. Biol. Macromol.* **2018**, doi:10.1016/j.ijbiomac.2018.06.089.

321.   Sukyai, P.; Anongjanya, P.; Bunyahwuthakul, N.; Kongsin, K.; Harnkarnsujarit, N.; Sukatta, U.; Sothornvit, R.; Chollakup, R. Effect of cellulose nanocrystals from sugarcane bagasse on whey protein isolate-based films. *Food Res. Int.* **2018**, doi:10.1016/j.foodres.2018.02.052.

322.   Salari, M.; Sowti Khiabani, M.; Rezaei Mokarram, R.; Ghanbarzadeh, B.; Samadi Kafil, H. Development and evaluation of chitosan based active nanocomposite films containing bacterial cellulose nanocrystals and   silver   nanoparticles.   *Food   Hydrocoll.   **2018**, doi:10.1016/j.foodhyd.2018.05.037.

323.   Wang, L.F.; Shankar, S.; Rhim, J.W. Properties of alginate-based films reinforced with cellulose fibers and cellulose nanowhiskers isolated   from   mulberry   pulp.   *Food   Hydrocoll.   **2017**, doi:10.1016/j.foodhyd.2016.08.041.

324.   Mujtaba, M.; Salaberria, A.M.; Andres, M.A.; Kaya, M.; Gunyakti, A.; Labidi, J. Utilization of flax (Linum usitatissimum) cellulose nanocrystals as reinforcing material for chitosan films. *Int. J. Biol. Macromol.* **2017**, doi:10.1016/j.ijbiomac.2017.06.127.

325.   Pirozzi, A.; Pataro, G.; Donsì, F.; Ferrari, G. Edible Coating and Pulsed Light to Increase the Shelf Life of Food Products. *Food Eng. Rev.* 2020.

326.   Mujtaba, M.; Akyuz, L.; Koc, B.; Kaya, M.; Ilk, S.; Cansaran-Duman, D.; Martinez, A.S.; Cakmak, Y.S.; Labidi, J.; Boufi, S. Novel, multifunctional mucilage composite films incorporated with cellulose nanofibers. *Food Hydrocoll.* **2019**, doi:10.1016/j.foodhyd.2018.10.021.

327.   Ranjbaryan, S.; Pourfathi, B.; Almasi, H. Reinforcing and release controlling effect of cellulose nanofiber in sodium caseinate films activated by nanoemulsified cinnamon essential oil. *Food Packag. Shelf Life* **2019**, doi:10.1016/j.fpsl.2019.100341.

328.   Ortiz, C.M.; Salgado, P.R.; Dufresne, A.; Mauri, A.N. Microfibrillated cellulose addition improved the physicochemical and bioactive properties of biodegradable films based on soy protein and clove essential oil. *Food Hydrocoll.* **2018**, doi:10.1016/j.foodhyd.2018.01.011.

329.   Zhang, W.; Zhang, Y.; Cao, J.; Jiang, W. Improving the performance of edible food packaging films by using nanocellulose as an additive. *Int. J. Biol. Macromol.* 2021.

330.   Roy, S.; Rhim, J.-W. Gelatin/agar-based functional film integrated with Pickering emulsion of clove essential oil stabilized with nanocellulose for active packaging applications. *Colloids Surfaces A Physicochem. Eng. Asp.* **2021**, 127220, doi:https://doi.org/10.1016/j.colsurfa.2021.127220.

331.   Montero, Y.; Souza, A.G.; Oliveira, É.R.; Rosa, D. dos S. Nanocellulose functionalized with cinnamon essential oil: A potential application in active biodegradable packaging for strawberry. *Sustain. Mater. Technol.* **2021**, doi:10.1016/j.susmat.2021.e00289.

332.   Lu, Q.; Yu, X.; Yagoub, A.E.G.A.; Wahia, H.; Zhou, C. Application and challenge of nanocellulose in the food industry. *Food Biosci.* **2021**, *43*, 101285, doi:10.1016/J.FBIO.2021.101285.

333.   Hassan, M.Z.; Sapuan, S.M.; Roslan, S.A.; Aziz, S.A.; Sarip, S. Optimization of tensile behavior of banana pseudo-stem (Musa acuminate) fiber reinforced epoxy composites using response surface methodology. *J. Mater. Res. Technol.* **2019**, *8*, 3517–3528, doi:10.1016/J.JMRT.2019.06.026.

334.   Velásquez-Cock, J.; Serpa, A.; Vélez, L.; Gañán, P.; Gómez Hoyos, C.; Castro, C.; Duizer, L.; Goff, H.D.; Zuluaga, R. Influence of cellulose nanofibrils on the structural elements of ice cream. *Food Hydrocoll.* **2019**, *87*, 204–213, doi:10.1016/J.FOODHYD.2018.07.035.

335.   Qi, W.; Wu, J.; Shu, Y.; Wang, H.; Rao, W.; Xu, H.N.; Zhang, Z. Microstructure and physiochemical properties of meat sausages based on nanocellulose-stabilized emulsions. *Int. J. Biol. Macromol.* **2020**, *152*, 567–575, doi:10.1016/J.IJBIOMAC.2020.02.285.

336.   Corral, M.L.; Cerrutti, P.; Vázquez, A.; Califano, A. Bacterial nanocellulose as a potential additive for wheat bread. *Food Hydrocoll.* **2017**, *67*, 189–196, doi:10.1016/J.FOODHYD.2016.11.037.

337.   Dai, H.; Wu, J.; Zhang, H.; Chen, Y.; Ma, L.; Huang, H.; Huang, Y.; Zhang, Y. Recent advances on cellulose nanocrystals for Pickering emulsions: Development and challenge. *Trends Food Sci. Technol.* 2020.

338.   Wu, J.; Ma, G.H. Recent Studies of Pickering Emulsions: Particles Make the Difference. *Small* 2016.

339.   Baek, J.; Wahid-Pedro, F.; Kim, K.; Kim, K.; Tam, K.C. Phosphorylated-CNC/modified-chitosan nanocomplexes for the stabilization of Pickering emulsions. *Carbohydr. Polym.* **2019**, doi:10.1016/j.carbpol.2018.11.006.

340.   Yee Khine, Y.; Stenzel, M.H. Surface modified cellulose nanomaterials: a source of non-spherical nanoparticles for drug delivery. *Mater. Horiz.* **2020**, *7*, 1727, doi:10.1039/c9mh01727e.

341.   Moohan, J.; Stewart, S.A.; Espinosa, E.; Rosal, A.; Rodríguez, A.; Larrañeta, E.; Donnelly, R.F.; Domínguez-Robles, J. Cellulose Nanofibers and Other Biopolymers for Biomedical Applications. A Review. *Appl. Sci.* **2020**, *10*, 65, doi:10.3390/app10010065.

342.   Luo, H.; Cha, R.; Li, J.; Hao, W.; Zhang, Y.; Zhou, F. Advances in tissue engineering of nanocellulose-based scaffolds: A review. *Carbohydr.   Polym.   **2019**,   224,   115144, doi:10.1016/J.CARBPOL.2019.115144.

343.   Kolakovic, R.; Peltonen, L.; Laukkanen, A.; Hellman, M.; Laaksonen, P.; Linder, M.B.; Hirvonen, J.; Laaksonen, T. Evaluation of drug interactions with nanofibrillar cellulose. *Eur. J. Pharm. Biopharm.* **2013**, *85*, 1238–1244, doi:10.1016/J.EJPB.2013.05.015.

344.   Löbmann, K.; Wohlert, J.; Müllertz, A.; Wågberg, L.; Svagan, A.J.; Löbmann, K.; Müllertz, A.; Svagan, A.J.; Wohlert, J.; Wågberg, L. Cellulose Nanopaper and Nanofoam for Patient-Tailored Drug Delivery. *Adv. Mater. Interfaces* **2017**, *4*, 1600655, doi:10.1002/admi.201600655.

345.   Gao, J.; Li, Q.; Chen, W.; Liu, Y.; Yu, H. Self-Assembly of Nanocellulose and Indomethacin into Hierarchically Ordered Structures with High Encapsulation Efficiency for Sustained Release Applications. *Chempluschem* **2014**, *79*, 725–731, doi:10.1002/cplu.201300434.

346.   Bannow, J.; Benjamins, J.W.; Wohlert, J.; Löbmann, K.; Svagan, A.J. Solid nanofoams based on cellulose nanofibers and indomethacin—the effect of processing parameters and drug content on material   structure. *Int.   J.   Pharm.*   **2017**,   *526*,   291–299, doi:10.1016/J.IJPHARM.2017.04.041.

347.   Valo, H.; Arola, S.; Laaksonen, P.; Torkkeli, M.; Peltonen, L.; Linder, M.B.; Serimaa, R.; Kuga, S.; Hirvonen, J.; Laaksonen, T. Drug release from nanoparticles embedded in four different nanofibrillar cellulose aerogels. *Eur. J. Pharm. Sci.* **2013**, *50*, 69–77, doi:10.1016/J.EJPS.2013.02.023.

348.   Valo, H.; Kovalainen, M.; Laaksonen, P.; Häkkinen, M.; Auriola, S.; Peltonen, L.; Linder, M.; Järvinen, K.; Hirvonen, J.; Laaksonen, T. Immobilization of protein-coated drug nanoparticles in nanofibrillar cellulose matrices—Enhanced stability and release. *J. Control. Release* **2011**, *156*, 390–397, doi:10.1016/J.JCONREL.2011.07.016.

349.   Lin, N.; Huang, J.; Chang, P.R.; Feng, L.; Yu, J. Effect of polysaccharide nanocrystals on structure, properties, and drug release kinetics of alginate-based microspheres. *Colloids Surfaces B Biointerfaces* **2011**, *85*, 270–279, doi:10.1016/J.COLSURFB.2011.02.039.

350.   Zhang, Q.; Li, W.; Moran, C.; Zeng, J.; Chen, J.; Wen, L.-P.; Xia, Y. Seed-Mediated Synthesis of Ag Nanocubes with Controllable Edge Lengths in the Range of 30-200 nm and Comparison of Their Optical

Properties. *J. Am. Chem. Soc.* **2010**, *132*, 11372–11378, doi:10.1021/ja104931h.

351.	Jackson, J.K.; Letchford, K.; Wasserman, B.Z.; Ye, L.; Hamad, W.Y.; Burt1, H.M. The use of nanocrystalline cellulose for the binding and controlled release of drugs. *Int J Nanomedicine* **2011**, *6*, 321–330, doi:10.2147/IJN.S16749.

352.	Wang, S.; Sun, J.; Jia, Y.; Yang, L.; Wang, N.; Xianyu, Y.; Chen, W.; Li, X.; Cha, R.; Jiang, X. Nanocrystalline Cellulose-Assisted Generation of Silver Nanoparticles for Nonenzymatic Glucose Detection and Antibacterial Agent. *Biomacromolecules* **2016**, *17*, 2472–2478, doi:10.1021/acs.biomac.6b00642.

353.	Abdi, M.M.; Razalli, R.L.; Tahir, P.M.; Chaibakhsh, N.; Hassani, M.; Mir, M. Optimized fabrication of newly cholesterol biosensor based on nanocellulose. *Int. J. Biol. Macromol.* **2019**, *126*, 1213–1222, doi:10.1016/J.IJBIOMAC.2019.01.001.

354.	Ling, Z.; Xu, F.; Edwards, J.V.; Prevost, N.T.; Nam, S.; Condon, B.D.; French, A.D. Nanocellulose as a colorimetric biosensor for effective and facile detection of human neutrophil elastase. *Carbohydr. Polym.* **2019**, *216*, 360–368, doi:10.1016/J.CARBPOL.2019.04.027.

355.	Du, X.; Zhang, Z.; Liu, W.; Deng, Y. Nanocellulose-based conductive materials and their emerging applications in energy devices - A review. *Nano Energy* **2017**, *35*, 299–320, doi:10.1016/J.NANOEN.2017.04.001.

356.	Golmohammadi, H.; Morales-Narvaéz, E.; Naghdi, T.; Merkoç, A. Nanocellulose in Sensing and Biosensing. *Chem. Mater.* **2017**, *29*, 5426–5446, doi:10.1021/acs.chemmater.7b01170.

357.	Zheng, W.; Lv, R.; Na, B.; Liu, H.; Jin, T.; Yuan, D. Nanocellulose-mediated hybrid polyaniline electrodes for high performance flexible supercapacitors. *J. Mater. Chem. A* **2017**, *5*, 12969–12976, doi:10.1039/c7ta01990d.

358.	Zhang, Q.; Chen, C.; Chen, W.; Pastel, G.; Guo, X.; Liu, S.; Wang, Q.; Liu, Y.; Li, J.; Yu, H.; et al. Nanocellulose-Enabled, All-Nanofiber, High-Performance Supercapacitor. *Appl. Mater. Interfaces* **2019**, *11*, 5919–5927, doi:10.1021/acsami.8b17414.

359.	Sayed, D.M.; El-Deab, M.S.; Elshakre, M.E.; Allam, N.K. Nanocrystalline Cellulose Confined in Amorphous Carbon Fibers as Capacitor Material for Efficient Energy Storage. *J. Phys. Chem. C* **2020**, *124*, 7007–7015, doi:10.1021/acs.jpcc.9b12045.

360.	Xu, X.; Hsieh, Y.-L. Aqueous exfoliated graphene by amphiphilic nanocellulose and its application in moisture-responsive foldable actuators. *Nanoscale* **2019**, *1*, 11719–11729, doi:10.1039/c9nr01602c.

361.	Lang, A.W.; Österholm, A.M.; Reynolds, J.R.; Lang, A.W.; Reynolds, J.R.; Österholm, A.M. Paper-Based Electrochromic Devices

Enabled by Nanocellulose-Coated Substrates. *Adv. Funct. Mater.* **2019**, *29*, 1903487, doi:10.1002/adfm.201903487.

362.   Tao, J.; Wang, R.; Yu, H.; Chen, L.; Fang, D.; Tian, Y.; Xie, J.; Jia, D.; Liu, H.; Wang, J.; et al. Highly Transparent, Highly Thermally Stable Nanocellulose/Polymer Hybrid Substrates for Flexible OLED Devices. *Appl. Mater. Interfaces* **2020**, *12*, 9701–9709, doi:10.1021/acsami.0c01048.

363.   Chen, L.; Yu, H.; Dirican, M.; Fang, D.; Tian, Y.; Yan, C.; Xie, J.; Jia, D.; Liu, H.; Wang, J.; et al. Highly Transparent and Colorless Nanocellulose/Polyimide Substrates with Enhanced Thermal and Mechanical Properties for Flexible OLED Displays. *Adv. Mater. Interfaces* **2020**, *7*, 2000928, doi:10.1002/admi.202000928.

364.   Choi, H.Y.; Jeong, Y.G. Microstructures and piezoelectric performance of eco-friendly composite films based on nanocellulose and barium titanate nanoparticle. *Compos. Part B Eng.* **2019**, *168*, 58–65, doi:10.1016/J.COMPOSITESB.2018.12.072.

365.   Tam, K.C.; Mohammed, N.; Grishkewich, N. Cellulose nanomaterials: promising sustainable nanomaterials for application in water/wastewater treatment processes. *Environ. Sci. Nano* **2018**, *5*, 623–658, doi:10.1039/c7en01029j.

366.   Dankovich, T.A.; Gray, D.G. Bactericidal Paper Impregnated with Silver Nanoparticles for Point-of-Use Water Treatment. *Environ. Sci. Technol* **2011**, *45*, 1992–1998, doi:10.1021/es103302t.

367.   Nemoto, J.; Saito, T.; Isogai, A. Simple Freeze-Drying Procedure for Producing Nanocellulose Aerogel-Containing, High-Performance Air Filters. *Appl. Mater. Interfaces* **2015**, *7*, 19809–19815, doi:10.1021/acsami.5b05841.

368.   Wu, X.; Lu, C.; Zhou, Z.; Yuan, G.; Xiong, R.; Zhang, X. Green synthesis and formation mechanism of cellulose nanocrystal-supported gold nanoparticles with enhanced catalytic performance. *Environ. Sci. Nano* **2014**, *1*, 71–79, doi:10.1039/c3en00066d.

369.   Korhonen, J.T.; Kettunen, M.; Ras, R.H.A.; Ikkala, O. Hydrophobic Nanocellulose Aerogels as Floating, Sustainable, Reusable, and Recyclable Oil Absorbents. *Appl. Mater. Interfaces* **2011**, *3*, 1813–1816, doi:10.1021/am200475b.

370.   Lsraelachvili Be, J.; Wennerstrom, H. *Role of hydration and water structure in biological and colloidal interactions*; 1996; Vol. 379;.

371.   Huang, S.; Wang, D. A Simple NanocelluloseCoating for Self-Cleaning upon Water Action: Molecular Design of Stable Surface Hydrophilicity. *Angew. Chemie* **2017**, *56*, 9053–9057, doi:10.1002/ange.201703913.

372.   Wang, W.; Zhang, T.J.; Zhang, D.W.; Li, H.Y.; Ma, Y.R.; Qi, L.M.; Zhou, Y.L.; Zhang, X.X. Amperometric hydrogen peroxide biosensor based on the immobilization of heme proteins on gold nanoparticles–bacteria

cellulose nanofibers nanocomposite. *Talanta* **2011**, *84*, 71–77, doi:10.1016/J.TALANTA.2010.12.015.

373. Yu, X.; Tong, S.; Ge, M.; Wu, L.; Zuo, J.; Cao, C.; Song, W. Adsorption of heavy metal ions from aqueous solution by carboxylated cellulose nanocrystals. *J. Environ. Sci.* **2013**, *25*, 933–943, doi:10.1016/S1001-0742(12)60145-4.

374. Srivastava, S.; Kardam, A.; Raj, K.R. Nanotech Reinforcement onto Cellulosic Fibers: Green Remediation of Toxic Metals. *Int. J. Green Nanotechnol* **2012**, *4*, 46–53, doi:10.1080/19430892.2012.654744.

375. Ma, H.; Hsiao, B.S.; Chu, B. Ultrafine Cellulose Nanofibers as Efficient Adsorbents for Removal of UO2 2+ in Water. *Macro Lett.* **2012**, *1*, 213–216, doi:10.1021/mz200047q.

376. Sharma, P.R.; Chattopadhyay, A.; Sharma, S.K.; Geng, L.; Amiralian, N.; Martin, D.; Hsiao, B.S. Nanocellulose from Spinifex as an Effective Adsorbent to Remove Cadmium(II) from Water. *Sustain. Chem. Eng.* **2018**, *6*, 3279–3290, doi:10.1021/acssuschemeng.7b03473.

377. Bharathiraja, B.; Ebenezer Selvakumari, I.A.; Iyyappan, J.; Varjani, S. Itaconic acid: an effective sorbent for removal of pollutants from dye industry effluents. *Curr. Opin. Environ. Sci. Heal.* **2019**, *12*, 6–17, doi:10.1016/J.COESH.2019.07.004.

378. Roa, K.; Oyarce, E.; Boulett, A.; ALSamman, M.; Oyarzún, D.; Pizarro, G.D.C.; Sánchez, J. Lignocellulose-based materials and their application in the removal of dyes from water: A review. *Sustain. Mater. Technol.* **2021**, *29*, e00320, doi:10.1016/J.SUSMAT.2021.E00320.

379. Goetz, L.A.; Naseri, N.; Nair, S.S.; Karim, Z.; Mathew, A.P. All cellulose electrospun water purification membranes nanotextured using cellulose nanocrystals. *Cellulose* **2018**, *25*, 3011–3023, doi:10.1007/s10570-018-1751-1.

380. Jin, L.; Li, W.; Xu, Q.; Sun, Q. Amino-functionalized nanocrystalline cellulose as an adsorbent for anionic dyes. *Cellulose* **2015**, *22*, pages2443–2456, doi:10.1007/s10570-015-0649-4.

381. Ansaloni, L.; Salas-Gay, J.; Ligi, S.; Baschetti, M.G. Nanocellulose-based membranes for CO_2 capture. *J. Memb. Sci.* **2017**, *522*, 216–225, doi:10.1016/J.MEMSCI.2016.09.024.

382. Lehtonen, J.; Hassinen, J.; Kumar, A.A.; Johansson, L.-S.; Mäenpää, R.; Pahimanolis, N.; Pradeep, T.; Ikkala, O.; Rojas, O.J. Phosphorylated cellulose nanofibers exhibit exceptional capacity for uranium capture. *Cellulose* **2020**, *27*, 10719–10732, doi:10.1007/s10570-020-02971-8.

383. Kumar, R.; Sharma, R.K.; Singh, A.P. Grafting of cellulose with N-isopropylacrylamide and glycidyl methacrylate for efficient removal of Ni(II), Cu(II) and Pd(II) ions from aqueous solution. *Sep. Purif. Technol.* **2019**, *219*, 249–259, doi:10.1016/J.SEPPUR.2019.03.035.

384.	Kumar, R.; Sharma, R.K.; Singh, A.P. Cellulose based grafted biosorbents - Journey from lignocellulose biomass to toxic metal ions sorption applications - A review. *J. Mol. Liq.* **2017**, *232*, 62–93, doi:10.1016/J.MOLLIQ.2017.02.050.

385.	Zhang, X.; Wang, L.; Dong, S.; Zhang, X.; Wu, Q.I.; Zhao, L.; Shi, Y.; Library, W.O. Nanocellulose 3, 5-Dimethylphenylcarbamate Derivative Coated Chiral Stationary Phase: Preparation and Enantioseparation Performance. *Chirality* **2016**, *28*, 376–381, doi:10.1002/chir.22578.

386.	Dong, S.; Sun, Y.; Zhang, X.; Li, H.; Luo, G.; Zhao, L. Nanocellulose crystals derivative-silica hybrid sol open tubular capillary column for enantioseparation. *Carbohydr. Polym.* **2017**, *165*, 359–367, doi:10.1016/J.CARBPOL.2017.02.060.

387.	Zhang, J.-H.; Xie, S.-M.; Zhang, M.; Zi, M.; He, P.-G.; Yuan, L.-M. Novel Inorganic Mesoporous Material with Chiral Nematic Structure Derived from Nanocrystalline Cellulose for High-Resolution Gas Chromatographic Separations. *Anal. Chem* **2014**, *86*, 9595−9602, doi:10.1021/ac502073g.

388.	Ludwicka, K.; Jedrzejczak-Krzepkowska, M.; Kubiak, K.; Kolodziejczyk, M.; Pankiewicz, T.; Bielecki, S. Medical and Cosmetic Applications of Bacterial NanoCellulose. In *Bacterial Nanocellulose: From Biotechnology to Bio-Economy*; Gama, M., Dourado, F., Bielecki, S., Eds.; Elsevier, 2016; pp. 145–165 ISBN 978-0-444-63458-0.

389.	Meftahi, A.; Samyn, P.; Geravand, S.A.; Khajavi, R.; Alibkhshi, S.; Bechelany, M.; Barhoum, A. Nanocelluloses as skin biocompatible materials for skincare, cosmetics, and healthcare: Formulations, regulations, and emerging applications. *Carbohydr. Polym.* **2022**, *278*, 118956, doi:10.1016/J.CARBPOL.2021.118956.

390.	Zhang, Z.; Zhang, B.; Grishkewich, N.; Berry, R.; Tam, K.C. Cinnamate-Functionalized Cellulose Nanocrystals as UV-Shielding Nanofillers in Sunscreen and Transparent Polymer Films. *Adv. Sustain. Syst.* **2019**, *3*, 1800156, doi:10.1002/adsu.201800156.

391.	Dufresne, A. Nanocellulose Processing Properties and Potential Applications. *Curr. For. Reports* **2019**, *5*, 76–89, doi:10.1007/s40725-019-00088-1.

392.	Pastrana, H.; Avila, A.; Tsai, C.S.J. Nanomaterials in Cosmetic Products: the Challenges with regard to Current Legal Frameworks and Consumer Exposure. *Nanoethics* **2018**, *12*, 123–137, doi:10.1007/s11569-018-0317-x.

Chapter I

Chapter II
Objectives and work plan

1. Objectives of the work

In recent years, cellulose has received increasing interest as a renewable raw material for producing biodegradable polymeric products and contributing to replacing fossil resources, considering their depletion, fluctuation in oil prices, and the negative environmental impacts [1]. Among the available sources of renewable feedstock for cellulose isolation, lignocellulosic biomass, including agricultural residues, stands out [2]. These residues are used today, in the best of cases and in small quantities, as organic compost and as cattle feed. However, most of these residues are simply burnt in the field causing air pollution and risk of fire. Moreover, if these residues are not removed, they can support infestations, causing potential environmental issues. Therefore, new strategies for the exploitation of agri-food residues (AFRs) represent a great opportunity of more sustainable routes for the recovery of high value-added compounds, as well as for mitigating their environmental burden.

In this scenario, the main challenge of this Ph.D. thesis work is to develop a green technology platform for an efficient and sustainable valorization of AFRs, ensuring the recovery of high-added value compounds, cellulose and nanocellulose (NCs) to be used as building blocks to develop more eco-friendly advanced materials.

The key innovation of proposed strategy is the integration of novel and/or more consolidated technologies to recover cellulose from AFRs at various degrees of hierarchical organization, by co-extracting bioactive molecules, cascading different physical processes (such as high-pressure homogenization HPH and ball milling BM), chemical and enzymatic hydrolysis of increasing complexity (Figure II.1).
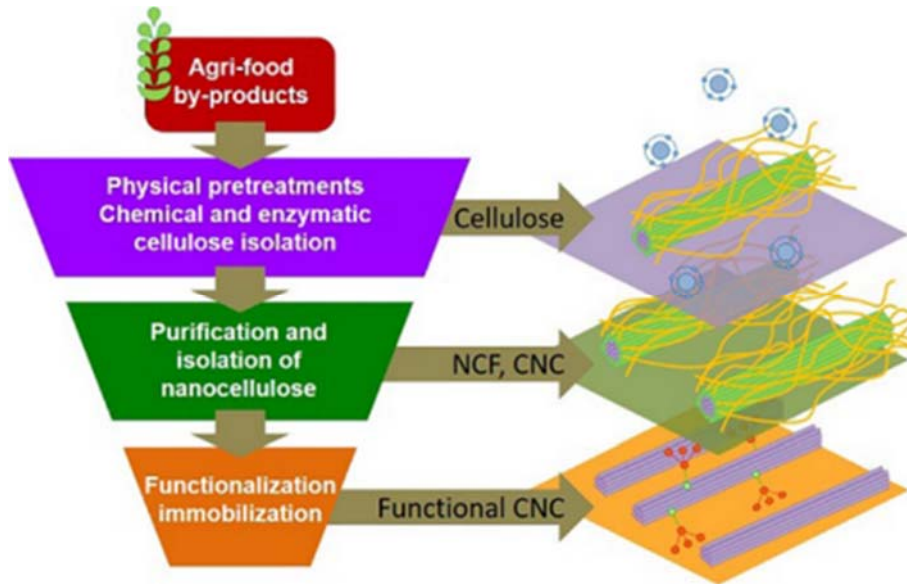
Figure II.1 *Envisioned recovery of different hierarchical NCs structures from AFRs, for advanced applications [3].*

2. Experimental plan

In order to achieve these goals, the project has been articulated as schematised in the following table (Table II.1).

Table II.1 *Ph.D. thesis main work plan.*

Biomass	Target compounds	Process design	Potential applications
Hemp cake Sunflower cake Roasted coffee beans White grape pomace Red grape pomace Bran Rice husk Wheat middlings	Bioactive compounds	Chemical treatments *(Solid/Liquid extraction, TEMPO-mediated oxidation, acid and alkaline hydrolysis)* Mechanical treatments *(HPH, PFI-beater, BM)*	Pickering emulsions Capillary suspensions Edible coating Aerogels for wastewater treatment
Tomato pomace Barley straw	Bioactive compounds		
	Cellulose	Combination of chemical and mechanical treatments	
	Nanocellulose		
Cellulose	Nanocellulose	Combination of chemical and mechanical treatments	CO_2 adsorption

More in detail, as reported in Figure II.2, the results of this thesis work have been structured in two chapters:

Bioactive compounds, cellulose, and NCs extraction

This chapter proposes a biorefinery approach for the utilization of AFRs for the recovery of valuable compounds carried out through an optimization of conventional solid/liquid extraction conditions. The main outcomes in terms of extract composition and its antioxidant power are presented and discussed. Moreover, the effect of HPH technology on the release of high value-added intracellular compounds from AFRs was performed with the aim to increase phenolics extraction yields with the use of purely physical process and without the usage of chemicals. For the sake of comparison, the efficiency of HPH-assisted extraction tests was compared to those observed in conventional solvent diffusion processes.

In this cascade of operations, this chapter focused also on the recovery of cellulose and the isolation of NCs. In particular, the HPH fluid-mechanical treatment is here exploited for the first time to increase the efficiency of mild chemical hydrolysis processing for isolation of cellulose with a defibrillated structure from AFRs, further contributing to the valorization of side streams very rich in bioactive compounds. Moreover, the isolation of cellulose has been also achieved through the Kombucha tea fermentation process using AFRs as substitutes for sucrose substrate. The cellulose-based pellicle formed at the air-liquid interface, called Symbiotic Culture of Bacteria and Yeast (SCOBY), forms a strong gel biofilm of crystalline microfibrils and absence of impurities of pectin, lignin, and hemicelluloses as well as environmentally friendly. The resulting cellulose pulp from AFRs was characterized and then its hierarchical structure disassembled by means chemical or purely mechanical treatments in order to obtain NCs. Moreover, it has been also evaluated the effect of mechanical treatments on commercial pure cellulose, to compare the physico-chemical, structural, morphological, and functional properties of NCs isolated from AFRs.

Advanced and innovative applications

The obtained materials have been used as target compounds in different field of application. In particular, NCs and bioactive compounds with different morphological and physical properties have been exploited to design advanced functional materials, such as: (i) Pickering emulsions and (ii) capillary suspensions oleocolloids for food applications; (iii) aerogels for the treatment of dye-contaminated wastewater due to its high surface area and versatile surface chemistry; (iv) edible coatings to improve polysaccharide-based packaging material properties (such as mechanical and thermal properties, antibacterial properties, oxygen and water vapor permeability); and (v) and amine modification for CO_2 capture.

Chapter II
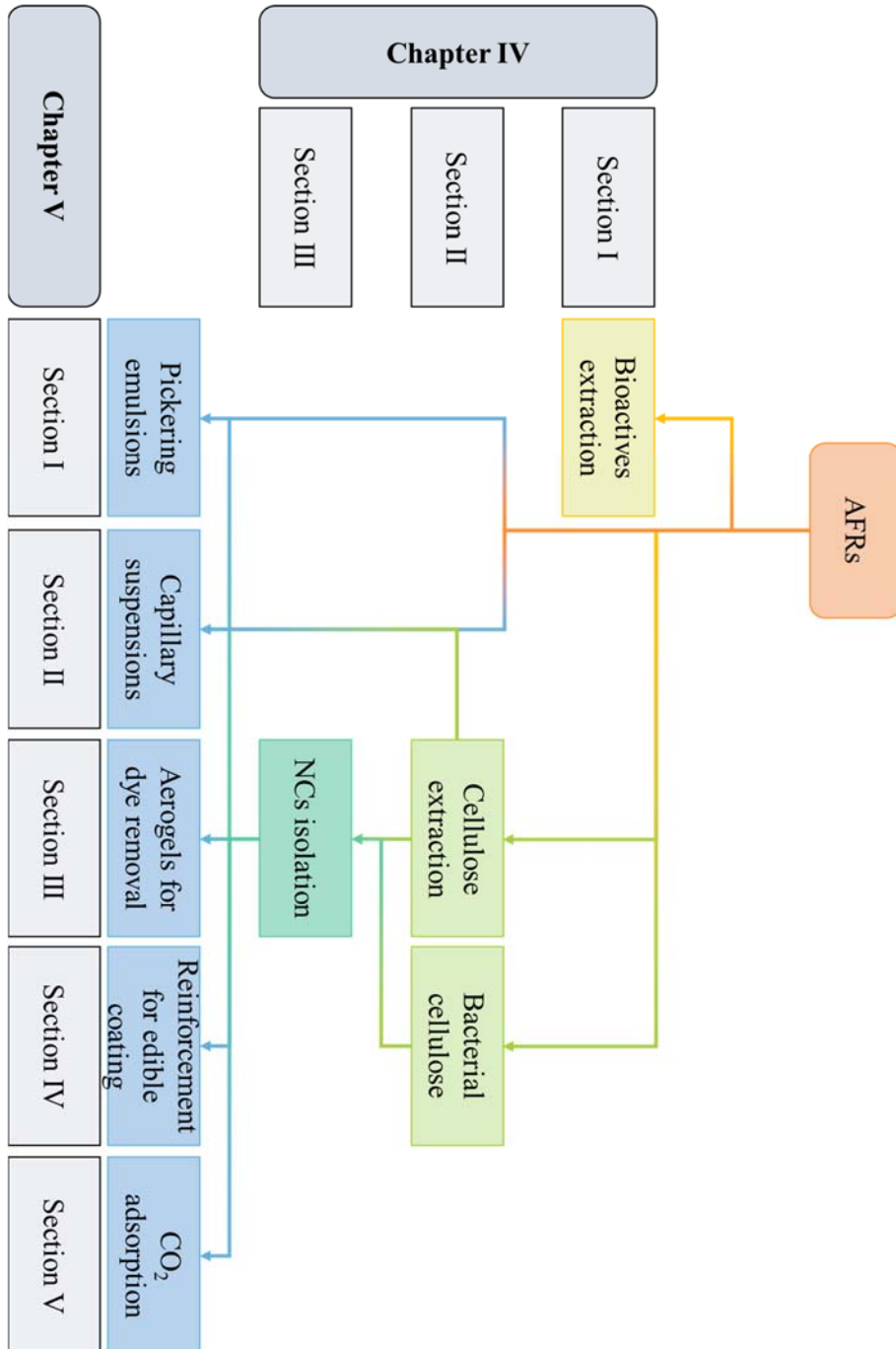
Figure II.2 *Process flow diagram from AFRs to innovative applications through different steps of valuable bioactive compounds extraction, cellulose production and NCs isolation.*

94

3. References

1. Araújo, D.J.C.; Machado, A.V.; Vilarinho, M.C.L.G. Availability and Suitability of Agroindustrial Residues as Feedstock for Cellulose-Based Materials: Brazil Case Study. *Waste and Biomass Valorization* **2019**, doi:10.1007/s12649-018-0291-0.
2. Pirozzi, A.; Ferrari, G.; Donsì, F. Cellulose Isolation from Tomato Pomace Pretreated by High-Pressure Homogenization. *Foods* **2022**, doi:10.3390/foods11030266.
3. PANACEA Available online: https://sites.google.com/unitn.it/panacea/home?authuser=0.

Chapter II

Chapter III
Materials and methods

1. AFRs from food sectors

The biomasses selected and used as raw materials in this thesis work are listed in the following table (Table III.1). The choice of these biomasses arises, first of all, from their amount and rich content of value-added derivatives (bioactive compounds and non-starch-polysaccharides). Secondly, the selection of these biomasses was also performed taking into account their availability throughout the year, since different food by-products cover different period of the year, thus avoiding overlapping and dead periods during the experimental work.

Table III.1 *AFRs biomasses selected to be valorized through the recovery of valuable compounds, cellulose extraction, and nanocellulose isolation.*

AFRs		Target compounds	Availability
	Hemp cake	Bioactive compounds (Polyphenols)	Autumn/Winter (October – March)
	Sunflower cake	Bioactive compounds (Polyphenols)	Autumn/Winter (October – March)
	Roasted coffee beans	Bioactive compounds (Polyphenols)	All year
	White grape pomace	Bioactive compounds (Polyphenols)	Summer/Autumn (September – October)
	Red grape pomace	Bioactive compounds (Polyphenols)	Summer/Autumn (September – October)
	Wheat middlings	Bioactive compounds (Polyphenols)	Autumn/Winter/Spring (October – July)
	Wheat bran	Bioactive compounds (Polyphenols)	Autumn/Winter/Spring (October – July)
	Rice husk	Bioactive compounds (Polyphenols)	Autumn/Winter/Summer (November – June)
	Tomato pomace	Bioactive compounds (Polyphenols) Cellulose Nanocellulose	Summer/Autumn (June – October)
	Barley straw	Cellulose Nanocellulose	Summer/Autumn/Winter (August – February)

Chapter III

All raw materials are dried residues (with humidity less than 10% on dry matter), except tomato and grape pomace, which were stored in aluminium trays and frozen at -20 °C until used.

2. Nonthermal mechanical systems

This paragraph covers the various methods of mechanical cell disruption and homogenization that have been used for processing AFRs and cellulosic materials throughout the whole experimental analysis. Treatments were used for high value-added compounds isolation, cellulose extraction processes as well as for the further defibrillation of cellulose and, therefore, converting cellulose to nanocellulose (NCs), as explained in more detail in chapter IV.

2.1. High-Shear Mixing (HSM)

HSM (Ultra Turrax T-25, IKA Labortechnik, Staufen, Germany) (Figure III.1) system was used as a gentle pre-treatment prior to perform High-Pressure Homogenization (HPH) treatment with the aim of (i) disaggregating cell clusters of food residues, which consequently lead to mechanical lyse of plant tissue; (ii) dispersing and/or dissolving immiscible mixtures with components of different phases; and (iii) pre-emulsifying activity. The HSH is essentially a stirring device at high speed (3,000 - 35,000 rpm 800 W) which consisted of a stator-rotor assembly made of stainless steel. The relative motion of the rotating and stationary parts of the mixer generates shearing forces (the driving principle) mixing the components in suspension. Due to friction, a significant temperature rise should be expected with the use of HSM. In order to avoid an excessive temperature increase, the suspensions were always kept in an ice-water bath during processing.
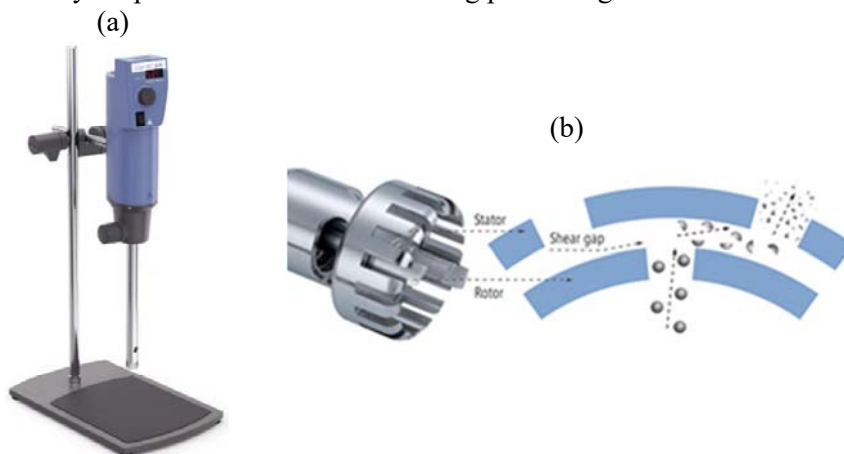
Figure III.1 *High-Shear Mixing (HSM) technology: (a) Ultraturrax T-25 system and (b) schematization of the rotor-stator working principle.*

2.2. HPH technology

HPH process is the purely physical technology of subdividing large particles in suspensions into a large number of small particles having a smaller size, down to nanometer range. The disruption of particles during HPH treatment occurs through different fluid-mechanical stresses: shearing effect, stress, turbulence, and hydrodynamic cavitation. The entire process occurs within the homogenization valve, and the overall disintegration efficiency depends on the specific valve geometry and design and flow conditions. The HPH technology applied during the experimental activities of this work is different for the specific valve geometry and, therefore, for operating conditions: the in-house developed unit used at the University of Salerno (available at ProdAl Scarl research centre) (§ III.2.2.1), and the lab-scale plant used at the University of Córdoba during the pre-doctoral visiting research internship (§ III.2.2.2).

2.2.1. In-house developed unit (at the University of Salerno)

The in-house developed laboratory scale HPH system used at the University of Salerno is shown in Figure III.2. Briefly, the unit consisted mainly of a homogenization orifice valve (model WS1973, Maximator JET GmbH, Schweinfurt, Germany) of different sizes and an air driven high-pressure pump (model DXHF-683, Haskel EGAR S.r.l., Milan, Italy). Pressure is first intensified by the high-pressure pump that pressurizes the product suspension which results in a fluid pressurization system. The high pressure generated can be up to 300 MPa and acts as the driving force that results in the flow of the fluid through and beyond the homogenization valve. The homogenization valve (Figure III.2c) consists of a small orifice (80 - 200 μm) in between the valve and the valve seat. The pressure drop across the orifice could be changed in the range between 80 and 200 MPa, while the volumetric flow rate of the suspension changed from 10 to 22 mL/s depending on the orifice diameter used and therefore on the selected pressure. In order to prevent excessive heating, after each pass, the suspensions were cooled by water flowing through a tube-in-tube exchanger, located downstream of the orifice valve.

(a)
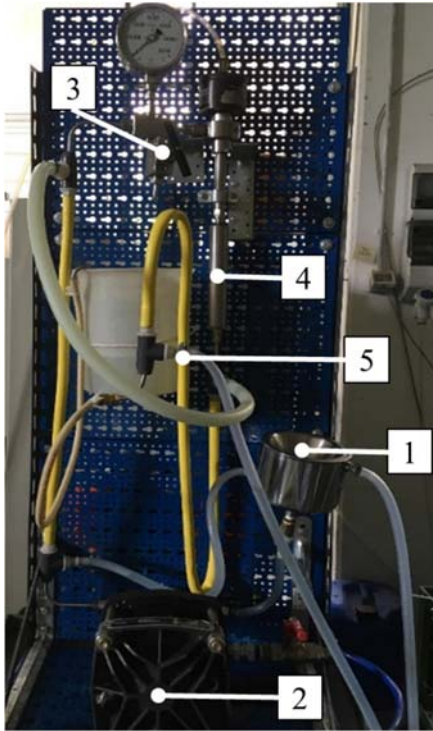
1	Jacketed inlet/collection tank
2	High-pressure pump
3	3-way ball valve
4	Homogenization valve
5	Cooling heat exchanger

(b)

(c)
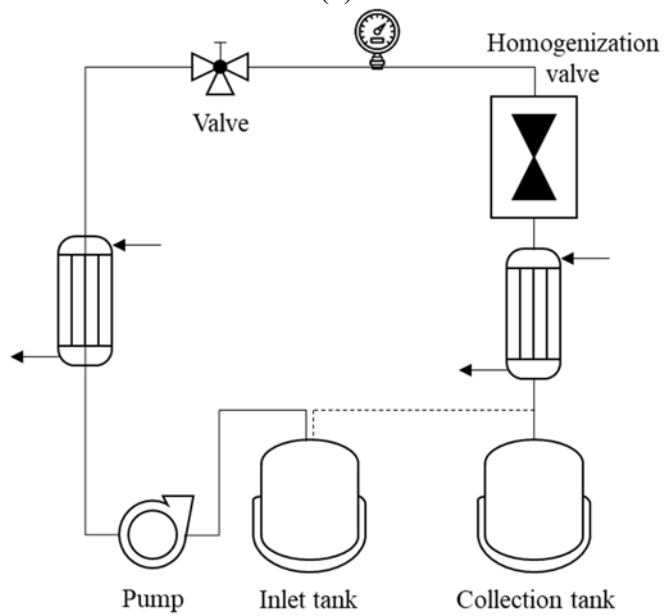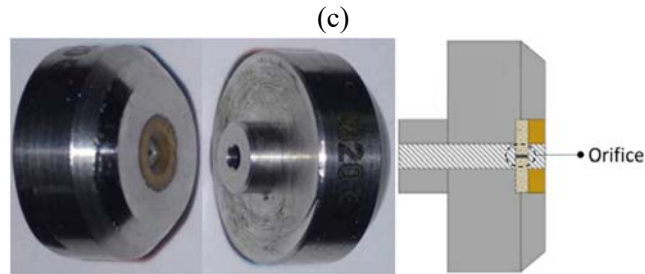
Figure III.2 *In-house developed HPH: (a) HPH plant available at ProdAl Scarl, (b) schematic representation of HPH system, and (c) homogenization orifice valve.*

HPH processing conditions used for the release of intracellular compounds, cellulose extraction, and NCs defibrillation were identified and in detailed illustrate in the specific chapter IV.

2.2.2. Lab-scale plant (at the University of Córdoba)

The lab-scale HPH system (PandaPLUS 2000, GEA Mechanical Equipment S.p.A., Düsseldorf, Germany) used at the University of Córdoba is shown in Figure III.3. PandaPLUS HPH technology consists of a high-pressure piston pump and a downstream two stages homogenizing valve. The pressure build-up within the HPH occurs by means of the piston pump which, with the help of ceramic pistons, ensure a volume flow of 2.5 mL/s that is independent of pressure. This system can operate at any pressure up to 200 MPa adjusted manually by hand-wheel.

(a) (b)
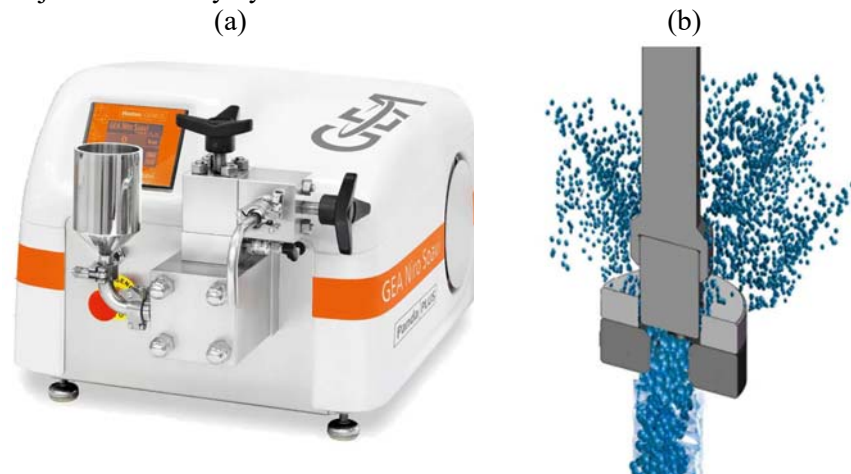
Figure III.3 *Lab-scale HPH: (a) PANDAPlus 2000 HPH plant and (b) homogenization orifice valve.*

2.3. Ball milling (BM) technology (at IPCB-CNR of Naples)

The planetary BM system (Retsch PM100, Haan, Germany) available at IPCB (Istituto per i Polimeri, Compositi e Biomateriali) of Consiglio Nazionale delle Ricerche (CNR) of Naples is shown in Figure III.4. The grinding jar (Figure III.4b) is arranged eccentrically on the sun wheel of the planetary ball mill. The direction of movement of the sun wheel is opposite to that of the grinding jars in the ratio 1:2. The grinding balls in the jars are subjected to superimposed rotational movements, the so-called Coriolis forces. The difference in speeds between balls (usually stainless-steel spheres with a diameter of 10 mm) and jars produces an interaction between frictional and impact forces, which releases high dynamic energies. The interplay between these forces produces the high and very effective degree of size reduction of the planetary ball mill, both, in ball to ball and ball to wall interactions (Figure III.4c).
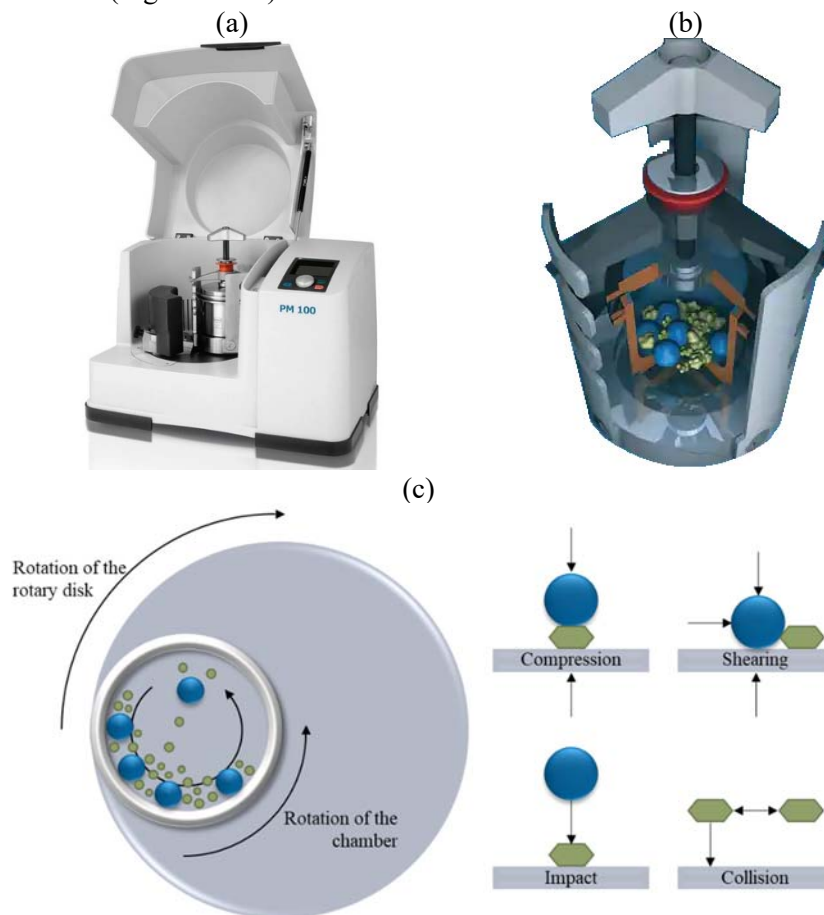
Figure III.4 *BM technology: (a) Retsch PM100 system, (b) grinding jar, and (c) schematisation of the BM working principle.*

3. Phytochemicals bioactive compounds extraction process

Phytochemical compounds, secondary metabolites of plants, herb, fruits, and vegetables, which provide certain color, flavor, or protection against pests and pathogens [1], can be recovered using various conventional and non-conventional extraction techniques. The conventional chemical methods for bioactive extraction are widely used because well established and easy to perform. The main limitations are related to the long duration of extraction, high cost to use high purity solvent, the use of heat treatment which will result in degradation of thermo-labile phytochemicals, as well as the limited application of the extracted phytochemicals in foods as solvents may pose harmful effects when ingested. Therefore, alternative approaches involving nonthermal or solvent-free extraction methods are highly desirable for application of phytochemicals in the food industry.

3.1. Conventional solid-liquid extraction (SLE)

The process of conventional SLE from AFRs was carried out using an orbital incubator (Stuart SI50, Salford Scientific Supplies Ltd, Salford, Manchester, England) at 25 °C and 160 rpm. Raw material (20 g) was mixed with 200 mL of the solvent (methanol, ethanol, and acetone) at different dilutions with distilled water (ranging from 20 to 100% v/v) and kept at room temperature up to 24 h. Then, the extract was centrifuged (PK121R model, ALC International, Cologno Monzese, Milan, IT) at 10,000×g-forces at 4 °C for 10 min to obtain clear supernatants, which were used for further quali-quantitative analyses (Figure III.5). Extractions were performed in duplicate.
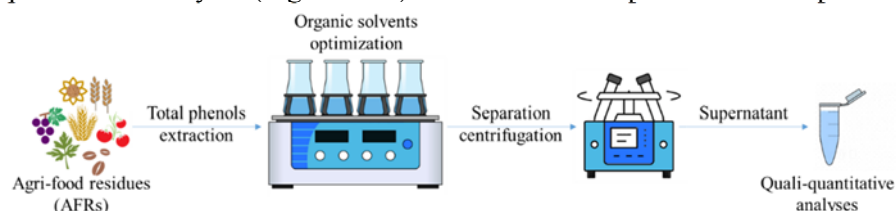
Figure III.5 *Simplification of conventional extraction procedure carried out on AFRs raw materials.*

Response Surface Methodology (RSM) model for the design of experiments (DOE) was used for modelling and optimization of conventional solid-liquid extraction. A factorial experiment involving two factors (the type of solvent, discrete numeric factor, and solvent concentration) was used to optimize the polyphenols extraction yield. I-Optimal Design was applied in this study, using Design-Expert 11.1.2.0 software (Statease Inc., Minneapolis, MN, U.S.) to determine the number of experiments to be evaluated for the optimization of the two independent and the response variables.

The experiments with two replications were fitted with a second-order polynomial Equation III.1.

$$Y_1 = \beta_0 + \sum_j \beta_j X_j + \sum \sum_{i<j} \beta_{ij} X_i X_j + \varepsilon \qquad \text{(III.1)}$$

In this equation, the values of the total phenols, used as the response variable (Y_1), were related to the experimental factors ($X_{i,j}$ with i,j = 1, 2). The coefficients of the polynomial model correspond to a constant term (β_0), linear effects (β_j), and pure second-order interaction effects (β_{ij}) obtained by the multiple nonlinear regression method, with ε being the model error.

The performance and adequacy of the developed RSM model were assessed following statistical parameters estimated using analysis of variance (ANOVA): determination coefficients (R^2, Adj R^2), the coefficient of variation (CV), and probability values (p-value).

3.2. HPH-assisted extraction

One of the emerging applications is the use of HPH nonthermal technology for the extraction of phytochemicals, which requires polluting solvent-free approaches and short processing times. HPH-assisted extraction experiments were performed by firstly mixing raw materials suspended in distilled water at 5 wt% using HSM (§ III.2.1) equipped with an S25-N18 G rotor and operated at 20,000 rpm in an ice bath to avoid any temperature increase. The HSM suspensions after 5 min of processing were, subsequently, submitted to HPH processing using in-house developed unit (§ III.2.2.1). HPH was carried out using an orifice valve assembly (orifice diameter ranging between 150 and 200 µm) at 80 - 100 MPa for up to 20 passes. After each pass, the suspensions were cooled down in a tube-in-tube heat exchanger set at different temperatures, to ensure that the product temperature was ranging between 5 and 50 °C. Then, the extract was centrifuged (PK121R model, ALC International, Cologno Monzese, Milan, IT) at 10,000×g-forces at 4 °C for 10 min to obtain clear supernatants, which were used for further quali-quantitative analyses (Figure III.6). Extractions were performed in duplicate.
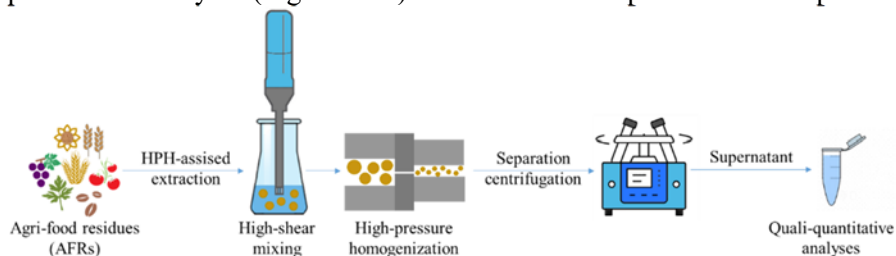
Figure III.6 *Simplification of the HPH-assisted extraction procedure carried out on AFRs raw materials.*

4. Cellulose fiber isolation process

Cellulose isolation from AFRs requires a top-down chemical deconstructing strategy, conventionally based on strong acid hydrolysis. This process is the most widely used strategy because it is inexpensive and can induce the breakdown of the fibrous cell walls, remove the lignin and hemicellulose fraction, and, thus, expose the cellulose for extraction [2]. However, there are several disadvantages in using this conventional approach, such as corrosion of equipment, environmental damage, as well as safety issues [3]. For these reasons, the increase in efficiency of these isolation methods, while decreasing the severity of the operating conditions, is highly desirable. In this scenario, the aim of this work is to develop an efficient process to isolate cellulose from AFRs via (i) mild chemical hydrolysis; (ii) the combination of mechanical treatments by HPH technology and mild chemical hydrolysis processes [4]; (iii) pulping process; and (iv) bacterial fermentation.

4.1. Mild chemical hydrolysis

Mild chemical hydrolysis was performed to extract cellulose fiber from tomato pomace, mainly composed of skins and seeds, kindly provided by the industrial processing company Salvati Mario & C. spa (Mercato San Severino, Italy), and from wheat bran. The tomato pomace was dried in an oven at 50 °C for 48 h. The dried material was milled in a lab knife grinder and sieved to a final particle size ≤ 2 mm. The milled pomace (sample TP) was packed in vacuum-sealed flexible pouches (multilayer packaging OPP30-A19-LDPE70, Di Mauro Officine Grafiche S.p.A., Cava de' Tirreni, Italy) and kept at 5 °C until used. In contrast, the humidity of wheat bran was $7.66 \pm 0.09\%$, therefore no drying process needed before cellulose isolation process.

Cellulose from tomato pomace was extracted through a cascade chemical route, consisting of three consecutive steps (Figure III.7). Initially (first step), the samples were treated with a 4.7% v/v H_2SO_4 solution (1:10 $m_{Sample}:v_{Solution}$) in a static autoclave at 121 °C for 45 min to hydrolyze polysaccharides and acid-soluble polyphenols. After acid hydrolysis, the samples were removed from the autoclave and rapidly cooled under running water. The second step consisted of the alkaline hydrolysis carried out by using 4 N NaOH solution (1:10 $m_{Sample}:v_{Solution}$) at 25 °C for 24 h under continuous stirring to dissolve the remaining hemicellulose, lignin, and other polysaccharides. Finally, in the third step, the samples were bleached with 4% H_2O_2 solution, with pH adjusted to 11.5 with NaOH (1:10 $m_{Sample}:v_{Solution}$), at 45 °C for 8 h under continuous stirring. At the end of each step, the solid residue and liquors were separated through vacuum filtration. Liquors were recovered and used for further characterization. Meanwhile, solid residues were washed by flushing distilled water until the pH of the eluted water reached neutral values, and

dried in an oven at 50 °C for 24 h. The resulting cellulose pulp was dried to be used for further characterization.
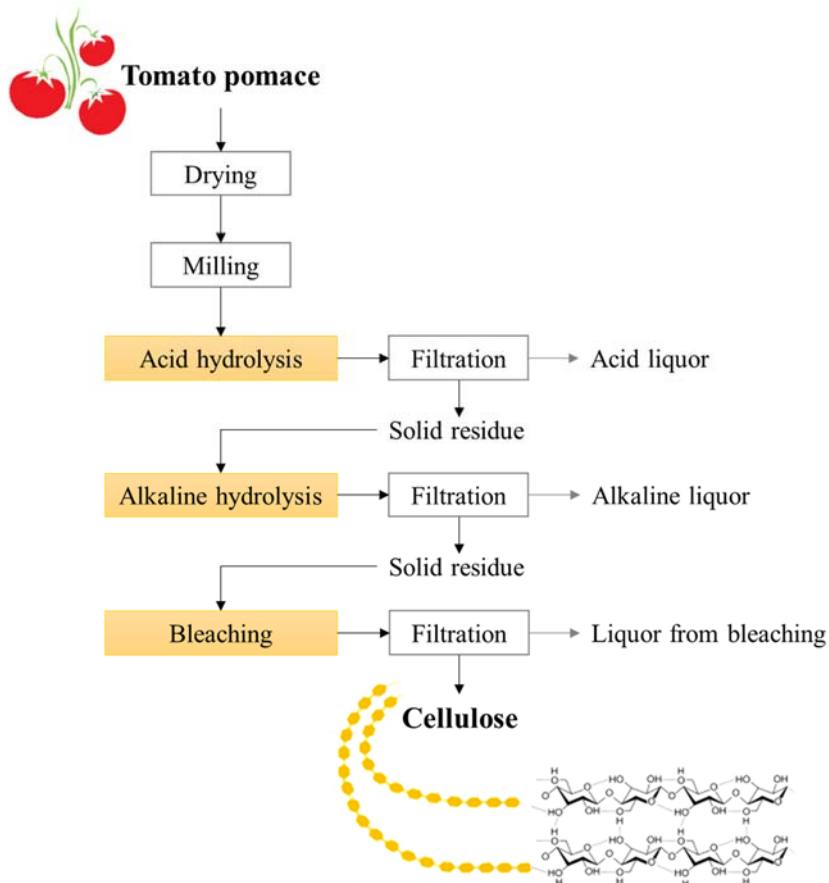
Figure III.7 *Schematic diagram of the procedures for extracting cellulose from tomato pomace through cascade of mild chemical hydrolysis.*

4.2. HPH-assisted chemical hydrolysis

The HPH fluid-mechanical treatment is exploited for the first time to increase the efficiency of mild chemical hydrolysis processing for isolation of cellulose with a defibrillated structure from tomato pomace. To evaluate the effect of HPH treatment it has been applied at different level of chemical step: before acid hydrolysis, before alkaline hydrolysis and before bleaching step, as shown in Figure III.8. In particular, the HPH treatment applied after each chemical steps follows the procedure described below.

The tomato pomace was suspended in bidistilled water at 0.5 wt% on dry weight. Then, the suspension was subjected to HSM at 20,000 rpm for 10 min with the Ultra Turrax device (§ III.2.1) equipped with an S25-N18 G rotor in an ice bath, to avoid any temperature rises. Subsequently, the obtained

suspension was treated by HPH using orifice diameter of 200 µm at 80 MPa and 25 °C for up to 20 passes, using an in-house developed system (§ III.2.2.1). At the end of the HPH treatment, the suspension was concentrated by using an R-200/205 Rotavapor (BÜCHI Labortechnik AG, Flawil, Switzerland) until achieving a volume reduction of up to 70%, prior to being freeze-dried in a 25 L VirTis Genesis freeze-drier (SP Scientific Products, Stone Ridge, NY, USA) at 7 Pa for 72 h. The HPH-treated freeze-dried sample was then packed in vacuum-sealed flexible pouches and stored under refrigerated conditions before proceeding to the isolation of cellulose through the chemical hydrolysis steps.
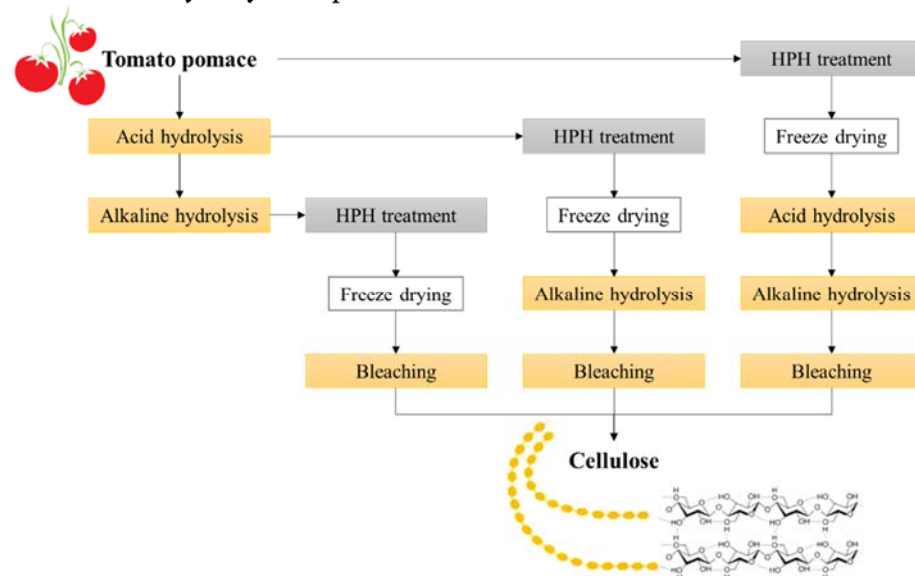
Figure III.8 *Schematic diagram of the procedures for extracting cellulose from tomato pomace through HPH-assisted chemical hydrolysis.*

4.3. Pulping process

Cellulose fibers were isolated from barley straw AFRs through pulping process (Figure III.9) by alkaline hydrolysis in a 15 lt reactor equipped with an external jacket to ensure the desired treatment temperature and a motor to achieve the stirring of pulp suspension rotating the reaction vessel by means of a horizontal axis. The barley straw was subjected to a soda pulping process (NaOH at 7 wt%$_{DM}$) for 150 min at 100 °C with a liquid/solid ratio of 10:1. The selected conditions entailed the minimum alkaline treatment concentration, temperature, and time for satisfactory cellulose pulp formation. After the pulping process, the cellulosic pulp was washed, dispersed in a pulp disintegrator for 30 min at 1,200 rpm, and then fed to a refiner mechanical pulping with a clearance between rotor and stator refiner plates about 5

107

(Sprout-Bauer refiner) for facilitating the generation of shorter fibers. Finally, the pulp was filtered by sieving through a 0.14 mm mesh size and, after centrifugation to remove excess water, was dried at 60 °C for 24 h. Afterward, the obtained cellulose pulp was subjected to a bleaching process to eliminate the lignin contained in the fibers. Briefly, 0.3 wt% on dry basis of $NaClO_2$ was added in acidified conditions (2 v% of acetic acid) to a 3 wt% on dry basis cellulose pulp suspension at 80 °C for 1 h. This treatment was repeated three times to achieve the final bleached cellulose fibers. By means of the bleaching process, purified cellulose pulp was obtained, although in the case of unbleached pulp, residual lignin content remained in the final product.
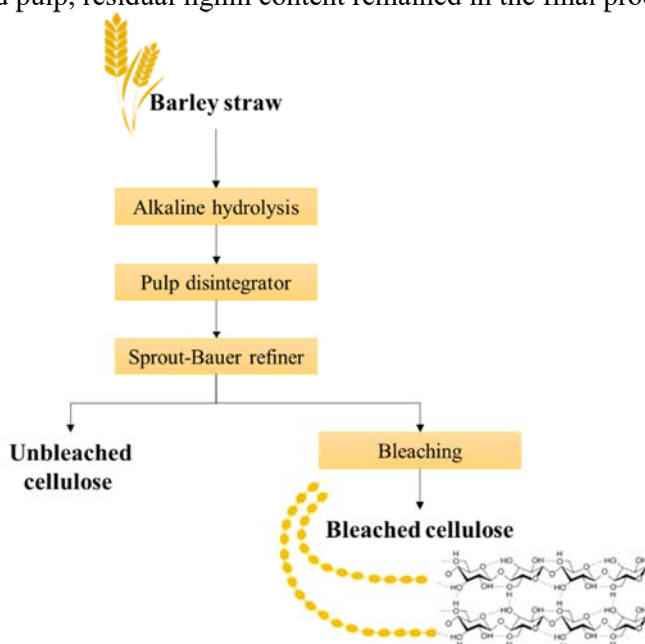
Figure III.9 *Schematic diagram of the procedures for extracting cellulose from barley straw through pulping process.*

4.4. Bacterial cellulose

SCOBY bacterial cellulose hydrogels were obtained in a static culture. Culture medium was composed of 80 g/L sucrose and 4 bags of black tea per litre of culture, at from the Department of Biochemistry of the University of Naples Federico II. Moreover, the micronized AFRs (HPH-TP and HPH-WM) in this study have been used at 13 g/L in substitution of sucrose in culture media for the production of bacterial cellulose. The container was covered with woven cotton fabric and left to stand in open air without direct sunlight to allow BC hydrogel to form on the air-liquid interface. The obtained BC hydrogel was kept in refrigerated conditions prior to further characterization and utilizations.

5. NCs isolation process

To obtain nanostructured cellulose, different top-down approaches have been evaluated (Figure III.10), including chemical and mechanical treatments and a combination of these treatments applied on (ligno)cellulosic fibers isolated from agricultural biomass.
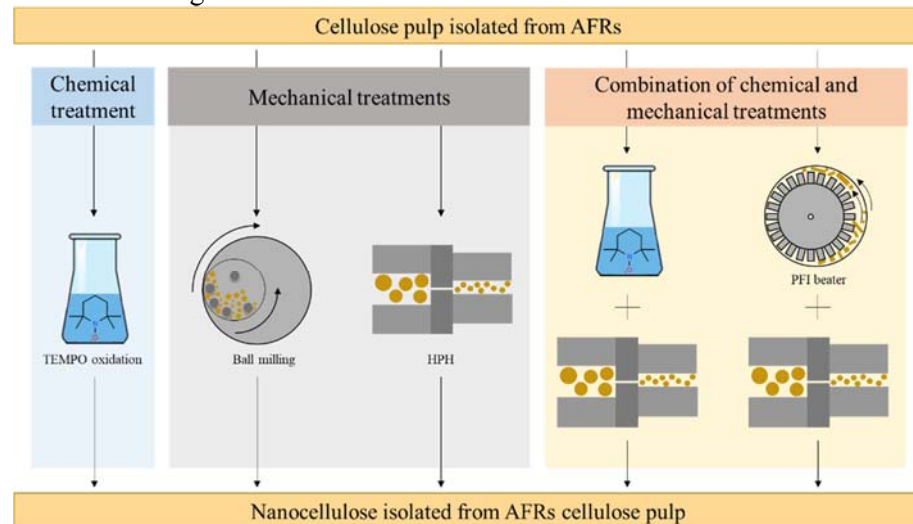
Figure III.10 *Schematisation of the combined chemical and mechanical treatment proposed in this work for NCs isolation from AFRs cellulosic pulp.*

Table III.2 *Summary of treatments and operating conditions for NCs isolation from commercial cellulose and AFRs.*

Cellulosic materials	Cellulose concentration (g/L)	Treatment applied	Conditions	Type of isolated NCs
CHEMICAL TREATMENTS				
Softwood kraft pulp Celeste 85	12.5	TEMPO-mediated oxidation	$C_9H_{19}N = 0.083$ wt% NaBr = 0.5 wt% t = 4 h	CNCs
Softwood kraft pulp Celeste 85	12.5	TEMPO-mediated oxidation	$C_9H_{19}N = 0.013$ wt% NaBr = 0.5 wt% t = 2 h	CNFs
MECHICAL TREATMENTS				
Cellulose Arbocel® BWW40 fibers	-	Ball milling	$V_{steel\ cup} = 125$ mL # steel spheres = 25 $d_{spheres} = 10$ mm $ratio_{spheres/cellulose} = 10:1$ t = 30 min	CNFs

Cellulose Arbocel® BWW40 fibers	-	Ball milling	$V_{steel\ cup}$ = 125 mL # steel spheres = 25 $d_{spheres}$ = 10 mm $ratio_{spheres/cellulose}$= 10:1 t = 60 min	CNFs

Cellulose Arbocel® BWW40 fibers	5	High-pressure homogenization	P = 80 MPa
			# passes = 20
			T = 5 °C
				CNFs

Tomato pomace	5	High-pressure homogenization	P = 80 MPa
			# passes = 20
			T = 5 °C
				CNFs

Bacterial cellulose	0.8	High shear mixing	v = 20,000 rpm t = 10 min T = 5 °C	MBC
COMBINATION OF CHEMICAL AND MECHANICAL TREATMENTS				
Barley straw	10	TEMPO-mediated oxidation	$C_9H_{19}N$ = 0.016 wt% NaBr = 0.1 wt% t = 2 h	(L)CNFs

		High-pressure homogenization	P = 30-90 MPa
			# passes = 10
			T = 5 °C	

Barley straw	100	PFI beater	$C_9H_{19}N$ = 0.016 wt% NaBr = 0.1 wt% t = 2 h	(L)CNFs
		High-pressure homogenization	v = 20,000 rpm P = 3 N/m t = 15 min	

5.1. Chemical treatments

NCs, in the form of nanocrystals (CNCs) and nanofibers (CNFs), were obtained through TEMPO-mediated oxidation, by controlling the intensity of the process (changing catalyst concentration and processing time), of northern bleached softwood kraft pulp Celeste 85 (kind gift of SCA, Sundsvall, Sweden), at laboratories of the Department of Physics of the University of Trento.

TEMPO-mediated oxidation was performed according to the method of Saito and Isogai [5] slightly modified as herein reported. In order to obtain CNCs, 5 g of Celeste 85 pulp was swollen in 400 mL distilled water. 83 mg of 2,2,6,6-Tetramethylpiperidine-1oxyl (TEMPO, $C_9H_{19}N$, ≥ 98.0%, Alfa Aesar Chemicals, Ward Hill MA, USA), the reaction catalyst, and 0.5 g of sodium bromide (NaBr, ≥ 99.99%, Carlo Erba, Milan, Italy), the catalyst re-cycling, were solubilized in 100 mL H_2O and added to the pulp suspension.

The reaction was started by adding 18 mL of sodium hypochlorite containing 6 - 14% active chlorine (NaClO, Sigma Aldrich, Milan, Italy) which is the primary oxidant. The pH of the reaction mixture was kept in the interval 10.5 - 11 by adding NaOH until it remained constant as occurred after 4 h. Then, the suspension was rinsed several times with distilled water and tip sonicated at 80% power delivered in the suspension aliquots of 35 mL volume by a Bandelin Sonuplus ultrasonicator system (Berlin, Germany).

CNFs were obtained with the same procedure except that a lower amount of TEMPO catalyst (12.5 mg instead of 83 mg) was used, and the reaction was stopped after 2 h. Finally, the suspension was rinsed several times with distilled water and tip sonicated at 80% power delivered in the suspension aliquots of 35 mL volume by a Bandelin Sonuplus ultrasonicator system (Berlin, Germany).

5.2. Mechanical treatments

5.2.1. BM treatment

Ball-milled cellulose particles were produced from commercial cellulose Arbocel® BWW40 fibers through BM at IPCB-CNR of Naples. Cellulose was preliminarily dried at 90 °C under vacuum for 24 h, and then samples (10.0 ± 0.1 g) were treated in a Retsch PM100 planetary ball-milling system (Haan, Germany), using a 125 mL steel milling cup and 25 steel spheres with a diameter of 10 mm [6]. The weight ratio of spheres/cellulose was about 10:1. The BM process was carried out for 30 min or 60 min.

5.2.2. HPH process

The HPH treatment was tested for its known ability to defibrillate cellulose [7]. Commercial cellulose Arbocel® BWW40 fibers, cellulose pulp isolated from tomato pomace was dispersed in distilled water at 5 g/L. Samples (200 mL) were pre-treated using a shear mixer (Ultra Turrax T-25, IKA Labortechnik, Germany) at 20,000 rpm for 5 min, within an ice bath, before HPH treatment at 80 MPa for 10 min at a flow rate of 22 mL/s, using an in-house developed unit, equipped with a 200 μm diameter orifice valve (model WS1973, Maximator JET GmbH, Schweinfurt). The use of smaller orifice valves (and, hence, of higher operating pressures) was not possible because of valve clogging. Tube-in-tube heat exchangers, with cold water at 5 °C, were placed immediately up-stream and downstream of the orifice valve to ensure that the product temperature was always kept < 10 °C. The obtained suspensions were stored at 4 °C until use.

5.2.2. HSM process

The HSM treatment was tested to micronize bacterial cellulose into microfibers. Scoby biofilms by-product of Kombucha tea fermentation process changing the culture media were dispersed in distilled water at 5 g/L and treated using a shear mixer (Ultra Turrax T-25, IKA Labortechnik, Germany) at 20,000 rpm for 10 min, within an ice bath. The obtained suspensions were stored at 4 °C until use.

5.3. Combination of chemical and mechanical treatments

The objective of this thesis work was not only to evaluate the efficacy of a single chemical or mechanical treatment on the isolation of NCs from AFRs cellulose pulp, but also to assess the feasibility of a combination of treatments to further improve the delamination of the cellulose fibers, as well as to tuning the physico-chemical properties of obtained nanostructured cellulose. Therefore, to fulfill this purpose, hurdle approaches have been proposed by using two independent pre-treatments prior to mechanical HPH process: (i) chemical process by TEMPO-mediated oxidation and (ii) mechanical beating by mechanical refining. Following both procedures on barley straw cellulose pulp, (ligno)cellulose CNFs were obtained at the University of Córdoba.

The TEMPO-mediated oxidation pre-treatment was carried out by suspending cellulose fibers at a final concentration of 10 g/L in distilled water containing TEMPO catalyst (0.016 wt%$_{DM}$) and sodium bromide (0.1 wt%$_{DM}$). The TEMPO-mediated oxidation was started by adding a specific amount of NaClO solution to obtain an oxidative power of 5 mmol/g on dry basis with continuous stirring at room temperature. The pH of suspension was maintained at 10 by adding NaOH solution (0.5 M) until no NaOH consumption was observed. After about 2 h of reaction time, 100 mL of ethanol was added to stop the oxidation reaction, and the oxidized fibers were filtered and washed several times with distilled water [10].

On the other hand, the mechanical pre-treatment was carried out by refining the cellulose fibers suspension at 100 g/L 20,000 rpm in a PFI beater (Mill PFI type, Metrotec, Kirchheim, Germany) to reach a Schopper–Riegler Degree (ºSR) of 90, according to ISO 5264-2:2002 [11,12].

A 10 g/L suspension of pre-treated fibers were subjected to a nanofibrillation process in a high-pressure homogenizer (PandaPlus 2000, GEA Niro, Düsseldorf, Germany) following 4 passes at 300 bars, 3 passes at 600 bars and 3 passes at 900 bars [8,9]. After this treatment, the suspension was cooled down at room temperature and stored at 4 °C before further chemico-physical characterization.

6. Papers and nanopapers formation

In the sector of paper and pulp industry, NCs have gained great interest because of their abundant availability, renewable and eco-friendly nature. Nanopaper is a fascinating free-standing thin film material and it is advantageous over traditional pulp paper due to its mechanical properties (such as high strength), optical transparency, thermal stability, smoothness, etc. Therefore, in this thesis an effort has been perfused to evaluate the properties of papers and nanopapers obtained using cellulosic pulp and NCs isolated, respectively, isolated from barley straw and how the intrinsic characteristics of NCs allow to modify the papers material properties. The cellulosic pulp and NCs were dispersed in a pulp disintegrator at a final concentration 5 g/L. The suspension was filtered under vacuum at -600 mbar until removal of supernatant water in a sheet former (Rapid Kothen, ISO 5269-2). Afterward, sheets were dried at 85 °C between two nylon sieves to prevent adherence and two cardboards until the papers and nanopapers were completely dried (Figure III.11). All papers were stored for 48 h in a conditioned room at 24 °C and 50% RH before characterization.
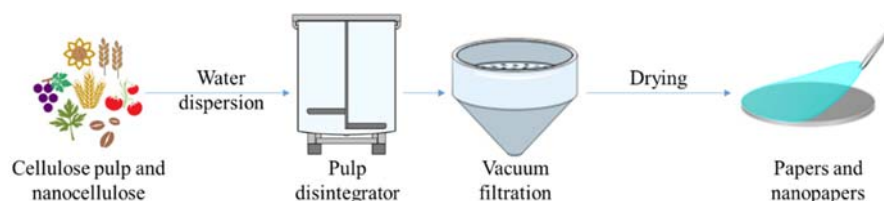
Figure III.11 *Simplification of papers and nanopapers formation procedure carried out on cellulose pulp and NCs.*

7. Analytical determinations

The composition of raw materials, the bioactivity of high-added compounds extracted, and the characterization of cellulose and NCs were determined by applying the official analytical methods described in the following sections.

7.1. Raw materials characterization

7.1.1. Moisture and ash content

In order to calculate the component content of different AFRs, the dry matter content is essential to make analytical results for the different parameters comparable. Moisture and ash content were gravimetrically determined by drying at 105 °C in an air-force oven (AOAC Method 950.46), and at 525 °C in a muffle (AOAC Method 923.02), respectively. The dry mass

content was expressed as g of dry matter per g of sample (g_{DM}/g), while the ash content was expressed as g of ashes per g of dry sample (g/g_{DM}).

7.1.2. Total protein analysis

Total protein content was determined by the Kjeldahl method, following the procedures described by the Association of Official Analytical Chemists International, as indicated above (AOAC Method 954.01), using a traditional Kjeldahl apparatus (Model UDK 126 D, VELP Scientifica Srl, Usmate Velate, Italy) with adjustable heaters for individual flasks. The digestion flasks had a total capacity of 500 mL and a 50-mL class A buret was used after distillation for titrations. Reagents used in this analysis were sulfuric acid (H_2SO_4, 98%, Sigma-Aldrich, St. Louis, MO, USA), copper(II) sulfate pentahydrate ($CuSO_4 \cdot 5H_2O$, ACS Reagent, Fisher Scientific, Waltham, MA, USA), potassium phosphate monobasic (K_2SO_4, $\geq$ 99.5%, Honeywell Fluka Charlotte, NC, USA), 40 wt% sodium hydroxide solution (NaOH, PanReac, Barcelona, Spain), and chloridric acid (HCl, 36.5 - 38.0%, ACS Reagent, PanReac). Water used was purified by Milli-Q water purification system (Barnstead™ Pacific TII Water, Thermo Scientific).

For this assay, 1 g of grounded sample (ca 0.7 - 1 mm) was mixed with 20 mL of deionized water into a Kjeldahl tube. The material is digested in the tube with H_2SO_4 (12 mL) to convert the protein N to $(NH_4)_2SO_4$ at a boiling point elevated by the addition of K_2SO_4 with the catalyst (7.0 g K_2SO_4 + 0.8 g $CuSO_4$) to enhance the reaction rate. If mixture foams, 3 mL 30 - 35% H_2O_2 was slowly added. The nitrogen in the sample is thus converted to nonvolatile ammonium sulphate. After cooling and dilution of the digest by adding 80 mL of distilled water, the ammonium sulphate is converted to volatile ammonia gas by heating with 40% NaOH. The ammonia is steam-distilled into an excess of boric acid solution, where it is trapped by forming ammonium borate. The amount of H_3BO_3 receiving solution formed is determined by titration using standard 0.10 M HCl to violet endpoint. To obtain the crude protein content of raw materials, the N content was multiplied by a factor that reflects the percentage of N in the sample protein. A general conversion factor of 6.25 is applied. The crude protein content was expressed as g of Kjeldahl nitrogen per g of dry sample (g/g_{DM}).

7.1.3. Fat analysis

Total fat was quantified by gravimetry after extraction (AOAC Method 920.39), using the Randall modification of the standard Soxhlet method to reduce the time needed for extraction process. Reagents used in this analysis were ethanol (C_2H_5OH, 99.9%, VWR Chemicals, Radnor, PA, USA), chloridric acid (HCl, 36.5 - 38.0%, ACS GR, PanReac), petroleum ether (C_6H_{14}, ACS Reagent, Sigma-Aldrich), and diethyl ether (($C_2H_5)_2O$, $\geq$ 98%,

VWR Chemicals). Used water was purified by Milli-Q water purification system (Barnstead™ Pacific TII Water, Thermo Scientific).

Briefly, 2 g of grounded sample (ca 0.7 - 1 mm) was mixed with 2 mL C_2H_6O and 10 mL HCl. The extraction system was then kept under gentle agitation at 80 °C for 30 min. After this stage, 50 mL of a miscible solution of petroleum ether and diethyl ether (1:1) solvents was added. The mixture of petroleum ether and diethyl ether was used as the main solvent for lipids extraction, in replacement of more toxic and high environmental impact solvents such as hexane and isopropanol, which are commonly used for this purpose. After extraction, the solvent was released by a rotary-evaporator using a R-200/205 Rotavapor (BÜCHI Labortechnik AG, Flawil, Switzerland) and the last traces were removed by placing the flask with the extract in a heater at 80 °C overnight. Lipid content was gravimetrically determined from the difference in weight of samples before and after drying and it was expressed as g of lipids per g of dry sample (g/g_{DM}).

7.1.4. Determination of dietary fiber composition

The procedures for the determination of total dietary fiber (TDF) content as outlined in this section is based on the methods ACC Method 32-05.01 and AOAC Method 985.29, using Megazyme Total Dietary Fiber Kit (Megazyme Ltd, Bray Ireland), that involves enzyme treatment steps. Reagents used in this analysis were sodium hydroxide solution (NaOH, PanReac), chloridric acid (HCl, 36.5 - 38.0%, ACS GR, PanReac), ethanol (C_2H_5OH, 99.9%, VWR Chemicals), acetone (CH_3COCH_3, $\geq$ 99%, VWR Chemicals), α-amylase, protease and amyloglucosidase (Megazyme Ltd). Water used was purified by Milli-Q water purification system (Barnstead™ Pacific TII Water, Thermo Scientific).

1 g of dried grounded sample (ca 0.3 - 0.5 mm) in 50 mL phosphate buffer (pH = 6.0) was incubated at 98 - 100 °C for 15 min with heat-stable α-amylase to give gelatinisation, hydrolysis and depolymerization of starch. After cooling down to room temperature, the pH was adjusted at 7.5 by adding 10 mL 0.275 N NaOH solution. 100 μL of protease solution was added to solubilize and depolymerize proteins and incubated at 60 °C with continuous agitation for 30 min. After cooling down to room temperature, the pH was adjusted at 4.5 by adding 10 mL 0.325 N HCl solution. 200 μL amyloglucosidase was added to hydrolyze starch fragments to glucose and the suspension was incubated for 30 min at 60 °C with continuous agitation. Finally, 280 mL 95% EtOH pre-heated to 60°C was added to precipitate soluble fiber and remove depolymerized protein and glucose (from starch). The residue was filtered; washed with three 20 mL portions of 78% EtOH, two 10 mL portions of 95% EtOH, and two 10 mL portions of acetone; dried; and weighed. Analyse residue from one sample of set of duplicates for protein (§ III.7.1.2), using N x 6.25 as conversion factor.

The other duplicate was used to determine the ash content (§ III.7.1.1). The percentage TDF is determined using Equation III.2:

$$TDF\ (\%\ w/w) \qquad\qquad\qquad (III.2)$$

$$= \frac{Sample\ residue\ (mg) - Protein\ (\%) - Ash\ (\%)}{Initial\ sample\ (mg)} \cdot 100$$

7.1.5 Cellulose, hemicelluloses, and lignin content

The cellulose, hemicelluloses and lignin content were determined using the gravimetric method according to the methods reported by the Technical Association of Pulp and Paper Industry (TAPPI). Reagents used in this analysis were toluene ($C_6H_5CH_3$, 99.8%, Sigma-Aldrich), ethanol (C_2H_5OH, 99.9%, VWR Chemicals), sulfuric acid (H_2SO_4, 98%, Sigma-Aldrich), sulphuric acid (H_2SO_4, 98%, Sigma-Aldrich), 40 wt% sodium hydroxide solution (NaOH, PanReac), acetic acid glacial (CH_3COOH, ≥ 99.7% ACS Reagent, VWR Chemicals), and sodium chlorite ($ClNaO_2$, 80%, Alfa Aesar Chemicals,). Water used was purified by Milli-Q water purification system (Barnstead™ Pacific TII Water, Thermo Scientific).

Prior to the gravimetric component determination, a 6 h Soxhlet extraction with a mixture of toluene and 96% ethanol (2:1) is employed according to TAPPI (T-264 om-82) [13] and ASTM (E1721-01) methods to remove compounds, which are not part of the biomass, and which may interfere with the further analyses. These extractives are sugars, phenolic compounds, and part of water-soluble polysaccharides according to the biomass type.

The lignin content of biomass samples was determined in accordance with TAPPI T-222 om-22 methodology [14]. In this method, 1 g of the obtained extractive-free sample was subjected to acid hydrolysis 72% H_2SO_4 solution (15 mL) for 2 h at room temperature to hydrolyze and solubilize the carbohydrates. The sample was then diluted with water to obtain a final sulphuric acid concentration of 3 wt% and further boiled for 4 h. Next, lignin was allowed to settle before being filtered. The residue was washed using hot water until reaching a neutral pH. The dried insoluble residue represents the lignin content.

Cellulose extraction, based on the TAPPI T-203 method, was obtained by alkaline treatment with soda and acetic acid applied on extractive-free samples from the first isolation step. Ideally, holocellulose contains only cellulose and hemicellulose. The procedure used for preparing holocellulose involves the treatment of the 2.5 g milled extractive-free samples with an acid solution (80 mL) at 70 °C for 6 h. Sodium chlorite (2.6 mL at 25%) was added every hour during 6 h. The mixture was then cooled down and the residue is filtered and washed with distilled water. The residue was finally dried at room temperature; an aliquot is weighted and dried at 105 °C for the determination of the holocellulose content.

The first step subjects the biomass sample to a concentrated acid that disrupts the non-covalent interactions between biomass polymers. The second step permits the optimization of the whole polymer hydrolysis while minimizing the degradation of monomeric sugars. It must be pointed out that degradations of sugars are unavoidable during these two steps of hydrolysis.

α-cellulose is defined as the residue of holocellulose insoluble in a 17.5 wt% NaOH solution. It is considered to represent the undamaged higher molecular weight cellulose in the wood or biomass sample. 5 g of holocellulose was added to a 17.5 wt% NaOH solution (100 mL) at room temperature for a 30 min incubating period. The residue was filtered and washed firstly two times with distilled water and then filtered again. Then, the addition of 15 mL of a 10 wt% glacial acetic acid solution served at hydrolyzing the degraded cellulose and hemicelluloses. The residue was filtered and washed with hot water, and dried at 105 °C. The amount of α-cellulose was finally determined gravimetrically. Hemicelluloses are more readily hydrolyzed compared to cellulose because of their branched and amorphous nature.

The determination of each component of the chemical characterization was performed in triplicate and the means and standard deviations were calculated.

7.2. Bioactives and liquor side streams composition

7.2.1. Total phenolic compounds (TPC)

Total phenols were quantified through the Folin-Ciocalteau assay [15] adopted to study natural antioxidant compounds; it measures the capacity of a compound to reduce the Folin's reagent, giving an estimation of its antioxidant capacity. Reagents used in this analysis were Folin-Ciocalteau's reagent (VWR Chemicals), and sodium carbonate anhydrous (Na_2CO_3, $\geq 99.5\%$, ACS Reagent, PanReac). Water used was purified by Milli-Q water purification system (Barnstead™ Pacific TII Water, Thermo Scientific).

Briefly, a sample of extract or liquor (1 mL opportunely diluted with distilled water) was added to Folin-Ciocalteau's reagent (5 mL at 10% v/v) and allowed to stand for 5 min at room temperature. Then, 7.5 wt% sodium carbonate solution (4 mL) was added to the mixture. After vortexing for 1 min, the mixture was incubated at room temperature for 60 min in darkness. The absorbance of the reacting mixture was then read at 765 nm using a V-650 Ultraviolet–visible (UV-Vis) spectrophotometer (Jasco Inc., Easton, MD, USA). Total phenols were expressed as milligrams of gallic acid equivalents per gram of dry samples (mg_{GAE}/g_{DM}), by means of a calibration curve obtained with a gallic acid standard at different concentrations (10 - 100 mg/L).

For the detection of the total content of phenolic compounds in liquors, the 280-index method was also used [4]: the sample was opportunely diluted with distilled water, and absorbance was directly read at 280 nm, which is the characteristic absorption wavelength of a benzene ring. Phenols were expressed as milligrams of gallic acid equivalents per gram of dry samples (mg_{GAE}/g_{DM}), by means of a calibration curve obtained with gallic acid standard solutions (5 - 20 mg/L).

7.2.2. High Performance Liquid Chromatographic (HPLC) analysis

The identification and quantification of chlorogenic acid, caffeic acid, gallic acid, quercetin 3-glucoside, epicatechin, and rutin contained in the extracts were carried out by High Performance Liquid Chromatographic (HPLC-DAD) analysis. HPLC analysis for single phenolic compounds determination was performed in a Waters 1525 Separation Module coupled to a photodiode array detector Waters 2996 (Waters Corporation, USA). Reagents used in this analysis were phosphoric acid (H_3PO_4, 85 - 90%, Honeywell Fluka Charlotte), and methanol (CH_3OH, $\geq$ 99.8%, VWR Chemicals). Water used was purified by Milli-Q water purification system (Barnstead™ Pacific TII Water, Thermo Scientific).

Before the injection, all the collected extracts were filtered with 0.45 μm filters. For phenols determination, the mobile phase consisted of phosphoric acid (0.1 %, eluent A) and methanol (100%, eluent B). The gradient elution program was used as follows: 0 - 30 min from 5% B to 80% B, 30 - 33 min 80% B, 33 - 35 min from 80% B to 5% B. The flow rate of the mobile phase and the injection volume was respectively 0.8 mL/min and 5 μL. Chromatograms were acquired at the fixed wavelength comparing the HPLC retention time and visible absorption spectra with those of commercial standard, and the content was expressed as mg of ascorbic acid per g of dried sample (mg_{AA}/g_{DM}).

7.2.3. Reducing activity (FRAP assay)

The reducing capacity of extracts and liquors was evaluated with the FRAP (ferric reducing antioxidant power) assay carried out according to the method described by Benzie and Strain (1996) [16] with some modifications. Reagents used in this analysis were 2,4,6-Tris (2-pyridyl)-s-triazine ($C_{18}H_{12}N_6$, 99%, Fisher Scientific), chloridric acid (HCl, 36.5 - 38.0%, ACS GR, PanReac), and iron (III)chloride hexahydrate ($FeCl_3 \cdot 6H_2O$, $\geq$ 98%, Sigma-Aldrich. Water used was purified by Milli-Q water purification system (Barnstead™ Pacific TII Water, Thermo Scientific).

The FRAP working solution was prepared by freshly mixing 0.3 M sodium acetate buffer, 10 mM TPTZ (2,4,6-Tris (2-pyridyl)-s-triazine) solution in 40 mM HCl, and 20 mM ferric solution at a ratio of 10:1:1 (v/v/v). Freshly prepared FRAP reagent solution (2.5 mL) was mixed with 0.5 mL of an

opportunely diluted sample and incubated for 10 min at ambient temperature. The change in absorbance due to the reduction of ferric-tripyridyltriazine (Fe III-TPTZ) complex by the antioxidants present in the samples was measured at 593 nm using a V-650 UV-Vis spectrophotometer (Jasco Europe Srl, Cremella, Italy) against blank (applying the same analysis conditions). Ascorbic acid was used as the standard for the calibration curve, and the FRAP values were expressed as ascorbic acid equivalents present in dried sample (mg_{AA}/g_{DW}).

7.2.4. Structural carbohydrates and lignin determination

Liquid fractions resulting from the side streams of chemical hydrolysis for cellulose isolation were analyzed for acid soluble lignin, cellulose, hemicellulose, and acetic acid using Megazyme Total Dietary Fiber Kit (Megazyme Ltd), as described in the following sections.

7.2.4.1. Acid soluble lignin content

Acid soluble lignin was determined by reading the absorbance at 320 nm in a V-650 UV-Vis spectrophotometer (Jasco Inc.). Soluble lignin was expressed as g of lignin present in 100 g of residue fibers ($g_{Soluble\ lignin}/100\ g_{Residue\ fiber}$).

7.2.4.2 D-Glucose concentration

Cellulose content was evaluated from the D-glucose concentration by using the GOPOD-format kit assay (K-Gluc assay, Megazyme, Lansing, MI, USA) based on the glucose oxidase/peroxidase reaction. The reactions involved are:

$$D - Glucose\ +\ O_2\ +\ H_2O\ \xrightarrow{(Glucose\ oxidase)}\ D - gluconate\ +\ H_2O_2$$

$$2\ H_2O_2 + p - hydroxybenzoic\ acid\ +\ 4 - aminoantipyrine$$
$$\downarrow (Peroxidase)$$
$$quinoneimine\ dye\ +\ 4H_2O$$
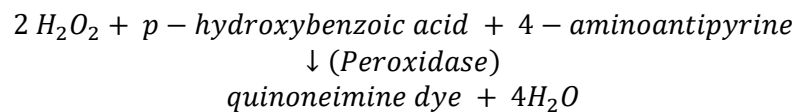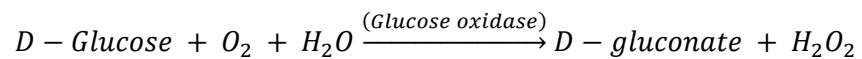
3.0 mL of GOPOD Reagent was added to 0.1 mL of sample solution and incubate at 40 - 50°C for 20 min. The absorbance of the reacting mixture was then read at 510 nm using a V-650 Ultraviolet–visible (UV-Vis) spectrophotometer (Jasco Inc.) against the reagent blank. Then D-glucose concentration was multiplied by the correction factor of 0.88 to obtain cellulose content, expressed as g of glucan present in 100 g of residue fibers ($g_{Glucan}/100\ g_{Residue\ fiber}$).

Chapter III

7.2.4.3. D-Xylose concentration

Hemicellulose concentration was quantified from the xylose concentration (K-Xylose assay, Megazyme) based on the interconversion of the α- and β-anomeric forms of D-xylose catalysed by xylose mutarotase. The reactions involved are:

$$\alpha - D - Xylose \xrightleftharpoons{(Xylose\ mutarotase)} \beta - D - xylose$$
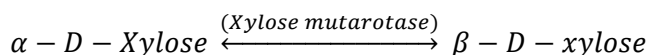
The β-D-xylose is oxidised by NAD^+ to D-xylonic acid in the presence of β-xylose dehydrogenase at pH 7.5, according to the following reaction:

$$\beta - D - Xylose\ +\ NAD^+ \xrightarrow{(\beta - xylose\ dehydrogenase)} D - xylonic\ acid\ +\ NADH\ +\ H^+$$
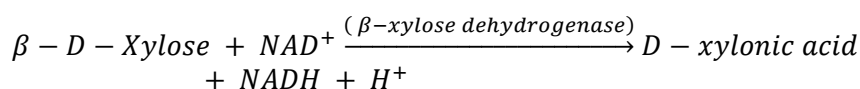
The amount of NADH formed in this reaction is stoichiometric with the amount of D-xylose.

2.0 mL of distilled water was added to 0.1 mL of sample solution with 0.4 mL of buffer (pH = 7.5), 0.4 mL of NAD^+/ATP, and 0.02 mL of hexokinase suspension. The mixture was incubated at room temperature for 5 min. Afterwards, 0.05 mL of XDH/XMR solution was added and let react for 6 min. The absorbance of the reacting mixture and of the reagent blank (prepared as aforementioned with distilled water instead of sample) was then read at 340 nm using a V-650 Ultraviolet-visible (UV-Vis) spectrophotometer (Jasco Inc.). The absorbance of the reacting mixture was multiplied by the correction factor of 0.90. Hemicellulose values were expressed as g of xylose present in 100 g of residue fibers (g_{Xylose}/100 $g_{Residue\ fiber}$).

7.2.4.4. Acetic acid concentration

Acetic acid concentration was determined by using the AK/PTA format kit assay (K-Acetrm assay, Megazyme), based on the conversion of acetic acid (acetate) into acetyl-phosphate and adenosine-5'-diphosphate with acetate kinase in the presence of ATP. The reactions involved are:

$$Acetic\ acid\ +\ ATP \xrightarrow{(Acetate\ kinase)} Acetyl - phosphate\ +\ Adenosine - 5' - diphosphate$$

$$Acetyl - phosphate \ + \ Coenzyme \ A \xrightarrow{\ (Phosphotransacetylase)\ } Acetyl \\ - CoA \ + \ Pi$$

$$Adenosine - 5' - diphosphate \ + \ Phosphoenolpyruvate \\ \xrightarrow{\ (Pyruvate\ kinase)\ } Pyruvate \ + \ ATP$$

$$Pyruvate \ + \ NADH \ + \ H^+ \xrightarrow{\ (D-lactate\ dehydrogenase)\ } D - lactic \ acid \\ + \ NAD^+$$
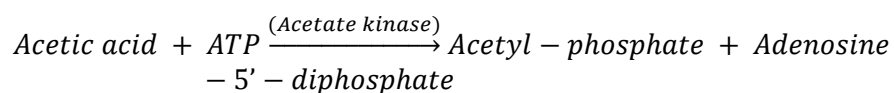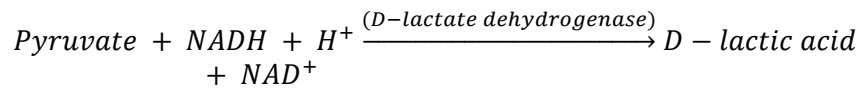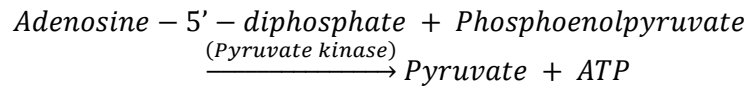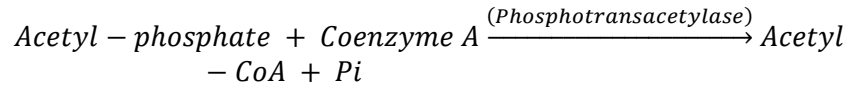
The amount of NAD^+ formed in the above reaction pathway is stoichiometric with the amount of acetic acid. It corresponds to NADH consumption which is measured by the decrease in absorbance at 340 nm. Acetic acid values were expressed as g of acetic acid present in 100 g of residue fibers ($g_{Acetic\ acid}/100\ g_{Residue\ fiber}$).

7.2.5. Dialysis purification

The liquor was centrifuged at 5,000 rpm for 15 min to remove the sediments. The supernatant was dialyzed against water for several days until the dialysate become neutral. The dialyzed suspension was then sonicated (Elmasonic S30H, Elma Schmidbauer GmbH, Singen, Germany) in an ice bath for 5 min at 40% amplitude to disrupt the large aggregates and get a uniform suspension. Afterward, the suspension was freeze-dried and stored at 4 °C for future characterization.

7.2.5.1. Fourier Transform Infrared Spectroscopy (FT-IR) analysis

Fourier-transform infrared (FT-IR) spectroscopy in attenuated total reflectance (ATR) mode was performed on freeze-dried solid residue after dialysis by a PerkinElmer Spectrum One FTIR spectrometer (Waltham, MA, USA), equipped with an ATR module, using a resolution of 4 cm^{-1} and 16 scan collections.

7.2.5.2. Scanning Electron Microscopy (SEM) analysis

The solid residues from liquors were analyzed by using a Scanning Electron Microscopy (SEM) at IPCB-CNR of Naples. The samples were dehydrated at room temperature, mounted on aluminium stub, and coated by 10 nm thick gold palladium alloy sputter coater before observation in a high-resolution FEI Quanta 200 FEG (FEI, Eindhoven, The Netherlands) at 20,000× magnification.

Chapter III

7.3. Cellulose pulp characterization

7.3.1. Cumulative yield of isolation

The yield of obtained cellulose (%) was calculated as the ratio between the weight of cellulose obtained after the treatments and the initial cellulose weight of AFRs, as shown in Equation III.3:

$$Yield\ (\%) = \frac{W_{Residue\ fiber}}{W_{AFRs}} \cdot \frac{W_{Glucan}}{W_{Residue\ fiber}} \cdot \frac{1}{\frac{W_{Cellulose}}{W_{AFRs}}} \qquad (III.3)$$
$$\cdot\ 100$$

7.3.2. Structural carbohydrate and lignin determination

The cellulose residues obtained after chemical treatments were subjected to a strong acid hydrolysis followed by dilute acid hydrolysis for the quantification of cellulose, hemicellulose, and lignin contents, according to Sluiter et al. 2011 [17]. The reagent used for the following hydrolysis is sulfuric acid (H_2SO_4, 98%, Sigma-Aldrich).

The cellulose residues were treated with 72% H_2SO_4 solution (0.2:1 m_{Sample}:$v_{Solution}$) at 30 °C in a water bath for 60 min. Then, distilled water was added to obtain a final concentration in H_2SO_4 equal to 3% v/v and the mixture was autoclaved at 121 °C for 60 min. After cooling down at room temperature, the solid fraction was separated from the liquid one by using Robu™ borosilicate glass filter crucible (Thermo Fisher Scientific, Waltham, MA, USA) with a porosity of 2 (40 - 100 μm pore size). The solid residue was analyzed for moisture (according to AOAC 950.46, § III.7.1.1) and ash content (according to AOAC 923.02, § III.7.1.1) to determine the acid in-soluble lignin fraction. Meanwhile, liquid fraction was analyzed for acid soluble lignin, cellulose, hemicellulose and acetic acid using Megazyme Total Dietary Fiber Kit (Megazyme Ltd), as described in the § III.7.2.4.1 - 7.2.4.4.

7.3.3. FT-IR analysis

FT-IR spectroscopy was used to obtain the spectra of the cellulose pulp samples, an FT-IR-4100 series spectrophotometer (Jasco Europe Srl, Cremella, Italy) at ambient conditions using a single-reflectance horizontal ATR cell (ATR-PRO 470-H with a diamond prism, Jasco Europe Srl). The infrared spectra were collected in absorbance mode from an accumulation of 128 scans over the wavenumber regions of 4000 - 400 cm^{-1} at a resolution of 4 cm^{-1}. Three repetitions from each sample were used for each spectra measurement. The resulting averaged spectra were smoothed with five-point under adaptive-smoothing function to remove the eventual noises and then baseline modification was applied.

7.3.4. Morphological analysis

A qualitative determination of the structural properties of isolated cellulose through different treatments was performed by using an optical microscopy and Scanning Electron Microscopy (SEM) analysis.

7.3.4.1. Optical microscopy analysis

The morphology of celluloses was observed with an optical microscope (Nikon Eclipse TE 2000S, Nikon instruments Europe B.V., Amsterdam, The Netherlands) with a 10× objective, coupled to a DS Camera Control Unit (DS-5M-L1, Nikon Instruments Europe B.V, Amsterdam, The Netherlands) for image acquisition and analysis.

7.3.4.2. SEM analysis

The morphological features of cellulose were analyzed by using SEM as previously described in § 7.2.5.2.

7.3.5. Particle Size Distribution (PSD)

The size distributions of isolated cellulose particles in aqueous suspensions (1 wt%$_{DM}$) were measured by laser diffraction at 25 °C with a Mastersizer 2000 instrument (Malvern instrument Ltd., Mal-vern, UK), using the Fraunhofer approximation, which does not require knowledge of the optical properties of the sample, as reported by Pirozzi et al. 2021 [6]. The temperature of the cell was maintained at 25 ± 0.5 °C, and an average of triplicates was determined. The surface-weighted mean diameter D[3,2] and volume-weighted mean diameter D[4,3] were evaluated according to Equation III.4 and III.5, respectively:

$$D[3,2] = \frac{\sum_i n_i d_i^3}{\sum_i n_i d_i^2} \qquad \text{(III.4)}$$

$$D[4,3] = \frac{\sum_i n_i d_i^4}{\sum_i n_i d_i^3} \qquad \text{(III.5)}$$

where n_i is the number of particles of diameter d_i.

Additionally, characteristic diameters d(0.1), d(0.5), and d(0.9) were evaluated, corresponding to the 10th, 50th (median value), and 90th percentile of the cumulative size distribution of the suspensions.

The relative span factors were calculated according to Equation III.6, to express the distribution width of the droplet size distribution:

$$Span = \frac{d(0.9) - d(0.1)}{d(0.5)} \qquad \text{(III.6)}$$

7.3.6. Water contact angle

The contact angles (Θ) of water on the isolated cellulose were measured by the sessile drop method [18], using a contact-angle meter (KSV Instruments LTD CAM 200, Helsinki, Finland), equipped with an image analysis software. Briefly, a drop of about 2 µL of distilled water was gently dispensed on the cellulose (placed on the instrument stand to be aligned horizontally in the contact point with the water drop) using a 500 µL syringe (Hamilton, Switzerland) with a 0.71mm diameter needle. Measurements were made each 1 s for a total of 30 s to evaluate the contact angle changes over time. The contact angle measurements were carried out in open air at room temperature (24 ± 1 °C), in situ. Contact angles were measured in triplicate, and the average contact angle was calculated as the mean value over the 30 s measurement.

7.4. NCs characterization

NCs or their suspensions have been characterized by a variety of techniques to evaluate features and properties in terms of structural, physico-chemical, and mechanical properties, and to assess their availability to be used in various innovative applications.

7.4.1. Nanofibrillation yields and nanosized fraction

The nanofibrillation yield and nanosized fraction of NCs suspensions consist in the determination of the nanoscale particle fraction in the suspension by a gravimetric method, according to the protocol described by Besbes et al. (2011) [10] and Naderi et al. (2015) [19], respectively. The dry weight of the non-nanometric material precipitated during centrifugation compared to the dry weight of the initial suspension was used to inversely determine the nanofibrillation yield and nanosized fraction.

7.4.2. Morphological analysis

The morphological properties of nanostructured cellulose were performed by using optical microscopy, SEM, and Atomic Force Microscopy (AFM) analysis to point out the geometrical dimensions and shape which vary based on their origin, extraction methods, and manufacturing conditions, which in turn affects the suspension rheology and colloidal behaviors [20].

7.4.2.1. Optical microscopy analysis

The optical microscopy for the evaluation of NCs suspensions was performed using the method reported in § III 7.3.4.

7.4.2.2. SEM analysis

The morphological features of NCs were analyzed by using SEM as previously described in § 7.2.5.2.

7.4.2.3. Atomic Force Microscopy (AFM) analysis

Atomic Force Microscopy (AFM) images were acquired using a NT-MDT P47H probe microscope (Apeldoorn, Netherlands) scanning operated in the semi-contact mode (tip spring constant = 40 N m^{-1}) at laboratories of the Department of Physics of the University of Trento. Detailed information on the size and morphology of the isolated NCs was obtained by analyzing these images with the Gwyddion 2.59 software.

7.4.3. Carboxyl content

The carboxyl content was determined using conductimetric titration [10,19,21]. The pH of NCs suspension at 0.25 wt%$_{DM}$ was adjusted at 2.7 using HCl solution (0.1 M) to exchange the sodium cations bound to the carboxyl groups by hydrogen ions. When a stable suspension was obtained, the mixture was titrated with NaOH solution (0.1 M). The titration curves showed the presence of a strong acid corresponding to the excess of HCl and a weak acid corresponding to the carboxylate content, the total amount of carboxyl groups, expressed as the average mmols of -COOH groups per gram of NCs, was calculated from the Equation III.7:

$$C_{COOH} = \frac{(V_2 - V_1) \cdot C_{NaOH}}{g_{NCs}} \qquad \text{(III.7)}$$

where C_{COOH} is the carboxyl content; V_2 and V_1 are the equivalent volumes of added NaOH solution; C_{NaOH} is the concentration of NaOH solution; g_{NCs} is the weight of NCs on dry basis.

7.4.4. Cationic demand

The cationic demand was determined using a particle charge detector Mütek PCD 05 (BTG Instruments, Schweden, Säffle) following the methodology described by Espinosa et al. (2016) [9] and Carrasco et al. (1998) [22]. Briefly, 15 ml of NCs suspension at 0.2 wt%$_{DM}$ was mixed with 25 mL of cationic polymer polydiallyldimethylammonium chloride (polyDADMAC 0.001 N) during 5 min with magnetic stirring. Then, the mixture was centrifuged for 90 min at 4,000 rpm. The supernatant was put in the Mütek equipment and anionic polymer (Pes-Na) was then added to the sample drop by drop until the equipment reached the value of 0 mV. The volume of anionic polymer consumed was used to calculate the cationic demand through Equation III.8:

$$CD \qquad\qquad\qquad\qquad\qquad\qquad\text{(III.8)}$$

$$= \frac{(C_{Ply-\text{DADMAC}} - V_{Poly-\text{DADMAC}}) - (C_{Pes-Na} - V_{Pes-Na})}{g_{NCs}}$$

where CD is the cationic demand; V_i is the volume of polymer used; C_i is the concentration of polymer; g_{NCs} is the weight of NCs on dry basis.

7.4.5. FT-IR analysis

The effect of the chemical and mechanical treatments used on chemistry structure of CNFs was examined by FT-IR spectra (FT-IR Spectrum Two series spectrophotometer, PerkinElmer, Waltham, Massachusetts, United States) at ambient conditions. The infrared spectra were obtained in transmittance mode collected 40 scans over the wavenumber regions of 4000 - 400 cm^{-1} with a resolution of 4 cm^{-1} on NCs previously dried in an air oven at 60 °C for 24 h.

7.4.6. Crystallinity index

The X-ray Spectra for the different CNFs were measured by using a Bruker D8 Discover with a monochromatic source Cu Kα1 over an angular range of 7 - 50° at a scan speed of 1.56°/min. The crystallinity index (CI) was calculated by using the empirical Equation III.9 [23]:

$$CI = \frac{I_{200} - I_{am}}{I_{200}} \cdot 100 \qquad\qquad\text{(III.9)}$$

where I_{200} is the intensity of the 2 0 0 peak (I_{200} 2θ = 22°) and I_{am} is the intensity minimum between the peaks at 2 0 0 and 1 1 0 (I_{am} 2θ = 15°).

7.4.7. ζ-potential

The ζ-potential values were measured by dynamic light scattering (DLS) and electrophoretic mobility using a Zetasizer (ZSP, Malvern Instruments Ltd., Worcestershire, UK) at 25 °C. The CNFs suspensions previously diluted to 0.1 wt%$_{DM}$ with deionized water were stirred for 30 s with T-25 Ultra Turrax device (IKA® -Werke GmbH & Co. KG, Staufen, Germany) equipped with an S18N-19 G rotor. The analysis was realized in triplicate, and mean value and standard deviation were calculated.

7.4.8. PSD analysis

The size distributions of isolated NCs in aqueous suspensions (1 wt%$_{DM}$) were measured by laser diffraction at 25 °C with a Mastersizer 2000 instrument (Malvern instrument Ltd., Mal-vern, UK), as described previously in § III.7.3.5.

7.4.9. Turbidity

The turbidity of the NCs suspensions was measured before being diluted to 0.1 wt%$_{DM}$ and stirred for 10 min with T-25 Ultra Turrax device (IKA® - Werke GmbH & Co. KG, Staufen, Germany) equipped with an S18N-19 G rotor, was measured with a portable turbidimeter (TN/3025 model, LabProcess, Barcelona, Spain). Three measures were carried out for each suspension and the results were expressed as the average with the unity NTU refers to Nephelometric Turbidity Units.

7.4.10. Intrinsic viscosity

The intrinsic viscosity (η) of 0.2 wt%$_{DM}$ of NCs suspensions was determined according to the ISO 5351:2010 standard and the degree of polymerization (DP) is related to the intrinsic viscosity, by the Equations III.10 and III.11 [24]:

$$DP(< 950): DP = \frac{\eta_s}{0.42} \qquad \text{(III.10)}$$

$$DP(> 950): DP = \frac{\eta_s}{2.28} \qquad \text{(III.11)}$$

The measurements were made five times, and the mean value and standard deviation were calculated.

7.4.11. Interfacial tension and three-phase contact angle

The interfacial tensions of NCs (0.5 wt%$_{DM}$) were measured by using the pendant drop method using a contact-angle meter (KSV Instruments LTD CAM 200, Helsinki, Finland), equipped with an image analysis software. Briefly, a syringe equipped with a stainless-steel needle (0.71 mm in diameter) filled with the aqueous phase containing nanoparticles was submerged into the oil phase within a glass cuvette. The initial volume of the formed drop during the whole experiment was about 30 μL. The optical contact angle meter recorded the change of the oil/water interface, and the Young-Laplace equation was used to calculate the interfacial tension. Distilled water was used as the control. The interfacial tension (γ) measurements were performed for 2,500 s, and the equilibrium interfacial tension values were estimated using the exponential decay model of Equation III.12 [25]:

$$\gamma = \gamma_\infty + (\gamma_0 - \gamma_\infty)e^{-\frac{t}{\tau_r}} \qquad \text{(III.12)}$$

where γ_∞ is the asymptotic interfacial tension, γ_0 is the initial interfacial tension, τ_r is the characteristic time for the arrangement of the molecules at the water-oil interface, and t is the time variable.

Chapter III

7.4.12. Tensile strength and Young's modulus of papers and nanopapers

The tensile properties were measured with Lloyd LF Plus Tensile Test Machine (Lloyd Instruments Ltd, Bognor Regis, United Kindom) equipped with a 1 kN load cell, following the standard NF Q03-004. The mechanical properties of the papers and nanopapers were evaluated by tensile tests, performed on rectangular samples (10 cm length and 15 mm width) with an initial gauge length of 10 cm and crosshead speed of 10 mm/min. The thickness was measured using a high accuracy Digital Micrometer (Mitutoyo Europe GmbH, Elgoibar, Spain). Young's modulus was calculated from the resulting stress-strain curves. The measurements were done at room temperature and at least nine samples were tested. Results have been expressed as a mean value ± standard deviation.

7.4.13. Porosity of papers and nanopapers

The porosity was calculated from the papers and nanopapers basis weight and thickness, using the following Equation III.13, as reported by Desmaisons et al. 2017 [26]:

$$P = \left(1 - \frac{BW}{\varepsilon \cdot \rho_C}\right) \cdot 100 \qquad \text{(III.13)}$$

where BW is the basis weight (kg/m^2), ε is the thickness (m), and ρ_C is the density of cellulose, considered as 1540 kg/m^3.

8. Statistical analysis

Experiments were repeated in triplicates Significant differences at ($p < 0.05$) were assessed with SPSS 20 (SPSS Inc., Chicago, IL, USA) statistical package through one-way analysis of variance (ANOVA) and Tukey's test. The data were normally distributed.

9. References

1.   Puri, M.; Sharma, D.; Barrow, C.J. Enzyme-assisted extraction of bioactives from plants. *Trends Biotechnol.* **2012**, *30*, 37–44, doi:10.1016/j.tibtech.2011.06.014.

2.   Hafid, H.S.; Omar, F.N.; Zhu, J.; Wakisaka, M. Enhanced crystallinity and thermal properties of cellulose from rice husk using acid hydrolysis treatment. *Carbohydr. Polym.* **2021**, doi:10.1016/j.carbpol.2021.117789.

3.   Wu, C.; McClements, D.J.; He, M.; Zheng, L.; Tian, T.; Teng, F.; Li, Y. Preparation and characterization of okara nanocellulose fabricated using

sonication or high-pressure homogenization treatments. *Carbohydr. Polym.* **2021**, doi:10.1016/j.carbpol.2020.117364.

4. Pirozzi, A.; Ferrari, G.; Donsì, F. Cellulose Isolation from Tomato Pomace Pretreated by High-Pressure Homogenization. *Foods* **2022**, *11*, 266, doi:doi.org/10.3390/foods11030266.

5. Saito, T.; Isogai, A. TEMPO-Mediated Oxidation of Native Cellulose . The Effect of Oxidation Conditions on Chemical and Crystal Structures of the Water-Insoluble Fractions. *Biomacromolecules* **2004**, *5*, 1983–1989.

6. Pirozzi, A.; Capuano, R.; Avolio, R.; Gentile, G.; Ferrari, G.; Donsì, F. O/W pickering emulsions stabilized with cellulose nanofibrils produced through different mechanical treatments. *Foods* **2021**, doi:10.3390/foods10081886.

7. Turbak, A.F.; Snyder, F.W.; Sandberg, K.R. Microfibrillated cellulose, a new cellulose product: Properties, uses, and commercial potential. *J. Appl. Polym. Sci., Appl. Polym. Symp.* **1983**.

8. Espinosa, E.; Sánchez, R.; González, Z.; Domínguez-Robles, J.; Ferrari, B.; Rodríguez, A. Rapidly growing vegetables as new sources for lignocellulose nanofibre isolation: Physicochemical, thermal and rheological characterisation. *Carbohydr. Polym.* **2017**, doi:10.1016/j.carbpol.2017.07.055.

9. Espinosa, E.; Tarrés, Q.; Delgado-Aguilar, M.; González, I.; Mutjé, P.; Rodríguez, A. Suitability of wheat straw semichemical pulp for the fabrication of lignocellulosic nanofibres and their application to papermaking slurries. *Cellulose* **2016**, *23*, 837–852, doi:10.1007/s10570-015-0807-8.

10. Besbes, I.; Alila, S.; Boufi, S. Nanofibrillated cellulose from TEMPO-oxidized eucalyptus fibres: Effect of the carboxyl content. *Carbohydr. Polym.* **2011**, doi:10.1016/j.carbpol.2010.12.052.

11. Espinosa, E.; Domínguez-Robles, J.; Sánchez, R.; Tarrés, Q.; Rodríguez, A. The effect of pre-treatment on the production of lignocellulosic nanofibers and their application as a reinforcing agent in paper. *Cellulose* **2017**, doi:10.1007/s10570-017-1281-2.

12. Espinosa, E.; Sánchez, R.; Otero, R.; Domínguez-Robles, J.; Rodríguez, A. A comparative study of the suitability of different cereal straws for lignocellulose nanofibers isolation. *Int. J. Biol. Macromol.* **2017**, *103*, 990–999, doi:10.1016/J.IJBIOMAC.2017.05.156.

13. Tappi Standard: TAPPI T-264 cm-07. Preparation of wood for chemical analysis 2007.

14. Tappi Standard: TAPPI T-222 om-22. Acid-insoluble lignin in wood and pulp 2006.

15. Slinkard, K.; Singleton, V. Total phenol analysis: automation and comparison with manual methods. *Am. J. Enol. Vitic.* **1977**.

16. Benzie, I.F.F.; Strain, J.J. The ferric reducing ability of plasma (FRAP) as a measure of "antioxidant power": The FRAP assay. *Anal. Biochem.* **1996**, doi:10.1006/abio.1996.0292.

17. Sluiter, A.; Hames, B.; Ruiz, R.; Scarlata, C.; Sluiter, J.; Templeton, D. Determination of structural carbohydrates and lignin in biomass. *Natl. Renew. Energy Lab.* **2010**.

18. Pirozzi, A.; Grosso, V. Del; Ferrari, G.; Donsì, F. Edible coatings containing oregano essential oil nanoemulsion for improving postharvest quality and shelf life of tomatoes. *Foods* **2020**, *9*, 1605, doi:https://doi.org/10.3390/foods9111605.

19. Naderi, A.; Lindström, T.; Sundström, J. Repeated homogenization, a route for decreasing the energy consumption in the manufacturing process of carboxymethylated nanofibrillated cellulose? *Cellulose* **2015**, doi:10.1007/s10570-015-0576-4.

20. Trache, D.; Tarchoun, A.F.; Derradji, M.; Hamidon, T.S.; Masruchin, N.; Brosse, N.; Hussin, M.H. Nanocellulose: From Fundamentals to Advanced Applications. *Front. Chem.* 2020.

21. Saito, T.; Kimura, S.; Nishiyama, Y.; Isogai, A. Cellulose nanofibers prepared by TEMPO-mediated oxidation of native cellulose. *Biomacromolecules* **2007**, doi:10.1021/bm0703970.

22. Carrasco, F.; Mutjé, P.; Pelach, M.A. Control of retention in paper-making by colloid titration and zeta potential techniques. *Wood Sci. Technol.* **1998**, doi:10.1007/BF00702595.

23. Segal, L.; Creely, J.J.; Martin, A.E.; Conrad, C.M. An Empirical Method for Estimating the Degree of Crystallinity of Native Cellulose Using the X-Ray Diffractometer. *Text. Res. J.* **1959**, doi:10.1177/004051755902901003.

24. Marx-Figini, M. The acid-catalyzed degradation of cellulose linters in distinct ranges of degree of polymerization. *J. Appl. Polym. Sci.* **1987**, doi:10.1002/app.1987.070330621.

25. Mauriello, E.; Ferrari, G.; Donsì, F. Effect of formulation on properties, stability, carvacrol release and antimicrobial activity of carvacrol emulsions. *Colloids Surfaces B Biointerfaces* **2021**, doi:10.1016/j.colsurfb.2020.111424.

26. Espinosa, E.; Rol, F.; Bras, J.; Rodríguez, A. Production of lignocellulose nanofibers from wheat straw by different fibrillation methods. Comparison of its viability in cardboard recycling process. *J. Clean. Prod.* **2019**, doi:10.1016/j.jclepro.2019.118083.

Chapter IV
Bioactive compounds, cellulose, and nanocellulose extraction

Section IV.1 – *Bioactives extraction optimization from AFRs*

Section IV.2 – *Cellulose isolation from AFRs*

Section IV.3 – *Nanocellulose isolation*

The Sustainable Development Goal has as its main objective the reduction of food waste through several approaches such as the re-use of agro-industrial by-products available in huge amounts and their exploitation through complete valorization of their high-valuable compounds. The extraction of the bioactive compounds through conventional methods has been used for a long time, whilst the advanced novel nonthermal and green treatments technologies are debated in the present chapter leading to the development of new, ecologically friendly, and high-efficiency processes. Apart from the extraction of bioactive compounds with beneficial properties to human health, this chapter addresses also the promising and innovative methodologies for the isolation of cellulose from agri-food residues (AFRs). In particular, mild chemical hydrolysis and mechanical treatments or a combination of them have been exploited as effective treatment techniques for delignification and cellulose recovery. Moreover, further valorization of isolated cellulose is investigated through top-down deconstructing strategies to obtain cellulose nanoparticles, improving the economic viability and sustainability of biomass biorefineries.

Chapter IV

Section IV.1
Bioactives extraction optimization from AFRs

This section aimed to optimize the conventional solid-liquid extraction (SLE) process using central composite design for response surface methodology from response surface methodology (RSM) with the aim to intensify the extractability of phenolic compounds from different AFRs. Total phenols extracted (mg_{GAE}/g_{DM}) were used as response variable to identify the optimal extraction conditions in terms of the most effective organic solvent (acetone, ethanol, or methanol) and solvent concentration (0 - 100% solvent in water) at fixed temperature (25 ± 1 °C) and sold/liquid ratio (1:10). The extracted compounds were analyzed also via HPLC-PDA analysis. Additionally, this section was further focused on the investigation of HPH-assisted extraction with the aim to sustainably intensify the extractability of phenolic compounds with high antioxidant activity maintaining the stability of these phytochemicals. The latter was performed without the use of organic solvents on different aqueous suspensions of AFRs at different temperatures (5, 25, and 50 °C) at fixed pressure (80 MPa), number of passes (20) and sold/liquid ratio (1:50). Results revealed that, at a fixed extraction pressure (80 MPa), the application of HPH at optimal temperature operating condition (25 °C) has the potential to significantly improve the bioactive compounds recovery by requiring less time and no solvents than conventional extraction methods, with the added benefit of using low temperatures and ensuring high extraction yields for temperature-sensitive compounds, without degradation phenomena during HPH application. Moreover, micronization treatment of AFRs water suspensions allowed to reduce their size distribution below the visual detection limit, due to the disruption of individual plant cells, increasing in this way the suspension stability against sedimentation. Remarkably, also the release of bioactive compounds in the aqueous suspension was influenced by the size reduction and the consequent increase of their porosity and surface area.

Chapter IV

IV.1.1. Specific goal and work plan

Agri-food industries are particularly responsible for the generation of high volumes of organic wastes (biomasses), reaching up to 140 billion tons per year [1], although a considerable part of this is not related to food wastage issues [2]. Disposal of these residues represents a cost to the food processor and has a negative impact on the environment. On the other hand, these materials can be considered as largely available by-products and low-cost sources of value-added compounds (including polyphenols, anthocyanins, tannins, and vitamins), whose recovery represents a valuable opportunity. Therefore, the exploitation of AFRs is a formidable challenge, since it might improve the sustainability of food industry production and create economic and social benefits, mitigating at the same time their environmental burden [3]. Especially, the recovered gamut of bioactive compounds with high commercial value has a potential application as natural additives or active ingredients in food, cosmetic, and pharmaceutical products. "Zero waste economy" prospective is a new eco-innovative concept which is based on the use of waste like a raw material for novel food products and ingredients and applications [4]. The recovery of bioactive fractions by conventional and modern technologies and their further valorization in different applications and industries is schematically illustrated in Figure IV.1.
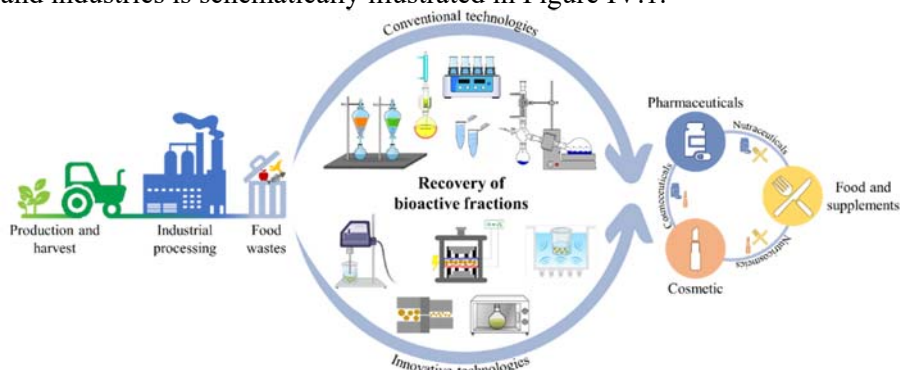
Figure IV.1 *Recovery of bioactive fractions from AFRs by conventional and innovative technologies for different applications.*

The recovery of bioactive compounds via conventional solid-liquid extraction (SLE) techniques is a well-established method for the recovery of valuable compounds from food wastes/by-products, due to its ease of operability and scalability. Despite this, SLE method is limited by the presence of the cell envelope (membranes and wall) in plant tissues, which exerts a significant resistance against mass transfer phenomena of solvents and target intracellular compounds, slowing down the solvent extraction process. Nevertheless, extraction yield is usually high, but the usage of solvents involved in the extraction process is generally toxic and harmful.

134

In addition, due to the uncomplete removal of solvents, the extracted phytochemicals may have adverse effects on human health, causing potential implications on the extract quality, such as loss of functionality of the desired compounds, and on the applications. Although this issue may be solved by using food-grade solvents, there are other challenges as well. These include long duration of extraction, high cost to use high-purity solvent, and the use of heat treatment. which results in the degradation of thermolabile phytochemicals [5-7]. Considering the mentioned drawbacks of the conventional extraction methods, intensive efforts have been made for the development of more efficient, sustainable, and ecologically friendly extraction technologies, such as enzyme-assisted extraction, supercritical fluid extraction, microwave-assisted extraction, and ultrasound-assisted extraction [8].

An alternative approach involving solvent-free extraction methods has been investigated in this work. In this frame, high-pressure homogenization (HPH) has gained great interest as nonthermal and easily scalable cell disruption technique of plant tissue, which induces the rupture of cell envelops, thus enhancing the extractability of target intracellular compounds from food by-products matrices, with reduced time, and without the usage of organic solvents, especially considering the safety issue related to the final products to be used as food supplements, pharmaceutical and/or cosmeceutical applications. However, to date, limited studies demonstrated the feasibility of the HPH impact on the extractability of phenolic compounds from AFRs. Furthermore, in order to fully exploit the potential benefits and advantages derived from the application of HPH-assisted extraction over the conventional SLE process, it should be emphasized that an optimization step is required. To this regard, response surface methodology (RSM) is a statistical tool that, by means of appropriate design and analysis of experiments, enables to gain insight on the effect of the different processing variables and their interactions on target response variables, while minimizing the count of experimental runs. As described in detail in chapter III, RSM has been successfully applied for optimizing SLE processing conditions, evaluating the effect of different organic solvents and solvent concentration on the total phenols content of AFRs tissues, with the aim to define the minimum treatment severity that maximizes the extraction yield. The selected solvents and concentration for the SLE process were used to perfume the extraction kinetic, with regard to define the optimal extraction time. The composition of polyphenols in the obtained extracts and their antioxidant properties were evaluated using HPLC-PDA analysis and FRAP analysis, respectively. Afterwards, HPH-assisted extraction at 80 MPa for 10 min (which corresponds to 20 equivalent passes) with water as the process medium has been applied on different AFRs to optimize temperature conditions (5, 20, and 50 °C). HPH-assisted extraction impact was evaluated on extraction yields of total phenolic and antioxidant activity by FRAP method (Figure IV.2).

Chapter IV

IV.1.2. Short materials and methods
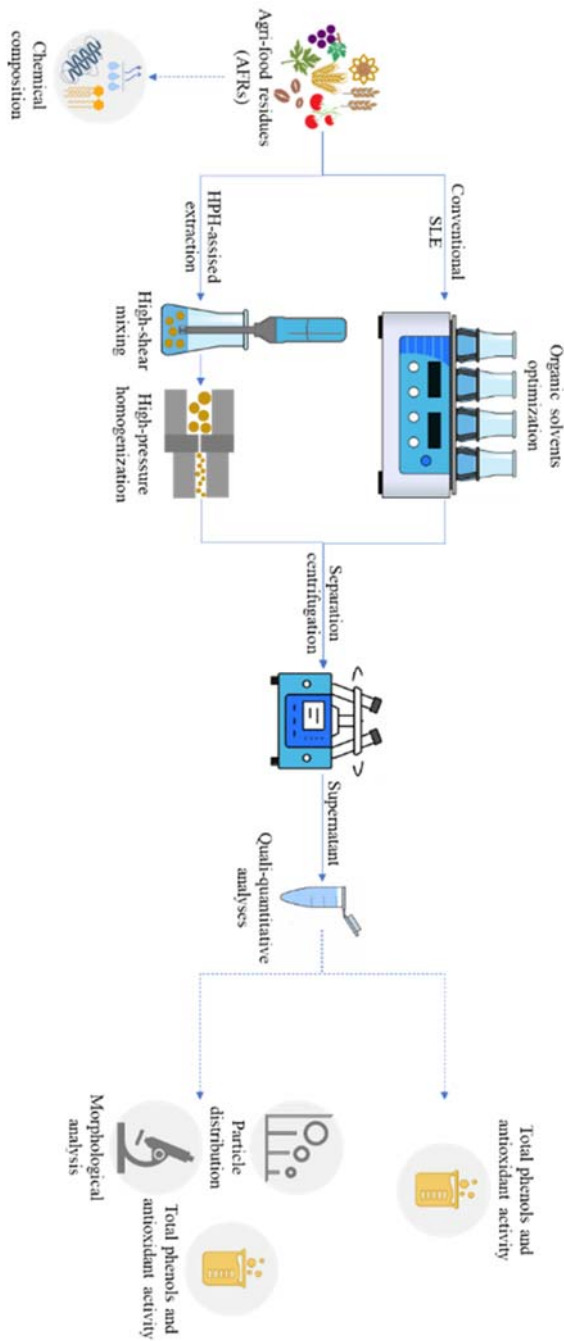
Figure IV.2 *Schematic representation of the methodology used for bioactives extraction optimization from AFRs.*

IV.1.2.1. AFRs raw material characterization

Moisture (method 950.46), ash (method 923.02), protein (method 954.01), and fats (method 920.39) analyses were performed using methodologies recommended by the Association of Official Analytical Chemists International (AOAC), as described in detail in § III.7.1.1 - 7.1.3. Carbohydrate content was calculated by difference. All analyzes were performed in triplicate.

IV.1.2.2. Experimental design for SLE extraction

Response surface methodology (RSM) was used to establish the relationship between response variables and process variables, to determine the optimal extraction conditions of SLE process, which maximize the total phenols compounds. A second-order polynomial model reported in Equation IV.1 was used to predict the response variable as a function of the investigated independent factors, as explained in § III.3.1.

$$Y_1 = \beta_0 + \sum_j \beta_j X_j + \sum \sum_{i<j} \beta_{ij} X_i X_j + \varepsilon \qquad \text{(IV.1)}$$

IV.1.2.3. HPH-assisted total phenols extraction

HPH-assisted extraction of AFRs was carried out in a house-developed unit (§ III.2.2.1) using an orifice valve assembly (orifice diameter 200 μm) at 80 MPa for up to 20 passes, as schematized in Figure III.6.

IV.1.2.4. Analytical determinations

The extracts from SLE and HPH-assisted extraction process were quali-quantitatively analyzed in terms of total phenolic compounds (TPC and HPLC) and antioxidant power (FRAP and DPPH), as previously reported in § III.7.2.1. - 7.2.3. In addition, a qualitative determination of the structural of HPH extracts was performed by using an optical microscopy (§ III.7.3.4.1) and their size distributions was measured by laser diffraction at 25 °C with a Mastersizer 2000 instrument (§ III.7.3.5).

IV.1.3. Results and discussion

IV.1.3.1. Characterization of AFRs raw materials

The characterization of AFRs raw material used in the present study is shown in Table IV.1.

Chapter IV

Table IV.1 *Chemical composition of AFRs raw materials.*

	Hemp cake	Sunflower cake	Roasted coffee beans	White grape pomace	Red grape pomace	Wheat middlings	Wheat bran	Tomato pomace	Rice husk
Moisture (%)	7.99 ± 0.06	10.75 ± 0.06	5.97 ± 0.04	80.41 ± 1.99	62.58 ± 2.21	10.59 ± 0.01	11.54 ± 0.10	80.70 ± 0.83	6.72 ± 0.13
Ash (%DM)	6.40 ± 0.04	5.93 ± 0.03	5.10 ± 0.81	10.52 ± 3.08	35.88 ± 5.80	3.79 ± 0.25	5.83 ± 0.60	4.90 ± 0.27	18.71 ± 0.23
Protein (%DM)	24.78 ± 0.49	24.30 ± 1.24	16.96 ± 0.41	58.13 ± 7.95	51.88 ± 1.77	18.53 ± 1.21	19.10 ± 0.40	14.65 ± 0.21	2.56 ± 0.25
Fat (%DM)	5.30 ± 0.09	2.30 ± 0.21	1.00 ± 0.02	1.55 ± 0.14	2.70 ± 0.33	0.79 ± 0.06	0.85 ± 0.10	1.20 ± 0.14	0.82 ± 0.15
Carbohydrates (%DM)	63.52 ± 0.49	68.47 ± 1.24	76.94 ± 0.91	29.80 ± 9.84	9.54 ± 3.55	76.90 ± 1.23	74.22 ± 0.72	79.25 ± 0.34	76.44 ± 0.34

It can be observed that the moisture, ash, lipid, protein, and carbohydrate content are in agreement with those found in literature [3,9-14]. Minor differences in chemical composition between this work and those found in the literature can be explained by differences in climate and soil conditions, variety, agricultural practices, post-harvest management, and genetic characteristics of the analyzed samples.

IV.1.3.2. RSM analysis and optimization of the conventional extraction process

Hemp cake and sunflower cake, by-products from oilseed cakes and sunflower oil refining, respectively, can be considered as a rich source of polyphenols, mainly located in the hull [15]. Spent coffee grounds from the industrial production of soluble coffee [16], lignocellulosic AFRs such as wheat bran, wheat middlings, rice husk [17]; and other wastes from the wood industry have been widely described as a clean source of phenolic compounds, mainly deriving from hydrothermal and/or autohydrolysis processing of lignin [1]. Additionally, also the main by-products of tomato processing and wine industry, i.e. tomato and grape pomace, respectively, contain mainly phenolic compounds such as flavanones and flavonols, quercetin, rutin, and kaempferol glycoside derivatives [18]. Polyphenols still present in these AFRs could be recovered and exploited for application in a variety of sectors given their high health-beneficial properties, such as cardioprotective, neuroprotective, anti-inflammatory, anticarcinogenic, antioxidant, and antimicrobial activities [19]. To this purpose, the RSM optimization was used to explore the effect of type of organic solvent and solvent concentration on the resulting total phenols recovery form AFRs obtained by conventional extraction. The data obtained from the I-Optimal experiment design were fitted to a second-order polynomial equation (Equation III.1). The values and significance of the regression coefficients of the predicted polynomial models and corresponding p values for each variable of different AFRs are reported in Table IV.2.

Table IV.2 *Analysis of variance (ANOVA) of the second-order polynomial model for the total phenols extraction with SLE technique of different AFRs.*

	Hemp cake	Sunflower cake	Roasted coffee beans	White grape pomace	Red grape pomace	Wheat middlings	Wheat bran	Tomato pomace	Rice husk
β_0	2.4097	12.5876	60.0919	2.9259	60.0919	3.7882	4.4755	24.2936	1.8468
β_1	0.8787	1.2737	-5.3765*	0.7430*	-5.3765*	-0.2182	-0.4736	-2.8697	-0.0739
β_2	0.3159	-1.7485*	-22.9276***	0.3731	-22.9276***	-1.0747**	-0.5966*	1.0038	-0.4464**
β_{12}	-0.1868	1.6693	7.0167*	1.3365**	7.0167*	0.6802*	0.1830	-3.4695	0.2559*
β_{11}	0.03793	-1.2115	-2.3723	0.8089	-2.3723	0.2276	0.1973	1.2223	0.0650
β_{22}	-0.9154*	-5.7743*	-29.1726***	-0.6145	-29.1726**	-1.1829**	-1.1467*	-1.6931	-0.8612**
R^2	0.5536	0.9194	0.9780	0.8285	0.9780	0.9275	0.7433	0.5575	0.9435
Adj-R^2	0.4880	0.7315	0.9266	0.7283	0.9266	0.7585	0.5444	0.4751	0.8118
C.V. (%)	33.04	19.29	12.10	25.19	12.10	13.44	16.61	16.36	14.33

*$p < 0.05$ **$p \leq 0.01$ ***$p \leq 0.001$

Depending on the matrices, factors β_1 and β_2, as well as the combinations of factors β_{12} and β_{22}, presented a statistically significant effect ($p < 0.05$) on extracts. In contrast, in all extracts, β_{11} quadratic term was not significant ($p > 0.05$) for the total phenols variable of the AFRs extracts. Moreover, by analysis of variance, the R^2 value of the models was higher than 0.74 and the Adj-R^2 value did not differ significantly from R^2 value, which showed that the regression model fitted well the experimental data of the system. Only two samples were not fitted well by the model ($R^2 \geq 0.56$). Another parameter that made evident the adequacy of the model was the coefficient of variation (CV, %) which suggests a lower spread of data values relative to the mean.

The 3D response surface plots, shown in Figure IV.3, graphically represent the multilinear regression of the total phenols as a function of type of solvent and solvent concentration (Equation III.1). The ultimate aim of the 3D response surface plots is to enable the prediction of the optimum values of the independent variables (solvent type and solvent concentration) that maximize the response variable (total phenols).

(a) Hemp cake

(b) Sunflower cake

(c) Roasted coffee beans

(d) White grape pomace
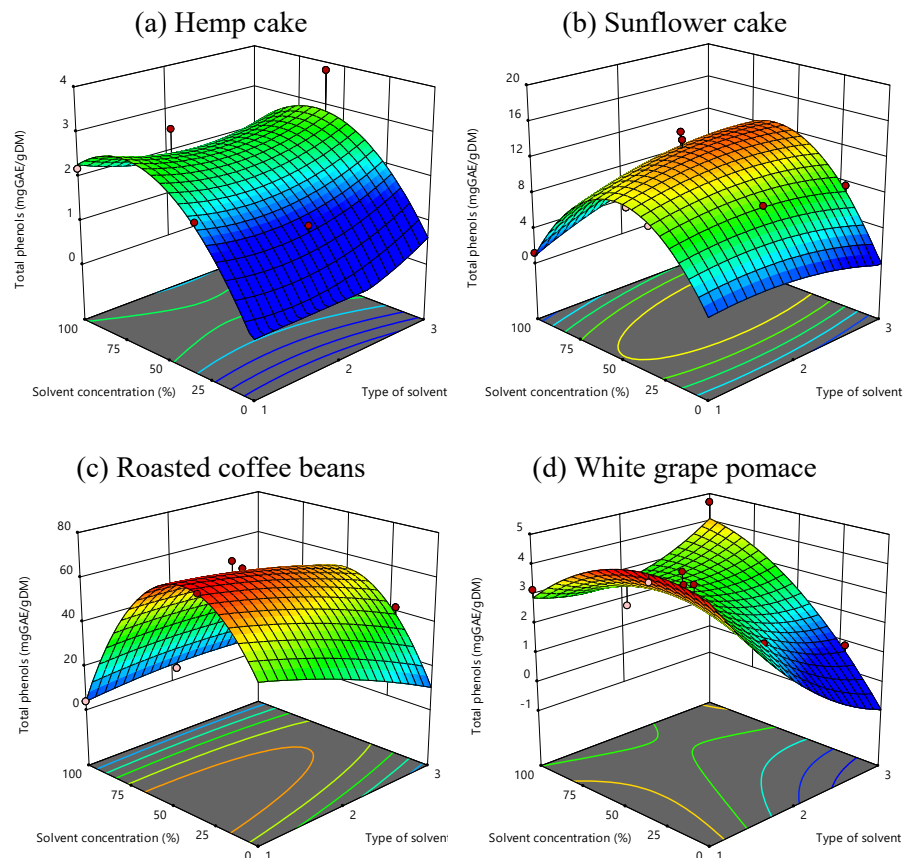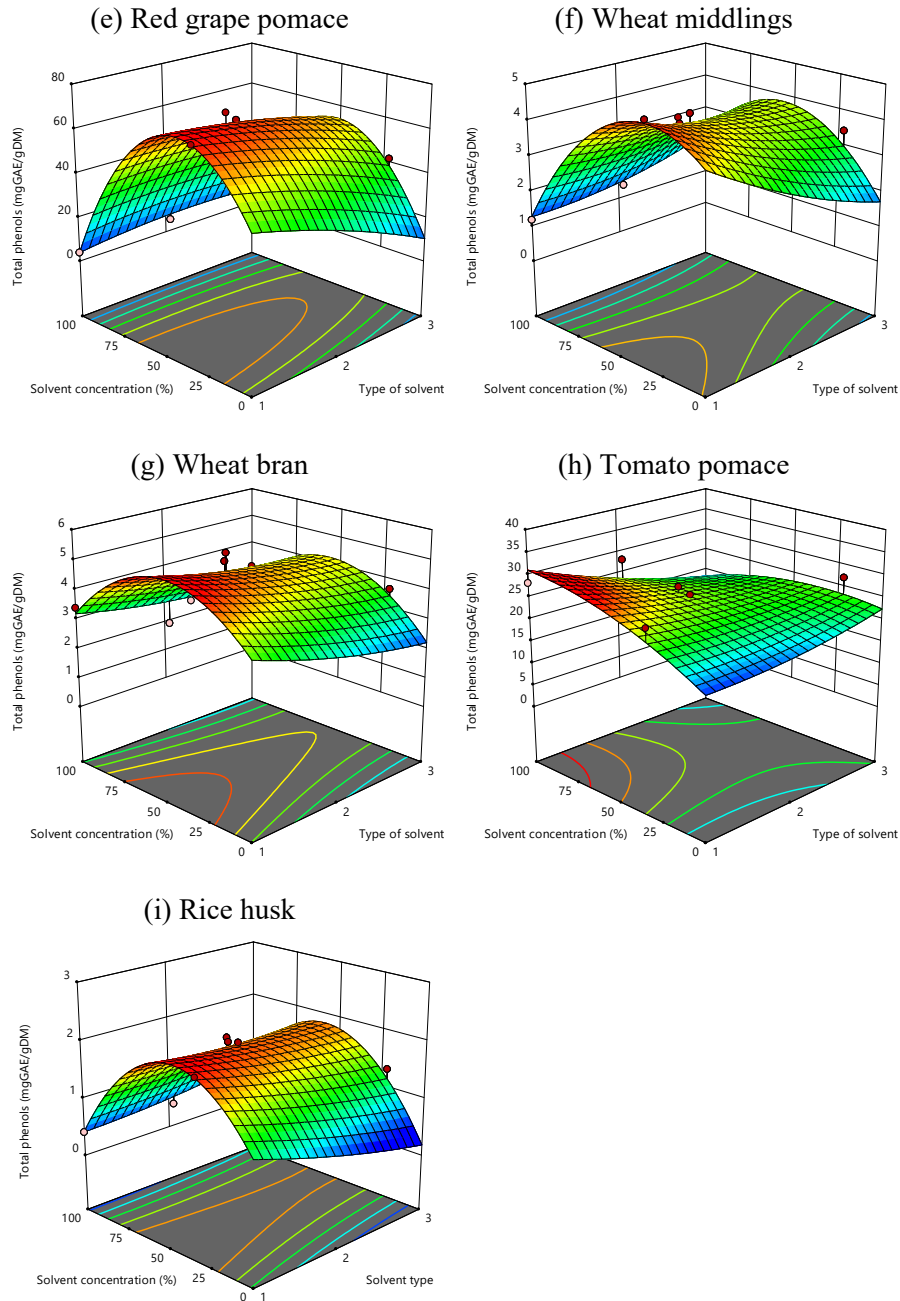
Figure IV.3 *Response surface plots for the total phenols (mg$_{GAE}$/g$_{DM}$) extraction of AFRs as a function of type of solvent and solvent concentration (%).*

In the first place, results suggest that the pure solvents have a negative effect on the concentration of phenolic compounds in the extracts.

Particularly, water-alcohols mixtures have been revealed to be more efficient in extracting phenolic constituents than the corresponding mono-component solvent systems. This phenomenon can be caused by an improvement in the mass transfer caused by the fraction of water present in the solvent. The water causes swelling of the raw material that facilitates the entry of solvent into the cell, improving the extraction yields [20], especially polar compounds stored in the vacuoles. Considering that using solvent-water mixtures more compounds are extracted from internal organelles, the polarity of the solvent plays a fundamental role for their solubilization, thus allowing a higher concentration of total phenols in the extracts [21]. From these results, the optimal solvent and solvent-water mixture ratio have been selected that enabled the achievement of the highest extraction yield, were defined.

According to these results, further investigations of the extractability of bioactive compounds from AFRs during 24 h were performed under the defined optimal extraction time conditions. Time of extraction is in fact an important parameter to be optimized in order to minimize energy costs of the process. To this purpose, Figure IV.4 shows the kinetics of polyphenols extraction from AFRs using the previously optimum water-solvent mixture at 25 °C and solid-solvent ratio 1:10. The kinetics curves are fitted by Langmuir model (Equation IV.2).

$$C\left(\frac{mg_{GAE}}{g_{DM}}\right) = C_{Max}\frac{t}{\tau + t} \qquad (IV.2)$$

where C_{Max} is the saturation concentration of phenols compounds extraction (mg_{GAE}/g_{DM}), t is the extraction time (min), and τ is time at which half of the maximum concentration of total phenols that can be extracted (min).

(a) Hemp cake
Methanol 60 v%
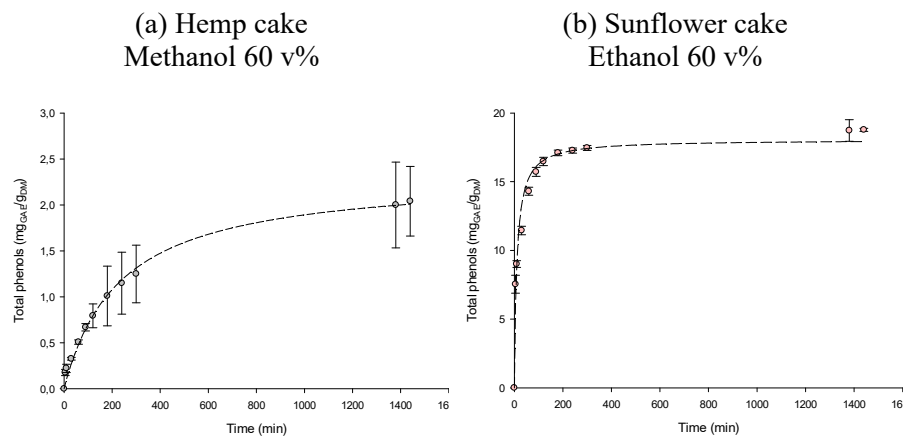
(b) Sunflower cake
Ethanol 60 v%

(c) Roasted coffee beans
Acetone 40 v%
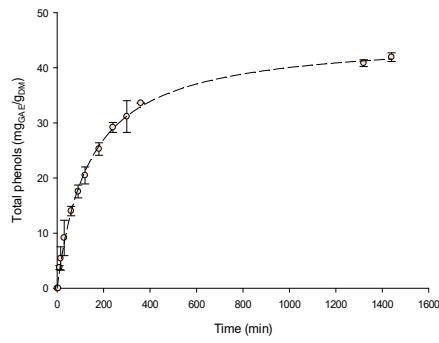
(d) White grape pomace
Acetone 20 v%
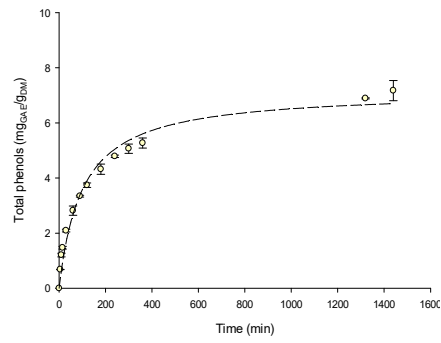
(e) Red grape pomace
Acetone 60 v%
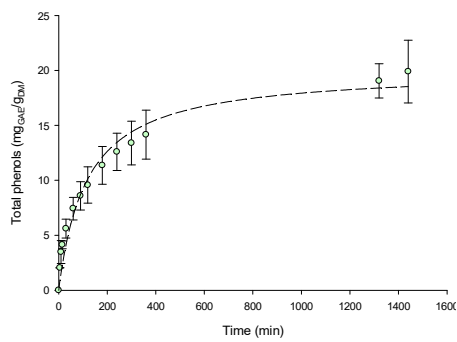
(f) Wheat middlings
Water
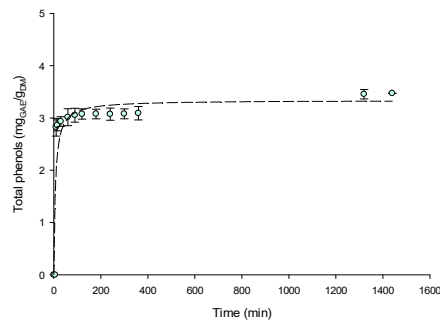
(g) Wheat bran
Water
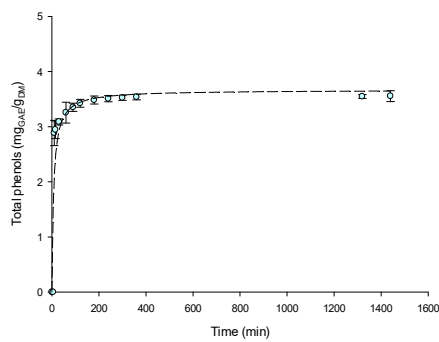
(h) Tomato pomace
Acetone 80 v%
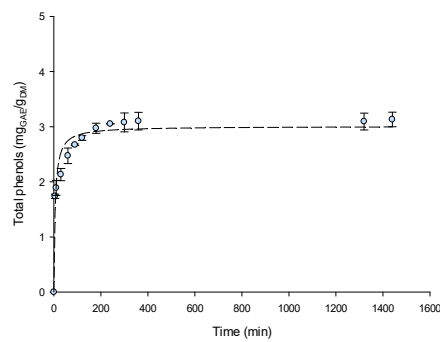
(i) Rice husk
Ethanol 50 v%
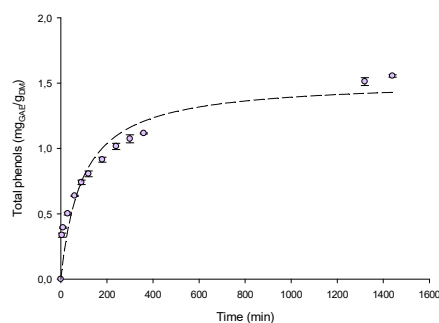
Figure IV.4 *Extraction kinetics of total phenols from AFRs at 25 °C and solid-solvent ratio 1:10. Dotted lines represent the Langmuir fitting curve (Equation IV.2).*

Independently on the investigated sample, goodness of the fitting of the Langmuir kinetic models for all experimental data was confirmed by the values of the coefficients of determination, as shown in Table IV.3.

Table IV.3 *Fitting parameters and coefficients of determination for the fitting of the data of Figure IV.4, using Equation IV.2.*

	C_{Max} (mg_{GAE}/g_{DM})	τ (min)	R^2	Adj-R^2
Hemp cake	2.333	232.711	0.991	0.909
Sunflower cake	18.057	10.943	0.974	0.971
Roasted coffee beans	45.579	137.989	0.998	0.997
White grape pomace	7.169	100.811	0.975	0.973
Red grape pomace	20.039	117.523	0.964	0.961
Wheat middlings	3.339	6.909	0.807	0.791
Wheat bran	3.666	7.767	0.845	0.832
Tomato pomace	3.007	5.698	0.952	0.947
Rice husk	1.523	93.498	0.917	0.909

It could be observed that for every studied raw material, the amount of extracted polyphenols increased continuously with time. The rate of extraction decreased progressively, and the extraction was completed at the end of the experimental runs (after 24 h extraction). From the extraction curves, it is obviously clear that the content of polyphenols was not exactly the same in the fractions of different AFRs. Moreover, the different particle size of different materials affects the kinetic of polyphenols extraction. The results obtained by extraction from the finest fraction of the AFRs, i.e. wheat middlings (Figure IV.4f) and wheat bran (Figure IV.4g) with d < 0.1 mm and d < 0.5 mm, respectively, confirm that the saturation yield of extraction has been achieved with less extraction time. The higher contact surface between the solvent and the fine solid particles favored the extraction of polyphenols.

The kinetics of the extraction from these fine particles was very fast and the yields were almost constant after the first 1 h of extraction. As a result, the high initial rate of polyphenols extraction was followed by a slower extraction rate, and asymptotically approaching an equilibrium concentration.

Figure IV.5 summarizes the total phenols content of extracts obtained from different AFRs with the optimal extraction conditions.
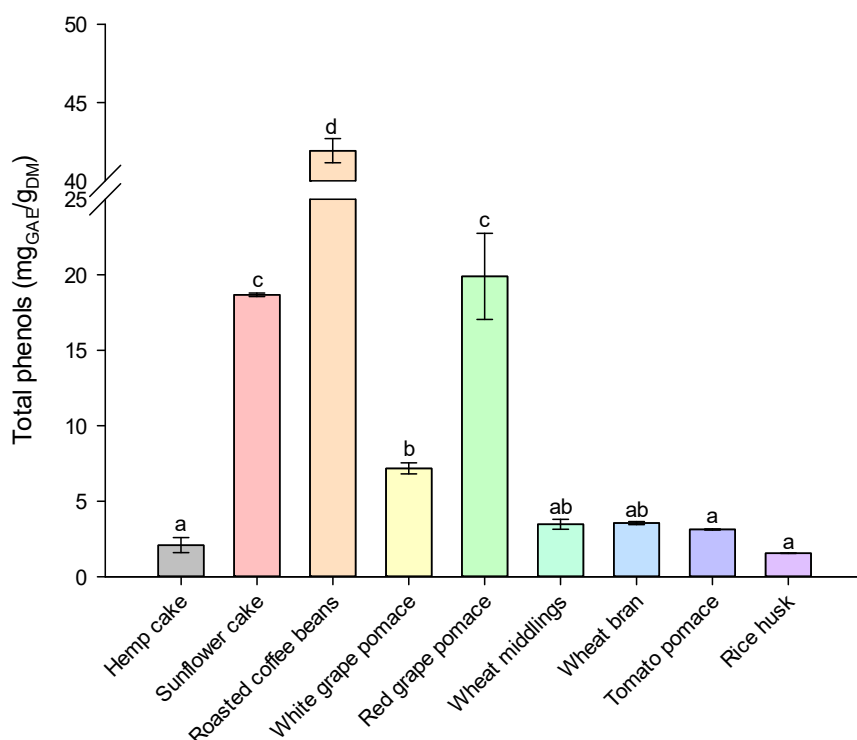
Figure IV.5 *Total phenols content of extracts obtained after a SLE extraction at 25 °C from AFRs, after 24 h of diffusion. Different letters above the bars indicate significant differences among the mean values (p < 0.05).*

It can be seen that all of the wastes contained large amounts of total phenolics, the measured phenolic content ranging from about 2 to 42 mg_{GAE}/g_{DM}. These values are in line with those reported previously in literature, where the total phenols for roasted coffee beans are higher than those found for other agri-industrial wastes [16], such as hemp cake [15], sunflower cake [10], grape pomace [22], tomato pomace [23], and lignocellulosic by-products [24], which were below 20 mg mg_{GAE}/g_{DM}. In conclusion, the examination of the results supports the suitability of AFRs as a source of phenolic compounds. Furthermore, a qualitative identification of

phenolic compounds in extracts form is conducted using HPLC analysis with a UV-Vis diode array detector (DAD) (Figure IV.6).

(a) Hemp cake

(b) Sunflower cake

(c) Roasted coffee beans

(d) White grape pomace

(e) Red grape pomace

(f) Wheat middlings

(g) Wheat bran

(h) Tomato pomace

(i) Rice husk
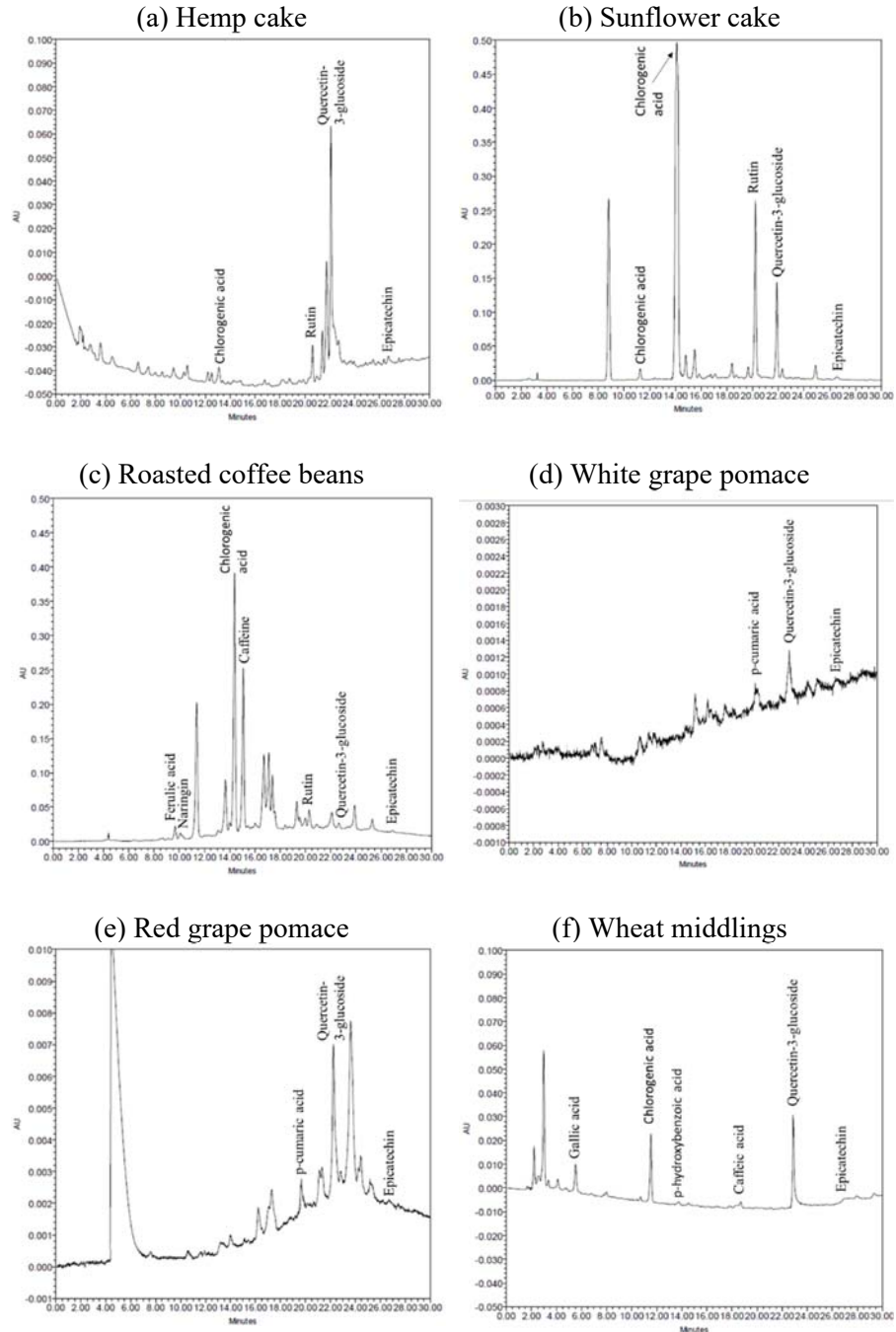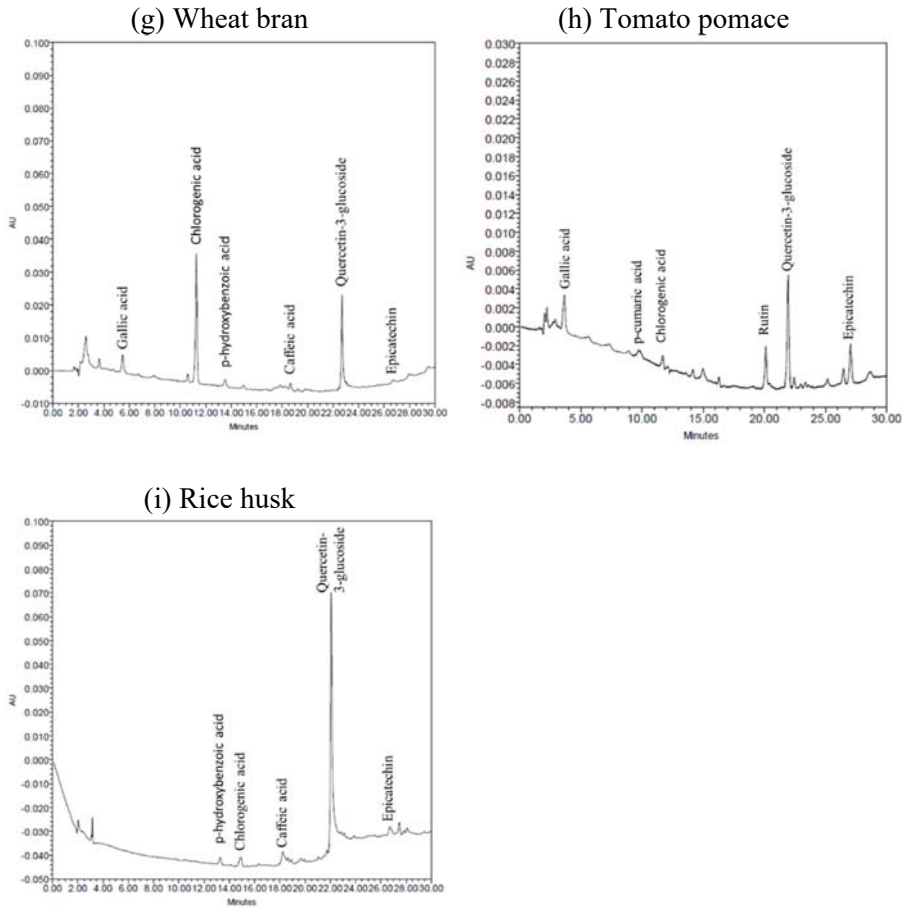
Figure IV.6 *HPLC-PDA chromatograms of extracts obtained after 24 h of SLE at 25 °C from AFRs.*

As shown in Figure VI.6, a wide variety of phytochemical components was observed in the extracts. Chlorogenic acid and quercetine-3-glucoside are the major phenolic acids regardless of the AFRs analyzed. This data supports the aforementioned results of total phenols and, therefore, the antioxidant activities of phytochemicals extracted from AFRs were evaluated below (Figure IV.7).
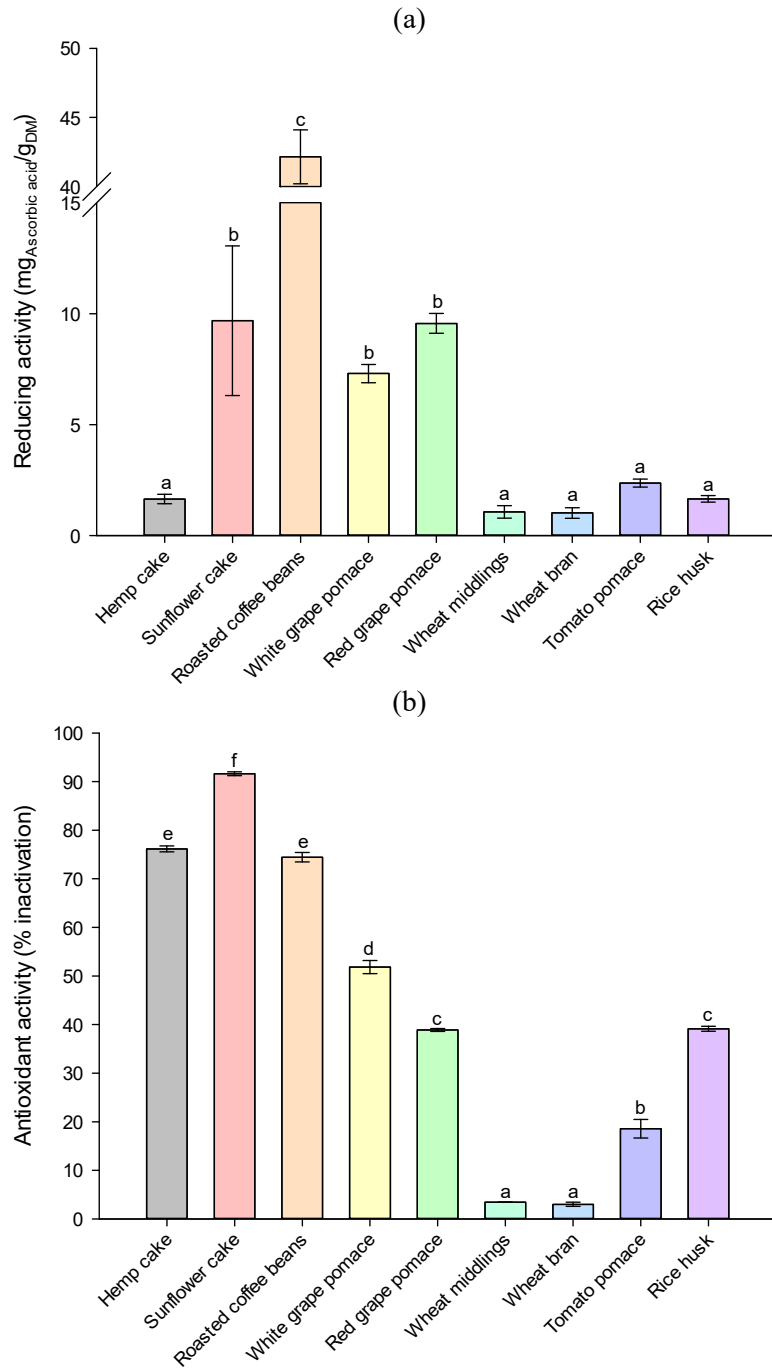
Figure IV.7 *Antioxidant activity of extracts obtained after a SLE extraction at 25 °C from AFRs, after 24 h of diffusion: (a) FRAP and (b) DPPH assay. Different letters above the bars indicate significant differences among the mean values ($p < 0.05$).*

Chapter IV

The effect of solvent over antioxidant capacity of extracts was presented positively for FRAP (Figure IV.7a) and negatively for DPPH (Figure IV.7b). The positive effect of the organic solvent concentration over FRAP response and the low response to DPPH radical could be due to the low ability to reduce Fe^{3+}, suggesting a higher concentration of hydrophobic phenols [25]. Furthermore, the DPPH did not present a correlation with the total phenolic content of the extracts ($p > 0.05$). Despite that, in agreement with previous findings, the behavior of the antioxidant activity in the case of FRAP analysis appeared very similar to that achieved for total phenols concentration. This similarity indicates, as expected, that phenolic compounds present in the AFRs extract are probably the main responsible for its antioxidant capacity. In particular, from the results illustrated in Figure IV.5 and Figure IV.7a, it clearly appears that the extracts derived from the roasted coffee beans possessed a higher antioxidant activity than other extracts at the selected optimal extraction temperature, which was likely due to the high amount of phenolic compounds recovered. Nevertheless, because all phenolic compounds do not show antiradical power, the correlation between polyphenols of AFRs extracts and their antioxidant capacity (FRAP) must be carefully studied. The correlation existing between the total phenols contents and their antioxidant powers could be described by means of a linear function ($y = 0.852 \cdot x$, $R^2 = 0.929$, data not shown). This confirmed that a strong positive correlation was found between the total phenols and antioxidant activity, with a Pearson correlation coefficient of about 0.954, indicating that the global antioxidant activity of the extracts is mostly associated with the phenolic compounds.

IV.1.3.3. Effect of HPH treatment on bioactive compounds extraction

Conventionally, phytochemicals are recovered from plant materials using solid-liquid extraction techniques. In this Ph.D. work, an approach based on the use of HPH assisted extraction and only water as extraction solvent has been investigated used for the extraction of phytochemicals from several AFRs. The hypothesis is that the usage of HPH mechanical and nonthermal processes may increase the extractability of intracellular compounds, such as phytochemicals. Moreover, the effect of extraction temperature on total phenols extraction (Figure IV.8a) and their antioxidant activity (Figure IV.8b) was evaluated at different operating parameters. In this process, as previously reported in § IV.1.2.3, the suspensions are forced through a small orifice (200 µm). The AFRs particles at higher lignocellulosic material content and with rigid structure agglomerate to form a larger mass which in turn clogs the orifice and prevents materials from going through the HPH treatment chamber. Therefore, the disadvantage of this process is the impossibility of treating some of the raw material selected, such as hemp and sunflower cake, grape pomace, and rice husk.
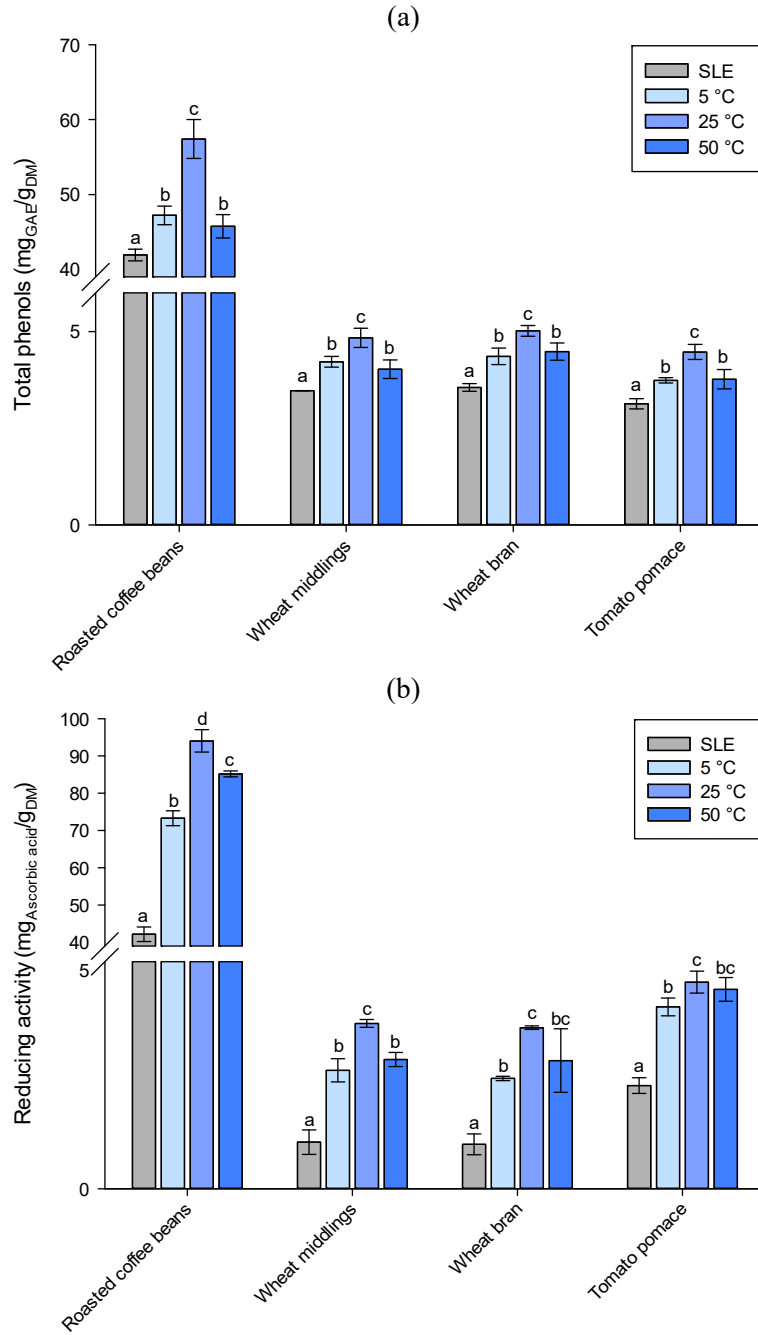
Figure IV.8 *(a) Total phenols and (b) reducing activity obtained of AFRs extracts through (▦) SLE extraction with organic solvent at optimum operating conditions and HPH-assisted extraction in water at (▢) 5 °C, (▣) 25 °C, and (▣) 50 °C. Different letters above the bars indicate significant differences among the mean values (p < 0.05).*

With HPH treatment at 80 MPa and 5 °C for 20 passes using water as the process medium an increase of 13%, 21%, 23%, and 19% in phenols extraction yield was obtained compared to SLE process for roasted coffee beans, wheat middlings, wheat bran, and tomato pomace, respectively. The obtained results show also a very clear influence of the treatment temperature on the extraction of polyphenols. HPH-assisted extraction of phenolic acids at room temperature further improved the extraction yield of about 21%. Generally, the temperature has a positive effect on the extraction of phenolic compounds from vegetal sources [26,27]. The observed positive effect of temperature could be explained by the higher solubility of polyphenols, the higher diffusivities of the extracted molecules and the improved mass transfer at higher temperatures [21]. On the other hand, subjecting AFRs to high temperatures (around 50 °C), might lead to the release of certain phenolic compounds while simultaneously triggering possible thermal oxidation or degradation of others [27]. For example, when Rajha et al. (2013) compared the water extraction yield of phenolic compounds form Cabernet Sauvignon grape by-products in a range of temperature between 33 and 50 °C, they found that diffusion time had a quadratic negative effect on TPC, showing a maximum TPC value at 30 h [28]. This is because long extraction time could lead to a reversed effect on the phenolic compounds likely due to oxidation or degradation reactions triggered by oxygen present in the head space of test flasks, which would be accelerated at higher temperatures [28]. Nevertheless, it is worth noting that, regardless the AFRs, the positive correlation between the phenols concentration and reducing activity leads to achieving a Pearson correlation coefficient higher than 0.999, which indicates that the antioxidant activity is completely caused by the extracted phenolic compounds.

The phenolic compounds extraction from HPH-treated AFRs and the exposure of antioxidant functional groups, which improves the antioxidant capacity, are strongly related to the microfluidization process. It effectively increases the specific surface area of vegetable materials by size reduction and more importantly loosens their microstructure, exposing more functional groups to the surrounding liquid phase, and even creating pores or cavities inside them.

IV.1.3.4. Effect of HPH treatment on physical characteristics of

AFRs suspensions

Mechanical treatments induced a measurable disruption of the vegetable tissue, which became more evident after HPH process. Visually, as shown in Figure IV.9, the AFRs suspensions became more homogeneous in appearance in comparison with HSM-treated samples. These observations can be correlated with the microscopical observations (Figure IV.10), which show that HSM micronization caused only the fragmentation of the tissue into

smaller cell aggregates, with negligible effects on cell wall integrity. Along with improving functional and physicochemical properties, HPH treatment also improves the progressively individual cell disruption, as suggested by the large fraction of filamentous debris appearing in the suspension, likely as the result of cell wall breakage. The significant variation in size and shape of samples before and after HPH process could be attributed to the fluid-mechanical stresses occur during the treatment, which improved the trimming of the particles along their length. Accordingly, the results achieved by Jurić et al. (2019) for tomato peels [29] and Wang et al. (2013) for wheat bran [30] are in agreement with the results of the present study.
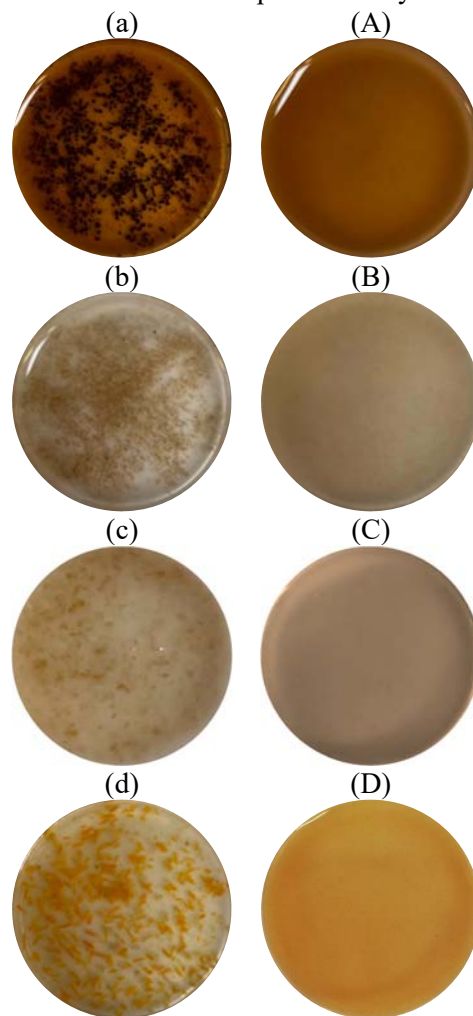
Figure IV.9 *Visual observations of roasted (a) coffee beans, (b) wheat middlings, (c) wheat bran, and (d) tomato pomace in water suspension. Lowercase letters indicate AFRs suspensions after HSM treatment; capital letters indicate AFRs suspensions after HPH treatment.*

(a)

(A)

(b)

(B)

(c)

(C)

(d)

(D)
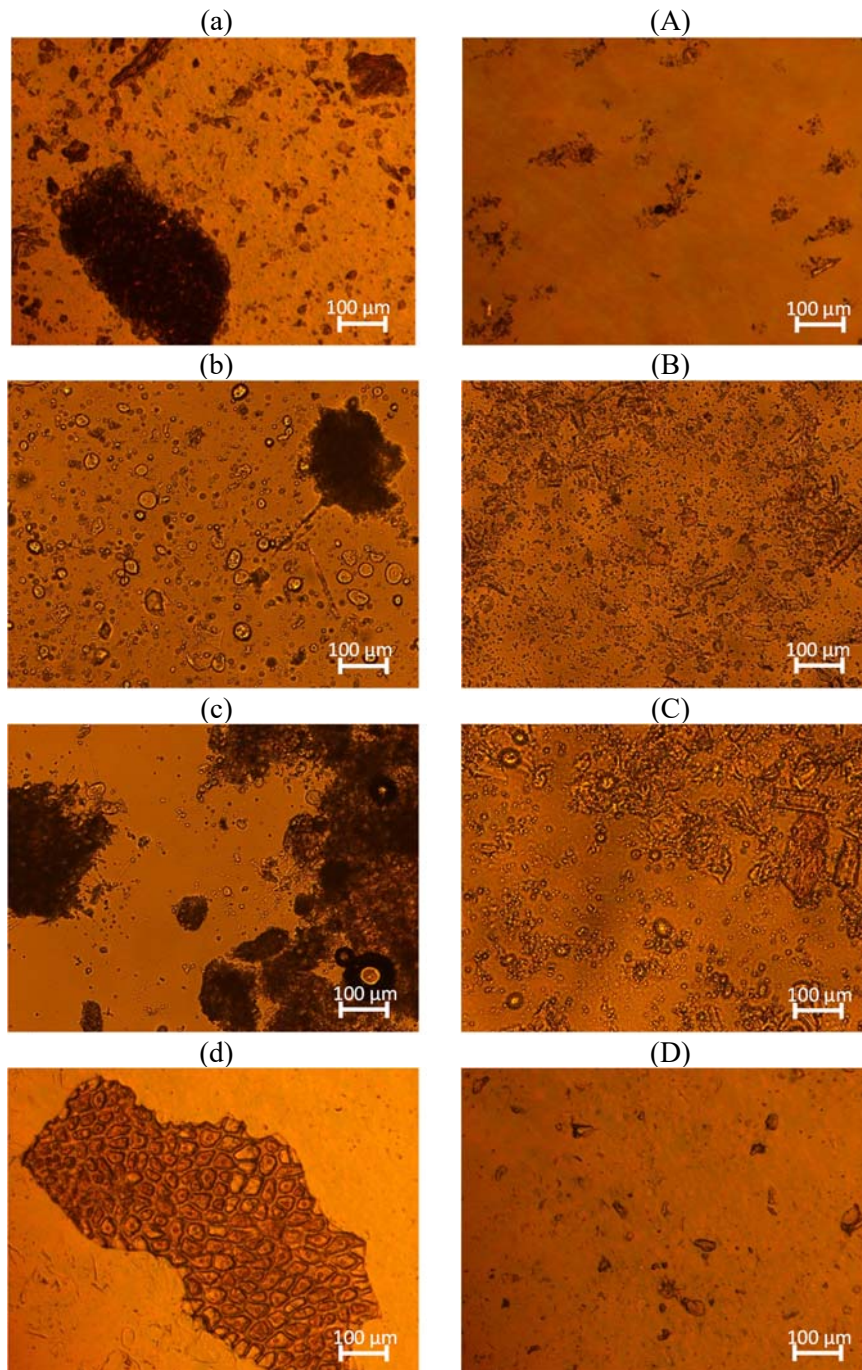
Figure IV.10 *Brighfield micrographs of (a) roasted coffee beans, (b) wheat middlings, (c) wheat bran, and (d) tomato pomace in water suspension. Lowercase letters indicate AFRs suspensions after HSM treatment; capital letters indicate AFRs suspensions after HPH treatment.*

The extent of the cell disruption related to the size reduction can be desumed from the particle size distribution curves reported in Figure IV.11.

(a)

(b)

(c)

(d)
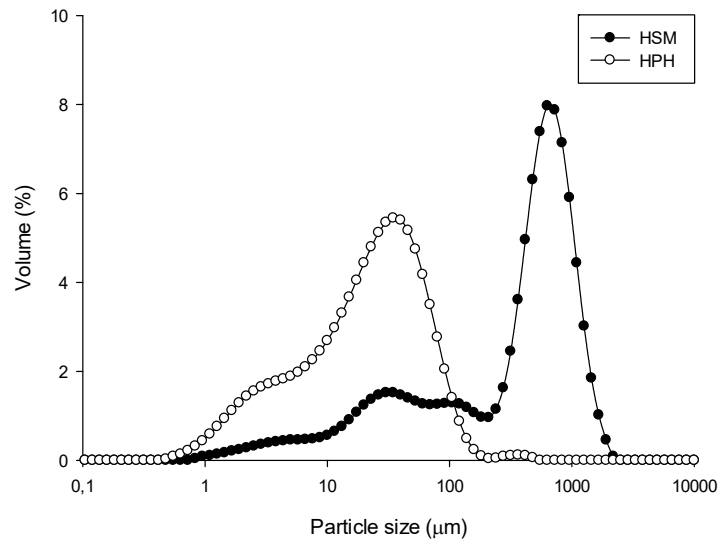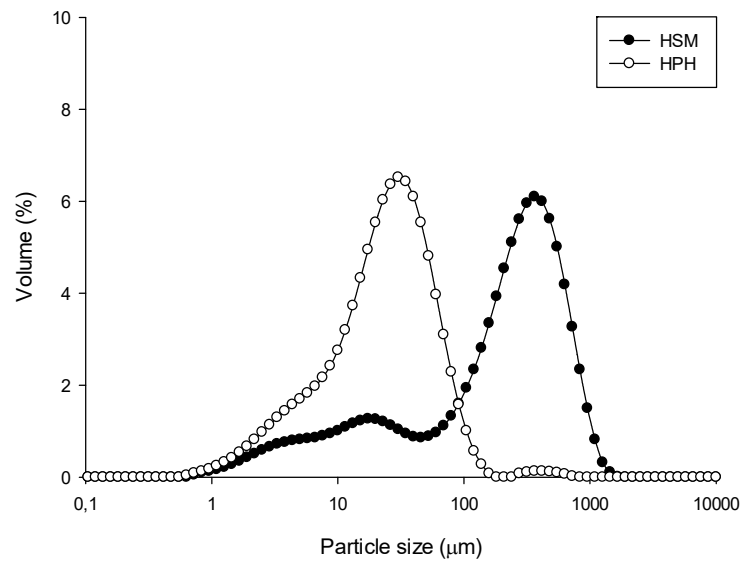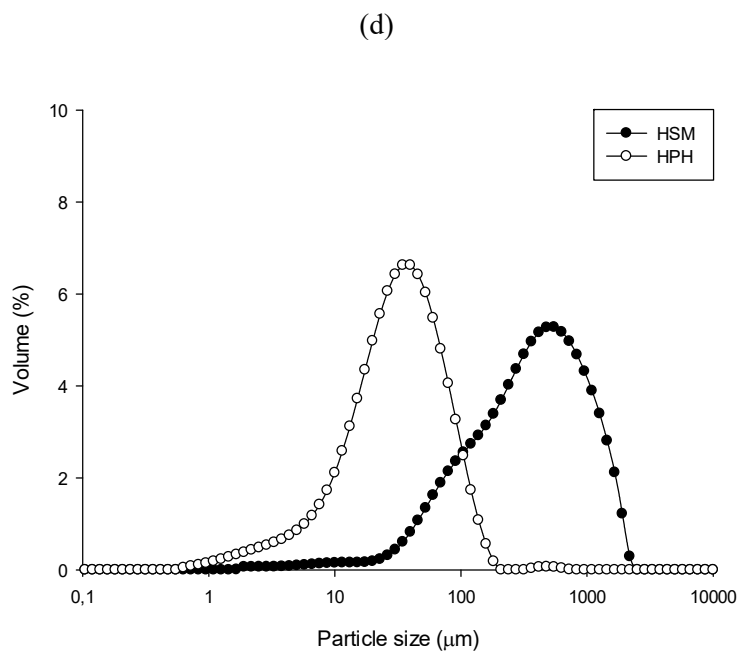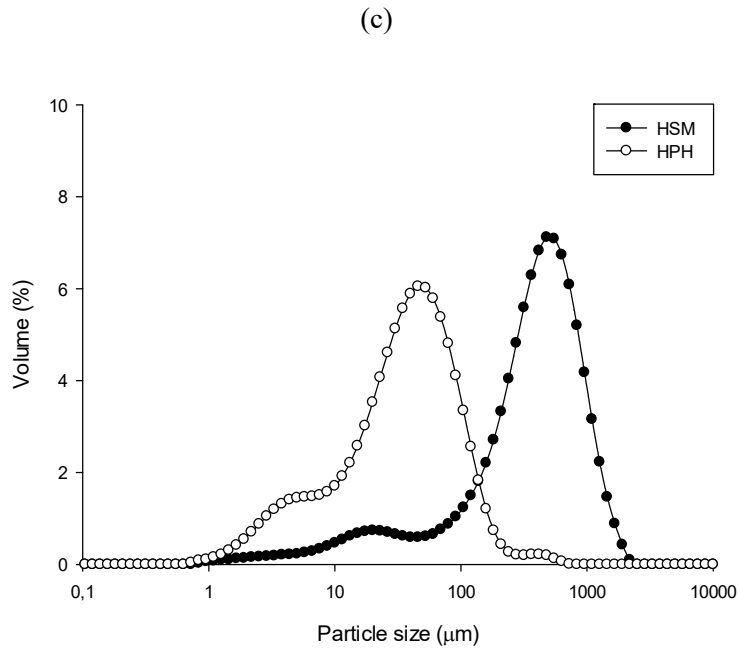
Figure IV.11 *Particle size distribution of (a) roasted coffee beans, (b) wheat middlings, (c) wheat bran, and (d) tomato pomace in-water-suspensions treated by HSM and HPH.*

Table IV.4 *Characteristic diameters (μm) of the particle size distribution of the AFRs aqueous suspensions treated by HSM and HPH.*

	Roasted coffee beans		Wheat middlings		Wheat bran		Tomato pomace	
	HSM	*HPH*	*HSM*	*HPH*	*HSM*	*HPH*	*HSM*	*HPH*
d(0.1)	1.83 ± 0.14	2.75 ± 0.01	8.55 ± 0.13	4.40 ± 0.05	36.28 ± 2.08	5.04 ± 0.01	67.20 ± 0.89	7.78 ± 0.14
d(0.5)	451.45 ± 16.90	21.31 ± 0.09	220.64 ± 3.02	22.62 ± 0.25	374.70 ± 4.63	34.41 ± 0.11	349.43 ± 6.29	29.97 ± 0.25
d(0.9)	978.34 ± 18.41	65.03 ± 0.30	595.37 ± 8.92	59.55 ± 0.48	898.21 ± 6.77	97.22 ± 1.30	1089.82 ± 51.78	78.22 ± 0.50
D[4,3]	468.85 ± 16.74	29.90 ± 0.42	266.08 ± 5.17	30.68 ± 0.36	438.26 ± 3.54	47.30 ± 1.20	473.18 ± 16.09	38.47 ± 1.06
D[3,2]	34.51 ± 2.13	7.53 ± 0.05	21.80 ± 0.31	10.43 ± 0.14	52.85 ± 1.17	13.23 ± 0.03	113.74 ± 1.97	14.47 ± 0.16

Chapter IV

The particle size of the suspension is described in Table IV.4, through the characteristic diameters d(0.1), d(0.5), d(0.9), D[4,3], and D[3,2] as a function of applied treatment. Both micronization methods resulted in smaller particle sizes compared to the non-micronized samples. Also, the smallest particle size has been seen when HPH was employed on the AFRs water suspensions.

More specifically, the HPH treatment also caused a significant reduction in diameters corresponding to the 10th, 50th and 90th percentile of the cumulative distribution (d(0.1), d(0.5), d(0.9), respectively, with a decrease in the distribution width (expressed as d(0.9) - d(0.1)) spanning ranging between 580 to 1020 μm for HSM and between 55 to 90 μm for HPH. Interestingly, the size distribution in terms of volumetric (D[4,3]) weighted decreased by ~94%, 88%, 89%, and 92% for roasted coffee beans, wheat middlings, wheat bran, and tomato pomace, respectively. While the surface weighted mean diameters (D[3,2]) exhibited a change by ~78%, 52%, 75%, and 87% for roasted coffee beans, wheat middlings, wheat bran, and tomato pomace, respectively, slightly fewer than D[4,3]. Nevertheless, small particles are more difficult to micronize [31,32], HPH treatment allowed to decrease both D[4,3], greatly influenced by the presence of large particles, and D[3,2] influenced by the smaller ones. Particle size variation also leads to change the stability characteristics of the AFRs water suspensions. The larger particles in suspension have a tendency of sedimentation due to shear force arising from internal instability [33]. Meanwhile, very small particle sizes lead to increase in interaction with sample network, which increases stability [34].

Remarkably, HSM treatment is not able to destroy individual plant cells, whereas HPH treatment does. In particular, the plant cells are completely disrupted, increasing (i) the suspension stability against sedimentation and (ii) the release in the suspension of most of the intracellular content. These results are consistent with the aforementioned results of the bioactive compounds release in water upon micronization treatment, which also induced an enhanced bioaccessibility of the antioxidant compounds, generally contained inside the cells.

IV.1.4. Conclusions

The water suspensions of AFRs represent a by-product with high added value. The present work clearly demonstrated that the antioxidant functional groups of phenolic compounds of AFRs exhibited antioxidant capacity when they are exposed to the surrounding liquid phase.

The results for the SLE conventional extraction of polyphenols are presented. Here, different organic solvents, as well as the influence of water in the extracting organic solvent are discussed concerning equilibrium and mass transport kinetics. The SLE studies confirmed that this process has a significant effect on the extraction of high-valuable active compounds. Moreover, the kinetic study plays a very important role in evaluating the

158

extraction process because it allows estimation of the cost-effectiveness of the process in saving time, money, and energy. Although phenols extraction with SLE is efficient, it is necessary to not overlook the fact that the use of chemicals and the processing time are the main technological advantages.

The micronization process through HPH mechanical treatment (80 MPa for 10 min at 25 °C) significantly increased the exposure of the phenolic compounds and the associated antioxidant capacity with respect to SLE. This study clearly substantiates the merits of particle size reduction leading to a higher extractability of polyphenols.

Thus, in view of the exploitation of AFRs derived from the industrial transformation, HPH treatment led to a more efficient recovery of phenolic compounds decreasing the extraction time and without the usage of solvents, which have negative effects from economical and environmental points of view, respectively. In this way the valorization of AFRs leads to a greater diversity of natural products to be used as food supplements or in cosmetics formulation, while lowering economical and environmental impact.

Chapter IV

Section IV.2
Cellulose isolation from AFRs

This section proposes a biorefinery approach for the exploitation of different valuable compounds of AFRs, such as tomato pomace (TP) and barley straw (BS), through top-down chemical deconstructing strategy, mainly based on mild acid hydrolysis and a combination of chemical hydrolysis with HPH mechanical treatment. In particular, the cellulose pulp was isolated using different combinations of chemical and physical processes, by applying HPH treatment (i) directly on the raw material; (ii) after the acid hydrolysis; and (iii) after alkaline hydrolysis. As an alternative approach, this section focused also on bacterial cellulose (BC) isolation through bottom-up green constructing strategy derived from the biofilm by-product of Kombucha tea fermentation process, using sucrose or micronized AFRs (in particular tomato pomace and wheat middlings) as a substitute for sucrose source in the culture media. Results show that these isolation routes allowed to achieve cellulose pulp with tailored morphological properties from underused lignocellulose feedstocks or by-products of fermentation process, evaluated through light scattering for particle size distribution, optical and scanning electron microscopy, and FT-IR analysis. Moreover, the mild chemical process produced side streams rich in bioactive molecules, evaluated in terms of total phenols and reducing activity. From the overall results collected in this section, an efficient cellulose extraction has been accomplished along with the valorization of the value-added compounds still contained in the AFRs biomass, subjected to further studies of nanostructured cellulose, as described in § IV - section IV.3. In summary, this study provides a feasible solution to deconstruct cellulose from lignocellulosic AFRs and to construct bacterial cellulose from fermentation of Kombucha tea, which has potential applications in the future as green advanced functional materials, with both processes accopained by the recovery of side streams rich in bioactive compounds (acid or alkaline liquors, or Kombucha beverage).

IV.2.1. Specific goal and work plan

In recent years, cellulose has received increasing interest as a renewable raw material for the production of biodegradable polymeric products, contributing to replace fossil resources, considering their depletion, fluctuation in oil price and the negative environmental impacts [35]. Cellulose is a linear homopolymer of glucose $(C_6H_{12}O_6)_n$, consisting of repeated units of D-glucose in a $^4C_1$ conformation. In the global scenario, among the available sources of renewable feedstock for cellulose isolation, lignocellulosic biomass, including agricultural residues, stands out. In contrast, the use of the vastly available by-products and wastes, also known as AFRs, is currently limited to livestock feed, providing a limited added value, or landfill or energy production by combustion, causing potential environmental issues [36]. Therefore, new strategies for the exploitation of AFRs represent a great opportunity for more sustainable routes for the recovery of high value-added compounds, as well as for mitigating their environmental burden. To date, research has primarily focused on the production of cellulose from lignocellulosic waste, such as coconut husk fibers [37], cassava bagasse [38], hazelnut shells [39], rice husk [14,40,41], wheat straw [39-41], oat hull [45], and okara [46,47]. All these biomasses mainly consist of three natural organic polymers, cellulose, hemicellulose, and lignin, and contain also small amounts of proteins, pectin, and other extractives (e.g. bioactive molecules).

Among the different side-streams from agriculture, lignocellulosic biomass, such as straws from cereal plants (barley straw, BS; wheat bran, WB; and rice husk, RH), is the most abundant renewable biomass on Earth, with approximately 200 billion tons per year of lignocellulosic biomass supply by worldwide from the forestry residue and agricultural wastes [45-49]. In addition, also tomato processing industry represents an interesting case study for enhancing and integrating synergic solutions for waste management, considering that tomato is one of the most widely cultivated vegetable crops in Mediterranean countries. It is one of the largest primary vegetable crops. As such, tomato processing industry is responsible for the production of large amounts of solid waste (~ 3 - 4% of the fresh processed tomatoes weight, also known at tomato pomace, TP), which creates a major disposal problem in terms of costs and environmental impacts [53].

Nowadays, BS, WB, and RH are mainly buried in soil or burnt in the field causing air pollution and fire risk, used as organic compost and as cattle feed. These uses do not add value to agricultural activity and are not sufficient to manage all waste generated in agricultural activity [54]. Meanwhile, TP is partially exploited for the organic extraction of lycopene [55,56], a powerful natural antioxidant carotenoid widely used in food, pharmaceutical and cosmetic products [57]. More recently, TP has been investigated as feedstock for anaerobic digestion to produce biogas [55,58,59]. However, these AFRs can also be exploited to recover cellulose, because it is a good source of the

complex carbohydrates composing the lignocellulosic plant cell wall, i.e. cellulose, hemicelluloses and lignin as well as other minor components (Figure IV.12).
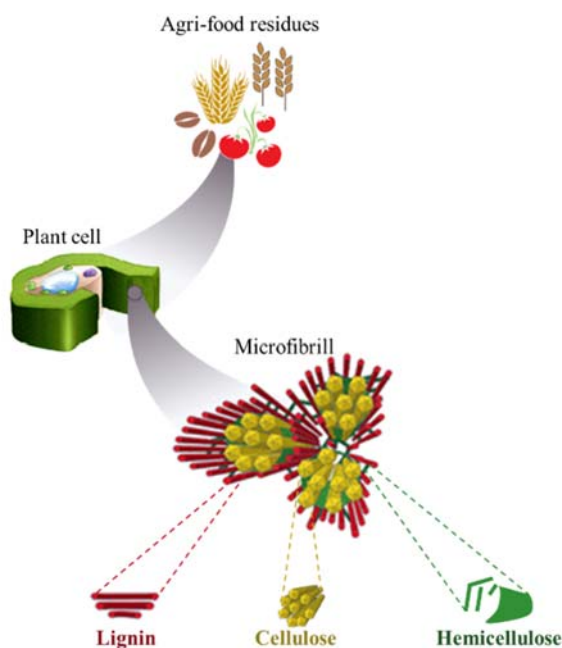
Figure IV.12 *Schematic representation of top-down deconstructing strategy for cellulose isolation from AFRs cell wall.*

In general, cellulose isolation from AFRs requires a top-down chemical deconstructing strategy, conventionally based on chemical or enzymatic hydrolysis. More in detail, the isolation process is based on strong acid hydrolysis (such as 63 - 72% H_2SO_4 [60,61], 42% HCl [62,63], or 77 - 83% H_3PO_4 [64]), followed by alkaline hydrolysis (1 - 10% NaOH [62-64]) and a bleaching process to remove residual pigments (1 - 2% NaClO [68–70] or 5 - 15% H_2O_2 [71,72]). Chemical hydrolysis is the most widely used strategy because it is inexpensive and is able to induce the breakdown of the fibrous cell walls, remove the lignin and hemicellulose fraction, and, thus, expose the cellulose for extraction [73]. However, there are several disadvantages in using this conventional approach, such as corrosion of equipment, environmental damage as well as safety issues [47]. For these reasons, the increase in efficiency of these isolation methods, while decreasing the severity of the operating conditions, is highly desirable. However, available data show intrinsic limitations in the cellulose extraction that can be obtained: lower acid concentrations are reported to produce particles characterized by highly amorphous regions with low-crystallinity, therefore, reducing yield and purity of cellulose [74].

Chapter IV

In this scenario, the aim of this study is to develop an efficient process to isolate cellulose from different AFRs, via mild chemical hydrolysis processes (e.g. reducing alkali concentrations) and the combination of mechanical treatments by HPH and mild chemical hydrolysis processes for more sustainable cellulose production processes. The fluid-mechanical stresses on the biomass occurring within the interaction chambers during HPH treatment were previously reported to induce (i) a significant reduction in particle size; (ii) and increase in surface area [29]; as well as (iii) the disruption of the well-arranged cellulose-hemicellulose-lignin complexes, causing what is referred to as fiber activation or cellulose defibrillation [75]. The HPH fluid-mechanical treatment is here exploited for the first time to increase the efficiency of mild chemical hydrolysis processing for the isolation of cellulose with a defibrillated structure from AFRs. Moreover, it is also aimed to demonstrate that the selected mild chemical hydrolysis conditions are able to produce side streams very rich in bioactive compounds, further contributing to the valorization of the AFRs under study.

Another strategy adopted in this work is to isolate bacterial cellulose (BC) from Kombucha tea fermentation (Figure IV.13). Traditionally, BC is produced from expensive culture media, containing glucose as carbon source and other nutrient sources resulting in very high production costs, which limits the use of this material to very high value-added applications. The use of cheap carbon and nutrient sources is an interesting strategy to overcome this limitation and therefore to increase the competitiveness of this unique material. Mostly, the AFRs have abundant sugars such as glucose and fructose that could be bio-converted into useful products. Therefore, an interesting approach for improved production of BC with cheap and readily available substrate to bring down the cost of production, as well as for changing its biological properties is the use of a combination of carbon sources with two different symbiotic AFRs consortia: HPH micronized TP and WM.
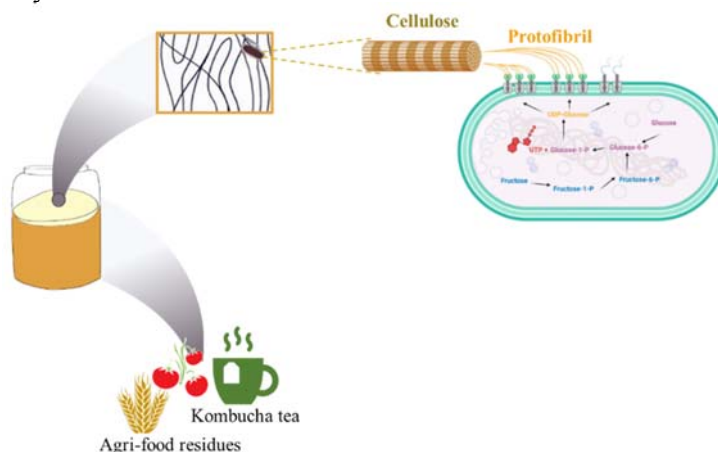
Figure IV.13 *Schematic representation of bottom-up constructing strategy for bacterial cellulose from Kombucha tea fermentation.*

The hypothesis was that it is suitable to use Kombucha symbiotic community of bacteria and yeast (SCOBY) to produce BC taking advantage of the low-cost media and high purity of isolated cellulose. This new approach contributes to reducing the use of chemicals and treatments for efficient cellulose isolation while taking advantage of different phytochemical compounds, which provide bioactive properties to cellulose itself.

IV.2.2. Short material and methods
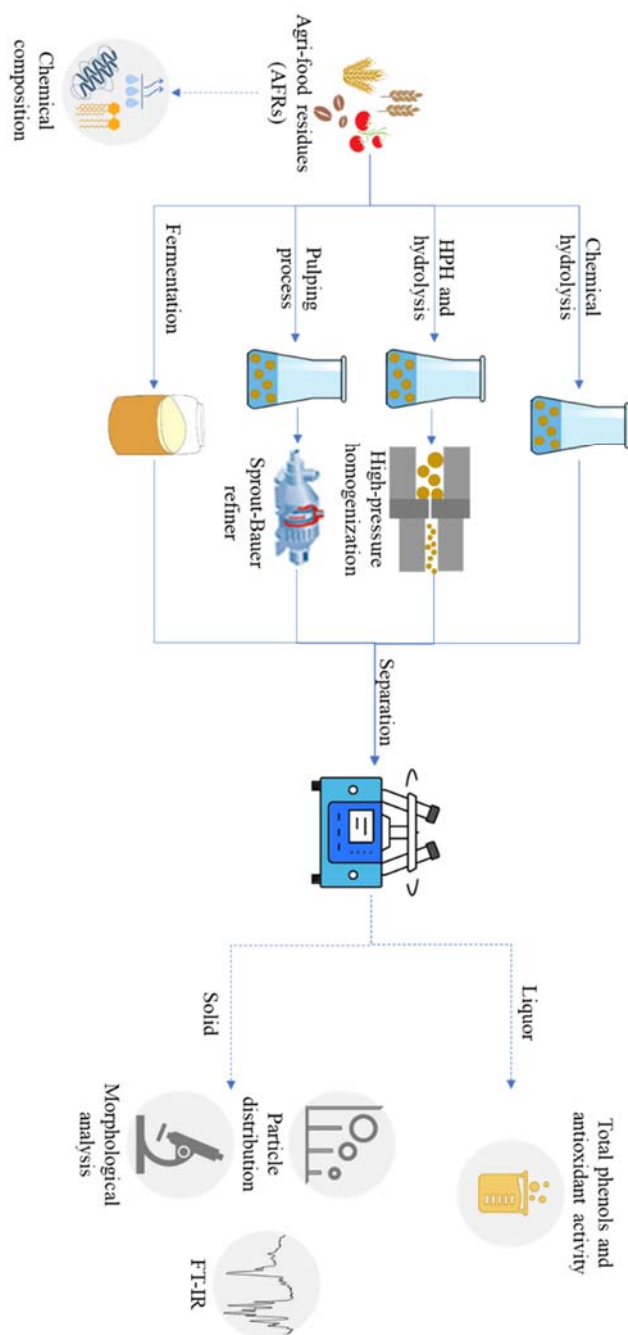
Figure IV.14 Schematic representation of methodology used for cellulose isolation from AFRs.

IV.2.2.1. Cellulose, hemicelluloses, and lignin content of AFRs

The cellulose and hemicellulose were determined using the gravimetric method according to TAPPI T-203, while lignin content according to TAPPI T-222 om-22 methodology, as described in detail in § III.7.1.5. Prior to the gravimetric component determination, extractives (such as sugars, phenolic compounds, and part of water-soluble polysaccharides) have been removed according to TAPPI method (T-264 om-82) [13] and ASTM E1721-01. All analysis were performed in triplicate and the means and standard deviations were calculated.

IV.2.2.2. Cellulose isolation processes

The processes adopted to isolate cellulose from AFRs are summarized in Table IV.5. More in detail the treatments are (i) mild chemical hydrolysis (as described in detail in § III.4.1); (ii) the combination of mechanical treatments by HPH technology and mild chemical hydrolysis processes (as described in detail in § III.4.2); (iii) pulping process (as described in detail in § III.4.3); and (iv) bacterial fermentation (as described in detail in § III.4.4).

Table IV.5 *Summary of treatments and operating conditions for cellulose isolation from AFRs.*

AFRs raw materials	Treatment applied	Conditions
MILD CHEMICAL HYDROLYSIS		
Tomato pomace (TP)	Chemical hydrolysis	
	• Acid hydrolysis	$H_2SO_4 = 4.7\%$ v/v
		$T = 121$ °C
		$t = 45$ min
	• Alkaline hydrolysis	NaOH = 4 N
		$T = 25$ °C
		$t = 24$ h
	• Bleaching	$H_2O_2 = 4\%$
		pH = 11.5
		$T = 45$ °C
		$t = 8$ h
HPH-ASSISTED CHEMICAL HYDROLYSIS		
Tomato pomace (TP)	HPH treatment	$P = 80$ MPa
		$T = 25$ °C
		# passes = 20
	Chemical hydrolysis	
	• Acid hydrolysis	$H_2SO_4 = 4.7\%$ v/v
		$T = 121$ °C
		$t = 45$ min
	• Alkaline hydrolysis	NaOH = 4 N
		$T = 25$ °C
		$t = 24$ h
	• Bleaching	$H_2O_2 = 4\%$
		pH = 11.5
		$T = 45$ °C
		$t = 8$ h

PULPING PROCESS		
Barley straw (BS)	Chemical hydrolysis	
	•Alkaline hydrolysis	NaOH = 0.7% w/v
		T = 120 °C
		t = 150 min
	• Bleaching	NaClO$_2$ = 30% w/w
		pH = 4.5
		t = 3 h
	Sprout-Bauer refiner	Distance rotor - stator plates = 5
BACTERIAL FERMENTATION		
Scoby	Fermentation process	Sucrose = 80 g/L
		Black tea = 4 bags/L
Scoby HPH-TP	Fermentation process	HPH-TP = 13 g/L
		Black tea = 4 bags/L
Scoby HPH-WM	Fermentation process	HPH-WM = 13 g/L
		Black tea = 4 bags/L

IV.2.2.3. Liquor side streams characterization

Side streams from cellulose isolation process, very rich in bioactive compounds, were characterized in terms of total phenolic compounds (TPC and HPLC) and antioxidant power (FRAP), as previously reported in § III.7.2.1 - 7.2.3. The structural carbohydrates have been also determined according to the methodology described in § III.7.2.4. In addition, the liquor was dialyzed against water and freeze-dried in order to analyze their functional groups by FT-IR spectroscopy (§ III.7.2.5.1) and determine the structural features performed by qualitative SEM microscopy (§ III.7.2.5.2).

IV.2.2.4. Cellulose pulp characterization

The cumulative cellulose yield (§ III.7.3.1) aimed to demonstrate the cellulose extraction efficiency of HPH treatment in combination with mild chemical hydrolysis processing. The cellulose residues obtained after each treatment were subjected to strong acid hydrolysis to determine the lignin, cellulose, and hemicellulose content, as described in § III.7.3.2. Moreover, to investigate the chemical structure of the isolated cellulose pulp by identifying the functional groups and evaluating the structural changes that occurred during the applied treatments, the FT-IR analysis was performed (§ III.7.3.3). The morphology of the isolated cellulose was observed using optical microscopy (§ III.7.3.4.1) and SEM (§ III.7.3.4.2). Finally, the particle size distribution and contact angle analysis were performed as described § III.7.3.5 and § III.7.3.6, respectively.

The cellulosic pulp from barley straw was dispersed in a pulp disintegrator, filtered under vacuum and dried between two nylon sieves to obtain papers (§ III.6). Mechanical properties and porosity have been determined on paper sheets as described in § III.7.4.12 and § III.7.4.13, respectively.

IV.2.3. Results and discussion

IV.2.3.1. Lignocellulosic biomass composition of AFRs

The lignocellulosic biomass composition of AFRs is reported in Table IV.6. The barley straw cellulose composition agrees well with previous data published by Lara-Serrano et al. (2019), which reported that cellulose, hemicellulose, and lignin content is 31.09%, 27.23%, and 18.77%, respectively [76]. In addition, also the cellulose composition of wheat bran, tomato pomace, and rice husk is in agreement with values reported by Rahman et al. (2021) [77], Kheiralla et al. (2018) [78] and Johar et al. (2012) [14], respectively. Nevertheless, some little variations in the chemical composition concentration of AFRs could be attributed to the type of paddy, climatic, geographical conditions, and sample preparation.

Table IV.6 *Cellulose composition of AFRs raw materials.*

	Barley straw	Wheat bran	Tomato pomace	Rice husk
Extractives ($\%_{DM}$)	10.24 ± 0.24	10.73 ± 0.52	8.24 ± 0.42	5.02 ± 1.31
Cellulose ($\%_{DM}$)	34.86 ± 0.33	13.55 ± 1.68	32.09 ± 2.24	40.38 ± 5.80
Hemicellulose ($\%_{DM}$)	22.80 ± 0.59	37.63 ± 0.95	26.62 ± 1.57	34.53 ± 4.96
Lignin ($\%_{DM}$)	11.88 ± 1.45	36.32 ± 0.91	30.54 ± 1.71	22.31 ± 3.92

IV.2.3.2. HPH-assisted chemical hydrolysis

A possible strategy to improve cellulose extractability is the use of HPH physical treatments in different phases of the chemical process. Figure IV.15 summarizes the treatments carried out on TP and the abbreviations used for each solid residue and side stream liquors.
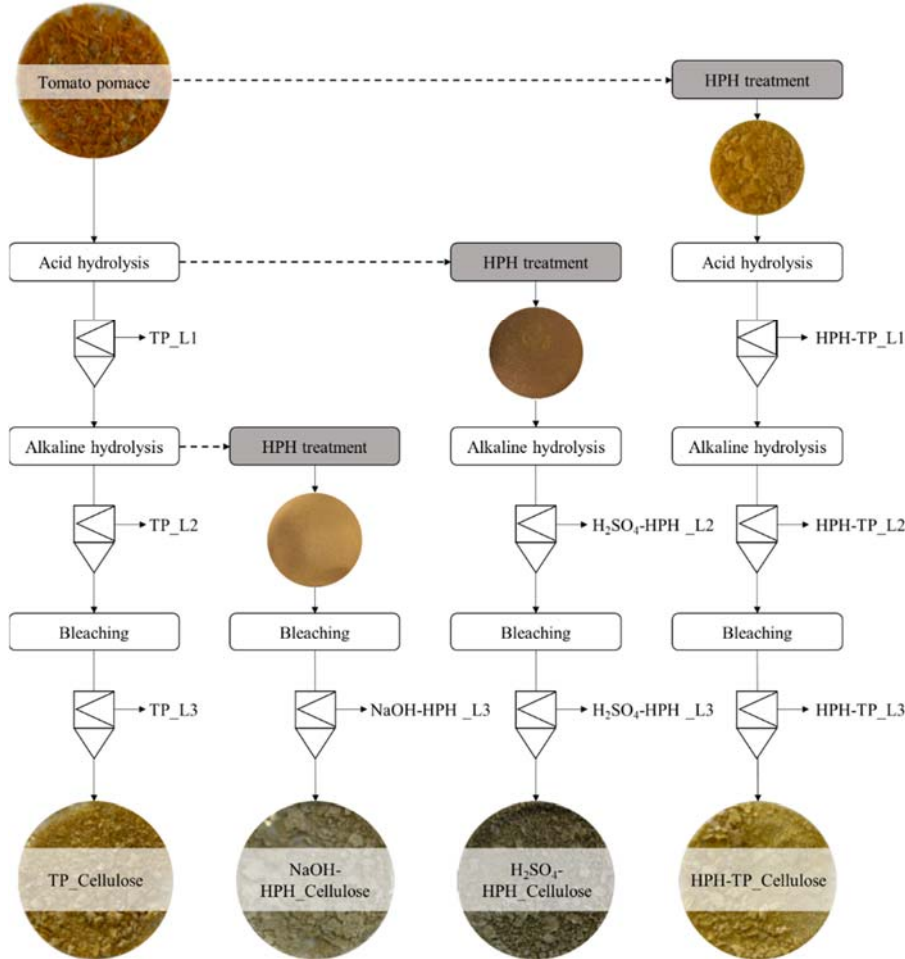
Figure IV.15 *Schematic representation of acid-alkaline fractionation process combined with HPH mechanical treatment on tomato pomace.*

Chemical and morphological characteristics of isolated cellulose

The applied HPH treatment influenced the composition of the fiber (Table IV.7) by reducing the resistance between the cellulose chain and disrupting the intermolecular and intramolecular hydrogen bonds [79]. HPH caused a significant ($p < 0.05$) increase in cellulose content, which correlates well with the observed decrease in lignin content. The lignin-containing fibers are subjected to intense collision, shearing, and cavitation, and the fibers are more likely to break up into uniform defibrillated cellulose of micrometric size during the HPH treatment [80]. Furthermore, the mild chemical hydrolysis cascade process (Figure III.7) applied to tomato pomace (TP) to obtain cellulose reached a cumulative yield, calculated with Equation III.3, of about $61.72 \pm 0.50\%$. The HPH treatment applied at different stages of hydrolysis

(Figure III.8) contributed to obtaining a significantly ($p < 0.05$) higher cellulose yield (Table IV.7). With respect to tomato pomace an increase in cellulose isolation of about 21% has been achieved for HPH treatment applied on raw material. In contrast, only a slight increase in cellulose isolation ($\sim 6\%$) has been obtained for HPH treatment applied after acid or alkaline hydrolysis. These results can be attributed to the effect of the mechanical treatment, which has a disruptive effect on the raw material structure as well as on bonds of the lignocellulosic structure, making cellulose isolation more efficient. Moreover, HPH treatment also influenced cellulose morphology and structure, as well as the biological activity of the liquors obtained at the end of each chemical hydrolysis step.

Table IV.7 *Cellulose yield from HPH-assisted chemical hydrolysis on TP at different level of cascade process.*

	TP_Cellulose	NaOH-HPH_Cellulose	H_2SO_4-HPH_Cellulose	HPH-TP_Cellulose
Cellulose (%$_{Residue\ fiber}$)	29.33 ± 1.52	31.51 ± 0.17	32.12 ± 0.24	37.72 ± 0.79
Hemicellulose (%$_{Residue\ fiber}$)	18.74 ± 0.52	2.17 ± 0.07	2.18 ± 0.10	4.62 ± 0.65
Lignin (%$_{Residue\ fiber}$)	0.74 ± 0.03	0.94 ± 0.03	0.97 ± 0.08	0.76 ± 0.02
Cumulative yield (%$_{DM}$)	61.72 ± 0.50	65.47 ± 0.36	65.07 ± 0.51	74.38 ± 0.41

In addition to yield, FT-IR spectra of extracted celluloses (Figure IV.16) were also measured to investigate the chemical structure by identifying the functional groups of different materials and evaluating the structural changes that occurred due to the applied treatment [3]. For example, FT-IR was used to identify protein and starch changes caused by high hydrostatic pressure [81,82] and sonication or the effect of HPH in nanocellulose isolation [46]. All spectra showed some signature characteristic bands of celluloses without any remarkable difference between the samples, including absorption peaks at 3300 and 2902 cm^{-1} because of the presence of H-bonded OH group stretching and C-H stretching vibration groups [83], respectively. The spectrum of cellulose is characterized by absorption peaks between 950 and 1100 cm^{-1} because of the presence of C-O and C=C stretching vibration groups [84]. In particular, the peak at 1028 cm^{-1} is attributed to the C-O-C pyranose ring stretching vibration [83,85] and 897 cm^{-1} at C-O-C stretching at the β-(1-4)glycosidic linkages between sugar units [86]. The absence peak around 1500 cm^{-1} (C=C aromatic skeletal vibrations stretching of the benzene ring) corresponding to the aromatic ring of lignin [85] from the spectrum of all cellulose pulp attested for the efficient lignin removal during the bleaching process. Thus, the accessibility of functional groups is facilitated, making the fibers more amenable to functionalization by chemical or physical pre-treatments and favoring their subsequent defibrillation. Based on Figure IV.16, it can be concluded that the cellulose isolated from HPH-treated TP at different level of chemical hydrolysis had a similar chemical structure as TP cellulose, suggesting that the chemical groups and conformation of the

cellulose structure were not altered or destroyed by the mechanical treatment. Finally, it must be highlighted that no absorption peaks were detected at 1540 cm^{-1}, suggesting that the samples did not contain any residual protein.
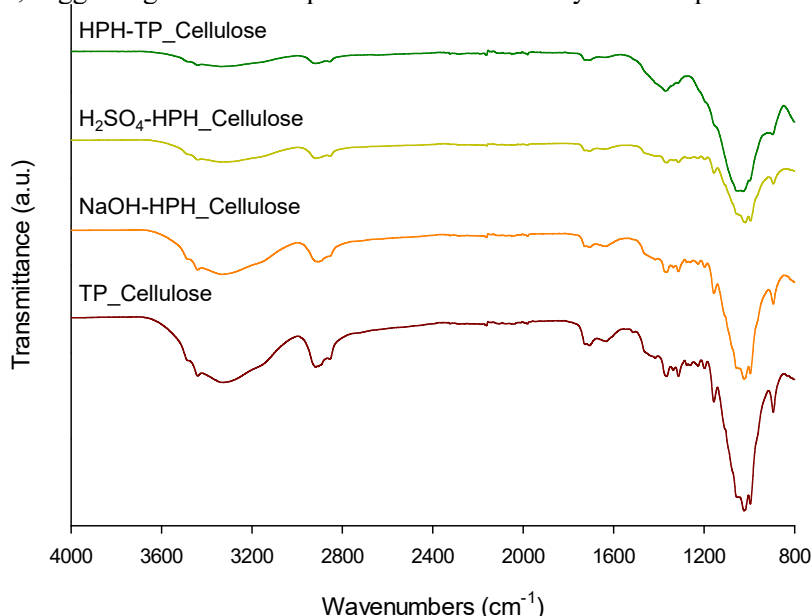
Figure IV.16 *FT-IR spectra of cellulose pulp isolated from TP with different combinations of HPH treatment and chemical hydrolysis.*

The morphology of the isolated cellulose after the HPH-assisted chemical hydrolysis was observed using optical microscopy (Figure IV.17a-d) and SEM (Figure IV.17e-h). The cellulose fibers from TP appeared in the form of agglomerates of irregular morphology, where the original cell structure could be clearly detected. The cellulose fibers isolated from TP with HPH-assisted chemical hydrolysis (at different levels of cascade steps) were, instead, completely different, with smaller agglomerates of irregular shape, including long needle-like debris with length from 600 to 950 μm and width from 10 to 30 μm. The significant variation in size and shape between TP_Cellulose and the others cellulose pulp could be attributed to the fluid-mechanical stresses exerted by the HPH treatment, which improved the cellulose defibrillation and contributed to trimming down the length of the fibers. SEM analysis (Figure IV.17e-h) confirmed the optical microscopy observations. Cellulose from TP is characterized by a thickness of approximately 20 μm and is organized in individual sheets corresponding to the peel cell layers. In contrast, cellulose from NaOH-HPH, H$_2$SO$_4$-HPH, and HPH-TP exhibited a high defibrillation degree, with individual fibers separating from fiber bundles. Moreover, in HPH-TP cellulose, the sheets observed for TP are fragmented in small pieces (with an average size of about 100 μm) and a honeycomb-like structure characterized by large cavities and high void fraction. This structure ensures

a significantly larger specific surface area than TP cellulose, improving the techno-functional properties of cellulose (which is sometimes referred to as fiber activation [87–89]). For example, HPH-activated TP fibers demonstrated a remarkable capability to act as stabilizers in Pickering emulsions [90].
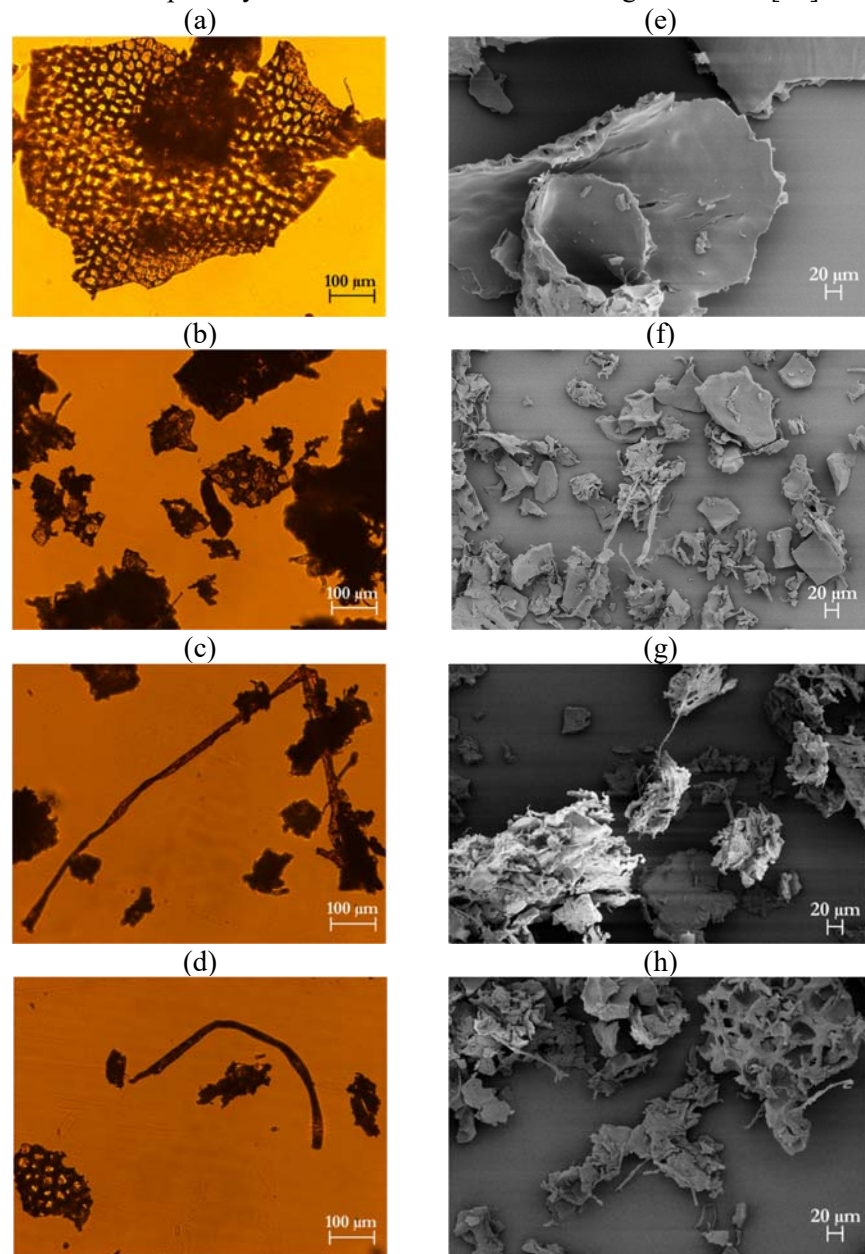
Figure IV.17 *Optical microscopy (a-d) at 10× magnification and SEM (e-h) images at 500× magnification of TP_Cellulose (a, e), NaOH-HPH_Cellulose (b, f), H_2SO_4-HPH_Cellulose (c, g), and HPH-TP_Cellulose (d, h).*

Chapter IV

Particle size distribution analysis showed that TP, NaOH, and HPH-TP cellulose particles presented a unimodal distribution and symmetrical curves, with low Span values ranging from 2.17 to 3.23 and the main peaks located approximately at 40 µm and 100 µm (Figure IV.18). For H_2SO_4-HPH_Cellulose the distribution curve is bimodal with large width of distribution (Span = 6.08), indicating the presence of particles in a broad size range of 140 µm to 710 µm. Moreover, the 90th percentile of TP, NaOH, and HPH-TP cellulose particles was ranged between 152 and 179 µm, while for H_2SO_4-HPH_Cellulose it was 854 µm. These results further proved the efficiency of HPH treatment applied at beginning or at the end of acid-alkaline fractionation process in the disintegration of plant tissues, indicating that the fluid-mechanical stresses generated by the treatment are strong enough for separating the multifibrillar structure into elementary fibers with a length of about 150-180 µm. Nevertheless, when HPH treatment is applied after acid hydrolysis, aggregation and swelling of particles occurred. The microscopy images of cellulose particles in Figure IV.17 confirm the statements above and prove the effectiveness combination of chemical and mechanical processes on the disintegration of fiber bundles and separation of elementary fibers from the surface.
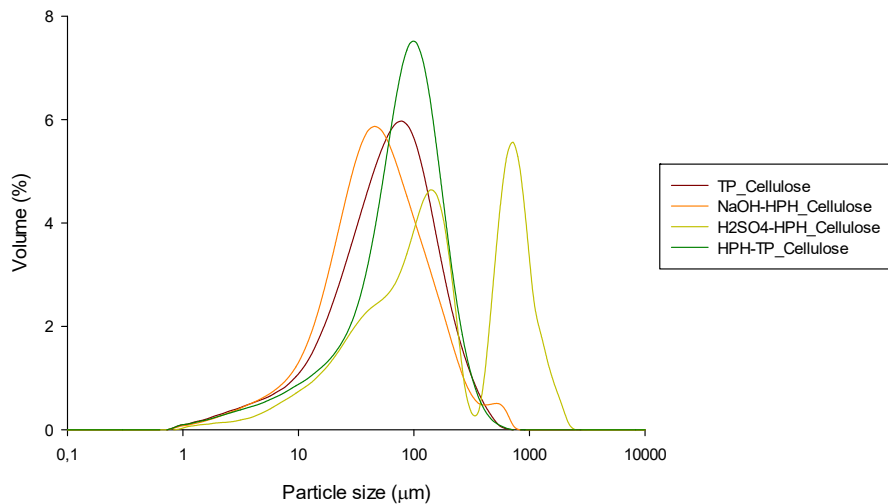
Figure IV.18 *Particle size distribution of cellulose pulp isolated from tomato pomace.*

Finally, contact angle analysis has been used to evaluate the hydrophobicity behavior and the wettability of cellulose surfaces and to assess their suitability for different applications in the presence of water. Figure IV.19 shows that the wettability for the TP_Cellulose is lower than all cellulose pulp isolated through HPH-assisted hydrolysis. This result could be explained by the difference in surface morphology: the open and porous

surface makes it more easily accessible to water compared to the tightly packed and dense surface of cellulose pulp [91]. The application of HPH treatment at different level of chemical cascade process reduced the number of surface hydroxyl groups [92] and therefore increased the water contact angle compared to chemical hydrolysis.
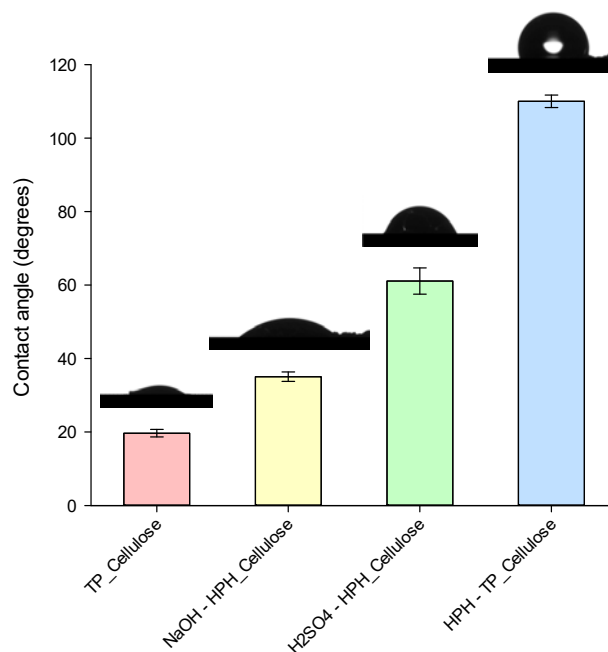
Figure IV.19 *Contact angle of water on cellulose pulp isolated from tomato pomace.*

Biological properties of side streams liquors

Besides its outstanding extraction yield and efficiency of cellulose isolation, as well as the change in morphology and chemico-physical properties occurring with the application of HPH treatment at different level of chemical cascade process treatments, this work aimed also to demonstrate that the selected process is able to produce side streams very rich in bioactive compounds, further contributing to the valorization of the AFRs.

Based on Folin's polyphenols determination (Figure IV.20), the acid hydrolysis step released higher amounts of total phenolic compounds than the successive alkaline hydrolysis and bleaching. Considering the total phenols quantification based on the 280-index method, the release yields obtained were notably higher than the values estimated with the Folin method. However, it should be considered that the 280 nm reading is also used to estimate the sugar degradation products, which can be generated by the acid hydrolysis of the hemicellulose fraction [93,94], with a consequent overestimation of phenols content. Detoxification is, therefore, generally

required to preserve the hemicellulose sugars removing the compounds that affect fermentation. The combination of the detoxification process with the recovery of phenols as high value-added compounds represents an interesting and widely investigated opportunity. Similar results were obtained in the evaluation of the reducing activity, with the acid liquor showing higher activity than the alkaline one, likely due to the preservation of phenolic compounds at acid conditions (Figure IV.20c).

(a)
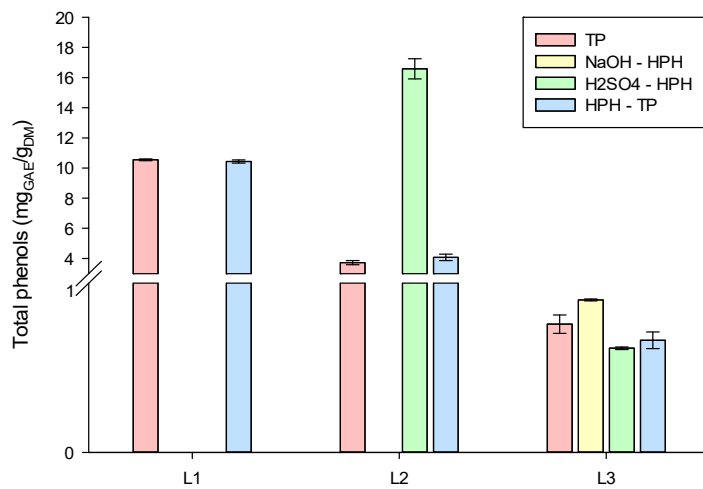
(b)
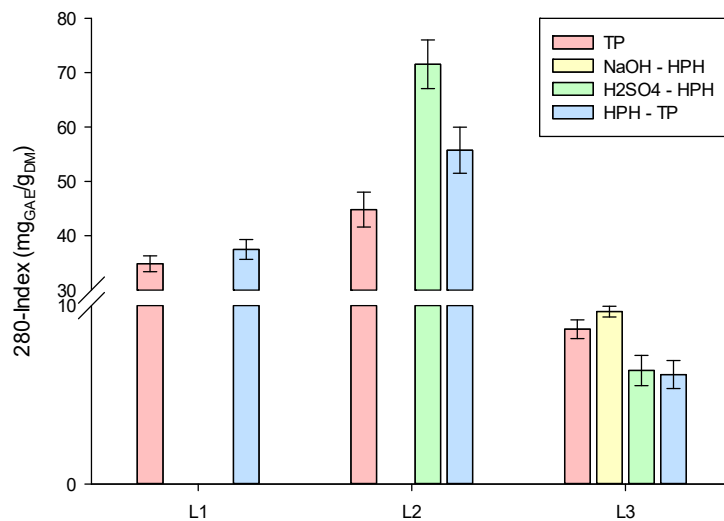
(c)
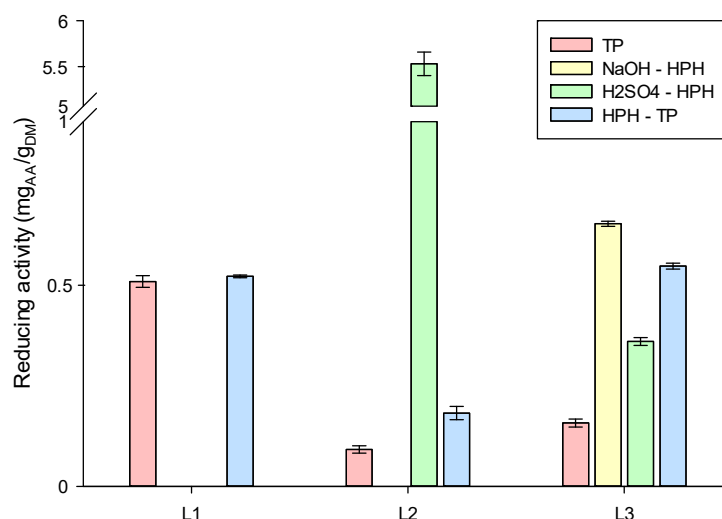
Figure IV.20 *(a) Total phenols, (b) 280-Index, and (c) reducing activity in the liquor from acid and alkaline hydrolysis and bleaching. Values are reported as mean (n = 5) ± standard deviations.*

Release yields of total phenols are significantly higher than the yields obtained from tomato pomace through optimized solvent extraction with acetone at 80 v% under agitation at 180 rpm at 25 °C for 24 h, as shown in Figure IV.8. In particular, total phenols content extracted with acetone at 80% v/v was about 3.13 ± 0.03 mg$_{GAE}$/g$_{DM}$, whereas significantly ($p < 0.05$) higher values were obtained in the liquor from acid hydrolysis. These findings suggest that the side streams of the lignocellulosic fractionation process (liquor from the different hydrolysis phases) can be exploited to efficiently recover phenolic compounds, replacing the conventionally applied solvent extraction step, hence contributing to enhancing the sustainability and economic viability of the cellulose recovery process from AFRs.

Structural carbohydrates, structural characteristics of liquors

Based on these results, acid-alkaline fractionation process followed by bleaching step combined with HPH mechanical treatment allowed to efficiently isolate cellulose pulp with different properties, depending on the treatment used, and at the same time recovery antioxidants from the side streams liquors. In addition, to provide a complete characterization of liquors composition recovered in each step, structural carbohydrates have been determined, as well as morphological and structural properties through SEM and FT-IR analysis, respectively.

Chapter IV

Acid treatment hydrolyses hemicellulose to monosaccharides; meanwhile, alkaline hydrolysis helps solubilize and extract lignin from the biomass by affecting acetyl group in hemicellulose and linkages of lignin-carbohydrate ester [95]. Consequentially, liquors recovered after H_2SO_4 (named liquors L1) and after NaOH (named liquors L2) treatment are rich in hemicellulose and lignin, respectively. This is confirmed by structural carbohydrate analysis, since they have a negligible content of cellulose (< 0.1 $g_{Glucan}/100\ g_{DM}$), and higher content of hemicellulose in all L1 liquors.

Regarding FT-IR analysis of freeze-dried liquors after dialysis, graphs in Figure IV.21a and Figure IV.21b presented typical hemicellulose and lignin bands, respectively. that correspond to their aromatic structure.
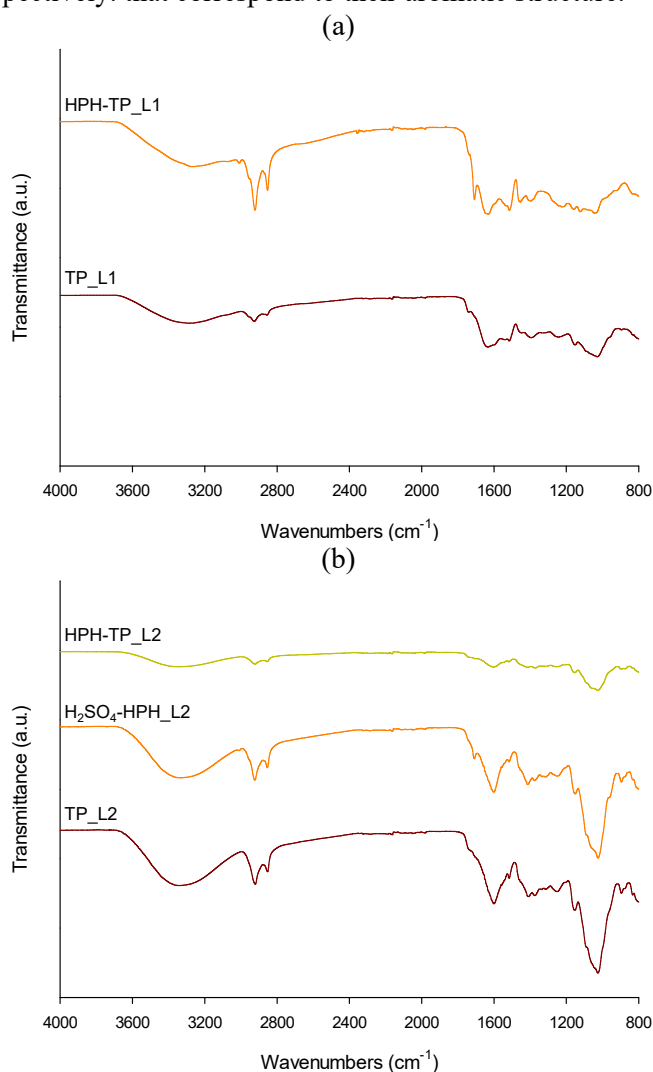
Figure IV.21 *FT-IR spectra of liquors after (a) acid hydrolysis and (b) alkaline hydrolysis.*

Within the range of 3300 to 2800 cm^{-1} and 1800 to 800 cm^{-1}, cellulose, hemicelluloses, and lignin have their own characteristic absorption peaks due to the hydroxy groups and many C-H bonds in their structures. According to the previous literature, the bands C=O stretching vibration in the O=C-OH group of the glucuronic acid unit at 1734 cm^{-1} corresponds to hemicelluloses [96] (Figure IV.21a), and the C-O stretching in the O=C-O group at 1268 cm^{-1}, belonged to hemicelluloses was derived from both hemicelluloses and lignin [97]. The band of the aromatic skeletal vibrations, together with the C=C stretch vibrations in lignin, were clearly identified at 1603 cm^{-1} (Figure IV.21b). Three other bands of lignin, i.e., the aromatic skeletal vibration (C=C-C) at 1509 cm^{-1} and C-H in-plane deformation with aromatic ring stretching at 1424 cm^{-1}, were also characteristic peaks of lignin [86]. The C-H bending in cellulose, hemicellulose, and lignin (aliphatic C-H stretching in methyl and phenolic alcohol) was observed at 1370 cm^{-1} [98]. Although several FT-IR bands of different components were overlapped, the spectra of lyophilized liquors still provide important clues, including hemicellulose and lignin composition of liquors after acid and alkaline hydrolysis, respectively, as well as other changes in peak intensity for chemical compounds for understanding the applied treatment processing.

The microstructures of solid residues after acid and alkaline hydrolysis were observed by SEM. As shown in Figure IV.22, the SEM images of TP_L1 exhibited an irregular shape with interconnected microspheres (Figure IV.22d) characteristic of hemicellulose particles [99]. HPH-TP_L1 presented a more homogeneous spherical structure (Figure IV.22h), with an average diameter at 1-2 μm. This homogeneous morphology could be attributed to the mechanical pre-treatment on tomato pomace which contributed to reduce hydroxyl groups (as previously found also for contact angle on cellulose pulp) and preventing the microparticles from aggregating.

TP_L1   HPH-TP_L1
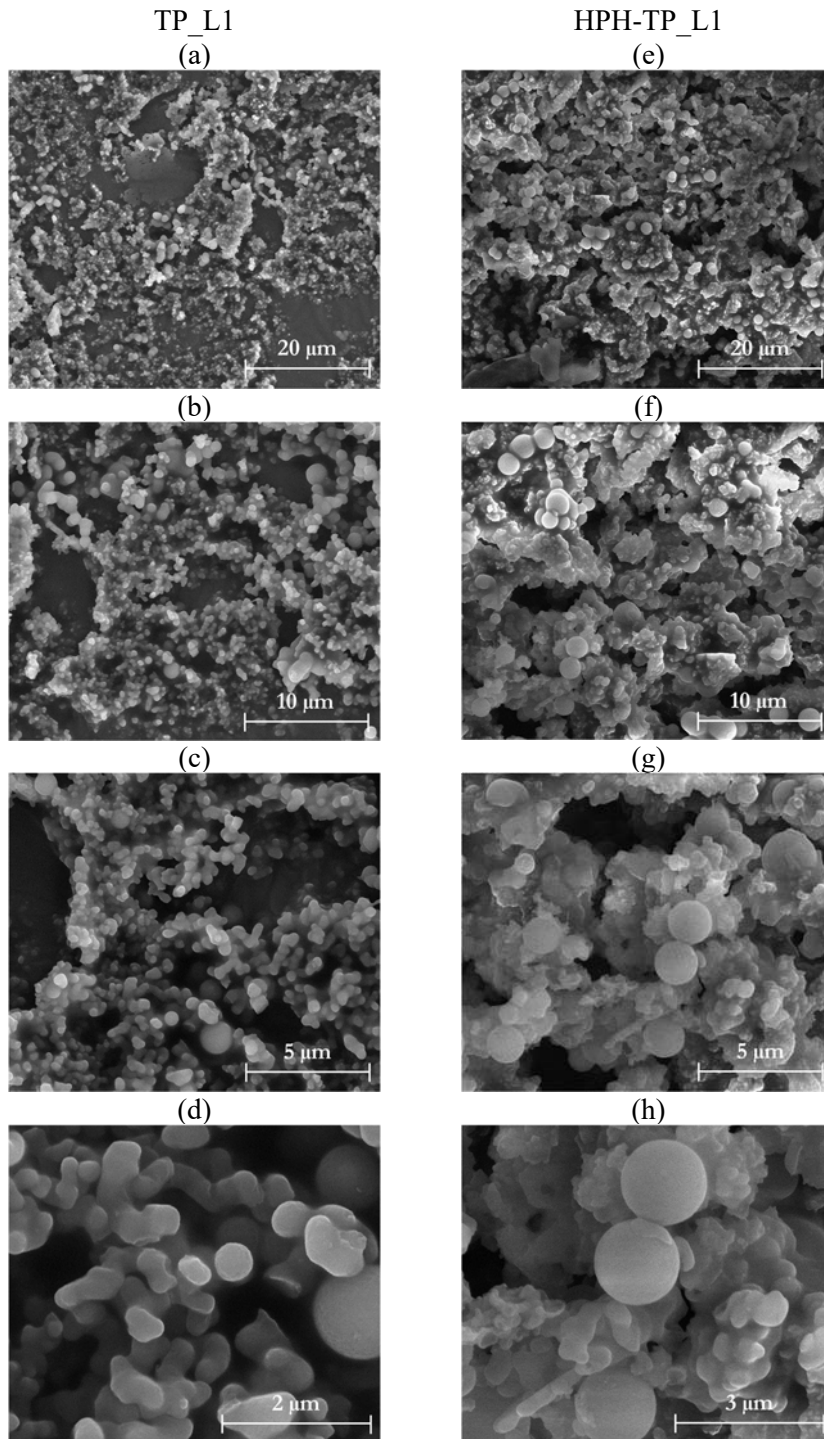
Figure IV.22 *SEM images of liquor after acid hydrolysis from (a-d) TP and (e-h) HPH-TP.*

The surface morphology of the freeze-dried liquors after alkaline hydrolysis is observed in SEM image in Figure IV.23.
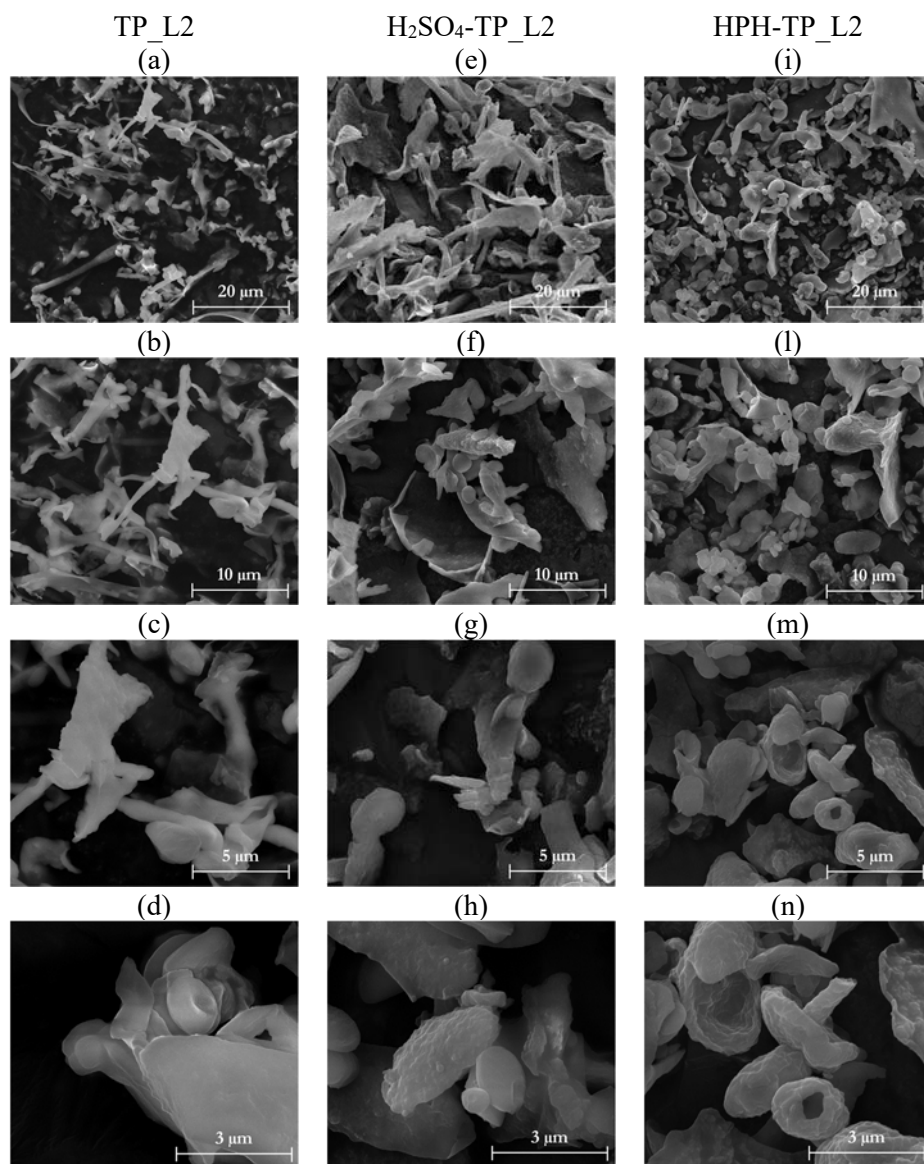
Figure IV.23 *SEM images of liquor after alkaline hydrolysis from (a-d) TP, (e-h) HPH-TP, and (i-n) H₂SO₄-HPH.*

We can see that particles show a typical morphology for lignin powders, with irregular semi-spherical shapes with different particle sizes. Comparing the surface morphology of TP_L2 with H₂SO₄-TP_L2 and HPPH-TP_L2, changes occurred due to the combination of chemical hydrolysis with

mechanical HPH treatment. TP_L2 appeared granulated with grains of compact structure and different sizes, while when HPH is applied at different levels of the cascade process particles have a rounded or shape with open volumes on the rough surface. Such a result indicates the application of fluido-mechanical stresses with HPH played an important role in the formation of lignin-based microsphere with modified surface (Figure IV.23d, h, n).

IV.2.3.3. Pulping process

After the exploitation of HPH treatment at different steps of acid-alkaline fractionation process to improve tomato pomace biomass delignification and at the same time recover high-added valuable compounds in side streams, a pulping process on barley straw (BS) lignocellulosic biomass has been established to carry out a complete cellulose recovery from agri-food waste in an environment-friendly manner (Figure IV.24). As expected from a lignocellulosic material, the main components of BS are the non-starch polysaccharides, with about 35% cellulose, 23% hemicellulose and 12% lignin, respectively. Such reduced percentage of lignin (less than or equal to 20%) makes easier its whole extraction from the fibers and gives the pulp relatively high values of specific volume, dimensional stability, and rigidity [100,101].

Figure IV.24 *Schematic representation of pulping process on barley straw.*

The chemical constituents of unbleached and bleached cellulose pulps are shown in Table IV.8. After the pulping process, the BS-UB shows a 36% increase in the cellulosic fraction, and a slight decrease in hemicellulose, while the lignin content was constant with values close to 22%. To prevent future interfering effects of lignin on the fibrillation behavior [102], a bleaching treatment was carried out to completely remove it from the sample. The used bleaching process allowed to efficiently and selectively extract lignin with a yield of 91% and without the dissolution of hemicellulose, which acts as a physical barrier inhibiting the microfibrils aggregation during the homogenization process [103]. The accessory non-structural components of barley straw are hydrophilic and lipophilic extractives, which are extracted with hot water or organic solvents (such as ethanol), respectively [104], and ashes. After the pulping process, the extractable and ashes were reduced. In particular, for bleached barley straw pulp, it is worth noting that the ash content is lower than 1% and this makes them suitable as pulp supplement materials [105]. Regarding the cumulative yield, the pulping process applied allows to obtain a high yield extraction of cellulose higher than 75%; meanwhile, the bleaching process contributed to efficiently extract cellulose (yield > 95%), removing at the same time lignin and ashes and therefore improving the quality of extracted cellulose.

Table IV.8 *Chemical characterization for barley straw unbleached cellulose pulp (BS-UB) and barley straw bleached cellulose pulp (BS-B) and cellulose yield extraction.*

	Barley straw	
	BS-UB	*BS-B*
Ashes (%$_{DM}$)	1.41 ± 0.01	0.82 ± 0.01
Cellulose (%$_{DM}$)	47.41 ± 0.70	60.66 ± 0.48
Hemicellulose (%$_{DM}$)	21.48 ± 0.13	21.73 ± 0.16
Lignin (%$_{DM}$)	10.30 ± 0.70	1.09 ± 0.04
Cumulative yield (%$_{DM}$)	95.84 ± 3.67	77.02 ± 2.75

In addition to yield, FT-IR spectra of extracted celluloses (Figure IV.25) were also measured to evaluate the structural changes that occurred during the applied treatments [3] and investigate the effect of bleaching conditions on quality of the celluloses. All spectra showed some signature characteristic bands of celluloses, including absorption peaks at 3300 and 2902 cm^{-1} because the presence of H-bonded OH group stretching and C-H stretching vibration groups [83], respectively. In addition, the peak at 1028 cm^{-1} is attributed to the C-O-C pyranose ring stretching vibration [83,85] and 897 cm^{-1} at C-O-C stretching at the β-(1-4)glycosidic linkages between sugar units [86]. The next peak detected in the spectra of unbleached cellulose pulp is around 1500 cm^{-1} (C=C aromatic skeletal vibrations stretching of the benzene ring), corresponding to the aromatic ring of lignin [85]. The absence of this band from the spectrum of bleached cellulose pulp confirmed the efficient lignin removal during the bleaching process. Thus, the accessibility of functional

groups is facilitated, making the fibers more amenable to functionalization by chemical or physical pre-treatments and favoring their subsequent defibrillation.
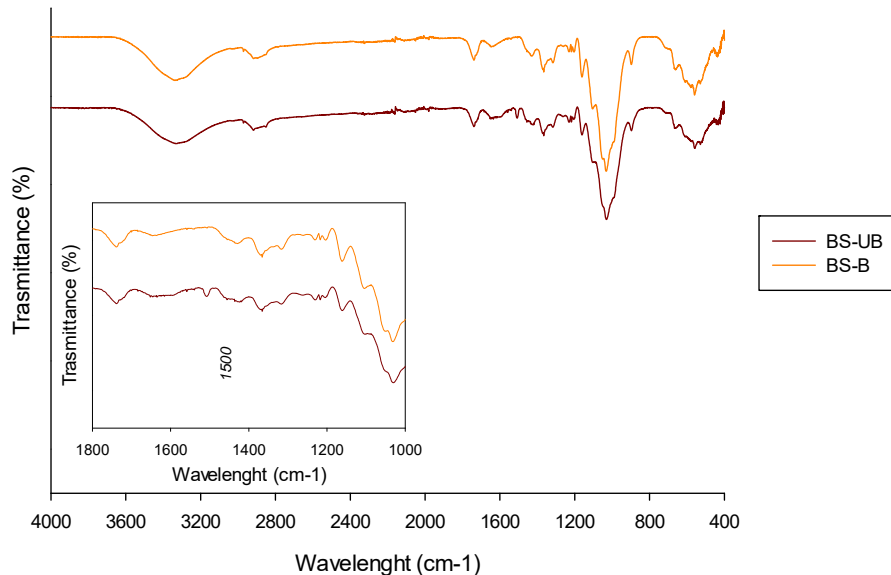
Figure IV.25 *FT-IR spectra of unbleached (BS-UB) and bleached (BS-B) cellulose pulps.*

The microstructures of (un)bleached cellulose pulp were observed by optical microscopy (Figure IV.26). As can be seen from the microphotography, BS-UB fibers (10.3% lignin) were straight and rod-like; meanwhile, BS-B fibers (1.1% lignin) were partially collapsed and showed comparatively more kinks and curved appearance due to the bleaching chemical treatment [106]. Moreover, BS-B individual structures show higher birefringence because of the large anisotropy of the polarizability derived from its anisotropic molecular structure and high polarity [107].
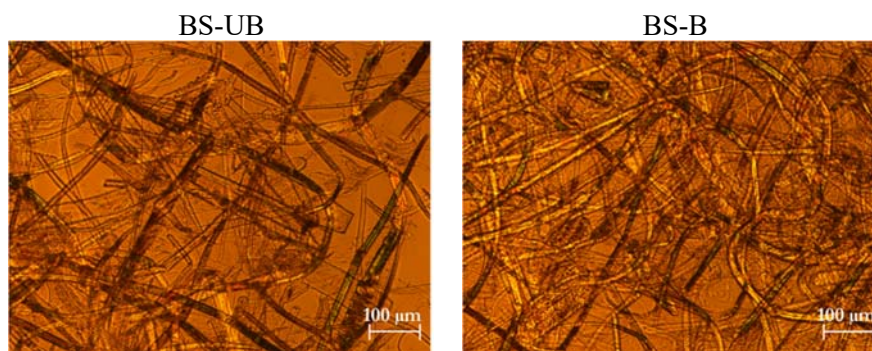
Figure IV.26 *Optical microscopy images at 10x magnification of unbleached and bleached cellulose pulps.*

184

From optical microscopy, birefringence provides information about the whole molecular structure of cellulose. Meredith (1946) highlighted that Young's modulus and strength of cellulose fibers are highly correlated with birefringence [108]. The mechanical properties of cellulose fibers, in turn, can be attributed to the formation of intra- and interfibrillar hydrogen and carbonyl bonds [109]. Mechanical properties and porosity of the derived papers using extracted (un)bleached cellulose pulps are reported in Table IV.9. Tensile strength of paper prepared with BS-UB increased up to 187% after the bleaching process.

It is important to highlight also the impact that porosity has on overall mechanical features. Porosity is a parameter that describes the empty spaces (filled with air) between the fibers. The reduction in porosity is an important feature because of its close relationship with mechanical properties: less-porous paper has been reported to improve mechanical properties of the paper owing to the increased hydrogen bonding [110]. The direct conclusion of this was that the increase in tensile strength and the decrease in porosity could be speculated to be a consequence of bleaching, which contributed to greater hydrogen bonding between fibers and to longitudinally oriented cellulose fiber structure [72].

Table IV.9 *Mechanical properties from the elongation analysis and porosity of papers obtained from BS (un)bleached cellulose pulp.*

| | Barley straw | |
	BS-UB	BS-B
Young's Modulus (GPa)	1.58 ± 0.52	2.55 ± 1.05
Tensile strength (MPa)	3.98 ± 0.91	11.44 ± 1.27
Load at break (N)	12.06 ± 1.87	25.85 ± 0.40
Strain at Break (%)	1.10 ± 0.20	1.72 ± 0.38
Porosity (%)	85.23 ± 2.96	79.49 ±1.29

IV.2.3.3. Bacterial fermentation

A static culture of SCOBY bacterial cellulose hydrogel was carried out by using HPH-micronized food wastes as carbon sources (Figure IV.27), to lower the cost of BC production and reduced environmental hazards [111].
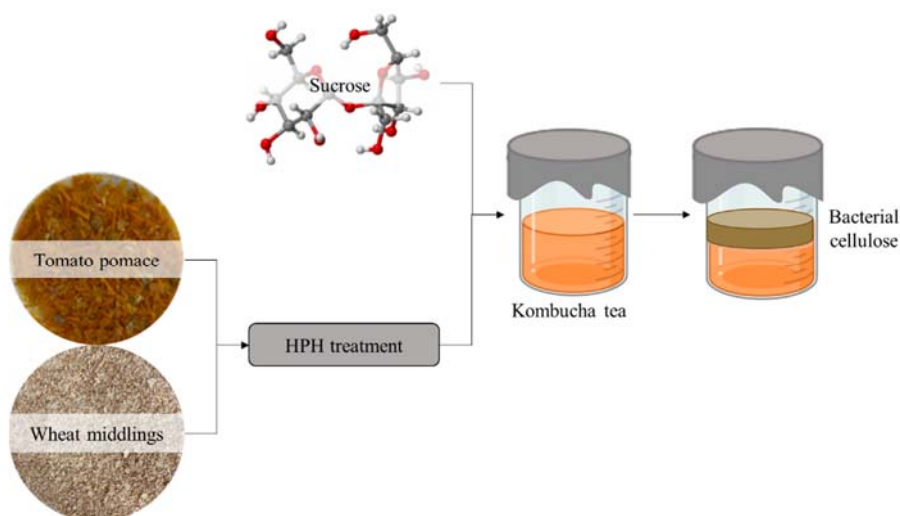
Figure IV.27 *Schematic representation of bacterial cellulose culture medium.*

When incubated under the specified conditions in tea broth, SCOBY produced a visible bacterial cellulose (BC) film suring incubation. When a fully-formed BC film was visible on the liquid-air surface, it was ready to be harvested. Overall, it was found that Kombucha consortium has been successfully cultivated on a tomato pomace and wheat middlings AFRs previously micronized by HPH (§ IV.1.3.3), proving its versatility in utilizing them as alternative carbon and nitrogen sources. Scoby films produced by Kombucha tea consortia in the various culture media showed a homogeneous, thick appearance with no cracks, flexibility, and a characteristic amber coloration (orange-brown color) of the fermentation culture (Figure IV.28). As can be seen, the BC pellicle produced in sucrose medium was much thicker than that in HPH-TP or HPH-WM. Furthermore, micronized AFRs are homogeneously integrated into the bacterial cellulose structure, locking the nutritive compounds and improving the biological properties of obtained cellulose. A higher intensity of red and brown color in films was observed for those obtained from Kombucha consortium cultivated on HPH-treated tomato pomace (Figure IV.28b) and wheat middlings, respectively. Therefore, the color change was significant for native films and perceptible to the human eye. Keeping integral materials without any purification stages is to preserve the bioactivity of incorporated high-valuable compounds, and more accessibility in the surrounding medium phase due to the micronization process applied directly in AFRs raw materials. Moreover, the color could protect food from light degradation contrary to colorless films.

(a) (b) (c)
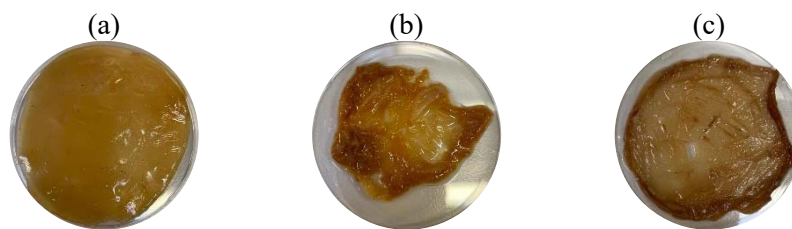
Figure IV.28 *Representative images of the microbial cellulose films from (a) Scoby, (b) Scoby + HPH-TP, and (c) Scoby + HPH-WM.*

In the present investigations, the usage of HPH-treated tomato pomace or wheat middlings (13 g/L) in Kombucha tea medium resulted in substantial productions of bacterial cellulose with relatively lower in comparison to that of in Kombucha medium containing sucrose as the carbon source (~ 6 g/L).

IV.2.4. Conclusions

Lignocellulosic biomass is a complex biopolymer that is primarily composed of cellulose, hemicellulose, and lignin. Multistep biorefinery processes are necessary to ensure the deconstruction of noncellulosic content in lignocellulosic biomass, while maintaining cellulose product for further hydrolysis into nanocellulose material. In this section, extensive research for AFRs biomass valorization has been carried out by experimenting numerous technological challenges based on the nature of the feedstock including mild chemical hydrolysis, acid-alkaline fractionation process in combination with mechanical treatments and pulping process to isolate cellulose and biological treatments. In this innovative field, alternatives to petroleum-based fuels and chemicals have been achieved, with sustainable biorefinery processes that include the principles of circular economy, and green chemistry strategies and ensure that the technology used is environmentally friendly and economically viable. The promising chemical (such as hydrophilicity, chirality, degradability, and broad chemical variability) and mechanical (non-toxic, biocompatible, renewable, and biodegradable) properties of cellulose have aroused increasing interest as building blocks for the development of new biomaterials, especially through advanced nanotechnology tools, enabled further promotion of its techno-functional attributes. Each cellulose isolation procedure has a distinct specificity for altering the chemical and physical structure of lignocellulosic materials. The advantages and disadvantages of these treatments are reported in Table IV.10, with the corresponding most promising application. This survey shows the effectiveness among these processes of HPH process as pre-treatment technique for cellulose recovery owing to its potential to simplify the disruption of lignocellulosic matrices. HPH enhances the accessibility of lignocellulosic biomass through fluido-mechanical stress (high shear, turbulence, and hydrodynamic cavitation) and cell wall disruption suitable for cellulose recovery.

Table IV.10 *Cellulose isolation from AFRs: advantages and application for each biorefinery process.*

AFRs raw materials	Treatment applied	Remarks	Applications
MILD CHEMICAL HYDROLYSIS			
Tomato pomace (TP)	Acid hydrolysis Alkaline hydrolysis Bleaching	Mild acid reaction conditions Removal of hemicellulose and lignin Higher reaction rates Cellulose swelling	Cellulosic fiber isolated from tomato pomace could be used to improve the strength of biopolymer in biodegradable food packaging.
HPH-ASSISTED CHEMICAL HYDROLYSIS			
Tomato pomace (TP)	HPH treatment Chemical hydrolysis Acid hydrolysis Alkaline hydrolysis Bleaching	Increase the accessibility and the yield extraction of cellulose High-defibrillated cellulose pulp Mild acid reaction conditions Removal of hemicellulose and lignin Production of side streams very rich in bioactive compounds with high antioxidant capacity	The synergistic effect of HPH treatment and acid-alkaline fractionation process resulted in fiber activation and high defibrillation of cellulose with improved the techno-functional properties, capable to act as stabilizers in Pickering emulsions for example. Moreover, within the cellulose isolation, this process allowed to recovery phenolic compounds in the side streams which could be an excellent enhancer in functionalized packaging materials.
PULPING PROCESS			
Barley straw (BS)	Chemical hydrolysis Alkaline hydrolysis Bleaching Sprout-Bauer refiner	Efficient removal of hemicellulose and lignin Higher pulp yields Simple and time-saving process	Cellulose is suitable to influence the mechanical properties of paper substrate.
BACTERIAL FERMENTATION			
Scoby Scoby HPH-TP Scoby HPH-WM	Fermentation process	Reduction of culture media costs High degree of cellulose polymerization Cellulose with tailor-made properties	Considering its properties, bacterial cellulose represents a promising alternative for the reinforcement of food edible coatings.

Section IV.3
Nanocellulose isolation

The development of process engineering approaches to integrate the production of high value-added biobased products, such as nanocellulose (NCs), is crucial to improve the financial performance and sustainability of AFRs biomass biorefineries. Here, the feasibility of applying chemical, mechanical, and a combination of treatments to obtain NCs was evaluated using cellulose pulp isolated from AFRs and commercial pure cellulose as a model feedstock. A systematic analysis of the structural properties of the nanomaterials obtained after each process revealed that different treatments allowed to extract cellulose nanoparticles with different morphological and physical properties. These findings demonstrated that NCs could be successfully extracted, in the form of nanofibrils (CNFs) and nanocrystals (CNCs), and their properties tuned according to the final application and starting raw material based on the selected sustainable integrated processes reported here, developing the biobased circular economy.

IV.3.1. Specific goal and work plan

In addition to increasing interest in cellulose material as a renewable raw material to replace fossil resources and its isolations process, cellulose nanoparticles (NCs) combine nanotechnology with sustainable and environmentally friendly processes, with excellent intrinsic properties, such as impressive physical properties, high mechanical strength, specific surface area, aspect ratio, crystallinity, and purity, low thermal expansion and density, renewability, biocompatibility, biodegradability, and transparency [112–115]. Owing to their hierarchical order in a supramolecular structure and

organization given by the hydrogen bond network between hydroxyl groups, nanoparticles can be efficiently isolated from cellulose [116]. In general, for obtaining cellulose nanocrystals (CNCs) an acid hydrolysis would be carried out, while the attainment of cellulose nanofibers (CNFs) is produced with mechanical treatments [117,118] (Figure IV.29). The size, shape, and characteristics of these materials depend mainly on the preparation techniques and starting source. CNCs are crystalline regions of macromolecules that are tightly entangled by hydrogen bonding interactions in cellulose; CNCs consist of cylindrical, elongated, less flexible, and rod-like nanoparticles with 4 - 70 nm in width, 100 - 6,000 nm in length, and 54 - 88% crystallinity index [119]. CNFs present an entangled network structure with flexible, longer and wide nanofibers (20 - 100 nm in width and >10,000 nm in length), and lower crystallinity with respect to CNCs [120].
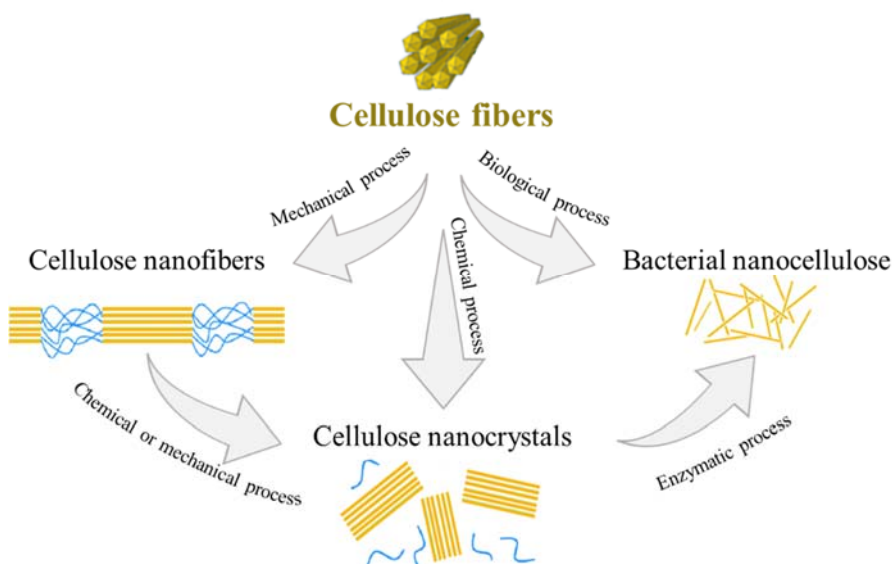
Figure IV.29 *Schematic representation of deconstructing strategy for NCs isolation from cellulose fibers.*

The high production cost of NCs is mainly attributed to cost of energy consumption and generated chemical waste post-treatment during the preparation process [121].

In this scenario, to address the issue of green and energy-saving process, and in the biorefinery context of low-cost and recyclable by-products, several approaches have been developed during the Ph.D. activities for the preparation of NCs from AFRs cellulose pulp according to the specific application and starting raw material. In this approach, the influence on NCs structural and physical characteristics resulting from (i) TEMPO-mediated oxidation; (ii) BM and HPH mechanical; and (iii) combination of chemical and mechanical treatments were investigated (Figure IV.30).

Bioactive compounds, cellulose, and nanocellulose extraction

The nanocellulosic materials were fully characterized by scanning electron microscopy (SEM), X-ray diffraction (XRD), Fourier transform infrared spectroscopy (FT-IR), zeta potential measurements, and interfacial tension analysis. The results demonstrated that the processes were effective in extracting NCs with tuning properties, offering a potential green and sustainable route that can be applied in future biorefineries.

IV.3.2. Short material and methods
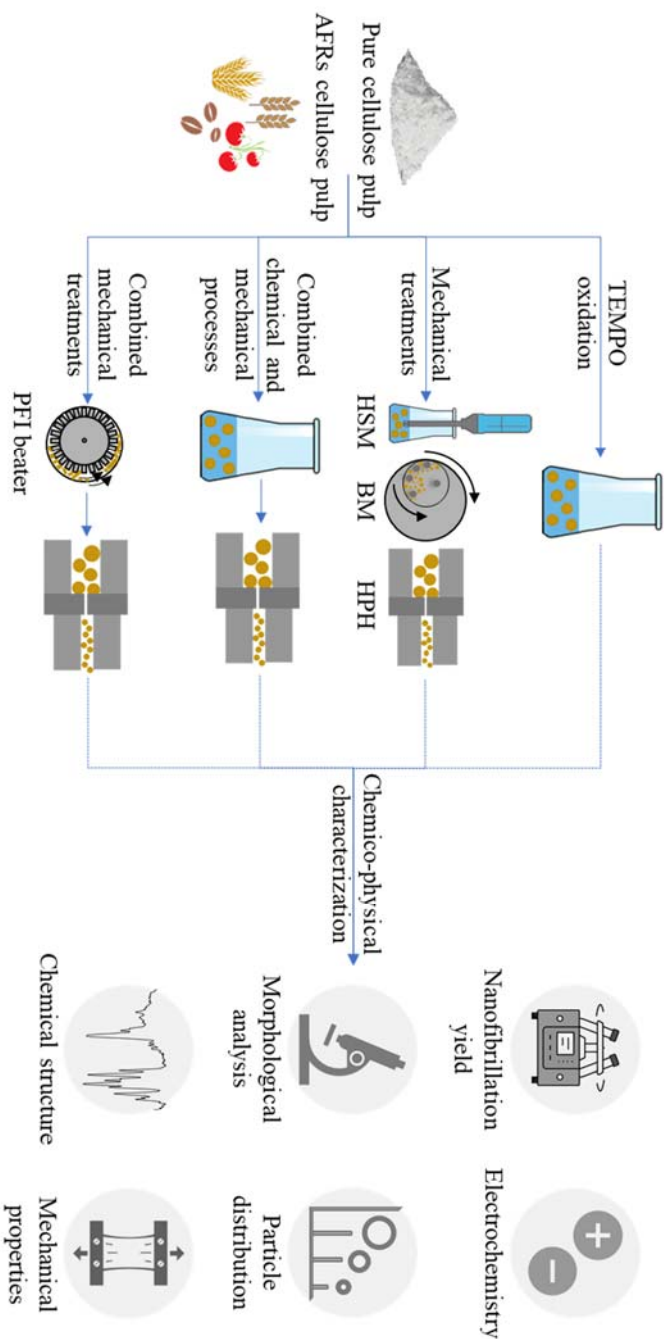
Figure IV.30 *Schematic representation of methodology used for NCs isolation from different (AFRs) cellulose pulp.*

IV.3.2.1. Nanocellulose isolation processes

The processes adopted to isolate NCs are summarized in Table IV.11. More in detail the treatments are (i) TEMPO-mediated oxidation (as described in detail in § III.5.1); (ii) mechanical treatments, i.e. HSM, BM or HPH (as described in detail in § III.5.2); (iii) the combination of TEMPO oxidation and HPH treatment (as described in detail in § III.5.3); and (iv) the combination of PFI beater and HPH treatment (as described in detail in § III.5.3).

Table IV.11 *Summary of treatments and operating conditions for NCs isolation.*

Cellulose pulp	Treatment applied	Conditions
CHEMICAL OXIDATION		
Northern bleached softwood kraft pulp Celeste 85	TEMPO-mediated oxidation	$C_9H_{19}N$ = 0.025 - 0.166% w/v NaBr = 0.001% w/v NaClO = 0.036% v/v/ pH = 10.5 - 11 t = 2 - 4 h
MECHANICAL TREATMENTS		
Commercial cellulose Arbocel® BWW40 fibers	BM	10:1 spheres/cellulose t = 30 - 60 min
	HPH	P = 80 MPa T = 25 °C # passes = 20
Tomato pomace cellulose pulp	HPH	P = 80 MPa T = 25 °C # passes = 20
Bacterial cellulose	HSM	v = 20,000 rpm t = 10 min
COMBINATION OF CHEMICAL AND MECHANICAL TREATMENTS		
Barley straw cellulose pulp	TEMPO-mediated oxidation	$C_9H_{19}N$ = 0.016% w/v NaBr = 0.1% w/v NaClO = 0.08% w/v/ pH = 10 t = 2
	HPH	P = 30, 60, 90 MPa T = 25 °C # passes = 10
COMBINATION OF MECHANICAL TREATMENTS		
Barley straw cellulose pulp	PFI beater	v = 20,000 rpm ºSR = 90
	HPH	P = 30, 60, 90 MPa T = 25 °C # passes = 10

IV.3.2.2. Nanocellulose characterization

The chemico-physical characterization aimed to highlight the effect of different processes on NCs properties, through investigating the morphology features (optical microscopy § III.7.4.2.1, SEM - § III.7.4.2.2, and AFM - § III.7.4.2.3), the chemical structure (FT-IR analysis - III.7.4.5 and cristallinity idex - III.7.4.6), electrochemistry characterization (carboxyl content - § III.7.4.3, cationic demand - § III.7.4.4, ζ-potential - § III.7.4.7, and interfacial tension - § III.7.4.11), particle dimensions (PSD - § III.7.4.8), rheological feature (intrinsic viscosity - § III.7.4.10), and mechanical properties (tensile strength and Young's modulus - § III.7.4.12), among others reported in detail in section § III.7.4.

IV.3.3. Results and discussion

IV.3.3.1. Chemical process on pure cellulose

In this work, two types of nanocellulosic materials, CNCs and CNFs, were obtained from the TEMPO-mediated oxidation of commercial cellulose raw material, by controlling the intensity of the process (changing catalyst concentration and processing time). The morphological, topological, and size features of CNCs and CNFs were evaluated through AFM. Representative images of the CNCs and CNFs are reported in Figure IV.31, with CNCs characterized by a needle-like structure, and CNFs by a fibrous network. The statistical analysis of the CNCs' size, performed on a data set of 900 CNCs individually resolved in the AFM images, indicated a length of 170 ± 90 nm and a width of 3.0 ± 0.5 nm. A rigorous statistical analysis of CNFs size was not possible, because of the entanglement propensity of the flexible and disordered regions still present in the fibers, which are clearly visible in the AFM images. However, an average fiber width of the order of 10 nm and a length of a few micrometers can be estimated.
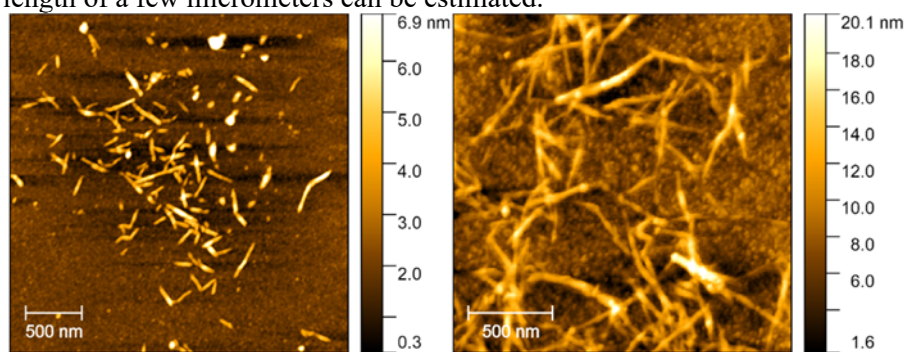
Figure IV.31 *AFM images of CNCs (left panel) and CNFs (right panel).*

FT-IR spectroscopy was used to analyze the functional groups of the NC samples. The representative spectra of CNCs (black trace) and CNFs (red trace) reported in Figure IV.32 show the typical features of cellulose nanostructures. In particular, the C-H rocking at 910 cm^{-1}, the C-O bond vibrations in the range 1030 - 1100 cm^{-1}, the antisymmetric stretching vibration of the C-O-C glycosidic bond at 1160 cm^{-1}, the stretching vibration of the C-H bond at 2900 cm^{-1} and a large band ascribable to the stretching vibrations of the O-H bonds of the primary and secondary hydroxyl groups in the range 3200 - 3500 cm^{-1} can be observed [122]. The strong peak at 1620 cm^{-1} can be assigned to the carboxylates introduced by the TEMPO-mediated oxidation. The different extent of oxidation of CNCs and CNFs appears evident when comparing the carboxylate peak intensities of the traces of Figure IV.32 normalized to the peak at 2900 cm^{-1}, which should be unaffected by the TEMPO-mediated reaction. The normalized spectra show larger oxidation of the CNCs with respect to CNFs, according to the milder oxidation conditions used to obtain the larger size and preserve some amorphous regions of CNFs.
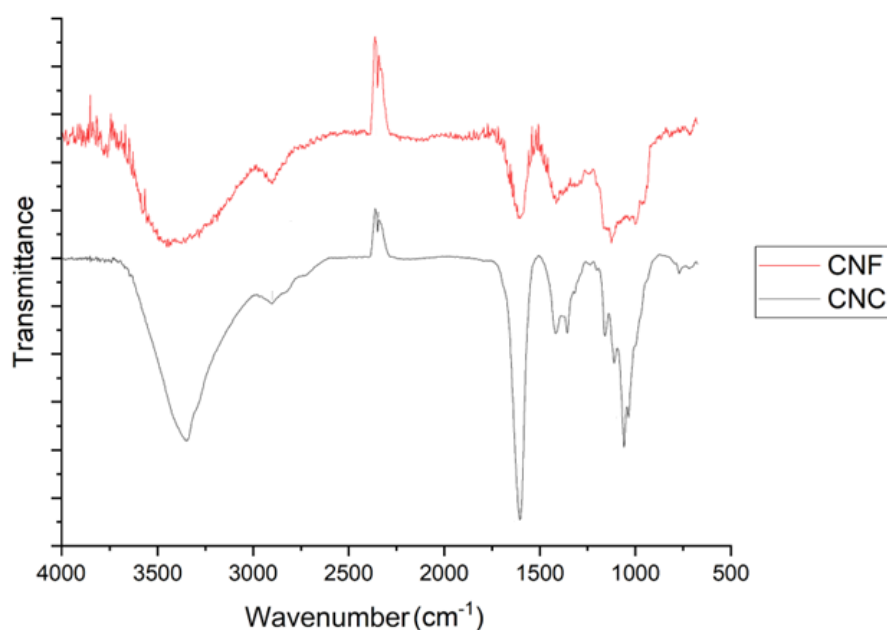
Figure IV.32 *FT-IR spectra of CNCs and CNFs isolated from commercial cellulose with TEMPO-mediated oxidation treatment.*

The FT-IR data were confirmed by the conductometric titrations which provided degree of oxidation values (Equation III.7) of 0.6 ± 0.2 µmol/mg and 1.4 ± 0.1 µmol/mg, of CNFs and CNCs, respectively.

Chapter IV

Figure IV.33 shows the dynamic adsorption behavior of CNCs and CNFs at the water-oil interface, investigated by monitoring the change of the interfacial tension (γ) with adsorption time (0 - 2,500 s) at 25 °C. The addition of both CNCs and CNFs to deionized water caused a significant reduction in the interfacial tension of the oil-water interface. More specifically, a higher reduction was observed for CNFs than for CNCs. The interfacial tension of water rapidly decreased during the initial 500 s, because of the adsorption of the more hydrophilic oil components, before gradually reaching equilibrium. The interfacial tension of CNCs and CNFs decreased over time, tending towards equilibrium values (γ_∞), which were estimated using an exponential decay model (Equation III.12) at 16.7 and 13.8 mN/m, respectively. The γ_∞ value for CNCs' was slightly lower than the one estimated for pure water (19.2 mN/m), indicating the reduced ability of the CNCs particles to act onto the oil-water interface. In contrast, CNFs particles are effectively adsorbed at the O/W interface, reducing its free energy, suggesting that, according to interfacial tension measurements, CNFs particles have the potential to be more effective in stabilizing O/W Pickering emulsions.
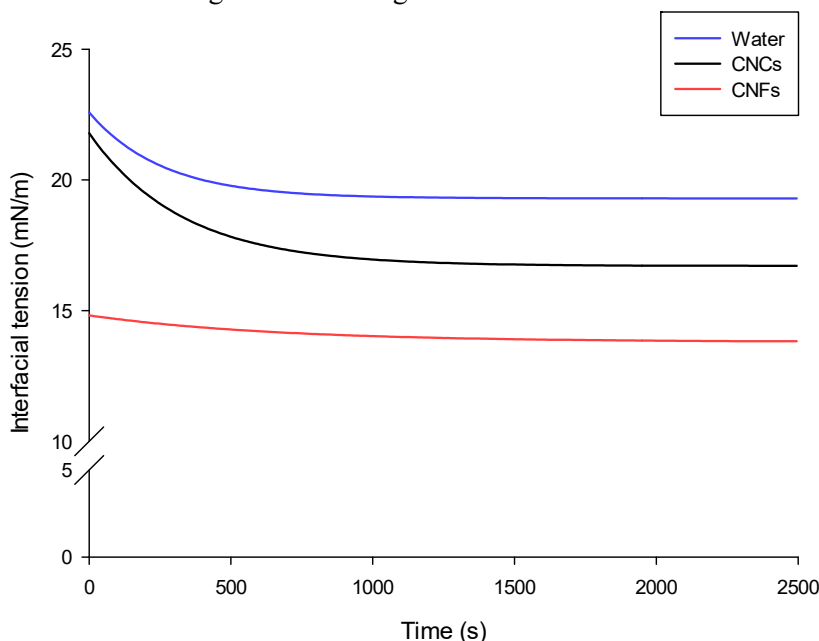
Figure IV.33 *Peanut oil-water interfacial tension for pure water, CNCs and CNFs aqueous suspensions at 0.5 wt%.*

The ζ-potential of the CNCs and CNFs was also measured, to obtain indications about the colloidal stability of the different cellulose suspensions. Generally, a stable particle suspension should be characterized by ζ-potential values greater than 30 mV of absolute value, to promote sufficient interparticle electrostatic repulsion forces for their stabilization [123].

196

Both CNCs and CNFs suspensions, whose visual appearance is shown in Figure IV.34, are characterized by high ζ-potential values, of -37.0 ± 2.35 mV at a natural pH $= 6.4 \pm 0.2$ and -52.97 ± 4.55 mV at a natural pH $= 6.8 \pm 0.4$ for CNCs and CNFs, respectively. These high ζ-potential values support the hypothesis that both suspensions might exhibit good colloidal stability. CNFs exhibited a higher absolute ζ-potential value than CNCs. It must be highlighted that, based on FT-IR results, which show a higher presence of carboxylate groups for CNCs particles, it would be expected an opposite effect on ζ-potential values of CNCs and CNFs, with higher absolute values for the formers. Further studies are needed to better elucidate the reasons that might the influence electro-kinetic phenomena of NCs, such as pKa of the carboxylate groups, counter ions effects, etc…
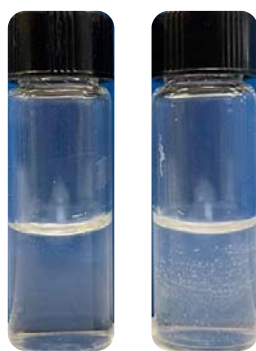
Figure IV.34 *Suspensions of CNCs (on the left) and CNFs (on the right).*

Finally, Figure IV.35 shows the size distribution, an extensively used method for determining the particle size distribution in colloidal suspensions. The average size of CNCs in suspension is about 300 nm, and the average particle size of CNFs is 700 nm. There are clearly differences in the size for NCs type; nevertheless, the compositions of all samples have a multi-modal particle size, which provides a no uniformity distribution with three populations. In the case of CNCs a first population is observed around 20 - 100 nm, another one at 200 - 1,700 nm and the last one at 2,500 - 7,000 nm. Meanwhile, CNFs present the populations at 10 - 80 nm, 150 - 700 nm and 4,000 - 7,000 nm. The first peaks could be attributed to individual cellulose nanofibers, whereas the others could be related to the orientation of fibers in the fluid during the analysis [124] as well as to cellulose nanoparticle aggregates [125].
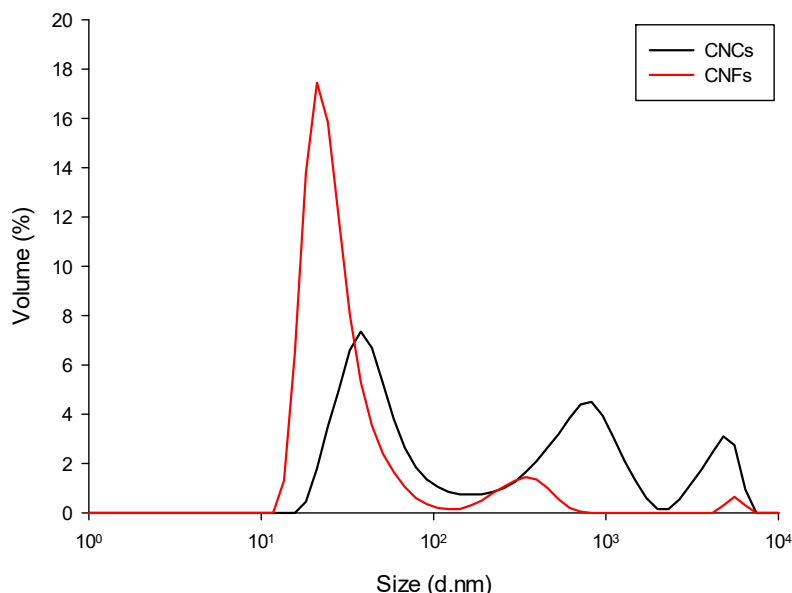
Figure IV.35 *Size distribution of CNCs and CNFs aqueous suspensions at 0.5 wt%.*

It can be concluded that the CNCs and CNFs are characterized by similar chemical composition, except for different content of carboxylate groups. In contrast, the particle dimension and morphology are clearly different: CNCs are needle-shaped, while CNFs are elongated, and partly disordered fibers, with a nanosized, roughly spherical cross-section.

IV.3.3.2. Mechanical treatments on pure cellulose

The morphological and structural parameters of NCs structures obtained from commercial cellulose via mechanical treatments (called BM30-CNFs, BM30-CNFs, and HPH-CNFs for BM at 30 min, BM at 60 min and HPH treatment, respectively) were investigated through optical microscopy (Figure IV.36) and SEM analysis (Figure IV.37).

Native cellulose (Figure IV.36a) exhibited a fibrous structure and the typical birefringence under polarized light. The mechanical processes caused irreversible alterations in the cellulosic fibers, increasing their bonding potentials. BM-CNFs (at 30 and 60 min) significantly differed in fiber length from native. BM treatments, due to the efficient disintegration of long cellulose chains, facilitated the production of nanoparticles characterized by a relatively constant cross-section and high birefringence properties (Figure IV.36b-c). In contrast, HPH-CNFs (Figure IV.36) exhibited a less ordered and uniform structure. The micrometric cellulose particles which can be observed after mechanical treatments can be attributed to the residual aggregated fibril bundles after partially removing the cellulose amorphous region [126]. These

198

bundles are characterized by a large variation in cross-section (irregular widths), and typical lengths in the range of $\sim$10 - 100 μm. The observation that the birefringence property observed under polarized light did not significantly change with the HPH treatments suggests that mechanical processes are likely to cause the structural disruption of cellulose fibers, without affecting the crystalline organization of the treated cellulose fibers.
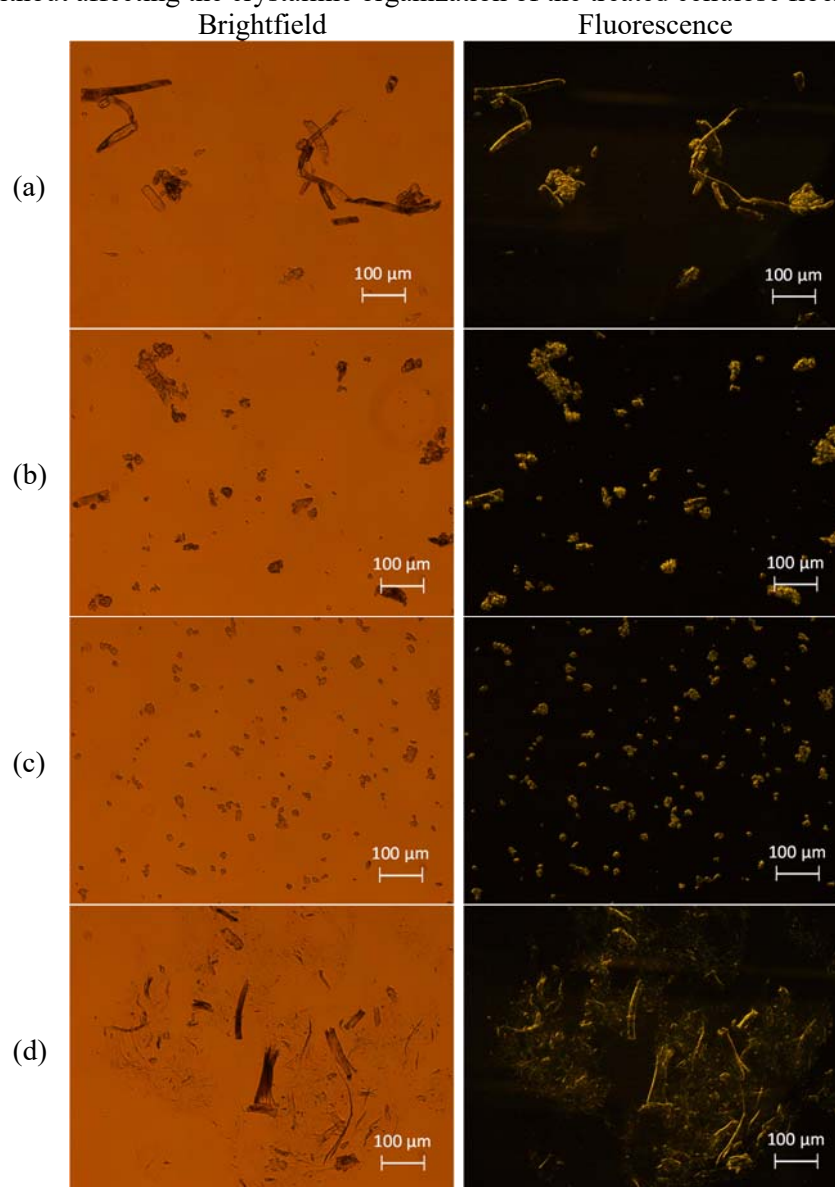
Figure IV.36 *Brightfield (left column) and fluorescence (right column) micrographs of (a) untreated cellulose, (b) BM30-CNFs, (c) BM60-CNFs, and (d) HPH-CNFs.*

SEM analysis confirmed the effect of the processes on the morphology of the samples. Indeed, SEM images reported in Figure IV.37a-b revealed the fibrous structure of untreated cellulose, with an approximate diameter of about 20 µm and an approximate length of 200 µm. The BM process induced a progressive disruption of the cellulose fibrous structure, with the formation of well-separated cellulose particles with an irregular shape and a lateral size is in the range of 10 - 50 µm, slightly lower in the case of cellulose treated for 60 min (Figure IV.37c-e). At higher magnifications (Figures IV.37d-f), the BM cellulose showed a compact morphology that did not evidence the presence of typical cellulose fibrils. In stark contrast, for the HPH-CNFs the original structure of the cellulose fibers is still evident in Figure IV.37g. Nevertheless, the HPH processes of cellulose aqueous suspensions induced the obtainment of a cellulose-based material that, after air drying at room temperature, produced the formation of a compact film (Figures IV.37g-h). The good film-forming ability can be ascribed to the pronounced defibrillation of the original structures, clearly evidenced in Figures IV.37h and the establishment of strong interactions between the nanosized cellulose fibrils during the drying process.

(a)

(b)

100 µm

5 µm

(c)

(d)

10 µm

3 µm
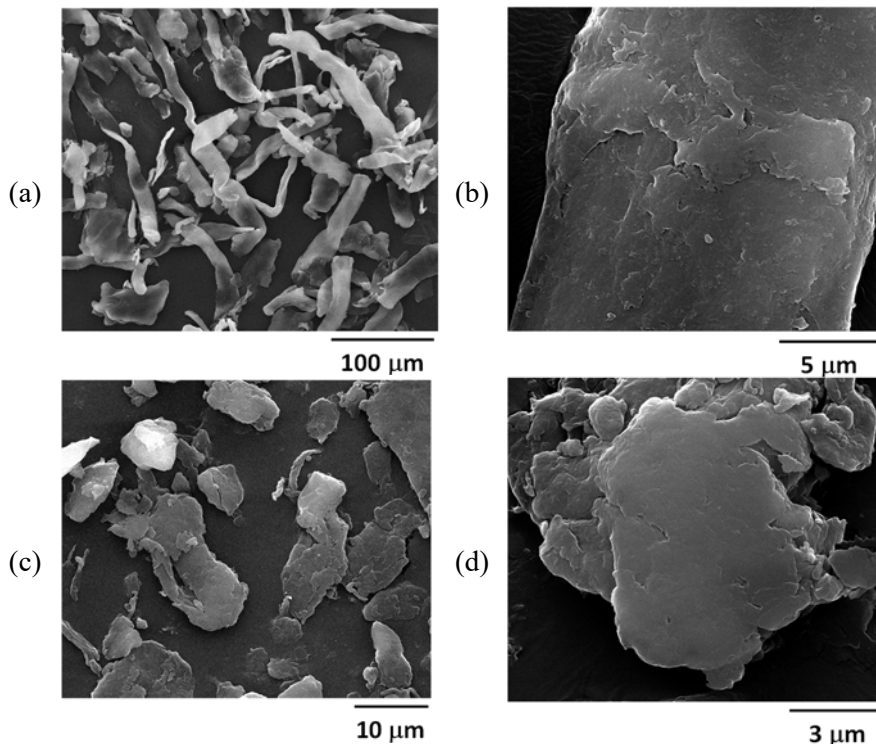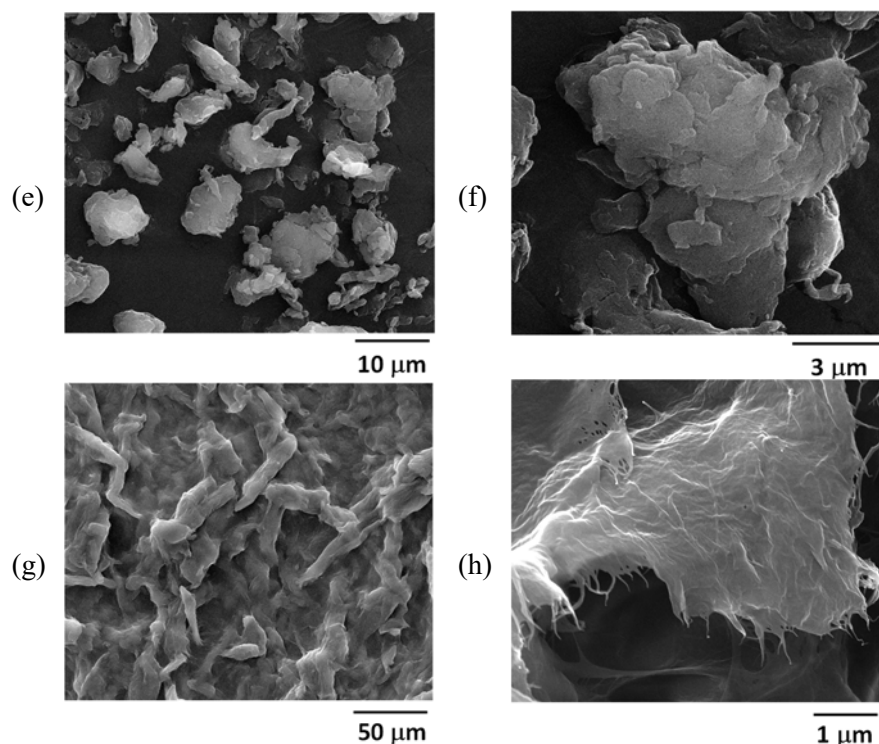
Figure IV.37 *SEM images of (a, b) untreated cellulose, (c, d) BM30-CNFs, (e, f) BM60-CNFs, and (g, h) HPH-CNFs.*

The effect of the suspended particles, processed with different mechanical treatments, on the interfacial tension at the O/W interface, is a predictor for a possible application of nanoparticles in the formation and stabilization of Pickering emulsion, as well as its mean droplet size [127]. In general, the higher the interfacial tension, the more resistant the whole system is to deformation and the more likely phase separation between the two liquids occur. The interfacial tension of pure water in oil, which was used as a control experiment, decreased from an initial value of $\gamma_0 = 15.2$ mN/m tending to an asymptotic value $\gamma_\infty = 5.7$ mN/m (Table IV.12), following an exponential decay trend (Equation III.12). Remarkably, the interfacial tension values of the particle suspensions in the oil phase were significantly affected by the nature of the dispersed particles. BM nanocellulose showed lower values of asymptotic interfacial tension ($\gamma_\infty = 5.0$ and 5.9 mN/m, respectively for BM30-CNFs and BM60-CNFs) than untreated cellulose ($\gamma_\infty = 6.2$ mN/m), but higher values than HPH-CNFs ($\gamma_\infty = 3.6$ mN/m). It is possible that, in the case of ball-milled cellulose, which exhibited a uniform particle size distribution and the smallest mean diameters, interfacial deformability is hindered by the resulting hard particles [128]. This hypothesis is in accordance with the observation that both initial and asymptotic interfacial tensions of BM30-CNFs were lower than for BM60-CNFs suspension.

Chapter IV

The significantly lower initial and asymptotic interfacial tension values measured for HPH-CNFs than control pure water in oil, untreated cellulose, as well as the BM-CNFs suspensions, could be likely ascribed to the morphology changes induced by HPH, promoting defibrillation but less efficient fiber breakage than BM. Especially when considering the characteristic times τ_r, which can be related to the molecular relaxation time, required for cellulose to adsorb and rearrange at the interface [129], is longer for HPH-CNFs, it can be hypothesized that more flexible fibers are generated by HPH, which are capable of adapting to the curved interfacial surface. Interestingly, no statistical difference can be observed between the τ_r values for BM30-CNFs and HPH-CNFs, while more intense BM processing (BM60-CNFs) causes a significant decrease in τ_r. This issue deserves, in future work, deeper investigation to relate the techno-functional properties of the obtained cellulose with its morphological features. As a final remark, it must be highlighted that the decrease in interfacial tension induced by the suspended cellulose particles was of a rather small entity in comparison with the interfacial tension values reached by highly surface-active molecules like surfactants and proteins [128,130].

Table IV.12 *Effect of different mechanical treatments on cellulose dispersed in water (0.5 wt%) on the oil-water interfacial tension dynamic parameters (γ_0, γ_∞, and τ_r) in comparison with pure water and untreated cellulose suspensions (0.5 wt%).*

	γ_0 (mN/m)	γ_∞ (mN/m)	τ_r (s)	R^2
Water	15.20 ± 0.47^d	5.71 ± 0.25^{cd}	44.13 ± 0.96^b	0.9966
Cellulose	14.95 ± 0.38^d	6.23 ± 0.67^d	37.14 ± 1.46^b	0.9948
BM30-CNFs	12.73 ± 0.18^c	4.98 ± 0.97^{bc}	63.29 ± 0.57^c	0.9976
BM60-CNFs	15.06 ± 0.71^d	5.93 ± 0.31^{cd}	26.97 ± 2.15^a	0.9926
HPH-CNFs	9.85 ± 0.17^a	3.62 ± 0.22^a	66.95 ± 3.67^c	0.9916

Different letters denote significant differences ($p < 0.05$) among the different samples within each column ($n = 5$).

Table IV.13 reports the particle size distribution of pure cellulose, BM30-CNFs, BM60-CNFs, and HPH-CNFs in terms of d(0.1), d(0.5), and d(0.9), as well as of D[4,3] and D[3,2]. Remarkably, the particle size of cellulose was significantly reduced after BM treatment (D[4,3] decreased by ~55%, D[3,2] of ~45-50%), but longer BM treatment times did not significantly change the size distribution. This is evident also when considering the diameters corresponding to the 10th, 50th, and 90th percentiles, with statistically significant differences ($p < 0.05$) observed only for d(0.9). The HPH treatment also caused a significant reduction of cellulose particle size (D[4,3] decreased by ~45%, D[3,2] of ~28%). Interestingly, the surface mean diameter D[3,2] decreased less than the volume mean diameter D[4,3] and was significantly higher than for BM samples, suggesting that less compact fibers, characterized by a higher surface area, are formed by HPH, in agreement with optical microscopy and SEM observations (Figures IV.36 and IV.37). Moreover, it

can also be observed that the HPH treatment is less efficient than BM, with generally higher values of the diameters corresponding to the 10th, 50th, and 90th percentiles. However, the size distribution data, with the help of the microscopic images (see Figures IV.36 and IV.37), suggest that HPH induced not only almost complete cell disruption but also cellulose defibrillation. Further studies are required to better clarify the aspects related to processing unrefined biomass for cellulose defibrillation.

Table IV.13 *Effect of different mechanical treatments of cellulose dispersed in water on particle size distribution (expressed as characteristic diameters) in comparison with untreated cellulose suspensions.*

	Cellulose	BM30-CNFs	BM60-CNFs	HPH-CNFs
d(0.1) (μm)	14.20 ± 017^a	7.16 ± 0.14^c	6.89 ± 0.12^c	9.56 ± 0.11^b
d(0.5) (μm)	53.23 ± 2.24^a	31.69 ± 0.34^b	30.66 ± 0.32^{bc}	32.04 ± 0.12^b
d(0.9) (μm)	206.46 ± 13.96^a	88.82 ± 0.69^c	82.93 ± 0.59^d	108.73 ± 1.16^b
D[4,3] (μm)	100.43 ± 5.32^a	45.01 ± 0.65^c	44.99 ± 0.49^c	54.44 ± 0.43^b
D[3,2] (μm)	23.25 ± 0.29^a	12.79 ± 0.18^d	11.68 ± 0.17^d	16.85 ± 0.12^b

Different letters denote significant differences ($p < 0.05$) among the different samples within each row (n = 3).

IV.3.3.3. HPH mechanical treatment on tomato pomace cellulose

pulp

The impact of HPH treatment on deconstructing cellulose pulp isolated from tomato pomace with different cascade operations was assessed using electron microscopy (Figure IV.38). After homogenization, these relatively thick cellulose fibers were disrupted and thinner fibers. Nevertheless, the electron microscopy images indicated that the fibers in the cellulose samples were agglomerated, which was probably caused by strong hydrogen bonding between the cellulose fibers during the sample preparation process [46], i.e. the drying step necessary for that analysis. At higher magnitudes, SEM analysis indicated that mechanical treatments caused surface erosion ("fluffing") and defibrillation of the cellulose fibers. Some differences have been revealed among samples depending on the treatment used to isolate the cellulosic pulp. It was observed that for TP-CNFs the external part displayed a rigid, relatively rough, and still intact structure (Figure IV.38a). With HPH treatment after acid or alkaline hydrolysis, the vascular bundles and conduit structures were significantly fragmented (Figure IV.38b,c), indicating higher cellulose accessibility. In particular, H_2SO_4-HPH_CNFs showed ultra-thin blade shape containing a few fibers. Meanwhile, the HPH-TP_CNFs had a circular shape, with some of the particles aggregated (Figure IV.38d), indicating that the micronization on both cellulose isolation process and the further nanoparticles deconstruction affects the morphology of NCs.

(a)

(b)

(c)

(d)
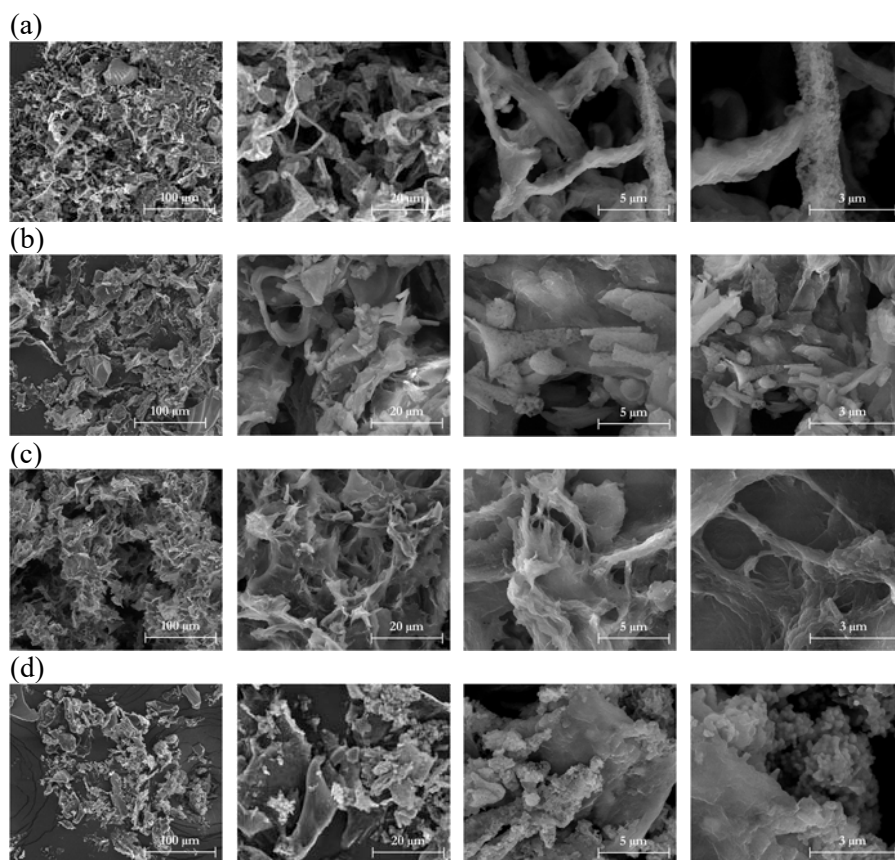
Figure IV.38 *SEM images at 1,000×, 5,000×, 20,000×, and 40,000× magnification (first, second, third, and fourth column, respectively) of (a) TP-CNFs, (b) NaOH-HPH_CNFs, (c) H₂SO₄-HPH_CNFs, and (d) HPH-TP_CNFs.*

FT-IR was used to analyze the surface chemical groups of the CNFs (Figure IV.39). There was no visual difference in the response of FT-IR spectra to different CNFs samples. The characteristic peaks were almost the same in accordance with the finding that particle size and shape had an inadequate influence on the FT-IR absorption bands [131], and a weak absorption peak was identified at 1737 cm^{-1}, attributed to the stretching vibration of C=O group of carboxyl. The characteristic peaks of the cellulose molecule include the bending vibrations of -CH$_2$ and -OCH at 1426 cm^{-1}, the stretching vibration of C-O at 1161 cm^{-1}, and the bending vibration of the C$_1$-H at 897 cm^{-1}. These results indicate that mechanical treatment changes the microstructures of the cellulose fibers while retaining their chemical features; indeed, the spectra of both the cellulose and cellulose nanofibers showed similar peaks (Figure IV.16 and IV.32, respectively), which were not

destroyed by the intense disruptive forces (hydrodynamic cavitation, turbulence, and high shear) associated homogenization.
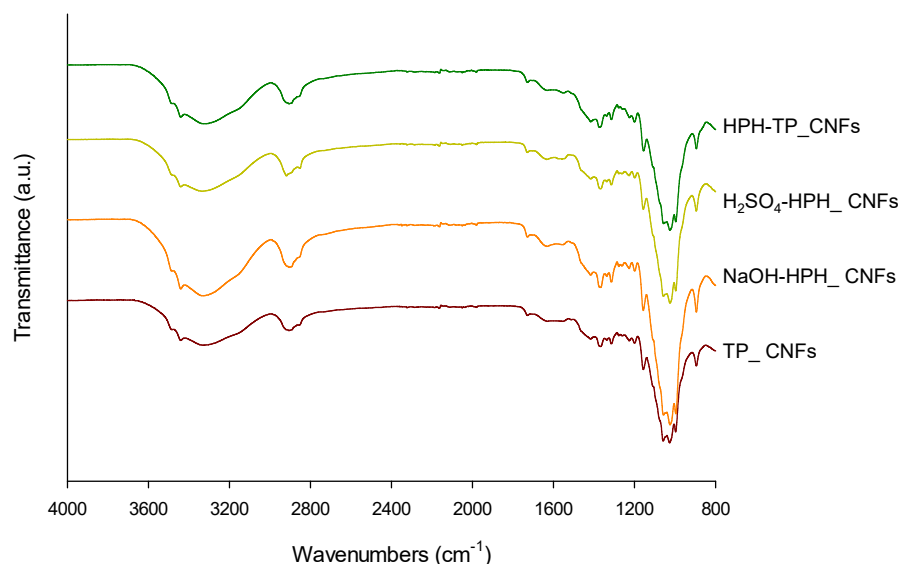
Figure IV.39 *FT-IR spectra of CNFs isolated from tomato pomace through the combination of HPH treatment and mild acid-alkaline hydrolysis.*

The dynamic adsorption behavior of CNFs at the water-oil interface was investigated by monitoring the change of the dynamic interfacial tension (γ) of NCs water suspensions (0.5 wt%) with adsorption time (0 - 1,000 s) (Figure IV.40). The initial interfacial tension value (γ_0) ranged between 13 and 16 mM/m and had a gradual decrease to an equilibrium value (γ_∞) between 10 and 12 mM/m over time (following the exponential decay trend described by Equation III.12 and fitting parameters reported in Table IV.14). The results indicated that all samples could rapidly absorb at the oil-water interface (about 333 s), causing the reduction of interfacial tension, and then gradually reached equilibrium. Nevertheless, the physical properties of the smaller particles (i.e. size, amorphous shape, surface roughness) can affect surface and interfacial activity [128]. As a consequence, the highest defibrillation and hydrophobicity of HPH-TP_CNFs contributed to their adsorption at oil-water interfaces [90], indicating that the rate of HPH-TP_CNFs particles adsorbed on the oil-water interface was increased [132]. However, this decrease in interfacial tension was rather small in comparison with the interfacial tension values of highly surface active molecules like surfactants and proteins [133]. Based on the interfacial tension data, it can be expected that HPH-TP_CNFs could be more suitable for the further stabilization of Pickering emulsions, of interest in the fields of biomedicine, food, and cosmetics [134] than the other NCs samples.
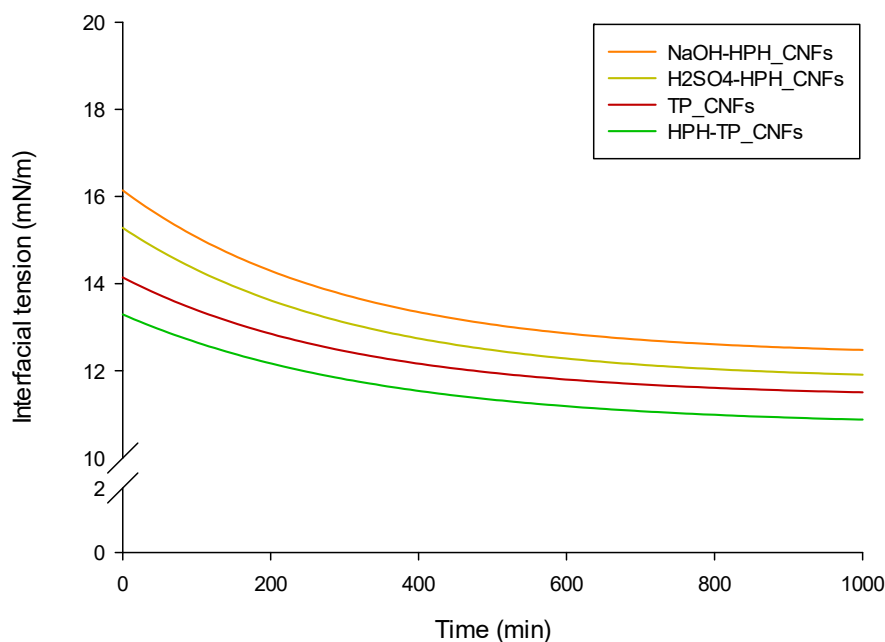
Figure IV.40 *Peanut oil-water interfacial tension for aqueous suspensions at 0.5 wt% CNFs from cellulose isolated through mild acid-alkaline fractionation process in combination with HPH treatment.*

Table IV.14 *Effect of HPH treatment on CNFs dispersed in water (0.5 wt%) on the oil-water interfacial tension dynamic parameters (γ_0, γ_∞, and τ_r).*

	γ_0 (mN/m)	γ_∞ (mN/m)	τ_r (s)	R^2
TP_CNFs	14.14 ± 0.44^b	11.39 ± 0.10^a	333.33 ± 1.02^a	0.9851
NaOH-HPH_CNFs	16.04 ± 0.62^a	12.34 ± 0.39^b	333.33 ± 0.98^a	0.9887
H$_2$SO$_4$-HPH_CNFs	15.28 ± 0.39^a	11.77 ± 0.11^a	333.33 ± 0.79^a	0.9836
HPH-TP_CNFs	13.30 ± 0.41^b	10.74 ± 0.27^a	333.33 ± 0.87^a	0.9813

Different letters denote significant differences (p < 0.05) among the different samples within each column (n = 5).

The particle size distribution of NCs in suspension is represented in Figure IV.41. From the DLS curve, it was noticed that all CNFs particles were accumulated in the range of 10 and 100 μm with a narrow and sharp peak at around 40 μm diameter, except for TP-CNFs which displayed the minimum and maximum particle sizes approximately of 56 and 595 μm, respectively. DLS analysis integrates any particle to spherical particles of equivalent volume; hence, CNFs measurement is expressed as a hydrodynamic apparent particle size without taking into account the morphology of the fibers. Besides particle size distribution, the formation of CNFs aggregates also causes the increase in particle dimension. Indeed, the obtained results are in agreement with the morphology analysis (Figures IV.37 and IV.38), which exhibited high particle agglomeration with a diameter range of 100 - 200 nm and several micrometers in length, therefore at least one dimension in the nano range.
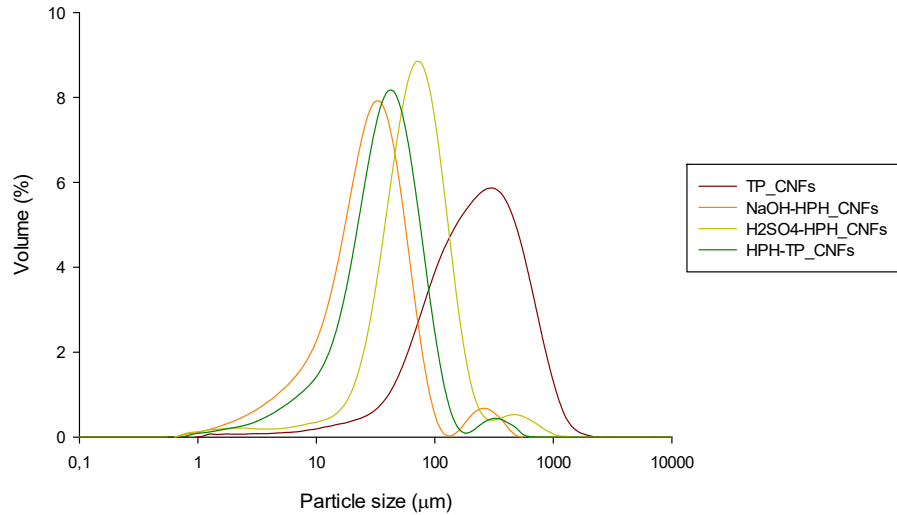
Figure IV.41 *Size distribution of aqueous suspensions at 0.5 wt% CNFs from cellulose isolated through mild acid-alkaline fractionation process in combination with HPH treatment.*

IV.3.3.4. HSM mechanical treatment on bacterial cellulose

Optical microscopy images in Figure IV.42 evidenced the size and aspect of bacterial microfibers (MBCs) obtained via HSM mechanical destructuration of Kombucha membranes. The micrographs clearly show the various morphological features of the cellulose sheets after the mechanical treatment, which can be gradually peeled off from the cellulose fibers.

Scoby	Scoby + HPH-TP	Scoby + HPH-WM
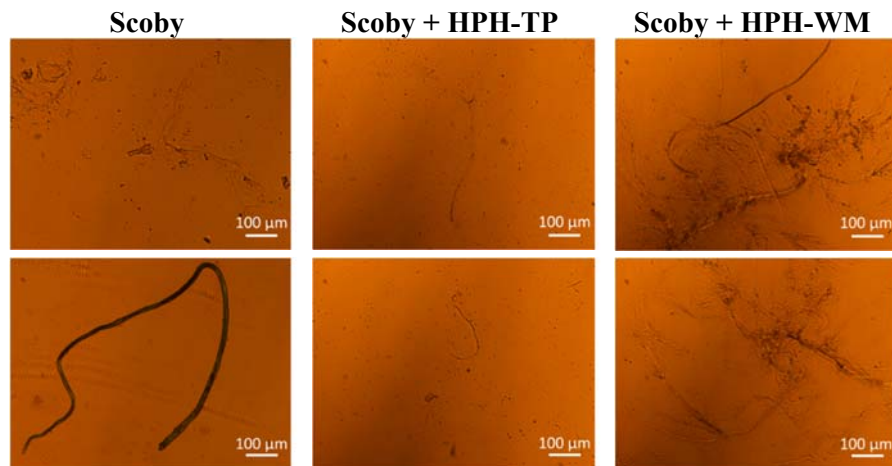
Figure IV.42 *Optical microscopy images of bacterial microfibrils isolated through HSM treatment.*

Chapter IV

FT-IR spectra of microfluidized samples of BC via HSM were taken in order to detect any peak shift that could be attributed to BC produced in Kombucha tea media with the addition of different micronized AFRs (Figure IV.43). The spectra are very similar to each other, independently of the added micronized AFRs in the culture media, indicating that the polymer had almost similar chemical structure. MBCs show absorption bands at 3400 - 3200 cm^{-1} attributed to a hydrogen-bonding region which contains signals from inter and intramolecular interactions of cellulose (OH-) and hydroxyl groups stretching vibrations due to water and carbohydrates [135–138]. Moreover, absorption bands at 2392 and 2369 cm^{-1} correspond to different stretching modes of C-H in methyl (CH$_3$) and methylene (CH$_2$) functional groups associated to cellulose [139]. In the range from 1800 to 1500 cm^{-1}, the band at 1650 cm^{-1} was assigned to the bending of O-H bonds in absorbed water molecules and also to polyphenols contribution [139,140]. Particularly, those antioxidant compounds that are present in tea extracts absorb at 1638 cm^{-1} and resulted in a marked signal, being more intense compared to the spectra of the other herbal extracts [141,142]. Therefore, the FT-IR results provide supportive evidence, as shown in Figure IV.42 (morphological properties), no structural changes in the polymer chains of BC occur among the change in culture media of bacterial polymers.
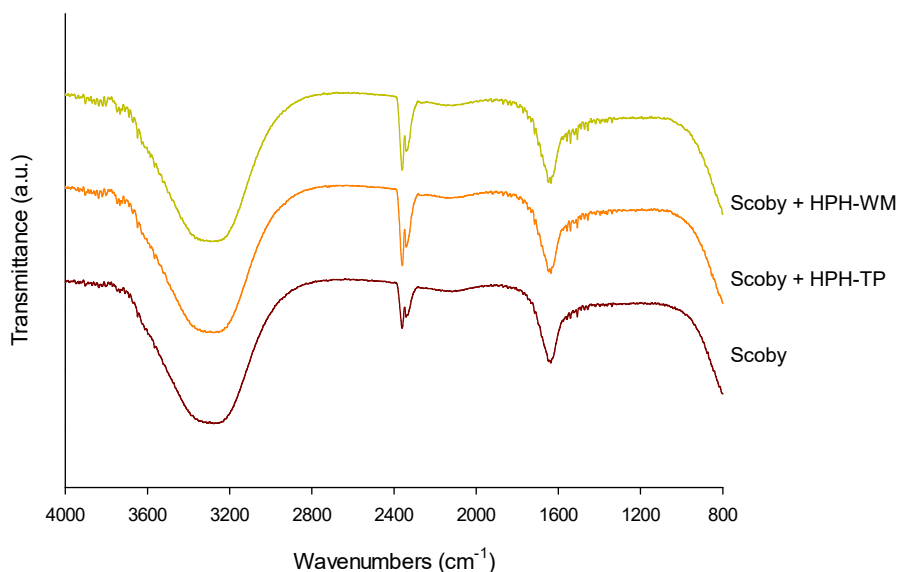
Figure IV.43 *FT-IR spectra of bacterial microfibrils isolated through HSM treatment.*

Also in the case of MBC with DLS might be considered an inappropriate analytical method to evaluate the dimensions of cellulose nano-/microfibrils, since they are not particles with a relative sphericity. Nevertheless, PDS analyzes could evidence a general trend of transition size distribution

(monomodal, bimodal, etc) after the mechanical disruption in microfibrils through HSM treatment as a function of added AFRs in culture media. This aspect can be seen in Figure IV.44 and Table IV.15, where the particle size distribution and characteristic diameters, respectively, of bacterial cellulose after HSM micronization were presented. If for the Scoby there can still be observed populations with average diameters of 306 μm, which is the length of microfibrils, for the Scoby with HPH-treated AFRs the decreasing trend of average diameters from 306 μm to 65 and 42 µm for HPH-TP and HPH-WM, respectively, are better evidenced since MBC forms microaggregates with a higher relative sphericity.
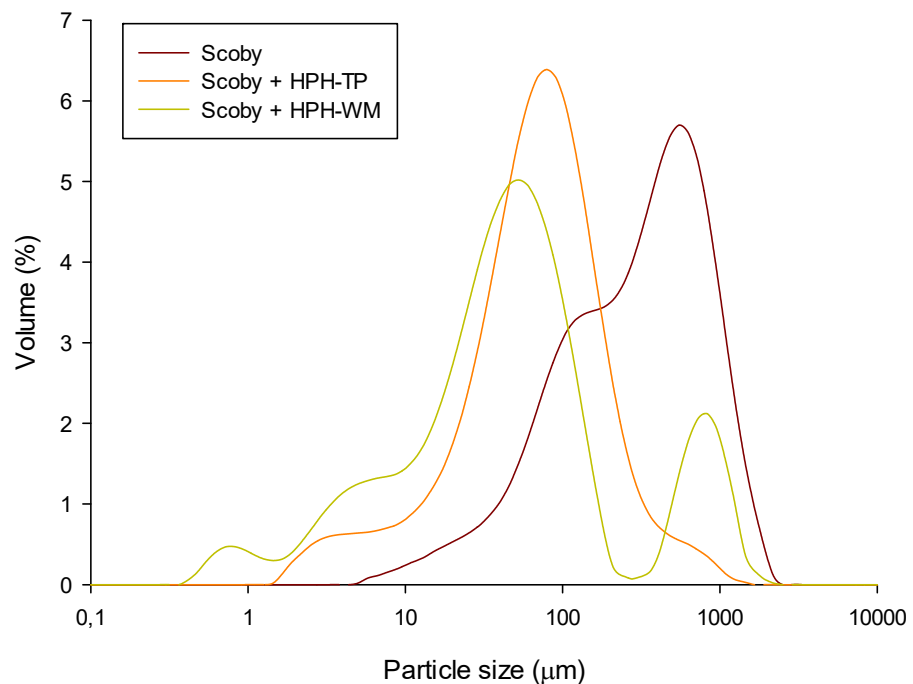
Figure IV.44 *Size distribution of aqueous suspensions at 0.5 wt% CNFs from cellulose isolated through mild acid-alkaline fractionation process in combination with HPH treatment.*

Table IV.15 *Effect of HSM mechanical treatments on bacterial cellulose dispersed in water on particle size distribution (expressed as characteristic diameters).*

	Scoby	**Scoby + HPH-TP**	**Scoby + HPH-WM**
d(0.1) (μm)	54.88	13.35	4.71
d(0.5) (μm)	306.38	64.99	42.42
d(0.9) (μm)	896.71	194.64	595.42
D[4,3] (μm)	402.63	97.79	145.43
D[3,2] (μm)	116.47	25.98	10.11

IV.3.3.6. Chemical and mechanical combined processes on barley

straw cellulose pulp

The characterization of the cellulose nanofibers isolated from unbleached cellulose pulp (designed as LCNFs) and bleached cellulose pulp (designed as CNFs) through TEMPO-mediated oxidation pre-treatment (designed as LCNF-TO and CNF-TO) or PFI beater mechanical pre-treatment (designed as LCNF-PFI and CNF-PFI) are summarized in Table IV.16.

The characteristics of the final CNFs are dependent on the pre-treatment used during their production. Notably, CNFs obtained from bleached cellulose pulp presented a higher nanofibrillation yield than those obtained from unbleached ones, due to the high lignin content still present in the pulp. This shows that the lignin content can have a greater influence on the nanofibrillation process. Moreover, also the applied pre-treatment is one of the most influential factors: in particular, a much higher nanofibrillation yield was obtained for CNFs obtained through TEMPO-mediated oxidation treatment. This was also observed for LCNFs with an increase in nanofibrillation yields for that isolated with TEMPO-mediated oxidation than that with PFI pre-treatment. The increased yield is due to the conversion of C6 primary hydroxyl groups into carboxylic groups without leaving residual aldehyde groups by the TEMPO-mediated oxidation [143,144]. The presence of such groups produces repulsion between fibers, facilitating the dismantling of the cellulose fiber structures by shearing forces [145].

Taking into consideration the carboxyl content, it was observed that the TEMPO-mediated oxidation of both BS-UB and BS-B cellulosic pulp produced chemical changes on the surface of the fibers, with a higher carboxyl content than the PFI pre-treated fibers. The significant increase in carboxyl content of about 280 and 500 μmol/g for LCNF-TO and CNF-TO, respectively, with respect to the (L)CNF-PFI causes an easier fibrillation of cellulose probably because (i) the carboxyl groups generate negative charges that bring forth repulsive forces between microfbrils [146] within the cell wall contributing to loosen the microfibrils cohesion held by hydrogen bonding; and (ii) the oxidation favors the hydration and the swelling of the fibers making them more flexible and the crystalline zone more accessible [147]. Less colloidal stability of the nanofibrillated suspension is the consequence of the protonation of the -COO$^-$ into -COOH, rendering not viable the repulsion among nanofibers to take place. Based on the above results, one can rule in a strong relation of carboxyl content to the nanofibrillation yield of the fiber, which is then reflected in the colloidal stability of the NCs suspension through electrostatic effects. A linear curve ($f(x) = y_0 + a \cdot x$) is capable of adequately describing the observed relation with the corresponding fitting parameters reported in Table IV.17.

Apart from the carboxyl content, also the cationic demand is strongly related to the nanofibrillation yield, as shown in Figure IV.45. The higher efficiency in the nanofibrillation process results in a larger exposed surface area and therefore higher surface charge of the cellulosic fibers. The determination of the cationic demand has been evaluated through cationization, by evaluating the surface adsorption mechanisms of polyDADMAC. In particular, two mechanism occur at the same time: (i) strong ionic interactions formed between the -CH_2-O- groups of cellulose fibers in alkaline medium and the quaternary ammonium groups of polyDADMAC [148]; and (ii) surface interactions due to London-Van Der Waals forces [100]. Defined the specific surface area of a single poly-DADMAC molecule, it would be then possible to theoretically calculate the specific surface area and then the theoretical diameter of NCs. On the other hand, a lower viscosity is observed for the CNF-TO, which sample showed the highest carboxyl content and yield of fibrillation. It is likely that the electrostatic repulsion resulting from the presence of a high level of ionized carboxyl groups on the surface of the nanofibers reduces the extent of the interaction among resulting in a lower viscosity of the suspension [147]. This effect accounts equally for the lowest turbidity and therefore the higher transparency of the CNF-TO.

A method for assessing the colloidal stability of dispersed nanoparticles is the measurement of zeta potential, a parameter associated with the electrokinetic properties of a particle in dispersion. The zeta potential was similar for both LCNFs (-19.13 ± 6.92 mV at pH 7.5 and -20.00 ± 0.75 at pH 6.5 for LCNF-TO and LCNF-PFI, respectively), which was significantly lower ($p < 0.05$) than that of the CNFs, which was -63.97 ± 4.41 mV and -25.77 ± 1.21 mV for CNF-TO and CNF-PFI, respectively. Considering that the effect of pH on zeta potential was negligible [149], pulp composition and pre-treatment affect the zeta potential the most (which are also the most significant parameters affecting the NCs length) which implies that the size is a dominant factor in predicting how NCs move in an electric field.

Table IV.16 *Cellulose nanofiber isolated from barley straw cellulose pulps characteristics.*

		LCNF-TO	CNF-TO	LCNF-PFI	CNF-PFI
Nanofibrillation yield	(%)	61.24 ± 1.00[c]	89.70 ± 0.87[d]	16.08 ± 0.35[a]	26.17 ± 0.45[b]
Cationic demand	(μeq/g)	624.80 ± 35.15[b]	732.40 ± 40.05[c]	292.96 ± 21.82[a]	333.49 ± 37.29[c]
Carboxyl content	(μmol/g)	431.11 ± 109.03[c]	653.06 ± 41.72[b]	153.32 ± 11.33[a]	157.55 ± 88.60[a]
Viscosity	(ml/g)	225.15 ± 23.20[a]	189.69 ± 28.71[a]	518.09 ± 14.36[b]	512.78 ± 23.21[b]
Polymerization degree	(-)	536.07 ± 55.23[a]	451.65 ± 68.36[a]	1233.56 ± 34.18[b]	1220.90 ± 55.26[b]
Turbidity	(NTU)	56.95 ± 2.47[b]	15.02 ± 3.44[a]	289.50 ± 9.19[d]	189.05 ± 10.39[c]
pH	(-)	7.56 ± 0.22[b]	7.16 ± 0.15[b]	6.48 ± 0.16[a]	6.27 ± 0.35[a]
ζ-potential	(mV)	-19.13 ± 6.92[b]	-63.97 ± 4.41[a]	-20.00 ± 0.75[b]	-25.77 ± 1.21[b]

Different letters denote significant differences ($p < 0.05$) among the different samples within each row (n = 3).
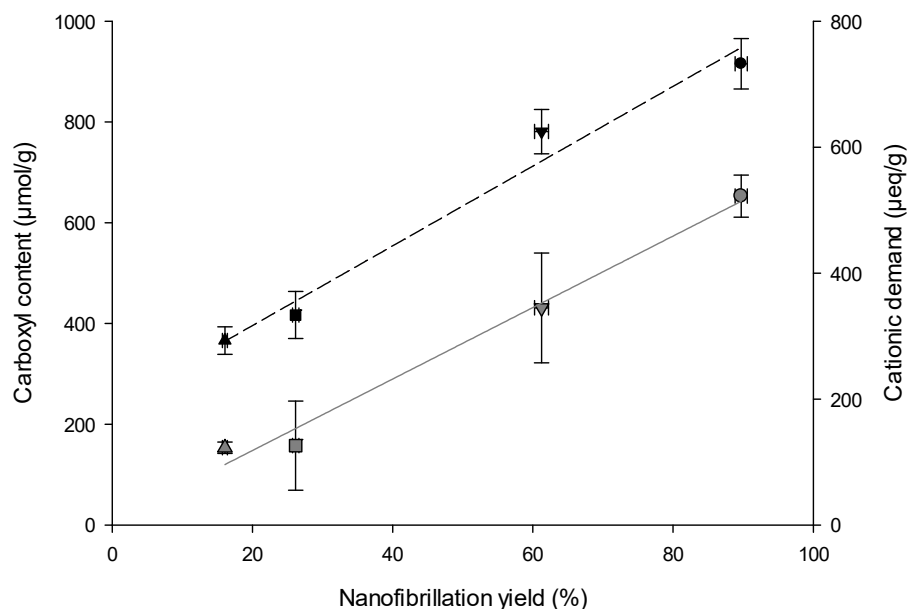
Figure IV.45 *Nanofibrillation yield of fibers according to the carboxyl content and cationc demand for (△) LCNF-TO, (□) CNF-TO, (▽) LCNF-PFI and (○) CNF-PFI. Gray dash line represents the fitting curve of carboxyl content, black solid line represents the fitting curve of cationic demand.*

Table IV.17 *Fitting parameters and coefficient of determination for the fitting of the data in Figure IV.45, using equation $f(x) = y_0 + a \cdot x$*

Parameters	Values	
	Carboxyl content	Cationic demand
y_0	6.038	190.023
a	7.096	6.333
R^2	0.986	0.976
Adj R^2	0.979	0.964

The quality of nanofibers, evaluated using different parameters through a unique quantitative grade index, calculated with Equation IV.3 as proposed by Desmaisons et al. (2017) [150], has been evaluated to (i) show the relationship between the characteristics of the final (L)CNFs and the pre-treatment used for their isolation; and (ii) to highlight the influence of their final properties on the efficiency in the removal of cationic contaminants.

$$QI = 0.30 \cdot x_1 - 0.03 \cdot x_2 - 0.071 \cdot x_3^2 + 2.54 \cdot x_3 - 5.35 \quad \text{(IV.3)}$$
$$\cdot \ln(x_4) + 59.9$$

where x_1 is the nanosize fraction (%), x_2 is the turbidity (NTU), x_3 is the Young's modulus (GPa), and x_4 is the macro-size (μm^2).

Figure IV.46a confirms that CNFs obtained from bleached cellulose pulp through TEMPO-mediated oxidation pre-treatment possess a better quality index than those produced from unbleached cellulose pulp with mechanical pre-treatment. In particular, CNF-TO presents a significantly higher QI than those produced with mechanical pre-treatment (69.0% and 68.3% for LCNF-PFI and CNF- PFI, respectively). TEMPO chemical pre-treatment eases the defibrillation process by creating repulsion between the fibers consequently weakening the structure allows to obtain the better-quality CNFs (72.6% and 85.6% for LCNF-TO and CNF-TO, respectively). Moreover, among TEMPO-mediated oxidation NCs, that one isolated from BS-B leads to increase in nanofibrillation and therefore the production of a higher CNF quality.

Furthermore, a clear correlation was found between quality index and nanofibrillation yield (Figure IV.46b). TEMPO chemical pre-treatment easing the defibrillation process by creating repulsion between the fibers consequently weakening the structure allows to obtain the better quality CNF. Moreover, among TEMPO-mediated oxidation NCs, the one isolated from unbleached cellulose pulp leads to increase in nanofibrillation and therefore the production of a higher CNF quality.

(a)

(b)

Parameters	Value
y_0	68.01
a	0.23
b	0.05
R^2	0.997
Adj R^2	0.992
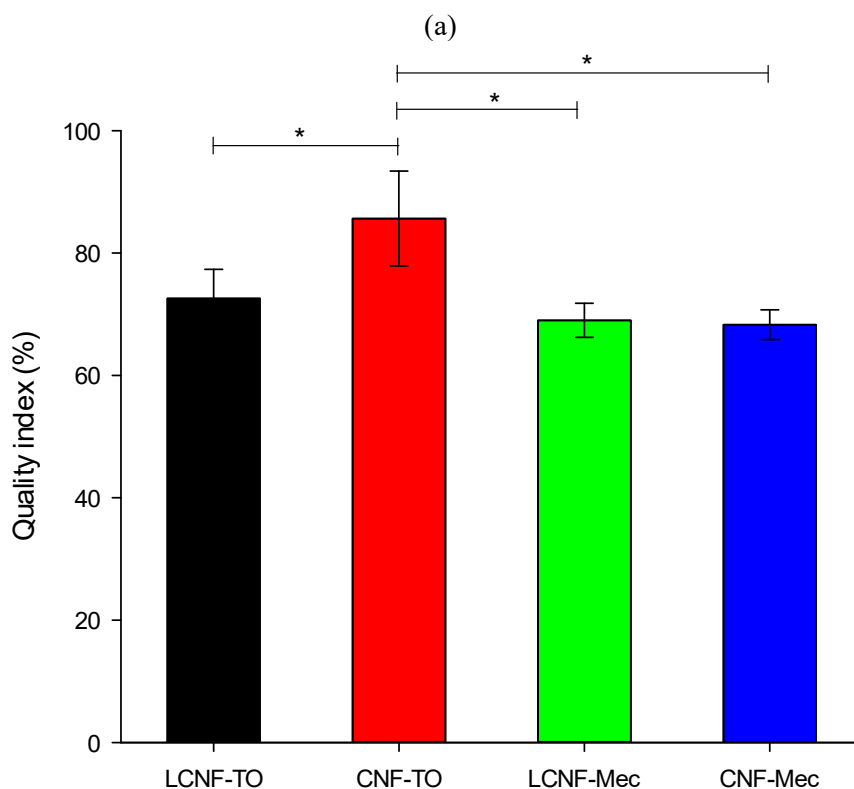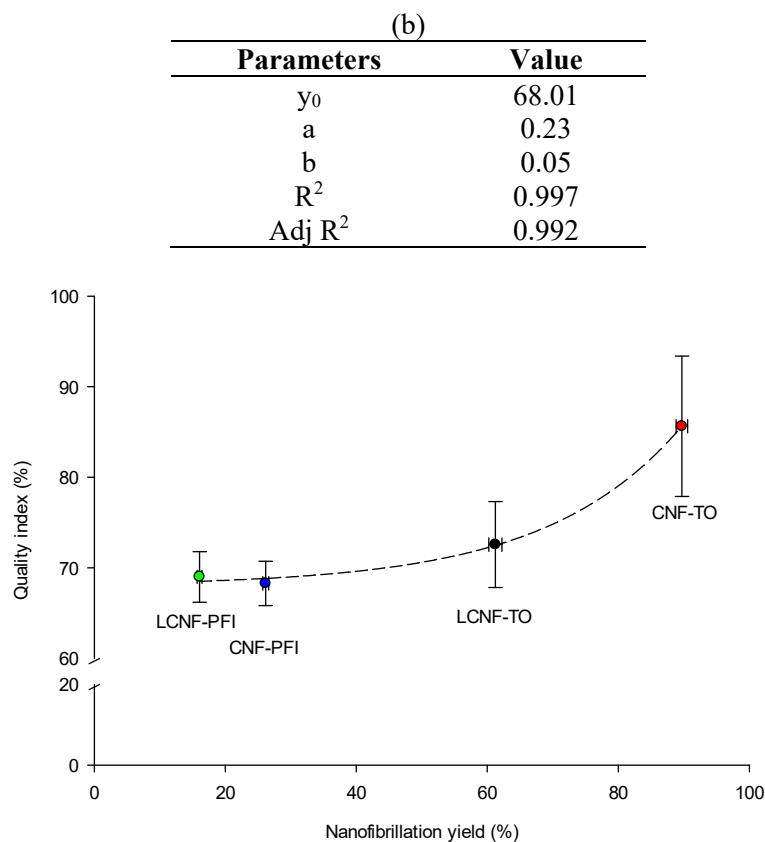
Figure IV.46 *Quality index: (a) influence of pre-treatments on cellulose pulp and (b) relation between quality index and nanofibrillation yield.*

The morphology of extracted celluloses under different pre-treatments was observed using visual analysis and optical microscope (Figure IV.47). Visually, it is clearly shown (Figure IV.47a) that, apart from LCNF-PFI which exhibited a slight separation of phases, all NCs formed stable suspension in water with a gel-like state. Moreover, at 1% solid content, the high transparency of CNF-TO suspension is visibly observed, as expected from its fibrillation yield of about 90%. Furthermore, the size and shape of cellulose fibers could be easily observed under optical microscope (Figure IV.47b). In general, considerable morphological differences of the cellulose fibers occurred along with type of pre-treatment applied. NCs isolated with PFI pre-treatment showed long-shaped morphology with length from 100 to 1,000 μm and width from 5 to 25 μm depending on the effect of bleaching process. The fibers from TEMPO-mediated oxidation pre-treatment had shorter length than that from mechanical pre-treatment, indicating that the chemical process caused more damages to the cellulose fibers by trimming down the length of fibers. Moreover, the morphology of CNF-TO was completely different from other three NCs, showing agglomerates of irregular particles with some

needle-like debris between them. The significant size reduction of cellulose fibers could be attributed to excessive oxidation.
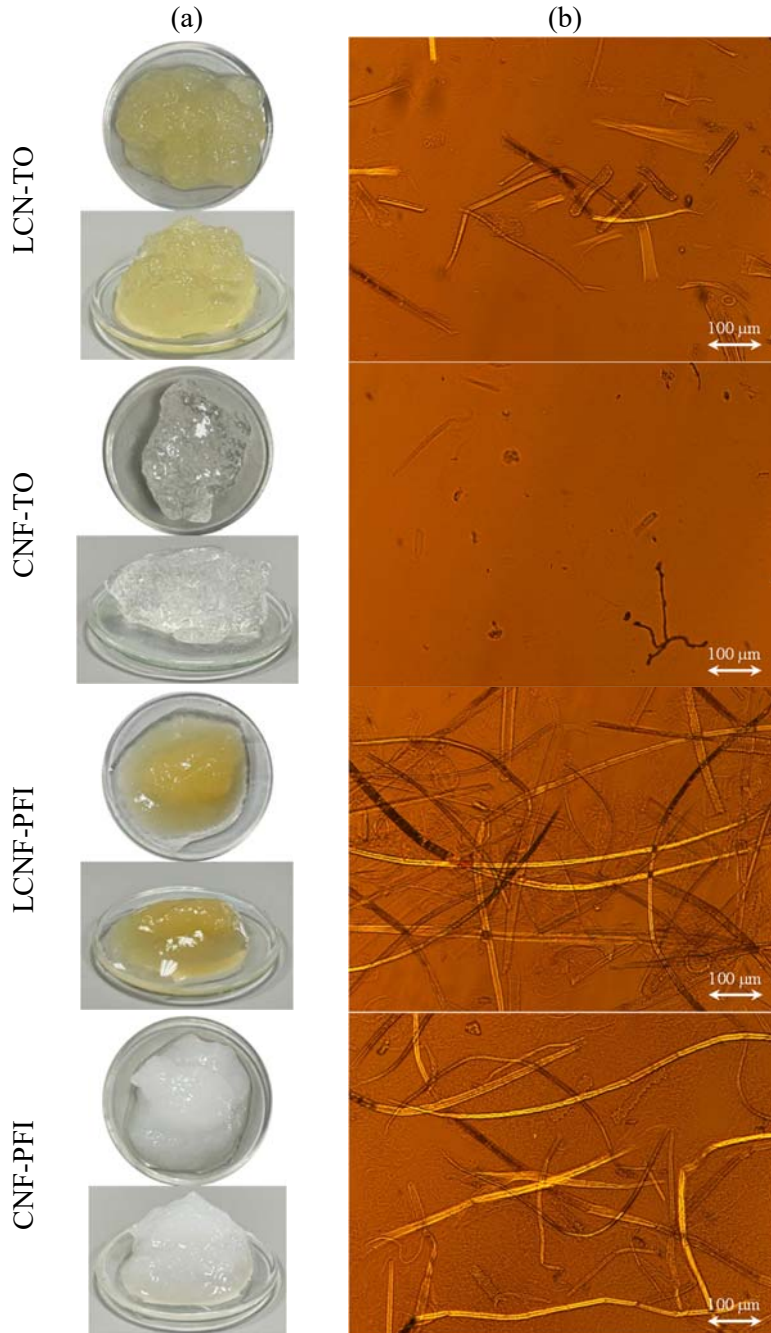
Figure IV.47 *Visual observation (column a) and optical microscope (column b) images of celluloses extracted from unbleached and bleached barley straw cellulose pulp through chemical and mechanical pre-treatments.*

XRD analysis was performed to investigate the crystalline behavior of extracted NCs. The XRD patterns of all samples (Figure IV.48) showed major peaks at $2\theta = 16°$ and $22°$ which indicated the presence of cellulose I_β structure [151]. The crystallinity index (CrI), used to indicate the order of crystallinity, was affected by each pre-treatment: LCNF-PFI < CNF-PFI < LCNF-TO < CNF-TO, which was $48.83 \pm 2.07\%$, $54.26 \pm 1.87\%$, $58.30 \pm 2.41\%$, and $61.97 \pm 0.96\%$, respectively, using Segal's empirical method. It was noticeable that TEMPO-extracted NCs from bleached cellulose pulp consisted of higher crystallinity compared to other NCs. This is the result of impurities removal, such as amorphous non-cellulosic compounds (lignin and ashes), due to the bleaching treatment and the decay of amorphous regions with a consequent rearrangement of the crystalline regions into a more ordered structure due to the oxidation reaction.
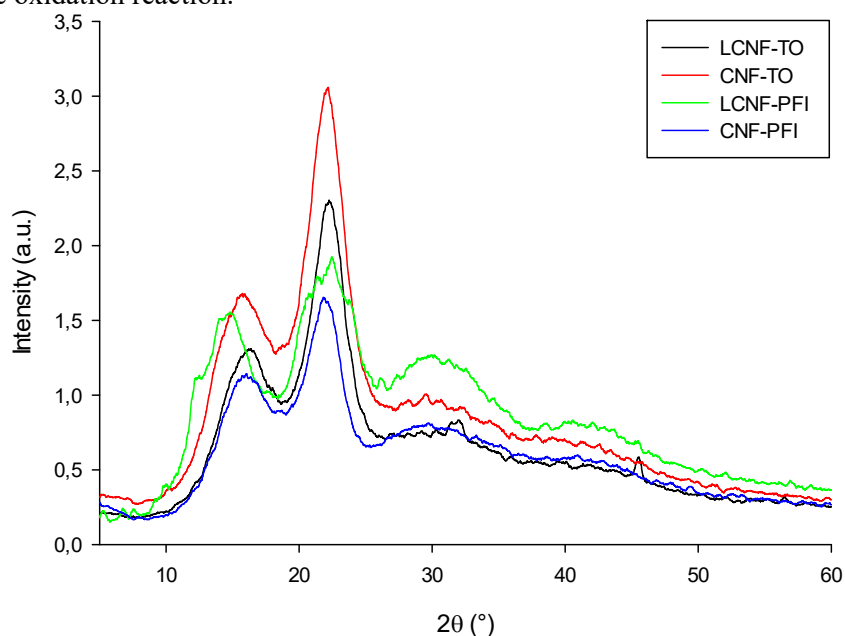
Figure IV.48 *XRD patterns for cellulose nanofibers extracted from unbleached and bleached barley straw cellulose pulp.*

The FT-IR spectra of the different NCs are shown in Figure IV.49. In general, similar results to cellulose pulp were found for all spectrum of NCs, which showed some signature characteristic bands, including 3300, 2900, 1030, and 900 cm^{-1}, which belonged to O-H stretching, C-H stretching, C-H deformation, C-O-C pyranose ring stretching vibration, and β-glycosidic linkages, respectively. All the spectra had a peak at around 1620 cm^{-1} attributed to the H-O-H bending of adsorbed water within cellulose samples [152]. The highest peak intensity of both LCNF-TO and CNF-TO at around 1030 cm^{-1} could be attributed to the carbonyl bonds present in the cellulose skeleton [153].

217
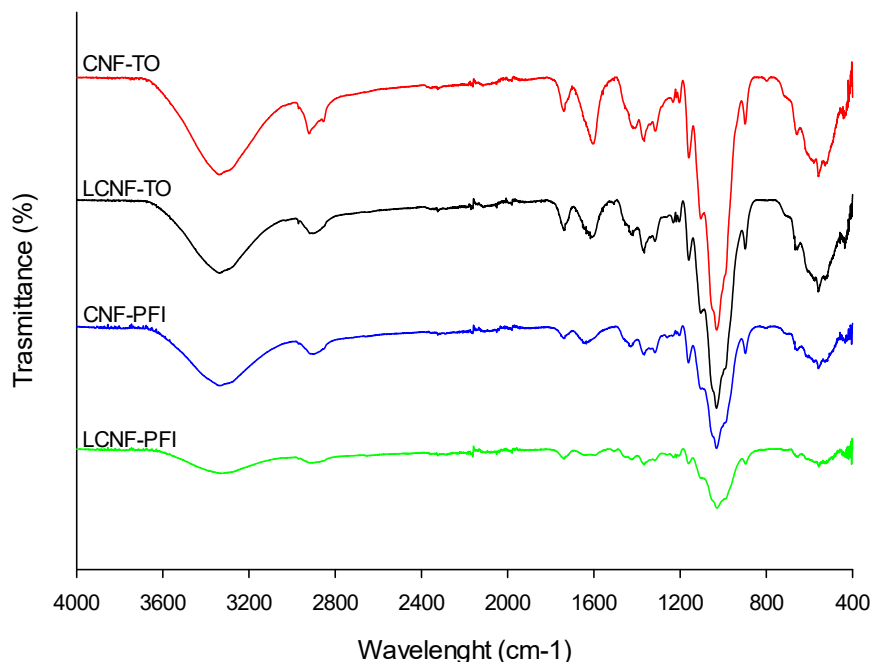
Figure IV.49 *FT-IR spectra of NCs isolated through TEMPO-mediated oxidation and PFI pre-treatments applied to unbleached and bleached cellulose pulp from barley straw.*

Papers from BS-UB and BS-B cellulose pulp exhibited a homogenous surface but with large and macroscopically heterogeneous spots and visible white agglomerates. In contrast, nanopapers prepared from CNFs suspension generally showed semi-transparent and smooth appearance without any holes. Mechanical properties and porosity of the derived papers and nanopapers using extracted cellulose pulp and isolated cellulose nanofibers are reported in Table IV.18. Nanopapers containing NCs complex isolated with mechanical pre-treated exhibited the highest tensile strength and load at break among all the papers. Due to the number of links among fibers, the type of links, and the intrinsic resistance of the fiber, LCNF-PFI and CNF-PFI possess a better adhesion between the cellulose fibers, resulting in superior mechanical strength of film. Especially, nanopaper formed from the LCNF-PFI and CNF-PFI suspensions exhibited the highest tensile strength value (28.62 ± 2.13 and 28.92 ± 3.50 MPa, respectively), being notably higher than that of pure CNF-TO (65 and 68% increase, respectively). A lower tensile strength causes a reduction in flexibility. Furthermore, the crosslinking among mechanical pre-treated complexed NC network enabled the enhancement of the strain at break of the nanopaper, with an increase respect to CNF-TO of 105 and 207% for LCNF-PFI and CNF-PFI, respectively. This improvement was likely due to the enhanced interactions between NCs constituents of the nanopaper, promoted by the electrostatic forces [154].

Table IV.18 *Mechanical properties from the elongation analysis of different papers and nanopapers.*

		Young's Modulus (GPa)	Tensile strength (MPa)	Load at break (N)	Strain at Break (%)
Pulp	BS-UB	1.58 ± 0.52^a	3.98 ± 0.91^a	12.06 ± 1.87^a	1.10 ± 0.20^a
	BS-B	2.55 ± 1.05^a	11.44 ± 1.27^b	25.85 ± 0.40^b	1.72 ± 0.38^b
Nanofiber	LCNF-TO	30.08 ± 0.26^d	7.63 ± 1.04^{ab}	9.49 ± 0.98^a	1.02 ± 0.06^a
	CNF-TO	37.27 ± 1.24^e	17.33 ± 0.15^c	9.02 ± 0.35^a	0.86 ± 0.28^a
	LCNF-PFI	9.59 ± 1.04^c	28.62 ± 2.13^d	31.48 ± 2.28^c	1.76 ± 0.17^b
	CNF-PFI	4.36 ± 0.68^b	28.92 ± 3.50^d	28.99 ± 0.73^c	1.79 ± 0.19^b

Different letters denote significant differences ($p < 0.05$) among the different samples within each column ($n = 3$).

Figure IV.50 shows the apparent density of nanopapers, from which it is possible to deduce a significant increase after bleaching treatment for both chemical and mechanical pre-treated NCs. Higher apparent density most likely thanks to stronger hydrogen bonds as well as particle sizes being better matched to the surface in absence of impurities [155]. Interestingly, the density and porosity of the nanopaper were strongly influenced by the nature of NC instead of pre-treatment. This indicated that the elimination of lignin allowed to control pore sizes within the paper and porosity of the paper. As a result, the reduction in porosity of the paper has been reported to improve mechanical properties (as confirmed in Table IV.18) of the paper owing to the increased hydrogen bonding introduced by CNF with high surface area [110].
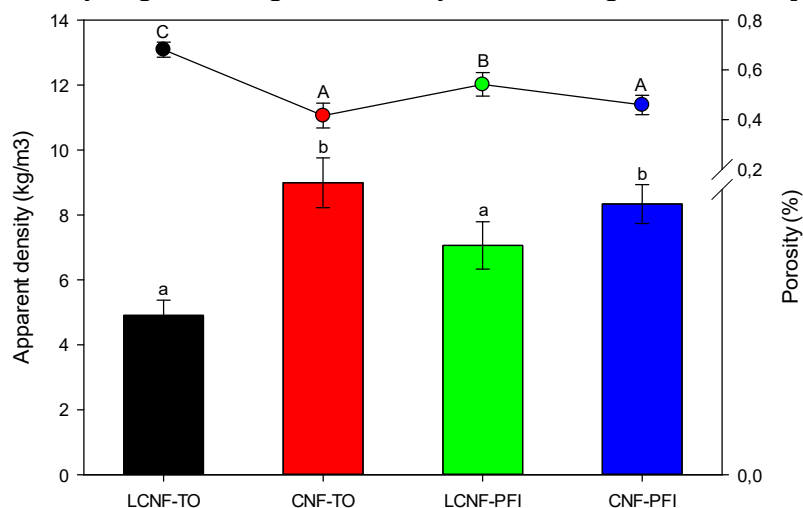
Figure IV.50 *Apparent density (vertical bars) and porosity (simple line) of nanopapers formed from extracted NCs. Different lowercase and uppercase letters indicate significant differences ($p < 0.05$) between samples for apparent density and porosity, respectively.*

IV.3.4. Conclusions

To enhance the overall performance of cellulose polymer isolated from AFRs, as described in the previous section, efforts have been made to improve their intrinsic properties by disrupting the strong hydrogen bonds between cellulose molecules and fibrils and obtaining cellulose nanoparticles. In summary, results show that both HPH and TEMPO-mediated oxidation can be used to prepare NCs from both pure cellulose or AFRs cellulose pulp with improved functional performance, such as defibrillated structure, gelling, and high colloidal stability. The mean particle diameter varies according to the input cellulosic material as well as the applied treatment, while the ζ-potential raised negative values for all samples thanks to the intensity of chemical treatment or the mechanical disruptive forces. The main findings demonstrated that NCs could be successfully isolated and their properties tuned according to the final application and starting cellulosic material (Table IV.19) based on the selected sustainable integrated processes (the combination of TEMPO-oxidation or PFI beater mechanical treatment with homogenization), developing the biobased circular economy. Overall, the use of AFRs to prepare high-performance NCs to achieve high-value utilization of agricultural waste provides new ideas and new methods for the preparation of NCs. Pushing the usage of NCs into new and innovative advanced applications, to create materials with tunable and improved characteristics will be of particular interest for the next chapter, especially the exploitation of AFRs as cost-effective commercial sources of NCs.

Table IV.19 *NCs isolation from (AFRs) cellulose pulp: advantages and application for each nanomaterials.*

Cellulose pulp	Treatment	Remarks	Applications
CHEMICAL OXIDATION			
Northern bleached softwood kraft pulp Celeste 85	TEMPO-mediated oxidation	CNCs and CNFs with width of 3 and 10 nm, respectively and length of 170 nm and several micrometres, respectively, CNCs are needle-shaped, while CNFs are elongated, and partly disordered fibers, with a nanosized, roughly spherical cross section. CNFs particles present the ability to act onto the O/W interface	NCs reinforcing agents to hydrophobic polymer for nanocomposites CNFs O/W Pickering stabilizer
MECHANICAL TREATMENTS			
Commercial cellulose Arbocel® BWW40 fibers	BM	CNFs characterized by a constant cross-section, high birefringence properties, and well-separated particles with an irregular shape and a lateral size is in the range of 10 - 50 µm. Interfacial deformability is hindered by the resulting hard particles	Performance-enhancement additive in composite materials

	HPH	CNFs exhibited a no ordered and uniform particle distribution but with high defibrillated structure. Flexible fibers capable of adapting to the curved interfacial surface	O/W Pickering stabilizer
Tomato pomace cellulose pulp	HPH	Thinner fibers with high erosion and defibrillation of surface and hydrophobicity contributed to their adsorption at oil-water interfaces	O/W Pickering stabilizer
Bacterial cellulose	HSM	Individual microfibrils with entangled network structure with average diameter of 40 - 300 μm.	Additive in edible coating to form strengthened composites increasing the antimicrobial properties
COMBINATION OF CHEMICAL AND MECHANICAL TREATMENTS			
Barley straw cellulose pulp	TEMPO-mediated oxidation + HPH	Gel-like materials with short length (< 100 μm), 2 - 5 μm in width and crystallinity of 58 - 62%. Low flexibility and high porosity due to the decrease in mechanical properties	Performance-enhancement additive in traditional papermaking Novel nanocomposite to eliminate contaminants from industrial effluents Promising materials for the amine modification and future capture of CO_2
COMBINATION OF MECHANICAL TREATMENTS			
Barley straw cellulose pulp	PFI beater + HPH	Gel-like materials with long-shaped morphology (length from 100 to 1,000 μm and width from 5 to 25 μm) and crystallinity of 49 - 54%. Good adhesion between the cellulose fibers, resulting in high mechanical strength.	Performance-enhancement additive in traditional papermaking Adsorption materials Promising materials for the amine modification and future capture of CO_2

Chapter IV

IV.4. References

1.   Panzella, L.; Moccia, F.; Nasti, R.; Marzorati, S.; Verotta, L.; Napolitano, A. Bioactive Phenolic Compounds From Agri-Food Wastes: An Update on Green and Sustainable Extraction Methodologies. *Front. Nutr.* **2020**, *7*, 1–27, doi:10.3389/fnut.2020.00060.

2.   Zuin, V.G.; Ramin, L.Z. Green and Sustainable Separation of Natural Products from Agro-Industrial Waste: Challenges, Potentialities, and Perspectives on Emerging Approaches. In *Chemistry and Chemical Technologies in Waste Valorization. Topics in Current Chemistry Collections.*; Lin, C.S.K., Ed.; Springer, Cham, 2018; pp. 229–282 ISBN 978-3-319-90653-9.

3.   Pirozzi, A.; Ferrari, G.; Donsì, F. Cellulose Isolation from Tomato Pomace Pretreated by High-Pressure Homogenization. *Foods* **2022**, *11*, 266, doi:doi.org/10.3390/foods11030266.

4.   AlfredoCassano; M.Galanakis, C. Membrane technologies for the fractionation of compounds recovered from cereal processing by-products. In *Sustainable Recovery and Reutilization of Cereal Processing By-Products*; Galanakis, C.M., Ed.; Sawston, 2018; pp. 159–187.

5.   Puri, M.; Sharma, D.; Barrow, C.J. Enzyme-assisted extraction of bioactives from plants. *Trends Biotechnol.* **2012**, *30*, 37–44, doi:10.1016/j.tibtech.2011.06.014.

6.   Patil, P.D.; Patil, S.P.; Kelkar, R.K.; Patil, N.P.; Pise, P. V.; Nadar, S.S. Enzyme-assisted supercritical fluid extraction: An integral approach to extract bioactive compounds. *Trends Food Sci. Technol.* **2021**, *116*, 357–369, doi:10.1016/j.tifs.2021.07.032.

7.   Wen, L.; Zhang, Z.; Sun, D.W.; Sivagnanam, S.P.; Tiwari, B.K. Combination of emerging technologies for the extraction of bioactive compounds. *Crit. Rev. Food Sci. Nutr.* **2020**, *60*, 1826–1841, doi:10.1080/10408398.2019.1602823.

8.   Fărcaş, A.C.; Socaci, S.A.; Nemeş, S.A.; Salanţă, L.C.; Chiş, M.S.; Pop, C.R.; Borşa, A.; Diaconeasa, Z.; Vodnar, D.C. Cereal Waste Valorization through Conventional and Current Extraction Techniques—An Up-to-Date Overview. *Foods* **2022**, *11*, 1–34, doi:10.3390/foods11162454.

9.   Kotecka-Majchrzak, K.; Kasałka-Czarna, N.; Montowska, M.; Spychaj, A.; Mikołajczak, B. The effect of hemp cake (Cannabis sativa L.) on the characteristics of meatballs stored in refrigerated conditions. *Molecules* **2021**, *26*, doi:10.3390/molecules26175284.

10.   Náthia-Neves, G.; Alonso, E. Valorization of sunflower by-product using microwave-assisted extraction to obtain a rich protein flour: Recovery of chlorogenic acid, phenolic content and antioxidant capacity. *Food Bioprod. Process.* **2021**, *125*, 57–67, doi:https://doi.org/10.1016/j.fbp.2020.10.008.

11.   Alamri, E.; Rozan, M.; Bayomy, H. A study of chemical Composition, Antioxidants, and volatile compounds in roasted Arabic coffee: Chemical

Composition, Antioxidants and volatile compounds in Roasted Arabic Coffee. *Saudi J. Biol. Sci.* **2022**, *29*, 3133–3139, doi:10.1016/j.sjbs.2022.03.025.

12. Deng, Q.; Penner, M.H.; Zhao, Y. Chemical composition of dietary fiber and polyphenols of five different varieties of wine grape pomace skins. *Food Res. Int.* **2011**, *44*, 2712–2720, doi:10.1016/j.foodres.2011.05.026.

13. Babu, C.R.; Harsha, K.; Sheik, K.B.; Viswanatha, C.K. Wheat bran-Composition and nutritional quality: A review. *Adv. Biotechnol. Microbiol.* **2018**, *9*, 1–7, doi:10.19080/AIBM.2018.09.555754.

14. Johar, N.; Ahmad, I.; Dufresne, A. Extraction, preparation and characterization of cellulose fibres and nanocrystals from rice husk. *Ind. Crops Prod.* **2012**, doi:10.1016/j.indcrop.2011.12.016.

15. Feng, X.; Sun, G.; Fang, Z. Effect of Hempseed Cake (Cannabis sativa L.) Incorporation on the Physicochemical and Antioxidant Properties of Reconstructed Potato Chips. *Foods* **2022**, *11*, 211, doi:https://doi.org/10.3390/foods11020211.

16. Panusa, A.; Zuorro, A.; Lavecchia, R.; Marrosu, G.; Petrucci, R. Recovery of Natural Antioxidants from Spent Coffee Grounds. *J. Agric. Food Chem.* **2013**, *61*, 4162–4168, doi:https://doi.org/10.1021/jf4005719.

17. Laddomada, B.; Caretto, S.; Mita, G. Wheat bran phenolic acids: Bioavailability and stability in whole wheat-based foods. *Molecules* 2015.

18. Kelebek, H.; Selli, S.; Kadiroğlu, P.; Kola, O.; Kesen, S.; Uçar, B.; Çetiner, B. Bioactive compounds and antioxidant potential in tomato pastes as affected by hot and cold break process. *Food Chem.* **2017**, doi:10.1016/j.foodchem.2016.09.190.

19. Karami, S.; Rahimi, M.; Babaei, A. An overview on the antioxidant, anti-inflammatory, antimicrobial and anti-cancer activity of grape extract. *Biomed. Res. Clin. Pract.* **2018**, *3*, 1–4, doi:10.15761/brcp.1000162.

20. Both, S.; Chemat, F.; Strube, J. Extraction of polyphenols from black tea - Conventional and ultrasound assisted extraction. *Ultrason. Sonochem.* **2014**, *21*, 1030–1034, doi:10.1016/j.ultsonch.2013.11.005.

21. Galvan D'Alessandro, L.; Kriaa, K.; Nikov, I.; Dimitrov, K. Ultrasound assisted extraction of polyphenols from black chokeberry. *Sep. Purif. Technol.* **2012**, *93*, 42–47, doi:10.1016/j.seppur.2012.03.024.

22. Bao, Y.; Reddivari, L.; Jen-Yi Huang Enhancement of phenolic compounds extraction from grape pomace by high voltage atmospheric cold plasma. *LWT* **2020**, *133*, 109970, doi:https://doi.org/10.1016/j.lwt.2020.109970.

23. Bao, Y.; Reddivari, L.; Huang, J.-Y. Development of cold plasma pretreatment for improving phenolics extractability from tomato pomace. *Innov. Food Sci. Emerg. Technol.* **2020**, *65*, 102445, doi:https://doi.org/10.1016/j.ifset.2020.102445.

24. Wang, J.; Sun, B.; Cao, Y.; Tian, Y.; Li, X. Optimisation of ultrasound-assisted extraction of phenolic compounds from wheat bran. *Food*

Chem. **2008**, *106*, 804–810, doi:https://doi.org/10.1016/j.foodchem.2007.06.062.

25. Castañeda-Valbuena, D.; Ayora-Talavera, T.; Luján-Hidalgo, C.; Álvarez-Gutiérrez, P.; Martínez-Galero, N.; Meza-Gordillo, R. Ultrasound extraction conditions effect on antioxidant capacity of mango by-product extracts. *Food Bioprod. Process.* **2021**, *127*, 212–224, doi:10.1016/j.fbp.2021.03.002.

26. Bucić-Kojić, A.; Planinić, M.; Tomas, S.; Bilić, M.; Velić, D. Study of solid-liquid extraction kinetics of total polyphenols from grape seeds. *J. Food Eng.* **2007**, *81*, 236–242, doi:10.1016/j.jfoodeng.2006.10.027.

27. Spigno, G.; Tramelli, L.; De Faveri, D.M. Effects of extraction time, temperature and solvent on concentration and antioxidant activity of grape marc phenolics. *J. Food Eng.* **2007**, doi:10.1016/j.jfoodeng.2006.10.021.

28. N. Rajha, H.; Darra, N. El; Vorobiev, E.; Louka, N.; Maroun, R.G. An Environment Friendly, Low-Cost Extraction Process of Phenolic Compounds from Grape Byproducts. Optimization by Multi-Response Surface Methodology. *Food Nutr. Sci.* **2013**, *04*, 650–659, doi:10.4236/fns.2013.46084.

29. Jurić, S.; Ferrari, G.; Velikov, K.P.; Donsì, F. High-pressure homogenization treatment to recover bioactive compounds from tomato peels. *J. Food Eng.* **2019**, *262*, 170–180, doi:10.1016/j.jfoodeng.2019.06.011.

30. Wang, T.; Raddatz, J.; Chen, G. Effects of microfluidization on antioxidant properties of wheat bran. *J. Cereal Sci.* **2013**, *58*, 380–386, doi:10.1016/j.jcs.2013.07.010.

31. Bengtsson, H.; Tornberg, E. Physicochemical characterization of fruit and vegetable fiber suspensions. I: Effect of homogenization. *J. Texture Stud.* **2011**, *42*, 268–280, doi:10.1111/j.1745-4603.2010.00275.x.

32. Mustafa, W.; Pataro, G.; Ferrari, G.; Donsì, F. Novel approaches to oil structuring via the addition of high-pressure homogenized agri-food residues and water forming capillary bridges. *J. Food Eng.* **2018**, *236*, 9–18, doi:10.1016/J.JFOODENG.2018.05.003.

33. Sato, A.C.K.; Cunha, R.L. Effect of particle size on rheological properties of jaboticaba pulp. *J. Food Eng.* **2009**, *91*, 566–570, doi:10.1016/j.jfoodeng.2008.10.005.

34. Labaky, P.; Dahdouh, L.; Ricci, J.; Wisniewski, C.; Pallet, D.; Louka, N.; Grosmaire, L. Impact of ripening on the physical properties of mango purees and application of simultaneous rheometry and in situ FTIR spectroscopy for rapid identification of biochemical and rheological changes. *J. Food Eng.* **2021**, *300*, 110507, doi:10.1016/j.jfoodeng.2021.110507.

35. Araújo, D.J.C.; Machado, A.V.; Vilarinho, M.C.L.G. Availability and Suitability of Agroindustrial Residues as Feedstock for Cellulose-Based Materials: Brazil Case Study. *Waste and Biomass Valorization* **2019**, doi:10.1007/s12649-018-0291-0.

36. Collazo-Bigliardi, S.; Ortega-Toro, R.; Chiralt Boix, A. Isolation and characterisation of microcrystalline cellulose and cellulose nanocrystals from coffee husk and comparative study with rice husk. *Carbohydr. Polym.* **2018**, doi:10.1016/j.carbpol.2018.03.022.

37. Rosa, M.F.; Medeiros, E.S.; Malmonge, J.A.; Gregorski, K.S.; Wood, D.F.; Mattoso, L.H.C.; Glenn, G.; Orts, W.J.; Imam, S.H. Cellulose nanowhiskers from coconut husk fibers: Effect of preparation conditions on their thermal and morphological behavior. *Carbohydr. Polym.* **2010**, doi:10.1016/j.carbpol.2010.01.059.

38. Pasquini, D.; Teixeira, E. de M.; Curvelo, A.A. da S.; Belgacem, M.N.; Dufresne, A. Extraction of cellulose whiskers from cassava bagasse and their applications as reinforcing agent in natural rubber. *Ind. Crops Prod.* **2010**, doi:10.1016/j.indcrop.2010.06.022.

39. Vadivel, V.; Moncalvo, A.; Dordoni, R.; Spigno, G. Effects of an acid/alkaline treatment on the release of antioxidants and cellulose from different agro-food wastes. *Waste Manag.* **2017**, doi:10.1016/j.wasman.2017.03.010.

40. Rosa, S.M.L.; Rehman, N.; De Miranda, M.I.G.; Nachtigall, S.M.B.; Bica, C.I.D. Chlorine-free extraction of cellulose from rice husk and whisker isolation. *Carbohydr. Polym.* **2012**, doi:10.1016/j.carbpol.2011.08.084.

41. Oliveira, J.P. de; Bruni, G.P.; Lima, K.O.; Halal, S.L.M. El; Rosa, G.S. da; Dias, A.R.G.; Zavareze, E. da R. Cellulose fibers extracted from rice and oat husks and their application in hydrogel. *Food Chem.* **2017**, doi:10.1016/j.foodchem.2016.10.048.

42. Li, J.B.; Dong, H.L.; Xiu, H.J.; Zhang, M.Y.; Reddy, K.S.; Zhang, X.F.; Ji, Y. Extraction, separation and refining of microcrystalline cellulose from wheat straw using various pretreatments. *Int. J. Agric. Biol. Eng.* **2016**, doi:10.3965/j.ijabe.20160902.1386.

43. Li, H.; Zhang, H.; Xiong, L.; Chen, X.; Wang, C.; Huang, C.; Chen, X. Isolation of Cellulose from Wheat Straw and Its Utilization for the Preparation of Carboxymethyl Cellulose. *Fibers Polym.* **2019**, doi:10.1007/s12221-019-7717-6.

44. Alemdar, A.; Sain, M. Isolation and characterization of nanofibers from agricultural residues - Wheat straw and soy hulls. *Bioresour. Technol.* **2008**, doi:10.1016/j.biortech.2007.04.029.

45. Debiagi, F.; Faria-Tischer, P.C.S.; Mali, S. A Green Approach Based on Reactive Extrusion to Produce Nanofibrillated Cellulose from Oat Hull. *Waste and Biomass Valorization* **2021**, doi:10.1007/s12649-020-01025-1.

46. Wu, C.; McClements, D.J.; He, M.; Zheng, L.; Tian, T.; Teng, F.; Li, Y. Preparation and characterization of okara nanocellulose fabricated using sonication or high-pressure homogenization treatments. *Carbohydr. Polym.* **2021**, doi:10.1016/j.carbpol.2020.117364.

47. Wu, C.; McClements, D.J.; He, M.; Huang, Y.; Zhu, H.; Jiang, L.; Teng, F.; Li, Y. Okara nanocellulose fabricated using combined chemical and

mechanical treatments: Structure and properties. *J. Mol. Liq.* **2021**, doi:10.1016/j.molliq.2021.116231.

48. Sánchez, Ó.J.; Cardona, C.A. Trends in biotechnological production of fuel ethanol from different feedstocks. *Bioresour. Technol.* 2008.

49. Yang, Z.; Xu, S.; Ma, X.; Wang, S. Characterization and acetylation behavior of bamboo pulp. *Wood Sci. Technol.* **2008**, doi:10.1007/s00226-008-0194-5.

50. Ragauskas, A.J.; Williams, C.K.; Davison, B.H.; Britovsek, G.; Cairney, J.; Eckert, C.A.; Frederick, W.J.; Hallett, J.P.; Leak, D.J.; Liotta, C.L.; et al. The path forward for biofuels and biomaterials. *Science (80-.).* 2006.

51. McKendry, P. Energy production from biomass (part 1): Overview of biomass. *Bioresour. Technol.* **2002**, doi:10.1016/S0960-8524(01)00118-3.

52. Das, A.M.; Hazarika, M.P.; Goswami, M.; Yadav, A.; Khound, P. Extraction of cellulose from agricultural waste using Montmorillonite K-10/LiOH and its conversion to renewable energy: Biofuel by using Myrothecium gramineum. *Carbohydr. Polym.* **2016**, doi:10.1016/j.carbpol.2015.12.070.

53. Urbonaviciene, D.; Viskelis, P. The cis-lycopene isomers composition in supercritical CO2 extracted tomato by-products. *LWT - Food Sci. Technol.* **2017**, doi:10.1016/j.lwt.2017.03.034.

54. Sánchez, R.; Espinosa, E.; Domínguez-Robles, J.; Loaiza, J.M.; Rodríguez, A. Isolation and characterization of lignocellulose nanofibers from different wheat straw pulps. *Int. J. Biol. Macromol.* **2016**, doi:10.1016/j.ijbiomac.2016.08.019.

55. Scaglia, B.; D'Incecco, P.; Squillace, P.; Dell'Orto, M.; De Nisi, P.; Pellegrino, L.; Botto, A.; Cavicchi, C.; Adani, F. Development of a tomato pomace biorefinery based on a CO2-supercritical extraction process for the production of a high value lycopene product, bioenergy and digestate. *J. Clean. Prod.* **2020**, doi:10.1016/j.jclepro.2019.118650.

56. Squillace, P.; Adani, F.; Scaglia, B. Supercritical CO2 extraction of tomato pomace: Evaluation of the solubility of lycopene in tomato oil as limiting factor of the process performance. *Food Chem.* **2020**, doi:10.1016/j.foodchem.2020.126224.

57. Zuknik, M.H.; Nik Norulaini, N.A.; Mohd Omar, A.K. Supercritical carbon dioxide extraction of lycopene: A review. *J. Food Eng.* 2012.

58. Achmon, Y.; Claypool, J.T.; Pace, S.; Simmons, B.A.; Singer, S.W.; Simmons, C.W. Assessment of biogas production and microbial ecology in a high solid anaerobic digestion of major California food processing residues. *Bioresour. Technol. Reports* **2019**, doi:10.1016/j.biteb.2018.11.007.

59. Chiariotti, A.; Rossi, E.; Scalella, R.; La Mantia, M.C.; Monti, F.; Santangelo, E. Anaerobic codigestion of tomato pomace (Peels plus seeds) with buffalo sludge improves methane production. In Proceedings of the European Biomass Conference and Exhibition Proceedings; 2021.

60. Selim, I.Z.; Zikry, A.A.F.; Gaber, S.H. Physicochemical properties of prepared cellulose sulfates: II. From linen pulp bleached by the H2O2 method. *Polym. - Plast. Technol. Eng.* **2004**, doi:10.1081/PPT-200030194.

61. Roman, M.; Winter, W.T. Effect of sulfate groups from sulfuric acid hydrolysis on the thermal degradation behavior of bacterial cellulose. *Biomacromolecules* **2004**, doi:10.1021/bm034519+.

62. Cheng, M.; Qin, Z.; Chen, Y.; Hu, S.; Ren, Z.; Zhu, M. Efficient Extraction of Cellulose Nanocrystals through Hydrochloric Acid Hydrolysis Catalyzed by Inorganic Chlorides under Hydrothermal Conditions. *ACS Sustain. Chem. Eng.* **2017**, doi:10.1021/acssuschemeng.6b03194.

63. Higgins, F.J.; Ho, G.E. Hydrolysis of cellulose using HCl: A comparison between liquid phase and gaseous phase processes. *Agric. Wastes* **1982**, doi:10.1016/0141-4607(82)90019-1.

64. Chen, H. Lignocellulose biorefinery feedstock engineering. In *Lignocellulose Biorefinery Engineering*; 2015.

65. Bandyopadhyay-Ghosh, S.; Ghosh, S.B.; Sain, M. The use of biobased nanofibres in composites. In *Biofiber Reinforcements in Composite Materials*; 2015 ISBN 9781782421276.

66. Bali, G.; Meng, X.; Deneff, J.I.; Sun, Q.; Ragauskas, A.J. The effect of alkaline pretreatment methods on cellulose structure and accessibility. *ChemSusChem* **2015**, doi:10.1002/cssc.201402752.

67. Oriez, V.; Peydecastaing, J.; Pontalier, P.-Y. Lignocellulosic Biomass Mild Alkaline Fractionation and Resulting Extract Purification Processes: Conditions, Yields, and Purities. *Clean Technol.* **2020**, doi:10.3390/cleantechnol2010007.

68. Jonoobi, M.; Harun, J.; Shakeri, A.; Misra, M.; Oksmand, K. Chemical composition, crystallinity, and thermal degradation of bleached and unbleached kenaf bast (Hibiscus cannabinus) pulp and nanofibers. *BioResources* **2009**, doi:10.15376/biores.4.2.626-639.

69. Shin, H.K.; Pyo Jeun, J.; Bin Kim, H.; Hyun Kang, P. Isolation of cellulose fibers from kenaf using electron beam. *Radiat. Phys. Chem.* **2012**, doi:10.1016/j.radphyschem.2011.10.010.

70. Chen, W.; Yu, H.; Liu, Y.; Chen, P.; Zhang, M.; Hai, Y. Individualization of cellulose nanofibers from wood using high-intensity ultrasonication combined with chemical pretreatments. *Carbohydr. Polym.* **2011**, doi:10.1016/j.carbpol.2010.10.040.

71. Fitriana, N.E.; Suwanto, A.; Jatmiko, T.H.; Mursiti, S.; Prasetyo, D.J. Cellulose extraction from sugar palm (Arenga pinnata) fibre by alkaline and peroxide treatments. In Proceedings of the IOP Conference Series: Earth and Environmental Science; 2020.

72. Wu, Y.; Wu, J.; Yang, F.; Tang, C.; Huang, Q. Effect of H2O2 bleaching treatment on the properties of finished transparent wood. *Polymers (Basel).* **2019**, doi:10.3390/polym11050776.

73. Hafid, H.S.; Omar, F.N.; Zhu, J.; Wakisaka, M. Enhanced crystallinity and thermal properties of cellulose from rice husk using acid hydrolysis treatment. *Carbohydr. Polym.* **2021**, doi:10.1016/j.carbpol.2021.117789.

74. Nagarajan, K.J.; Ramanujam, N.R.; Sanjay, M.R.; Siengchin, S.; Surya Rajan, B.; Sathick Basha, K.; Madhu, P.; Raghav, G.R. A comprehensive review on cellulose nanocrystals and cellulose nanofibers: Pretreatment, preparation, and characterization. *Polym. Compos.* 2021.

75. Jin, S.; Zhang, G.; Zhang, P.; Fan, S.; Li, F. High-pressure homogenization pretreatment of four different lignocellulosic biomass for enhancing enzymatic digestibility. *Bioresour. Technol.* **2015**, doi:10.1016/j.biortech.2015.01.069.

76. Lara-Serrano, M.; Morales-delaRosa, S.; Campos-Martín, J.M.; Fierro, J.L.G. Fractionation of lignocellulosic biomass by selective precipitation from ionic liquid dissolution. *Appl. Sci.* **2019**, *9*, doi:10.3390/app9091862.

77. Rahman, A.; Fehrenbach, J.; Ulven, C.; Simsek, S.; Hossain, K. Utilization of wheat-bran cellulosic fibers as reinforcement in bio-based polypropylene composite. *Ind. Crops Prod.* **2021**, *172*, 114028, doi:10.1016/j.indcrop.2021.114028.

78. ZH, K.; Gendy, N.S. El; HA, A.; THT, S.; MMD, H. Upgrading of Tomato (Solanum lycopersicum) Agroindustrial Wastes. *J. Microb. Biochem. Technol.* **2018**, *10*, 46–48, doi:10.4172/1948-5948.1000394.

79. FU, T.-K.; WANG, Y.-H.; LI, J.-H.; WEI, X.-Y.; WANG, F. Effect Of High Pressure Homogenization (HPH) On The Rheological Properties Of Pineapple Leaf Cellulose/[BMIM]Cl Solution. *DEStech Trans. Eng. Technol. Res.* **2017**, doi:10.12783/dtetr/mdm2016/4922.

80. Yan, Z.; Yi, C.; Liu, T.; Yang, J.; Ma, H.; Sha, L.; Guo, D.; Zhao, H.; Zhang, X.; Wang, W. Effect of Lignin containing Highly Fibrillated Cellulose on the Adsorption Behavior of an Organic Dye. *BioResources* **2021**, *16*, 6560–6576.

81. Larrea-Wachtendorff, D.; Tabilo-Munizaga, G.; Moreno-Osorio, L.; Villalobos-Carvajal, R.; Pérez-Won, M. Protein Changes Caused by High Hydrostatic Pressure (HHP): A Study Using Differential Scanning Calorimetry (DSC) and Fourier Transform Infrared (FTIR) Spectroscopy. *Food Eng. Rev.* **2015**, doi:10.1007/s12393-015-9107-1.

82. Larrea-Wachtendorff, D.; Tabilo-Munizaga, G.; Ferrari, G. Potato starch hydrogels produced by high hydrostatic pressure (HHP): A first approach. *Polymers (Basel).* **2019**, doi:10.3390/polym11101673.

83. Ling, Z.; Tang, W.; Su, Y.; Shao, L.; Wang, P.; Ren, Y.; Huang, C. Promoting enzymatic hydrolysis of aggregated bamboo crystalline cellulose by fast microwave-assisted dicarboxylic acid deep eutectic solvents pretreatments. *Bioresour. Technol.* **2021**, *333*, 125122, doi:10.1016/j.biortech.2021.125122.

84. Liu, X.; Renard, C.M.G.C.; Bureau, S.; Le Bourvellec, C. Revisiting the contribution of ATR-FTIR spectroscopy to characterize plant cell wall polysaccharides. *Carbohydr. Polym.* **2021**, doi:10.1016/j.carbpol.2021.117935.

85. Kubovský, I.; Kačíková, D.; Kačík, F. Structural Changes of Oak Wood Main Components Caused by Thermal Modification. *Polymers (Basel).* **2020**, *12*, 485, doi:10.3390/polym12020485.

86. Zhuang, J.; Li, M.; Pu, Y.; Ragauskas, A.J.; Yoo, C.G. Observation of Potential Contaminants in Processed Biomass Using Fourier Transform Infrared Spectroscopy. *Appl. Sci.* **2020**, *10*, 4345, doi:10.3390/app10124345.

87. Bi, C.H.; Yan, Z.M.; Wang, P.L.; Alkhatib, A.; Zhu, J.Y.; Zou, H.C.; Sun, D.Y.; Zhu, X. Di; Gao, F.; Shi, W.T.; et al. Effect of high pressure homogenization treatment on the rheological properties of citrus peel fiber/corn oil emulsion. *J. Sci. Food Agric.* **2020**, doi:10.1002/jsfa.10398.

88. Hua, X.; Xu, S.; Wang, M.; Chen, Y.; Yang, H.; Yang, R. Effects of high-speed homogenization and high-pressure homogenization on structure of tomato residue fibers. *Food Chem.* **2017**, doi:10.1016/j.foodchem.2017.04.003.

89. Zhu, X.; Lundberg, B.; Cheng, Y.; Shan, L.; Xing, J.; Peng, P.; Chen, P.; Huang, X.; Li, D.; Ruan, R. Effect of high-pressure homogenization on the flow properties of citrus peel fibers. *J. Food Process Eng.* **2018**, doi:10.1111/jfpe.12659.

90. Pirozzi, A.; Capuano, R.; Avolio, R.; Gentile, G.; Ferrari, G.; Donsì, F. O/W pickering emulsions stabilized with cellulose nanofibrils produced through different mechanical treatments. *Foods* **2021**, doi:10.3390/foods10081886.

91. Guo, J.; Filpponen, I.; Johansson, L.S.; Heiβler, S.; Li, L.; Levkin, P.; Rojas, O.J. Micro-patterns on nanocellulose films and paper by photo-induced thiol–yne click coupling: a facile method toward wetting with spatial resolution. *Cellulose* **2018**, *25*, 367–375, doi:10.1007/s10570-017-1593-2.

92. Xu, Y.; Yang, S.; Zhao, P.; Wu, M.; Song, X.; Ragauskas, A.J. Effect of endoglucanase and high-pressure homogenization post-treatments on mechanically grinded cellulose nanofibrils and their film performance. *Carbohydr. Polym.* **2021**, *253*, 117253, doi:10.1016/j.carbpol.2020.117253.

93. Spigno, G.; Pizzorno, T.; De Faveri, D.M. Cellulose and hemicelluloses recovery from grape stalks. *Bioresour. Technol.* **2008**, doi:10.1016/j.biortech.2007.08.044.

94. Arslan, Y.; Eken-Saraçoĝlu, N. Effects of pretreatment methods for hazelnut shell hydrolysate fermentation with Pichia Stipitis to ethanol. *Bioresour. Technol.* **2010**, doi:10.1016/j.biortech.2010.05.085.

95. Hassan, N.S.; Badri, K.H. Lignin recovery from alkaline hydrolysis and glycerolysis of oil palm fiber. *AIP Conf. Proc.* **2014**, *1614*, 433–438, doi:10.1063/1.4895236.

Chapter IV

96.   Cheng, S.; Huang, A.; Wang, S.; Zhang, Q. Effect of different heat treatment temperatures on the chemical composition and structure of chinese fir wood. *BioResources* **2016**, *11*, 4006–4016, doi:10.15376/biores.11.2.4006-4016.

97.   Yang, H.; Yan, R.; Chen, H.; Lee, D.H.; Zheng, C. Characteristics of hemicellulose, cellulose and lignin pyrolysis. *Fuel* **2007**, *86*, 1781–1788, doi:10.1016/j.fuel.2006.12.013.

98.   Xu, F.; Sun, J.X.; Sun, R.; Fowler, P.; Baird, M.S. Comparative study of organosolv lignins from wheat straw. *Ind. Crops Prod.* **2006**, *23*, 180–193, doi:10.1016/j.indcrop.2005.05.008.

99.   Wei, Y.; Chen, W.; Liu, C.; Wang, H. Facial synthesis of adsorbent from hemicelluloses for Cr(VI) adsorption. *Molecules* **2021**, *26*, doi:10.3390/molecules26051443.

100.   Espinosa, E.; Tarrés, Q.; Delgado-Aguilar, M.; González, I.; Mutjé, P.; Rodríguez, A. Suitability of wheat straw semichemical pulp for the fabrication of lignocellulosic nanofibres and their application to papermaking slurries. *Cellulose* **2016**, *23*, 837–852, doi:10.1007/s10570-015-0807-8.

101.   Tang, K.; Hao, X.; Wei, Q.; Zhou, X. Effects of Lignin Chemistry on Cellulose Extraction Performance Towards Crop Straw/Stalk. *Chiang Mai J. Sci.* **2020**, *47*, 1204–1215.

102.   Hubbe, M.A. Water vapor barrier properties of coated and filled microfibrillated cellulose composite films. *BioResources* **2011**, *6*, 4370–4388.

103.   Chaker, A.; Alila, S.; Mutje, P.; Rei, M.; Sami, V. Key role of the hemicellulose content and the cell morphology on the nanofibrillation effectiveness of cellulose pulps. *Cellulose* **2013**, *20*, 2863–2875, doi:10.1007/s10570-013-0036-y.

104.   Soon, L.; Chiang, L. Influence of different extraction solvents on lipophilic extractives of Acacia hybrid in different wood portions. *Asian J. Appl. Sci.* **2012**, *5*, 107–116, doi:10.3923/ajaps.2012.107.116.

105.   Ververis, C.; Georghiou, K.; Danielidis, D.; Hatzinikolaou, D.G.; Santas, P.; Santa, R.; Corleti, V. Cellulose, hemicelluloses, lignin and ash content of some organic materials and their suitability for use as paper pulp supplements. *Bioresour. Technol.* **2007**, *98*, 296–301, doi:10.1016/j.biortech.2006.01.007.

106.   Oliaei, E.; Lindén, P.A.; Wu, Q.; Berthold, F.; Berglund, L.; Lindström, T. Microfibrillated lignocellulose (MFLC) and nanopaper films from unbleached kraft softwood pulp. *Cellulose* **2020**, *27*, 2325–2341, doi:10.1007/s10570-019-02934-8.

107.   Uetani, K.; Koga, H.; Nogi, M. Estimation of the Intrinsic Birefringence of Cellulose Using Bacterial Cellulose Nanofiber Films. *ACS Macro Lett.* **2019**, *8*, 250–254, doi:10.1021/acsmacrolett.9b00024.

108.   Meredith, R. Molecular orientation and the tensile properties of cotton fibres. *J. Text. Inst. Trans.* **1946**, *37*, T205–T218, doi:10.1080/19447024608659812.

109.   Niskanen, I.; Zhang, K.; Karzarjeddi, M.; Liimatainen, H.; Shibata, S.; Hagen, N.; Heikkilä, R.; Yoda, H.; Otani, Y. Optical Properties of Cellulose Nanofibre Films at High Temperatures. *J. Polym. Res.* **2022**, *29*, 1–11, doi:10.1007/s10965-022-03019-0.

110.   González, I.; Alcalà, M.; Chinga-Carrasco, G.; Vilaseca, F.; Boufi, S.; Mutjé, P. From paper to nanopaper: evolution of mechanical and physical properties. *Cellulose* **2014**, *21*, 2599–2609, doi:10.1007/s10570-014-0341-0.

111.   Islam, M.U.; Ullah, M.W.; Khan, S.; Shah, N.; Park, J.K. Strategies for cost-effective and enhanced production of bacterial cellulose. *Int. J. Biol. Macromol.* **2017**, *102*, 1166–1173, doi:10.1016/j.ijbiomac.2017.04.110.

112.   Saba, N.; Jawaid, M. Recent advances in nanocellulose-based polymer nanocomposites. In *Cellulose-Reinforced Nanofibre Composites: Production, Properties and Applications*; 2017 ISBN 9780081009659.

113.   Trache, D.; Tarchoun, A.F.; Derradji, M.; Hamidon, T.S.; Masruchin, N.; Brosse, N.; Hussin, M.H. Nanocellulose: From Fundamentals to Advanced Applications. *Front. Chem.* 2020.

114.   Fukuzumi, H.; Saito, T.; Iwata, T.; Kumamoto, Y.; Isogai, A. Transparent and high gas barrier films of cellulose nanofibers prepared by TEMPO-mediated oxidation. *Biomacromolecules* **2009**, doi:10.1021/bm801065u.

115.   Abdul Khalil, H.P.S.; Bhat, A.H.; Ireana Yusra, A.F. Green composites from sustainable cellulose nanofibrils: A review. *Carbohydr. Polym.* 2012.

116.   Dufresne, A. Nanocellulose: A new ageless bionanomaterial. *Mater. Today* 2013.

117.   Rajinipriya, M.; Nagalakshmaiah, M.; Robert, M.; Elkoun, S. Importance of Agricultural and Industrial Waste in the Field of Nanocellulose and Recent Industrial Developments of Wood Based Nanocellulose: A Review. *ACS Sustain. Chem. Eng.* **2018**, *6*, 2807–2828, doi:10.1021/acssuschemeng.7b03437.

118.   Mateo, S.; Peinado, S.; Morillas-Gutiérrez, F.; La Rubia, M.D.; Moya, A.J. Nanocellulose from agricultural wastes: Products and applications—a review. *Processes* **2021**, *9*, doi:10.3390/pr9091594.

119.   Naz, S.; Ali, J.S.; Zia, M. Nanocellulose isolation characterization and applications: a journey from non-remedial to biomedical claims. *Bio-Design Manuf.* **2019**, *2*, 187–212, doi:10.1007/s42242-019-00049-4.

120.   Charreau, H.; Cavallo, E.; Foresti, M.L. Patents involving nanocellulose: Analysis of their evolution since 2010. *Carbohydr. Polym.* **2020**, *237*, 116039, doi:10.1016/j.carbpol.2020.116039.

121.   Thomas, B.; Raj, M.C.; B, A.K.; H, R.M.; Joy, J.; Moores, A.; Drisko, G.L.; Sanchez, M. Nanocellulose, a Versatile Green Platform: From Biosources to Materials and Their Applications. *Chem. Rev.* **2018**, *118*, 11575–11625, doi:10.1021/acs.chemrev.7b00627.

122.   Foster, E.J.; Moon, R.J.; Agarwal, U.P.; Bortner, M.J.; Bras, J.; Camarero-Espinosa, S.; Chan, K.J.; Clift, M.J.D.; Cranston, E.D.; Eichhorn, S.J.; et al. Current characterization methods for cellulose nanomaterials. *Chem. Soc. Rev* **2018**, *47*, 2609, doi:10.1039/c6cs00895j.

123.   Hunter, R.J. Zeta Potential in Colloid Science 1st Edition. *Acad. Press* **2013**.

124.   Espinosa, E.; Sánchez, R.; Otero, R.; Domínguez-Robles, J.; Rodríguez, A. A comparative study of the suitability of different cereal straws for lignocellulose nanofibers isolation. *Int. J. Biol. Macromol.* **2017**, *103*, 990–999, doi:10.1016/J.IJBIOMAC.2017.05.156.

125.   Cai, J.; Zhang, L.; Liu, S.; Liu, Y.; Xu, X.; Chen, X.; Chu, B.; Guo, X.; Xu, J.; Cheng, H.; et al. Dynamic Self-Assembly Induced Rapid Dissolution of Cellulose at Low Temperatures. *Macromolecules* **2008**, *41*, 9345–9351, doi:10.1021/ma801110g.

126.   Ni, Y.; Li, J.; Fan, L. Production of nanocellulose with different length from ginkgo seed shells and applications for oil in water Pickering emulsions. *Int. J. Biol. Macromol.* **2020**, doi:10.1016/j.ijbiomac.2020.01.263.

127.   Abe, M.; Ogura, T.; Imura, T.; Misono, T.; Sakai, K.; Tsuchiya, K.; Torigoe, K.; Endo, T. *Measurement Techniques and Practices of Colloid and Interface Phenomena*; Abe, M., Ed.; Springer Nature Singapore, 2019;

128.   Tamayo Tenorio, A.; Gieteling, J.; Nikiforidis, C. V.; Boom, R.M.; van der Goot, A.J. Interfacial properties of green leaf cellulosic particles. *Food Hydrocoll.* **2017**, doi:10.1016/j.foodhyd.2017.04.030.

129.   Li, Q.; Xie, B.; Wang, Y.; Wang, Y.; Peng, L.; Li, Y.; Li, B.; Liu, S. Cellulose nanofibrils from Miscanthus floridulus straw as green particle emulsifier for O/W Pickering emulsion. *Food Hydrocoll.* **2019**, doi:10.1016/j.foodhyd.2019.105214.

130.   Seta, L.; Baldino, N.; Gabriele, D.; Lupi, F.R.; Cindio, B. de Rheology and adsorption behaviour of β-casein and β-lactoglobulin mixed layers at the sunflower oil/water interface. *Colloids Surfaces A Physicochem. Eng. Asp.* **2014**, doi:10.1016/j.colsurfa.2013.10.041.

131.   Yang, Y.; Zhang, M.; Zhao, J.; Wang, D. Effects of particle size on biomass pretreatment and hydrolysis performances in bioethanol conversion. *Biomass Convers. Biorefinery* **2022**, doi:10.1007/s13399-021-02169-3.

132. Lei, Y.; Zhang, X.; Li, J.; Chen, Y.; Liang, H.; Li, Y.; Li, B.; Luo, X.; Pei, Y.; Liu, S. Nanocellulose from bamboo shoots as perfect Pickering stabilizer: Effect of the emulsification process on the interfacial and emulsifying properties. *Food Biosci.* **2022**, *46*, 101596, doi:10.1016/j.fbio.2022.101596.

133. Du, K.; Glogowski, E.; Emrick, T.; Russell, T.P.; Dinsmore, A.D. Adsorption energy of nano- and microparticles at liquid-liquid interfaces. *Langmuir* **2010**, *26*, 12518–12522, doi:10.1021/la100497h.

134. Bao, C.; Chen, X.; Liu, C.; Liao, Y.; Huang, Y.; Hao, L.; Yan, H.; Lin, Q. Extraction of cellulose nanocrystals from microcrystalline cellulose for the stabilization of cetyltrimethylammonium bromide-enhanced Pickering emulsions. *Colloids Surfaces A Physicochem. Eng. Asp.* **2021**, doi:10.1016/j.colsurfa.2020.125442.

135. Coma, M.E.; Peltzer, M.A.; Delgado, J.F.; Salvay, A.G. Water kefir grains as an innovative source of materials: Study of plasticiser content on film properties. *Eur. Polym. J.* **2019**, *120*, 109234, doi:10.1016/j.eurpolymj.2019.109234.

136. Dima, S.O.; Panaitescu, D.M.; Orban, C.; Ghiurea, M.; Doncea, S.M.; Fierascu, R.C.; Nistor, C.L.; Alexandrescu, E.; Nicolae, C.A.; Trica, B.; et al. Bacterial nanocellulose from side-streams of kombucha beverages production: Preparation and physical-chemical properties. *Polymers (Basel).* **2017**, *9*, 5–10, doi:10.3390/polym9080374.

137. Sharma, C.; Bhardwaj, N.K. Biotransformation of fermented black tea into bacterial nanocellulose via symbiotic interplay of microorganisms. *Int. J. Biol. Macromol.* **2019**, *132*, 166–177, doi:10.1016/j.ijbiomac.2019.03.202.

138. Ramírez Tapias, Y.A.; Di Monte, M.V.; Peltzer, M.A.; Salvay, A.G. Bacterial cellulose films production by Kombucha symbiotic community cultured on different herbal infusions. *Food Chem.* **2022**, *372*, doi:10.1016/j.foodchem.2021.131346.

139. Cerrutti, P.; Roldán, P.; García, R.M.; Galvagno, M.A.; Vázquez, A.; Foresti, M.L. Production of bacterial nanocellulose from wine industry residues: Importance of fermentation time on pellicle characteristics. *J. Appl. Polym. Sci.* **2016**, *133*, 1–9, doi:10.1002/app.43109.

140. Sharma, C.; Bhardwaj, N.K. Fabrication of natural-origin antibacterial nanocellulose films using bio-extracts for potential use in biomedical industry. *Int. J. Biol. Macromol.* **2020**, *145*, 914–925, doi:10.1016/j.ijbiomac.2019.09.182.

141. Gullón, B.; Eibes, G.; Moreira, M.T.; Herrera, R.; Labidi, J.; Gullón, P. Yerba mate waste: A sustainable resource of antioxidant compounds. *Ind. Crops Prod.* **2018**, *113*, 398–405, doi:10.1016/j.indcrop.2018.01.064.

142. Medina Jaramillo, C.; Gutiérrez, T.J.; Goyanes, S.; Bernal, C.; Famá, L. Biodegradability and plasticizing effect of yerba mate extract on

cassava starch edible films. *Carbohydr. Polym.* **2016**, *151*, 150–159, doi:10.1016/j.carbpol.2016.05.025.

143. Saito, T.; Isogai, A. TEMPO-mediated oxidation of native cellulose. The effect of oxidation conditions on chemical and crystal structures of the water-insoluble fractions. *Biomacromolecules* **2004**, *5*, 1983–1989, doi:10.1021/bm0497769.

144. Shibata, I.; Isogai, A. Depolymerization of cellouronic acid during TEMPO-mediated oxidation. *Cellulose* **2003**, *10*, 151–158.

145. Espinosa, E.; Sánchez, R.; González, Z.; Domínguez-Robles, J.; Ferrari, B.; Rodríguez, A. Rapidly growing vegetables as new sources for lignocellulose nanofibre isolation: Physicochemical, thermal and rheological characterisation. *Carbohydr. Polym.* **2017**, doi:10.1016/j.carbpol.2017.07.055.

146. Saito, T.; Nishiyama, Y.; Putaux, J.; Vignon, M.; Isogai, A. Homogeneous Suspensions of Individualized Microfibrils from TEMPO-Catalyzed Oxidation of Native Cellulose. *Biomacromolecules* **2006**, *7*, 1687–1691.

147. Besbes, I.; Alila, S.; Boufi, S. Nanofibrillated cellulose from TEMPO-oxidized eucalyptus fibres: Effect of the carboxyl content. *Carbohydr. Polym.* **2011**, doi:10.1016/j.carbpol.2010.12.052.

148. Aguado, R.; Tarr, Q.; Mutj, P.; Angels, M.; Delgado-aguilar, M. Industrial Crops & Products Non-covalently cationized nanocellulose from hemp: Kinetics, key properties, and paper strengthening. *Ind. Crop. Prod.* **2022**, *188*, 115582, doi:10.1016/j.indcrop.2022.115582.

149. Vanderfleet, O.M.; Osorio, D.A.; Cranston, E.D. Optimization of cellulose nanocrystal length and surface charge density through phosphoric acid hydrolysis. *Philos Trans A Math Phys Eng Sci* **2018**, *376*, 20170041, doi:10.1098/rsta.2017.0041.

150. Desmaisons, J.; Boutonnet, E.; Rueff, M.; Dufresne, A.; Bras, J. A new quality index for benchmarking of different cellulose nanofibrils. *Carbohydr. Polym.* **2017**, doi:10.1016/j.carbpol.2017.06.032.

151. Cui, F.; Li, H.; Chen, C.; Wang, Z.; Liu, X.; Jiang, G.; Cheng, T. Cattail fibers as source of cellulose to prepare a novel type of composite aerogel adsorbent for the removal of enrofloxacin in wastewater. *Int. J. Biol. Macromol.* **2021**, *191*, 171–181.

152. Jia, N.; Li, S.M.; Ma, M.G.; Zhu, J.F.; Sun, R.C. Synthesis and characterization of cellulose-silica composite fiber in ethanol/water mixed solvents. *BioResources* **2011**, *6*, 1186–1195, doi:10.15376/biores.6.2.1186-1195.

153. Morcillo-Martín, R.; Espinosa, E.; Rabasco-Vílchez, L.; Sanchez, L.M.; de Haro, J.; Rodríguez, A. Cellulose Nanofiber-Based Aerogels from Wheat Straw: Influence of Surface Load and Lignin Content on Their Properties and Dye Removal Capacity. *Biomolecules* **2022**, doi:10.3390/biom12020232.

154.   Zhang, K.; Ismail, M.Y.; Liimatainen, H. Water-resistant nanopaper with tunable water barrier and mechanical properties from assembled complexes of oppositely charged cellulosic nanomaterials. *Food Hydrocoll.* **2021**, *120*, 106983, doi:10.1016/j.foodhyd.2021.106983.

155.   Perdoch, W.; Cao, Z.; Florczak, P.; Markiewicz, R.; Jarek, M.; Olejnik, K.; Mazela, B. Influence of Nanocellulose Structure on Paper Reinforcement. *Molecules* **2022**, *27*, 4696.

Chapter IV

Chapter V
Advanced and innovative applications

Section V.1 – *NCs-stabilized Pickering emulsions*

Section V.2 – *NCs capillary suspensions for oil structuring*

Section V.3 – *NCs-based aerogels for the removal of pollutants from wastewater*

Section V.4 – *Reinforcement materials for edible coatings*

Section V.5 – *Amine-modified NCs for CO_2 capture via adsorption*

Cellulose materials and in particular cellulose in the form of nanostructures have been proved in the previous chapter to be one of the most prominent green materials of modern times, owing to their attractive and excellent characteristics such as abundance, high aspect ratio, good mechanical properties, renewability, and biocompatibility. The abundant hydroxyl functional groups allow a wide range of functionalization via chemical reactions, leading to developing various materials with tunable features. In this chapter, recent advances in the preparation, modification, and emerging application of nanocellulose (NCs) are described and discussed, with special emphasis on Pickering emulsifiers, oleocolloids, adsorption, and nanocomposites. These research activities have been conducted to fulfill current needs in advanced application, and achieve the feasibility of the final materials, in particular (i) develop new methods/process to produce NCs-based materials; (ii) exploit NCs for advanced materials based on the specific feedstock, isolation process, and final properties; and (iii) decrease the energy- and time-consumption of the NCs-based materials.

Chapter V

Section V.1
NCs-stabilized Pickering emulsions

Nanostructured cellulosic material, nanofibrils (CNFs) and nanocrystals (CNCs), obtained through different mechanical treatments (i.e. BM and HPH) or TEMPO-mediated oxidation by changing catalyst concentration and processing time, were tested in the stabilization of Pickering emulsions, fabricated through high-pressure homogenization (HPH). Moreover, this section aimed also at studying the stabilization of O/W Pickering emulsions using HPH micronized tomato pomace. Results showed that both CNFs and CNCs provided efficient steric and electrostatic stabilization of the oil-in-water emulsions. Remarkably, the strong inter-droplet interactions, observed when CNFs were used as stabilizers, because of long fibers with higher flexibility and fibrils entanglement in the continuous phase, resulted in a 3D fibrous network emulsion, with higher viscosity than CNCs-stabilized emulsions, and higher tendency towards flocculation. HPH-treated tomato pomace gave similar results in terms of particle morphology and interfacial tension, and slightly lower emulsion stabilization capability than HPH-treated cellulose, suggesting that the used mechanical disruption process does not require cellulose isolation for its efficient defibrillation. Therefore, the HPH treatment significantly affected the nanofibrils interfacial layer, promoting the emulsifying ability of CNFs, and increasing stability against coalescence. In contrast, CNCs-stabilized emulsions exhibited, along with lower viscosity, higher interfacial activity, and emulsion stabilization capability, without any phase separation during 10 months of refrigerated storage. Emulsion stability tests, carried out at 4 °C for 28 d or under centrifugation at different pH values (2.0, 7.0, and 12.0), revealed that CNFs limited the occurrence of coalescence phenomena and significantly slowed down gravitational separation. Remarkably, it can be concluded that NCs with tailored emulsifying properties can be easily obtained through the regulation of the process intensity of TEMPO-mediated oxidation of pulp cellulose or changing the mechanical

treatments, opening the way to the production of new ingredients for the food and cosmetic industries.

V.1.1. Specific goal and work plan

Emulsions are mixtures of two immiscible liquids, with one of them finely dispersed in the form of small droplets into the continuous phase of the other liquid [1], for example, oil droplets dispersed in water (O/W emulsions). Since emulsions are thermodynamically unstable systems, tending towards complete phase separation, their properties are bound to change over time. The rate of change of emulsion properties, and in particular droplet size distribution, in comparison with the expected shelf life of the product containing the emulsion, defines emulsion kinetic stability [2]. Different mechanisms accelerate emulsion instability phenomena. Physical instability mechanisms include flocculation, coalescence, Ostwald ripening, gravitational separation, and phase inversion [3], whereas the most common sources of chemical instability are lipid oxidation and degradation of functional ingredients, such as aroma, flavor, or health-beneficial compounds [4]. A (kinetically) stable emulsion can resist the environmental stimuli experienced during emulsion incorporation into the final product, and subsequent transformation, storage, and preparation, such as exposure to extremes of temperature, pH, ion concentration, radiation, or shearing [3]. Optimal emulsion performance, in terms of ease of preparation and stability over time, is ensured by the proper selection of interfacial agents, such as surfactants or polymeric emulsifiers, which reduce the interfacial tension between the two phases, stabilizing the emulsion droplet during emulsification and storage, and therefore delaying phase separation.

Emulsions can be efficiently stabilized also by colloidal particles, instead of surfactants or emulsifiers molecules, forming the so-called Pickering emulsions [3]. Solid particles irreversibly adsorb at the liquid/liquid interfaces because of their high interfacial adsorption energy, forming a dense film around the oil droplets, which prevents droplet coalescence mainly through steric repulsion [5], maintaining excellent stability over time regardless of the external environmental stimuli. Moreover, since several edible natural substances (e.g., polysaccharides, proteins, and lipids) can be used as solid particulate stabilizing materials, Pickering emulsions generally exhibit lower toxicity and better biocompatibility and food compatibility than emulsions stabilized by surfactants [6], which is matter of health and environmental concerns. Many researchers have focused on the utilization of proteins for this purpose, derived from animal, plant, or microbial sources [7]. Although protein particles can be produced in nanometric size, protein-based particle-stabilized emulsions are generally sensitive to coalescence at pH around their isoelectric points and are susceptible to proteolytic enzymes [8].

Recently, polysaccharide-based particles have attracted increasing attention as potential stabilizers in multi-phase food systems. Among polysaccharides, nanostructured cellulose is particularly suitable for the stabilization of edible Pickering emulsions, of interest in the fields of biomedicine, food, and cosmetics [6]. Nanosized cellulosic materials (NCs) possess several advantages deriving from their nanometric sizes, such as high tensile strength, stiffness, and surface functional groups. When used as a stabilizer in O/W emulsions, NCs are reported to significantly enhance the properties and performance in comparison with conventional systems [9].

NCs are generally prepared using a top-down approach to isolate the semi-crystalline individual nanofibers or extract the crystalline portion. The chosen process and its processing conditions determine the type of NCs produced: cellulose nanocrystals (CNCs) are produced from chemical and enzymatic treatments, and cellulose nanofibrils (CNFs) are obtained by either mechanical or chemical treatments [10–12], with high and low aspect ratios, respectively. In particular, while the diameter of CNFs is in the nanoscale, i.e., less than 100 nm, their length is typically up to a few micrometers, and disordered regions are still present in the fibrils. Conversely, CNCs are rod-like crystalline structures, with diameters of 2 - 25 nm and lengths from 100 to 750 nm [13]. The tuning of the structure of these nanomaterials, while preserving the similar chemical nature, offers an interesting opportunity to investigate the effect of the physical (i.e. morphological) parameters on the characteristics and stability of the Pickering emulsions. More specifically, the exploitation of different types of cellulose-based nanomaterials, such as CNFs and CNCs, represents a promising strategy to increase the technologic and profitable potential of NCs in the fabrication of food-grade Pickering emulsions, due to their unique properties and excellent sustainability, biocompatibility, and renewability.

This section aimed to investigate the structure effect of different cellulose nanoparticles, such as CNFs and CNCs, obtained by TEMPO-mediated oxidation or mechanical treatments from cellulose pulp and HPH-micronized tomato pomace, on the production and stabilization of oil-in-water Pickering emulsions (Figure V.1). In particular, the correlation between the physicochemical properties of different NCs with emulsion properties (mean diameter, ζ-potential, microstructure, and rheological properties) is investigated to understand how to improve emulsions behavior and stability over time in function of isolated NCs.

V.1.2. Specific material and methods
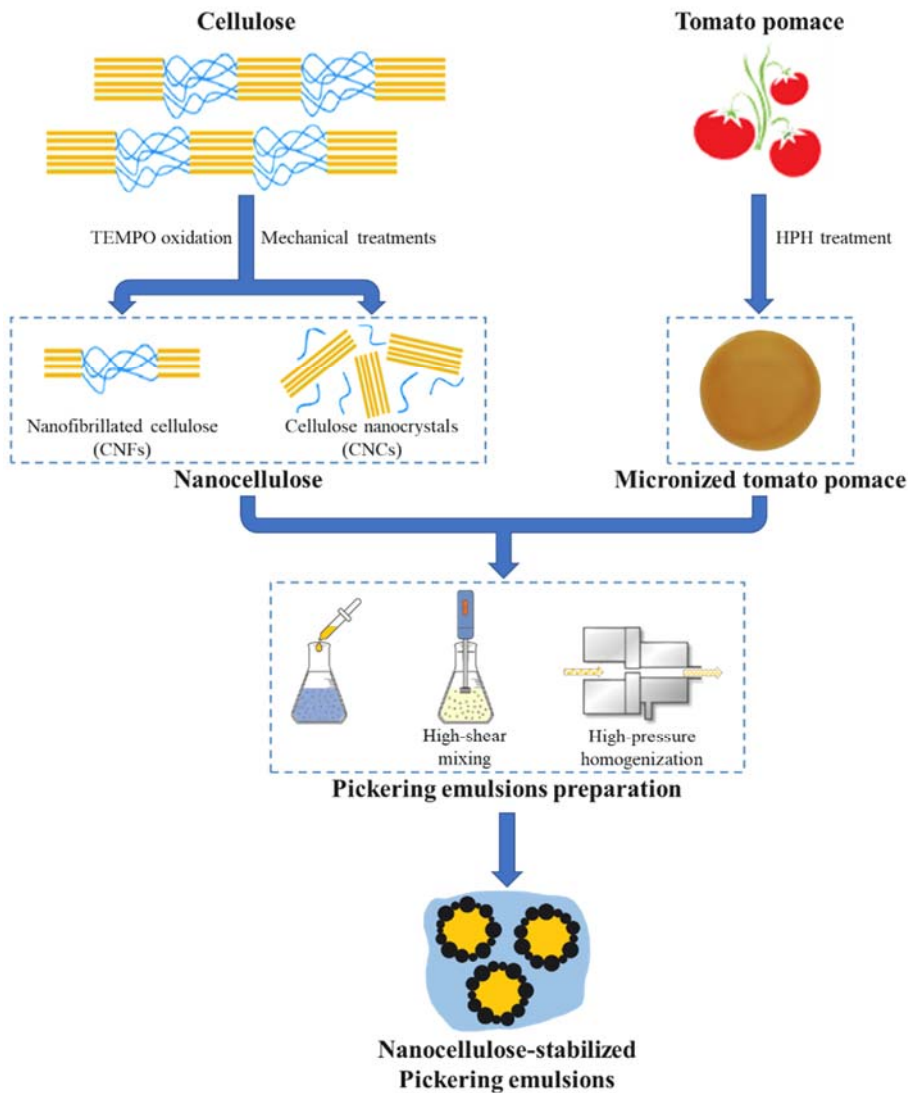
Figure V.1 *Schematic representation of methodology used for Pickering emulsion preparation stabilized by NCs and HPH micronized tomato pomace.*

V.1.2.1. Materials

NCs were obtained thought TEMPO-mediated oxidation of northern bleached softwood kraft pulp Celeste 85, as described in detail in section § III.5.1, and identified as CNCs-C85 and CNFs-C85. NCs were also obtained through BM and HPH treatment on Commercial cellulose Arbocel® BWW40,

as described in detail in sections § III.5.2.1 and § III.5.2.2, respectively. Nanoparticles are identified as BM30-CNFs and BM60-CNFs for ball milled cellulose pulp and HPH-CNFs for HPH-treated cellulose pulp. Tomato pomace has been micronized through HPH treatment (sample HPH-TP) as described in section § III.3.2.

Peanut oil, purchased from a local market (Olio di Semi di Arachide Giglio Oro, Firenze, Italy), was used as the oil phase. Its composition (on weight basis, based on manufacture's specification) comprises 18 wt% of saturated fatty acids, 46 wt% of monounsaturated fatty acids, and 28 wt% of polyunsaturated fatty acids.

All reagents were of analytical grade unless otherwise stated. Micro-pure deionized water was used throughout the experiments.

V.1.2.2. Preparation of Pickering emulsions

Coarse oil-in-water emulsions were prepared by mixing peanut oil (5 wt%) with the aqueous phase (95 wt%) containing 0.5 wt% of NCs or HPH-TP in ultrapure H_2O, in a high-shear mixer (HSM) (MIULab MT-30K Handheld Homogenizer, Hangzhou, China) at 35,000 rpm for 5 min in an ice bath. The obtained coarse emulsions were then treated through a HPH process at 80 MPa for 15 equivalent passes, with the heat exchangers set at 5 °C, in a lab set-up (orifice-type homogenizer) previously described in detail by Pirozzi et al. (2021) [14].

V.1.2.3. Pickering emulsions characterization

The microscopic structure of Pickering emulsions was observed using the optical inverted microscope Nikon Eclipse equipped with a polarization filter, with a 10× objective, coupled to a DS Camera Control for image acquisition and analysis, as described in § III.7.3.4.1. Prepared solutions were observed also using a polarizing light to observe NCs birefringence. The anisotropic properties and the microstructure of the different Pickering emulsions were also measured with the same microscope. For fluorescence measurements, 10 μL of Nile Red (1 mg/mL in ethanol) was added to 100 μL of collected samples to stain the oil phase before observations.

The emulsions size distributions were measured by laser diffraction using a Mastersizer 2000 instrument (§ III.7.3.5), using the Fraunhofer approximation, which does not require knowledge of the optical properties of the sample. The temperature of the cell was maintained at 25 ± 0.5 °C. Characteristic diameters d(0.1), d(0.5), and d(0.9), corresponding to the 10th, 50th (median value), and 90th percentile of the cumulative size distribution of the suspensions, were evaluated. Additionally, the surface-weighted mean diameter D[3,2] and volume-weighted mean diameter D[4,3] were determined according to Equations III.4 and III.5. The relative span factors were

calculated according to Equation III.6, to express the distribution width of the droplet size distribution.

The surface coverage (SC) of NCs of the internal phase of the Pickering emulsions was given by the theoretical maximum surface area by the particles (SP) divided by the total surface displayed by the oil droplets (S_d) according to the following equation [15–17]:

$$SC = \frac{S_P}{S_d} = \frac{m_P \cdot D[3,2]}{6 \cdot h \cdot \rho_P \cdot V} \tag{V.1}$$

where m_P is the mass of particles in the Pickering emulsion (g), D[3,2] is the surface-weighted mean diameter, h is the thickness of cellulose fibers, ρ_P is the cellulose density (1.6 g cm^{-3}) and V is the volume of oil used in the Pickering emulsion (mL).

The rheological properties of Pickering emulsions were characterized by using a rotational rheometer (AR 2000 rheometer, TA instruments, Newcastle, DE, USA), equipped with a concentric cylinder (15 mm stator inner diameter, 28 mm rotor outer diameter, 42 mm cylinder immersed height, 2° cone angle). Viscosity curves were obtained by changing the shear rate from 0.1 s^{-1} up to a rate of 200 s^{-1} and the temperature was set at 20 °C. The viscosity measurements were repeated five times for each emulsion. Newtonian model (Equation V.2) and Power Law (Ostwaldde-Waele) models (Equation V.3) [18] were used to fit the experimental data.

$$\tau = \eta \cdot \dot{\gamma} \tag{V.2}$$
$$\tau = K \cdot \dot{\gamma}^n \tag{V.3}$$

where τ is the shear stress, η is the viscosity, K is the consistency index, n is the flow behavior index, and $\dot{\gamma}$ is the shear rate.

The emulsion's stability was determined according to the turbidimetric method [19]. The absorbance values of freshly prepared emulsions (t_0) and after 30 min (t_{30}) were read at 500 nm against a blank (dilution solution) following the introduction of 50 μL of emulsion into 5 mL of 0.1 wt% sodium dodecyl sulfate (SDS) solution. The emulsifying activity index (EAI) and the emulsion stability index (ESI) were calculated using Equation V.4 and V.5, respectively.

$$EAI \left(\frac{m^2}{g}\right) = 2 \cdot \frac{T}{(1 - \vartheta) \cdot C \cdot 1{,}000} \tag{V.4}$$

$$ESI \left(-\right) = \frac{EAI_{t_0}}{EAI_{t_0} - EAI_{t_{30}}} \cdot 100 \tag{V.5}$$

where T is the turbidity, ϑ is the volume fraction of oil used to form the emulsion, and C (g mL^{-1}) is the initial concentration of NCs. EAI_{t0} and EAI_{t30} are the emulsifying activity indexes calculated at 0 and 30 min, respectively. The turbidity was calculated by using Equation V.6:

$$T = 2.303 \cdot \frac{A \cdot DF}{OP} \tag{V.6}$$

where A is the absorbance of the sample at t_0 and 500 nm, DF is the dilution factor, and OP is the optical path (1 cm, in the used equipment).

V.1.2.4. Influence of environmental stimuli on emulsions stability

Emulsion stability was assessed by visual observation and monitored by taking photos for a storage period of at least one month at 4 °C. Moreover, accelerated stability tests against gravitational separation were also conducted, by centrifuging the emulsions at 3,500 rpm for 10 and 20 min, which are considered equivalent to a gravitational acceleration field applied for around six and twelve months, respectively [20]. The effects on the stability of the Pickering emulsions of pH over storage were investigated through microstructure observation and rheological analysis. The pH of the emulsions was adjusted from 2 to 12 using 0.1 mol/L of HCl solution and 0.1 mol/L of NaOH solution.

V.1.2.5. Statistical analysis

Statistically significant differences ($p < 0.05$) between the means were evaluated using a one-way analysis of variance (ANOVA), performed with SPSS 20 (SPSS Inc., Chicago, IL, USA) statistical package, and Tukey's test. At least three replicates were conducted for each analysis otherwise specified. All the data were reported in the form of mean ± SD.

V.1.3. Results and discussion

V.1.3.1. Characteristics of Pickering emulsions

The digital pictures and optical microscopic images, and of freshly prepared Pickering emulsions stabilized with NCs and with HPH-TP at 5 wt% oil phase are shown in Figure V.2. In the right column of Figure V.2, cellulose and oil are distinguishable in the fluorescence micrographs, where the cellulose birefringence can be recognized by yellowish shades, and the Nile-red stained oil is also evident as red domains. The oil droplets of CNFs-C85 stabilized emulsions showed a spherical structure with a uniform size of about 3 μm (Figure V.2b). When the stabilizer was CNCs-C85, the emulsion was still uniform in size, but the particles, characterized by a greater rigidity, were not able to completely cover the oil droplets, remaining partly dispersed in the aqueous phase (Figure V.2a). Nevertheless, no phase separation occurs during storage at 4 °C (data not shown). The appearance of the emulsions prepared with BM-CNFs, shown in Figure V.2c-d, suggests that the cellulose particles do not completely cover the oil droplets, but remain largely dispersed in the aqueous phase. This effect is also confirmed by the fluorescence micrographs

in Figure V.2a-b (corresponding to the brightfield micrographs in the left column), which highlights the uniform fiber dispersion in water as a green shade observed in the entire continuous phase. This agrees well with the limited stability of these emulsions, associated with droplet coalescence, causing complete phase separation within 24 h after preparation (data not shown). Interestingly, for the emulsions prepared with HPH-CNFs and HPH-TP (Figure V.2e-f), the particles form large irregular domains aggregated around the oil droplets, efficiently entrapping them and maintaining the oil in emulsified form. In the case of HPH-CNFs and HPH-TP emulsions, no fluorescent reflection was observed in the continuous phase. This observation indicates that these solid particles are mainly aggregated around the oil droplets and close to the oil-water interface, leading to the efficient stabilization of the Pickering emulsions. In these emulsions, no coalescence phenomena were observed over 28 d at 4 °C (no evidence of oiling off), but only gravitational separation and associated creaming. Vigorous mixing was sufficient to form again the emulsion. These systems displayed outstanding stability against droplet coalescence likely as a consequence of steric stabilization due to the different cellulose configuration in comparison with BM cellulose, and also possibly to the thickening effect of the aqueous phase due to the longer cellulose chains [21]. Different efficiency in O/W stabilization can be related to the difference in morphological properties (shape and size) of nanoparticles cellulose chains: flexible and defibrillated nanocellulose (CNFs-C85, HPH-CNFs and HPH-TP) are likely to diffuse faster, and better cover smaller oil droplets. Another possible reason for this phenomenon was the aggregation of nanofibrillated cellulose and thickening effect of the aqueous phase due to the longer cellulose chains: therefore, entrapping of the oil droplets was more efficient, and a 3D emulsified structure was promoted. It can be speculated that the improved capacity of entanglement allows to bridge the neighbouring droplets to create an entangled droplet fiber 3D network.

Brightfield   **Fluorescence**

(a)

(b)
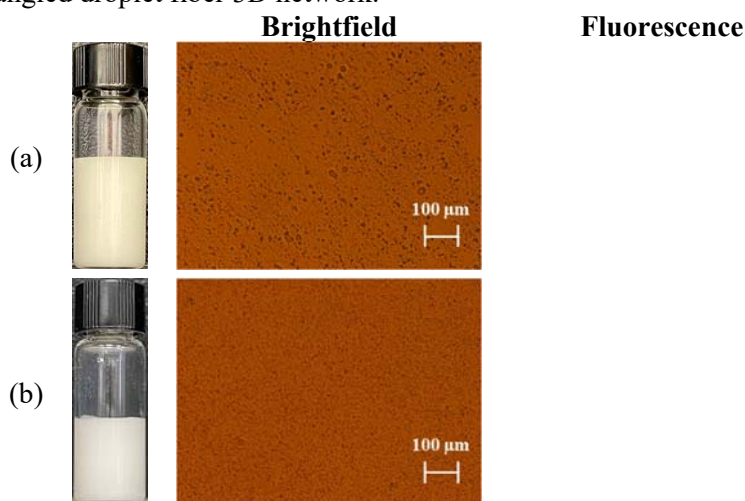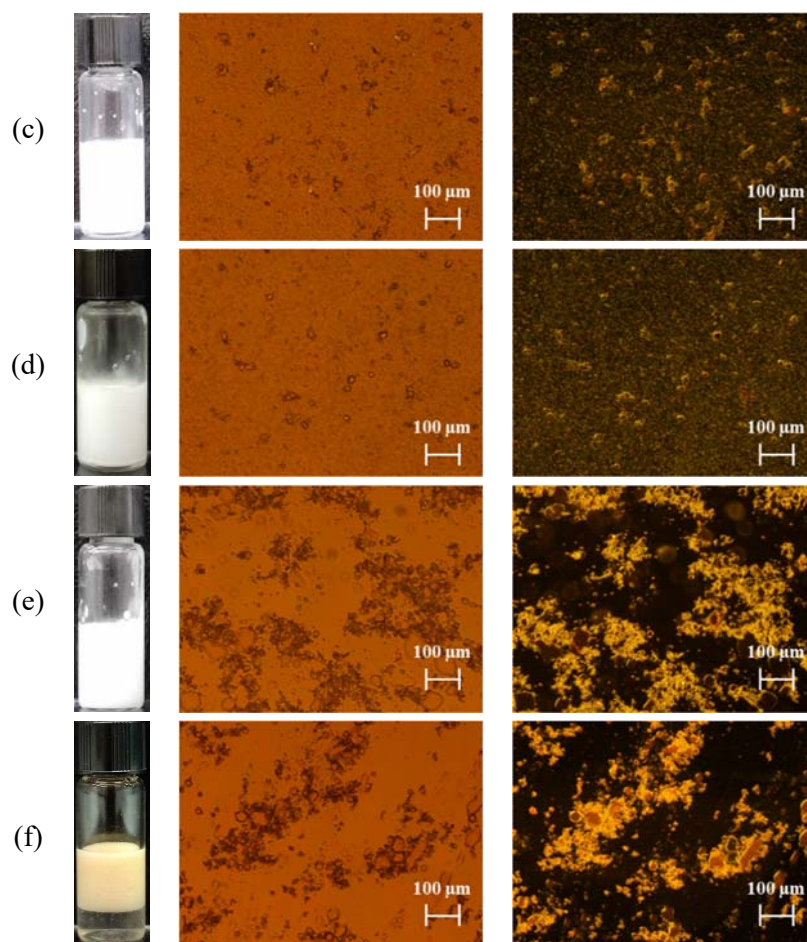
Figure V.2 *Comparison between brightfield (left column) and fluorescence (right column) micrographs of emulsion stabilized with (a) CNCs-C85, (b) CNFs-C85, (c) BM30-CNFs, (d) BM60-CNFs, (e) HPH-CNFs, and (f) HPH-TP.*

Generally, the differences in interfacial tension and ζ-potential (§ IV.3.3.1) can be related to the observed difference in emulsifying performance, such as ability to act onto the oil-water interface, the promotion of droplet formation, and the increase of droplet stability induced by electrostatic repulsion [6]. Remarkably, despite the differences in interfacial tension and ζ-potential, all NCs samples excluding BM-CNFs, displayed outstanding stability against droplet coalescence, without any phase separation under refrigerated storage at 4 °C, likely because of the efficient steric and electrostatic stabilization.

Chapter V

In order to further understand the mechanisms of Pickering emulsion stabilization with NCs, the droplet size distribution (Figure V.3) and mean droplet diameters (Table V.1) of the emulsions were measured. The particle size distribution of emulsions stabilized with NCs isolated via TEMPO-mediated oxidation presented a monomodal and narrower droplet size distribution (peak around 1 μm and span of 1.2 and 1.4 for CNCs and CNFs, respectively). Meanwhile, the particle size distribution of emulsions stabilized with NCs isolated via mechanical processes was multimodal, with two or more peaks in the distribution curve within a range from 1 to 100 μm. It can be observed that the measured size distributions are coherent with the micrographs of Figure V.2. Indeed, BM-CNFs and HPH-treated materials displayed no-uniform droplets in dimension, while the Pickering emulsions with CNCs-C85 or CNFs-C85 became uniform and displayed many smaller droplets in dimension. Furthermore, the droplet size distribution of mechanical-treated samples is characterized by d(0.9) in the range of 54 - 84 μm. On the other hand, d(0.9) of CNCs-C85 and CNFs-C85 stabilized Pickering emulsions is in the micrometric size range, of about 2 and 3 μm, respectively. The volume mean diameters D[4,3] were in the range of 1 - 23 μm, the surface mean diameters D[3,2] in the range of 1 - 10 μm (Table V.1). Low D[3,2] values are generally associated with higher kinetic stability because of the reduction of the effects of the gravitational phase separation, this, in turn, is due to the fact that the droplets separation velocity is proportional to the square radius [22].
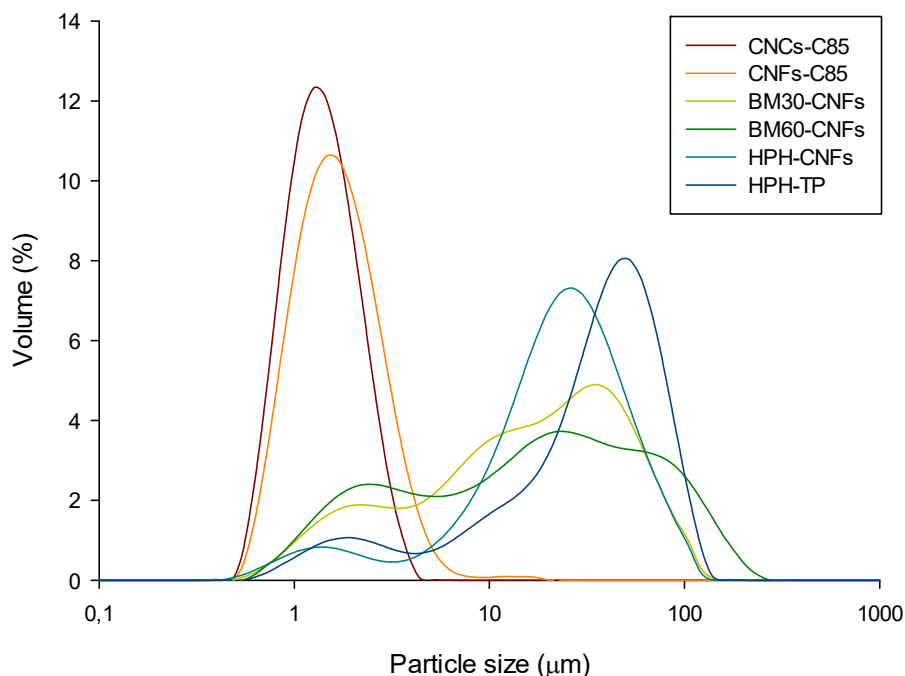
Figure V.3 *Droplet size distribution of the oil-in-water Pickering emulsion.*

Table V.1 *Particle size distribution (expressed as characteristic diameters) of Pickering emulsions.*

	CNCs-C85	CNFs-C85	BM30-CNFs	BM60-CNFs	HPH-CNFs	HPH-TP
d(0,1)	0.75	0.83	1.92	1.79	5.02	3.82
d(0,5)	1.27	1.50	15.60	16.65	21.75	34.40
d(0,9)	2.23	2.93	54.44	84.25	53.85	72.73
D[4,3]	1.40	1.77	22.90	31.11	26.38	37.05
D[3,2]	1.18	1.37	5.70	5.44	8.45	9.83

In addition, to evaluate the influence of particle types on the stabilization of emulsion, the surface coverage has been determined, by investigating the relationship between the size of the emulsions as a function of the volume fraction of dispersed phase (i.e. oil) and estimating the emulsion coverage as the maximum number of particles entrapped at the droplet interface. The percentage coverage of the emulsions stabilized with TEMPO-mediated oxidation isolation process of NCs was higher than 100% (377% and 131% for CNCs and CNFs, respectively). This could be ascribed to the content, physical size, and morphology of NCs, whose fibrous particles linked or overlapped at the oil-water surface. Meanwhile, the surface coverage of emulsions stabilized with mechanical-treated samples was less than 100% (11%, 17%, 81%, and 47% for BM30-CNFs, BM60-CNFs, HPH-CNFs, and HPH-TP, respectively). Based on these results, it can be inferred that the CNCs-C85, CNFs-C85, and HPH-CNFs particles had a significant influence on the O/W interface, where they likely associate and form a three-dimensional network entrapping the emulsion droplets and inhibiting them from freely moving, hence contributing to improving emulsion stability.

The strong interaction between the nanomaterials and the oil droplets, as suggested by the present data, can promote the physical stability of the Pickering emulsions, by (i) increasing the viscosity of the continuous phase; (ii) reducing the emulsion droplets size; and/or (iii) reducing the difference in density between the continuous phase and the disperse one [6,23–26].

Therefore, the rheological properties of the emulsions have been evaluated for interpreting the effect of morphological properties of NCs on the viscosity of the emulsions, in relation to their stability, through flow measurements in steady-state conditions. The viscosity of Pickering emulsions (Figure V.4) showed the typical non-Newtonian shear thinning behavior, i.e. the apparent viscosity decreased at increasing shear rate, with a in the entire shear rate range of 0.1 to 100 s^{-1}. The decrease in viscosity can be linked to the structural deformation of emulsion, since the breakdown of the entangled three-dimensional networks of nanofiber bundles [27,28] and their orientation along flow lines upon the shear force application [29]. CNFs-C85 favored the increase of emulsion apparent viscosity values [30] with respect to the same amount (mg/mL) of CNCs-C85, due to their peculiar morphological properties. The long, flexible, and defibrillated fibers interacted strongly in the O/W emulsion system and consequently formed internal entanglements in the continuous phase.

These results suggest that CNFs-C85 particles are prone to strongly interact through Van der Waals forces and/or hydrogen bonds in the continuous phase, with a consequent increase in viscosity. The strong 3D emulsion network formed leads to restricted movement of the oil droplets and improved emulsion stability. Different mechanical treatments on cellulose influenced also the rheological behavior of Pickering stabilized emulsions. It can be noticed that both emulsions stabilized with BM cellulose demonstrated the occurrence of hysteresis (data not shown) within the range of shear rate investigated, suggesting significant instability during shearing. Moreover, it was observed that the HPH-CNFs emulsion viscosity displayed higher viscosity values, indicating strengthened attractive forces between the emulsion droplets, which likely contributed to forming a three-dimensional network structure of the highly flexible fibers shown in Figure V.2e. This consideration is in very good agreement with the observed emulsion microstructure and the interfacial tension measurements.
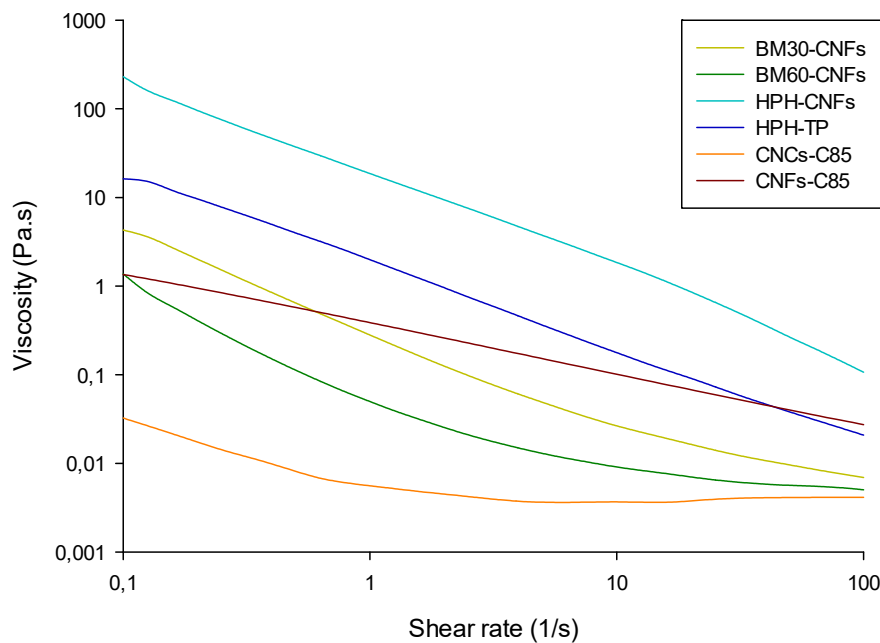
Figure V.4 *Flow measurements (viscosity as a function of shear rate) in steady-state conditions of freshly prepared emulsion. Each flow curve is the average of five measurements.*

V.1.3.2. Stability of Pickering emulsions stabilized with chemical

isolated NCs

To examine the long-term stability of different types of NCs on Pickering emulsions, the change in the microstructure and the mean droplet diameter upon aging for 10 months at 4 °C was monitored. Figures V.5 displays microscope images of the emulsions stabilized by CNCs-C85 and CNFs-C85. Visual observations show that CNCs-C85 could efficiently stabilize the Pickering emulsions, without showing any sign of precipitation or flocculation during the entire storage period. The appearance of CNCs-C85 stabilized emulsion suggested no occurrence of phase separation after 10 months. Emulsion droplet size distribution exhibited some changes over the storage period, with the appearance of a peak at smaller size and the reduction in volume of the initially observed peak. This phenomenon can be attributed to the onset of coalescence, which caused an initial increase in droplet size, associated with the reduction of the surface area to be covered by the CNCs-C85 particles, with the suspension in water of CNCs-C85 particles no more adsorbed at the O/W surface. At the same time, the reduction of the O/W specific surface is also reported to increase the surface coverage of droplets, whereby a network structure is formed that prevents oil droplets from further condensing together into larger droplets [31]. In contrast, flocculation of the emulsions prepared with CNFs-C85 can be clearly observed at the end of the storage period, through the formation of aggregates visibly by naked eye and through optical microscopy (Figure V.5). This instability phenomenon can be ascribed to bridging flocculation, in agreement with the observed increase in CNFs-C85 emulsion viscosity because of fiber entanglements in the continuous phase.

(a)   (b)
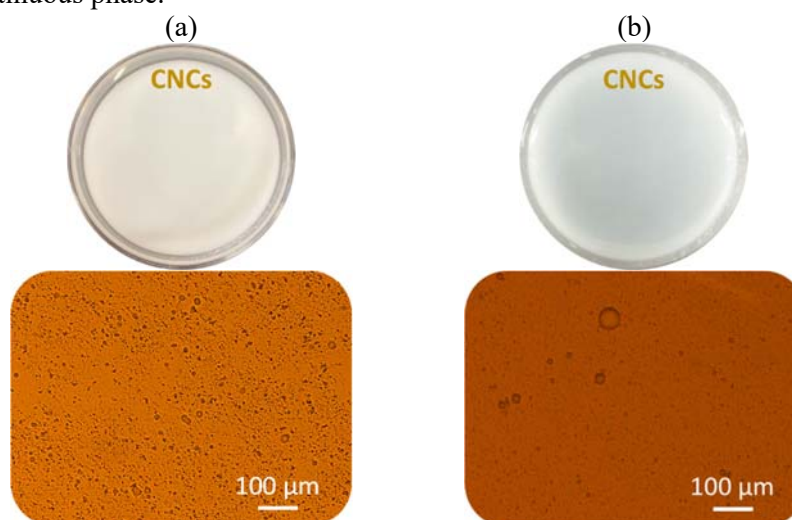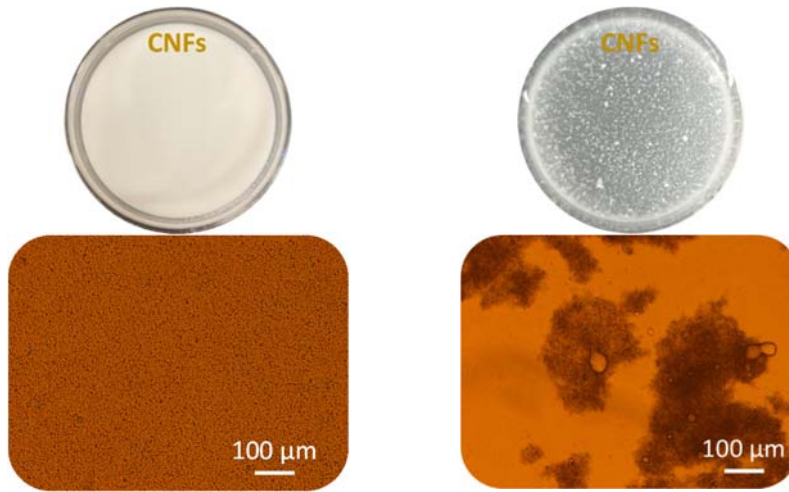
Figure V.5 *Visual observation and micrographs of (a) freshly prepared Pickering emulsions and (b) emulsions after 10 months of storage at 5 °C (10x of magnification) stabilized by CNCs-C85 and CNFs-C85 at first and second row, respectively.*

The formation of aggregates is clearly visible also from the particle size distribution data in Figure V.6, which might be due to CNFs-C85 chain interactions which led to droplet flocculation through particle bridging mechanism at O/W interface.
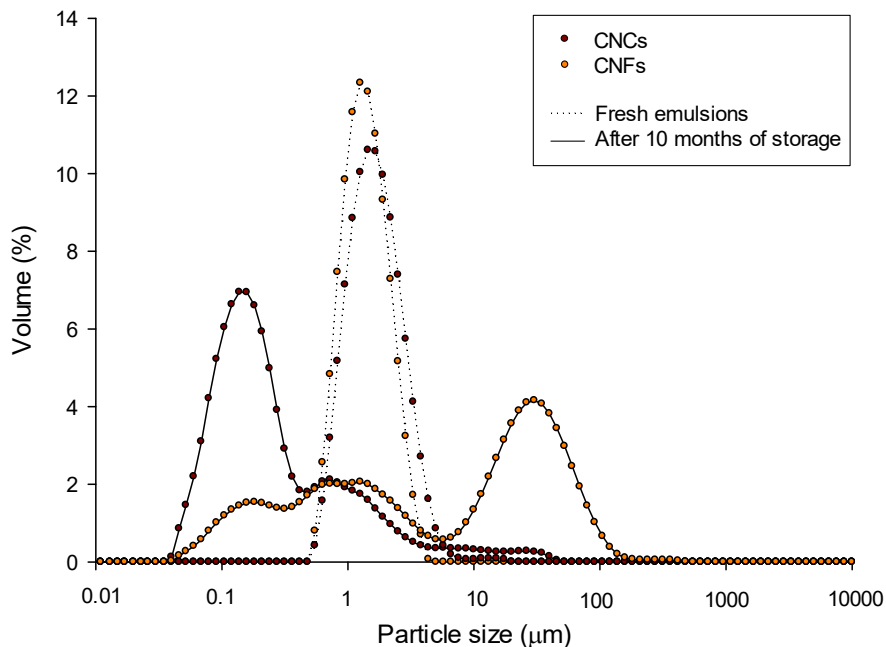
Figure V.6 *Droplet size distributions of CNCs-C85 and CNFs-C85 stabilized emulsions on day 0 (··· dotted line) and 10 months (— solid line).*

252

The emulsifying activity and emulsion stability, the most important parameters to estimate the emulsifier ability to form a stable emulsion, were determined for both fresh emulsions and emulsions stored for 10 months at refrigerated conditions. EAI and ESI, evaluated through Equations V.4 and V.5 and reported in the Table V.2, are greatly dependent on the hydrophobicity and the ionic charge of CNCs-C85 and CNFs-C85. After preparation, a significantly ($p < 0.05$) higher value of the index of the interfacial area stabilized per unit of weight (EAI = 186 ± 4 m^2/g) was observed for CNCs-C85. This phenomenon was attributed to the smaller molecules that could quickly diffuse and adsorb onto the oil-water interface [32,33]. Simultaneously, ESI was 0.14 ± 0.03 and 0.33 ± 0.09% for CNCs-C85 and CNFs-C85 stabilized emulsions, respectively. ESI of CNFs-C85 emulsion was significantly ($p < 0.05$) higher than for the CNCs-C85 stabilized emulsion, likely because of the higher molecular flexibility of CNFs-C85, an important factor for forming a compact interfacial layer and promoting emulsion stability. After the storage period, emulsions exhibited lower EAI values than those freshly prepared, but constant ESI values. The capability to stabilize emulsions (ESI) was higher in CNFs-C85 stabilized emulsions mainly because of the higher viscosity of the continuous phase, which slowed down gravitational separation phenomena.

Table V.2 *Emulsifying activity (EAI) and emulsion stability (ESI) parameters of Pickering emulsions stabilized by CNCs-C85 and CNFs-C85.*

	Fresh emulsions		After 10 months of storage	
	CNCs-C85	CNFs-C85	CNCs-C85	CNFs-C85
EAI (m^2/g)	186.03 ± 4.40[d]	150.02 ± 2.98[c]	54.27 ± 4.02[b]	45.23 ± 4.16[a]
ESI (%)	0.14 ± 0.03[a]	0.33 ± 0.09[b]	0.17 ± 0.10[a]	0.32 ± 0.02[b]

Different letters denote significant differences ($p < 0.05$) among the different samples within each row (n = 3).

V.1.3.3. Stability of Pickering emulsions stabilized with mechanical isolated NCs

The influence of pH on the physical stability of the Pickering emulsion stabilized by BM-CNFs, HPH-CNFs and HPH-TP is of interest for application in processed foods as well as during gastrointestinal digestion [34]. The stability of emulsions stored at 4 °C for 28 d at different pH values (2.0, 7.0, and 12.0) was evaluated upon centrifugation (3,500 rpm for 10 and 20 min) in terms of changes in microstructure (Figure V.7).

In Figure V.7, the red, yellow, and dark regions represent oil droplets, cellulose, and water, respectively. The oil phase is always completely encapsulated by water inside the emulsions in the form of spherical droplets.

Chapter V

Large oil droplets for all emulsions were observed under acidic conditions (pH = 2.0), thus indicating substantial droplet aggregation and low emulsion stability across this pH range [35].

During the storage period, creaming (dense layer floating on the top) and/or sedimentation (pellet layer at the bottom) occur for emulsions stabilized with BM30-CNFs and BM60-CNFs, as a consequence of gravitational separation. This observation indicates the poor stability of these emulsions, which is particularly evident at low pH, where a clear serum is formed. Moreover, some oiling off is also observed, suggesting the occurrence of coalescence phenomena.

When compared with the emulsion stabilized by BM-treated cellulose, HPH-CNFs, and HPH-TP provided better coverage of the oil droplets' surface, thus increasing the dimensional resistance among droplets, which reduced coalescence of the droplets also by changing the pH environmental factor (no oiling off observed after 28 d or centrifugation). In particular, for HPH-CNFs no creaming nor sedimentation was observed during storage, suggesting the high stabilization efficiency of the resulting emulsion at all tested pH values. In the case of HPH-TP, clear serum appeared at the bottom already from day 0, with some evidence of sedimentation only at pH = 2. In general, HPH-treated systems produced more stable emulsions than BM-treated cellulose. However, in the case of tomato pomace, a higher solid content is likely necessary to compensate for the fact that cellulose is only a fraction of the overall solids (about 37% on dry matter), and, therefore, lower emulsification ability is recorded.
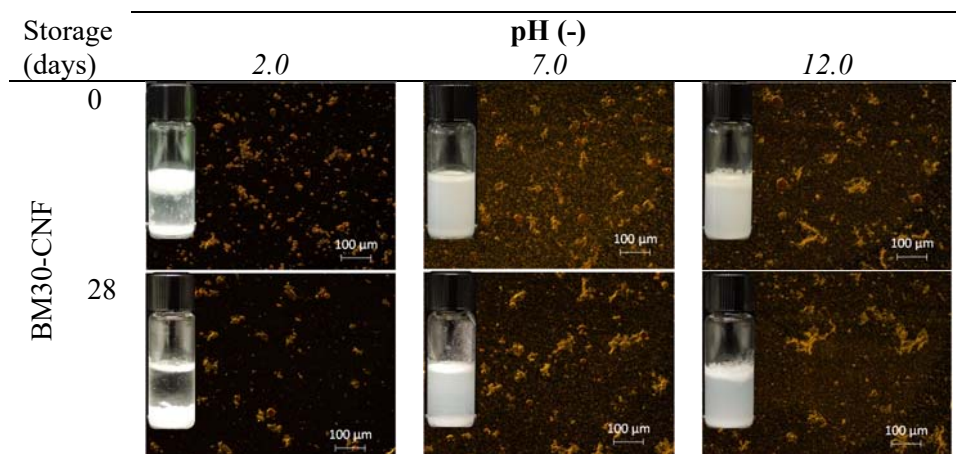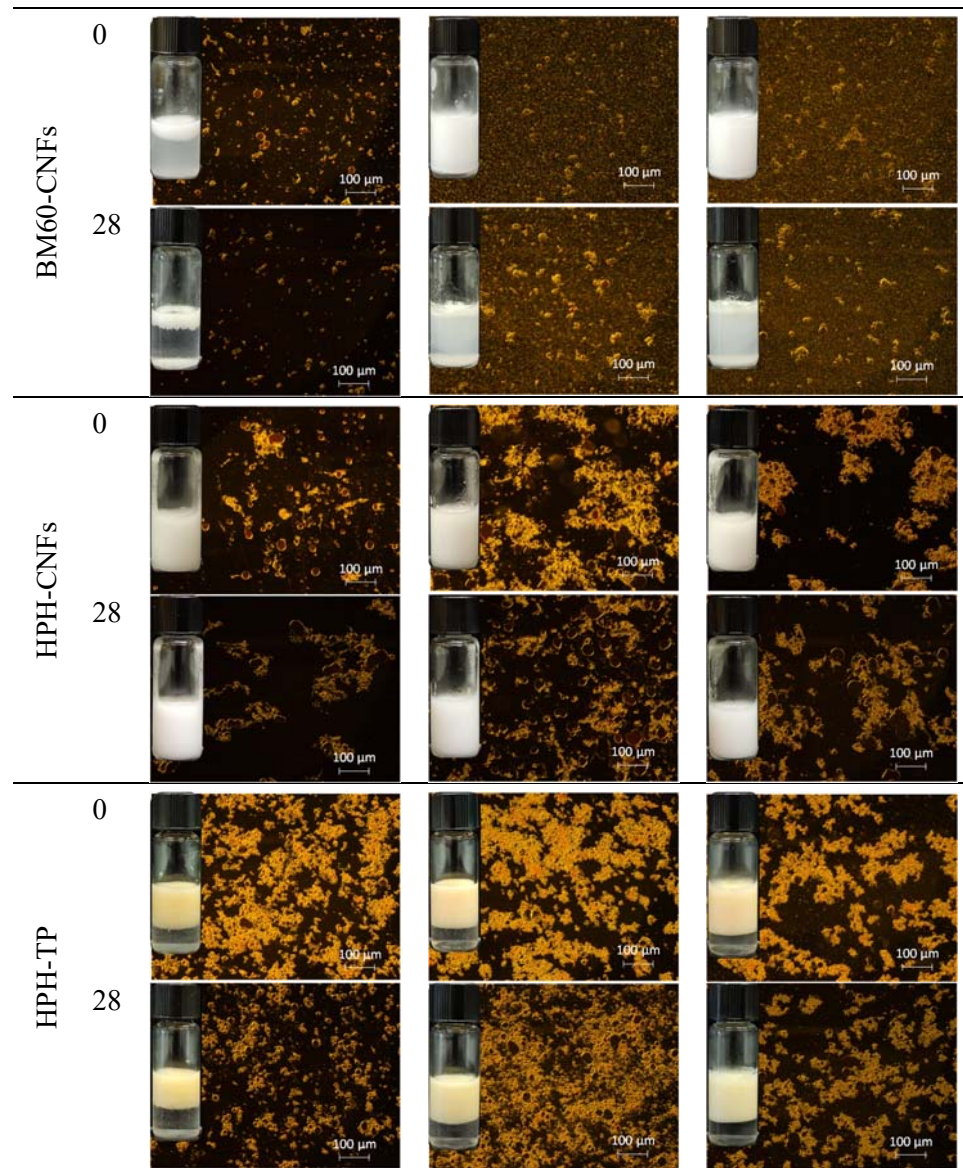
Figure V.7 *Fluorescence microscopy and visual images of emulsions stabilized by cellulose and tomato pomace subjected to different mechanical treatments over 28 d of storage at 4 °C at different pH values.*

The change of emulsion rheological properties over time provides important pieces of information for interpreting storage stability, as the increase of viscosity could retard droplets movement and delay the creaming process [36]. Table V.3 shows that the viscosity of all emulsions is lower in acidic conditions, which may be due to the weak viscoelasticity of the interfacial layer.

Moreover, the viscosity of all emulsions decreased with increasing storage time. Only HPH-CNFs stabilized emulsion is not significantly affected by the storage; this effect could be ascribed to the stronger interaction between molecules presented. HPH-CNFs and HPH-TP exhibited the highest viscosity among all the emulsions, regardless of the storage and pH conditions. Based on the aforementioned discussion about the microstructure analysis, the enhanced viscosity was beneficial to increase the stability of emulsions stabilized with HPH-CNFs and HPH-TP, with better resistance to droplet aggregation over the entire storage and centrifugal forces.

Table V.3 *Viscosity values for each emulsion as a function of storage period and pH environmental conditions.*

pH = 2.0		Viscosity (Pa·s)			
		BM30-CNFs	BM60- CNFs	HPH- CNFs	HPH-TP
Storage period	0	0.032 ± 0.001^c	0.023 ± 0.001^b	14.820 ± 0.940^a	1.548 ± 0.214^c
(day)	28	0.024 ± 0.001^b	0.015 ± 0.002^a	14.293 ± 0.446^a	1.337 ± 0.068^{bc}
Centrifugation	10 min	0.023 ± 0.003^b	0.018 ± 0.002^a	14.502 ± 0.314^a	1.261 ± 0.017^b
at 3,500 rpm	20 min	0.019 ± 0.001^a	0.015 ± 0.003^a	14.404 ± 0.142^a	0.836 ± 0.066^a
pH = 7.0		Viscosity (Pa·s)			
		BM30- CNFs	BM60- CNFs	HPH- CNFs	HPH-TP
Storage period	0	0.381 ± 0.006^d	0.069 ± 0.002^c	21.138 ± 0.889^a	1.015 ± 0.148^b
(day)	28	0.182 ± 0.009^c	0.049 ± 0.001^b	20.053 ± 0.487^a	0.819 ± 0.014^{ab}
Centrifugation	10 min	0.157 ± 0.002^b	0.026 ± 0.006^a	18.623 ± 1.743^a	0.747 ± 0.071^a
at 3,500 rpm	20 min	0.138 ± 0.002^a	0.018 ± 0.003^a	17.733 ± 2.020^a	0.739 ± 0.144^a
pH = 12.0		Viscosity (Pa·s)			
		BM30- CNFs	BM60- CNFs	HPH- CNFs	HPH-TP
Storage period	0	0.043 ± 0.001^c	0.029 ± 0.002^c	6.858 ± 0.104^b	0.615 ± 0.034^b
(day)	28	0.025 ± 0.001^b	0.019 ± 0.001^b	4.902 ± 1.434^a	0.309 ± 0.021^{ab}
Centrifugation	10 min	0.020 ± 0.002^a	0.020 ± 0.001^b	4.333 ± 0.305^a	0.203 ± 0.023^a
at 3,500 rpm	20 min	0.018 ± 0.002^a	0.015 ± 0.002^a	4.334 ± 0.298^a	0.129 ± 0.064^a

The letters indicate significant differences ($p < 0.05$) for the same sample during the storage period (n = 5).

Therefore, HPH-CNFs emulsion with higher viscosity prevents mobilization of the continuous phase between the oil droplets, resulting in a more stable emulsion. Additionally, microscopic inspections were carried out to evaluate the stability of the prepared emulsions by observing their ability to resist physical changes under pH environmental factors after centrifugation at 35,000 rpm for 10 and 20 min. As seen from Figure V.8, the oil in water emulsions prepared with all particles showed phase separation under acid conditions. However, emulsions stabilized with HPH-CNFs and HPH-TP allowed for increased oil droplet stabilization.
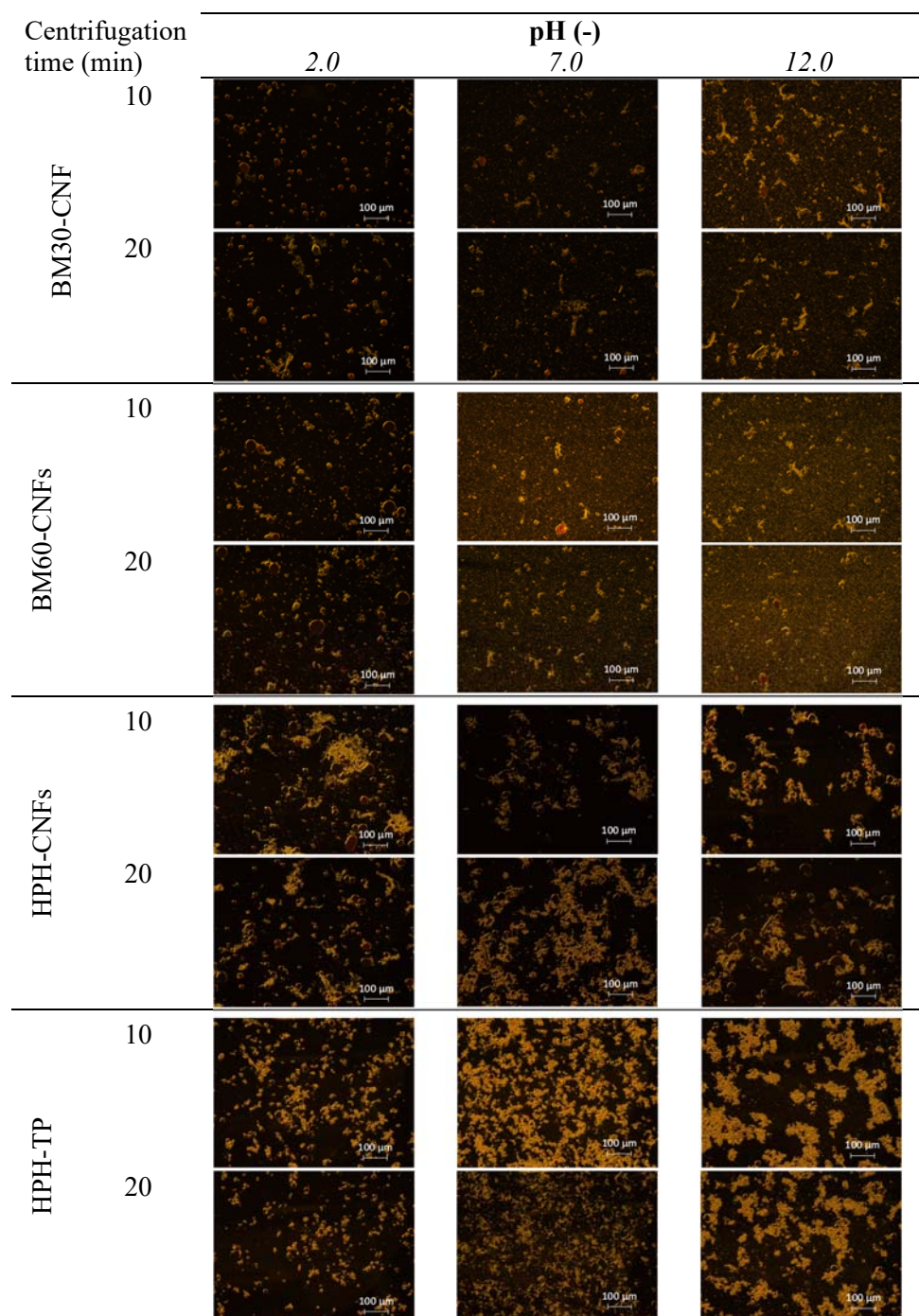
Figure V.8 *Fluorescence micrographs of emulsion stabilized with BM30-CNFs, BM60-CNFs, HPH-CNFs, and HPH-TP under different pH values during storage period at 4 °C.*

Chapter V

V.1.4. Conclusions

This section investigated the influence of different NCs on the stabilization of O/W Pickering emulsions. TEMPO-mediated oxidation at different processing time and catalyst concentration is applied on softwood kraft pulp Celeste 85 to obtain CNCs-C85 and CNFs-C85, meanwhile BM for 30 and 60 min and HPH were the mechanical treatment investigated to obtain CNFs from Commercial cellulose Arbocel®. The results show that the obtained CNCs-C85, with a needle-like structure of ~3 nm in thickness and ~170 nm in length, and CNFs-C85, characterized by a fibrous structure of ~10 nm in thickness and a few micrometers in length, were both able to stabilize 5 wt% sunflower oil-based Pickering emulsions at a dosage of 0.5% wt. Despite the significant morphological differences, CNCs-C85 and CNFs-C85 contribute to forming an interconnected network structure of the emulsion droplets, promoting their efficient steric and electrostatic stabilization. In addition, also HPH-CNFs, characterized by fibril bundles with a length in the range of ∼10–100 μm and irregular width, exhibited higher mobility and flexibility at the oil-water interface, resulting in an efficient emulsifying ability at different pH values, with the fibrils wrapping around the oil droplets for their stabilization. On the contrary, despite BM-CNFs showed a fine and uniform size distribution, the resulting emulsions exhibited oil droplets not completely covered by cellulose fibrils, and, therefore, significantly lower stability. The hypothesis that the higher stability of emulsions stabilized by HPH-treated cellulose is due to the entanglement of fibrils around the droplets to form a 3D network was supported by viscosity measurements: with HPH-CNFs and HPH-TP emulsions exhibiting significantly higher viscosity than other emulsions. The present results, hence, provide specific and relevant outcomes about how tailoring the properties of the nanostructured cellulose during fabrication may represent a simple strategy to affect the behavior and stability of Pickering emulsions. More specifically, CNCs-C85 and BM-CNFs can be exploited in the stabilization of emulsions for low-viscosity applications, such as drinks and beverages, due to the finer attainable emulsion size and span values. In contrast, HPH-CNFs and HPH-TP could be exploited in creams, sauces and dressings, due to the higher apparent viscosity and stronger 3D-network formed by entangled fibers.

Section V.2
NCs capillary suspensions for oil structuring

Oleogels have been proposed as suitable systems for replacing unhealthy saturated fats in food preparations. This section aimed at structuring sunflower oil through capillary suspensions using solid fraction wheat middlings (WM), a residue of the wheat milling process, as structurant. For the first time, high-pressure homogenization (HPH) was applied directly on the WM-in-oil-dispersion to reduce the particle size dimensions, induce fiber activation and release the high value-added intracellular compounds into sunflower vegetable oil. The optimized formulation of WM-in-oil-dispersion was then used in the preparation of capillary suspension, through the addition of water as a secondary immiscible fluid. Water addition drastically altered the rheological behavior and the strength of the oil suspensions due to the establishing capillary forces and the percolating particle network formation. The strength of the capillary bridges resulted to depend on the particle size of the WM, the surface properties of the solid particles, and the fraction of added water (ranging between 5 and 80% w/w with respect to the oil). The oil dispersion at 30% w/w of WM solid fraction treated by HPH (80 MPa for 10 min) with the addition of 50% w/w of water exhibited apparent yield stress > 300 Pa, corresponding to a gel-like behavior. These results highlight that the obtained oleocolloids are a very promising material for the formulation of healthier and more sustainable food products as an alternative for solid fats with many potential applications based on (i) the reduction of the overall caloric content; (ii) the addition of benefits related to dietary fibers of AFRs; and (iii) the oil stability against oxidation related to antioxidant bioactive compounds.

V.2.1. Specific goal and work plan

Low-fat products currently represent a relevant trend in food science, to support healthier eating with a familiar mouthfeel, but without penalizing taste. Several studies showed correlation between saturated fat consumption and the increase of Low Density Lipoprotein (LDL) cholesterol and Apolipoprotein B (ApoB protein) [37], which are considered the main heart disease risk factor [38]. Vegetable oil structuring methods have recently emerged as a promising strategy for reducing or replacing unhealthy (or negatively perceived by consumers) fats in food products [39]. The main requirement for the texture of food products prepared with fat replaces is mimicking regular/full-fat products, to gain consumers' acceptance [40]. For example, emulsions with adequate droplet size distribution, are reported to contribute to reproducing mouthfeel and stability of full-fat products. In particular, a widely studied pathway for fat replacement is based on the use of particle-stabilized Pickering emulsions [41–43], whose droplets cluster together forming spherical agglomerates that maintain excellent stability over time regardless of the external environmental stimuli [14]. Recently, it was determined that adding a small amount of a secondary immiscible fluid in the continuous phase of particle suspensions can create a sample-spanning particle network [44,45]. This phenomenon can be attributed to the capillary bridge forces of the two fluids on the solid particles, causing particle agglomeration and, if the mass fraction of solids is sufficient, the formation of a network of particles within the bulk fluid [46]. In this case, the rheological properties of the ternary solid-liquid-liquid systems are dramatically altered by the transition from a fluid-like to a gel-like state (from a weak to a strong gel) [44,46,47]. The transition in the suspension is associated with two distinct states: the pendular state, where the secondary (or minority) fluid preferentially wets the particles, because of higher affinity than the primary fluid, and the capillary state, where the secondary fluid wets the particles less well than the primary fluid [44]. Both the capillary state and pendular state are controlled by the capillary forces and are strongly influenced by changes in the amount of secondary fluid, the material properties, as well as interfacial and wetting properties of the ternary system [48]. For all these reasons, capillary suspensions represent a potential alternative route for the formulation of novel structured food products [49] with vegetable oils, with the additional advantage of reducing the caloric content, because part of the fats is replaced by a secondary fluid, such as water, and solid particles, such as fibrous materials. In this scenario, different agri-food residues (AFRs), such as tomato peels and spent coffee grounds [45], and different fractions of yellow peas processing [50], have shown an excellent ability to structure vegetable oils [51], through the addition of a small amount of a secondary immiscible fluid.

This work aimed at addressing the use of wheat middlings (WM), rich in fibers, as a sunflower oil-structuring material for obtaining gel-like products without the use of unhealthy fats or undesired additives, but only water as secondary fluid (Figure V.9). The WM is a by-product of wheat milling, consisting of finer particles of endosperm, typically used as animal feed, because they provide a source of energy, amino acids, and phosphorus [52–54]. More specifically, this study aims to elucidate the mechanism of network formation of WM particles when micronized using HPH, as well as their possible contribution in slowing down lipid oxidation.

V.2.2. Specific material and methods
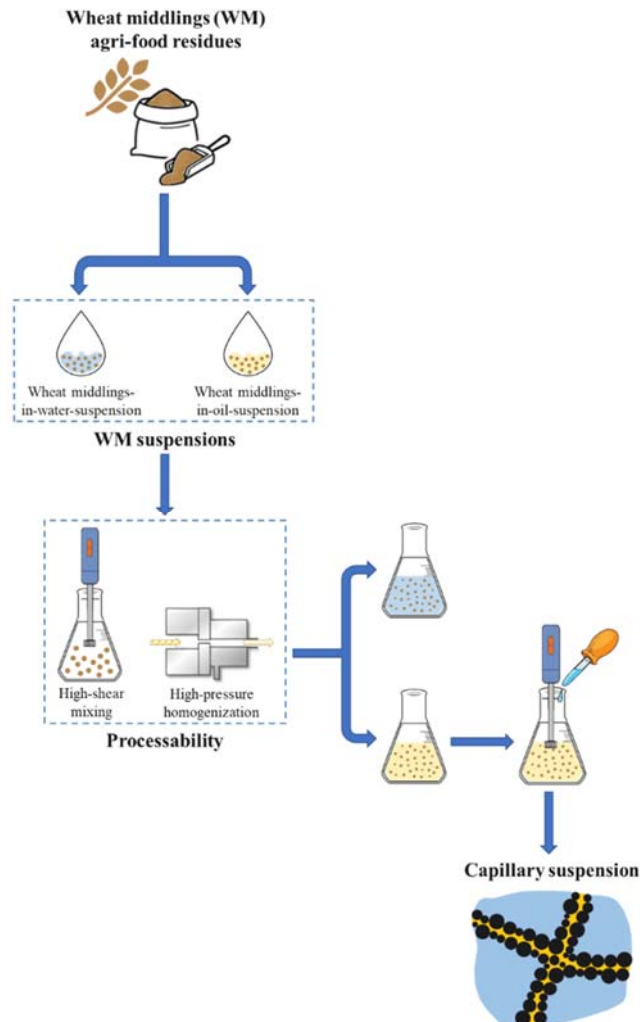
Figure V.9 *Schematic representation of methodology used for oleocolloid preparation stabilized by WM residues.*

V.2.2.1. Materials

The wheat middlings (WM), collected from a local milling industry (Molini Giardullo Di Giardullo Silvia E C. S.n.c., Albanella (SA), Italy), as described in detail in section § III.1, were packed in vacuum-sealed flexible pouches (multilayer packaging OPP30-A19-LDPE70, Di Mauro Officine Grafiche S.p.A., Cava de' Tirreni (SA), Italy) and stored at room temperature until used. The moisture content of WM was $11.54 \pm 0.10\%$.

Sunflower oil was purchased from a local market (Olio di Semi di Girasole Basso, San Michele di Serino (AV), Italy). Its composition (on weight basis) comprises 10.3% wt of saturated fatty acids, 19.5 wt% of monounsaturated fatty acids, and 65.7 wt% of polyunsaturated fatty acids.

All reagents were of analytical grade unless otherwise stated. Micro-pure deionized water was used throughout the experiments.

V.2.2.2. Preparation of wheat middlings-in-oil dispersion by

mechanical treatments

WM particles were dispersed in sunflower oil at a solid mass fraction (ϕ, defined as the ratio of the solid weight to the total sample weight) ranging between 5 and 30 wt%, using a high-shear mixer (HSM) (Ultra Turrax T25, IKA Labortechnik, Germany) at 20,000 rpm (50,176 g centrifugal force equivalent) for 5 min within an ice bath. The obtained suspensions were then subjected to HPH treatment at 80 MPa for 10 min at a flow rate of 22 mL/s using an in-house developed system equipped with a 200 μm diameter orifice valve (model WS1973, Maximator JET GmbH, Schweinfurt, Germany) and a tube-in-tube heat exchanger, to avoid the increase in product temperature, using cooling water at 10 °C. The abbreviation used was HSM-O-5, which refers to the mechanical treatment applied on the continuous phase at certain solid fraction.

V.2.2.3. Characterization of oil dispersions

The particle size distribution of the samples micronized by HSM or HPH was measured by laser diffraction using a Malvern Mastersizer 2000 (Malvern Instruments Ltd., UK). The oil phase of WM-in-oil dispersions was substituted by water by washing three times the suspensions with saponin from quillaja bark (Sigma-Aldrich, St. Louis, MO, USA) at 0.5 wt% in water, followed by centrifugation at a centrifugal force of 5,300 g. From the particle size distribution, the diameters corresponding to the 10th, 50th and 90th percentile of the cumulative distribution (d(0.1), d(0.5) and d(0.9), respectively), the volume-based mean diameter (D[4,3]), and the surface-based mean diameter (D[3,2]) were calculated, as previously described §

III.7.3.5. The temperature of the cell was maintained at 25 ± 0.5 °C, and the mean value of three replicates was determined.

The hydration and oil binding properties of WM particles are related to their chemical structure and particle size [55]. The particle swelling was determined according to a previously reported method [50]. Briefly, WM was dispersed in distilled water at two different concentrations (5 and 7 wt%) and allowed to swell overnight under continuous stirring at 20 °C. Then, 2 g of each aqueous dispersion was centrifuged for 30 min at 25 °C and 1,626 g force equivalent and, after removing the supernatant, the pellet was weighed. The maximum amount of water absorbed per g of WM (WA_{max}) was calculated as the average of each WM concentration used (determined in triplicate):

$$WA_{max} \left(\frac{g_{water}}{g_{WM}} \right) = \frac{\sum_{i=1}^{3} \frac{P_{water,i} - SC}{SC}}{3} \qquad (V.7)$$

where $P_{water,i}$ is the weight of pellet after centrifuging of each WM concentration dispersed in water and SC is the solid content of the sample.

The water absorption capacity (WAC) is the capacity of middlings particles to absorb water when dispersed in water, expressed as:

$$WAC = \frac{100 \cdot \left(\frac{WC}{SC} \right)}{WA_{max}} \qquad (V.8)$$

where WC is the water content (g).

When WAC is lower than 100%, the solid content is exposed to less water than its maximum absorption capacity (corresponding to 100%); whilst for WAC higher to 100% the particles have adsorbed excess water.

The same procedure was carried out to calculate oil holding capacity (OAC).

$$OA_{max} \left(\frac{g_{oil}}{g_{WM}} \right) = \frac{\sum_{i=1}^{3} \frac{P_{oil,i} - SC}{SC}}{3} \qquad (V.9)$$

$$OAC = \frac{100 \cdot \left(\frac{OC}{SC} \right)}{OA_{max}} \qquad (V.10)$$

where OA_{max} is the maximum oil absorption calculated and P_{oil} is the weight of pellet after centrifuging the dispersion of particles in oil.

The structure of capillary suspensions and their strength depends on the particle size distribution, as well as on the interfacial tension between the fluids [56] and the wetting properties of both liquids, which are all taken into account by the three-phase contact angle measurement [48]. The three-phase contact angle was measured for HSM-O-5 and HPH-O-5 with the sessile drop method, as previously described [49], using a contact angle meter (CAM 200, KSV Instruments Ltd., Helsinki, Finland). Each dispersion was placed in a quartz cuvette and left for 24 h at room temperature to allow separation by the gravity of the solid particles from the oil phase. Subsequently, the secondary fluid (distilled water) was placed in a 500 µL syringe (Hamilton Company,

Bonaduz, Switzerland) with a 0.72 mm diameter stainless steel needle, to form a drop of about 2 μL in the cuvette filled with the oil phase for two-third of its volume and with the solid particles onto the bottom. Drop formation triggered the activation of a camera, which recorded the shape of the drop once deposited on the particle layer for 100 s at 1 s time intervals. An image analyzer software (CAM 101, KSV Instruments Ltd., Helsinki, Finland) was used to measure the angle formed between the surface in contact with the drop, and the tangent to the drop of liquid at the point of contact with the surface, on both sides of the image. For each drop formed, values of the contact angles were averaged over time and side. Measurements were repeated five times for each sample. Results are expressed as an average of the values during the 100 s.

V.2.2.4. Preparation of capillary suspensions

The capillary suspensions were obtained by adding dropwise distilled water as a secondary fluid at saturation ratio S (Equation V.11) comprised between 0.05 and 0.70 to the HPH-treated WM-in-oil dispersions at constant particle volumetric fraction $\phi = 30\%$ w/w (HPH-O-5) under HSM at 20,000 rpm for 10 min within an ice bath [56].

$$S = \frac{V_{water}}{V_{oil} + V_{water}} \tag{V.11}$$

V.2.2.5. Characterization of capillary suspensions

The morphology of oil dispersions and capillary suspensions was observed with an optical microscope (Nikon Eclipse TE 2000S, Nikon instruments Europe B.V., Amsterdam, The Netherlands), coupled to a DS Camera Control Unit (DS-5M-L1, Nikon Instruments Europe B.V, Amsterdam, The Netherlands) for image acquisition and analysis, as described in § III.7.3.4.1.

Rheological measurements were performed in a rotational rheometer (AR 2000 rheometer, TA instruments, Newcastle, DE, USA), equipped with a concentric cylinder (15 mm stator inner diameter, 28 mm rotor outer diameter, 42 mm cylinder immersed height, 2° cone angle) and plate-cone geometry (40 mm diameter, 2° cone angle and 1 mm fixed gap width) based on the sample to be analyzed. The apparent yield stress, i.e. the stress at which the sample begins to flow irreversibly, was evaluated using a shear rate ramping. More in detail it was found by the intercept point between the y-axis and a tangent line into the stress vs. shear rate curve at the point where the curve slope does not significantly change as the shear rate increases. Flow curves were obtained by continuously varying the shear rate from 0.1 s^{-1} up to a rate of 200 s^{-1} at 20 °C. Measurements were repeated five times on two independently prepared samples, and are reported as means ± standard deviations for apparent yield stress.

V.2.2.6. Accelerated oxidation stability test

The primary oxidation compounds analysis is always carried out by the peroxide value (PV) to assess the quality of oil at its stability. For the Schaal oven, accelerated stability test approximately 1 g of each sample was put in vials and stored in an oven at 65 ± 2 °C in absence of light after 15-days of storage [57]. The PV value was determined iodometrically (visually) with a starch indicator and a sodium thiosulfate standard solution according to ISO 3960:2007 (International Organization for Standardization).

V.2.2.7. Statistical analysis

All experiments and analysis were performed in triplicate on independently prepared samples, otherwise specified, and the mean and standard deviation (SD) of the experimental values were calculated. Statistically significant differences ($p \leq 0.05$) among the mean values were assessed by one-way ANOVA and the Tukey's test ($p < 0.05$), using statistical software SPSS (version 20, SPSS Inc., Chicago, IL, USA).

V.2.3. Results and discussion

V.2.3.1. Water and oil holding capacities

Water and oil holding capacities describe the ability of solid particles to adsorb and retain bound, hydrodynamic, capillary, and physically entrapped water and oil, respectively [58]. WM particles are very rich in starch and fiber, especially cellulose, which positively influences water adsorption, whereas the presence of natural oil, wax, and fat hinders water molecules from penetrating inside the fiber [59]. The maximum water adsorption of WM is about 4.5 ± 0.3 g_{water}/g_{WM}, suggesting that water fills the void space of the WM anisotropic particles, which is important, as high water penetration was reported to play a significant role in the structuring of capillary suspension in starch particles [49]. Moreover, the solid particles with high water holding capacity can be used as functional ingredients to avoid synaeresis and to modify the viscosity and texture of different formulated foods [60]. The maximum WM oil absorption is about 2.8 ± 0.9 g_{oil}/g_{WM}, reaching only half of the value of maximum water adsorption.

The water and oil holding capacities (WAC and OAC, Equations V.8 and V.10) represent the ability of a material to retain water and oil, respectively, after centrifugation. In general, the ability of a material to adsorb water is strictly correlated to its dietary fiber content. The hydration properties of dietary fibers, in turn, are related to the chemical structure of the component polysaccharides, and other factors such as porosity, particle size, ionic form, pH, temperature, ionic strength, type of ions in solution and stresses upon

fibers [61]. WM particles are characterized by a high level of fibers, which leads to the higher values of maximum adsorbed water. OA_{max} instead, is closely associated with the chemical structure of the plant polysaccharides and depends on surface properties, overall charge density, particle size, the insoluble fiber contents, and the hydrophobic nature of the fiber particles [62]. The micronization process by HPH treatment altered the physical structure of WM due to the fluido-mechanical stresses that occur during the treatment, and, therefore, also the water and oil holding capacity, which is generally related to its structure, density, and the nature and number of water and oil-binding sites, respectively. It could then be expected that the size reduction caused by the HPH treatment increases the surface area and expose more water binding sites (polar groups or uronic acid groups) to the surrounding water [63], leading to increase the WA_{max} [64]. Nevertheless, results (Figure V.10) suggest that the fluid-mechanical stresses that occur during HPH treatment induced the collapse of WM fiber matrix and pores, hence negatively affecting the hydration properties of the materials. In fact, HPH treatment increased the exposure of hydrophobic groups of WM and the mutual attraction of fibers; consequently, as shown in Figure V.10 the WA_{max} of HPH-treated sample was lower than for the untreated one. Additionally, in the case of oil holding capability, HPH treatment does not influence the physical entrapment of oil.
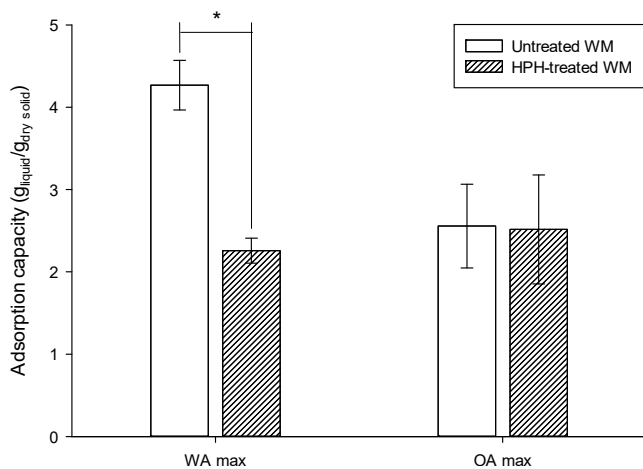
Figure V.10 *Water (WA_{max}) and oil holding capacity (OA_{max}) of untreated and HPH-treated WM. Asterisk represents significant differences at p < 0.05.*

V.2.3.2. Wheat middlings-in-oil-dispersions

Particle size and shape are crucial factors in dictating the rheological properties of oil dispersions [65]. Remarkably, the particle size distribution of WM-in-oil-dispersion at 5 wt% is slightly different from the one recorded for water-dispersion at the same particle mass fraction (see § IV.1.3.3). This can be due to the procedure used for particle size analysis of oil dispersions, which

required the removal of the oil by washing three times the sample with distilled water and surfactant. However, it is also likely that the different affinity of WM for water and oil as demonstrated by the values of water and oil holding capability, may have influenced the effect of the HPH process on particle disruption [66]. More specifically, when WM particles are processed in water, a greater effect on particle size reduction by HPH process was achieved (Figure V.11) because of the larger volume of particles when wetted with water, deriving by the better WM water-absorbing ability than oil.

(a)

(b)
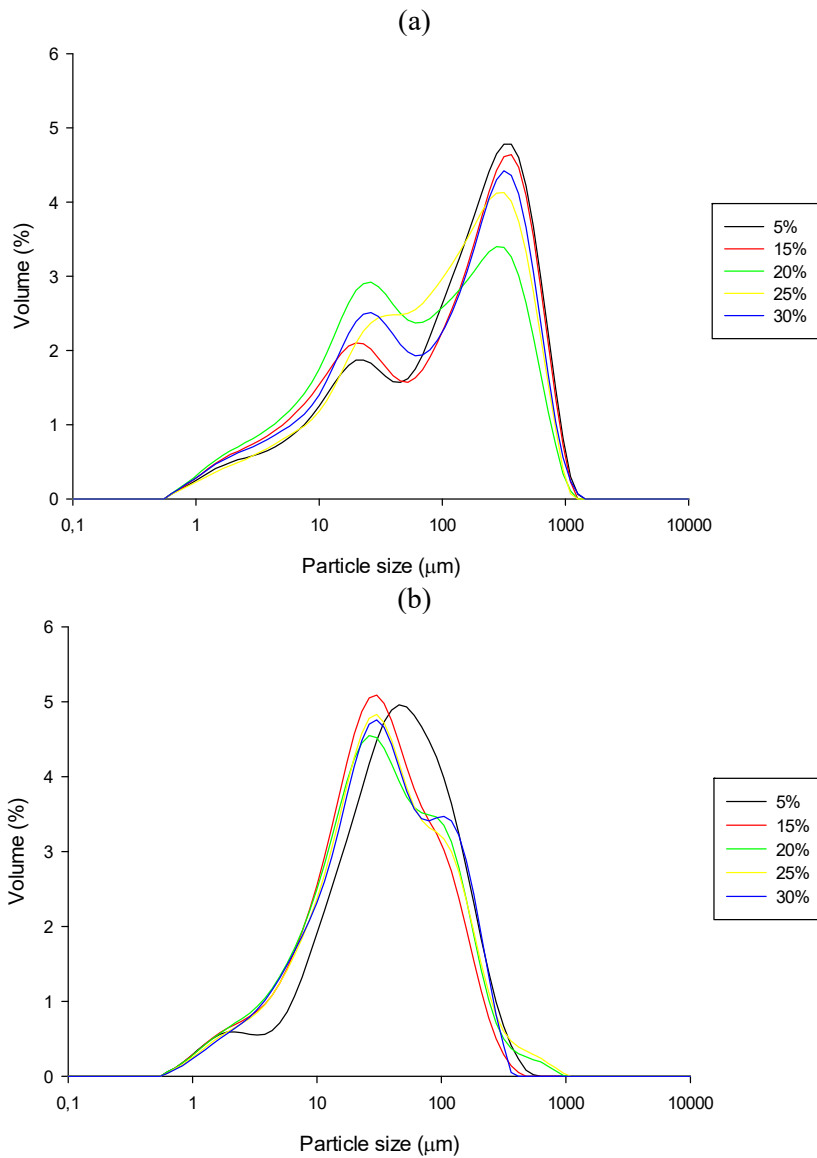
Figure V.11 *Particle size distribution of WM-in-oil-dispersions treated with (a) HSM and (b) HPH at different particle mass fractions.*

Chapter V

Because of the relevant role on size distribution of the sample preparation procedure, the particle size distribution for WM-in-oil-dispersions treated by HSM and HPH, shown in Figure V.11a and V.11b respectively, have, therefore, be considered only as qualitative analysis, which gives information on the effect of the two different mechanical treatments on oil dispersions. The WM-based oil dispersions produced through HPH exhibited a narrower and more homogeneous distribution than HSM-treated samples for all particle mass fractions tested, with a reduction of about 14%, 68% and 71% for the 10th, 50th and 90th percentile of the cumulative distribution, respectively. The HSM-treated WM-in-oil-dispersions exhibited a bimodal distribution with a peak at about 450 μm and a broader shoulder at a smaller size of about 20 μm (Figure V.11a). In contrast, the particle size distribution of the HPH-treated WM-in-oil-dispersions displayed a dominant size at about 20 μm with only a minor shoulder at a larger size, suggesting that also in oil the WM particles were broken down by the HPH treatment into cell wall fragments, cellular material, fiber particles and polymers.

The capability of WM particles to structure the oil phase was preliminarily assessed through visual observations (Figure V.12) immediately after the HPH treatment and after leaving the oil dispersions at room temperature for 24 h and 48 h.
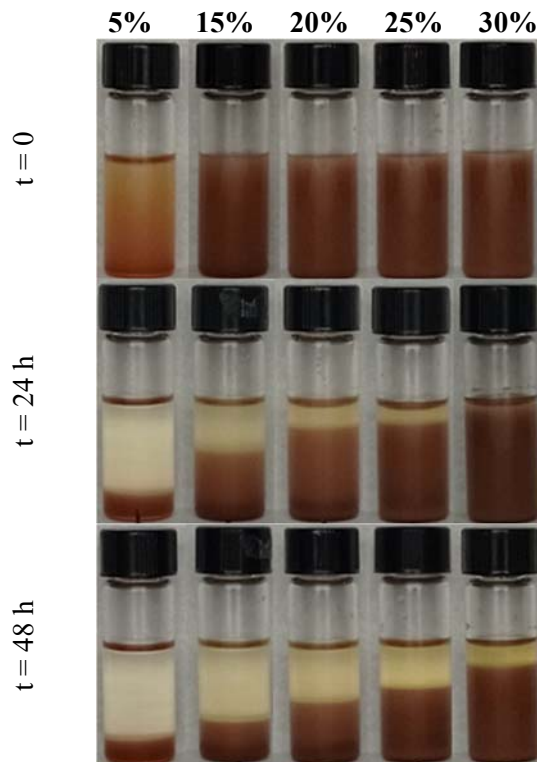
Figure V.12 *Pictures of the different WM-in-oil-dispersions prepared by HPH treatment, after 0, 24, and 48 h.*

WM-in-oil-dispersions displayed a different sedimentation degree, which depended on the particle mass fraction, as shown in Figure V.12. At 5 wt%, the majority of the solid particles settled at the bottom of the vials already after 24 h. When increasing the particle mass fraction, the sedimentation phenomenon required longer times, due to the strong interparticle interactions occurring. At $\phi = 30$ wt% of WM particles the oil dispersion displayed a very homogeneous, paste-like appearance, indicating that the continuous oil phase is able to lubricate the particles.

Samples with higher particle concentrations are more kinetically stable, because, as highlighted by the micrographs in Figure V.13, the particles are tightly packed together, forming a particle network more resistant to sedimentation.
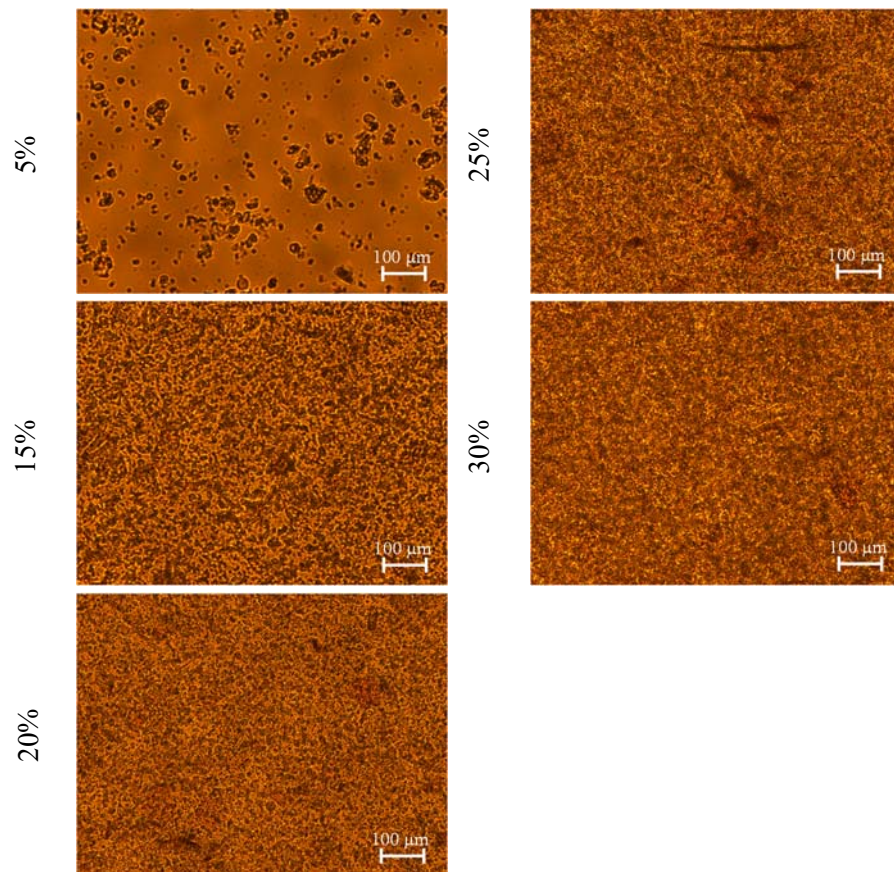
Figure V.13 *Optical micrographs at 10× magnification for HPH treated WM-in oil-dispersions at different mass fractions.*

Figure V.13 clearly shows the differences between 5 and 15 wt% particle mass fraction, where at 5 wt% particle interaction leads to well-separated aggregates, whereas at 15 wt%, a network structure is developed. Such network apparently becomes stronger when increasing the particle fraction, as suggested by the rheological properties of WM-oil-dispersions, shown in Figure V.14.
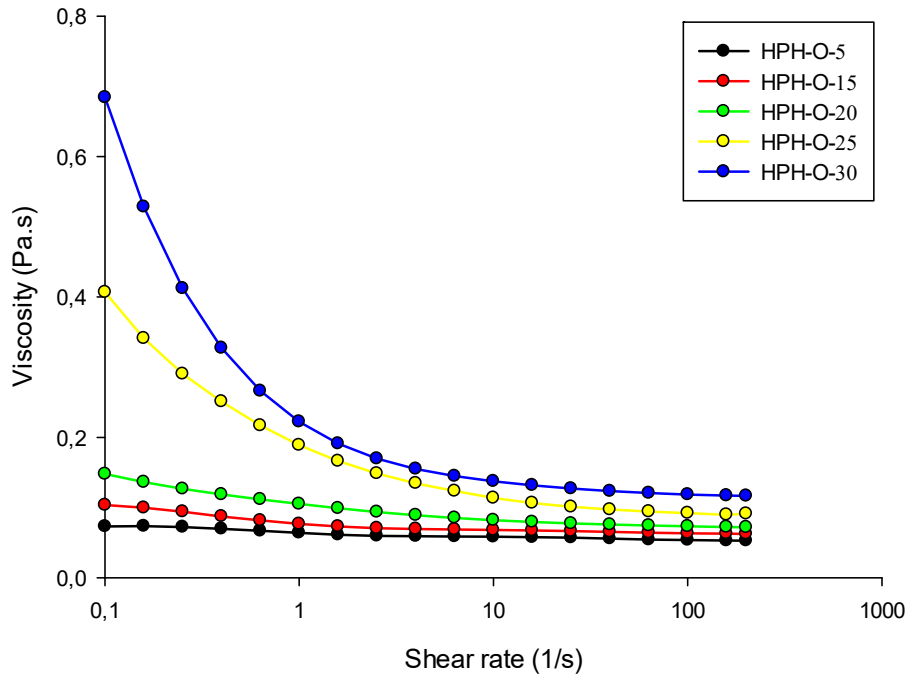
Figure V.14 *Flow curves for HPH treated WM-in-oil-dispersions at different particle mass fractions ϕ.*

The results of the shear-controlled tests (Figure V.14) show that the flow curves of WM-in-oil-dispersions are characterized by an increase in viscosity η, as a function of the particle mass fraction. More specifically, the fluid curves shape shows a transition from Newtonian behavior, with the viscosity being independent on shear rate, to a non-Newtonian shear-thinning response, where the viscosity decreases with an increase in shear rate. The shear-thinning behavior can be related to the breakage of the aggregates, to the change in the shape of particles and the particle orientation in the flow direction, as it has been observed also for pea fiber dispersions in oil [50]. This behavior could be fitted by the power-law model (Equation V.2). For all WM-in-oil-dispersions, the power-law index is greater than or equal to 0 indicating that the fluid is shear-thickening and the severity of shear-thinning behavior increases with the increase in ϕ, as shown by the parameters reported in Table V.4.

Table V.4 *Fitting parameters and coefficients of determination for the fitting of the data of Figure V.14, using Equation V.2.*

	k	n	R^2	Adj-R^2
$\phi = 5\%$	0.06	1.00	n.a.	n.a.
$\phi = 15\%$	0.08	1.05	0.7517	0.7399
$\phi = 20\%$	0.11	1.13	0.9698	0.9684
$\phi = 25\%$	0.19	1.36	0.9834	0.9826
$\phi = 30\%$	0.25	1.46	0.9848	0.9840

n.a.: not available because the HPH-O- $\phi 1$ curve is not adequately fitted by a power-law model

To better understand the characteristics of the materials under examination, the apparent yield stress as a function of the solid mass fraction has been determined (Figure V.15) as previous reported in Mustafa et al. 2018 [45] using the continuous shear stress or shear rate ramp, from low to high stress or rate.
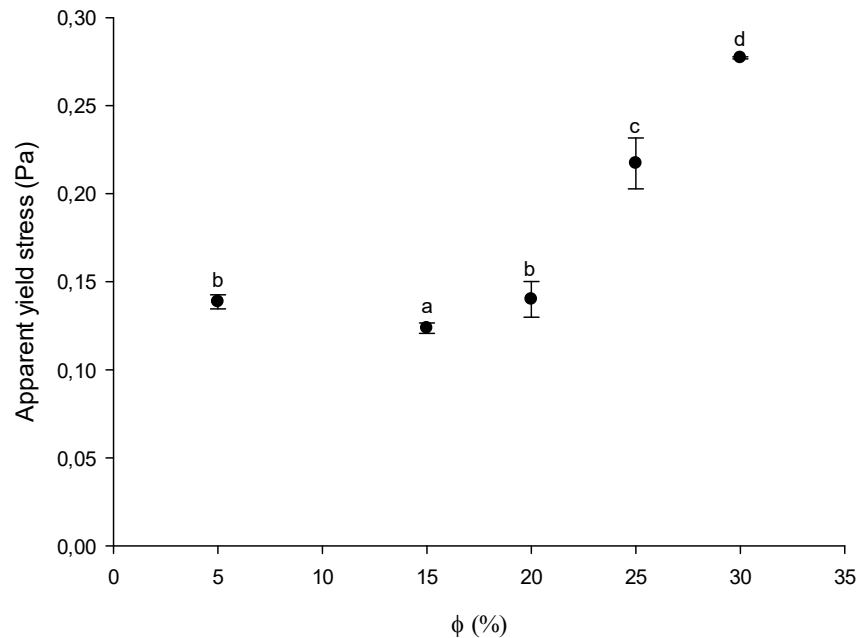
Figure V.15 *Apparent yield stress for WM-in-oil-dispersions as a function of solid mass fractions. Different letters denote statistically significant (p < 0.05) differences.*

The yield stress is an important characteristic of structured fluids because it provides an indication of the gel stability. Higher apparent yield stress for mass fraction of 25 and 30 wt% of WM in oil respectively suggest a more compact structure, which prevents the material to undergo phase separation, sedimentation or aggregation, because of stronger particle-particle interactions and the formation of strong particle network. In conclusion, the results of Figure V.15 suggest that the structuring of oil suspensions could be achieved when the mass fraction of WM is higher than 20 wt%.

V.2.3.3. *Wheat middlings-in-oil-dispersions in the presence of water*

To addition of a secondary fluid with high affinity for the solid particles, such as water, can be expected to drastically affect the gel structure. To check the interactions of the HSM- and HPH-treated WM particles with the secondary fluid in the presence of oil as a continuous phase, the three-phase contact angles (Figure V.16) were measured.
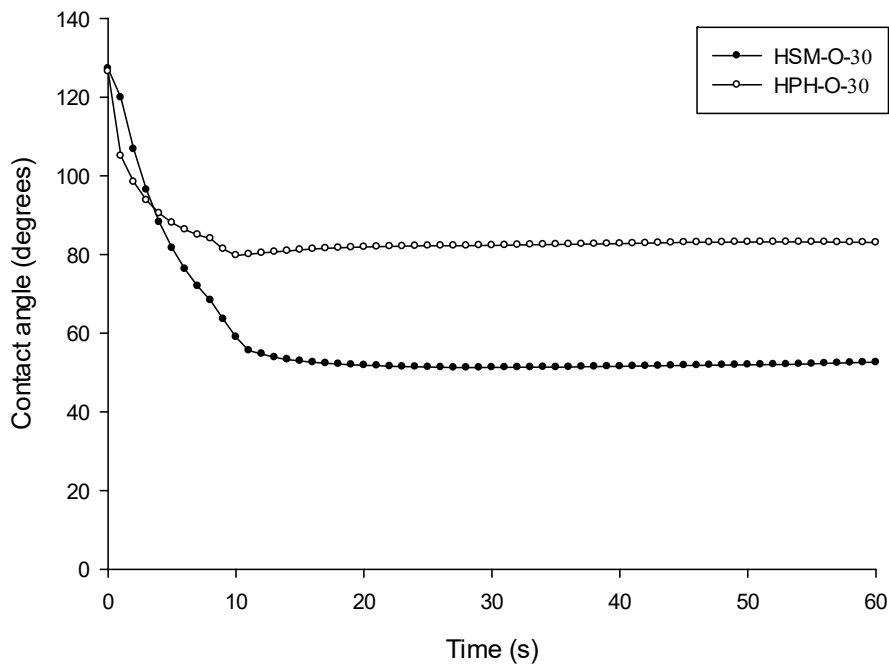
Figure V.16 *Contact angle curves for HSM (―●―) and HPH (―○―) treated WM-in-oil-dispersions at ϕ = 30 wt% of particle mass fraction. Each curve is the average of three measurements.*

The three-phase contact angle curves recorded over 60 s were fitted with an exponential decay equation (Equation III.12), and the fitting parameters are reported in Table V.5.

Table V.5 *Three-phase contact angle parameters of the WM-in-oil-dispersions (ϕ = 30% w/w) treated by HSM and HPH.*

	HSM-O-30	HPH-O-30
γ_0	132.18°	124.83°
γ_∞	51.12°	82.50°
τ_r	4.87 s	2.10 s
R^2	0.9936	0.9868
Adj-R^2	0.9873	0.9738

In general, the contact angle γ is a quantitative measure of the wetting capability of a solid by a liquid: γ < 90° indicates that the liquid wets well the solid, γ ≈ 90° indicates that the liquid spreads on the solid surface, and γ > 90° represents a non-wetting condition. As expected, WM particles are characterized by a three-phase contact angle with oil and water lower than 90°, in agreement with the hydrophilic nature of the organic polymeric chains constituting WM; therefore, it can be desumed that WM dispersions in oil are arranged in a pendular state upon water addition. The three-phase contact angle for HSM-treated WM particles decreased from an initial value of 132.2° to an asymptotic value of 51.1°, following an exponential decay trend (Equation III.12). In contrast, the contact angle for HPH-treated WM particles tended toward an asymptotic value of 90°. The observed differences can be attributed to the different mechanical treatments applied to WM-in-oil-dispersions. It is possible that HPH treatment caused an increase in porosity and, therefore, the oil, in which WM is dispersed, could have interacted with the hydrophobic parts of the particles, leading to their partial saturation [67]. On the contrary, porous effects were less enhanced for HSM-treated systems. In any case, this different behavior apparently did not negatively influence the water-binding ability of HPH-treated WM particles.

V.2.3.4. Capillary suspensions characterization

The addition of water as a secondary fluid into HPH-O-30 (WM-in-oil-dispersion at ϕ = 0.30 treated with HPH) was exploited to promote to form capillary suspensions, through the formation of capillary bridges and the development of a 3D network.

The formation of a capillary network is observed when a secondary fluid (e.g. water) is added to a particle suspension in an immiscible fluid (e.g. oil), where the particle surface exhibit affinity for the secondary fluid (e.g. prevalently hydrophilic nature of the particle surface). The formation of a capillary suspension is accompanied by the transition from a fluid-like to a gel-like behavior, with higher consistency and firmness as the saturation ratio S increases, as shown in Figure V.17.

(a)
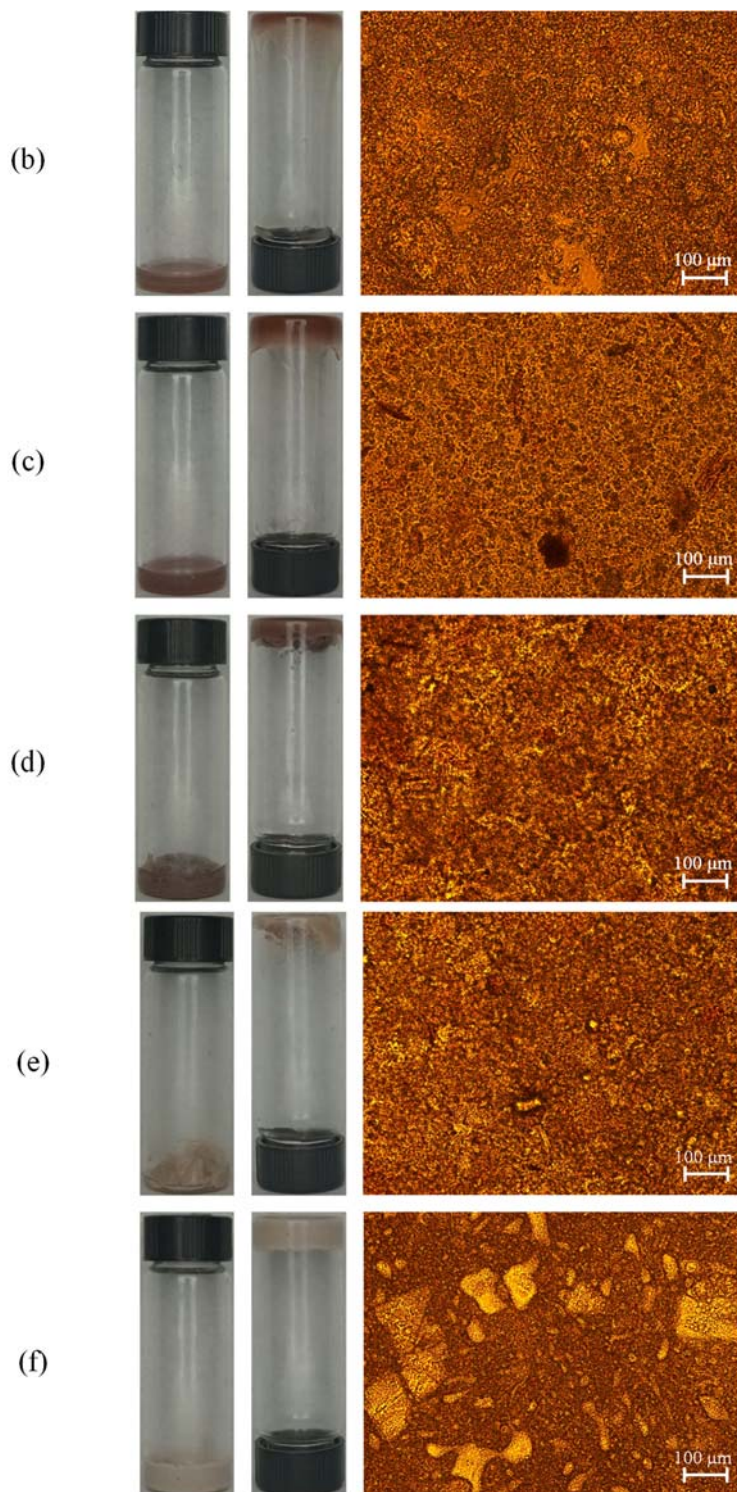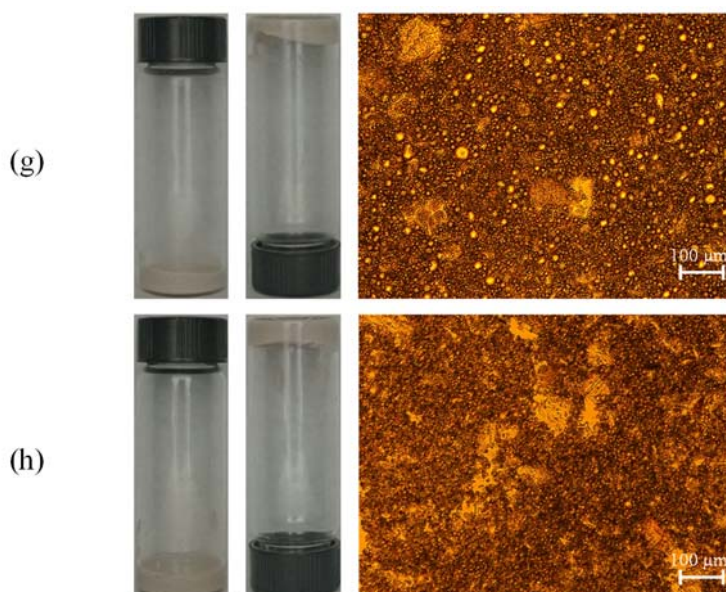
Figure V.17 *Visual and microscopic images of HPH suspensions prepared from HPH-O-30 at varying water addition: (a) S = 0.00; (b) S = 0.05; (c) S = 0.15; (d) S = 0.30; (e) S = 0.40; (f) S = 0.50; (g) S = 0.60; (h) S = 0.70.*

The sample at S = 0.05 displayed a very weak gel-like behavior, similar to the HPH-O-30 sample (S = 0.00). Also, the micrographs for these two samples are very similar to each other (Figures V.17a and V.17b), where no interconnected water-rich aggregates can be observed. As water addition increased, small water-rich aggregates, indicated by the enlarged dark area in the microscopic images, were obtained. For even higher water addition (S ≥ 0.50), a very compact homogeneous structure was obtained, where water acted as a ligand for particle cluster formation. The size of the formed clusters is in many cases greater than 100 μm and they can entrap the oil phase, forming a homogeneous gel. For S = 0.50, the water absorbed is close to 60% of the WAC value, which means that the system is getting close to phase inversion. The WM-in-oil-dispersions with S > 0.50 exhibited the formation of oil droplets in the aqueous phase, suggesting the occurrence of phase inversion (Figures V.17g and V.17h). This effect was previously reported by Calabrese et al. 2021, where oil-in-water emulsion droplets were observed for S = 0.40 [50]. Overall, the augmented gel-like behavior and the formation of capillary bridges' network upon water addition, strongly suggest that capillary forces control the rheological behavior of the ternary blend [50].

The rheological behavior of the capillary suspensions is reported in Figure V.18. Coherently with the micrographs of Figure V.17, the flow curves of Figure V.18 demonstrate the formation of a capillary network structure, becoming stronger when increasing the S up to 50%, which can be explained by the formation of swollen aggregates interconnect via a 3D network.
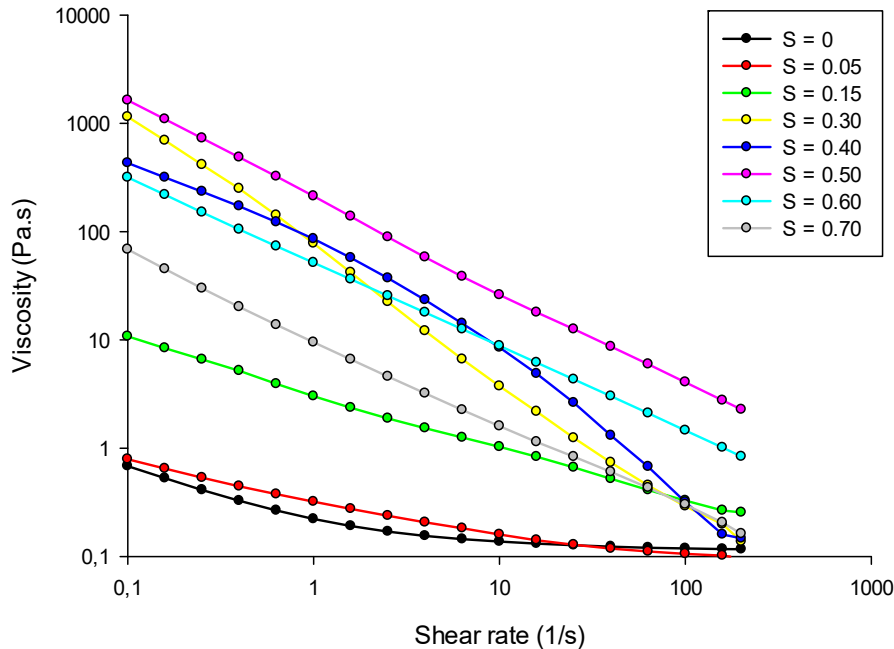
Figure V.18 *Flow curves for HPH-treated WM-in-oil-dispersions at ϕ = 30% w/w as a function of saturation degree.*

In comparison with the black curve, representing the oil dispersion without water addition, and characterized by lower viscosity values than all the other samples, the addition of water caused a measurable and significant viscosity increase. All samples showed a shear-thinning behavior, which was more pronounced for S = 0.50, when the majority of added water led to the bridge network formation. This state, which is called funicular [68], is typically disrupted at higher shear rate, as shown in Figure V.18. Being WM particles preferentially wetted by water, particle swelling and the capillary forces between neighboring particles are expected to play a dominant role in the rheological behavior of the mixtures [46]. The capillary suspension at S = 0.30 exhibited a high value of viscosity at low shear rate, followed by a rapid decrease when shear rate increased, even at values lower than the sample with S = 0.15. This behavior could be explained by looking at the image in Figure V.17d: the sample shows high inhomogeneity, which can be associated with the formation of a pendular state, where the formed bridges are strong enough to increase viscosity but not enough to form a strong network that does not break during the test. Similar behavior has been found for the sample with a saturation ratio S = 0.40.

Each capillary suspension was also characterized by measuring the apparent yield stress, as shown in Figure V.19, displayed as a function of saturation ratio.
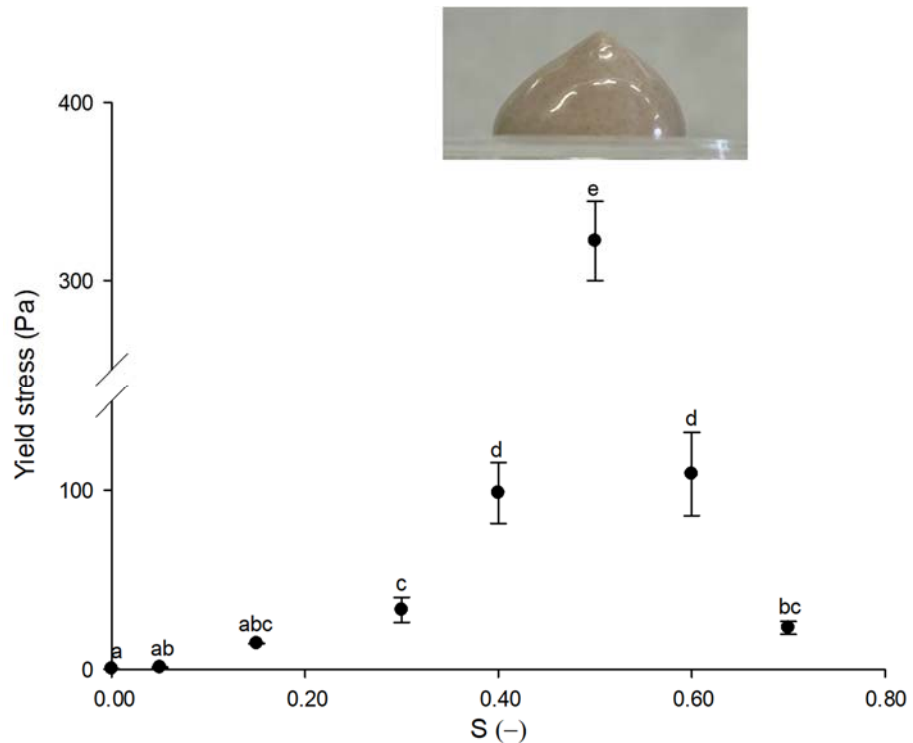
Figure V.19 *Apparent yield stress for WM-in-oil-dispersions at ϕ = 30% w/w as a function of saturation degree. Different letters denote statistically significant (p < 0.05) differences. On the top, the visual image of capillary suspension at S = 0.50.*

The addition of water changed dramatically the propriety of the suspension, as shown by the apparent yield stress, which increased progressively with the water content due to the increase of the network strength, up to a maximum value reached at S = 0.50. At higher S values, the apparent yield stress dropped, suggesting the occurrence of phase inversion. Remarkably, the apparent yield stress at S = 0.50 was three orders of magnitude higher than the particle in oil dispersion (S = 0.00). This value corresponds to the peak yield stress, denoting the creation of a network in which water acts as a bridge between the particles forming the so-called capillary bridges, which are much stronger with respect to the Van Der Waals forces that act in a simple suspension [46]. The results deal with other works, in which capillary suspension exhibits an increase in the yield stress with increasing amounts of added secondary fluid [45,50], until the maximum yield stress is achieved with 0.50 of saturation ratio.

V.2.3.5. Oxidative stability of capillary suspensions

The 15-day period of storage in the accelerated Schaal oven test conditions (65 °C) correspond to 15 equivalent months at room temperature. A remarkable increase in peroxide values, which are the indicator of primary lipid oxidation, was noticed in pure sunflower oil. In contrast, WM-based capillary suspensions ensured the lowest PV in the oil, demonstrating that the proposed approach not only does not suffer the presence of water, but significantly improves the oxidation stability with respect to the pure oil due to the phenolic bioactive compounds with high antioxidant activity, contained in the WM particles (Figure V.20).
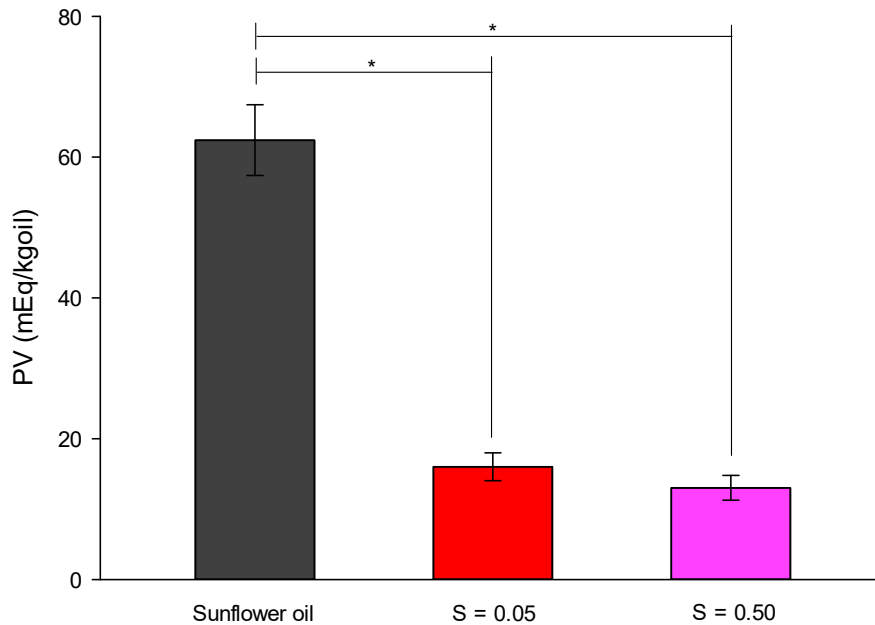
Figure V.20 *PV of capillary suspensions after a 15-day storage period at 65 °C.*

V.2.4. Conclusions

This section showed for the first time that wheat middlings AFRs can be valorized and exploited in sunflower oil structuring. Additionally, this work also demonstrated that the HPH mechanical treatment (80 MPa for 10 min) can be applied to the wheat middling particles directly in oil, to efficiently cause particle break-up, and, at the same time, to induce the activation of fibers, which is important in the formation of capillary bridges and a three-dimensional network, to regulate the apparent viscosity and yield stress of the capillary suspension, when water as secondary fluid is added.

Therefore, oil structuring with wheat middling treated by HPH approach offers many advantages in comparison with more conventional approaches based on oleogelation, namely: (i) a facile and versatile process, based only on physical processing, without the addition of undesired ingredients to the formulation (e.g. gelators); (ii) the replacement of part of the oil with the fibrous material and water, hence developing a more sustainable and health-beneficial oleogels in replacement of solid fats reducing the caloric intake, while ensuring the desired mouthfeel, as the oil will still constitute the continuous phase; (iii) the delivery of bioactive molecules, associated with the fibours particles from AFRs still rich in valuable compounds with an antioxidant, which effect on the decrease of oil oxidaion and on health-beneficial effects also on consumers; and (iv) the high transferability of the proposed approach, enabling to tune color, flavor, and taste of the structured oil, depending on the desired application. Further studies need to be addressed to further explore the application of these oleogels in spreads, creams, fillings or baking applications to evaluate the quality of these new products in terms of (i) texture of new low-fat food products in mimic regular full-fat products; (ii) in vitro digestion; (iii) microbial stability; and (iv) organoleptic properties.

Chapter V

Section V.3
NCs-based aerogels for the removal of pollutants from wastewater

Nanostructured cellulose has attracted attention for the fabrication of bio-absorbent aerogels, because of its remarkable properties and highly efficient, low-cost, biodegradable, and renewable sourcing. In this section, (ligno)cellulose nanofibers produced from barley straw by different pre-treatments and the quality index of the obtained suspensions has been evaluated for their application in wastewater decontamination systems. Although all the nanofibers exhibited quality indexes higher than 60%, cellulose nanofibers obtained after TEMPO-mediated catalytic oxidation pre-treatment excelled in quality, reaching a quality index of more than 90%. The application of nanofibers in the form of aerogels in wastewater decontamination demonstrated a contaminant removal capacity of more than 80% for those nanofibers with a quality index higher than 70%. Particularly, the high specific surface area of (L)CNF-TO allowed a higher affinity and interaction of the carboxyl groups with the contaminant. In addition, the analysis using the Langmuir adsorption isotherm model suggested a homogeneous adsorption of the contaminant on the aerogels. Therefore, the eco-friendly NCs-based aerogels would be a promising adsorbent material for effective wastewater treatment.

Chapter V

V.3.1. Specific goal and work plan

Along the whole food supply chain, 931 million tonnes of food wastes and by-products, also known as AFRs, were generated in 2019, 61% of which came from households, 26% from food service, and 13% from retail. This suggests that 17% of total global food production may be wasted (11% in households, 5% in food service, and 2% in retail) [69]. Food loss and waste are a big source of greenhouse gas emissions, making them a major contributor to the three planetary crises of climate change, nature and biodiversity loss, and pollution and waste. As awareness of human impact on the planet is increasing, the demand for new sustainable materials has grown rapidly in recent years, as evidenced by the UN agenda 2030 [70], in particular Sustainable Development Goal 12.3 aims to halve food waste and reduce food loss by 2030. In this scenario, the agricultural industry, in collaboration with the scientific community, has directed efforts toward the design of appropriate methods for the exploitation of AFRs to extract and purify high value-added compounds [71] including dietary fiber, antioxidants, oligosaccharides, vitamins, pectin, enzymes, pigments, organic acids inter alia, of special interest for innovative applications in different fields (i.e food ingredients, nutraceuticals, cosmeceutical, bioderived fine chemicals, biofuels, etc) [72,73]. It is currently known that the full use of waste with functional properties could lead the food industry to reduce residues and increase its profitability [74]. Therefore, the partial (or even total) use of industrial and agricultural wastes not only is an advantage from the environmental point of view for mitigating their environmental burden [75], but it could also solve some economic issues.

Among the different side-streams from agriculture, lignocellulosic biomass, such as straws from cereal plants (barley, oat, rye, and wheat, are rich in lignocellulose), is the most abundant renewable biomass on Earth, with approximately 200 billion tons per year of lignocellulosic biomass supply by worldwide from the forestry residue and agricultural wastes [76–80]. These biomasses are composed of cellulose, hemicelluloses, and lignin as well as other minor components. Among them, cellulose is the most abundant renewable organic carbohydrate polymer produced in the biosphere and widely distributed in higher plants, in several marine animals, and to a lesser degree in algae, fungi, bacteria, invertebrates, and even amoeba [81]. Cellulose is characterized by noteworthy structure and properties due to its unique molecular structure [82]. Owing to their hierarchical order in a supramolecular structure and organization given by the hydrogen bond network between hydroxyl groups, nanoparticles can be efficiently isolated from cellulose [83] via mechanical and chemical methods, or through their combination. Among the wide range of applications offered by NC, owing to its ultra-low density, high porosity, and large surface area as well as its wide

availability, NC-based aerogels represent a promising class of materials for water decontamination [84,85].

Effluent wastewater from different industries (textile, leather, paper printing, cosmetic, pharmaceutical, food, and technological applications) is a major source of environmental contamination from chemicals and dyes [86]. Owing its synthetic origin, dyes are a major concern due to their potential toxicity and adverse effects to human life and ecosystems. In particular, pollution from methylene blue, a cationic dye commonly used in textile manufacturing processes for dying cotton, wood, and silk, can lead to eye burns, breathing difficulties, nausea, vomiting, and methemoglobinemia [87–90]. These organic dyes are also stable at elevated temperature, under light exposure, heat, and in the presence of other chemical reactions [91]. In this scenario, the removal of organic dyes from wastewater before discharging is a crucial and very important aspect. During the past three decades, several physical methods, such as membrane filtration (nano-filtration, reverse osmosis, electrodialysis) [92], coagulation/flocculation [93], and irradiation [94], and other conventional chemical and biological decolorization methods, such as advanced oxidation processes [95], electrochemical degradation or ozonation [96], and decolorization by white-rot fungi [97], have been reported. Amongst these numerous techniques of dye removal, adsorption is the most widely employed method which gives the best results and can be used to remove different types of coloring materials [98,99] and moreover it is an effective and eco-friendly method due to its low-cost, high efficiency and without the generation of harmful substances [100] or secondary contamination [101].

For the adsorption process, NCs-based aerogels are the promising choice of adsorbent thanks to their features, such as large internal surface area, wide pore size distribution, rapid recovery from aqueous solutions, and low density, which are ideal for dye removal from wastewater, increasing greatly the adsorption capacity of the adsorbent.

The novelty of the study arises from the relationship between the quality index of (ligno)cellulose nanofibers purified from barley straw ((L)CNFs) (§ IV.3.3.6) and their application as wastewater decontaminant aerogels. For this purpose, the adsorption effect of pollutants from aerogels based on these (L)CNFs was analyzed by investigating in detail the kinetic and isothermal models of the process (Figure V.21). Finally, it was investigated in detail the quality index of NCs as the benchmarking parameter closely linked with adsorption efficiency of dye pollutants.

V.3.2. Specific material and methods
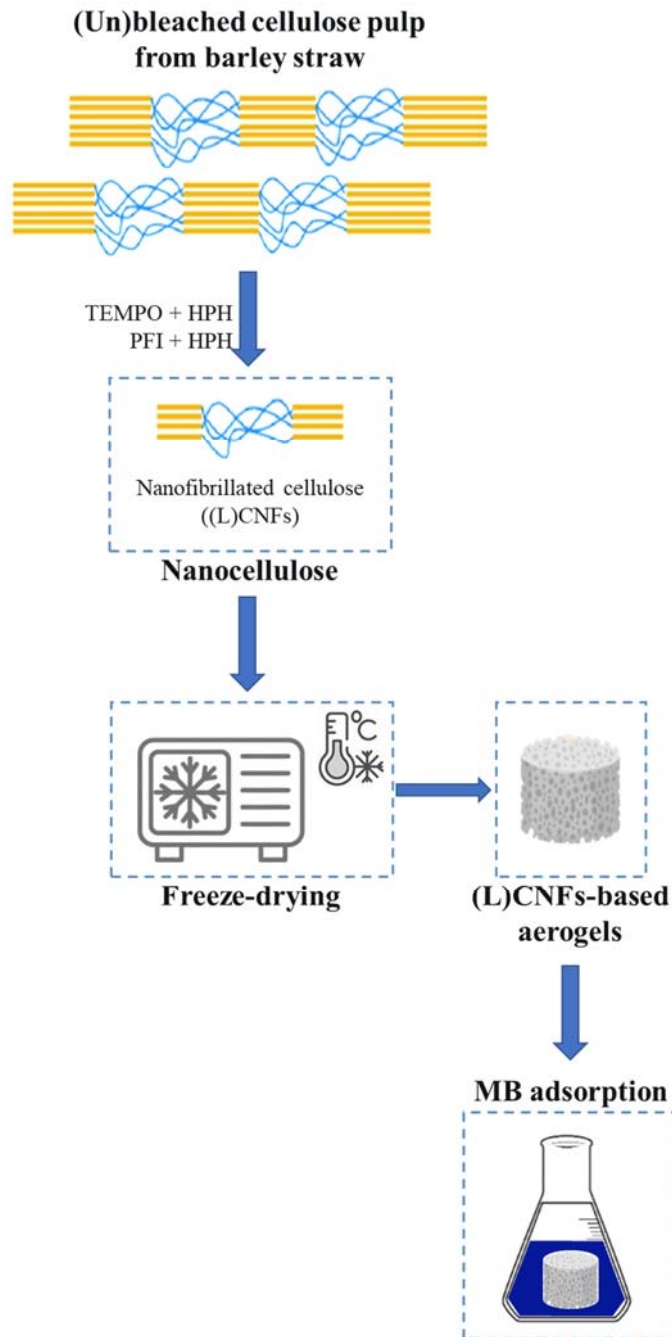
Figure V.21 *Schematic representation of methodology used for (L)CNFs-based aerogels production and utilization in dye removal.*

V.3.2.1. Materials

The (ligno)cellulose pulp was isolated from barley straw as described in § IV.2.3.3, and (L)CNFs have been obtained from the cellulose pulp through the combination of TEMPO-mediated oxidation or PFI beater with HPH, as described in detail in section § IV.3.3.6.

All reagents were of analytical grade unless otherwise stated. Micro-pure deionized water was used throughout the experiments.

V.3.2.2. Preparation and characterization of (L)CNFs-based

aerogels

(L)CNF suspensions at 0.5 wt%$_{DM}$ were prepared diluting the samples with distilled water and subsequently homogenizing at 20,000 rpm for 5 min with an Ultraturrax T18 (IKA-Werke GmbH & Co. KG, Staufen, Germany). Each suspension was frozen for 24 h prior to be subjected to freeze drying at -85 °C under 0.5 mBar for 72 h in a Lyoquest -85 lyophilizer (Telstar, Terrassa, Spain).

The porosity, a key property in the formation of aerogels due to its relationship with adsorption capacity [91], is calculated using the following equation [85]:

$$P = \left(1 - \frac{\rho_S}{\rho_C}\right) \cdot 100 \qquad (V.12)$$

where ρ_S is the apparent density of aerogels (obtained by the cylinder volume method using a digital calliper and digital balance with accuracy of 0.01 mm and 0.0001, respectively), and ρ_C is the density of cellulose (considered as 1540 kg/m^3).

The mechanical properties of cylinder aerogels (24 mm heigh and 28 mm diameter) were evaluated using Lloyd LF Plus Tensile Test Machine (Lloyd Instruments Ltd, Bognor Regis, United Kindom) equipped with a load cell of 1 kN by compression tests with a strain limit of 80%, based on the initial aerogels' height, at a speed of 2 mm/min.

The water contact angle (WCA) was measured in a Contact Angle Goniometer (Ossila Ltd, Sheffield, England), using the sessile drop method. A 10 µL droplet of deionized water was cast on the surface of the aerogel and the angle was measured from 0 to 10 s. The measurements were replicated 5 times and the results were expressed as average with their relative standard deviation.

V.3.2.3. Evaluation of dye removal efficiency

In this work, methylene blue (MB) solution was employed as typical cationic dye to simulate wastewater. All adsorption experiments were

performed by immersing the aerogel samples in 50 mL dye aqueous solution at 10 mg/L. The concentration of the dye solution during 24 h of adsorption was analyzed by UV–vis spectrophotometer (Lambda 25, Perkin Elmer Inc, Waltham, USA), using a calibration curve, obtained from the linear fitting (A_{664} nm = 0.2075 · C_{MB}, R^2 = 0.9991) of the measured absorbance (A_{664} nm) as a function of MB concentration (ranging from 0 to 10 mg/L). The percentage of dye removal during the adsorption kinetic was measured and calculated using the following relationship:

$$\% \, Dye \, removal = \left(\frac{C_i - C_t}{C_i}\right) \cdot 100 \qquad (V.13)$$

where C_i and C_t are the initial and after time t concentrations of dye (mg/L), respectively.

The amount of dye adsorbed Q_e (mg/g), onto aerogel was calculated from the mass balance equation as follows:

$$Q_e = \frac{C_i - C_e}{M} \cdot V \qquad (V.14)$$

where C_e is the equilibrium concentration of dye (mg/L), V is the volume of dye solution (L), and M is the mass of the adsorbent aerogel used (g).

Langmuir isotherm (Equation V.15) is used to describe adsorption equilibrium type and maximum adsorption capacity [100].

$$\frac{C_e}{Q_e} = \frac{1}{Q_m} \cdot C_e + \frac{1}{Q_m K_L} \qquad (V.15)$$

where Q_m is the maximum adsorption capacity (mg/g), and K_L is the Langmuir constant (L/mg).

Furthermore, the separation factor (R_L), calculated as in Equation V.16, is used to describe the essential characteristic of Langmuir isotherm: irreversible ($R_L = 0$); favorable ($0 < R_L < 1$); linear ($R_L = 1$); unfavourable ($R_L > 1$) [102].

$$R_L = \frac{1}{1 + K_L \cdot C_i} \qquad (V.16)$$

V.3.2.4. Statistical analysis

Experiments were repeated in triplicates and the values were expressed as mean ± standard deviation. Significant difference of *p < 0.05* was taken in a SPSS 20 (SPSS Inc., Chicago, USA) statistical package one-way analysis of variance (ANOVA) and Tukey's test. The data was normally distributed.

3.3. Results and discussion

V.3.3.1. (L)CNF-based aerogels

Aiming to establish a relationship between the QI of (L)CNFs (calculated using the Equation IV.3) and their potential applications, aerogels (Figure V.22) were prepared with these nanofibers to be applied as wastewater decontamination systems, due to their unique linear structure and mechanical properties as well as the presence of many hydroxyl groups, leading to an increase in the affinity of this adsorbent material with organic dyes.
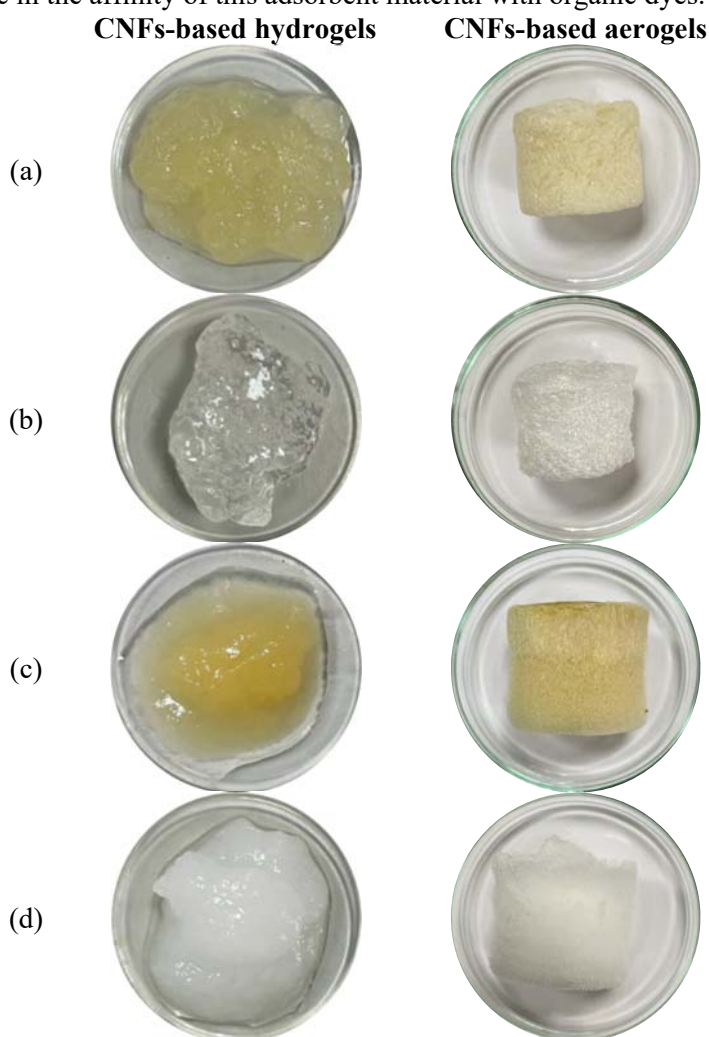
Figure V.22 *Aerogels materials obtained from (a) LCNFs-TO, (b) CNF-TO, (c)LCNF-PFI, and (d) CNF-PFI.*

Chapter V

To investigate the crucial factors for the handling and performance of adsorbent aerogels, the (L)CNFs-based aerogels obtained by freeze-drying hydrogels to preserve the internal pore structure were characterized by apparent density and the corresponding porosity, as well as by compression tests for mechanical properties (Table V.6). (L)CNFs aerogels, owing to the high strength of NCs and the stable porous structure, exhibit good mechanical performances under an external force, better than the traditional brittle SiO_2 aerogels that are usually broken easily under pressure [103]. Moreover, the Young's modulus of the (L)CNF-TO samples increased with respect to (L)CNF-PFI ones, owing to the strong hydrogen bonding of cellulose chains which can facilitate the formation of a strong network. As a result, at the same cellulose content, LCNF-TO and CNF-TO demonstrate a significant difference ($p < 0.05$) in compressive strength (of about ≈ 3 kPa) with respect to LCNF-PFI and CNF-PFI. Moreover, the tensile strength and compressive modulus have a direct relationship with the density of CNFs-based aerogels [104]. The NCs-based solid aerogels have the advantages to display low density ranging from 5 to 9 kg/m³, and the corresponding porosity higher than 99%, which greatly improves their water absorption and water retention, as well as their excellent ability to adsorb macromolecules. The compressive behavior of aerogels, plotted against relative density in Figure V.23a, is commonly described by power law dependence of Equation V.17 [105]:

$$E \propto \left(\frac{\rho_s}{\rho_c}\right)^n \qquad (V.17)$$

where the E is the Young's Modulus, ρ_s/ρ_c is the relative density, and n is the scaling exponent.

The power law predicts a scaling exponent of n = 3.708, suggesting that obtained materials have aerogel-like structure, in good agreement with previous studies on cellulose [106,107].

Table V.6 *Mechanical properties from the compression analysis, apparent density, and porosity of the different aerogels.*

	Young's Modulus (kPa)	Tensile strength (kPa)	Stiffness (kN/m)	Apparent density (kg/m³)	Porosity (%)
LCNF-TO	30.46 ± 2.19[c]	2.78 ± 0.32[b]	6.96 ± 0.48[b]	7.53 ± 0.50[c]	99.51 ± 0.03[b]
CNF-TO	33.91 ± 3.92[c]	3.09 ± 0.17[b]	7.23 ± 0.16[b]	9.08 ± 0.43[d]	99.41 ± 0.03[a]
LCNF-PFI	18.68 ± 2.71[a]	1.81 ± 0.05[a]	4.73 ± 0.85[a]	5.78 ± 0.40[a]	99.62 ± 0.03[d]
CNF-PFI	24.21 ± 1.72[b]	1.61 ± 0.18[a]	5.51 ± 0.78[a]	6.61 ± 0.16[b]	99.57 ± 0.01[c]

Different letters denote significant differences ($p < 0.05$) among the different samples within each column (n = 3).

(a)

(b)
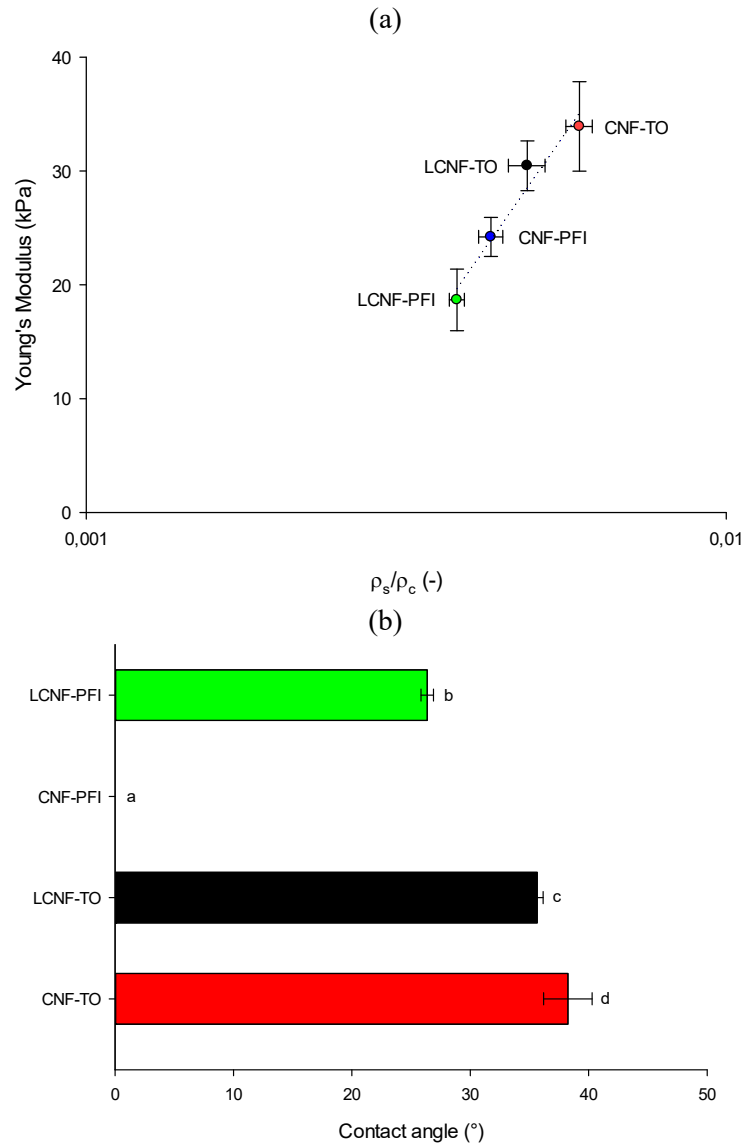
Figure V.23 *(a) Young's Modulus as a function of relative density (ρ_s/ρ_c) for CNFs-based aerogels. Dotted line represents the power law fitting curve (Equation V.17). (b) Average contact angle of water on aerogels. Different letters denote significant differences (p < 0.05).*

In order to further verify the feasibility for dye removal from water, the aerogels were characterized also in terms of wetting properties. Due to the large number of hydrophilic hydroxyl groups in cellulose, the water contact angle was lower than 40° for freeze-dried cellulose nanofiber aerogels, a part for CNF-PFI, into which a water droplet penetrates within 1 s, and therefore

the water contact angle was 0°. Hence, water droplets are not stood on the surface but adsorbed within 10 s, demonstrating the hydrophilic nature of CNFs-based aerogel.

V.3.3.2. Adsorption behavior of (L)CNF-based aerogels

The prepared adsorbent aerogels showed excellent Methylene blue (MB) adsorptions. Figure V.24 shows the adsorption kinetics of different (L)CNFs-based aerogels for MB solution at 10 mg/L. The results indicated that the adsorption rate increased rapidly at the beginning due to the high availability of hydroxyl and carboxyl groups present in the aerogel (negative charge) to interact with MB (positive charge), and then it gradually slowed down owing to the saturation of the adsorption sites inside the adsorbent. Therefore, the affinity for adsorption by the (L)CNFs-based aerogels was due to their functional groups (hydroxyl and carboxyl), as reported in Table V.7. The adsorption equilibrium has been reached at about 1, 4, 23, and 3.5 h after adsorption for LCNF-TO, CNF-TO, LCNF-PFI, and CNF-PFI, respectively. The slower adsorption obtained by CNF-PFI aerogel is mainly due to the low surface charge of nanofibers obtained by mechanical pre-treatment as well as the lower QI value. Meanwhile, despite LCNF-PFI exhibited a slight different QI value than CNF-PFI, the lignin content still present in the LCNFs had a significant effect on the adsorption properties owing to the formation of electrostatic interactions between the functional groups and cationic dye [85].
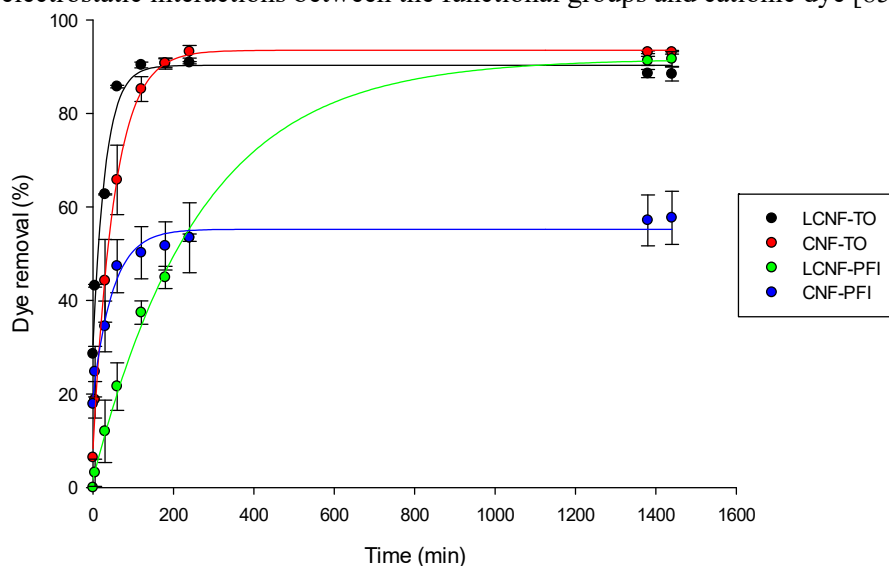
Figure V.24 *Effect of contact time on the adsorption capacity of Methylene blue cationic dye. Circles represent experimental data points and solid lines represent exponential decay fitting curves (Equation V.18).*

In addition, all samples exhibited the exponential decay relation (Equation 18) between adsorption time and percentage of dye removed. Therefore, Table V.7 showed the relevant kinetic parameters of graphs of kinetic model which has a higher R^2 value, and thereby it is suitable for describing the adsorption behavior of the MB cationic dye.

$$f(x) = y_0 + a \cdot e^{-b \cdot x} \qquad (V.18)$$

Table V.7 *Kinetic coefficients and fitting parameters for dyes adsorption model using Equation V.18.*

Parameters	Value			
	LCNF-TO	*CNF-TO*	*LCNF-PFI*	*CNF-PFI*
y_0	1.042 ± 0.025	0.708 ± 0.042	0.857 ± 0.111	4.765 ± 0.774
a	9.250 ± 0.484	9.283 ± 0.557	9.028 ± 0.661	5.231 ± 0.359
b	0.346 ± 0.004	0.043 ± 0.013	0.005 ± 0.001	0.377 ± 0.013
R^2	0.999 ± 0.001	0.997 ± 0.001	0.994 ± 0.004	0.947 ± 0.006
Adj R^2	0.998 ± 0.001	0.996 ± 0.001	0.992 ± 0.006	0.928 ± 0.008

The high initial concentration of MB (10 mg/L) promoted the adsorption amount of cellulose aerogels toward dye, which was ascribed to the higher driving forces between adsorbents and dye molecules. The LCNF-TO and CNF-TO-based aerogels allowed to reach the maximum equilibrium adsorption capacity of the MB (Figure V.25a), because the (L)CNF-TO have higher specific surface area, leading to a higher affinity and interaction of carboxyl groups with MB. This result is also confirmed from visual observations (Figure V.26), where it is clear visible how the MB solution became clearer after the treatment with aerogels. In addition, this finding indicated that a QI higher than 70% causes the adsorption process's efficiency of MB to increase, reaching the maximum equilibrium adsorption capacity.

(a)

(b)
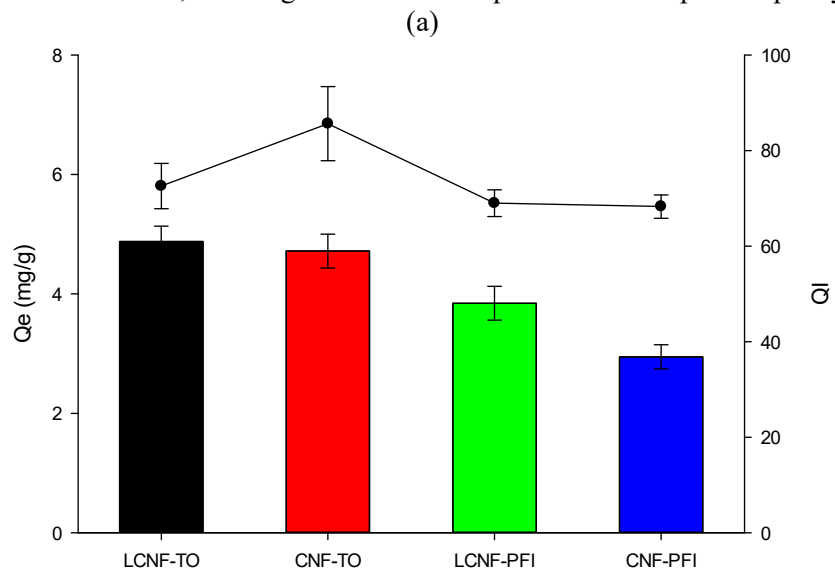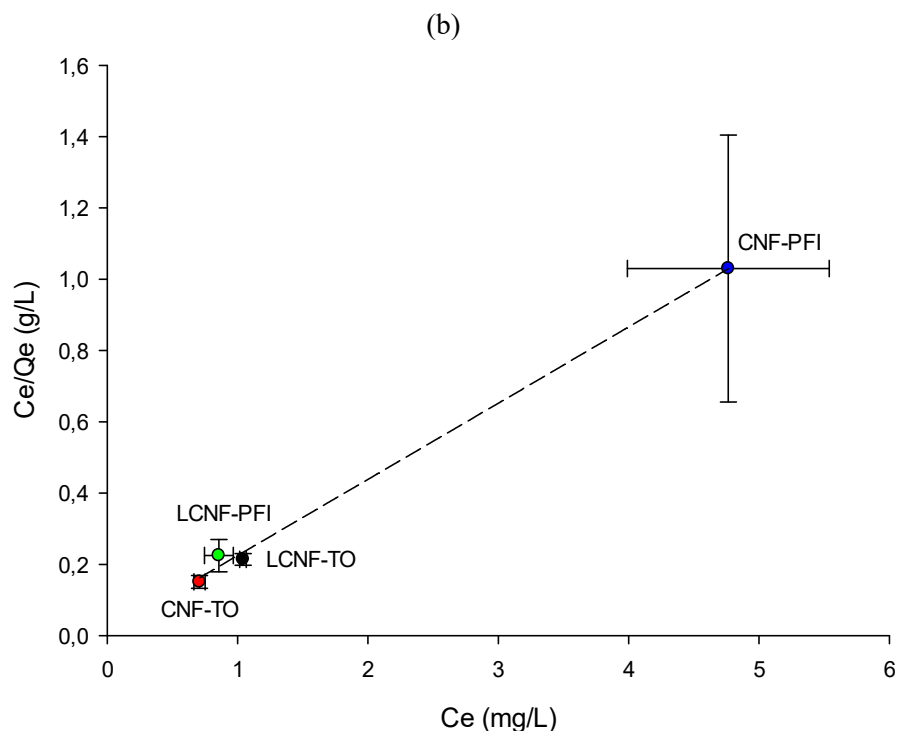
Figure V.25 *(a) Effects of different aerogels on the MB adsorption capacity (left y-axis, Q_e) and on the quality index (right y-axis, QI). (b) Langmuir isothermal adsorption model.*

Furthermore, the interaction between the adsorbent and adsorbate has been analyzed via the Langmuir adsorption isotherm model (Equation V.15) at 25 °C, as shown in Figure V.25b. Results indicated that NCs-based aerogels have homogeneous adsorption characteristics for MB with a maximum adsorption capacity of 4.677 mg/g. Moreover, the R_L value of MB adsorbed by (L)CNFs aerogels is less than 1 (Table V.8), demonstrating a favorable adsorption process owing to the strong intermolecular interaction between oxygen-containing groups of aerogels and hydrophilic segment of dye molecules.

Table V.8 *Langmuir isothermal adsorption fitting parameters of Equation V.15.*

Parameters	Value
Q_m	4.677
K_L	19.796
R^2	0.997
Adj R^2	0.996
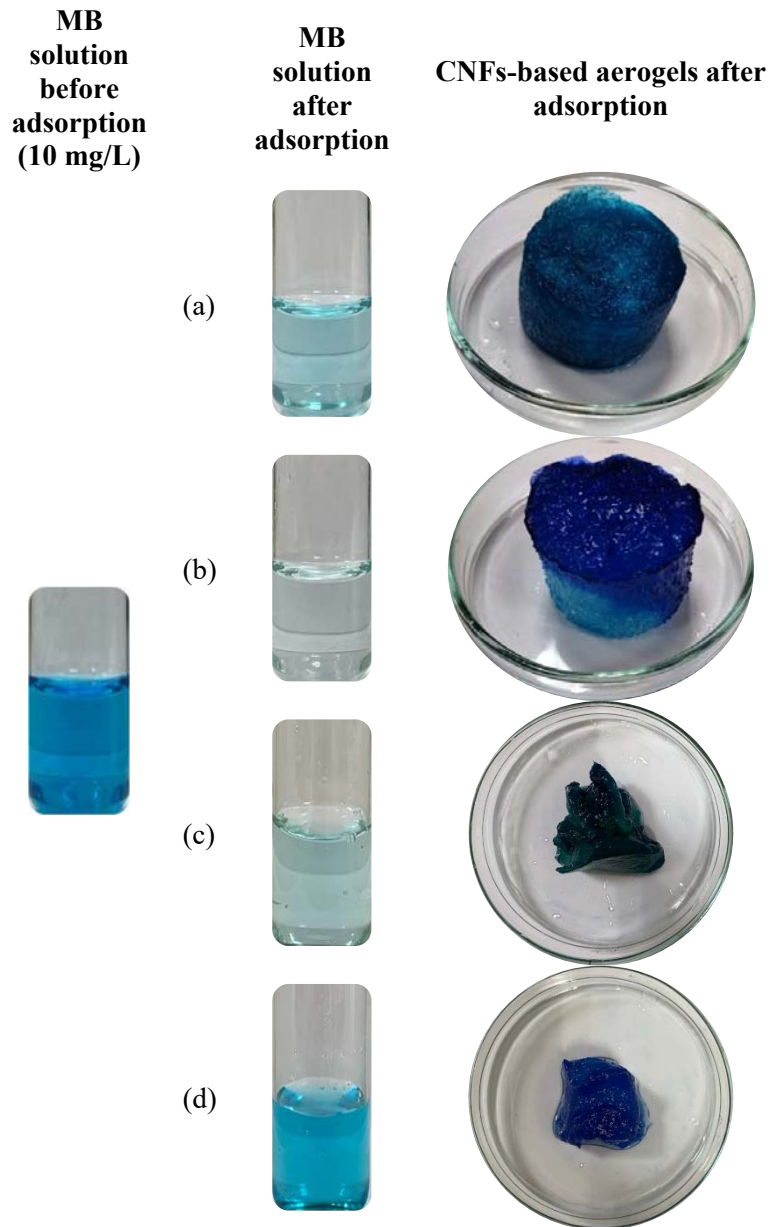
Figure V.26 *MB solution (left column) and aerogels materials (right column) of (a) LCNFs-TO, (b) CNF-TO, (c)LCNF-PFI, and (d) CNF-PFI, after 24 h adsorption test.*

V.3.4. Conclusions

In summary, porous, low density, and high porosity NCs-based aerogels have been successfully obtained using nanostructured cellulose isolated from barley straw by-products via chemical and mechanical pre-treatments. The quality index clearly characterization enabled to observe the relationship between the quality grade of different (ligno)cellulosic nanofibers and their adsorption behavior. Batch adsorption experiments indicated that (L)CNFs aerogels have high adsorption capacity for methylene blue, which could be ascribed to the internal porous structure and the electrostatic interaction between NCs and cationic dye molecules. In particular, all samples exhibited a MB capacity removal equal or higher than 90%, except nanofibers obtained by mechanical pre-treatment which have the lower quality index. Nevertheless, the effect of residual lignin content in NCs isolated via mechanical pre-treatment significantly improved the adsorption capacity in comparison with lignin-free CNFs-PFI. The excellent cationic dye removal efficiency of these lignin-nanocellulose can be explained as follows. At the beginning of batch adsorption experiment, cationic dye can undergo weak adsorption through hydrogen bonding and π–π accumulation with lignin. For longer time, deprotonated anionic functional groups, such as hydroxyl and carboxyl groups, present on the surface of lignin implement strong electrostatic interactions with cationic dye molecules and thus exhibit an adsorption capacity, reaching the final adsorption percentage of (L)CNF-TO. Furthermore, the equilibrium data was consistent with the Langmuir isothermal model, and the maximum theoretical adsorption capacity for MB was 4.88 mg/g. In this scenario, NCs-based aerogels with a quality index higher than 69% would be a promising adsorbent material for wastewater treatment owing to its low-cost and high adsorption capacity.

Section V.4
Reinforcement materials for edible coatings

The usage of edible coatings (ECs) represents an emerging approach for extending the shelf life of highly perishable foods, such as fresh fruits and vegetables. This section addresses, in particular, the use of NCs as reinforcing agents in film-forming solutions of sodium alginate to tailor the physicochemical, mechanical, and antimicrobial properties of composite coatings, focusing on the impact of NC origin and physical treatments on their structural properties (morphology, shape, and dimension) and their functionality. Moreover, to enhance their efficiency and functionality, ECs can be loaded with different bioactive compounds, such as essential oil, to develop specific functionalities, such as antimicrobial, antioxidant, flavoring, or even nutritive actions. However, the use of additives, to achieve the desired effect during foodstuff shelf life and, upon consumption, in the relevant biological environment, is severely limited by their scarce performance, especially for what concerns solubility, stability against environmental conditions during product manufacturing, storage, and bioavailability upon consumption. Nanoencapsulation can be seen as an attractive approach to overcoming these challenges. Among the different nanoencapsulation systems, NCs-stabilized Pickering emulsions have emerged as the most effective ones, because of their intrinsic low toxicity following their formulation with biocompatible and biodegradable materials.

V.4.1. Specific goal and work plan

Edible coatings represent a method to extend the shelf life and maintain the physical and gustatory characteristics of fresh produce, traditionally used in food storability [108]. The introduction of food-grade materials with more advanced properties and novel deposition methods has enabled the application of edible coatings in extremely thin layers on the food surface, providing an invisible physical barrier to oxygen, external microbial contamination, and

moisture absorption/desorption in food, without affecting its organoleptic properties [109–111]. More recently, the use of edible coatings has been further promoted by their functionalization with bioactive compounds, such as natural antimicrobial compounds, antioxidants, minerals, and vitamins, which contribute not only to improving safety and preserving the quality of food but also to delivering health benefits to the consumer [112,113]. Because of their high efficiency in reducing the occurrence of deteriorative processes, antimicrobial coatings have been widely studied for extending the shelf life of fish and meat products, as well as for high value-added fruits and vegetables [110].

Edible coatings can be applied onto the food surfaces by various methods, including spraying, dipping, spreading, and thin-film hydration [114]. Numerous studies have been conducted to date to assess the effect of edible coatings on preserving the quality and increasing the shelf life of fresh/fresh-cut fruits [115]. The coating efficiency in protecting food products was reported to depend on (i) the method of application; as well as on (ii) the nature of the coating ingredients and their concentrations [116]; (iii) the uniformity of wetting and spreading on the surface and on the adhesion, cohesion, and durability [117]; (iv) the capability to act as barriers against water or oils permeation; and (v) gas or vapors transmission [117,118].

Among different film-forming materials, alginates are widely used in the edible coating because of their wide availability and regulatory status. The U.S. Food and Drug Administration (FDA) classifies food-grade sodium alginate as generally regarded as safe (GRAS) [119] and lists its usage as an emulsifier, stabilizer, thickener, and gelling agent [120]. The European Commission (EC) lists alginic acid and its salts (E400–E404) as authorized food additives.

Recently, the incorporation of essential oils (EOs) as natural antimicrobial agents in edible coatings has received increasing attention to control the decay and extend the storage life of perishable foods [121–123]. Bergamot essential oil (BEO) has excellent antimicrobial properties and inhibits the growth of both gram-positive and gram-negative bacteria and fungi [124]. Moreover, the synergistic interaction between reinforcement agents and the polymeric material, through hydrogen bonding or ionic complexation, enables the ECs mechanical properties to be increased and permeability of moisture and gases to be reduced [125]. Among the different reinforcing agents, nanofillers or additives with their size lying in the range of 100 nm have attracted increasing attention. In this scenario, NCs emerged as a promising material for tailoring ECs properties in food preservation. For their nano-reinforcing effect in many different polymer matrices, NCs is mainly used.

This section addressed the development of active coatings for strawberries, which are one of the most popular and trending fruits across the world. The shelf-life extension of strawberries is of great industrial relevance, since they are readily perishable fruits, so special technology or handling is needed to

prevent damage arising from the poor logistics from rural and remote areas of cultivation as well as from the market storage, hence contributing to food waste reduction and maintaining the shelf life and human health benefits. From the aforementioned reasons, the objective of this work was to investigate the effect of coating formulation, based on sodium alginate at 2 wt%, reinforced with MBC or functionalized with bergamot essential oil as it is and in encapsulated forms using emulsions or MBC-stabilized Pickering emulsions (Figure V.27).

V.4.2. Specific material and methods
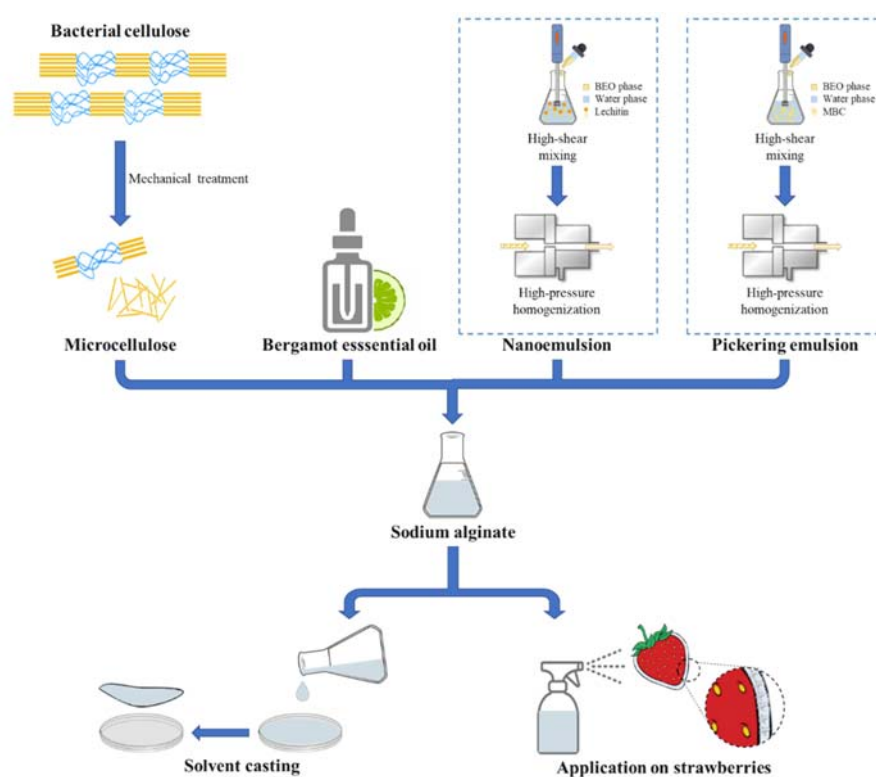
Figure V.27 *Schematic representation of methodology used for active edible coating.*

V.4.2.1. Materials

Fresh strawberries (*Fragaria × ananassa*) were purchased from a local supermarket (Salerno, Italy), and stored at 4 °C until used. Before each experiment, strawberries were selected based on similar shape and without any physical damage or visible signs of disease occurrence were subjected to the experimental treatments.

297

Chapter V

The bacterial cellulose, iolated from the Kombucha tea fermentation (§ IV.2.3.3), was treated through high shear mixing, as described in the section § IV.3.3.4, to obtain micronized baterial cellulose (MBC). Sodium alginate (Thermo Fisher GmbH, Kandel, Germany), bergamot essential oil (kindly supplied by Frey & Lau GmbH, Henstedt, Ulzburg, Germany) and lecithin (soy lecithin Solec IP, Milan, Italy) were used in coating formulations. Buffered peptone water, plate count agar, and agar dichloran rose bengal (all acquired from VWR International, Milan, Italy) were used in microbiological viability tests.

All chemicals and solvents used in this study were purchased from Sigma Aldrich (Milan, Italy) unless otherwise specified.

V.4.2.2. Preparation of emulsions and coating solutions

Nanoemulsion was produced by dispersing BEO in water, using lecithin as the emulsifier. A primary emulsion was prepared by mixing BEO with lecithin at different concentration and then adding the mixture to distilled water using a high-shear mixing (HSM) disperser (Ultra Turrax T25, IKA Labortechnik, Staufen, Germany) at 35,000 rpm for 5 min, based on previously optimized conditions [126]. The nanoemulsion was obtained by treating the primary emulsion by HPH at 80 MPa for 15 passes, using an in-house developed unit, equipped with a 200 μm diameter orifice valve (model WS1973, Maximator JET GmbH, Schweinfurt, Germany) and an air-driven Haskel pump (model DXHF-683, EGAR S.r.l., Milan, Italy).

Pickering emuslion was produced by dispersing BEO in water, using micronized bacterial cellulose as stabilizer. Coarse oil-in-water emulsions were prepared by BEO with MCB in water suspension at different concentrations, in a high-shear mixer (HSM) (MIULab MT-30K Handheld Homogenizer, Hangzhou, China) at 35,000 rpm for 5 min in an ice bath. The obtained coarse emulsions were then treated through a HPH process at 80 MPa for 15 equivalent passes, with the heat exchangers set at 5 °C, in a lab set-up (orifice-type homogenizer) previously described in detail by Pirozzi et al. (2021) [14].

Sodium alginate coating solutions were prepared by dissolving sodium alginate in distilled water followed by stirring with a magnetic stirrer, at 70 °C, until the solutions became clear [127–129]. The solutions were then sterilized in an autoclave at 121 °C for 10 min.

The active edible coating was prepared by mixing a sodium alginate solution of appropriate concentration with MBC, BEO or emulsions under magnetic stirring, to ensure a final coating solution of 2 wt% (optimized concentration) and an MBC, BEO or emulsions concentration of 0.5 or 1 wt%. All coating solutions were prepared in a laminar-flow hood (Faster Bio48/Faster UltraSafe, Milan, Italy) under aseptic conditions, using

autoclave-sterilized Milli-Q water. Details of the coating formulations used in this study are summarized in Table V.9.

Table V.9 *Sample codes and formulations.*

Sample code	Sodium alginate (wt%)	MBC (wt%)	Bergamot essential oil (wt%)	Nanoemulsion (wt%)	Pickering emulsion (wt%)
SA	2	-	-	-	-
SA_MBC 0.5	2	0.5	-	-	-
SA_MBC 1	2	1	-	-	-
SA_BEO 0.5	2	-	0.5	-	-
SA_BEO 1	2	-	1	-	-
SA_NE 0.5	2	-	-	0.5	-
SA_NE 1	2	-	-	1	-
SA_PE 0.5	2	-	-	-	0.5
SA_PE 1	2	-	-	-	1

V.4.2.3. Edible films characterization

1.5 mL of film-forming solutions (Table V.9) was poured onto Petri dishes and dried in a laminar-flow hood at 25 °C for 24 h to obtain edible films through solvent casting method.

Once the films completely dried off, thickness (δ) measurements at ten distinct points of the edible film were performed, using a digital micrometer (Micromaster Capa μ System, TESA Technology Italia s.r.l., Milan, Italy), and the mean values and standard deviations were determined.

The surface color was determined using a colorimeter CR400 Chroma Meter (Konika Minolta Inc., Japan). Color changes were quantified in the CIE L*a*b* color space. L* (lightness), a* (green-red chromaticity), and b* (blue-yellow chromaticity) were recorded and used to calculate the total color difference (ΔE) with respect to the control SA film and whiteness index (WI), according to the Equation V.19 and V.20, respectively. Before each analysis, the colorimeter was calibrated with a standard white plate. Ten readings were taken at random positions from sample, for two independently prepared films.

$$\Delta E = \sqrt{(L_0^* - L^*)^2 + (a_0^* - a^*)^2 + (b_0^* - b^*)^2} \qquad (V.19)$$

$$WI = 100 - \sqrt{(100 - L^*)^2 + a^{*2} + b^{*2}} \qquad (V.20)$$

Water vapor permeability (WVP) tests were conducted using the gravimetric method ASTM E96 [130] with some modifications. The used procedure is the dry-vial method, where each film sample was sealed over a vial circular opening of 2.6 cm^2 and stored at 25 °C in a chamber at controlled relative humidity (RH). More specifically, to maintain a 75% RH gradient across the film, anhydrous calcium chloride (0% RH) was placed inside the vial and a sodium chloride saturated solution (75% RH) was used in the chamber. The RH inside the vial was, therefore, always lower than the outside chamber. The weight gain of the vials over time was measured periodically

for 53 h to obtain the water vapor transmission rate (WVTR) of the films. Three replications were conducted for the same treatment. In calculating the WVTR, linear regressions ($R^2 > 0.99$) were carried out for the recorded weight gains. The WVTR was calculated from the slope of the straight line (g/s) divided by the cell area (m^2). The average of the ten measurements of the film thickness was used to calculate the WVP (g/Pa s m) from the WVTR results by the following equation:

$$WVP = \frac{WVTR}{S \cdot (RH_1 - RH_2)} \cdot \delta \qquad (V.21)$$

where WVTR is the slope obtained by plotting the final weight minus the initial weight of the sample versus time, S is the saturation vapor pressure of water (Pa) at the test temperature (25 °C), RH_1 and RH_2 is the relative humidity in the chamber and in the vial, respectively, δ is the film thickness (m). Under these conditions, the driving force $S \cdot (RH_1 - RH_2)$ is 1753,55 Pa [131].

Tensile properties of edible films are measured according to modified ASTM D882-12 standard method [132], by using a texture analyzer model TA-XT2a (Stable Microsystems, Godalming, United Kingdom). Rectangular strips of edible films are cut according to ASTM D6287-09 standard method [133] and stretched at fixed initial grip distance (50 mm) and cross-head speed (50 mm/min). Five samples (1.8×10 cm) of each film were evaluated. The tensile strength (TS) was calculated according to the Equation V.22:

$$TS = \frac{F_{Max}}{\delta \cdot h} \qquad (V.22)$$

where F_{Max} is the maximum force (N) required at break, δ is the film thickness (m), and h is the width (m) of the film.

V.4.2.4. Edible coatings on strawberries characterization

Before coating treatment, strawberries were washed with water for approximately 2 min and drained with blotting paper and let at room temperature until the fruit surface was completely dried. Then, sodium alginate film-forming solutions with 1 wt% of MBC, BEO or emulsions were vaporized with a manual spryer on strawberries surface. Subsequently, the coated strawberries were placed on perforated aluminum trays and let to dry in a laminar-flow hood at 23°C under aseptic conditions for 4 h. The strawberries were then stored at refregirated conditions (4 °C).

The contact angles (θ) of the film-forming solution on the strawberries were measured by the sessile drop method [134], using a contact-angle meter (KSV Instruments LTD CAM 200, Helsinki, Finland), equipped with an image analysis software. Briefly, a drop of about 2 μL of the film-forming solution was gently dispensed on the strawberries surface (placed on the instrument stand to be aligned horizontally in the contact point with the water drop) using a 500 μL syringe (Hamilton, Switzerland) with a 0.71 mm diameter needle. Measurements were made each 5 s for a total of 600 s to evaluate the contact angle changes over time. The contact angle measurements were carried out in open air at room temperature (24 ± 1 °C), *in situ*, for water as a control and the film-forming formulations, containing MBC, BEO, or emulsions at different concentrations, deposited on the strawberries surface. Contact angles were measured in triplicate, and the average contact angle was calculated as the mean value over the 600-s measurement.

Firmness was measured at 1 and 27 days of storage using a texture analyzer (Model TA-XT2, Stable Microsystems, England) equipped with flat end probe (P/10) and three replicates of penetration at different points. Measurements were made to a depth of 5 mm; penetration speed was 0.5 mm/s, and the cylinder plunger had a diameter of 10 mm. Firmness values are presented in Newton (N).

The changes in the endogenous microbial flora of strawberries, both for control and coated fruits stored at 4 °C for 27 days, were determined for total bacterial count and yeasts and molds count at storage days 1 and 27. The total bacterial count was measured using Plate Count Agar (PCA) medium, according to the procedures described by ISO 4833-1/2013, while yeasts and molds were determined using Agar Dichloran Rose Bengal (DRBC), according to the methods described by ISO 21527-1/2008. For each microbial determination, two tomatoes per coating formulation were analyzed, by recovering the microbial load using a filter stomacher bag containing buffered peptone water (1:5 mass ratio), which was aseptically homogenized in a Stomacher 400 Circulator (Seward, FermionX, provided by VWR International PBI s.r.l., Milan, Italy). Decimal dilutions were prepared with the same diluent and appropriate dilutions were included in culture media. For total bacterial count, inoculated Petri dishes were incubated at 30 °C for 72 h; for molds and yeasts count, the Petri dishes were incubated at 25 °C for 120 h. After incubation, colonies were enumerated and results were reported as log CFU/g of sample. All tests were performed in triplicate, and for each sample, the evaluation was carried out in duplicate for each dilution and analyzed according to ISO TS 19036:2006. The sensitivity of the analysis was ≥ 1 log CFU/g.

V.4.2.5. Statistical analysis

Treatments and analyses were performed in triplicate unless differently specified and the results were reported as means ± their respective standard deviations. Significance of differences between means were evaluated using a one-way analysis of variance (ANOVA), performed with SPSS 20 (SPSS IBM., Chicago, USA) statistical package, and Tukey's test ($p < 0.05$).

V.4.3. Results and discussion

V.4.3.1. Edible films

The aspect and appearance of the nine films were investigated using visual images, as shown in Figure V.28. In general, as additive content increased, a lower transparency of films was observed compared to the control film, showing active films of a slight gray color. Moreover, pores or cavities could be observed in the films containing lecithin-based nanoemulsions, which were associated with oil droplets embedded in the complex matrix. Indeed, emulsion weakened the interactions between chitosan molecules and increased the porosity of the film structure. Meanwhile, the structure of SA_MBC samples was homogeneous without cracks or pores, due to the good compatibility between sodium alginate and MBC-stabilized Pickering emulsions.
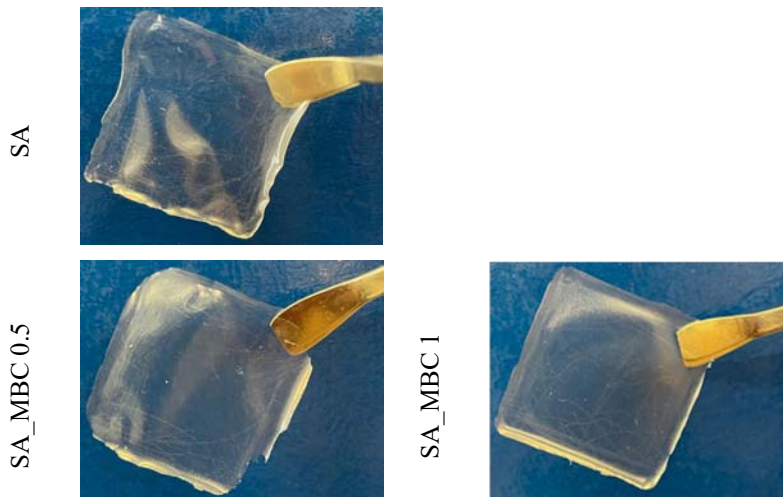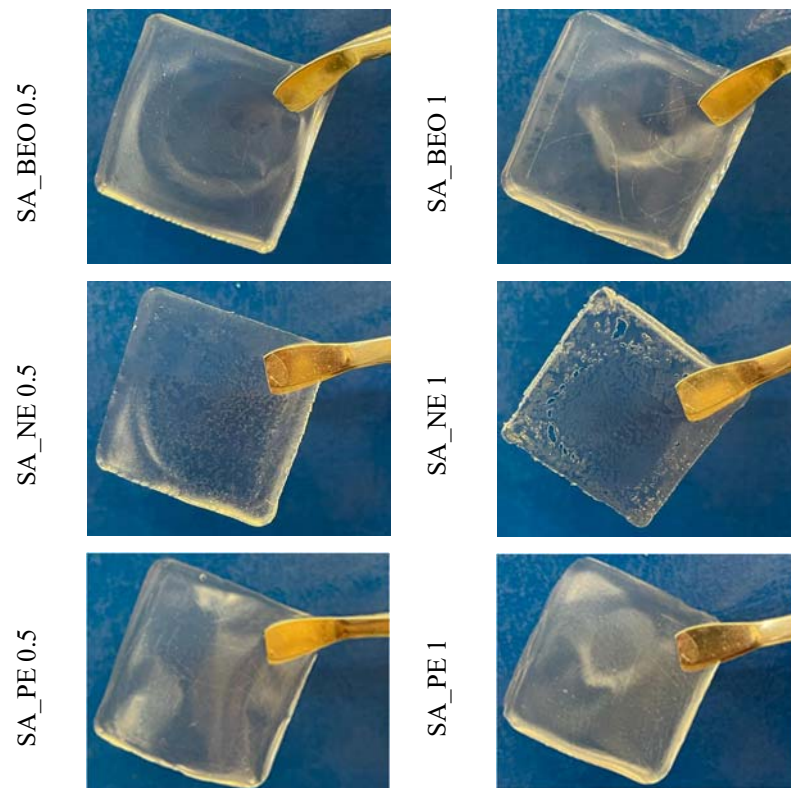
Figure V.28 *Visual appearance of the obtained edible films.*

A significant ($p < 0.05$) slight decrease in L* and a* (lightness) values and an increase in b* parameters with the addition of additives (Table V.10) was obtained. Concerning the total color difference (ΔE), a clearly significant ($p < 0.05$) increase was observed with additive concentration, being higher for films added with 1 wt% MBC, BEO or Pickering emulsion. However, WI values followed a decreasing tendency with increasing additives loading. It should be highlighted that the chromaticity parameters of the color CIELab space were obtained on a standard white plate, so the decrease in WI and L* values with respect to the control film may reflect a lower transparency. In this sense, the incorporation of OE contributes to intensifying the color of active films [135] due to their natural color, except for BEO which was not significant influenced color parameters with respect to SA control sample.

Significant differences between films were observed also regarding thickness (Table V.10), between 16 and 60 µm. Lower thickness values correspond to a well-organized and dense film network [136]. In this sense, thickness is an important issue to be considered as changes in structural, mechanical, thermal, or barrier properties should be expected in films presenting nonhomogeneous thickness values [137].

Table V.10 *Thickness and color coordinates of edible films.*

Edible film	Thickness (μm)	L*	a*	b*	ΔE	WI
SA	29.90 ± 3.60^{bc}	91.02 ± 0.07^{de}	2.97 ± 0.06^{d}	-4.19 ± 0.18^{a}	-	46.49 ± 0.20^{de}
SA_MBC 0.5	28.10 ± 1.45^{b}	89.03 ± 0.41^{abc}	3.06 ± 0.05^{d}	-1.81 ± 0.52^{bc}	2.94 ± 0.44^{c}	36.44 ± 0.66^{c}
SA_MBC 1	33.00 ± 2.36^{c}	88.87 ± 0.13^{ab}	3.07 ± 0.07^{d}	-0.24 ± 0.09^{c}	4.50 ± 0.31^{d}	33.32 ± 0.17^{b}
SA_BEO 0.5	17.30 ± 4.42^{a}	91.71 ± 0.24^{de}	2.87 ± 0.11^{cd}	-4.01 ± 0.36^{a}	0.23 ± 0.19^{a}	48.86 ± 0.45^{e}
SA_BEO 1	19.20 ± 2.53^{a}	91.53 ± 0.15^{e}	2.74 ± 0.08^{bcd}	-3.48 ± 0.35^{ab}	0.90 ± 0.15^{ab}	54.32 ± 0.39^{f}
SA_NE 0.5	16.10 ± 1.85^{a}	90.84 ± 0.36^{de}	2.57 ± 0.08^{abc}	-2.04 ± 0.27^{bc}	2.19 ± 0.20^{bc}	52.66 ± 0.46^{f}
SA_NE 1	26.80 ± 4.76^{b}	90.96 ± 0.53^{de}	2.38 ± 0.07^{ab}	-1.82 ± 0.41^{bc}	2.44 ± 0.45^{c}	54.65 ± 0.67^{f}
SA_PE 0.5	25.60 ± 3.20^{b}	89.86 ± 0.18^{bcd}	2.70 ± 0.03^{abcd}	-1.18 ± 0.29^{c}	3.24 ± 0.12^{cd}	44.25 ± 0.34^{d}
SA_PE 1	59.70 ± 2.54^{d}	87.65 ± 0.27^{a}	2.34 ± 0.03^{a}	4.27 ± 0.27^{d}	9.13 ± 0.15^{e}	11.88 ± 0.38^{a}

Different letters denote significant differences ($p < 0.05$) among the different samples within each column ($n = 10$).

Generally, mechanical resistance and gas barrier of the composite films should be highlighted since they are often subjected to external stress and should keep structural integrity during packaging, transportation, and storage [138]. The effects of the incorporated additives on the mechanical properties of composite films relied on their type and amount. Table V.11 shows the TS of the composite films slightly decreased from with the addition of both nanoemulsion and Pickering emulsion independently on the concentration. During the film formation, alginate molecules interact with each other through hydrogen bonding, which is responsible for the formation of network structure and maintenance of structural integrity [139]. The introduction of emulsions disrupted the ordered arrangement of the polymer matrix by interfering with the formation of inter- and/or intra-hydrogen bonds of alginate molecules, especially around dispersed O/W droplets [140]. However, the essential oil incorporated in sodium alginate film led to the increase of tensile strength, due to the specific interactions occur between the film and the oil constituents, such as crosslinks, structural arrangements of the components and the formation of heterogeneous biphasic structures [141].

Table V.11 *Physical properties TS and WVP of edible films with different concentrations of different additives.*

Edible film	TS (MPa)	WVP ($\times 10^{10}$ g/m Pa s)
SA	11.67 ± 0.81^{bc}	1.94 ± 0.40^{a}
SA_MBC 0.5	11.80 ± 0.85^{c}	1.97 ± 0.14^{a}
SA_MBC 1	10.16 ± 0.23^{abc}	2.01 ± 0.29^{a}
SA_BEO 0.5	16.40 ± 0.40^{d}	1.62 ± 0.31^{a}
SA_BEO 1	15.64 ± 0.07^{d}	1.58 ± 0.13^{a}
SA_NE 0.5	8.47 ± 0.78^{ab}	1.47 ± 0.60^{a}
SA_NE 1	8.16 ± 0.62^{a}	1.48 ± 0.29^{a}
SA_PE 0.5	10.24 ± 0.55^{abc}	1.88 ± 0.29^{a}
SA_PE 1	8.72 ± 0.43^{abc}	2.45 ± 0.54^{a}

Different letters denote significant differences ($p < 0.05$) among the different samples within each column (n = 3).

As it is well known, water plays a key role in food deterioration, which in turn influences various food properties such as odor, color, flavor, and nutrient content [142,143]. The film ability to degradation of the product is an important characteristic that affects the final product quality and food shelf-life. Therefore, water barrier properties should be taken into due account. As the film thickness increased, there was a slight reduced resistance to water vapor transfer across it and, as a consequence, a stagnant air layer formed, characterized by a high water vapor partial pressure on the inner film surface. Nevertheless, the incorporation of other compounds into the polymer matrix did not significantly (*p < 0.05*) contribute to the modification of SA film barrier behavior.

V.4.3.2. Effect of edible coating application on strawberries shelf life

The results of the previous section mostly covered only the properties and characteristics of the edible film. The present section findings are mainly on the effect of the coating solutions with the incorporation of additives at 1 wt% upon the strawberry fruit application and antimicrobial activities. Figure V.29 shows the appearance of strawberries on the last day of storage indicating that the color of the strawberry epidermis gradually changed with the applied edible coating.

Uncoated	SA	SA_MBC 1

SA_BEO 1	SA_NE 1	SA_PE 1
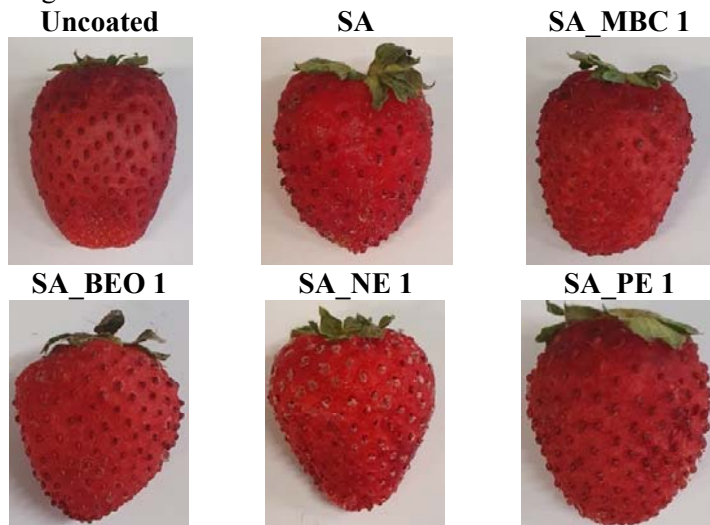
Figure V.29 *The color appearance of uncoated and coated strawberries in the last day of storage.*

The effect of the addition of MBC, BEO or emulsions in the sodium alginate coating solutions was investigated through contact-angle wettability analysis. The contact angle is one of the basic wetting properties of coating materials, indicating the hydrophilic/hydrophobic character of the film-forming solution. The contact angle values may range from 0° (complete and instantaneous spreading of the liquid onto the solid surface) to 180° (an unrealistic limit of absolutely no wetting) [144]. Therefore, the lower the contact angle, the higher the hydrophobicity of solutions [145]. The contact angles of droplets of sodium alginate film solutions deposited on the strawberries skin were similar to that of water (Figure V.30). This suggests a high interaction of the film solutions with the hydrophobic strawberry surface. It is clear that micronized bacterial cellulose addition caused a significant ($p < 0.05$) increase in the superficial hydrophilicity of the reinforced samples compared to that of sodium alginate or water.

Regarding this point, it is necessary to highlight that the mechanical treatment applied to bacterial cellulose caused the defibrillation of native fibers, resulting in alteration of their hydrophilicity [146]. The addition of BEO in pure form or stabilized in form of nanoemulsion and Pickering emulsion to the alginate film-forming solution significantly ($p < 0.05$) decreased the contact angle value of about 20, 38 and 34%, therefore further reducing the surface wettability with active coatings. The observed reduction in contact angle might be attributed to the essential oil providing more hydrophobic sites in the coating, and therefore reducing water attraction.
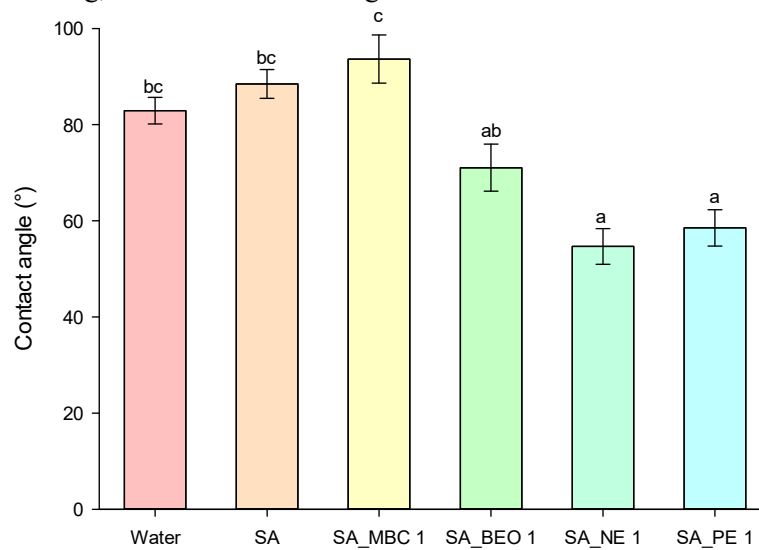
Figure V.30 *Average contact angle of water and coating solutions with or without additives. Different letters denote significant differences (p < 0.05).*

Changes in firmness of both uncoated and coated strawberries during storage at 4 °C are shown in Figure V.31. The firmness of the initial fruits ranged from 14.41 N to 18.89 N and decreased during storage, but this decrease was effectively delayed by sodium alginate active edible coatings. During the storage period, all the coated fruit firmness had changed including the uncoated fruits. However, SA_BEO 1 exhibited a slightly better performance in preventing firmness reduction. Therefore, the addition of BEO in the coating was able to maintain firmness well, with 3.98 N of firmness at the end of storage, as the highest value of firmness. Moreover, also the coating containing nanoemulsions (SA_NE 1) exhibited a slight high but significant difference with average firmness of 3.63 N. On the other hand, the application of Pickering emulsion (SA_PE 1) had an undesirable impact, with a drastic decrease in the firmness of the fruit. A possible reason that caused a loss of firmness in coated fruit was the effect of the emulsion added to the coating formulation: the firmness reduction may be induced by the water loss from fruit cells during storage, because of the presence of the Pickering emulsion,

causing lower cell turgor [111]. In addition, the hydrolysis of alginate as well as depolymerization occurring during the storage period have the potential to result in cell breakdown due to senescence and cause the flesh of the fruit to soften and reduce its texture or firmness [147,148].
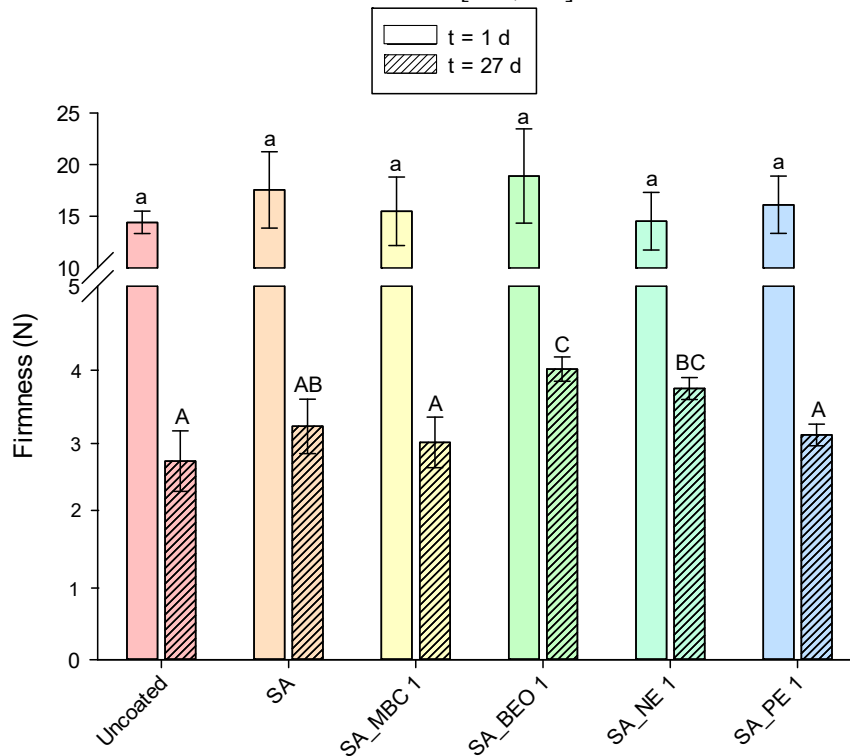
Figure V.31 *Effect of edible coating application on strawberries' firmness 27-d during storage at 4 °C. Different lowercase and uppercase letters show differences between treatment groups within 1 and 27 days, respectively (p < 0.05).*

The effect of different coating treatments on the bacterial counts and the number of yeasts and molds is given in Figure V.32. Initial bacterial counts determined for uncoated and coated strawberries ranged between 3.62 and 6.96 log CFU/g. The sodium alginate coating and coating reinforced with MBC contributed to a slight decrease in microbial growth when compared to control for 27 days. On the contrary, the use of the active coating, prepared with BEO, BEO nanoemulsion, and Pickering emulsion contributed to maintaining the total microbial count well below the acceptability limits, with values < 6 log CFU/g, and significantly lower (*p < 0.05*) than control and other coatings only at the beginning of storage, with an increase after 27 days. The number of yeast and molds in all treatments were below the limits of acceptability for those microorganisms in fresh fruit according to the Institute of Food Science and Technology (IFST), which is 6 log CFU/g [149].

Moreover, a significant difference between coated and control strawberries was observed already from the first days of storage. Notably, at the end of the shelf life, a reduced yeast and molds population was observed for coated fruits with SA or SA_MBC 1 in comparison with the SA_BEO 1, SA_NE 1, and SA_PE 1. Contrary to what was expected due to what observed during edible film characterization, the coated samples and the combination of MBC and BEO did not show sufficient antimicrobial activity. Further studfies must, therefore, be carried out in order to adjust coating formulations and exploit the potential benefits of reinforcing agents of MBC and antimicrobial activity of BEO.

(a)

(b)
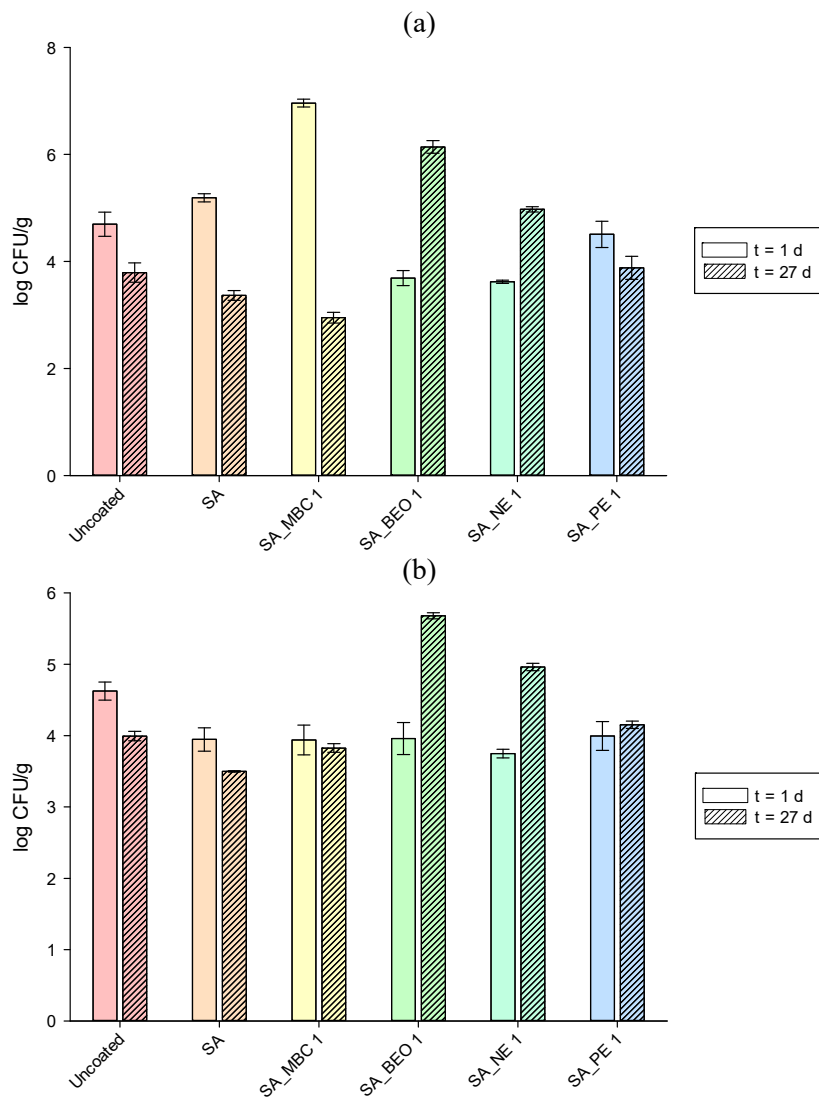
Figure V.32 *(a) Total microbial count and (b) yeast and molds over a 27 days storage period at 4 ± 1 °C of uncoated and coated strawberries.*

V.4.4. Conclusions

Physical characterization showed that the sodium alginate-based edible coating can be a proper carrier for encapsulating essential oil and being deposited as a thin layer onto fresh strawberries. Moreover, micronized bacterial cellulose can be a good reinforcing agent for improving mechanical and barrier properties of edible coatings. The results of the present section showed that the incorporation of additives at 1 wt% induced high adhesion of coating solution on the fruit surface, increasing at the same time the firmness during 27 days of storage at refrigerated conditions. Nevertheless, the antimicrobial properties of the edible films were not significantly enhanced when essential oils have been incorporated in pure form or in emulsion. This study, hence, provided preliminary data about the interactions between sodium alginate and bacterial cellulose and encapsulated essential oil, which would be a better way to (i) increase the mechanical properties of coatings; (ii) delivery and protect essential oils in antimicrobial films; and (iii) eliminate the negative effects of essential oils on physico-chemical characteristics of such edible films.

Section V.5
Amine-modified NCs for CO₂ capture via adsorption

In this section, cellulose nanofibers isolated from barley straw (ligno)cellulose pulp by combining chemical and mechanical treatments have been used to fabricate amine functionalized CNFs-based aerogels as promising materials for the capture of CO_2. The N-(2-aminoethyl)-3-aminopropyltri-methylsilane (AEAPMDS) and 3-Aminopropyl-triethoxysilane (APTS) CNFs-based aerogels were successfully fabricated by freeze-drying of CNFs hydrogels into which the amine group has been successfully introduced via C–O–Si bonds between NC and AEAPMDS or APTS. The impact of various parameters (temperature, type, and concentration of amine, and type of CNFs) on the properties of the as-prepared materials are systematically characterized through elemental analysis and potentially applied to capture CO_2 via covalent bonding. The purpose is to valorize AFRs and highlight the effective strategy available for a simple, environmentally safe, non-toxic, low-cost CO_2 capture by using amine-modified NCs for chemisorption.

V.5.1. Specific goal and work plan

The increase in the atmospheric carbon dioxide (CO_2) level has been demonstrated as being responsible for global warming and climate change. According to statistical data, the emission of CO_2 has mostly occurred from anthropogenic activities [150]. In order to mitigate the increasing concentration of CO_2, studies on the reduction of emissions are being actively conducted. In particular, CO_2 is inevitably generated due to the country's economic growth and accompanying development such as industrialization, urbanization, and transportation. In this scenario, at the 2015 UN Climate Change Conference, participants reached an agreement to create a global framework to prevent severe climate change by limiting global warming below 2 °C and striving to keep it below 1.5 °C [151]. According to the IPCC

Chapter V

(Intergovernmental Panel on Climate Change), reducing CO_2 emissions is essential if we are to keep the concentration of carbon dioxide in the atmosphere below 450 ppm by the end of 2100 and prevent climate change from becoming irreversible [152]. Methods for removing CO_2 from gas streams include (i) membranes; (ii) cryogenics; (iii) adsorption; and (iv) absorption, which can be classified into chemical or physical absorption based on the type of solvent used [153]. Membrane separation stands out for its ability to produce high-purity CO_2 streams, especially for power plants, and has several advantages, such as energy efficiency and continuous operation, compared to other methods [154]. Cryogenic separation of CO_2, which involves liquid CO_2 flow under high pressure, is mainly suitable for highly concentrated CO_2 streams but it is an expensive strategy due to the refrigeration step and the need for water removal [155]. Among others, adsorption is a relatively new approach to CO_2 removal and, together with absorption, is the most economical way to separate CO_2 from large flows [156]. This study focuses on the effectiveness of adsorption technology using nanomaterials, which depends largely on the exposed surface area, porosity, diffusion path, and availability of adsorption sites on the material, resulting from physical interactions between nanomaterials and CO_2 molecules [157]. The main studied and reported nanomaterial adsorbents with strong CO_2 adsorption are activated carbon, zeolites, metal-organic frameworks (MOFs), boron nitride (BN), and MXene [158].

Activated carbon is an abundant feedstock, low-cost materials, high available surface, and high adsorptive characteristics, such as high surface area, large porosity, and good thermal and chemical stability, making it ideal for physical adsorption of CO_2 under normal conditions [158,159]. Despite the easy adjustment of activated carbon porosity and surface area through pyrolysis and etching methods, which allow to meet the structural requirements of the adsorption process [160], the capacity and selectivity of activated carbon materials in terms of adsorption efficiency are limited by the weak physical interactions between CO_2 molecules and the material [161]. To enhance the efficiency of CO_2 physical adsorption, zeolite materials are utilized due to the stronger physical interactions between CO_2 molecules and the negative charges on the surface of zeolite. Moreover, zeolite materials are beneficial due to their abundant porosity, pore size, and high surface area and can be easily chemically modified according to specifications and scope of application CO_2 capture, making it to be a cost-effective technique for applying to control circumstances of flue gas [162]. The major disadvantage of zeolites is their weak CO_2 capture performance if the gas mixture contains water. Water will preferably interact with the cations due to the strong metal-dipole interactions, making part of the internal porosity unavailable for CO_2 capture and reducing the strength and heterogeneity of the internal electric field which made the materials so attractive for CO_2 capture [163]. This makes difficult the usage of zeolites for direct air capture in humid environments.

MOFs are a class of solid sorbents, which consist of inorganic-organic hybrid crystalline materials formed through the self-assembly of inorganic metal cations or clusters and organic ligands [164]. MOFs are porous materials with comparable or even better characteristics (i.e., high surface areas and uniform micropore size) when compared to zeolites and with tunable internal structures and properties, which make MOFs a promising alternative to traditional liquid and solid carbon capture sorbents [157]. The CO_2 adsorption enhancement is attributed to the pore enrichment effect of the nanomaterials. In this regard, the attention is turned to porous boron nitride as potential material for CO_2 adsorbent, due to unique B-N electronegativity, high thermal and chemical stabilities, and well recyclability in pollution management [165]. Different studies have been reported that the adsorption capacity of BN nanotubes (BNNTs) for CO_2 is better than carbon nanotubes (CNTs) [166,167]. Nevertheless, CO_2 molecules form weak interactions with uncharged BN nanomaterials and are weakly adsorbed. Hence, extensive work has been performed to enhance the CO_2 adsorption activity of BN by introducing functional group modification, making these nanomaterials highly effective absorbents [168]. Recently, nitrides (MXenes) have been proposed for CO_2 capture thanks to their intrinsic high surface areas [169]. Results highlight that the prepared MXene-supported adsorbents exhibit a large working capacity and a very stable cycling stability because of the synergetic effect [170].

Compared to physical adsorption, chemical adsorption has a higher sorption capacity and stronger interaction of materials with CO_2 molecules. Chemisorption is a chemical adsorption process where a molecule adsorbs onto a solid surface by spontaneous formation of a chemical bond-like hydrogen bonding, covalent and ionic bond [158]. The energy of chemisorption between gas molecules and adsorbents can differ considerably depending on the strength of the adsorbent and adsorbate specie bonding. Among different adsorbents, amine-modified nanomaterials have proven to be an effective solution for CO_2 chemical adsorption, due to their low energy consumption, chemical stability, and reversible nature [171].

As far as is known, no such study on the process variables optimization of the NCs amine modification to be used in CO_2 capture has been reported in literature. Therefore, the prime objective of the present section was to analyze the effect of process parameters and optimization of conditions using RSM approach. The variables employed in the experimental design were the type of NCs, the type and concentration of amine, and reaction temperature. Lastly, a study was carried out to analyze the CO_2 adsorption isotherm conducted at 298 K and pressure up to 1 bar. Meanwhile, desorption was performed by depressurizing CO_2 from 1 bar (Figure V.33).

V.5.2. Specific material and methods
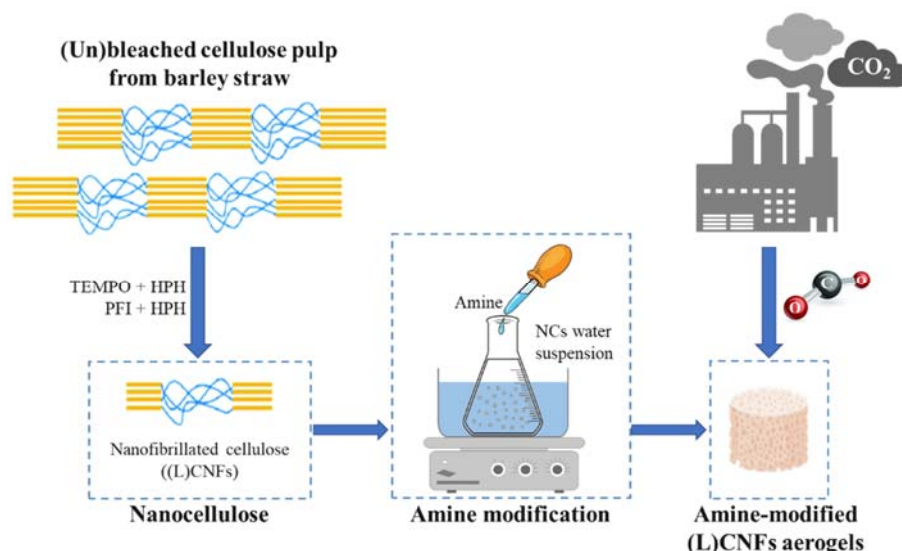
Figure V.33 *Schematic representation of methodology used to modify NCs with amine for CO_2 capture.*

V.5.2.1 Materials

The (ligno)cellulose pulp was isolated from barley straw as described in § IV.2.3.3, and (L)CNFs have been obtained from the cellulose pulp through the combination of TEMPO-mediated oxidation or PFI beater with HPH, as described in detail in section § IV.3.3.6.

All reagents were of analytical grade unless otherwise stated. Micro-pure deionized water was used throughout the experiments.

V.5.2.2. Preparation of amine-modified NCs aerogel

The previously dried (L)CNFs was dissolved in distilled water and treated in an ultrasonic cell distruptor with a constant power of 2000 W for 5 min to form a homogeneous solution of 2.5 wt%. N-2-Aminoethyl-3-aminopropyltri-methoxysilane (AEAPMDS) and 3-Aminopropyl-triethoxysilane (APTS) was added to this (L)CNFs hydrogels until the total silane concentration ranged between 2.5 and 10 wt% The suspension was sonicated for 45 s, followed by a spontaneous physical gelation route for 20 min at room temperature. Then, the prepared amino-modified (L)CNFs hydrogels were added into a bath, containing glycerol, at different temperatures (70 - 120 °C) and reacted for 24 h. Finally, freeze-drying was carried out to obtain AEAPMDS/APTS-(L)CNFs aerogels.

V.5.2.3. Experimental design for CO$_2$ capture

Response surface methodology (RSM) model for the design of experiments (DOE) was used for fitting and establishing the relationship between response variables (nitrogen content and CO$_2$ adsorption) and process variables (type of NCs, type of amine, amine concentration, and operating temperature), to determine the optimal processing conditions of the modification process, which maximize the nitrogen content as well as the higher CO$_2$ capture. I-Optimal Design was applied in this study, using Design-Expert 11.1.2.0 software (Statease Inc., Minneapolis, MN, U.S.) to determine the number of experiments to be evaluated for the optimization of the two independent and the response variables. A third-order polynomial model reported in Equation V.23 was used to predict the response variable as a function of the investigated independent factors.

$$Y_k = \beta_0 + \sum_{i=1}^{4} \beta_i X_i + \sum_{i=1}^{3} \sum_{j=i+1}^{4} \beta_{ij} X_i X_j + \sum_{i=1}^{2} \beta_{ii} X_i^2 \qquad (V.23)$$

$$+ \sum_{i=1}^{1} \sum_{j=i+1}^{3} \sum_{k=j+1}^{4} \beta_{ijk} X_i X_j X_k + \sum_{i=1}^{2} \beta_{iii} X_i^3$$

$$+ \sum_{i=1}^{2} \sum_{j=i+1}^{4} \beta_{iij} X_i^2 X_j + \sum_{i=1}^{3} \sum_{j=i+1}^{2} \beta_{ijj} X_i X_j^2$$

$$+ \varepsilon$$

In this equation, Y_k is the predicted response variables; $X_{i,j,k}$ are the independent variables; β_0, β_i, β_{ii}, β_{ij}, β_{iij}, β_{ijj}, and β_{ijk} correspond to a constant term, regression coefficients of the linear effects, quadratic, and interaction terms of the model, respectively, with ε being the model error.

V.5.2.4. Elemental analysis

The elemental analysis for carbon, hydrogen, and nitrogen was performed in a Euro EA3000 series elemental analyser (EuroVector SpA, Milano, Italy) to determine whether the modifier was successfully grafted onto the CNFs as well as to investigate the impact of different parameters on the modification process. Total oxidation of the sample (10 mg) was conducted at 1020 °C. Combustion products were separated in a chromatographic column (PTFA column for CHNS, 2 m; carrier gas, He, 70 kPa; purge flow, 80 mL/min; oxygen pressure, 35 kPa).

V.5.2.5. CO₂ adsorption isotherm

The amine-modified nanomaterials' CO_2 adsorption capacities were determined from their isotherms, measured volumetrically using a ASAP 2020 Analyzer (Micromeritics Instrument Corporation, Norcross, United States) at 25 °C. Prior to the measurements, samples were outgassed at 110 °C and 10^{-4} mbar during 8 h.

V.5.3. Results and discussion

V.5.3.1. Optimization of nitrogen content

The most common mechanism for CO_2 capture involves the formation of a zwitterion through the interaction of CO_2 and amines, followed by deprotonation of the zwitterion by a base to produce a carbamate [172–174]. The zwitterion mechanism is written as follows:

$$RNH_2 + CO_2(g) \leftrightarrow RNH_2^+CO_2^-$$
$$RNH_2^+CO_2^- + RNH_2 \leftrightarrow RNHCO_2^- + RNH_3^+$$
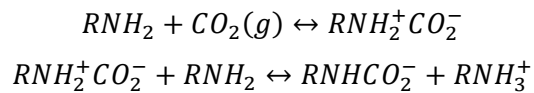
whereas the termolecular mechanism reads:

$$CO_2(g) + RNH_2 \cdots NH_2R \leftrightarrow RNHCO_2^- + RNH_3^+$$
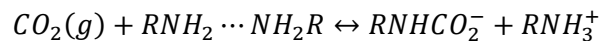
In this scenario, NCs have been studied as support for amine adsorbents for CO_2 capture. The sorbent materials were prepared using AEAPMDS and APTS that was grafted to (L)CNFs, as depicted in Figure V.34.
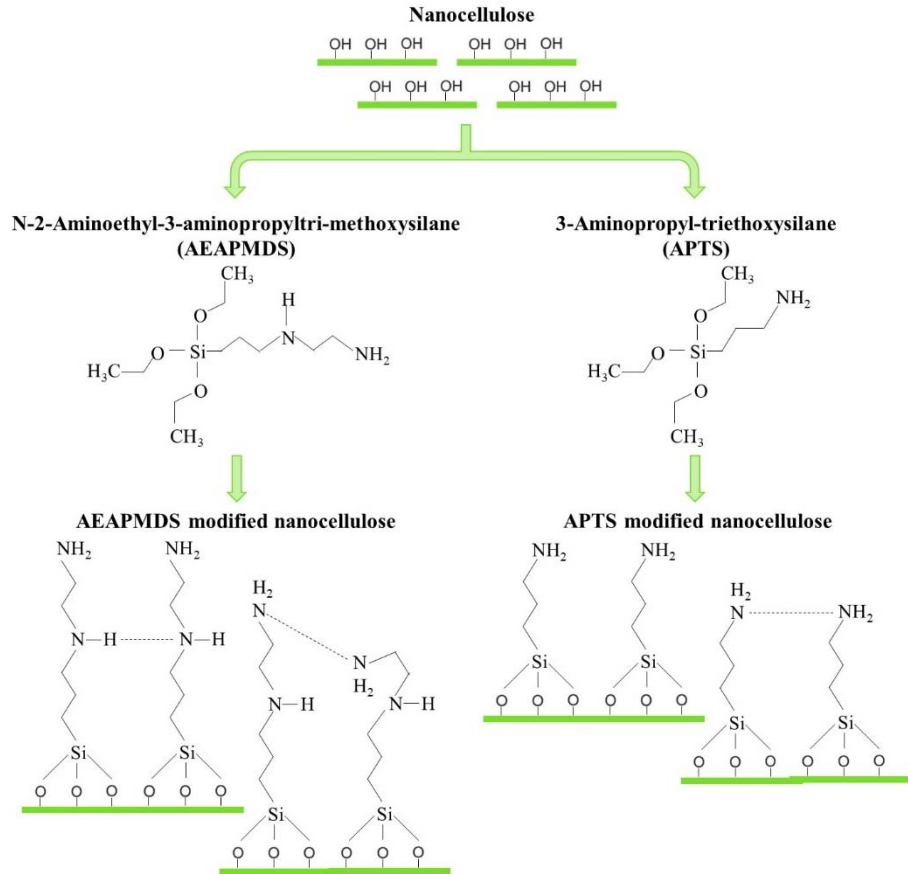
Figure V.34 *Schematic representation of amine materials used in this study supported by NCs.*

In order to gain insight into the underlying mechanism of (L)CNFs modification by amines, the RSM optimization was used to explore the effect of different parameters: type of NCs, type of amine, amine concentration, and operating temperature. The experimental data obtained from the I-Optimal experiment design were fitted by cubic model (Equation V.24), which was used to analyze and predict the optimal level for enhanced surface modification.

$$Y_1 = 8.180 + 2.300 \cdot X_1 - 0.463 \cdot X_2 + 0.575 \cdot X_3 + 1.860 \quad \text{(V.24)}$$
$$\cdot X_4 - 0.354 \cdot X_1 \cdot X_2 - 0.997 \cdot X_1 \cdot X_3$$
$$- 0.602 \cdot X_1 \cdot X_4 + 0.267 \cdot X_2 \cdot X_3 + 0.477$$
$$\cdot X_2 \cdot X_4 + 0.003 \cdot X_3 \cdot X_4 - 0.684 \cdot X_1^2$$
$$- 0.133 \cdot X_2^2 - 2.760 \cdot X_1 \cdot X_2 \cdot X_3 - 0.887$$
$$\cdot X_1 \cdot X_2 \cdot X_4 - 1.690 \cdot X_1 \cdot X_3 \cdot X_4$$

317

Chapter V

The significance of the regression coefficients of the predicted polynomial model are reported in Table V.12. As shown by the data in Table V.12, the regression coefficient (R^2 = 0.9742) values indicated that the developed regression model had satisfactory goodness of fit and confidence level. Furthermore, the adjusted regression coefficient (Adj-R^2 = 0.8453) is almost the same as R^2, indicating that only 2.36% of the data are not explained by the equation. The model F-value, lack-of-fit F-value, and P-value were used to evaluate the significance for the modification of (L)CNFs with AEAPMDS or APTS with a high degree of fitting. The model F-value of 7.56 revealed that the model is adequate; the coefficient of variation (C.V. %) value of 13.78 % also indicated the dependability and adequacy of the model. "Adeq Precision" measures the signal-to-noise ratio and a value ratio of 9.243 indicates an adequate signal in the model for the navigation of the design space.

Table V.12 *Analysis of variance (ANOVA) of the cubic model for the nitrogen content of amine-modified (L)CNFs.*

Parameters	Value
Mean	7.80
C.V. (%)	13.78
F-value	7.56
R^2	0.9742
Adj-R^2	0.8453
Adeq Precision	9.243

The response surface plots the nitrogen percentage of (L)CNFs after modification with amines, given by the interactions between four independent factors (Figure V.35). Therefore, the plots reveal the interaction between (L)CNFs and amine type as a function of amine concentration and operating temperature. Based on the outcomes of elemental analysis, it was found that the AEAPMDS-modified NCs were characterized by a higher concentration of nitrogen with respect to that modified with APTS. It can be assumed that amine was bonded to cellulosic nanoparticles. However, due to the chemical structure, not all hydroxyl groups of NCs are highly reactive [175]. According to observations presented in the literature, the attachment of modifying molecules takes place mainly at C6 and C2 and results from regioselectivity [176,177]. Nevertheless, the obtained nitrogen values were higher than those presented by Neves et al. (2021) and Kawalerczyk et al. (2022) [175,178]. Regarding the impact of AEAPMDS, it was observed that nitrogen content is proportional to the amount of AEAPMDS without, however, following a linear trend. The latter can be ascribed to the limited number of hydrogen groups, which were progressively consumed by AEAPMDS, resulting finally in a steady state. Under the present conditions, we observed that the nitrogen content was not increased in AEAPMDS-(L)CNFs upon increasing the operating temperature. These results showed that the temperature modification was not influenced the (L)CNFs modification process;

meanwhile, the type and the amount of amine added to NCs had a certain effect on the nitrogen content. The optimum reaction conditions, at fixed 24 h treatment time and solid-to-liquid ratio (w/w) of 1:10, were identified as follows: reaction temperature of 70 °C, and amine concentration of 8 wt%. Based on these optimum values, about 4% of the amount of AEAPMDS consumption can be effectively saved AEAPMDS as amine at 8 wt%.

(a)

319

(b)
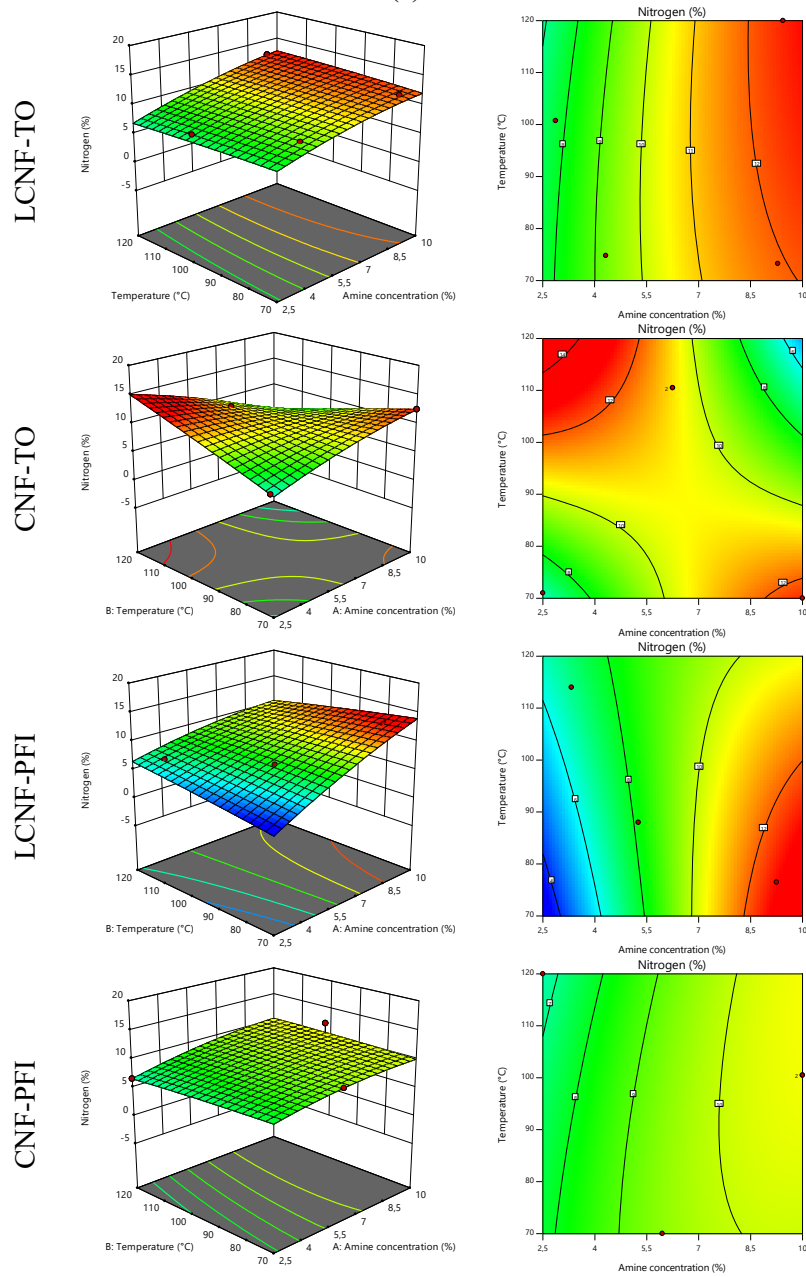
Figure V.35 *3D Surface (left column) and contour (right column) plots of interaction between independent parameters for nitrogen (%) after (a) AEAPMDS and (b) APTS modification of NCs.*

V.5.3.2. Optimization of CO_2 sorption

Next, the effect of (L)CNFs aerogel modified with the two amines at different concentrations on CO_2 capture was investigated. Response surface plots reported in Figure V.36 shows the interactions between reaction temperature and amine concentration of (L)CNFs modification process on the CO_2 adsorption at 25 °C, predicted by third-order polynomial model reported in Equation V.25.

$$Y_2 = 0.014 - 0.010 \cdot X_1 - 0.029 \cdot X_2 - 0.008 \cdot X_3 + 0.003 \qquad (V.25)$$
$$\cdot X_4 - 0.041 \cdot X_1 \cdot X_2 - 0.049 \cdot X_1 \cdot X_3$$
$$- 0.074 \cdot X_1 \cdot X_4 - 0.026 \cdot X_2 \cdot X_3 + 0.038$$
$$\cdot X_2 \cdot X_4 + 0.002 \cdot X_3 \cdot X_4 + 0.068 \cdot X_1^2$$
$$- 0.012 \cdot X_2^2 - 0.173 \cdot X_1 \cdot X_2 \cdot X_3 - 0.036$$
$$\cdot X_1 \cdot X_2 \cdot X_4 - 0.068 \cdot X_1 \cdot X_3 \cdot X_4$$

The significance of the regression coefficients of the predicted polynomial model is reported in Table V.13.

Table V.13 *Analysis of variance (ANOVA) of the cubic model for the CO_2 capture of amine-modified (L)CNFs.*

Parameters	Value
Mean	0.06
C.V. (%)	4.48
F-value	313.17
R^2	0.9994
Adj-R^2	0.9962
Adeq Precision	74.505

The interaction between investigated factors was significant ($p \leq 0.01$), suggesting that the combination of NCs, amine type and concentration, and reaction temperature vary the adsorption of CO_2. Moreover, the coefficients of the equation used for the fitting and the statistics used to test the adequacy of the model, are demonstrated to be well-fitted by the third-order polynomial equation expressing the relationship between the experimental parameters and the response variable. The p-value of the model was < 0.0001, which indicates that the model is significant, and therefore the independent variables of the model have a significant effect on the response. The model has a satisfactory level of adequacy (R^2= 0.9994), indicating a good agreement between the experimental data and the predicted values.

(a)

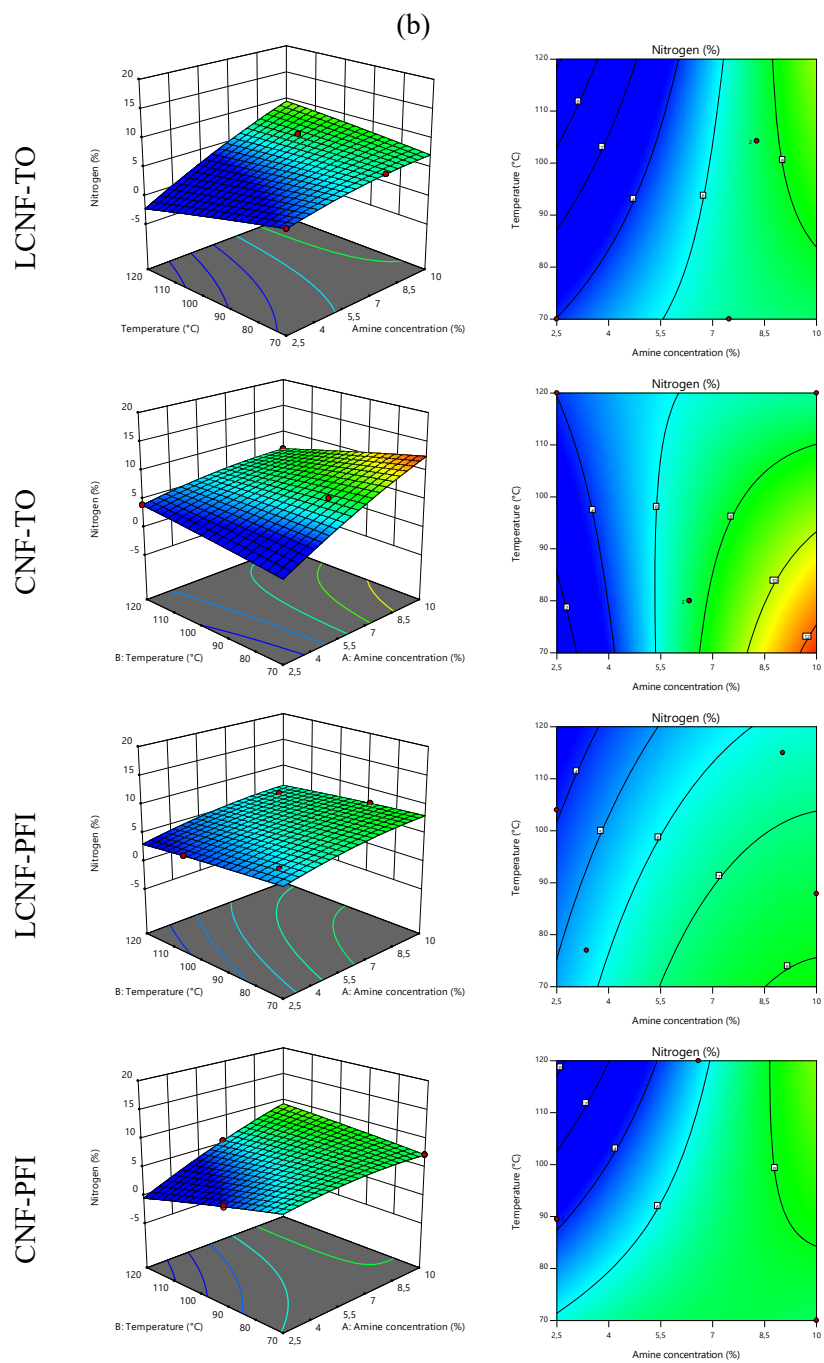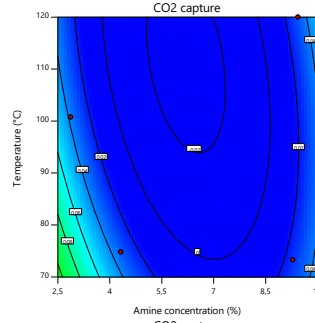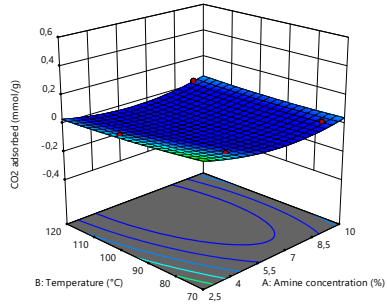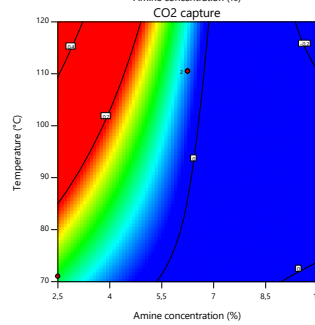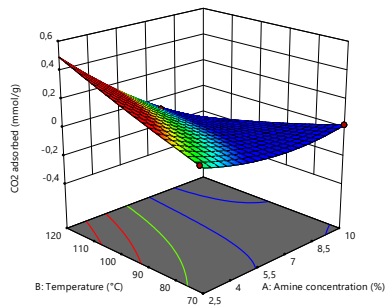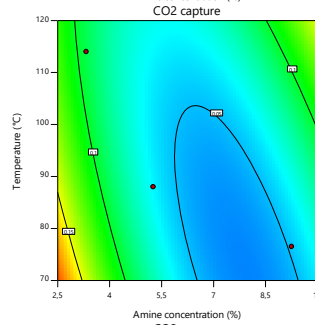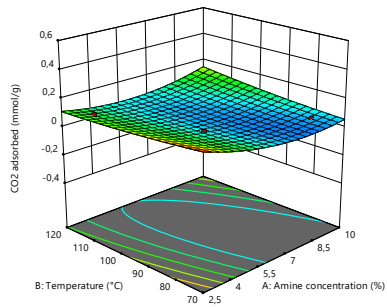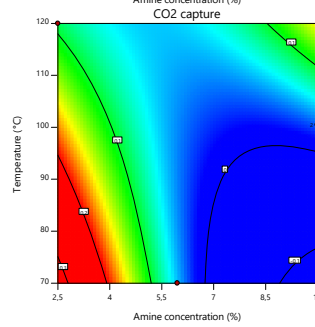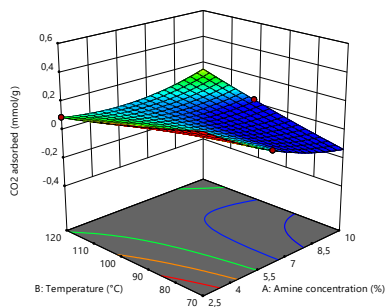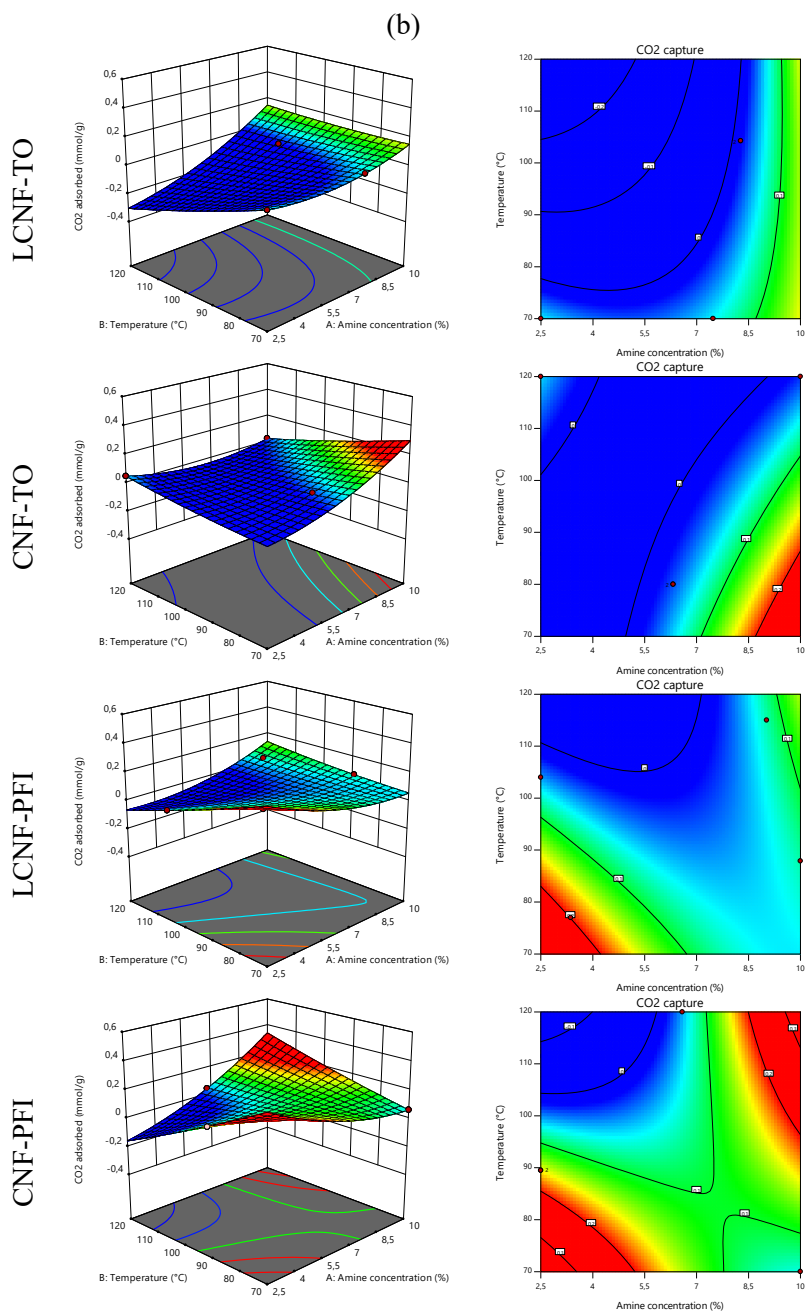**Figure V.36** *3D Surface (left column) and contour (right column) plots of interaction between independent parameters for CO₂ adsorption at 25 °C of (a) AEAPMDS and (b) APTS modified NCs.*

In the whole investigated domain, the increase in the temperature treatment induced a decrease in CO_2 capture, regardless the type of NCs and amine. More specifically, results in Figure V.37 clearly show that the CO_2 content was initially captured in amine-modified (L)CNFs, followed, however, by a substantial decrease at intermediate concentration. The reason of this volcano behavior is not clear, and it may be related to the formation of amino silanol by methoxy hydrolysis in amine at the beginning stages [179].
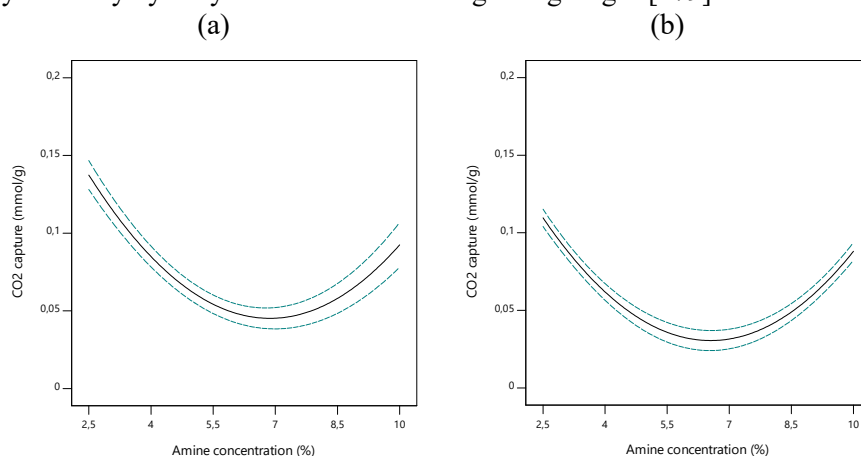
Figure V.37 *Dependence of CO_2 capture from amine concentration (solid line) with the indication of the 95% confidence interval bands (dashed lines), using (a) AEAPMDS and (b) APTS as amine for NCs modification.*

The sequence of adsorption capacity is demonstrated by AEAPDM_CNF-TO > APTS_CNF-PFI > APTS_CNF-TO > AEAPDM_CNF-PFI > APTS_LCNF-PFI > APTS_LCNF-TO > AEAPDM_LCNF-PFI > AEAPDM_LCNF-TO. Interestingly, as CO_2 gas is considered, the order of adsorption is inversely proportional to the N content of the modified-NCs. This may also be due to the hindrance effect when the modification occurred, and the silane is folded, especially for the intermediate and long-chain aminosilanes. The long-chain of aminosilane probably folded at –N of the amine as hydrogen bonding between –NH of aminosilanes occurred, as demonstrated by Nurul Hanisah et al. (2021) [180]. Furthermore, the other reason for the lower adsorption capacity with higher N content of the amino-modified-NCs is that the chemical adsorption occurred, which only allowed for monolayer adsorption. The short-chain aminosilane, with only one N-group used for grafting interaction, promotes physical adsorption, where multilayer adsorption is possible [180].

V.5.3.3. Adsorption kinetics

The CO_2 adsorption isotherm of CNF-TO modified with AEAPMDS (the optimized sample for the adsorption of CO_2) was tested to reveal their adsorption capacity for CO_2 and investigate the variation of adsorption capacity with the equilibrium pressure (Figure V.38). It was observed that the adsorption capacity increases with the increase in equilibrium pressures, which was attributed to the exothermic nature of adsorption. The adsorbed CO_2 amount from the desorption isotherm was higher than that of the adsorption isotherm in the gas phase, according to the usual trend where the desorption lies above the adsorption one [181].
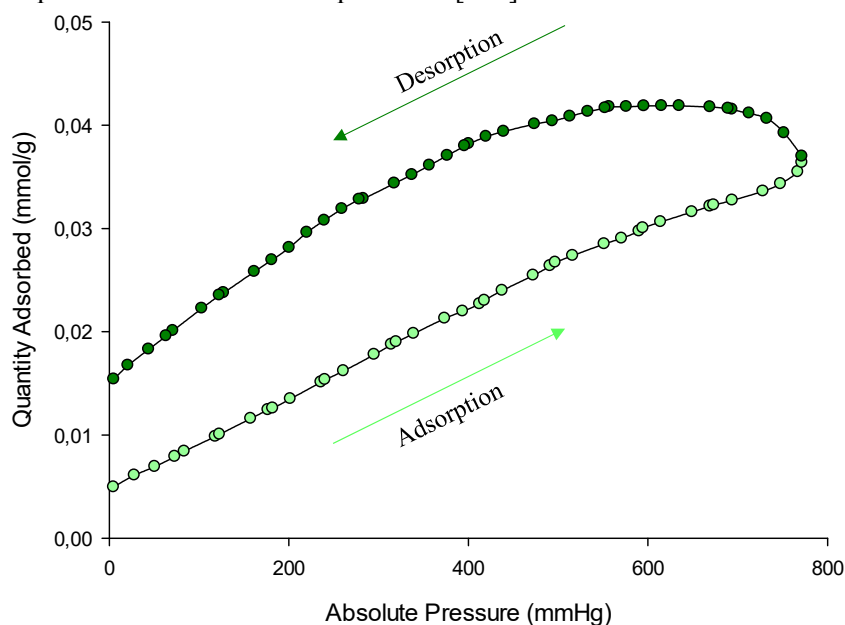
Figure V.38 *CO_2 adsorption isotherms of CNF-TO modified with AEAPMDS at 25 °C.*

The most efficient experimental equilibrium data for CO_2 adsorption isotherm at 25 °C was assessed by using isotherm models, such as Langmuir and Freundlich. This analysis studied the mechanism of CO_2 adsorption onto the adsorbent. These were well-established adsorption isotherms that were closely studied for explaining the adsorption mechanisms. Langmuir equation was derived theoretically through a kinetic approach that assumes that a homogeneous adsorption mechanism occurs on a monolayer [182]. According to the Langmuir model (Equation V.26), it assumes uniform energies of adsorption onto a surface and no transmigration of adsorbate in the plane of the surface [183]. The model parameters have been determined from the slope and intercept of plot fitted with the linearized form of the Langmuir model (Equation V.27).

Chapter V

The essential features of the Langmuir isotherm may be expressed in terms of equilibrium parameter R_L (Equation V.28), which is a dimensionless constant referred to as the separation factor or equilibrium parameter [184].

$$q = \frac{q_0 \cdot K_L \cdot P}{1 + K_L \cdot P} \qquad (V.26)$$

$$\frac{1}{q} = \frac{1}{q_0 \cdot K_L \cdot P} + \frac{1}{q_0} \qquad (V.27)$$

$$R_L = \frac{1}{1 + (1 + K_L \cdot C_0)} \qquad (V.28)$$

where q is the adsorption capacity (mmol/g), P is the CO_2 pressure (mmHg), K_L is the Langmuir isotherm constant that is related to the energy of adsorption, q_0 is the monolayer capacity (mmol/g), and C_0 is the initial concentration of the adsorbate (mmol/g).

From the Table V.14, the correlation coefficient is satisfactory (R^2 = 0.9940) and indicates good agreement with the experimental adsorption isotherm. The affinity between the adsorbate and adsorbent was predicted by using a dimensionless constant called separation factor or equilibrium parameter, R_L. The R_L value indicates the adsorption nature to be either unfavorable if $R_L > 1$, linear if $R_L = 1$, favorable if $0 < R_L < 1$ and irreversible if $R_L = 0$ [185]. The R_L value of 2.54×10^{-4} indicates that the equilibrium CO_2 adsorption at 25 °C was favorable.

Adsorption characteristics for the heterogeneous surface [186] can be described by fitting with the experimental data to the empirical equation proposed by Freundlich (Equation V.29), with the linearized formula of Freundlich isotherm expressed as Equation V.30. The constant K_F is an approximate indicator of adsorption capacity while 1/n is a function of the strength of adsorption in the adsorption process [187].

$$q = K_F \cdot P^{\frac{1}{n}} \qquad (V.29)$$

$$\log q = \frac{1}{n} \log P + \log K_F \qquad (V.30)$$

where K_F is Freundlich isotherm constant, and n is adsorption intensity.

Based on Table V.14, the Freundlich model fitted well and correctly describes the CO_2 adsorption isotherm at 25 °C with a correlation coefficient, $R^2 = 0.9980$. Opposite to the Langmuir model, the Freundlich model assumes that several layers of adsorbate can be attached to the adsorbent forming multilayer adsorption that will take place on the heterogeneous adsorbent. The importance of 1/n is the Freundlich intensity parameter that indicates the adsorption strength. A value of 1/n < 1 indicates a normal adsorption representing greater surface heterogeneity, while smaller values of 1/n represent that greater heterogeneity is expected. Meanwhile, 1/n > 1 corresponds to driving force or cooperative adsorption [188], which an adsorbate molecule adsorbed to adsorption site will facilitate next molecule to be adsorbed. In addition, n values indicate the type of adsorption, wherein n =

326

1 indicating the partition between two phases are independent of the pressure which is linear [188]. Meanwhile, $n < 1$ corresponds to chemical adsorption and $n > 1$ or lies between 1 to 10 is for physical adsorption with the adsorption is favorable [188,189]. Based on the parameters obtained in Table V.14, the n value is larger than 1, which indicates that the CO_2 adsorption onto adsorbents is favorable and the adsorption phenomenon is expected to be physisorption.

Table V.14 *Langmuir and Freundlich model parameters.*

Isotherm	Parameters	Values	
		Adsorption	**Desorption**
Langmuir	q_0	178.57 mmol/g	47.85 mmol/g
$q = \dfrac{q_0 \cdot K_L \cdot P}{1 + K_L \cdot P}$	K_L	140.00	696.67
	R^2	0.9940	0.8567
Freundlich	1/n; (n)	$4 \cdot 10^{-5}$; (25,000)	$3 \cdot 10^{-5}$; (33,333)
$q = K_F \cdot P^{\frac{1}{n}}$	K_F	1.01	1.05
	R^2	0.9980	0.9358

V.5.4. Conclusions

In this study, the synthesis of amine-functionalized nanofibrillated cellulose is experimentally investigated. In particular, the influences of experimental parameters, i.e. type of NCs, type of amine, amine concentration and processing temperature, on the nitrogen content and CO_2 adsorption capacity were successfully investigated by experimental design methodology. The ANOVA showed high coefficient of the determination values (R^2 of 0.9742 and $R^2 > 0.9994$ for nitrogen content and CO_2 capture, respectively). The reaction conditions relevant to the modification of CNF-TO by AEAPMDS were systematically explored through the analysis of adsorption kinetic. Adsorption and desorption isotherms were well described by the Langmuir and Freundlich models. This work demonstrates the potential of amination to functionalize fibers aerogels, offering new opportunities for the design of novel functional biomaterials with controlled properties.

V.6. References

1. Chen, L.; Ao, F.; Ge, X.; Shen, W. Food-grade pickering emulsions: Preparation, stabilization and applications. *Molecules* 2020, *25*.

2. Gonzalez Ortiz, D.; Pochat-Bohatier, C.; Cambedouzou, J.; Bechelany, M.; Miele, P. Current Trends in Pickering Emulsions: Particle Morphology and Applications. *Engineering* 2020, *6*.

3. Donsì, F.; Velikov, K.P. Encapsulation of food ingredients by single O/W and W/O nanoemulsions. In *Lipid-Based Nanostructures for Food Encapsulation Purposes*; Elsevier, 2019; pp. 37–87.

4. McClements, D.J.; Rao, J. Food-Grade nanoemulsions: Formulation, fabrication, properties, performance, Biological fate, and Potential Toxicity. *Crit. Rev. Food Sci. Nutr.* 2011, *51*.

5.   Cui, F.; Zhao, S.; Guan, X.; McClements, D.J.; Liu, X.; Liu, F.; Ngai, T. Polysaccharide-based Pickering emulsions: Formation, stabilization and applications. *Food Hydrocoll.* 2021, *119*.

6.   Dong, H.; Ding, Q.; Jiang, Y.; Li, X.; Han, W. Pickering emulsions stabilized by spherical cellulose nanocrystals. *Carbohydr. Polym.* **2021**, *265*, doi:10.1016/j.carbpol.2021.118101.

7.   Mauriello, E.; Ferrari, G.; Donsì, F. Effect of formulation on properties, stability, carvacrol release and antimicrobial activity of carvacrol emulsions. *Colloids Surfaces B Biointerfaces* **2021**, doi:10.1016/j.colsurfb.2020.111424.

8.   Sarkar, A.; Ademuyiwa, V.; Stubley, S.; Esa, N.H.; Goycoolea, F.M.; Qin, X.; Gonzalez, F.; Olvera, C. Pickering emulsions co-stabilized by composite protein/ polysaccharide particle-particle interfaces: Impact on in vitro gastric stability. *Food Hydrocoll.* **2018**, *84*, doi:10.1016/j.foodhyd.2018.06.019.

9.   Baek, J.; Wahid-Pedro, F.; Kim, K.; Kim, K.; Tam, K.C. Phosphorylated-CNC/modified-chitosan nanocomplexes for the stabilization of Pickering emulsions. *Carbohydr. Polym.* **2019**, doi:10.1016/j.carbpol.2018.11.006.

10.   Abdul Khalil, H.P.S.; Davoudpour, Y.; Islam, M.N.; Mustapha, A.; Sudesh, K.; Dungani, R.; Jawaid, M. Production and modification of nanofibrillated cellulose using various mechanical processes: A review. *Carbohydr. Polym.* 2014.

11.   Kargarzadeh, H.; Mariano, M.; Huang, J.; Lin, N.; Ahmad, I.; Dufresne, A.; Thomas, S. Recent developments on nanocellulose reinforced polymer nanocomposites: A review. *Polymer (Guildf).* 2017.

12.   Capron, I.; Rojas, O.J.; Bordes, R. Behavior of nanocelluloses at interfaces. *Curr. Opin. Colloid Interface Sci.* 2017.

13.   Rajinipriya, M.; Nagalakshmaiah, M.; Robert, M.; Elkoun, S. Importance of Agricultural and Industrial Waste in the Field of Nanocellulose and Recent Industrial Developments of Wood Based Nanocellulose: A Review. *ACS Sustain. Chem. Eng.* **2018**, *6*, 2807–2828, doi:10.1021/acssuschemeng.7b03437.

14.   Pirozzi, A.; Capuano, R.; Avolio, R.; Gentile, G.; Ferrari, G.; Donsì, F. O/W pickering emulsions stabilized with cellulose nanofibrils produced through different mechanical treatments. *Foods* **2021**, doi:10.3390/foods10081886.

15.   He, K.; Zhang, X.; Li, Y.; Li, B.; Liu, S. Water-insoluble dietary-fibers from Flammulina velutiper used as edible stabilizers for oil-in-water Pickering emulsions. *Food Hydrocoll.* **2020**, doi:10.1016/j.foodhyd.2019.105519.

16.   Hu, K.; McClements, D.J. Fabrication of biopolymer nanoparticles by antisolvent precipitation and electrostatic deposition: Zein-alginate core/shell

nanoparticles. *Food Hydrocoll.* **2015**, *44*, 101–108, doi:10.1016/J.FOODHYD.2014.09.015.

17. Kalashnikova, I.; Bizot, H.; Cathala, B.; Capron, I. New pickering emulsions stabilized by bacterial cellulose nanocrystals. *Langmuir* **2011**, doi:10.1021/la200971f.

18. Steffe, J.F. *Rheological methods in food engineering*; 1996; ISBN 0963203614.

19. De Maria, S.; Ferrari, G.; Maresca, P. Effects of high hydrostatic pressure on the conformational structure and the functional properties of bovine serum albumin. *Innov. Food Sci. Emerg. Technol.* **2016**, doi:10.1016/j.ifset.2015.11.025.

20. Restu, W.K.; Sampora, Y.; Meliana, Y.; Haryono, A. Effect of Accelerated Stability Test on Characteristics of Emulsion Systems with Chitosan as a Stabilizer. *Procedia Chem.* **2015**, doi:10.1016/j.proche.2015.12.031.

21. Wüstenberk, T. *Cellulose and cellulose derivatives in the food industry. Fundamental and applications*; 2014; ISBN 9780874216561.

22. Martins, L.S.; Gonçalves, R.; Santos, D.; Spinacé, M.A.S. Properties of Cellulose Nanofibers Extracted from Eucalyptus and their Emulsifying Role in the Oil-in-Water Pickering Emulsions. **2022**, *13*, 689–705, doi:10.1007/s12649-021-01498-8.

23. Kalashnikova, I.; Bizot, H.; Bertoncini, P.; Cathala, B.; Capron, I. Cellulosic nanorods of various aspect ratios for oil in water Pickering emulsions. *Soft Matter* **2013**, doi:10.1039/c2sm26472b.

24. Tang, K.; Hao, X.; Wei, Q.; Zhou, X. Effects of Lignin Chemistry on Cellulose Extraction Performance Towards Crop Straw/Stalk. *Chiang Mai J. Sci.* **2020**, *47*, 1204–1215.

25. Varanasi, S.; Henzel, L.; Mendoza, L.; Prathapan, R.; Batchelor, W.; Tabor, R.; Garnier, G. Pickering Emulsions Electrostatically Stabilized by Cellulose Nanocrystals. *Front. Chem.* **2018**, doi:10.3389/fchem.2018.00409.

26. Xu, Y.; Yang, S.; Zhao, P.; Wu, M.; Song, X.; Ragauskas, A.J. Effect of endoglucanase and high-pressure homogenization post-treatments on mechanically grinded cellulose nanofibrils and their film performance. *Carbohydr. Polym.* **2021**, *253*, 117253, doi:10.1016/j.carbpol.2020.117253.

27. Costa, A.L.R.; Gomes, A.; Cangussu, L.B.; Cunha, R.L.; de Oliveira, L.S.; Franca, A.S. Stabilization mechanisms of O/W emulsions by cellulose nanocrystals and sunflower protein. *Food Res. Int.* **2022**, *152*, 110930, doi:10.1016/j.foodres.2021.110930.

28. Reid, M.S.; Villalobos, M.; Cranston, E.D. Cellulose nanocrystal interactions probed by thin film swelling to predict dispersibility. *Nanoscale* **2016**, doi:10.1039/c6nr01737a.

29. Yuan, T.; Zeng, J.; Wang, B.; Cheng, Z.; Chen, K. Pickering emulsion stabilized by cellulosic fibers: Morphological properties-interfacial

stabilization-rheological behavior relationships. *Carbohydr. Polym.* **2021**, *269*, 118339, doi:10.1016/j.carbpol.2021.118339.

30.   Yuan, T.; Zeng, J.; Wang, B.; Cheng, Z.; Chen, K. Pickering emulsion stabilized by cellulosic fibers: Morphological properties-interfacial stabilization-rheological behavior relationships. *Carbohydr. Polym.* **2021**, doi:10.1016/j.carbpol.2021.118339.

31.   Ojala, J.; Visanko, M.; Laitinen, O.; Österberg, M.; Sirviö, J.A.; Liimatainen, H. Emulsion Stabilization with Functionalized Cellulose Nanoparticles Fabricated Using Deep Eutectic Solvents. *Molecules* **2018**, *23*, 2765, doi:10.3390/molecules23112765.

32.   Bao, X.; Yan, X.; Zhang, G.; Zhao, J.; Zeng, Z.; Yu, P.; Gong, D. Improving effect of phytase treatment on the functional properties and in vitro digestibility of protein isolate from Cinnamomum camphora seed kernel. *Lwt* **2022**, *155*, 112948, doi:10.1016/j.lwt.2021.112948.

33.   Liu, Y.; Xie, Y.P.; Ma, X.Y.; Liu, L.N.; Ke, Y.J. Preparation and properties of antioxidant peptides from wampee seed protein. *J. Food Meas. Charact.* **2022**, doi:10.1007/s11694-021-01164-6.

34.   Dai, L.; Sun, C.; Wei, Y.; Mao, L.; Gao, Y. Characterization of Pickering emulsion gels stabilized by zein/gum arabic complex colloidal nanoparticles. *Food Hydrocoll.* **2018**, doi:10.1016/j.foodhyd.2017.07.040.

35.   Zhang, X.; Qi, B.; Xie, F.; Hu, M.; Sun, Y.; Han, L.; Li, L.; Zhang, S.; Li, Y. Emulsion stability and dilatational rheological properties of soy/whey protein isolate complexes at the oil-water interface: Influence of pH. *Food Hydrocoll.* **2021**, doi:10.1016/j.foodhyd.2020.106391.

36.   Fernández Sosa, E.I.; Chaves, M.G.; Henao Ossa, J.S.; Quiroga, A.V.; Avanza, M.V. Protein isolates from Cajanus cajan L. as surfactant for o:w emulsions: pH and ionic strength influence on protein structure and emulsion stability. *Food Biosci.* **2021**, *42*, doi:10.1016/j.fbio.2021.101159.

37.   Liu, A.G.; Ford, N.A.; Hu, F.B.; Zelman, K.M.; Mozaffarian, D.; Kris-Etherton, P.M. A healthy approach to dietary fats: Understanding the science and taking action to reduce consumer confusion. *Nutr. J.* 2017.

38.   Ryoo, J.H.; Ha, E.H.; Kim, S.G.; Ryu, S.; Lee, D.W. Apolipoprotein B is highly associated with the risk of coronary heart disease as estimated by the framingham risk score in healthy Korean men. *J. Korean Med. Sci.* **2011**, doi:10.3346/jkms.2011.26.5.631.

39.   Hodson, L.; Skeaff, C.M.; Chisholm, W.A.H. The effect of replacing dietary saturated fat with polyunsaturated or monounsaturated fat on plasma lipids in free-living young adults. *Eur. J. Clin. Nutr.* **2001**, doi:10.1038/sj.ejcn.1601234.

40.   Le Révérend, B.J.D.; Norton, I.T.; Cox, P.W.; Spyropoulos, F. Colloidal aspects of eating. *Curr. Opin. Colloid Interface Sci.* 2010.

41.   Ghosh, S.; Rousseau, D. Fat crystals and water-in-oil emulsion stability. *Curr. Opin. Colloid Interface Sci.* 2011.

42. Rousseau, D. Fat crystals and emulsion stability - A review. *Food Res. Int.* 2000.

43. Rousseau, D.; Hodge, S.M. Stabilization of water-in-oil emulsions with continuous phase crystals. *Colloids Surfaces A Physicochem. Eng. Asp.* **2005**, doi:10.1016/j.colsurfa.2005.02.035.

44. Koos, E. Capillary suspensions: Particle networks formed through the capillary force. *Curr. Opin. Colloid Interface Sci.* 2014.

45. Mustafa, W.; Pataro, G.; Ferrari, G.; Donsì, F. Novel approaches to oil structuring via the addition of high-pressure homogenized agri-food residues and water forming capillary bridges. *J. Food Eng.* **2018**, *236*, 9–18, doi:10.1016/J.JFOODENG.2018.05.003.

46. Koos, E.; Willenbacher, N. Capillary forces in suspension rheology. *Science (80-.).* **2011**, doi:10.1126/science.1199243.

47. de Vries, A.; Jansen, D.; van der Linden, E.; Scholten, E. Tuning the rheological properties of protein-based oleogels by water addition and heat treatment. *Food Hydrocoll.* **2018**, doi:10.1016/j.foodhyd.2017.11.043.

48. Koos, E.; Johannsmeier, J.; Schwebler, L.; Willenbacher, N. Tuning suspension rheology using capillary forces. *Soft Matter* **2012**, doi:10.1039/c2sm25681a.

49. Hoffmann, S.; Koos, E.; Willenbacher, N. Using capillary bridges to tune stability and flow behavior of food suspensions. *Food Hydrocoll.* **2014**, doi:10.1016/j.foodhyd.2014.01.027.

50. Calabrese, V.; Gunes, D.Z.; Farrés, I.F. Rheological control of pea fibre dispersions in oil: The role of particle and water volume fractions. *Food Hydrocoll.* **2021**, doi:10.1016/j.foodhyd.2021.106988.

51. Ferrari, G.; Mustafa, W.; Donsì, F. Use of agri-food residues for oil structuring and functionalization. *Chem. Eng. Trans.* **2017**, doi:10.3303/CET1757306.

52. Galanakis, C.M. Concluding remarks and future perspectives. In *Sustainable Recovery and Reutilization of Cereal Processing By-Products*; 2018 ISBN 9780081022146.

53. Huang, Q.; Shi, C.X.; Su, Y.B.; Liu, Z.Y.; Li, D.F.; Liu, L.; Huang, C.F.; Piao, X.S.; Lai, C.H. Prediction of the digestible and metabolizable energy content of wheat milling by-products for growing pigs from chemical composition. *Anim. Feed Sci. Technol.* **2014**, doi:10.1016/j.anifeedsci.2014.06.009.

54. Rosenfelder, P.; Eklund, M.; Mosenthin, R. Nutritive value of wheat and wheat by-products in pig nutrition: A review. *Anim. Feed Sci. Technol.* 2013.

55. Fleury, N.; Lahaye, M. Chemical and physico-chemical characterisation of fibres from Laminaria digitata (kombu breton): A physiological approach. *J. Sci. Food Agric.* **1991**, doi:10.1002/jsfa.2740550307.

Chapter V

56.   Bossler, F.; Weyrauch, L.; Schmidt, R.; Koos, E. Influence of mixing conditions on the rheological properties and structure of capillary suspensions. *Colloids Surfaces A Physicochem. Eng. Asp.* **2017**, doi:10.1016/j.colsurfa.2017.01.026.

57.   Lužaić, T.Z.; Grahovac, N.L.; Hladni, N.T.; Romanić, R.S. Evaluation of oxidative stability of new cold-pressed sunflower oils during acceleratethermal stability tests. *Food Sci. Technol.* **2022**, *42*, 1–8, doi:10.1590/fst.67320.

58.   Damodaran, S.; Paraf, A. *Food proteins and their applications*; 2017; ISBN 9781351447539.

59.   Begum, H.A.; Tanni, T.R.; Shahid, M.A. Analysis of Water Absorption of Different Natural Fibers. *J. Text. Sci. Technol.* **2021**, doi:10.4236/jtst.2021.74013.

60.   Grigelmo-Miguel, N.; Martín-Belloso, O. Characterization of dietary fiber from orange juice extraction. *Food Res. Int.* **1999**, doi:10.1016/S0963-9969(98)00087-8.

61.   Elleuch, M.; Bedigian, D.; Roiseux, O.; Besbes, S.; Blecker, C.; Attia, H. Dietary fibre and fibre-rich by-products of food processing: Characterisation, technological functionality and commercial applications: A review. *Food Chem.* 2011.

62.   Huang, L.; Liu, J.; Addy, M.; Ding, B.; Cheng, Y.; Peng, P.; Wang, Y.; Liu, Y.; Chen, P.; Ruan, R. Physicochemical and emulsifying properties of orange fibers stabilized oil-in-water emulsions. *LWT* **2020**, doi:10.1016/j.lwt.2020.110054.

63.   Chen, J.; Gao, D.; Yang, L.; Gao, Y. Effect of microfluidization process on the functional properties of insoluble dietary fiber. *Food Res. Int.* **2013**, doi:10.1016/j.foodres.2013.09.025.

64.   Chau, C.F.; Wang, Y.T.; Wen, Y.L. Different micronization methods significantly improve the functionality of carrot insoluble fibre. *Food Chem.* **2007**, doi:10.1016/j.foodchem.2005.11.034.

65.   Mewis, J.; Wagner, N.J. *Colloidal suspension rheology*; 2011; ISBN 9780511977978.

66.   Su, D.; Zhu, X.; Wang, Y.; Li, D.; Wang, L. Effects of high-pressure homogenization on physical and thermal properties of citrus fiber. *LWT* **2019**, doi:10.1016/j.lwt.2019.108573.

67.   Ulbrich, M.; Flöter, E. Impact of high pressure homogenization modification of a cellulose based fiber product on water binding properties. *Food Hydrocoll.* **2014**, doi:10.1016/j.foodhyd.2014.04.020.

68.   Wang, L.F.; Shankar, S.; Rhim, J.W. Properties of alginate-based films reinforced with cellulose fibers and cellulose nanowhiskers isolated from mulberry pulp. *Food Hydrocoll.* **2017**, doi:10.1016/j.foodhyd.2016.08.041.

69.   UNEP *Food Waste Index Report 2021*; 2021; ISBN 9789280738513.

70. Assembly U.G Transforming Our World: The 2030 Agenda for Sustainable Development. In *A New Era in Global Health*; 2018.

71. Leyva-López, N.; Lizárraga-Velázquez, C.E.; Hernández, C.; Sánchez-Gutiérrez, E.Y. Exploitation of agro-industrial waste as potential source of bioactive compounds for aquaculture. *Foods* 2020.

72. Espinosa, E.; Rincón, E.; Morcillo-Martín, R.; Rabasco-Vílchez, L.; Rodríguez, A. Orange peel waste biorefinery in multi-component cascade approach: Polyphenolic compounds and nanocellulose for food packaging. *Ind. Crops Prod.* **2022**, *187*, doi:10.1016/j.indcrop.2022.115413.

73. Rincón, E.; Espinosa, E.; García-Domínguez, M.T.; Balu, A.M.; Vilaplana, F.; Serrano, L.; Jiménez-Quero, A. Bioactive pectic polysaccharides from bay tree pruning waste: Sequential subcritical water extraction and application in active food packaging. *Carbohydr. Polym.* **2021**, *272*, doi:10.1016/j.carbpol.2021.118477.

74. Ayala-Zavala, J.F.; Vega-Vega, V.; Rosas-Domínguez, C.; Palafox-Carlos, H.; Villa-Rodriguez, J.A.; Siddiqui, M.W.; Dávila-Aviña, J.E.; González-Aguilar, G.A. Agro-industrial potential of exotic fruit byproducts as a source of food additives. *Food Res. Int.* 2011.

75. Pirozzi, A.; Ferrari, G.; Donsì, F. Cellulose Isolation from Tomato Pomace Pretreated by High-Pressure Homogenization. *Foods* **2022**, doi:10.3390/foods11030266.

76. Sánchez, Ó.J.; Cardona, C.A. Trends in biotechnological production of fuel ethanol from different feedstocks. *Bioresour. Technol.* 2008.

77. Yang, Z.; Xu, S.; Ma, X.; Wang, S. Characterization and acetylation behavior of bamboo pulp. *Wood Sci. Technol.* **2008**, doi:10.1007/s00226-008-0194-5.

78. Ragauskas, A.J.; Williams, C.K.; Davison, B.H.; Britovsek, G.; Cairney, J.; Eckert, C.A.; Frederick, W.J.; Hallett, J.P.; Leak, D.J.; Liotta, C.L.; et al. The path forward for biofuels and biomaterials. *Science (80-.).* 2006.

79. McKendry, P. Energy production from biomass (part 1): Overview of biomass. *Bioresour. Technol.* **2002**, doi:10.1016/S0960-8524(01)00118-3.

80. Das, A.M.; Hazarika, M.P.; Goswami, M.; Yadav, A.; Khound, P. Extraction of cellulose from agricultural waste using Montmorillonite K-10/LiOH and its conversion to renewable energy: Biofuel by using Myrothecium gramineum. *Carbohydr. Polym.* **2016**, doi:10.1016/j.carbpol.2015.12.070.

81. Habibi, Y.; Lucia, L.A.; Rojas, O.J. Cellulose nanocrystals: Chemistry, self-assembly, and applications. *Chem. Rev.* **2010**, doi:10.1021/cr900339w.

82. Saba, N.; Jawaid, M. Recent advances in nanocellulose-based polymer nanocomposites. In *Cellulose-Reinforced Nanofibre Composites: Production, Properties and Applications*; 2017 ISBN 9780081009659.

83. Dufresne, A. Nanocellulose: A new ageless bionanomaterial. *Mater. Today* 2013.

84. Feng, J.; Nguyen, S.T.; Fan, Z.; Duong, H.M. Advanced fabrication and oil absorption properties of super-hydrophobic recycled cellulose aerogels. *Chem. Eng. J.* **2015**, *270*, 168–175, doi:10.1016/j.cej.2015.02.034.

85. Morcillo-Martín, R.; Espinosa, E.; Rabasco-Vílchez, L.; Sanchez, L.M.; de Haro, J.; Rodríguez, A. Cellulose Nanofiber-Based Aerogels from Wheat Straw: Influence of Surface Load and Lignin Content on Their Properties and Dye Removal Capacity. *Biomolecules* **2022**, doi:10.3390/biom12020232.

86. Carpenter, A.W.; De Lannoy, C.F.; Wiesner, M.R. Cellulose nanomaterials in water treatment technologies. *Environ. Sci. Technol.* **2015**, *49*, 5277–5287, doi:10.1021/es506351r.

87. Rafatullah, M.; Sulaiman, O.; Hashim, R.; Ahmad, A. Adsorption of methylene blue on low-cost adsorbents: A review. *J. Hazard. Mater.* **2010**, *177*, 70–80, doi:10.1016/j.jhazmat.2009.12.047.

88. Chcn, G.; Pan, J.; Han, B.; Yan, H. Adsorption of methylene blue on montmorillonite. *J. Dispers. Sci. Technol.* **1999**, *20*, 1179–1187, doi:10.1080/01932699908943843.

89. Tan, I.A.W.; Ahmad, A.L.; Hameed, B.H. Adsorption of basic dye on high-surface-area activated carbon prepared from coconut husk: Equilibrium, kinetic and thermodynamic studies. *J. Hazard. Mater.* **2008**, *154*, 337–346, doi:10.1016/j.jhazmat.2007.10.031.

90. Tan, I.A.W.; Ahmad, A.L.; Hameed, B.H. Adsorption of basic dye using activated carbon prepared from oil palm shell: batch and fixed bed studies. *Desalination* **2008**, *225*, 13–28, doi:10.1016/j.desal.2007.07.005.

91. Hasanpour, M.; Hatami, M. Photocatalytic performance of aerogels for organic dyes removal from wastewaters: Review study. *J. Mol. Liq.* **2020**, *309*, 113094, doi:10.1016/j.molliq.2020.113094.

92. Kadhim, R.J.; Al-Ani, F.H.; Al-Shaeli, M.; Alsalhy, Q.F.; Figoli, A. Removal of dyes using graphene oxide (Go) mixed matrix membranes. *Membranes (Basel).* **2020**, *10*, 1–24, doi:10.3390/membranes10120366.

93. Shi, B.; Li, G.; Wang, D.; Feng, C.; Tang, H. Removal of direct dyes by coagulation: The performance of preformed polymeric aluminum species. *J. Hazard. Mater.* **2007**, *143*, 567–574, doi:10.1016/j.jhazmat.2006.09.076.

94. Rehman, F.; Sayed, M.; Khan, J.A.; Khan, H.M. Removal of crystal violet dye from aqueous solution by gamma irradiation. *J. Chil. Chem. Soc.* **2017**, *62*, 3359–3364, doi:10.4067/S0717-97072017000100011.

95. Suzuki, N.; Okazaki, A.; Takagi, K.; Serizawa, I.; Hirami, Y.; Noguchi, H.; Pitchaimuthu, S.; Terashima, C.; Suzuki, T.; Ishida, N.; et al. Complete decomposition of sulfamethoxazole during an advanced oxidation process in a simple water treatment system. *Chemosphere* **2022**, *287*, 132029, doi:10.1016/j.chemosphere.2021.132029.

96.   Gorito, A.M.; Pesqueira, J.F.J.R.; Moreira, N.F.F.; Ribeiro, A.R.; Pereira, M.F.R.; Nunes, O.C.; Almeida, C.M.R.; Silva, A.M.T. Ozone-based water treatment (O3, O3/UV, O3/H2O2) for removal of organic micropollutants, bacteria inactivation and regrowth prevention. *J. Environ. Chem. Eng.* **2021**, *9*, 10–14, doi:10.1016/j.jece.2021.105315.

97.   Senthilkumar, S.; Perumalsamy, M.; Janardhana Prabhu, H. Decolorization potential of white-rot fungus Phanerochaete chrysosporium on synthetic dye bath effluent containing Amido black 10B. *J. Saudi Chem. Soc.* **2014**, *18*, 845–853, doi:10.1016/j.jscs.2011.10.010.

98.   Yagub, M.T.; Sen, T.K.; Afroze, S.; Ang, H.M. Dye and its removal from aqueous solution by adsorption: A review. *Adv. Colloid Interface Sci.* **2014**, *209*, 172–184, doi:10.1016/j.cis.2014.04.002.

99.   Jain, A.K.; Gupta, V.K.; Bhatnagar, A.; Suhas Utilization of industrial waste products as adsorbents for the removal of dyes. *J. Hazard. Mater.* **2003**, *101*, 31–42, doi:10.1016/S0304-3894(03)00146-8.

100.   Ma, M.; Chen, Y.; Zhao, X.; Tan, F.; Wang, Y.; Cao, Y.; Cai, W. Effective removal of cation dyes from aqueous solution using robust cellulose sponge. *J. Saudi Chem. Soc.* **2020**, *24*, 915–924, doi:10.1016/j.jscs.2020.09.008.

101.   Li, P.; Yang, C.; Xu, X.; Miao, C.; He, T.; Jiang, B.; Wu, W. Preparation of Bio-Based Aerogel and Its Adsorption Properties for Organic Dyes. *Gels* **2022**, *8*, 755.

102.   Liu, R.L.; Liu, Y.; Zhou, X.Y.; Zhang, Z.Q.; Zhang, J.; Dang, F.Q. Biomass-derived highly porous functional carbon fabricated by using a free-standing template for efficient removal of methylene blue. *Bioresour. Technol.* **2014**, *154*, 138–147, doi:10.1016/j.biortech.2013.12.034.

103.   Chen, Y.; Zhang, L.; Yang, Y.; Pang, B.; Xu, W.; Duan, G.; Jiang, S.; Zhang, K. Recent Progress on Nanocellulose Aerogels: Preparation, Modification, Composite Fabrication, Applications. *Adv. Mater.* **2021**, *33*, doi:10.1002/adma.202005569.

104.   Sehaqui, H.; Zhou, Q.; Berglund, L.A. High-porosity aerogels of high specific surface area prepared from nanofibrillated cellulose (NFC). *Compos. Sci. Technol.* **2011**, *71*, 1593–1599, doi:10.1016/j.compscitech.2011.07.003.

105.   Ali, Z.M.; Gibson, L.J. The structure and mechanics of nanofibrillar cellulose foams. *Soft Matter* **2013**, *9*, 1580–1588, doi:10.1039/c2sm27197d.

106.   Woignier, T.; Reynes, J.; Hafidi Alaoui, A.; Beurroies, I.; Phalippou, J. Different kinds of structure in aerogels: Relationships with the mechanical properties. *J. Non. Cryst. Solids* **1998**, *241*, 45–52, doi:10.1016/S0022-3093(98)00747-9.

107.   Sescousse, R.; Gavillon, R.; Budtova, T. Aerocellulose from cellulose-ionic liquid solutions: Preparation, properties and comparison with

cellulose-NaOH and cellulose-NMMO routes. *Carbohydr. Polym.* **2011**, *83*, 1766–1774, doi:10.1016/j.carbpol.2010.10.043.

108.   Zhao, Y. Edible coatings for extending shelf-life of fresh produce during postharvest-storage. In *Encyclopedia of Food Security and Sustainability*; 2019 ISBN 9780128126882.

109.   Al-Tayyar, N.A.; Youssef, A.M.; Al-Hindi, R.R. Edible coatings and antimicrobial nanoemulsions for enhancing shelf life and reducing foodborne pathogens of fruits and vegetables: A review. *Sustain. Mater. Technol.* 2020.

110.   Valdés, A.; Ramos, M.; Beltrán, A.; Jiménez, A.; Garrigós, M.C. State of the art of antimicrobial edible coatings for food packaging applications. *Coatings* **2017**, *7*, 1–23, doi:10.3390/coatings7040056.

111.   Maringgal, B.; Hashim, N.; Mohamed Amin Tawakkal, I.S.; Muda Mohamed, M.T. Recent advance in edible coating and its effect on fresh/fresh-cut fruits quality. *Trends Food Sci. Technol.* **2020**, *96*, 253–267, doi:10.1016/j.tifs.2019.12.024.

112.   Maria Leena, M.; Yoha, K.S.; Moses, J.A.; Anandharamakrishnan, C. Edible coating with resveratrol loaded electrospun zein nanofibers with enhanced bioaccessibility. *Food Biosci.* **2020**, doi:10.1016/j.fbio.2020.100669.

113.   Pirozzi, A.; Pataro, G.; Donsì, F.; Ferrari, G. Edible Coating and Pulsed Light to Increase the Shelf Life of Food Products. *Food Eng. Rev.* 2020.

114.   Ju, J.; Xie, Y.; Guo, Y.; Cheng, Y.; Qian, H.; Yao, W. Application of edible coating with essential oil in food preservation. *Crit. Rev. Food Sci. Nutr.* **2019**, *59*, 2467–2480, doi:10.1080/10408398.2018.1456402.

115.   Maringgal, B.; Hashim, N.; Mohamed Amin Tawakkal, I.S.; Muda Mohamed, M.T. Recent advance in edible coating and its effect on fresh/fresh-cut fruits quality. *Trends Food Sci. Technol.* **2020**, *96*, 253–267, doi:10.1016/j.tifs.2019.12.024.

116.   Thakur, R.; Pristijono, P.; Golding, J.B.; Stathopoulos, C.E.; Scarlett, C.J.; Bowyer, M.; Singh, S.P.; Vuong, Q. V. Amylose-lipid complex as a measure of variations in physical, mechanical and barrier attributes of rice starch- ι -carrageenan biodegradable edible film. *Food Packag. Shelf Life* **2017**, *14*, 108–115, doi:10.1016/j.fpsl.2017.10.002.

117.   Krochta, J.M. Edible protein films and coatings. In *Food Proteins and their Applications*; Damodaran, S., Ed.; CRC PRESS, 2019 ISBN 9780367401047.

118.   Paul, S.K. Edible Films and Coatings for Fruits and Vegetables. In *Encyclopedia of Renewable and Sustainable Materials*; 2020.

119.   U.S. FDA FOOD ADDITIVES PERMITTED FOR DIRECT ADDITION TO FOOD FOR HUMAN CONSUMPTION. *CFR - Code Fed. Regul. Title 21, Vol. 3, Part 172* 2019, 21CFR172.

120.	U.S. Food & Drug Administration Code for Federal Regulations Title 21 Part 184—Direct Food Substances Affirmed as Generally Recognized as Safe Available online: https://www.accessdata.fda.gov/scripts/cdrh/cfdocs/cfcfr/CFRSearch.cfm?fr =184.1724.

121.	Donsì, F.; Ferrari, G. Essential oil nanoemulsions as antimicrobial agents in food. *J. Biotechnol.* **2016**, *233*, 106–120, doi:10.1016/j.jbiotec.2016.07.005.

122.	Fathi, M.; Vinceković, M.; Jurić, S.; Viskić, M.; Režek Jambrak, A.; Donsì, F. Food-Grade Colloidal Systems for the Delivery of Essential Oils. *Food Rev. Int.* 2019.

123.	Das, S.; Vishakha, K.; Banerjee, S.; Mondal, S.; Ganguli, A. Sodium alginate-based edible coating containing nanoemulsion of Citrus sinensis essential oil eradicates planktonic and sessile cells of food-borne pathogens and increased quality attributes of tomatoes. *Int. J. Biol. Macromol.* **2020**, doi:10.1016/j.ijbiomac.2020.08.086.

124.	Memar, M.Y.; Raei, P.; Alizadeh, N.; Aghdam, M.A.; Kafil, H.S. Carvacrol and thymol: Strong antimicrobial agents against resistant isolates. *Rev. Med. Microbiol.* **2017**, *28*, 63–68, doi:10.1097/MRM.0000000000000100.

125.	Jafarzadeh, S.; Mohammadi Nafchi, A.; Salehabadi, A.; Oladzad-abbasabadi, N.; Jafari, S.M. Application of bio-nanocomposite films and edible coatings for extending the shelf life of fresh fruits and vegetables. *Adv. Colloid Interface Sci.* 2021.

126.	Ribes, S.; Fuentes, A.; Talens, P.; Barat, J.M.; Ferrari, G.; Donsì, F. Influence of emulsifier type on the antifungal activity of cinnamon leaf, lemon and bergamot oil nanoemulsions against Aspergillus niger. *Food Control* **2017**, *73*, 784–795, doi:10.1016/J.FOODCONT.2016.09.044.

127.	Hamedi, H.; Kargozari, M.; Shotorbani, P.M.; Mogadam, N.B.; Fahimdanesh, M. A novel bioactive edible coating based on sodium alginate and galbanum gum incorporated with essential oil of Ziziphora persica: The antioxidant and antimicrobial activity, and application in food model. *Food Hydrocoll.* **2017**, doi:10.1016/j.foodhyd.2017.05.014.

128.	Rangel-Marrónab, L.; Mani-Lópeza, E.; Paloua, E.; López-Malo, A. Effects of alginate-glycerol-citric acid concentrations on selected physical, mechanical, and barrier properties of papaya puree-based edible films and coatings, as evaluated by response surface methodology. *LWT* **2019**, *101*, 83–91, doi:https://doi.org/10.1016/j.lwt.2018.11.005.

129.	Medina-Jaramillo, C.; Quintero-Pimiento, C.; Gómez-Hoyos, C.; Zuluaga-Gallego, R.; López-Córdoba, A. Alginate-edible coatings for application on wild andean blueberries (Vaccinium meridionale swartz): Effect of the addition of nanofibrils isolated from cocoa by-products. *Polymers (Basel).* **2020**, doi:10.3390/POLYM12040824.

Chapter V

130.   ASTM International Standard Test Methods for Water Vapor Transmission of Organic Coating Films 1996.

131.   Mali, S.; Grossmann, M.V.E.; Garcia, M.A.; Martino, M.N.; Zaritzky, N.E. Microstructural characterization of yam starch films. *Carbohydr. Polym.* **2002**, *50*, 379–386, doi:10.1016/S0144-8617(02)00058-9.

132.   ASTM International Standard Test Method for Tensile Properties of Thin Plastic Sheeting 2012.

133.   ASTM International Standard Practice for Cutting Film and Sheeting Test Specimens 2009.

134.   Kwok, D.Y.; Neumann, A.W. *Contact angle measurement and contact angle interpretation*; 1999; Vol. 81; ISBN 1416978127.

135.   Pereda, M.; Dufresne, A.; Aranguren, M.I.; Marcovich, N.E. Polyelectrolyte films based on chitosan/olive oil and reinforced with cellulose nanocrystals. *Carbohydr. Polym.* **2014**, *101*, 1018–1026, doi:10.1016/j.carbpol.2013.10.046.

136.   Kokoszka, S.; Debeaufort, F.; Lenart, A.; Voilley, A. Water vapor permeability, thermal and wetting properties of whey protein isolate based edible films. *Int. Dairy J.* **2010**, *20*, 53–60, doi:10.1016/j.idairyj.2009.07.008.

137.   Bertuzzi, M.A.; Castro Vidaurre, E.F.; Armada, M.; Gottifredi, J.C. Water vapor permeability of edible starch based films. *J. Food Eng.* **2007**, *80*, 972–978, doi:10.1016/j.jfoodeng.2006.07.016.

138.   Xu, Y.; Chu, Y.; Feng, X.; Gao, C.; Wu, D.; Cheng, W.; Meng, L.; Zhang, Y.; Tang, X. Effects of zein stabilized clove essential oil Pickering emulsion on the structure and properties of chitosan-based edible films. *Int. J. Biol. Macromol.* **2020**, *156*, 111–119, doi:10.1016/j.ijbiomac.2020.04.027.

139.   Hou, L.; Wu, P. Exploring the hydrogen-bond structures in sodium alginate through two-dimensional correlation infrared spectroscopy. *Carbohydr. Polym.* **2019**, *205*, 420–426, doi:10.1016/j.carbpol.2018.10.091.

140.   Benavides, S.; Villalobos-Carvajal, R.; Reyes, J.E. Physical, mechanical and antibacterial properties of alginate film: Effect of the crosslinking degree and oregano essential oil concentration. *J. Food Eng.* **2012**, *110*, 232–239, doi:10.1016/j.jfoodeng.2011.05.023.

141.   Siracusa, V.; Romani, S.; Gigli, M.; Mannozzi, C.; Cecchini, J.P.; Tylewicz, U.; Lotti, N. Characterization of active edible films based on citral essential oil, alginate and pectin. *Materials (Basel).* **2018**, *11*, doi:10.3390/ma11101980.

142.   Wang, X.; Sun, X.; Liu, H.; Li, M.; Ma, Z. Barrier and mechanical properties of carrot puree films. *Food Bioprod. Process.* **2011**, *89*, 149–156, doi:10.1016/j.fbp.2010.03.012.

143.   Bonilla, J.; Atarés, L.; Vargas, M.; Chiralt, A. Effect of essential oils and homogenization conditions on properties of chitosan-based films. *Food Hydrocoll.* **2012**, *26*, 9–16, doi:10.1016/j.foodhyd.2011.03.015.

144. Ghanbarzadeh, B.; Musavi, M.; Oromiehie, A.R.; Rezayi, K.; Razmi Rad, E.; Milani, J. Effect of plasticizing sugars on water vapor permeability, surface energy and microstructure properties of zein films. *LWT - Food Sci. Technol.* **2007**, *40*, 1191–1197, doi:10.1016/j.lwt.2006.07.008.

145. Pirozzi, A.; Grosso, V. Del; Ferrari, G.; Donsì, F. Edible coatings containing oregano essential oil nanoemulsion for improving postharvest quality and shelf life of tomatoes. *Foods* **2020**, *9*, 1605, doi:https://doi.org/10.3390/foods9111605.

146. Ybañez, M.G.; Camacho, D.H. Designing hydrophobic bacterial cellulose film composites assisted by sound waves. *RSC Adv.* **2021**, *11*, 32873–32883, doi:10.1039/d1ra02908h.

147. Wigati, L.P.; Wardana, A.A.; Tanaka, F.; Tanaka, F. Strawberry preservation using combination of yam bean starch, agarwood Aetoxylon bouya essential oil, and calcium propionate edible coating during cold storage evaluated by TOPSIS-Shannon entropy. *Prog. Org. Coatings* **2023**, *175*, 107347, doi:10.1016/j.porgcoat.2022.107347.

148. Khodaei, D.; Hamidi-Esfahani, Z. Influence of bioactive edible coatings loaded with Lactobacillus plantarum on physicochemical properties of fresh strawberries. *Postharvest Biol. Technol.* **2019**, *156*, 110944, doi:10.1016/j.postharvbio.2019.110944.

149. Azarakhsh, N.; Osman, A.; Ghazali, H.M.; Tan, C.P.; Mohd Adzahan, N. Lemongrass essential oil incorporated into alginate-based edible coating for shelf-life extension and quality retention of fresh-cut pineapple. *Postharvest Biol. Technol.* **2014**, *88*, 1–7, doi:10.1016/j.postharvbio.2013.09.004.

150. Chiang, Y.C.; Yeh, C.Y.; Weng, C.H. Carbon dioxide adsorption on porous and functionalized activated carbon fibers. *Appl. Sci.* **2019**, *9*, doi:10.3390/app9101977.

151. Streck, C.; Keenlyside, P.; Unger, M. von The Paris agreement: A new beginning. *J. Eur. Environ. Plan. Law* **2016**, *13*, 3–29, doi:10.1080/02646811.2016.1133983.

152. Allen, M.; Babiker, M.; Chen, Y.; Coninck, H. de; Connors, S.; Diemen, R. van; Pauline, O.D.; Ebi, K.L.; Engelbrecht, F.; Ferrat, M.; et al. *Global warming of 1.5°C*; 2019;

153. Mancini, V.; Verdone, N.; Trinca, A.; Vilardi, G. Economic, environmental and exergy analysis of the decarbonisation of cement production cycle. *Energy Convers. Manag.* **2022**, *260*, 115577, doi:10.1016/j.enconman.2022.115577.

154. Rashid, M.; Hussain, Q.; Khan, K.S.; Alwabel, M.I.; Ahmad, M.; Alvi, S.; Riaz, M.; Xiongyun, S.; Manaf, A.; Azeem, M.; et al. *Carbon Sequestration in Alkaline Soils*; 2019; Vol. 2; ISBN 9783540228608.

155. Font-Palma, C.; Cann, D.; Udemu, C. Review of Cryogenic Carbon Capture Innovations and Their Potential Applications. *J. Carbon Res.* **2021**, *7*, 58, doi:10.3390/c7030058.

156.   Lee, J.W.; Kim, S.; Torres Pineda, I.; Kang, Y.T. Review of nanoabsorbents for capture enhancement of CO2 and its industrial applications with design criteria. *Renew. Sustain. Energy Rev.* **2021**, *138*, 110524, doi:10.1016/j.rser.2020.110524.

157.   Oschatz, M.; Antonietti, M. A search for selectivity to enable CO2 capture with porous adsorbents. *Energy Environ. Sci.* **2018**, *11*, 57–70, doi:10.1039/c7ee02110k.

158.   Firdaus, R.M.; Desforges, A.; Rahman Mohamed, A.; Vigolo, B. Progress in adsorption capacity of nanomaterials for carbon dioxide capture: A comparative study. *J. Clean. Prod.* **2021**, *328*, 129553, doi:10.1016/j.jclepro.2021.129553.

159.   Karimi, M.; Silva, J.A.C.; Gonçalves, C.N.D.P.; Diaz De Tuesta, J.L.; Rodrigues, A.E.; Gomes, H.T. CO2 Capture in Chemically and Thermally Modified Activated Carbons Using Breakthrough Measurements: Experimental and Modeling Study. *Ind. Eng. Chem. Res.* **2018**, *57*, 11154–11166, doi:10.1021/acs.iecr.8b00953.

160.   Sreńscek-Nazzal, J.; Kiełbasa, K. Advances in modification of commercial activated carbon for enhancement of CO2 capture. *Appl. Surf. Sci.* **2019**, *494*, 137–151, doi:10.1016/j.apsusc.2019.07.108.

161.   Coromina, H.M.; Walsh, D.A.; Mokaya, R. Biomass-derived activated carbon with simultaneously enhanced CO2 uptake for both pre and post combustion capture applications. *J. Mater. Chem. A* **2015**, *4*, 280–289, doi:10.1039/c5ta09202g.

162.   Santori, G.; Charalambous, C.; Ferrari, M.C.; Brandani, S. Adsorption artificial tree for atmospheric carbon dioxide capture, purification and compression. *Energy* **2018**, *162*, 1158–1168, doi:10.1016/j.energy.2018.08.090.

163.   Bonenfant, D.; Kharoune, M.; Niquette, P.; Mimeault, M.; Hausler, R. Advances in principal factors influencing carbon dioxide adsorption on zeolites. *Sci. Technol. Adv. Mater.* **2008**, *9*, doi:10.1088/1468-6996/9/1/013007.

164.   Furukawa, H.; Cordova, K.E.; O'Keeffe, M.; Yaghi, O.M. The chemistry and applications of metal-organic frameworks. *Science (80-.).* **2013**, *341*, doi:10.1126/science.1230444.

165.   Liu, Y.; Li, L.; Li, Q.; Lin, J.; Guo, Z.; Zhang, X.; Lu, Z.; Ma, Y.; Huang, Y.; Tang, C. Fluorine doped porous boron nitride for efficient CO2 capture and separation: A DFT study. *Appl. Surf. Sci.* **2021**, *556*, 149775, doi:10.1016/j.apsusc.2021.149775.

166.   Sun, Q.; Li, Z.; Searles, D.J.; Chen, Y.; Lu, G.; Du, A. Charge-controlled switchable CO2 capture on boron nitride nanomaterials. *J. Am. Chem. Soc.* **2013**, *135*, 8246–8253, doi:10.1021/ja400243r.

167.   Maurya, M.; Sappidi, P.K.; Singh, J.K. Selective Separation of CO2from Flue Gas Using Carbon and Boron Nitride Nanotubes as a

Membrane. *Energy and Fuels* **2020**, *34*, 7223–7231, doi:10.1021/acs.energyfuels.0c00311.

168.   Tian, L.; Liang, F.; Dong, L.; Li, J.; Jia, Q.; Zhang, H.; Yan, S.; Zhang, S. Preparation and enhanced adsorption properties for CO2 and dyes of amino-decorated hierarchical porous BCN aerogels. *J. Am. Ceram. Soc.* **2021**, *104*, 1110–1119, doi:10.1111/jace.17501.

169.   Morales-García, Á.; Fernández-Fernández, A.; Viñes, F.; Illas, F. CO2 abatement using two-dimensional MXene carbides. *J. Mater. Chem. A* **2018**, *6*, 3381–3385, doi:10.1039/c7ta11379j.

170.   Liu, F.Q.; Liu, X.; Sun, L.; Li, R.; Yin, C.X.; Wu, B. MXene-supported stable adsorbents for superior CO2capture. *J. Mater. Chem. A* **2021**, *9*, 12763–12771, doi:10.1039/d1ta01403j.

171.   Darunte, L.A.; Walton, K.S.; Sholl, D.S.; Jones, C.W. CO2 capture via adsorption in amine-functionalized sorbents. *Curr. Opin. Chem. Eng.* **2016**, *12*, 82–90, doi:10.1016/j.coche.2016.03.002.

172.   Mebane, D.S.; Kress, J.D.; Storlie, C.B.; Fauth, D.J.; Gray, M.L.; Li, K. Transport, zwitterions, and the role of water for CO2 adsorption in mesoporous silica-supported amine sorbents. *J. Phys. Chem. C* **2013**, *117*, 26617–26627, doi:10.1021/jp4076417.

173.   Didas, S.A.; Sakwa-Novak, M.A.; Foo, G.S.; Sievers, C.; Jones, C.W. Effect of amine surface coverage on the Co-adsorption of CO2 and water: Spectral deconvolution of adsorbed species. *J. Phys. Chem. Lett.* **2014**, *5*, 4194–4200, doi:10.1021/jz502032c.

174.   Pinto, M.L.; Mafra, L.; Guil, J.M.; Pires, J.; Rocha, J. Adsorption and activation of CO2 by amine-modified nanoporous materials studied by solid-state NMR and 13CO2 adsorption. *Chem. Mater.* **2011**, *23*, 1387–1395, doi:10.1021/cm1029563.

175.   Kawalerczyk, J.; Walkiewicz, J.; Dziurka, D.; Mirski, R.; Brózdowski, J. APTES-Modified Nanocellulose as the Formaldehyde Scavenger for UF Adhesive-Bonded Particleboard and Strawboard. *Polymers (Basel).* **2022**, *14*, 5037.

176.   Majdoub, M.; Essamlali, Y.; Amadine, O.; Ganetri, I.; Hafnaoui, A.; Khouloud, M.; Zahouily, M. Octadecylamine as chemical modifier for tuned hydrophobicity of surface modified cellulose : toward organophilic cellulose nanocrystals. *Cellulose* **2021**, *28*, 7717–7734, doi:10.1007/s10570-021-04044-w.

177.   Rico, D.; Koso, T. V; Kakko, T.; King, A.W.T. Crystallinity reduction and enhancement in the chemical reactivity of cellulose by non-dissolving pre-treatment with tetrabutylphosphonium acetate. **2020**, *6*, 5545–5562, doi:10.1007/s10570-020-03044-6.

178.   Neves, R.M.; Ornaghi, H.L.; Duchemin, B.; Zattera, A.J.; Amico, S.C. In-Depth Study of the Microcrystalline Cellulose Amino-Functionalization Efficiency. *Cellulose* **2021**, 1–23.

179.   Wang, X.; Zhang, Y.; Wang, S.; Jiang, H.; Liu, S.; Yao, Y.; Zhang, T.; Li, Q. Synthesis and characterization of amine-modified spherical nanocellulose aerogels. *J. Mater. Sci.* **2018**, *53*, 13304–13315, doi:10.1007/s10853-018-2595-7.

180.   Mohd, N.H.; Kargazadeh, H.; Miyamoto, M.; Uemiya, S.; Sharer, N.; Baharum, A.; Peng, T.L.; Ahmad, I.; Yarmo, M.A.; OthamanNurul, R.; et al. Aminosilanes grafted nanocrystalline cellulose from oil palm empty fruit bunch aerogel for carbon dioxide capture. *J. Mater. Res. Technol.* **2021**, *13*, 2287–2296, doi:10.1016/j.jmrt.2021.06.018.

181.   Abunowara, M.; Bustam, M.A.; Sufian, S.; Eldemerdash, U. Description of Carbon Dioxide Adsorption and Desorption onto Malaysian Coals under Subcritical Condition. *Procedia Eng.* **2016**, *148*, 600–608, doi:10.1016/j.proeng.2016.06.521.

182.   Vijayaraghavan, K.; Padmesh, T.V.N.; Palanivelu, K.; Velan, M. Biosorption of nickel(II) ions onto Sargassum wightii: Application of two-parameter and three-parameter isotherm models. *J. Hazard. Mater.* **2006**, *133*, 304–308, doi:10.1016/j.jhazmat.2005.10.016.

183.   Hameed, B.H.; Din, A.T.M.; Ahmad, A.L. Adsorption of methylene blue onto bamboo-based activated carbon: Kinetics and equilibrium studies. *J. Hazard. Mater.* **2007**, *141*, 819–825, doi:10.1016/j.jhazmat.2006.07.049.

184.   Weber, T.W.; Chakravorti, R.K. Pore and solid diffusion models for fixed-bed adsorbers. *AIChE J.* **1974**, *20*, 228–238, doi:10.1002/aic.690200204.

185.   Dada, A.O.; Olalekan, A..; Olatunya, A..; Dada, O. Langmuir, Freundlich, Temkin and Dubinin–Radushkevich Isotherms Studies of Equilibrium Sorption of Zn 2+ Unto Phosphoric Acid Modified Rice Husk. *IOSR J. Appl. Chem.* **2012**, *3*, 38–45, doi:10.9790/5736-0313845.

186.   Hutson, N.D.; Yang, R.T. Theoretical basis for the Dubinin-Radushkevitch (D-R) adsorption isotherm equation. *Adsorption* **1997**, *3*, 189–195, doi:10.1007/BF01650130.

187.   Voudrias, E.; Fytianos, K.; Bozani, E. Sorption-desorption isotherms of dyes from aqueous solutions and wastewaters with different sorbent meterials. *Glob. NEST J.* **2018**, *4*, 75–83, doi:10.30955/gnj.000233.

188.   Ishikawa, T.; Cai, W.Y.; Kandori, K. Characterization of the thermal decomposition products of δ-FeOOH by Fourier-transform infrared spectroscopy and N2 adsorption. *J. Chem. Soc. Faraday Trans.* **1992**, *88*, 1173–1177, doi:10.1039/FT9928801173.

189.   Bagheri, S.; Aghaei, H.; Ghaedi, M.; Asfaram, A.; Monajemi, M.; Bazrafshan, A.A. Synthesis of nanocomposites of iron oxide/gold (Fe3O4/Au) loaded on activated carbon and their application in water treatment by using sonochemistry: Optimization study. *Ultrason. Sonochem.* **2018**, *41*, 279–287, doi:10.1016/j.ultsonch.2017.09.031.

Chapter VI
# General conclusions and future perspectives

Large amounts of organic waste are generated in the agro-industrial processing cycle. The management of this waste, called AFRs, creates major costs, including both properly disposing of it and reducing the environmental impact. The circular bioeconomy initiative offers a clear perspective on food waste handling for minimizing environmental impact. Moreover, AFRs from processing industries can be a significant source of bioactive compounds that can be further exploited in the food additive, pharmaceutical, or cosmetics industries. The extraction of bioactive compounds from organic residues through conventional solid/liquid extraction methods is well documented, and despite their financial, environmental, and toxicity limitations, they are widely used because they can provide significant extraction yields. According to the findings of this thesis, the use of advanced extraction methods, i.e. HPH nonthermal process, has achieved considerable increase in phenolic yield with high antioxidant capacity and decrease in processing time without the usage of solvents, with remarkable economic and environmental consequences. AFRs could, therefore, represent a useful feedstock to establish a more sustainable global society through a biorefinery approach. In this scenario, the comprehensive utilization of these feedstocks has attracted considerable interest also for the isolation and recovery of cellulose. Extensive research in this thesis has been reported for biomass valorization, carried out through the combination of HPH and mild chemical hydrolysis. The presented results show the effectiveness of HPH as pre-treatment technique for cellulose recovery owing to its potential to enhance the accessibility of lignocellulosic biomass through fluido-mechanical stresses and cell wall disruption. Following these findings, it is possible to highlight the easier applicability of HPH-based methods that may represent the solution of choice for the efficient assisted extraction of bioactive compounds as well as a pre-treatment for mild chemical hydrolysis toward cellulose recovery.

Chapter VI

Moreover, the choice of the cellulose isolation methodology through non-conventional mild chemical hydrolysis is dictated not only by consideration of the advantages for cellulose yield, but also by the improved physico-chemical characteristics of the cellulosic materials that can extracted, which can be easily tuned for different advanced applications. Overall, the approach used enabled to reach remarkable yields (> 22%) of extraordinary high-quality grade cellulose, as demonstrated by spectroscopic and morphological analyses. Furthermore, despite it was demonstrated that top-down approaches for cellulose isolation from low-cost wastes can be successfully carried out, the biosynthesis of bacterial cellulose through bottom-up approaches was also investigated in culture media based on black tea and micronized AFRs as a substitute for sucrose source. The obtained results demonstrated that AFRs-based bacterial cellulose exhibited similar structure compared to bacterial cellulose grown with sucrose source, with outstanding antioxidant capacity in the film due to the incorporation of bioactive molecules from the AFRs culture broth in the matrix. Additionally, it represented a promising result which can bring down the cost of bacterial cellulose production.

Cellulose in nanostructured form (nanocellulose, NCs) is of considerable interest for several outstanding useful features such as high surface area, tailorability of surface chemistry, better mechanical characteristics, and anisotropic shape, among others. Extensive efforts have been devoted during this thesis to the cost-effective production of NCs from pure cellulose and from AFRs isolated cellulose, through chemical or mechanical processes, and their combination. To address the biocompatibility together with achieving the mechanical performances, the key issue was to investigate the effect of different treatment and processing conditions and define a cascade of operation according to the end-product application. Herein, NCs has extensively been used as green nanofiller for improving and modifying the varieties of advanced products, such as Pickering emulsion, oleocolloids, composite polymers, and aerogel-based material with high adsorption capacity.

In summary, this research provided the following outcomes:
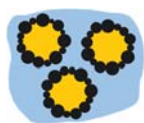
A complete and exhaustive study was reported for the production of Pickering emulsions stabilized with NCs, in form of nanocrystals and nanofibers, with good stability against external environmental stimuli, i.e. pH, temperature and NaCl.
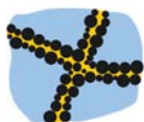
A novel approach for oil structuring was based on direct processing via HPH of oil suspension of lignocellulosic particles, such as wheat middlings, and subsequent addition of water to form a 3D network stabilized by interparticle capillary forces. This approach

344

offers many advantages in comparison with more conventional approaches based on oleogelation, namely: (i) a facile and versatile process, based only on physical processing, without the addition of undesired ingredients to the formulation (e.g. gelators); (ii) the replacement of part of the oil with the fibrous material and water, hence reducing the caloric intake, while ensuring the desired mouthfeel, as the oil will still constitute the continuous phase; (iii) the delivery of bioactive molecules, associated with the fibours particles, when obtained from agri-food residues or other biomass, still rich in valuable compounds, with an antioxidant effect on the oil and expected health-beneficial effects also on consumers; and (iv) the high transferability of the proposed approach, enabling to tune color, flavor, and taste of the structured oil, depending on the desired application.
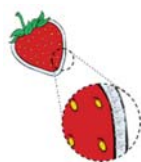
A feasibility study was carried out for the production of NCs-based edible films incorporated with essential oil or emulsions as sustainable food packaging systems with antioxidant/antimicrobial properties to prevent the oxidative deterioration of strawberries. The antimicrobial properties of the edible films were significantly enhanced when essential oil was incorporated, and the bacteriostatic effect of films depended mainly on the form of emulsion.

The suitability of NCs-based aerogels was assessed for applications in the areas of adsorption, due to the environmentally-friendly renewability, biocompatibility, and biodegradability of cellulose, as well as due to the excellent properties of NCs aerogels such as low density, high porosity, and a high specific surface area. Herein it was demonstrated the cationic dye adsorption efficiency of the NCs-based aerogel is higher than 80% and therefore can be considered promising adsorbent for the treatment of dye wastewater.

Advances in amine-functionalized cellulose nanomaterials for CO_2 capture was reported. Surface modification of NCs gave rise to a change of the predominant surface functional groups. An increase in the amount of chemisorbed on NCs has been achieved with the introduction of polar nitrogen functionalities. The amine-modified NCs-based aerogel was successfully

prepared by freeze-drying. The existence of basic nitrogen-containing functionalities was thought to lead to higher CO_2 uptakes; however, there was no explicit relationship between them. Despite this, the adsorption of CO_2 still confirmed that in this study, the influence of high porosity functionalized aerogels on CO_2 adsorption was prevailing.

Additional studies are still ongoing to investigate the effect of NCs on others innovative applications, such as food packaging and paper products. Further research activities need to be conducted to fill current gaps through the practical transition from laboratory scale to industrial or commercial production and achieve the feasibility of the final advanced materials and introduce them in the market, in particular, (i) application of life cycle assessment to the environmental aspects of NCs isolation from AFRs and NCs-based materials; (ii) elucidate the role and interaction between the proposed cascade isolation routes and the processed biomass, with the purpose of developing a technological platform to give value to disparate AFRs sources, thus increasing the availability of high-added molecules; and (iii) focus the research on the effects on the new food product quality with the addition of NCs-based Pickering emulsions or oleocolloids, in terms of the texture in food systems, in vitro digestion, microbial stability, and organoleptic and sensorial properties. Despite the above-mentioned challenges, NCs-based materials will certainly improve people's quality of life in the future through the development of the next generation of materials. Furthermore, the approach and the results achieved in the frame of this thesis work hopefully will represent a useful basis for opening up new scenarios in the frame of biorefinery processing, bearing in mind the "sustainability" concept to be fulfilled.